UNIVERSITÉ DE STRASBOURG

ÉCOLE DOCTORALE 222
[UMR 7515]

THÈSE présentée par :

[Taylan KARAKOÇ]

soutenue le : **11 octobre 2024**

pour obtenir le grade de : **Docteur de l'Université de Strasbourg**
Discipline/Spécialité : Chimie/Chimie-Physique

Elaboration de matériaux composites oxyde inorganique / carbone pour optimiser leurs performances électrochimiques dans les dispositifs de stockage d'énergie

-

Structural design of inorganic transition metal oxide / carbon composite materials for optimizing their electrochemical performance in energy storage devices

THÈSE dirigée par :	
[M. PRONKIN Sergey]	MCF, Université de Strasbourg
Codirecteur de thèse :	
[M. BEGIN Dominique]	DR, ICPEES CNRS
RAPPORTEURS :	
[M. DOERT Thomas]	Prof., Faculté de chimie et chimie alimentaire, TU Dresden, Allemagne
[Mme ROTH Christina]	Prof., Fakultät für Ingenieurwissenschaften, Universität Bayreuth, Allemagne

---

AUTRES MEMBRES DU JURY :	
[Mme GHIMBEU Camelia]	DR, IS2M (UMR-7361), CNRS-UHA
[M. FLEISCHMANN Simon]	DR, Helmholtz Institut Ulm, Karlsruhe Institut de Technolgie (KIT), Allemagne

Rîya dirêj bi gavên biçûk dest pê dike

Bi dinyê bişêwire, bi aqlê xwe bike

Her dar siyê ji koka xwe re nake

Her giha li ser koka xwe şîn dibe

Çiyayê bilind bê berf û bê rê nabin

Çiyayê bê gul weke mirovê bê dil

Kevir giran e di cihê xwe de

Rê rîya mirinê be jî tu her li pêş be

Rîya azadiyê, bi xwîna hevî rohnî dibe

Tirs berê mirinê nagirê

Xwîn bi xwînê nayê şûştin

Remerciements

Il est désormais temps de remercier les personnes qui m'ont donné l'opportunité de réaliser tout ce que j'ai pu entreprendre. Sergey et Dominique, comment vous remercier pour m'avoir donné cette chance. Vous êtes ceux qui m'ont permis d'être doctorant au sein de l'ICPEES. Merci pour tout. Dominique, je suis sans doute l'un de tes derniers doctorants tandis que pour toi Sergey j'ai pu être le premier à être sous ta direction. Quel hasard en y pensant. Dominique, je voulais te remercie sincèrement pour chacun de tes conseils, avis et aides que tu as pu m'apporter pendant mes premières années de recherche. Cette dernière année (et demi), on t'avait annoncé une mauvaise nouvelle mais tu as réussi à te battre et à persévérer tout en restant toi-même. J'espère que tu savoureras pleinement de ta retraite tant mérité avec toute ta santé. Merci pour tout Dom'. On entend souvent que la thèse est une partie de souffrance de la part de beaucoup de doctorants pour diverses raisons. Si tout s'est *bien* passé dans mon cas, je pense que c'est principalement grâce à toi Sergey. Tu n'as pas seulement été un superviseur mais bien plus que cela. Tu as été un professeur, un coach, un collègue, un camarade, un ami mais également un mentor. Tu m'as toujours encouragé et félicité dans tout ce que j'ai fait et pour ça, je t'en suis infiniment reconnaissant. Tu m'as toujours fait confiance quand j'avais une idée et su me donner confiance en moi. J'ai vraiment pu passer de très bons moments à tes côtés. Je souhaite à chaque futur doctorant d'avoir un superviseur comme toi. Tout cela n'aura pas été possible sans. J'espère toujours te revoir à l'avenir et pourquoi pas devenir collègue un jour. Qui sait de quoi l'avenir est fait ? J'aime à croire que cela fait le charme de la vie !

En ce qui concerne ce projet, je remercie tous les partenaires qui ont pu participer à sa création, son bon déroulement et à son aboutissement. Outre Sergey et Dominique, je tiens à remercier Sylvie ainsi que ses doctorants Théo et Joana qui ont pu me permettre de synthétiser et de caractériser bon nombre de nanoparticules d'oxyde de fer de par leur méthode. Merci à Sandrine ainsi qu'à Asma pour leur apport dans l'élaboration d'autres matériaux carbonés que sont les aérogels de carbones qui fut une découverte pour moi. Je remercie également dans les acteurs présents de l'ICCF, Katia, Malika, Régis et Batiste pour leur immense aide quant au développement approfondi des mes matériaux via fluoration et tests électrochimiques pour les applications en batterie lithium-ion.

Mon équipe a également été une part qui m'a permis de me développer en tant que chercheur en science électrochimique de par leur divers expertises dans ce domaine. Je remercie également les stagiaires et doctorants de cette équipe avec lesquels j'ai pu me développer personnellement et professionnellement.

Mes plus grands remerciements vont à ma famille et mes deux frères. Vous avez toujours été là pour moi, soutenu et accompagné dans ma vie, dans tous les moments. Deniz et Seyon, vous êtes ma fierté. Je suis fier d’avoir des frères tels que vous dans ma vie. A la vie comme à la mort, on sera toujours ensemble. Sans vous, je n’y serai sans doute jamais arriver. Je vous dédie aussi cette thèse. Elle est aussi pour mon peuple kurde, ma communauté pour qui je me battrai sans relâche et êtes ma fierté. Je n’oublierai jamais d’où je viens.

Ma famille, ailem, malbata min… Bu doktora ve her yaptığım şeyi size adıyorum. Hep yanımda oldunuz, 25 sene boyunca ve bu yaptığım tez sizin için de. Bakır ve Karakoç ailelerinde yeni bir doktor var artık.

Dayê, her tist ji bo te ye û bê te jîyan nabe… Tu gûla dilê min î û ez pir bextewar im ku keseke wekî te dayika min e. Ez ji te pir hez dikim! Ji bo her tiştê ku te bo min kiriye, ez te pir spas dikim. Ev tez ya te ye! Tu cana min î.

Je dédie cette thèse à toutes les personnes de l’immigration, à tous ceux qui comme moi sont des enfants d’immigrés, issues d’une basse classe sociale et ont grandi dans ces quartiers pauvres ont l’on nous a tous attroupés. Cette thèse, ce diplôme qui est censé être le plus haut pouvant être délivré, je l’ai fait pour nous. Ne baissez jamais les bras, accrochez-vous, poursuivez vos ambitions car on peut le faire. Vous n’êtes pas seuls dans ce combat, ne laissez jamais le racisme et la discrimination vaincre. On est plus fort que ça. Ceux qui comme moi sont originaires du Moyen-Orient et même ceux qui viennent d’Afrique, d’Asie, nous n’avons jamais été vraiment acceptés et nous nous sommes toujours battus pour montrer, prouver que l’on était comme les autres et que nous sommes chez nous. Notre combat ne s’arrêtera jamais et continuera toujours à le mener car c’est le nôtre. Vous pensiez pouvoir m’enfermer dans ces HLM depuis mon enfance et m’y voir, nous y voir rester ? Ma famille, mes proches et moi, on s’est battu et on sortira tous de là. Moi qui, comme beaucoup, rien ne nous destinait à faire des études mais rien n’est impossible.

Sonunda bu doktora, bu diploma asil bir amaca hizmet edecek mi? Fon bulmak, bencilce tanınma arzusuyla bilimsel araştırma yapmak, kapitalist hırsla ürün geliştirmek ya da her neyse... Sevdiklerime, halkıma, yoksula, haksıza, zulme uğrayana, dünyamıza yardım etmenin bir yolunu içtenlikle bulabilecek miyim? Bu soruyu sorduğuma göre, düşüncelerimin verdiği cevap hayır diye belirtileniyor. Bu işin içinde anlam göreceğim buydu işte. Bunca insanlar ölürken ben kendi bencil keyfime nasıl bakabilirim, namusumu bunda nasıl bulabilirim. Hayatıma bu gereksiz anlamı vermem de veremem. Yârdim ihtiyaç istenler yardım edemeyeceksem, mutsuza mutluluk getiremezsem, gönlü ve ruhu kafesin içinde yatan birine özgürlük yolunu gösteremezsem ve kendimi bu sözlerime rağmen kaybedersem, o zaman kahrolayım!

Ez nikarim dev jê berdim, divê ez berdewam bikim, pêş de herim. Ev dinya bi qasî zalim e ku jî xweş e. Lêbelê, divê ew ji bo her kesî bibiriqe, ferq nake em kî ne û ji ku ne. Ji ber vê yekê gerek e ku şer bikim. Bê tirs, bê şerm û bê xem. Eger rojekê ez soza xwe bixapînim, bila ez bê namûs bimirim. Mirin û jiyan di destê hev de ne. Ax jiyana me, ax dinya me, ax gelê me. Ewrî, baranî, bayî û tarî, roj dê her li wir be. Bihar bê zivistan nabe û azadî bê berxwedan nabe. Loma ez nahêlim.

Ax, 2020,

Delawer Omar

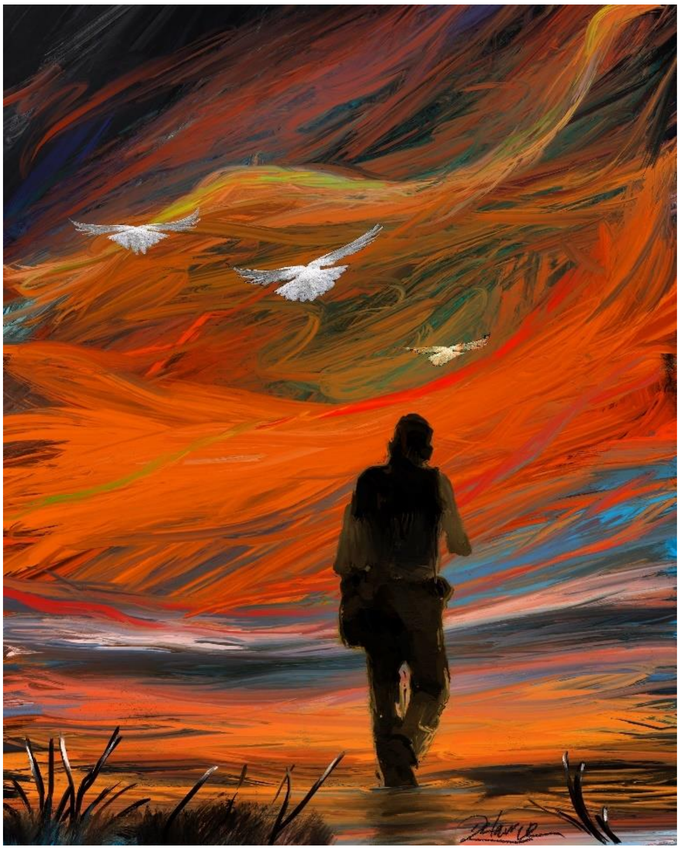

Rê, 2020,

Delawer Omar

Structural design of inorganic transition metal oxide / carbon composite materials for optimizing their electrochemical performance in energy storage devices

Abbreviations list

%	percentage
$(NH_4)_3Cit$	ammonium citrate tribasic
[ ]	concentration of species between the brackets
ΔG	free energy difference
°C	Celcius degree
µ	chemical potential
µF	microfarad
µL	microliter
µm	micrometer
5-HMF	5-hydroxymethylfurfural
∞	infinite
A	area
α	CPE constant
A/g	ampere per gram
$A^{\mp}$	adsorbate
AAO	anodized alumina oxide
AC	activated carbon
ACC	activated carbon synthetized with sucrose and citric acid
ACN	N-doped activated carbon
ACS	activated carbon synthetized from pure sucrose
AE	Advanced economies
AEI	anodic electrolyte interphase
Ag	silver
A_g	geometric surface area of substrate
AgCl	silver chloride
Ah/cm^3	ampere hour per cubic centimeter
Ah/g	ampere hour per gram
Al	aluminum
A_{mp}	micropore surface area
AN	acetonitrile
APS	Announced Pledges Scenario
Ar	argon

As	Arsenic
AsO_4^{3-}	arsenate
at.%	atomic percentage
ATR-FTIR	Attenuated Total Reflectance Fourier transform infrared spectroscopy
BET	Brunauer, Emmett and Teller
Bi	Bismuth
$BMIMBF_4$	1-butyl-3-methylimidazolium tetrafluoroborate
b_p	Boiling point
Br or Br_2	Bromine
$\vec{C}$	chiral vector
C_{60}	fullerene
C''	capacitive component of total impedance
C_2H_4	ethylene
Ca	calcium
$c_{A^{\mp}}$	concentration of adsorbate
CAM	conversion/alloying materials
Cd	Cadmium
$Cd(OH)_2$	Cadmium hydroxide
CDC	carbide-derived carbon
CDL	double-layer capacitance
CF_x	Carbon monofluoride
Cg	specific capacitance
CH_4	methane
Cl or Cl_2	Chlorine
cm^2	square centimeter
CND	carbon nanodot
CNF	carbon nanofiber
CNO	nano-onion
CN-PS	pseudocapacitance from nitrogen heteroatoms
CNT	carbon nanotube
Co	Cobalt
CO	carbon monoxide
CO_2	carbon dioxide
Co_3O_4	cobalt oxide spinel

Co_3O_4	cobalt spinel oxide
CoO	cobalt oxide
CPE	constant phase element
CQD	carbon quantum dot
Cs	specific surfacecapacitance
Cu	Cooper
CV	cyclic voltammetry
CVD	chemical vapor deposition
C_z	complex capacitance of the electrode
C_ϕ	pseudocapacitance
d	distance
D	diffusion coefficient
dB	decibel
DFT	density functional theory
$d_{interlayer}$	interlayer spacing
DMC	dimethyl carbonate
DME	1,2-dimethoxyethane
DMSO	dimethylsulfoxide
dp	pore diameter
e^-	electron
e.g.	exempli gratia
E_{max}	maximum operating voltage
EC	ethylene carbonate
E_{cell}	equilibrium potential or cell voltage
ECSA	electrochemical surface area
E_d	energy density
EDL	electrochemical double-layer
EDLC	electrochemical double-layer capacitance
EESD	Electrochemical energy storage device
EIS	Electrochemical impedance spectroscopy
EJ	Exajoules
EMD	Electrolytic manganese dioxide
EMDE	Emerging market and developing economies
EMF	Electromotive force

EMIM TFSI	ethyl-methylimidazolium bis(trifluormethylsulfonyl)imide
$E°$	Standard electrode potential
EPR	Electron paramagnetic resonance
EQCM	electrochemical quartz crystal microbalance
EROEI	Energy Returned on Energy Invested
EROI	Energy Return On Investment
ESOEI or $ESOI_e$	Energy Stored on Energy Invested
EU	European Union
EV	Electric vehicle
eV	electronvolt
EXAFS	extended X-ray absorption fine structure
ε_0	vacuum permittivity
ε	electrolyte’s dielectric constant
F	Faraday's constant
f	frequency
F or F_2	Fluor ; Farad
F/g	farad per gram
Fe	Iron
Fe_3O_4	iron spinel oxide, magnetite
FeF_2	iron fluoride
FLG	few-layer graphene
FWHM	full width at half maximum
g	gram
g	lateral interaction parameter
G	magnetic field
g/Ah	gram per ampere hour
g/L	gram per liter
G_v	bulk or volume free energy
Ga	Gallium
GCD	galvanostatic charge-discharge
GCPL	Galvanostatic charging with potential limitations
GO	graphene oxide
GPa	gigapascal
GQD	graphene quantum dot

H^+	Proton
H_2 or H	Hydrogen
H_2O	Water
H_2SO_4	Sulfuric acid
H_3PO_4	phosphoric acid
HCl	hydrochloric acid
HER	Hydrogen evolution reaction
HF	Hydrofluoric acid
Hg/HgO	mecury/mercury oxide
HNO_3	nitric acid
HOMO	highest occupied molecular orbital
Hz	Hertz
i	current
I or I_2	Iodine
i.e.	id est
IEA	International Energy Agency
Im(Z)	impedance imaginary component
In	Indium
IR	infrared
j	current density
K	Potassium ; Kelvin
k	constant
k_1	adsorption equilibrium constant
K_1	adsorption-to-desorption equilibrium constant
k_{-1}	desorption equilibrium constant
K_2SO_4	potassium sulfate
KBr	potassium bromide
KCl	potassium chloride
$KClO_3$	potassium chlorate
kJ/mol	Kilojoule per mole
$KMnO_4$	potassium permanganate
KOH	Potassium hydroxide
kOhm	kiloohm
Kt	kilotonne

kW/kg	kilowatt per kilogram
L	diffusion length
L	liter
l_1	average length of macropore
l_2	average length of mesopore
l_3	average length of micropore
L_a	average size of ordered sp2-domain
LCO	$LiCoO_2$
Li	Lithium
$Li_{1-x-y}M_xM'_yO_2$	Lithium layered oxides
Li_2CO_3	lithium carbonate
Li_2O	Lithium oxide
Li_2S	Lithium sulfide
$Li_2S_2O_4$	Lithium dithionite
LiB	Lithium ion battery
LiBr	Lithium bromide
LIC	lithium-ion capacitor
LiCl	Lithium chloride
$LiClO_4$	Lithium perchlorate
LiF	Lithium fluoride
LiI	Lithium iodide
$LiM_{2-x}M'_xO_4$	Lithium spinels
$LiMPO_4$ or $LiM_{1-x}M'_xPO_4$	phospho-olivines materials
LiOH	lithium hydroxide
$LiPF_6$	Lithium hexafluorophosphate
LMO	$LiMn_2O_4$
LNO	$LiNiO_2$
l_p	length of pores
LTO	lithium titanate oxide
LUMO	lowest unoccupied molecular orbital
M	Molar mass or metal
M	metal
$M°$	reduced metal
m^2	square meter

MA_{ads}	metal-adsorbate species
mAh/g	milliamperehour per gram
Mb/d	Million barrels per day
Mg	magnesium
mg	milligram
mg/cm^2	milligram per square centimeter
$MgCl_2$	magnesium chloride
MgH_2	magnesium hydride
m-GQT	multi-layer graphene quantum dot
MH	Metal hydride
mL	milliliter
mm	millimeter
Mn	manganese
$Mn(NO_3)_2$	manganese nitrate
$Mn(NO_3)_2 \cdot 2H_2O$	manganese nitrate dihydrate
$Mn(NO_3)_2 \cdot 4H_2O$	manganese nitrate tetrahydrate
$Mn(NO_3)_2 \cdot H_2O$	manganese nitrate monohydrate
Mn_3O_4	manganese spinel oxixe, hausmannite
MnO_2	manganese dioxide
$MnO_x(NO_3)_{2-x}$	manganese oxonitrate
MnOx-NC	manganese oxide synthetized with ammonium citrate
MnOx-NCG	manganese oxide synthetized with glycine and ammonium citrate
MnOx-NCU	manganese oxide synthetized with urea and ammonium citrate
MnOx-NG	manganese oxide synthetized with glycine
MOF	Metal-organic framework
MoO_2	molybdenum dioxide
MoO_4^{2-}	molybdate
MoS_2	molybdenum disulfide
m_p	Melting point
ms	millisecond
MSE	mercury/mercurous sulfate electrode
Mt	Megatonne
Mtce	Million tonnes of coal equivalent
mV/s	millvolt per second

mW	millwatt
MWCNT	multi-walled carbon nanotube
MΩ·cm	megaohm centimeter
N_2	nitrogen
N_2H_4	hydrazine
Na	Sodium
Na_2SO_4	sodium sulfate
$NaBH_4$	sodium borohydride
$NaClO_4$-	sodium perchlorate
NaOH	sodium hydroxide
NAP-XPS	Near ambient pressure X-ray photoelectron spectroscopy
Nb	niobium
Nb_2O_5	niobium pentoxide
NCA	$LiNi_{1-x-y}Co_xAl_yO_2$
n_{e-}	Number of electrons exchanged
NH_2CH_2COOH	glycine
NH_4Cl	ammonium chloride
NHE	normal hydrogen electrode
Ni	Nickel
$Ni(OH)_2$	Nickel hydroxide
NIC	sodium-ion capacitor
NiO	nickel oxide
NiOOH	Nickel oxyhydroxide
nm	nanometer
NMC	$LiNi_{1-x-y}Mn_xCo_yO_2$
NMD	Natural manganese dioxide
NMO	$LiNi_{1-x}Mn_xO_2$
NMP	N-methyl-2-pyrrolidone
NMR	Nuclear magnetic resonance
NZE	Net Zero Emissions
O_2 or O	Oxygen
OCV	Open-circuit voltage
OH^-	Hydroxide anion
OLC	onion-like carbon

Ox	oxidant
P	pressure
P_{max}	maximum power achievable
Pa	pascal
PANI	polyaniline
Pb	Lead
PbO_2	Lead dioxide
$PbSO_4$	Lead sulfate
PC	propylene carbonate
PDF	pair density function
PEO	poly(ethylene) oxide
pH	potential of hydrogen
pKa	acidity equilibrium constant
PO_4^{3-}	phosphate
ppb	part per billion
PSD	pore size distribution
Pt	platinum
PV	Photovoltaic
PVP	poly(2-vinylpyridine)
q	charge
Q	capacity
Q_{th}	Theoretical capacity
R	ideal gas constant
R_{ESR}	equivalent series resistance
r_1	average size of macropore
r_2	average size of mesopore
r_3	average size of micropore
r_{ads}	rate of adsorption
r_{des}	rate of desorption
Re(Z)	impedance real component
Red	reductant
rGO	reduced graphene oxide
RHE	reversible hydrogen electrode
RSN	Raspberry-shaped nanoparticle

RSN@TA@FLG	Raspberry-shaped nanoparticle attached to few-layer graphene with tannic acid surfactant
$RSN@TA@FLG_{100mg}$	RSN@TA@FLG particle using 100mg of freeze-dried FLG
$RSN@TA@FLG_{300mg}$	RSN@TA@FLG particle using 300mg of freeze-dried FLG
Ru	ruthenium
RuO_2	ruthenium oxide(IV)
S	Sulfur
s	second
$S\cdot cm^{-1}$	siemens per centimer
SAXS	small-angle X-ray scattering
Sb	Antimony
SCE	saturated calomel electrode
SCS	solution combustion synthesis
SEI	solid electrolyte interphase
s-GQD	single-layer graphene quantum dot
Si	silicon
SiC	silicon carbide
Sn	Tin
SO_2	Sulfur dioxide
SO_3^{2-}	sulfite
SO_4^{2-}	sulfate
$SOCl_2$	Thionyl chloride
SOHIO	Standard Oil Company
SSA	specific surface area
ssNMR	solid-state NMR
STEPS	Stated Policies Scenario
SWCNT	single-walled carbon nanotube
t	time
T	temperature
T_{ad}	adiabatic temperature
TBAOH	tetrabutylammonium hydroxide
Tcm	Trillion cubic metres
t_d	diffusion time

TD-DRIFTS	Temperature-Dependent Diffuse Reflectance Infrared Fourier Transform Spectroscopy
TEA	Tetraalkylammonium
TEGDME	Tetraethylene glycol dimethyl ether
TEM	transmission electron microscopy
TGA	Thermogravimetric analysis
TiC	titanium carbide
TiO_2	titanium(IV) oxide
TiS_2	titanium disulfide
TLM	transmission line model
T_{max}	maximum temperature
TMO	transition metal oxide
TOC	Total of organic compound
TPa	terapascal
upd	underpotential deposition
US	United States
V	Volt
V	potential
V_2O_5	vanadium pentoxide
V_{mp}	micropore volume
V_{p}	pore volume
V_{th}	Theoretical voltage window
W	watt
WEO	World Energy Outlook
Wh/g	Watt hour per gram
Wh/kg	Watt hour per kilogram
Wh/L	Watt hour per liter
WO_4^{2-}	tungstate
wt.%	weight percentage
x(N)	content in nitrogen
x(O)	content in oxygen
XeF_2	xenon difluoride
XPS	X-ray photoelectron spectroscopy
XRD	X-ray diffraction

Z	Electrochemical equivalents
Zn	Zinc
$ZnCl_2$	zinc chloride
ZnSe	zinc selenide
Z_p	impedance of a single semi-infinite pore
β	Brønsted barrier symmetry factor
γ_s	surface tension
γ_{sn}	surface energy normalized by the surface area
ΔE	Potential difference
ΔG_d	free energy linked to atoms to pass through the created interface
ΔG_{int}	free energy for the creation of an interphase
ΔG_{strain}	free energy associated with strain creations
$\Delta_r G$	Gibbs free energy change of a reaction
$\Delta_r H°$	Standard enthalpy of reaction
θ_A	surface coverage
λ	alternatice current penetration depth
$\tilde{\mu}$	electrochemical potential
μ_{e^-}	chemical potential of electron
μ_{Li}	chemical potential of lithium
μ_{Li}^{ex}	excess of chemical potential of lithium
μ_{Li^+}	chemical potential of lithium cation
µF/cm2	microfarad per square centimeter
ν	scan rate
ρ_c	volumetric density of porous material
ρ_g	volumetric density of compact carbon
σ	conductivity
ϕ	local electrostatic potential difference
φ	phase angle
Ω	Ohm
ω	angular frequency

Figures and tables list

Résumé

- **Introduction**

La transition vers les sources d'énergie renouvelables représente l'un des défis les plus importants de notre époque. Les effets de la pollution s'aggravent d'année en année en touchant la planète entière et engendrant une hausse du réchauffement climatique attendue pour +1,5 °C en 2030 d'après les prévisions les plus optimistes de l'Agence Internationale de l'Energie (IEA)[1]. A cela s'ajoute les problématiques liées à la constante croissance de la population mondiale envisagée à 9,7 milliards d'habitants en 2050 d'après le rapport des Nations Unies publié en 2022[2]. De nos jours, l'accès à l'électricité pour tous constitue un objectif essentiel ne serait-ce que pour subvenir aux besoins vitaux mais aussi pour l'amélioration des conditions de vie au quotidien. Pour atteindre cet objectif, il est nécessaire de disposer de dispositifs de stockage d'énergie « verts » réversibles très efficaces, tels que les dispositifs de stockage d'énergie électrochimique qui comprennent les batteries et les supercondensateurs[3–5]. Ces dispositifs ont la particularité d'avoir un taux élevé de conversion d'énergie chimique en énergie électrique (et vice versa), une large échelle de densité d'énergie (Wh/kg ou Wh/L) et de puissance (W/kg ou W/L) tout en opérant sans l'émission de gaz toxique. Les batteries, ou accumulateurs, sont des technologies de stockage et conversion de l'énergie très répandues et présents dans une vaste majorité de dispositifs électroniques. Elles se caractérisent par la conversion d'énergie électrique en chimique au niveau de la charge et de la restitution de l'énergie stockée en électricité au niveau de la décharge. Fondamentalement, le fonctionnement repose entre l'échange d'ions et électrons entre les deux électrodes de la batterie mettant en jeu de part et d'autre des demi-réactions redox. La différence de potentiel entre la cathode et l'anode est directement lié à l'énergie capable d'être stockée et réémise de par les principes fondamentaux de la thermodynamique. Globalement, pour l'exemple d'une batterie lithium-ion, le mécanisme de charge qui est non-spontanée se produit par la désinsertion d'ions Li^+ du matériau de cathode (généralement un oxyde de lithium et autres métaux) vers leur intercalation au sein du matériaux d'anode (plus communément du graphite) en passant via un électrolyte conducteur ionique (mais non conducteur électronique) et entraînant la circulation d'électrons au sein du circuit électrique. La décharge quant à elle, phénomène spontanée, ce fait par phénomène inverse. Les batteries permettent de stocker et de délivrer de l'énergie sur une longue période temps (haute densité d'énergie, ~250 Wh/kg) allant de quelques dizaines de minutes à plusieurs heures mais au détriment une faible vitesse de stockage/décharge d'énergie (faible densité de puissance, quelques kW/kg). Les supercondensateurs représentent quant à eux le deuxième dispositif de stockage d'énergie électrochimique. Ce dernier type de dispositif se caractérise par une longue durée de vie (plus de 10^6 de cyclages), des densités de puissance élevées (~10s kW/kg) mais des densités d'énergie faible (~10s de Wh/kg).

Les matériaux à base de carbone (carbone activé, carbones graphitiques…) et d'oxydes de métaux de transition, tels que les oxydes de manganèse et de fer, sont une source de matériaux abondants et peu toxiques pour la santé et l'environnement, faisant d'eux des matériaux de choix pour le développement de ces deux types de technologies. Les matériaux d'électrode en carbone poreux à grande surface spécifique permettent d'obtenir des supercondensateurs avec une charge/décharge très rapide et une grande stabilité lors des cycles grâce à leur mécanisme de stockage de charge électrostatique à l'intérieur de leurs pores. L'activation thermochimique de précurseurs riches en carbone avec des éléments de dopage en azote (N-dopé) pour développer un charbon actif poreux N-dopé très efficace avec une composition contrôlée pour des applications de supercondensateurs. Les propriétés électrochimiques des oxydes de métaux de transition, en particulier leur capacité spécifique (en mAh/g) théorique sont très élevé due à leur mécanisme de stockage de charge pseudocapacitif se basant par des réactions redox surfacique/sous-surfacique rapides et réversibles. A noter que leur capacité de charge et leur stabilité électrochimique dépendent fortement de leur cristallinité et de leur composition chimique. C'est pourquoi les méthodes de synthèse de ce type d'oxyde métalliques permettant une variation contrôlée de ces propriétés suscitent un vif intérêt. Ainsi, la conception et l'élaboration de ces oxydes par diverses voies de synthèses sont explorées, principalement par voies combustion de solution et ses modifications (combustion de xérogels) et, solvothermales.

- **Matériaux carbonés pour application en supercondensateur**
    - Carbone activé dopé à l'azote (N-dopé)

Les matériaux en carbone sont parmi les matériaux d'électrode les plus couramment utilisés pour les supercondensateurs, en particulier dans les condensateurs à double couche électrique (EDLC), qui s'appuient sur le mécanisme de charge au niveau de la double couche électrochimique à l'interface avec l'électrolyte. Les avantages des matériaux en carbone sont leur conductivité électrique élevée, leur stabilité électrochimique et la variabilité contrôlée de la structure et de la composition des matériaux. Les matériaux en carbone peuvent être synthétisés avec une grande variété de structures: de 0D (nanodots de carbone et points quantiques de carbone), à 1D (nanotubes et nanofibres de carbone), 2D (carbones de type graphène), à de nombreux carbones poreux 3D, par exemple les carbones activés (AC). Pour les électrodes EDLC, les matériaux carbonés à surface spécifique élevée (SSA) sont d'un grand intérêt, en particulier les AC.

Les carbones activés représente le groupe de matériaux de carbone ayant une surface spécifique (SSA) exceptionnellement élevée, proche du maximum théorique de la SSA pour une feuille de carbone *sp*^{2} étroitement emballée (couche de graphène unique) de 2680 m^2/g. Compte tenu de la valeur typique de la capacité interfaciale spécifique à la surface des matériaux en carbone Cs ≈ 5-10 µF/cm^2, on peut s'attendre à ce que la capacité spécifique de masse des électrodes en carbone soit de l'ordre de Cg ≈ 150-300 F/g. La capacité spécifique de masse élevée est fournie par la structure poreuse ouverte de l'AC avec une contribution prédominante des micropores (diamètre d < 2 nm). Le dopage par hétéroatomes comme l'azote est considéré comme une stratégie prometteuse pour améliorer les performances de ces électrodes par l'ajout de groupements fonctionnels actifs au mécanisme de stockage.

L'objectif est de synthétiser un matériau carboné modèle très performant pour investiguer l'influence du dopage à l'azote sur les performances électrochimiques du l'électrode. En ce sens, le sucrose est utilisé comme précurseur et source de carbone ne comportant pas de groupement azoté. Du citrate d'ammonium tribasique est ajouté en tant qu'agent dopant mais également comme source additionnel de carbone pouvant également réticuler le réseau carboné. Pour cela, le sucrose et le citrate d'ammonium sont dans un premier mélangés avec un ratio massique 1:1 et broyés finement avant d'être chauffé à 160°C pendant 5 heures pour conduire à la polycondensation du sucrose et réticuler la matrice carbonée. La matrice carbonée est ensuite broyée et mélangé avec une solution aqueuse concentrée en hydroxyde de potassium KOH pour respecter un ratio sucrose:citrate d'ammonium:KOH de 1:1:1 puis séché au four comme précédemment. Le KOH est utilisé pour activer et former les mésopores (2-50 nm) et micropores (<2 nm) lors la pyrolyse également appelée étape d'activation thermochimique. Enfin, le mélange est enfourné dans un four tubulaire sous argon et chauffé avec une rampe de montée de 10°C/min jusqu'à une température de maintien pendant une heure. Le matériau est chauffé à 700°C, 800°C et 900°C pour observer l'effet de la température de pyrolyse sur les propriétés du carbone activé final. Le carbone activé obtenu refroidi à température ambiante est lavé avec une solution diluée de HCl 3M et de l'eau ultrapure MilliQ (18,2 Ω·cm, COT < 1ppb). Les différentes étapes de la synthèse sont illustrées sur la Figure A[6].

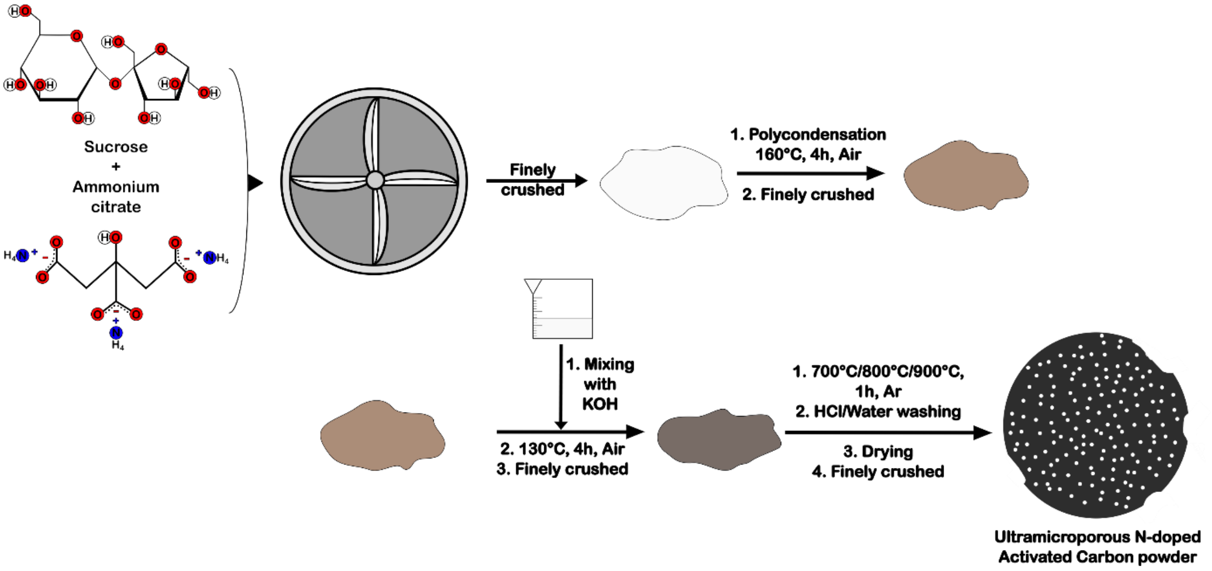

Figure A: Activation thermochimique par KOH d'un mélange de sucrose et de citrate d'ammonium pour former un carbone activé N-dopé[6]

Les échantillons de carbone activé N-dopé (ACN) ainsi que les intermédiaires réactionnels ont été caractérisés essentiellement par spectroscopie infrarouge et Raman, techniques d'adsorption-désorption de N_2 et CO_2, spectrométrie photoélectronique X (XPS), mesures de conductivité sur poudres et caractérisations électrochimiques (voltamétrie cyclique, cyclage galvanostatique avec limitations de potentiel et spectroscopie d'impédance électrochimique).

L'intermédiaire de polycondensation réticulé formé à partir du citrate d'ammonium et du sucrose contient des groupes amides et imides qui sont décomposés au-dessus de 600°C et résultant en la formation de fragments aromatiques azotés plus stables de la matrice carbonée. Cette décomposition se traduit également par une augmentation additionnelle de la surface spécifique des carbones N-dopé, confirmé par les mesures d'adsorption-désorption de gaz. Les mesures d'adsorption-désorption de gaz révèle que plus température de température est élevée, plus la surface spécifique est élevée ($SSA_{ACN700°C}$ = 556 m^2/g ; $SSA_{ACN800°C}$ = 1177 m^2/g ; $SSA_{ACN900°C}$ = 1534 m^2/g) avec distribution de taille de pores situées quasi-essentiellement au niveau des micropores (obtenu avec CO_2 et traitement Non-local DFT : $ACN_{700°C}$ = 0.23865 cm^3/g; $ACN_{800°C}$ = 0.51960 cm^3/g; $ACN_{900°C}$ = 0.66655 cm^3/g). Plus précisément, les mesures au CO_2 montrèrent une taille médiane du diamètre des pores aux alentours des 0,37-0,41 nm attestant du caractère ultramicroporeux (d<0,7 nm) des matériaux. Les données XPS quant à elles révélèrent une diminution de la teneur en azote plus la température de pyrolyse est élevée ($at.\%(N)_{ACN700°C}$ = 7,3% ; $at.\%(N)_{ACN800°C}$ = 3,6% ; $at.\%(N)_{ACN900°C}$ = 1,5%). De plus, en cas de température élevée la teneur en groupements pyridinique, pyrrolique et pyridinium diminue alors que celle en groupements amine, N-quaternaire et R-N oxydé augmente. Il est soutenu que les groupements pyrroliques peuvent apporter un effet pseudocapacitif et induire un stockage de charge accru. Les mesures de conductivité sur poudre montrent une augmentation de la conductivité électronique plus la température de pyrolyse est élevée par environ deux ordres de grandeur entre chaque palier ($\rho_{ACN700°C} \approx 19{,}5\ k\Omega \cdot cm$; $\rho_{ACN800°C} \approx 194\ \Omega \cdot cm$; $\rho_{ACN900°C} \approx 9{,}2\ \Omega \cdot cm$). Ceci est attendu en vue de la graphitisation du carbone amorphe qui commence aux alentours de 800°C et plus prononcée plus la température est élevée. Ainsi, le carbone activé synthétisé à 700°C présente une très faible conductivité électronique, ce qui est un désavantage pour des applications électroniques dans les dispositifs de stockage d'énergie. Le taux de graphitisation et l'augmentation de l'ordre au sein des structures est confirmé via les mesures Raman avec les rapports des intensités des pics D (défauts du réseau) et G (graphitisation) avec I_D/I_G et de la largeur à mi-hauteur du pic G qui diminue ($FWHM_{ACN700°C} = 117\ cm^{-1}$; $FWHM_{ACN800°C} = 103\ cm^{-1}$; $FWHM_{ACN700°C} = 81\ cm^{-1}$), respectivement. Les mesures électrochimiques ont été réalisées dans une cellule à 3 électrodes avec une contre électrode de platine, une électrode de référence en mercure/sulfate de mercure plongeant dans une solution saturée en K_2SO_4 et une électrode de travail avec 150 µg de matériau actif reposant sur un support en carbone vitreux dans un électrolyte d'acide sulfurique 1M H_2SO_4.

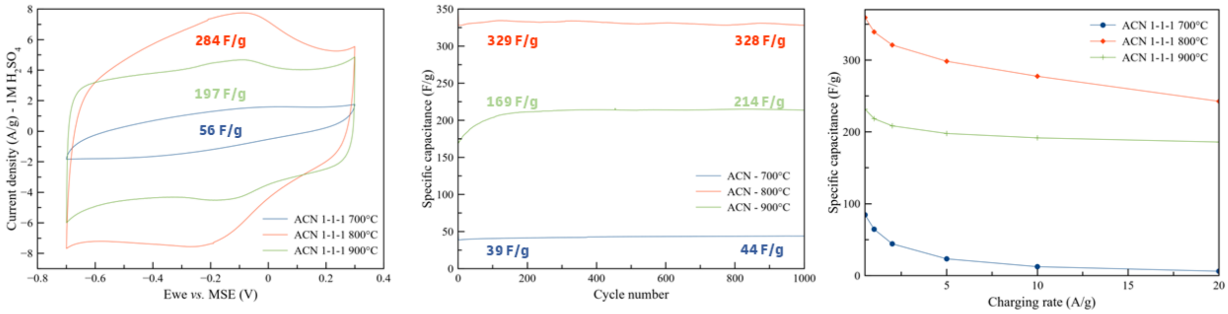

Figure B : Courbes de voltamétrie cyclique à 20 mV/s (gauche); test de cyclage galvanostatique à potentiel limité à 2 A/g (milieu) ; et à différentes vitesse de charge/décharge (droite)

Les performances sont les plus élevées pour le ACN-800°C malgré une plus faible surface spécifique qu'ACN-900°C et ce grâce aux groupements pyrroliques permettant de stocker plus de protons lors des cyclages dont la transition redox peut être visible sur les courbes de voltamétrie cycliques (Figure B). De plus, les divers groupements fonctionnels azotés et oxygénés augmentent la mouillabilité des pores et l'insertion de l'électrolyte.

- Influence de la fluoration

L'effet de fluoration sur ces matériaux a également été étudié. La fluoration à l'aide de difluorure de xénon XeF_2 sur des charbons actifs dopés à l'azote a été choisie pour étudier le rôle probable du dopage au fluor sur des composés déjà dopés à l'azote et révéler son impact sur les propriétés structurelles et les performances en tant que matériaux d'électrodes de supercondensateurs.

La fluoration à faible niveau sur un ACN-800°C plus désordonné a permis de réduire le nombre de liaisons pendantes, mais au détriment de la conductivité des matériaux, ce qui a entravé ses performances en tant que matériau d'électrode. Plus précisément, l'impact négatif de la fluoration sur cet échantillon pourrait être expliqué par une perte de conductivité électronique du matériau (augmentation du rapport O/C, perte du noyau de carbone sp^2 lors de la fixation du fluor) directement visible sur la forme de la courbe CV (Figure C).

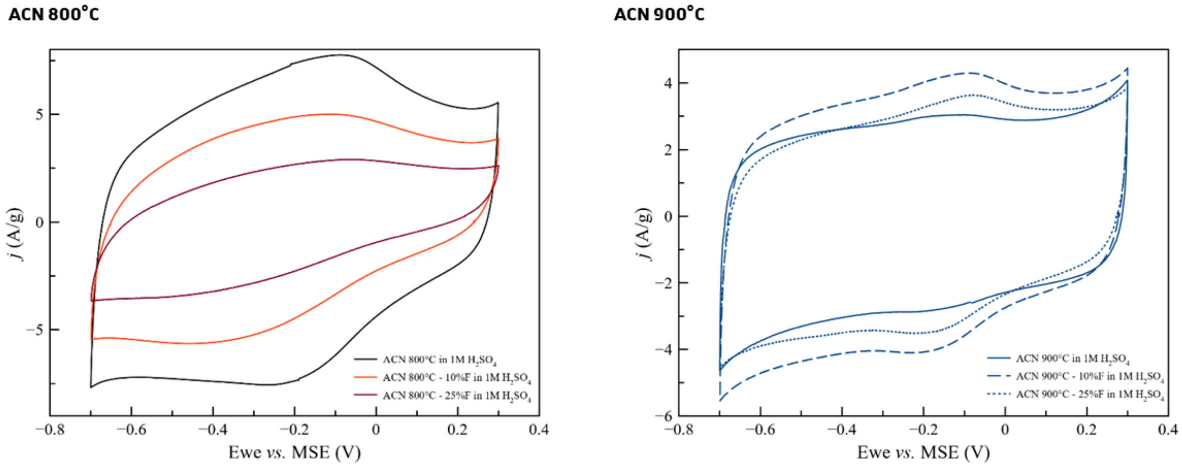

Figure C : Courbes de voltamétrie cyclique à 20 mV/s sur des carbones activés ACN-800°C (gauche) et ACN-900°C (droite) à différents taux de fluoration

Sur un matériau ACN-900°C plus ordonné, la fluoration a été plus facile à réaliser et a permis une légère augmentation des performances en raison de l'augmentation probable de la mouillabilité des pores et de l'accessibilité à l'électrolyte, sans affecter radicalement une matrice de carbone sp^2 déjà plus conductrice. Néanmoins, une forte fluoration aurait un effet négatif sur les deux échantillons avec une détérioration profonde de la matrice conductrice des charbons actifs.

- Etude *in situ* d'électrodes carbonées via spectroscopie d'impédance électrochimique

Une étude profonde sur trois carbones (ACN-800°C, Vulcan XC-72 et AC Norit) présentant des caractéristiques différentes a été réalisée par spectroscopie d'impédance électrochimique (EIS). L'analyse de la dépendance en fréquence de la capacité (complexe) d'un matériau d'électrode poreux permet de caractériser *in situ* sa structure poreuse et, en particulier, les conditions de polarisation d'une interface électrochimique à l'intérieur des pores. La capacité complexe est directement calculée à partir de l'impédance mesurée, corrigée de la résistance série de l'électrolyte. Afin d'analyser la capacité, nous avons utilisé un modèle géométrique simplifié de matériaux d'électrode poreux supposant trois générations de pores ramifiés hiérarchiquement (c'est-à-dire consécutifs). Cette technique d'analyse est complémentaire afin d'étudier en détail les propriétés des électrodes.

Le problème lié à la compréhension des propriétés électrochimiques des matériaux d'électrode poreux est que la réponse de l'interface électrochimique à l'intérieur du matériau poreux à la modulation du potentiel (ou du courant) varie en fonction de la position de l'interface à l'intérieur des pores. Cela crée des conditions locales non uniformes de potentiel interfacial à l'intérieur des pores uniques et, par conséquent, à l'intérieur du matériau. La réponse de l'interface électrochimique à la modulation du potentiel est caractérisée par l'impédance interfaciale locale spécifique à la surface Z_c (Ohm·m^2), qui est, par exemple, en l'absence de transfert de charge interfacial, déterminée par la capacité interfaciale spécifique à la surface C_s (F/m^2). La spectroscopie d'impédance est un outil polyvalent de l'étude de l'interface électrochimique électrode/électrolyte, intensivement utilisé dans les études du mécanisme des processus interfaciaux et dans la caractérisation de ces matériaux d'électrode. Dans un ensemble de travaux fondamentaux, DeLevi a démontré que la réponse à la modulation du potentiel d'une interface à l'intérieur d'un seul pore semi-infini peut être bien décrite par un modèle de ligne de transmission[7,8]. La solution de ce modèle peut être exprimée par l'équation de l'impédance d'un pore unique comme suit :

$$Z_p = \sqrt{R_s Z_s}\coth\sqrt{\frac{R_s}{Z_s}} = \sqrt{\frac{Z_c \rho}{2\pi^2 r^3}}\coth(l\sqrt{\frac{2\rho}{Z_c r}})$$

Au cours des décennies qui ont suivi les travaux de DeLevi, les modèles à ligne de transmission (TLM) de l’impédance des matériaux poreux Z_{em} ont été intensivement utilisés pour caractériser les propriétés électrochimiques des électrodes poreuses. Il a été démontré que l'analyse de la dépendance en fréquence de la capacité complexe de l'électrode, C_z, calculée à partir de Z_{em}, est un outil très utile pour caractériser la structure poreuse de l'électrode. Par exemple, pour évaluer la dépendance de l'impédance d'une électrode par rapport à la forme des pores[9], ou à la largeur de la distribution de la taille des pores[10]. Divers modèles très complexes ont été établis depuis pour caractériser ces matériaux d’électrodes. Cependant, l’une des difficultés rencontrées dans le développement des modèles de pores hiérarchiques est la grande quantité de paramètres géométriques utilisés, tels que la taille et la longueur de chaque génération de pores, et les facteurs de ramification. De ce fait, un modèle géométrique simplifié a été utilisé pour cette étude. Dans ce travail, nous proposons une double stratégie afin de développer un modèle géométrique simplifié mais cohérent pour les matériaux d'électrodes poreux, applicable à la modélisation des propriétés électrochimiques des matériaux poreux avec une grande variété de porosité. Premièrement, le modèle géométrique doit être cohérent avec la variété des paramètres structurels déterminés par des méthodes *ex situ*, à savoir la caractérisation par adsorption-désorption de gaz inerte avec la surface spécifique, le volume des pores, des micropores et la contribution relative à la surface des pores et des micropores. Deuxièmement, le modèle doit être cohérent avec les données électrochimiques obtenues pour différentes épaisseurs d'électrodes poreuses, en utilisant les mêmes paramètres pour la géométrie des pores internes et des paramètres ajustés pour les macropores.

La structure modèle d'une couche poreuse est représentée sur la Figure D. Nous supposons que la couche est composée de particules micrométriques formant des agglomérats alignés verticalement. La taille attendue de ces agglomérats est de quelques dizaines à quelques centaines de nm, et ces agglomérats forment donc le premier niveau de pores, que l'on appelle "macropores" avec une taille moyenne r_1 et une longueur l_1. À l'intérieur de ces particules se forment les pores du deuxième niveau, dont la taille prévue est de quelques nm à quelques dizaines de nm, et qui sont donc appelés "mésopores", de taille moyenne r_2 et de longueur l_2. Chacun des macropores est ramifié en une moyenne de r_{21} mésopores, qui sont répartis de manière aléatoire et uniforme sur la surface intérieure du macropores. À son tour, chaque mésopore se ramifie en r_{32} pores de troisième niveau, appelés "micropores", de taille moyenne r_3 et de longueur l_3. Les paramètres r_{21} et r_{32} sont appelés "facteurs de ramification".

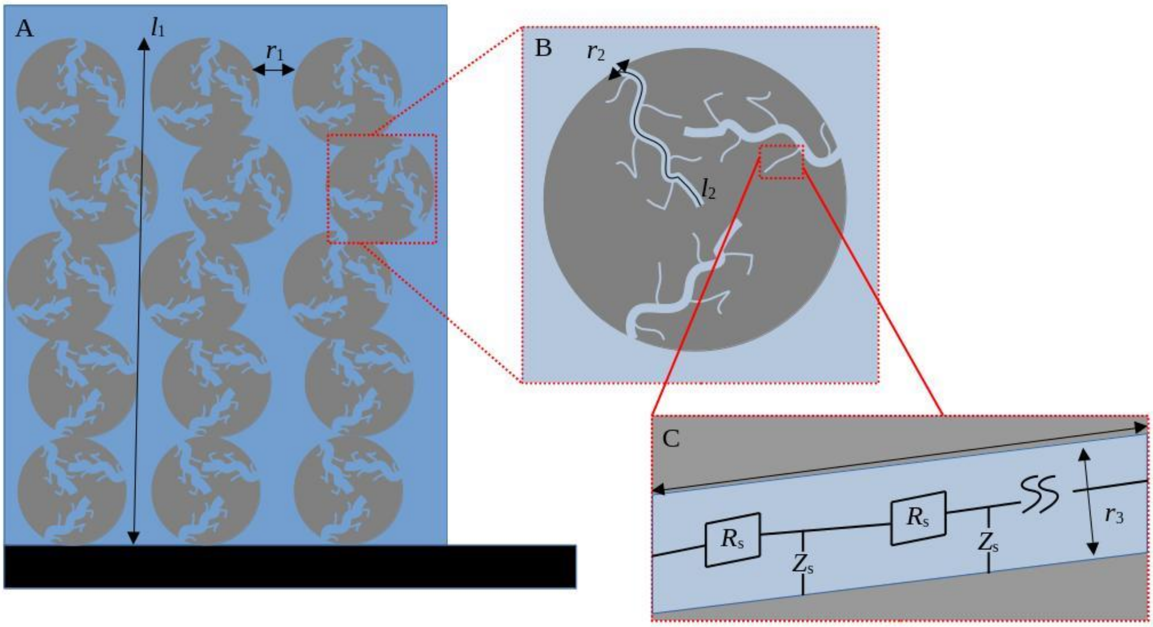

Figure D : Le diagramme représentant la structure du modèle d'une couche poreuse, composée d'agglomérats de particules orientés verticalement, séparés par des macropores (A) ; les particules contiennent des mésopores se ramifiant en micropores (B) ; l'impédance d'un pore unique est modélisée par une ligne de transmission (C).

Le modèle d'impédance d'un matériau poreux à base de carbone est quant à lui représenté par un ensemble de circuits équivalents, décrits sur la Figure E.

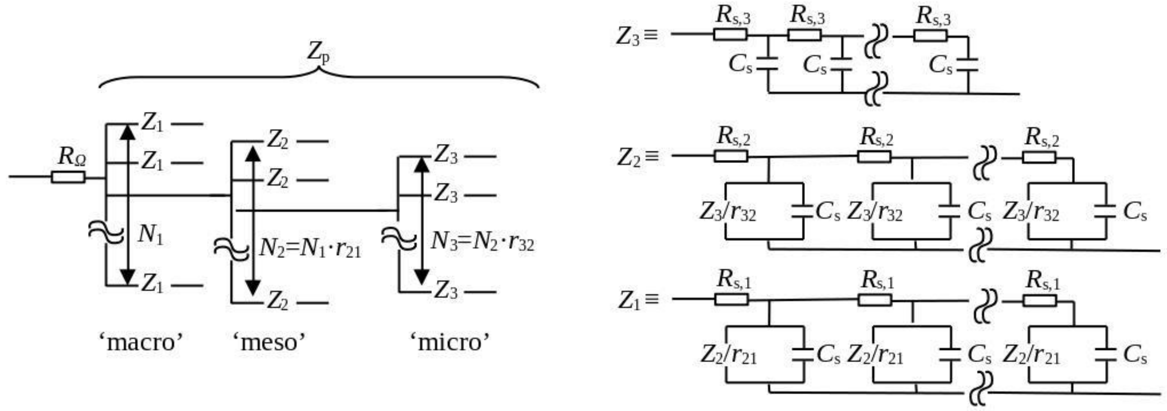

Figure E : Diagrammes représentant les circuits équivalents utilisés dans le modèle d'impédance des matériaux en carbone poreux

Les impédances Z_1, Z_2 et Z_3 correspondent à l'impédance d'un pore unique du i-ème niveau, Z_i, et sont calculées par l'équation de De Levie, similaire à l'équation présentée précédemment :

$$Z_i = \sqrt{R_{s,i} Z_{s,i}} \coth \sqrt{\frac{R_{s,i}}{Z_{s,i}}}$$

Différentes charges de matière active ont été testées pour permettre un ajustement supplémentaire des paramètres des "macropores". Le fitting du modèle géométrique avec les données expérimentales est présenté en Figure F, montrant un résultat assez qualitatif du modèle malgré sa simplification. De nombreux résultats et observations ont pu être obtenus à partir de ces expériences.

L'étude du carbone Vulcan XC-72 montre que plus de 60% des pores internes (7% en termes de volume total) contribuent à la surface interfaciale, 45% d'entre eux étant des micropores courts (dizaines de nanomètres). La modélisation de l'impédance et son ajustement avec le modèle géométrique ont permis de mieux comprendre la formation d'un réseau de mésopores, dû à des particules nanométriques qui coalescent pour former des agglomérats plus grands, se ramifiant en mésopores et micropores. Dans le cas du carbone AC Norit, les pores intérieurs représentent 36 % du volume total des pores et près de 99 % de la surface totale, avec 94 % de micropores. Les derniers sont plus étroits et plus longs que ce qui a été caractérisé pour le carbone Vulcan XC-72, entravant l'accessibilité des ions de l'électrolyte, ce qui donne une surface spécifique active électrochimique ECSA (460 m^2/g) inférieure à la surface mesurée de 732 m^2/g par adsorption-désorption de gaz d'azote, alors que pour le XC-72 les valeurs étaient plus proches (172 m^2/g pour l'ECSA contre 236 m^2/g d'après l'analyse BET).

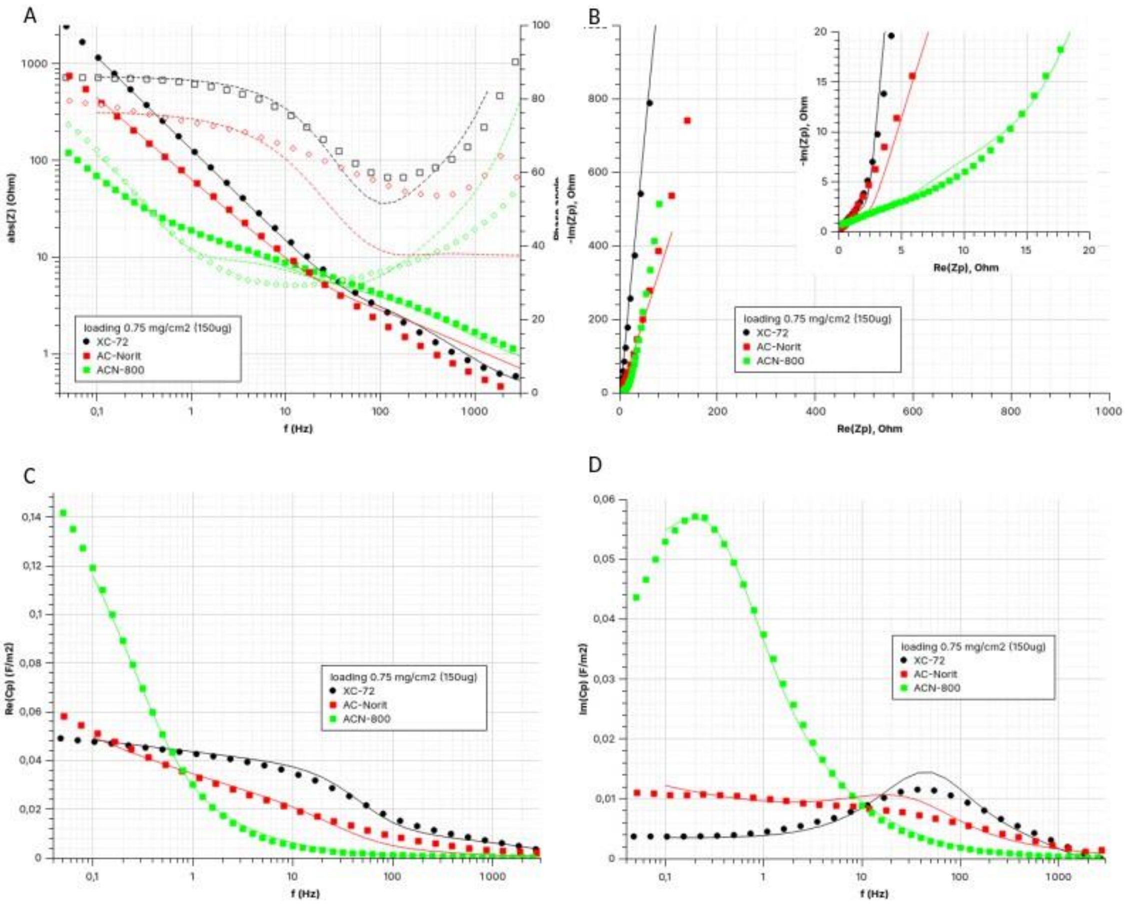

Figure F : Courbes de Bode et de Nyquist de l'impédance pour des dépôts de 0,75 µg/cm² de divers matériaux en carbone

La surface de l'interface étant presque constituée de micropores, leur capacité de polarisation déterminera directement la performance électrochimique du matériau AC Norit. Malgré un ajustement plus compliqué pour ce carbone de à la forme de réseau interconnecté quasi uniquement par les micropores, la modélisation a indiqué une polarisation non uniforme dans les pores internes, même à basses fréquences. Dans le cas de l'ACN-800°C, plus de 98% de l'interface est liée aux micropores étroits et longs avec une grande accessibilité pour les ions de l'électrolyte, ce qui explique la proximité entre l'ECSA et le SSA obtenu expérimentalement. Ce matériau de carbone serait formé de mésopores étroits et longs créant une ramification de micropores longs interconnectés. La polarisation de ces pores est nettement plus uniforme que celle de l'échantillon précédent, ce qui indique une dispersion plus étroite de ces micropores par rapport à l'AC Norit.

- **Synthèse par combustion de nanoparticules de Mn_3O_4 et leurs études pour supercondensateurs**

La synthèse par combustion de solution (SCS) repose sur la propagation d'une réaction exothermique autoalimentée tout le long medium aqueux voire sol-gel[11]. Elle consiste en la réaction entre un oxydant qui est généralement un nitrate de métal hydraté et d'un combustible (glycine, urée, sucrose, etc…) dans un solvant. Le mélange est ensuite placé directement sur une plaque chauffante ou un four jusqu'à atteindre la température d'ignition pour lancer la combustion. L'oxygène libéré par la décomposition du nitrate va réagir avec le combustible et s'auto-suffire via une réaction exothermique libérant une forte chaleur conduisant à la synthèse d'un oxyde métallique. La méthode de synthèse a été optimisée avec un séchage préalable à l'étuve pour 48h à 80°C pour former un xérogel et permettre une combustion rapide (30s-60s) et plus uniforme au sein du milieu réactionnel. La formation de la phase hausmannite Mn_3O_4 fut produite en essayant plusieurs conditions différentes. En outre, le nitrate de manganèse tétrahydraté $Mn(NO_3)_2{\cdot}4H_2O$ fut toujours utilisé comme précurseur métallique où a été ajouté soit de la glycine ou de l'urée comme combustible avec des ratio molaire différent. Les ratios molaires sont définis en équilibrant les molécules de dioxygène des deux demi-équations de décomposition du nitrate métallique et de la combustion du combustible. Les équations en considérant la glycine et l'urée sont écrites ci-dessous :

$$
\begin{aligned}
&3\,M^{\vartheta}(NO_3)_{\vartheta}\ \cdot m\,H_2O + \frac{5}{3}\varphi\vartheta\,Glycine + \frac{15}{4}\vartheta(\varphi-1)\,O_2 \\
&\qquad \rightleftarrows \frac{3\vartheta}{8}\,M_{\frac{8}{\vartheta}}O_4 + \vartheta\left(\frac{3}{2}+\frac{5}{6}\varphi\right)N_2 + \frac{10}{3}\varphi\vartheta\,CO_2 + \left(\frac{25}{6}\varphi\vartheta + 3m\right)H_2O
\end{aligned}
$$

$$
\begin{aligned}
&3\,M^{\vartheta}(NO_3)_{\vartheta}\ \cdot m\,H_2O + \frac{5}{2}\varphi\vartheta\,Urea + \frac{15}{4}\vartheta(\varphi-1)\,O_2 \\
&\qquad \rightleftarrows \frac{3\vartheta}{8}\,M_{\frac{8}{\vartheta}}O_4 + \vartheta\left(\frac{3}{2}+\frac{5}{2}\varphi\right)N_2 + \frac{5}{2}\varphi\vartheta\,CO_2 + (5\,\varphi\vartheta + 3m)H_2O
\end{aligned}
$$

avec ϑ la valence du cation métallique, et φ le coefficient indiquant si le milieu est équilibré en oxygène ($\varphi = 1$), appauvri ($\varphi < 1$) ou en excès ($\varphi > 1$). Les réactions décrites ne donnèrent cependant pas de phases pures mais essentiellement un mélange d'oxyde avec du Mn_3O_4, MnO et/ou Mn_2O_3 selon les précurseurs et leur ratio molaire. Du citrate d'ammonium fut ajouté afin de changer la coordination du cation métallique et ainsi d'envisager la création d'un complexe de citrate de manganèse plus stable lors de la décomposition et étudier son effet sur le produit final.

Les études DRIFTS accompagnées d'une analyse thermogravimétrique (ATG) ont permis de dégager quelques observations et conclusions intéressantes. La glycine et le nitrate de manganèse forment en fait un complexe de $[Mn(gly)(H_2O)_2](NO_3)_2$ ou de $[Mn(gly)(H_2O)_4](NO_3)_2$, ce qui garantit un mélange fin et uniforme des réactifs. En outre, ces complexes Mn(II)-glycine sont thermodynamiquement moins stables que de nombreux autres complexes de métaux de transition, leur décomposition se produisant à une température inférieure à celle de la glycine pure (160°C contre 220°C). La décomposition plus rapide du mélange glycine-nitrate de Mn(II) pourrait indiquer une énergie d'activation plus faible pour la réaction de décomposition que pour les réactifs purs séparés. Le rapport précurseur métallique/combustible a été modifié en utilisant la glycine et le nitrate de manganèse afin d'être en déficit d'oxygène, en équilibre ou en excès selon une équation de réaction idéale pour obtenir uniquement la phase Mn_3O_4 avec un dégagement de gaz plus contrôlé. Aucune phase pure pratique n'a été obtenue avec ces mélanges de nitrate de manganèse et glycine, avec l'obtention de Mn_3O_4, Mn_2O_3 et MnO. Ces synthèses ont permis d'obtenir des structures mésoporeuses de nanoparticules d'oxydes partiellement agglomérées d'environ 25-40 nm. Pour les milieux pauvres en oxygène, la principale phase obtenue était Mn_2O_3 alors que pour les milieux à l'équilibre ou en excès d'oxygène, un mélange de Mn_3O_4 (prédominant) et de MnO (mineur) était présent (Figure G). La présence de différentes phases d'oxyde dans un même mélange pourrait s'expliquer par la réduction partielle d'une phase (c'est-à-dire de Mn_3O_4 en MnO) due à la réaction de combustion à haute température, mais dont la présence n'est que mineure grâce à la libération efficace de chaleur par les espèces gazeuses produites. Mais cela peut également être dû à la précipitation partielle de l'hydroxyde de manganèse $Mn(OH)_2$ pendant l'évaporation du solvant en raison de sa plus faible solubilité par rapport au nitrate. Cet hydroxyde serait ensuite décomposé en MnO qui ne serait plus oxydé en raison de l'environnement pauvre en oxygène dans la réaction SCS. Cette dernière hypothèse tend à être plus exacte puisqu'un excès élevé d'oxygène n'a pas entraîné une plus grande quantité de MnO.

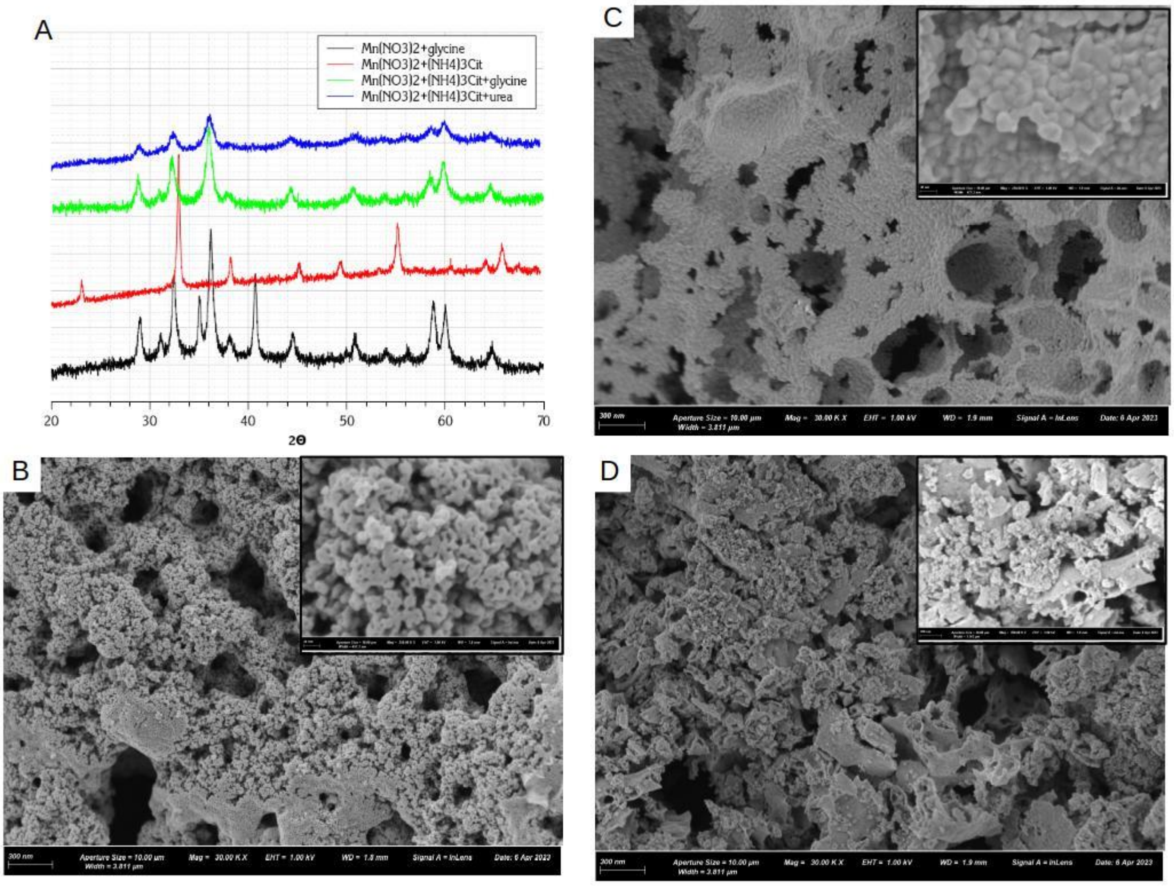

Figure G : Diagrammes XRD des oxydes de Mn synthétisés par SCS en utilisant les mélanges Mn nitrate/glycine (NG), Mn nitrate/citrate (NC), Mn nitrate/citrate/glycine (NCG) et Mn nitrate/citrate/urée (NCU) (A) Images SEM typiques de l'oxyde synthétisé avec NC (B), NCG (C), et NCU (D).

Du citrate d'ammonium a été ajouté pour tester son influence sur les produits obtenus en réalisant des mélanges nitrate de Mn/citrate d'ammonium (NC), nitrate de Mn/glycine/citrate d'ammonium (NCG) et nitrate de Mn/urée/citrate d'ammonium (NCU). Il est intéressant de noter que la présence de citrate d'ammonium a permis d'obtenir des phases pures dans chaque cas. Malgré une cinétique de décomposition plus lente (par rapport aux mélanges de glycine), on suppose que la principale source d'inhomogénéité des produits finaux est due à des complexes de manganèse (II) moins stables dans la solution initiale des réactifs qui, sinon, créeraient d'autres complexes métalliques, des sels secs ou même de l'hydroxyde. En effet, le ligand citrate d'ammonium permet la création de complexes forts et stables au cours du lent processus d'évaporation du solvant. Dans le cas de NC, seul Mn_2O_3 a été obtenu alors que pour NCG et NCU, la seule phase détectée était Mn_3O_4. Les raisons de l'obtention de l'hausmannite dans les deux derniers cas peuvent être dues aux températures plus élevées atteintes avec ces deux combustibles et à la décomposition de la glycine et des intermédiaires de l'urée qui consomment également de l'oxygène, diminuant ainsi la pression partielle locale de l'oxygène. Ces deux raisons favoriseraient la formation d'un oxyde Mn_3O_4 plus réduit que

Mn_2O_3. La phase Mn_3O_4 obtenue avec le mélange NCU présentait une SSA plus élevée et une taille de cristallite plus petite par rapport au mélange NCG, ce qui est attribué à la cinétique de décomposition plus rapide entraînant la formation de particules plus petites avec moins de frittage.

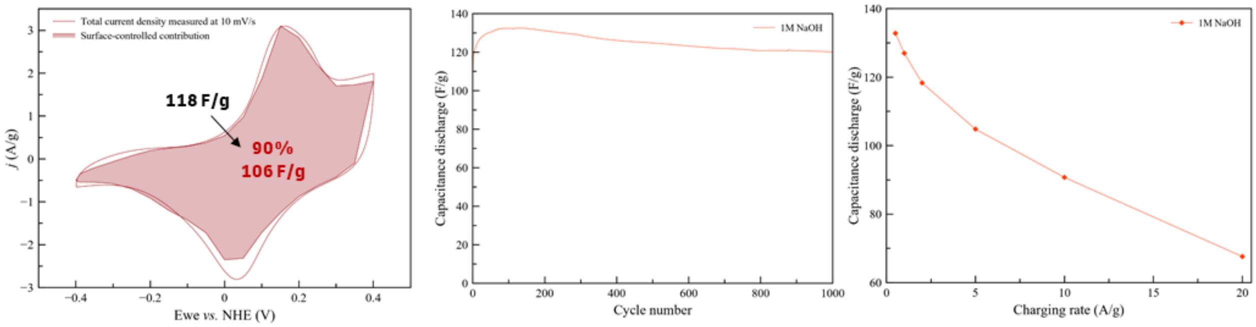

Figure H : Courbes de voltamétrie cyclique à 10 mV/s (gauche); test de cyclage galvanostatique à potentiel limité à 2 A/g (milieu) ; et à différentes vitesse de charge/décharge (droite)

Des tests électrochimiques sur ces matériaux ont été effectués pour des applications en tant qu'électrode de supercondensateur dans des milieux aqueux basiques. La comparaison des deux différents Mn_3O_4 obtenus soit par les mélanges NCG ou NCU en milieu aqueux basique a révélé des performances plus élevées pour celui obtenu par le mélange NCU. Cela s'explique par la surface spécifique plus élevée (35 m^2/g contre 24 m^2/g pour NCG) due à une taille de cristallite plus petite (11,3 nm contre 9,3 nm pour NCG), augmentant également le rapport surface-volume et donc l'interface entre les ions de l'électrolyte et le nombre plus élevé de sites actifs électrochimiques pour la pseudocapacité d'oxydoréduction de surface. Des performances allant jusqu'à 130 F/g ont pu être atteintes pour un taux de cyclage de 2 A/g, soit l'équivalent de 371 $\mu F/cm^2$. En outre, l'analyse effectuée à différents taux de balayage a permis de mettre en évidence le processus d'oxydoréduction de surface rapide et réversible, 90 % de la capacité totale étant fournie par la contribution contrôlée par la surface. Il est intéressant de noter que des applications pour les batteries lithium-ion sont également envisagées et planifiées pour ces matériaux d'oxyde de manganèse.

- **Synthèse par voie polyol de matériaux nanostructurés et composite à base d'oxyde fer Fe_3O_4 et de graphène pour des applications en batterie lithium-ion**

Le développement d'anodes de type conversion nanostructurées est très encouragé en raison de leurs capacités théoriques plus élevées que celles des anodes en graphite conventionnelles (c'est-à-dire > 372 mAh/g) pour les applications à haut débit et parce qu'elles offrent un potentiel plus élevé par rapport à Li^+/Li pour éviter le placage de lithium[12]. Pour les supercondensateurs, les propriétés électrochimiques des oxydes de métaux de transition sont particulièrement intéressantes en raison de leur mécanisme de stockage de charge pseudocapacitif basé sur des réactions redox de surface/sous-surface rapides et réversibles[13]. Les spinelles d'oxyde de fer Fe_3O_4 sont considérés comme un matériau prometteur pour les dispositifs de stockage d'énergie électrochimique en raison de leur abondance relativement élevée, de leur faible toxicité et de leur capacité théorique élevée de 924 mAh/g. La nanostructuration et l'ingénierie structurelle sont envisagées pour améliorer les performances des électrodes à base de Fe_3O_4 en augmentant la surface spécifique du matériau, son nombre de sites actifs électrochimiques accessibles et le mélange des composites pour obtenir une robustesse mécanique intéressante.

La voie polyol est utilisée pour permettre l'ingénierie de synthèse d'oxyde de fer de type spinelle Fe_3O_4 avec une structure creuse en forme de « framboise » composé de nanograins[14,15]. Du graphène ou plus précisément du few-layer graphène (FLG) est ajouté au mélange réactionnel afin de former un composite avec un support conducteur électroniquement. L'ajout de FLG pourrait à la fois augmenter la stabilité structurelle de l'oxyde de fer et apporter de la conductivité électronique. Ce type d'architecture est pensé pour renforcer la stabilité mécanique de l'oxyde lors de l'insertion et désinsertion du lithium créant une expansion volumique du matériaux. La synthèse est réalisée en mélangeant un précurseur de chlorure de fer $FeCl_3{\cdot}6H_2O$, d'acide succinique et d'urée (et de FLG dans le cadre d'un composite) dans de l'éthylène glycol. A noter que le FLG est formé par exfoliation avec une ultrasonotrode en milieu aqueux à partir de graphite expansé et d'acide tannique (TA) agissant comme surfactant[16], puis lyophilisé afin de l'ajouter au milieu polyol. Le mélange est ensuite scellé dans une chambre en Téflon et placer d'en un autoclave. Ce dernier est chauffé dans une étuve avec un programme de température consistant en la montée jusqu'à 200°C avec une rampe de 1,5°C/min et maintenu pendant 10h30 avant refroidissement jusqu'à température ambiante. La dispersion est lavée plusieurs fois avec un mélange d'éthanol/acétone via décantation magnétique grâce aux propriétés magnétiques des particules de Fe_3O_4. Trois synthèses ont été réalisées avec les particules d'oxyde seules (RSN), un composite avec l'ajout de 100 mg de ($RSN@FLG@TA_{100mg}$) et un autre composite avec l'ajout de 300mg ($RSN@FLG@TA_{300mg}$). Les caractérisations à la DRX révèlent bel et bien la formation de Fe_3O_4 ainsi que de la présence du FLG via la présence du pic graphitique. Les mesures d'adsorption-désorption de gaz au N_2 montre une augmentation de la surface spécifique avec l'ajout de FLG (SSA_{RSN} = 13 m^2/g ; $SSA_{RSN@FLG@TA100mg}$ = 29 m^2/g ; $SSA_{RSN@FLG@TA300mg}$ = 61 m^2/g). De plus, les observations par microscopie à balayage électronique (MEB) et par transmission (MET) montrent une diminution de la taille des oxydes de fer par ajout croissant de FLG@TA (Figure I) qui peut s'expliquer par la présence d'acide agissant comme encapsulant.

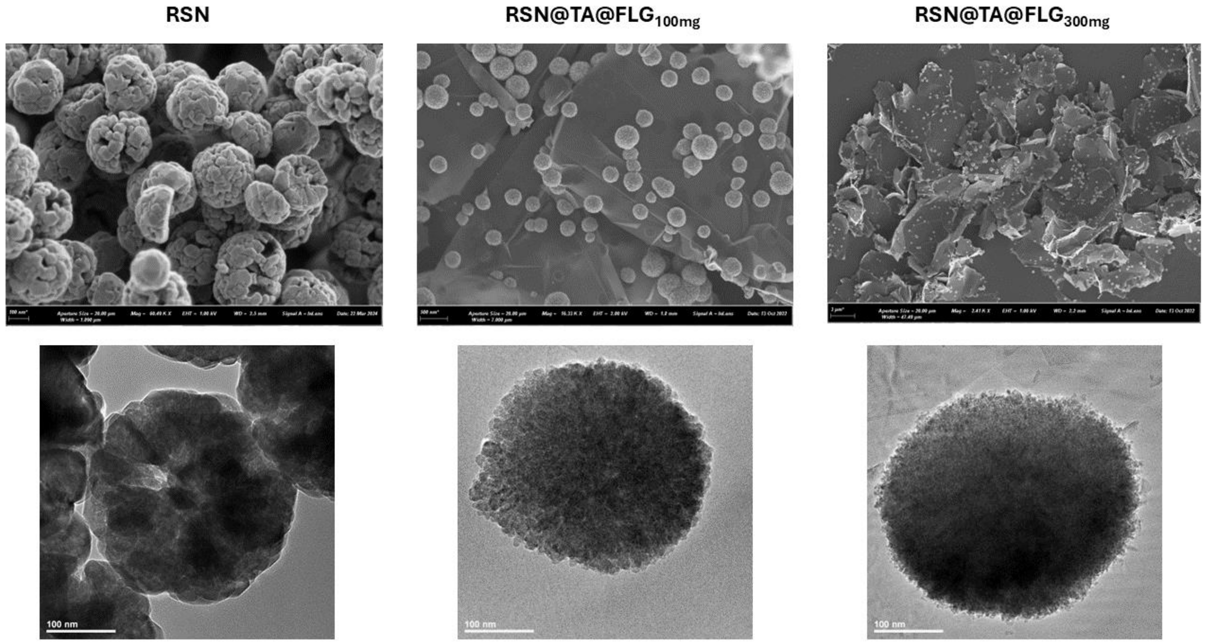
RSN

RSN@TA@FLG$_{100mg}$

RSN@TA@FLG$_{300mg}$

Figure I : Images MEB (haut) et MET (bas) des échantillons de RSN, RSN@TA@FLG$_{100mg}$ et RSN@TA@FLG$_{300mg}$

Pour les applications de supercondensateurs, des capacités de surface très élevées dépassant 350 µF/cm^2 en milieu basique (1M NaOH) ont été obtenues grâce à une réduction partielle de la taille des nanograins pour le composite RSN@TA@FLG$_{100mg}$ en raison de la présence d'acide tannique (voir données électrochimiques en Figure J). Ce mécanisme de stockage de charge est, comme pour l'oxyde de manganèse, dû à des phénomènes de pseudocapacité induits par l'oxydoréduction de surface avec les changements d'état de valence du fer. Le composite RSN@TA@FLG$_{100mg}$ a démontré les performances les plus élevées bien qu'il ait une surface spécifique intermédiaire (29 m^2/g) et une taille de nanograin (environ 10 nm) entre le RSN « pure » et les matériaux RSN@TA@FLG$_{300mg}$. Cela souligne l'obtention d'un mélange optimal à respecter entre le matériau actif RSN et le support FLG pour améliorer la performance électrochimique, la réversibilité du stockage, la stabilité mécanique des matériaux mais aussi la taille des nanograins influencée par la présence de l'acide tannique surfactant sur les surfaces FLG. Le RSN, et plus précisément le Fe_3O_4, étant le matériau actif pour le stockage électrochimique des charges, une quantité moindre de ce dernier dans la composition de l'électrode empêcherait l'obtention d'une capacité élevée, même si la surface spécifique est plus élevée ou la taille des nanograins plus petite. Un travail complémentaire pour une étude plus approfondie serait de synthétiser plus de composites mais avec plus de variations du FLG exfolié assisté par l'acide tannique pour analyser les tendances à la fois en termes de différences structurelles des matériaux (par exemple, la taille des particules, la surface spécifique, la forme) et en termes d'utilisation ultérieure du FLG exfolié.

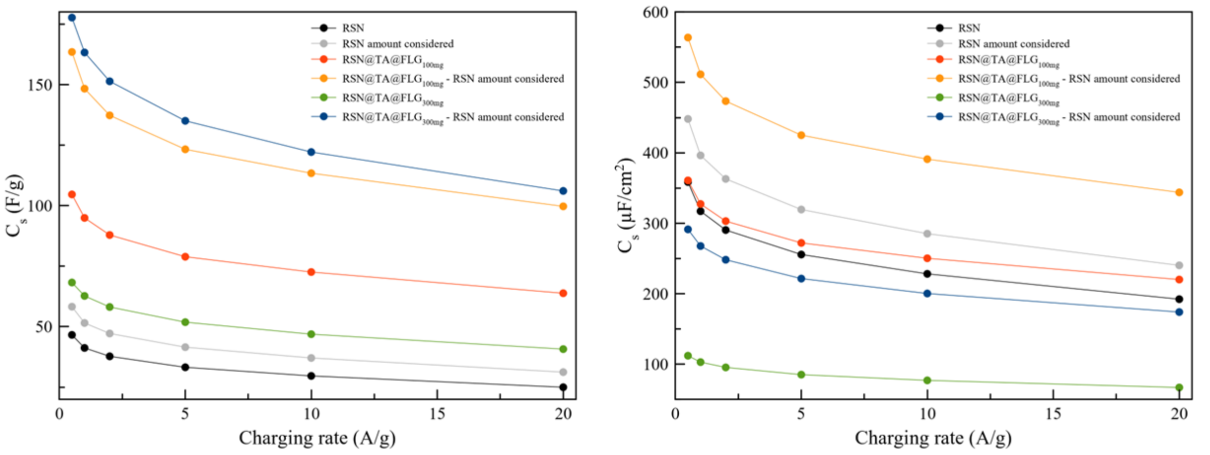

Figure J : Courbes galvanostatiques à différents taux de charge des électrodes normalisés à la masse de l'électrode (gauche) ou à la SSA du matériau actif d'après l'analyse BET (droite)

Les matériaux actifs sont testés en cellule pour batterie ion-lithium en préparant les électrodes. La formulation consiste en la mélange de la matière active et du noir d'acétylène (agent conducteur) dans un mortier, l'ajout d'un liant qu'est le polyfluorure de vinylidène (PVFD) dans du N-méthyl-2-pyrrolidone (NMP), déposé sur un disque en inox puis séché sous air (60°C) puis sous vide (110°C). L'assemblage se fait dans une cellule de type pile-bouton avec l'électrode de matière active testé, une électrode de contre et pseudo-référence qu'est une film couche de lithium métallique et un électrolyte organique qu'est 1M $LiPF_6$ EC/DEC (1:1) (LP40) avec des séparateurs en polypropylène. En ce qui concerne l'utilisation du Fe_3O_4 comme électrode négative de type réaction de conversion (également communément appelée électrode d'anode) une capacité théorique maximale d'environ 924 mAh/g est attendue pour une réaction prenant en compte un échange de 8 électronds. Cependant, la réaction de conversion implique généralement une énorme modification structurelle des matériaux actifs de l'électrode en raison de l'expansion du volume qui peut atteindre plus de 300 % du volume initial de l'électrode, ce qui implique des contraintes mécaniques et des fissures. Par conséquent, les composites d'oxyde de fer RSNs et FLG sont très prometteurs pour améliorer la stabilité de ces électrodes. Il a été observé que l'électrode nue à base de RSN ne conservait pas sa structure même après cinq cycles, ce qui s'accompagnait d'une chute de la capacité de rétention à près de 10 mAh/g après 50 cycles (Figure K, gauche). Cependant, les structures RSN des composites ne se sont pas effondrées même après des dizaines de cycles, ce qui met en évidence les avantages du support FLG. Leur cyclabilité et leur efficacité coulombienne ont été améliorées grâce aux nanoparticules de phase métallique de fer déposées sur les surfaces conductrices du FLG, ce qui a amélioré la réversibilité de la réaction tout en empêchant l'isolation électronique et spatiale de ces particules. Pour de telles applications, le composite avec la plus grande quantité de FLG a montré les meilleures performances, principalement soulignées par sa remarquable rétention de capacité de 27,0 % après 50 cycles, bien plus élevée que pour les autres échantillons. En outre, les électrodes composites ont présenté une capacité supplémentaire apportée par la présence de FLG, ce qui laisse supposer que le FLG participe également au stockage de la charge, comme visible sur les cycles de voltamétrie cyclique en Figure K (droite) avec un pic aux alentours de 0,58V vs. Li^+/Li. Cette "surcapacité" est étudiée à l'aide de la technique *operando* Raman afin d'évaluer les changements de pics Raman autorisés au cours des cycles de charge-décharge.

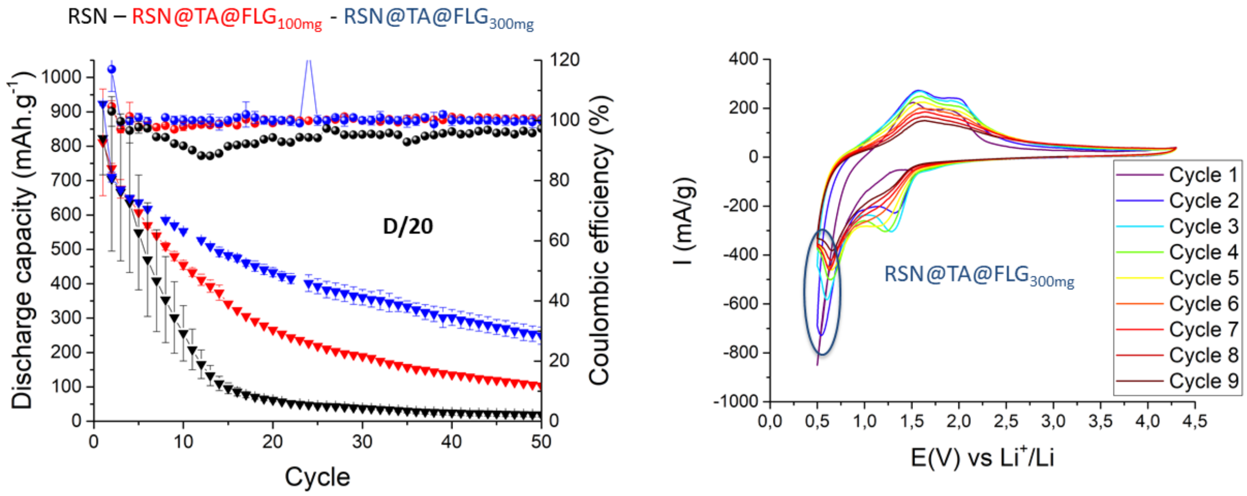

Figure K : Capacité de décharge et efficacité coulombique des matériaux en fonction de leur nombre de cycle pour les différents matériaux d'électrode testés à une vitesse de décharge de D/20 (gauche) ; voltamétrie cyclique réalisée à 0,2 mV/s pour l'électrode à base RSN@TA@FLG$_{300mg}$

- **Conclusion**

Le dopage en azote réalisé des carbones activés à partir de sucrose, de citrate d'ammonium et d'hydroxyde de potassium montrèrent de très haute performance (>320 F/g) pour des applications en supercondensateur. Cette étude permis de mettre en évidence l'augmentation des performances attribuées aux groupements fonctionnels azotés telles que les pyrroles en terme de contribution pseudocapacitif. La fluoration à faible teneur en fluor peut être utile afin d'améliorer légèrement les performances de matériaux carbonés qui présenterait une conductivité électronique déjà importante et peu de défauts structuraux pour obtenir une meilleure mouillabilité des pores et insertion des ions de l'électrolyte. L'étude par spectroscopie d'impédance électrochimique avec un modèle géométrique simple a été prouvée comme étant un modèle qui peut être appliqué à un grand nombre de carbone afin d'obtenir des informations pertinentes concernant l'accessibilité des pores, leur modulation par un potentiel, leur géométrie complexe et de manière générale, apporter une meilleure compréhension du mécanisme de stockage de charge.

La méthode de combustion de solution et les diverses caractérisations ont mis en évidence le rôle d'un agent complexant, le citrate d'ammonium, sur la formation d'oxyde de phase uniques. L'analyse *in situ* par TD-DRIFTS permit de réaliser des observations quant au rôle du complexe métallique formé dans le mélange initial des réactifs. En effet, les complexes métalliques Mn(II)-glycine formés se décomposent à des températures moins élevés que les réactifs seuls notamment dû à une moindre stabilité thermodynamique. L'ajout de citrate d'ammonium comme agent complexant révéla que l'uniformité et sa forte complexation des ions Mn^{2+} dans le mélange initial permit d'obtenir des oxydes de phases pures en empêchant au préalable la formation d'hydroxyde et d'autres sels/complexes métalliques par l'évaporation du solvant. De plus, des matériaux Mn_3O_4 avec des petites de cristallites ont été synthétisés qui proposent des performances intéressantes comme pseudocondensateurs (>100 F/g, >370 µF/cm^2). Ces matériaux sont aussi envisagés comme base d'électrode pour application dans des batteries rechargeables de type Li-ion et sont à l'ordre du jour pour de futurs expériences.

L'ingénierie de particules de Fe_3O_4 sous forme de « framboise » constitués de nanograins ainsi que leur composite avec des feuillets de graphène montrèrent des performances très élevées pour des batteries ion-lithium mais également en tant qu'électrodes de supercondensateurs. Pour cette dernière application, des capacitance à plus de 350 µF/cm^2 furent obtenus pour le composite RSN@TA@FLG$_{100mg}$ qui posséda une surface spécifique plus grande que les RSN seuls mais plus faible que pour le composite RSN@TA@FLG$_{300mg}$ et, des tailles de nanograins suivant la tendance inverse. Cela souligne l'importance apporté par la conductivité électronique apportée par le FLG mais également la prise en compte de la teneur en matériaux actifs dans l'électrode. En ce qui concerne les électrodes de type réaction de conversion, les matériaux composites montrèrent une nette supériorité en terme de stabilité quant aux RSN seuls. Les couches de FLG permettent de stabiliser la structure des RSN et d'empêcher de meilleure façon l'isolation spatiale et électronique des nanoparticules de fer métalliques reposant sur les surfaces de FLG suite à la réaction de conversion. L'échantillon RSN@TA@FLG$_{300mg}$ présenta une capacité en décharge à plus de 923 mAh/g et une rétention de capacité de 27,0% pour plus de cinquante cycles. Le FLG semble également participer au stockage de charge via un apport en capacité (« surcapacité »). L'effet de surcapacité apporté par le graphène est très intéressant et en cours d'investigation par mesure *operando* de spectroscopie Raman.

Introduction

Context: Energy needs in the current climate-related and socio-economic situations

Energy is a primordial source of life in its essence – from a pure biological and physico-chemical point of view as for our societies. Carbohydrates, lipids and proteins constitutes the main fuels for the human body in which their chemical energy is converted to other types of energy such as heat[17]. Besides this essential form of energy needed for the propagation of life and proper functioning of individuals, societies needs additional sources to sustain. Indeed, if energy is considered as the capacity to do work[18] then its production and use is translated in every components of our environment. Depending on the type of applications ranging from mere but essential food production and consumption to the operation of complex facilities with high technology machines, passing by heat regulator and source of light, energy is able to take a variety of forms (thermal, kinetic, potential, chemical, nuclear, electrical and others). Hence, it can be regarded as an index of life quality and different metrics have emerged in the field of energy economics such as the **Energy Return On Investment (EROI)** or also called **Energy Returned on Energy Invested (EROEI)** which refers to a ratio of a usable energy delivered by an energy carrier to energy required to deliver it[19,20]. The higher the ratio, the more viable the energy source is and for ratio ≤ 1, the source is considered as an « energy sink ». An energy storage related measure called the **Energy Stored on Energy Invested** (**ESOEI** or **ESOI$_e$**) – ratio of the electrical energy stored over the device's lifetime to the electrical energy needed to its building[21] – is more in link with the energy storage technologies production and efficiency problematic. The latter is becoming one of the main concerns of modern societies stressed by an increasing global energy need over the years and requirement for « green » energy source. According to the *World Population Prospects 2022: Summary and Results* [2], the United Nations' Department of Economic and Social Affairs project a global population growth to 8.5 billion in 2030, 9.7 billion for 2050 and about 10.4 billion for 2100 (Figure 1).

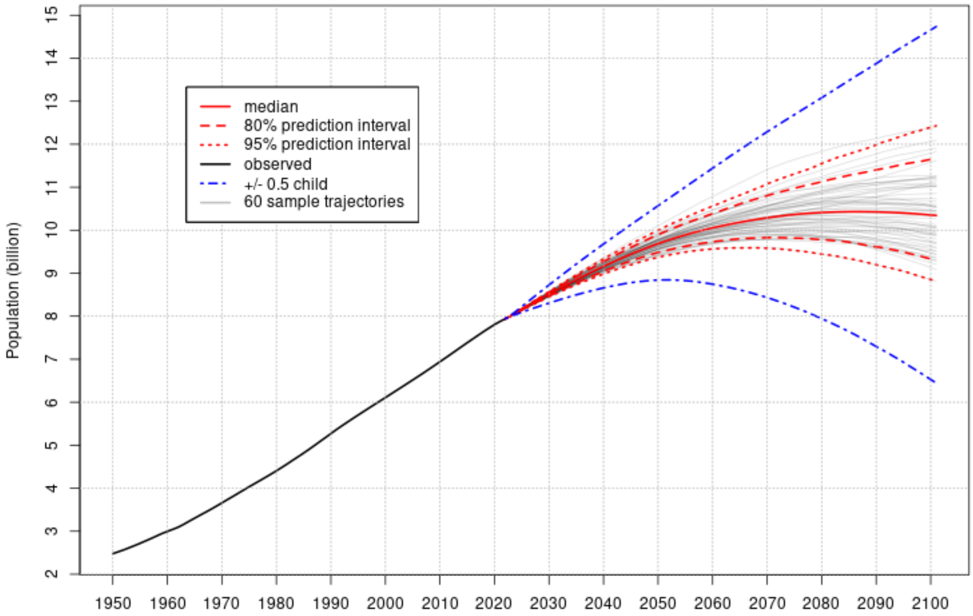

Figure 1: World total population with probabilistic projections plotted from the United Nations' World Population Prospects 2022 database[22]

World ever-increasing population growth is a major cause of concern since more people will necessitate energetic resources for their basic and greater needs. In fact, the energy problem constitutes a complex challenge that has to be tackled from every socio-economic aspects of the World and has been in the center of most of historical and geopolitical tensions and wars. In its annual *World Energy Outlook* (WEO) reports as well as in its various analyses and perspective works, the International Energy Agency (IEA) provides comprehensive studies on all the widely spread energy sources and linked technologies plus resources. Data, statistics and analyses are provided for over a hundred countries, giving rise to complete and precise projections for the upcoming years. Supported by diverse recommendations, roadmaps, tracking and forecasts, their reports not only take into account scientific data on the environment and climate but also consider current political policies, decisions and international cooperation on climate-related issues (e.g. Paris Agreements or Sustainable Development Goals) but also geopolitical conflicts (e.g. Russia-Ukraine war), economic trends (e.g. photovoltaic solar cells wide implementation or US, European Union and China's economic measures) or global health emergencies (e.g. COVID-19 pandemic). Considering these aspects, outlooks are given based on three different views of the future or *scenarios*. The **Stated Policies Scenario (STEPS)** is based on the up-to-date energy, climate and industry policies. Then the **Announced Pledges Scenario (APS)** presumes that every (inter-)national energy and climate objectives made by governments are encountered without time delay. A more challenging scenario for which the World should take for its best would be the **Net Zero Emissions by 2050 (NZE)** in which +1.5 °C would be the limit increase in global warming. According to the latest published *World Energy Outlook 2023* report[1], the global energy demand for 2030 in the STEPS scenario – a more down-to-earth scenario with nowadays policies – is expected to increase by 1.07% compared to 2022 to reach 670 exajoules (EJ, 1 EJ = 10^{18} Joules). However, in every scenario the need for renewables energies is in constant increase where all fossil fuels demand decline starting from 2030 (Figure 2).

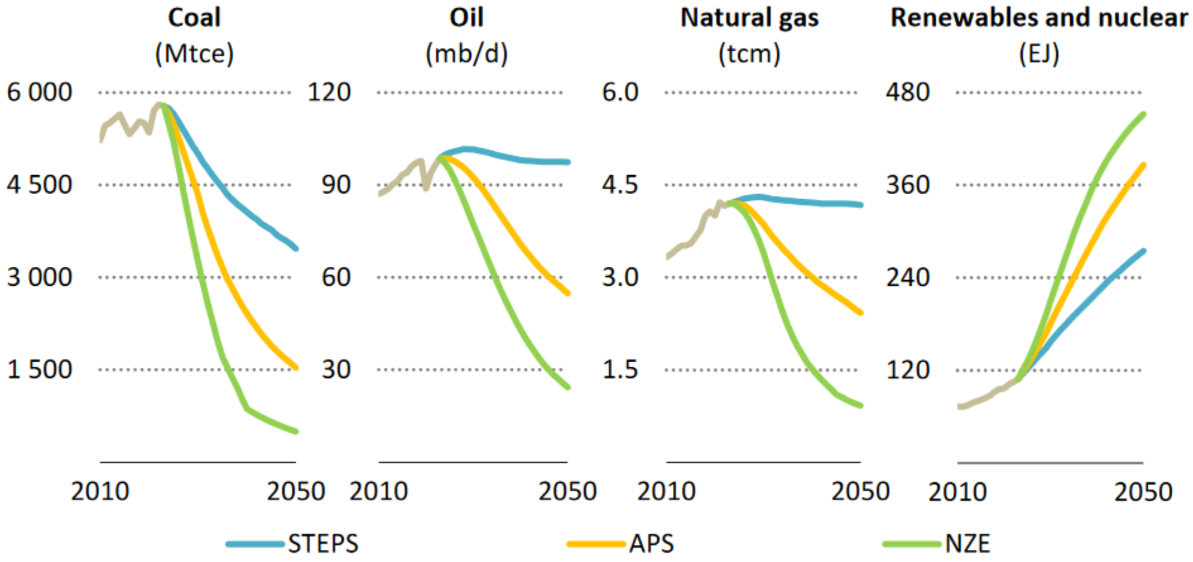

Figure 2: Global total energy demand by fuel and scenario, 2010-2050[2], with Mtce = million tonnes of coal equivalent; mb/d = million barrels per day; tcm = trillion cubic metres

The concealed target to achieve a significant decrease of CO_2 emissions over the years while fulfilling the requirements to provide enough energy in every sector of the World is to pass through the electrification of our surroundings. It implies the replacement of commonly used fossil fuels in diverse technologies and operating systems by electrically powered equals in most of the areas possible[23]. This includes industrial sector as well as the transport and building sectors in which the challenge is to achieve full decarbonization with shift to renewable source of energies – implying low-carbon – during electricity generation. Certainly, the electricity demand to accommodate all the necessities is for every sectors but also regions of the World (Figure 3), which face different issues depending on their population growth rate, economic situations of individuals and nations, political policies or even environment-related scarcity in primary needs.

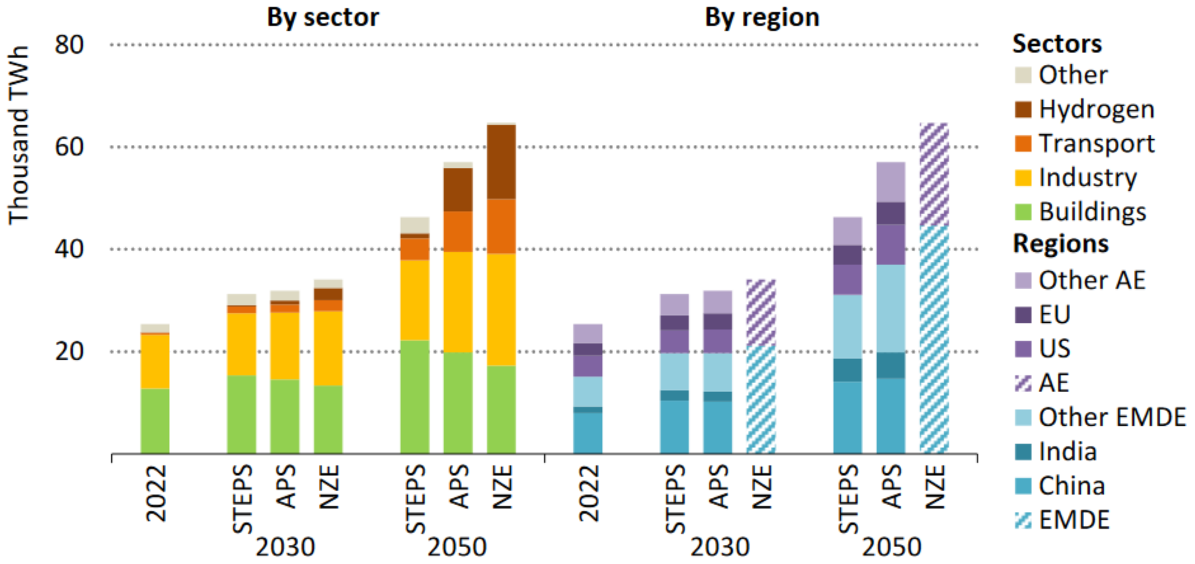

Figure 3: Electricity demand by sector and region, and by scenario[1]. EMDE: emerging market and developing economies; AE: advanced economies; US: United States; EU; European Union

Furthermore, not only the overall population growth affects the general electricity demand but also the raise in quality life of individuals subjected to better wages in advanced and developing countries. International cooperation pushes towards the development of low-carbon emission transportations like electric vehicles (EVs) or production of clean hydrogen. The IEA states that the transition to electric transportations represents one of the major plan to reduce drastically CO_2 emissions for 2050. Undoubtedly, those diverse strategies require the evolution of the current technologies and their development in bigger scale. This implies the extraction of crucial minerals and element for specific technologies and applications such as Silicon for photovoltaics (PVs), Copper for the grids, or Lithium for battery storage and EVs (Figure 4). Unfortunately, the uneven distribution of these elements on Earth is a source of diverse conflicts in the World and terrible working conditions (e.g. Cobalt extraction in DR Congo).

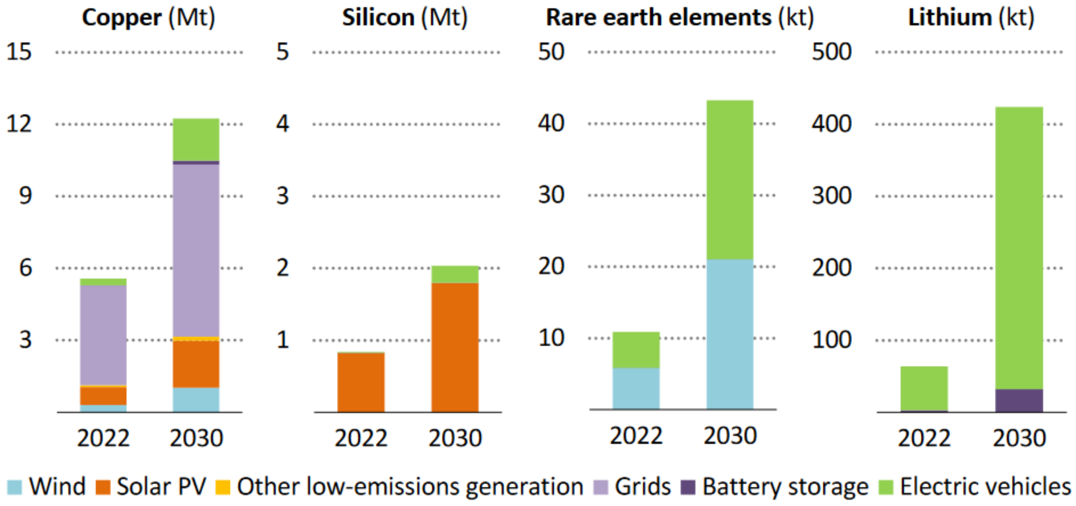

Figure 4: Critical minerals demand by technologies in the APS scenario for 2022 and 2030[1]

Electricity storage technologies are representing an indispensable part to reach these ecological and socio-economic goals. Different actors around the World push the cooperation to speed up electrification at the national and international scale. Among them, the BATTERY 2030+ roadmap is a large-scale research initiative from the European Union to accelerate development in the field of batteries at European level[24]. The main objectives of the initiative are to invent highly performant, sustainable, safe, affordable and long-life batteries while providing tools and advance technologies for the industry for a long-term European leadership in the transport and stationary markets as well as for future upcoming fields. Three themes are distinctly designed with their own aim such as the acceleration of discovery, optimization of battery materials, interfaces and cells; integration of smart sensing and self-healing functionalities to increase reliability, safety and life cycle; and introducing manufacturability and recyclability in the very beginning of research and development of batteries (Figure 5).

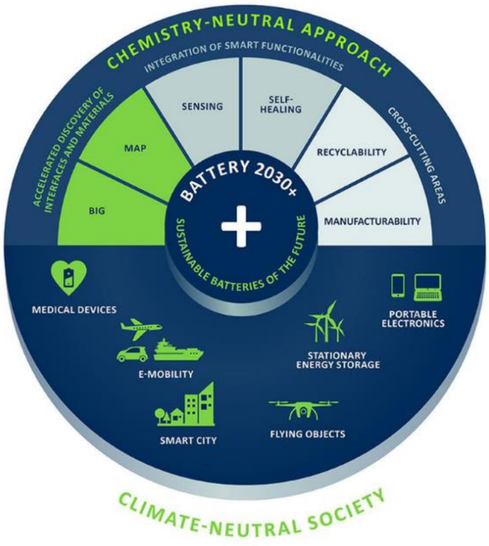

Figure 5: Illustrative approach of the BATTERY 2030+ initiative[24]

Electrochemical Energy Storage Devices

A brief history of batteries and supercapacitors

Electricity management and storage represent a vital point for the sustainability of societies and diverse technologies are under development to address the needs. Electrochemical energy storage devices (EESDs) play in our everyday life and will continue to play an important role for the future of energy storage due to their high conversion efficiency of chemical energy to electrical energy, high range of energy and power densities while operating without toxic gas emission. Nowadays, they can be found in different forms according to their applications – stationary or portable – in forms of batteries or electrochemical capacitors to cite the most famous and commonly used electrochemical cells.

- Batteries
    - Primary (non-rechargeable) batteries

Alessandro Volta presented the first trace of an electrochemical conversion reactor, or battery, in 1800 with the invention of the voltaic pile[25]. It is constituted of a stacking of units/cells, each one composed of copper and zinc disks separated by a kind of brine tissue/cloth acting as the electrolyte (Figure 6 middle). Voltaic pile represented a real revolution in comparison to the pre-existing Leyden jars – ancestor of capacitors – in the mid-18th century in which electrical charge was only stored physically between two electrical conductors separated by a dielectric material (e.g. glass) and released in one time. Continuous electricity and "stable" current flow were obtained, posing the basis of electrochemistry with chemical reaction and production of electricity and the influence of the latter on chemicals. Note that in this voltaic pile configuration, only the Zn is the electrochemically active species while the Cu serves as a metallic current collector (Figure 6 right). Indeed, here the Cu acts as a catalyst for the hydrogen evolution reaction (HER) and other chemically inert metal could be used instead at condition that it develops a weaker overpotential than the Zn towards the HER. This first battery is actually a Zn/H^+ pile with an electromotive force (EMF) – maximum potential difference between the two electrodes of the cell or "strength" of the pile – of about 0.76 V that can be calculated from the thermodynamics data of standard electrode potential[26] (Figure 6 left). The main drawback of this pile was the self-discharge at open-circuit voltage (OCV) with the reduction of proton at the Zn surface and a strong polarization due to the collection of hydrogen bubbles on the metallic current collector. This breakthrough technology allowed future chemists to isolate for the first time diverse element in relatively large quantity to study them including metallic lithium Li in from molten lithium chloride salt electrolysis in 1855 by Robert Wilhelm Bunsen[27] – an essential element for nowadays batteries. Due to drawbacks such as low potential and current, self-discharge or polarization, the voltaic pile needed to be improvement. Thus, scientists worked on the development of new configurations/architectures of the device, different composition of the electrodes or electrolyte.

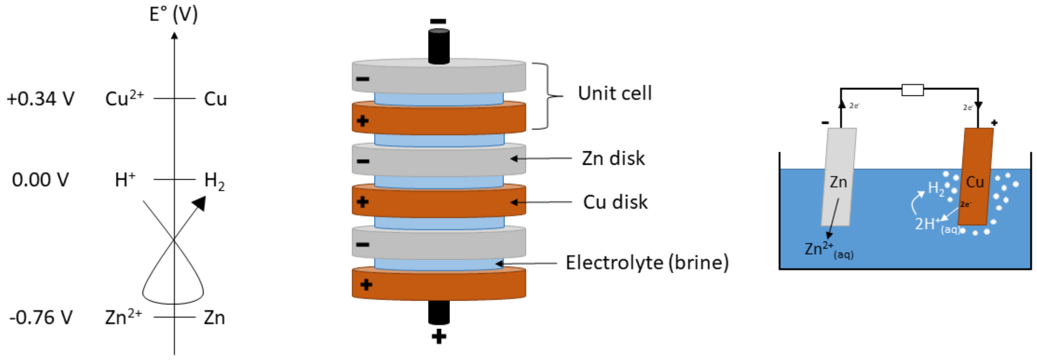

Figure 6: Standard electrode potentials showing the spontaneous oxydoreduction reaction between the proton H^+ and Zn (left); Voltaic cell stacking composed of three cells made of a Zn disk, Cu disk and brine as electrolyte (middle); illustrative scheme of a working cell of Zn and Cu disks in brine electrolyte (right)

Diverse primary systems derived from the Volta's pile came out with the Daniell cell in 1836 as a first major innovation to solve the hydrogen bubble formation[28,29]. John Frederic Daniell following works from Antoine César Becquerel proposed a two-compartment cell separating the Zn electrode in a sulfuric acid solution and the Cu electrode in a copper sulfate aqueous solution by a porous earthenware as membrane (Figure 7 middle-left). Zinc sulfate aqueous solution was then used instead of the sulfuric acid solution, both metal electrode plunging in an aqueous solution of their own ion salts (Cu^{2+} and Zn^{2+}). Each compartment is in direct contact between the oxidizing agent (M^{2+}) and the reducing agent (M^0) of the same redox couple. The two metal electrodes are connected by an electrical circuit and the ionic solutions by an electronically insulating ionic junction. Separating the flow of ions and electrons involved in an electrochemical reaction and thus producing a controllable reactor whose spontaneous behavior releases a quantity of work ($\Delta_r G$, Gibbs free energy change of a reaction) proportional to the number of electrons exchanged (n_{e-}) and the potential difference (ΔE) at which this reaction occurs (Figure 7 left). Hence, the active couples here are not H^+/H_2 and Zn^{2+}/Zn anymore but Cu^{2+}/Cu and Zn^{2+}/Zn. This has an impact to enhance the EMF to 1.10 V, enabling more electric energy release (ΔE proportional to the energy density of the device), limiting the self-discharge to the inter-diffusion of ions in the ionic junction membrane and the Zn metal electrode not being constantly consumed. Other configurations were designed out of the Daniell cell such as the gravity cell. Armand Callaud designed a cell consisting of a zinc sulfate solution floating in direct contact on top of a copper sulfate solution thanks to different densities (Figure 7 middle-right), so that the ionic junction is only limited to the interface between the two liquids[30]. The higher ionic diffusion at the interface results in higher currents due to a minimized internal resistance. Note that the electrodes can have various specific geometry such as crowfoot to maximize the contact surface with the electrolytes. However, this architecture implies that it can only be used in stationary conditions not to mix the solutions, necessitates a continuous work to limit the metal ions diffusion through the interface and, a regular maintenance by dilution of the ever-increasing concentration of zinc ions in the supernatant solution to keep a sufficient density difference. A different designed following Callaud's battery is the Meidinger's cell (Figure 7 right) in which the copper sulfate solution is in contact in a balloon containing copper sulfate crystals acting as a solid reservoir[31]. This particular cell allows enhancing the energy density with higher active species concentration and a constant imposed potential imposed by the solubility constant of both salts. Nevertheless, these first technologies were not applicable for transportation and required constant maintenance.

$$\Delta_r G = -n_{e^-} \cdot F \cdot \Delta E$$

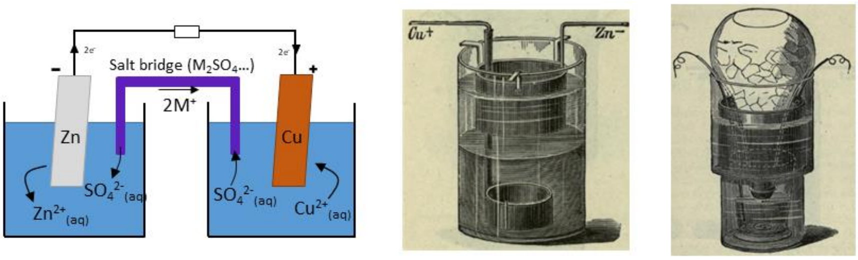

Figure 7: Relation between Gibbs free energy change of a reaction, the number of electron involved in it and the potential difference of the two half-reactions (left); Illustrative scheme of a Daniell cell (middle-left); Callaud's cell (middle-right)[31]; Meidinger's cell[31]

In parallel to these works and in order to resolve the issue of polarization of hydrogen bubbles forming at the surface of the current collector in voltaic piles, the research of batteries will take a different lead for the research of new materials and electrolytes. Indeed, one might think to "absorb" the hydrogen by a "depolarizing" material, Georges Lionel Leclanché created a battery of approximately 1.4-1.5 V EMF by using a natural manganese dioxide MnO_2 (NMD) at the cathode, mixed with carbon to offset the poor electronic conductivity of this oxide and conserve wetness, zinc at the anode and an ammonium chloride solution as electrolyte (Figure 8 left)[32]. According to the different degree of discharge, the cell reaction can see some variations also due to the complexity of the manganese oxide MnO_x non-stoichiometry. A general simple reaction considering ammonium chloride could be given as follow[33]:

$$2\,MnO_2\,(s) + Zn\,(s) + 2\,NH_4{}^+\,(aq) + 2\,Cl^-\,(aq) \rightarrow 2\,MnOOH\,(aq) + Zn(NH_3)_2Cl_2 \qquad (1)$$

The Leclanché wet cell was starting to be commercialized. However, the aqueous and liquid nature of the electrolyte had a tendency to dry out, rendering the cell unusable. For this reason, starch was added to the electrolyte in order to obtain a more viscous and less likely to leak cell. Later on, zinc chloride was added to the ammonium chloride aqueous electrolyte to improve the EMF slightly more for the second generation of Leclanché cell. Then, aqueous zinc chloride electrolyte was used alone providing better performance in terms of energy density per mass or volume, stability and a slightly slower self-discharge rate. In addition, the zinc chloride has the effect of reducing the corrosion on the Zn anode. In 1886-1887[34], Gassner modified the Leclanché cell by using ferric hydroxide $Fe(OH)_3$ and manganese dioxide MnO_2 as the cathode electrode and gypsum plaster to the electrolyte of ammonium and zinc chloride to obtain a not-leaking paste. This technology, known and popularized as the zinc-carbon battery, will mark the industrial history with a complete switch from wet cells to dry cells more useful and safe for portable usage. Unlike the glass jar for the Leclanché cell, the dry zinc-carbon cell had a solid and very robust cylindrical shape composed of a cathode mix enclosed with cloth and saturated electrolyte. This architectural conception reduced chemical undesired reactions, hence improving the cell's shelf life (Figure 8 middle and right). Ammonium chloride can also be omitted in following zinc-carbon generations.

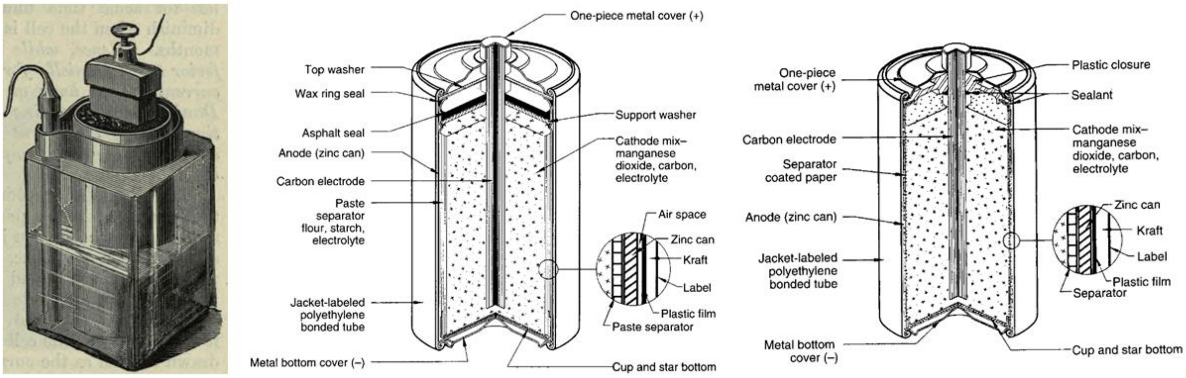

Figure 8: Illustrative scheme of a Leclanché cell as conceptualized primarily (left)[31]; Commercialized ''Eveready'' cylindrical Leclanché battery (middle)[33]; Commercialized ''Eveready'' cylindrical zinc chloride battery (right)[33]

More revolutionary, the switch from saline to alkaline electrolyte marked the importance on how the choice, and hence, the role of the electrolyte has an impact on the overall performance of the battery. The zinc-carbon or Leclanché battery was already a well implemented technology but the use of alkaline electrolyte in a similarly modified system, in comparison to saline/acidic electrolytes, revealed more advantages.

After the implementation of caustic electrolytes – mostly potassium hydroxide KOH – in these technologies in the late 1950s[33] , the Zn/MnO_2 alkaline batteries were recognized as clearly superior to the zinc-carbon batteries using the same electrode configuration except a more or less neutral electrolyte. The main advantages of such alkaline batteries compared to ammonium/zinc chloride electrolyte zinc-carbon batteries are higher energy density and capacity at various rates, enhanced low-temperature working performance, diminished leakage and internal resistance and, longer shelf life. The developed alkaline Zn/MnO_2 is essentially composed of a cathode mixture of electrolytic manganese dioxide (EMD) and carbon conductive agent (e.g. graphite), zinc powder as the main anode active material and potassium hydroxide as the electrolyte. EMD differs from the commonly used natural manganese dioxide ore (NMD) having greater purity, higher content of manganese – especially γ-MnO_2 being more active than manganese oxyhydroxide MnOOH found in greater quantity in NMD – and higher activity. The γ-MnO_2 used here – with a natural crystal structure name nsutite (Figure 9 right) – corresponds to an intergrowth of the β-MnO_2 (i.e. pyrolusite, Figure 9 left) and R-MnO_2 (ramsdellite, Figure 9 middle) forming 1 × 1 and 1 × 2 tunnels respectively[35,36], having a lower tendency to obstruct the surface during electrochemical product formation. Potassium hydroxide is used instead of sodium hydroxide mostly due to its higher ionic conductivity over a range of KOH weight composition in water, higher range of discharge rate and reduced cell gassing rate that could occur while zinc corrosion for instance. The anode zinc in powder form allows a higher specific surface area compared to a bulkier zinc metal plate for instance. It provides a lower concentration polarization due to a better distribution of the solid within the electrolyte phase in the anode cell. As a result, lower internal resistance is achieved and higher power density. Overtime, Hg is incorporated for the anode to form an amalgam with the Zn to prevent its corrosion. Indeed, zinc being unstable in water, it will produces H_2 gas due to water reduction limiting the performance and stability of such alkaline batteries.

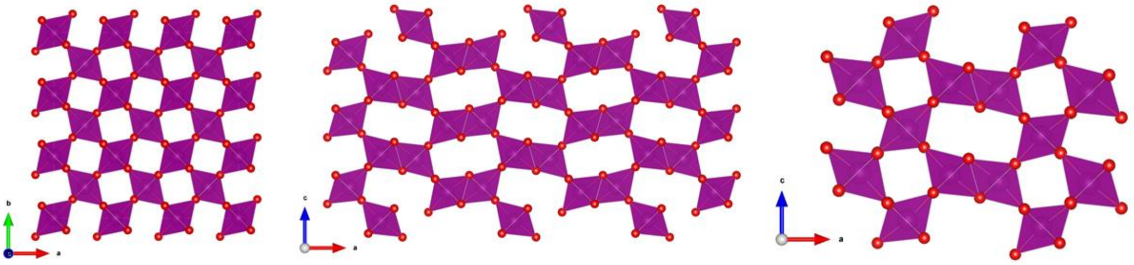

β-MnO_2
Pyrolusite

R-MnO_2
Ramsdellite

γ-MnO_2
Nsutite (intergrowth)

Figure 9: Figure 9: Crystal structures of β-MnO_2 Pyrolusite (left); R-MnO_2 Ramsdellite (middle); γ-MnO_2 intergrowth

After the "The Mercury-Containing and Rechargeable Battery Management Act - Public Law 104-142" in 1996[37], the use of mercury is no longer authorized in batteries due to toxicity, health and environmental issues. To overcome Hg usage, diverse strategies are explored. One is to use other metal cation additives of indium In, tin Sn, gallium Ga, lead Pb or even bismuth Bi having high hydrogen evolution reaction (HER) overpotential[38]. Furthermore, the used zinc might contain metal impurities of copper Cu^{2+}, nickel Ni^{2+} or others (i.e. iron Fe^{2+}, cobalt Co^{2+}, arsenic As^{3+} or antimony Sb^{3+}) which are active for the HER, a reaction that is needed to be avoided as mentioned. Hence, increasing the purity of the zinc (less active metal impurities towards HER), manganese sources (more γ-MnO_2 active phase), electrolyte and can container represents also a major strategy. Some ZnO is also added in the electrolyte to saturate it with Zn^{2+} and by so to thermodynamically push the reaction to avoid the metal zinc oxidation. The Zn electrode can also be alloyed with a small amount of aluminum Al to reduce the corrosion occurrence[39]. The alkaline Zn/MnO_2 is a great example of a technology that matured through decades of scientific and industrial research and is still widely commercialized and used worldwide

(Figure 10). In addition, since its development in the 1950’s - with one of its first prototype from Energizer in 1957[40] - the alkaline battery saw its energy density almost triple (<40-45 Wh/g to ~140 Wh/g) in the 2020’s[40,41].

1800
Volta’s pile
Zinc **anode**
Copper (current collector)
Proton H^+ **cathode**
Brine **electrolyte**

1836
Daniel cell
Zinc **anode**
Copper **cathode**
$ZnSO_4/CuSO_4$ aqueous **electrolyte**

1866
Leclanché cell
Zinc powder **anode**
Natural MnO_2 (NMD) with carbon conductive agent **cathode**
NH_4Cl **electrolyte**

1887 – 1950’s
Zinc-carbon battery
Zinc powder then Zn-Hg amalgam **anode**
Natural MnO_2 (NMD) then Electrolytic MnO_2 (EMD) with carbon conductive agent **cathode**
$ZnCl_2$(/NH_4Cl) **electrolyte**

1950’s – 1960’s
Alkaline battery
Zn-Hg amalgam **anode** (only Zn in 1996)
Electrolytic MnO_2 (EMD) with carbon conductive agent **cathode**
KOH **electrolyte**

Nowadays
Alkaline battery
Zn **anode**
Electrolytic MnO_2 (EMD) with carbon conductive agent **cathode**
KOH **electrolyte** and other **additives**

Figure 10: Development and evolution of alkaline batteries overtime[31,42–45]

To improve even more the performance of primary batteries, metal lithium is considered as a promising candidate as anode material electrode due to its very low molar mass and its high electrochemical equivalence (i.e. mass of an element transported by an electric charge) enabling higher theoretical capacities and energy densities, high voltage (up to ~4.0 V) and conductivity. It is without surprise that researchers dug for a high-performance primary lithium battery technology since the 1960’s and following decades. Lithium being highly reactive with water, non-aqueous aprotic organic/inorganic solvents with a salt – to ensure ionic conductivity – are used as electrolytes instead. Among the most commonly used polar organic solvents, acetonitrile, propylene carbonate, dimethylsulfoxide (DMSO), 1,2-dimethoxyethane (DME) or even methyl formate can be cited, each of them having different properties according to the desired application and performance (e.g. boiling/melting/flash points, density or specific conductivity for a specific lithium ionic conductive salt). Concerning inorganic solvents, thionyl chloride $SOCl_2$ or some sulfuryl chloride SO_2Cl_2 are usually found. In comparison to alkaline batteries mostly relying on Zn/MnO_2 electrodes and caustic KOH electrolyte, lithium primary cells can be categorized in different technologies using metal lithium in each but different electrolyte/solute composition and cathode materials, hence different lithium chemistries (Figure 11). The two most common are the cells using a soluble liquid/gaseous cathode with a salt-containing organic or inorganic electrolyte or, a solid cathode with salt-containing organic electrolyte. Soluble cathode cells have the advantages to have very limited self-discharge of the lithium anode due to the active cathode materials – the electrolyte or dissolve in it – passivating the anode through a reaction between the two electrodes and, designable in different manners to provide low to high discharge rates and with different capacity ranges. Solid cathode cells cannot provide high rates due to solid nature of the electrode but does not necessitate pressurizing a liquid or gas active material.

More for niche application such as in medicine with pacemakers, solid electrolyte cells also exist working for low rate for a very long shelf life (up to 20-25 years) without any leakage.

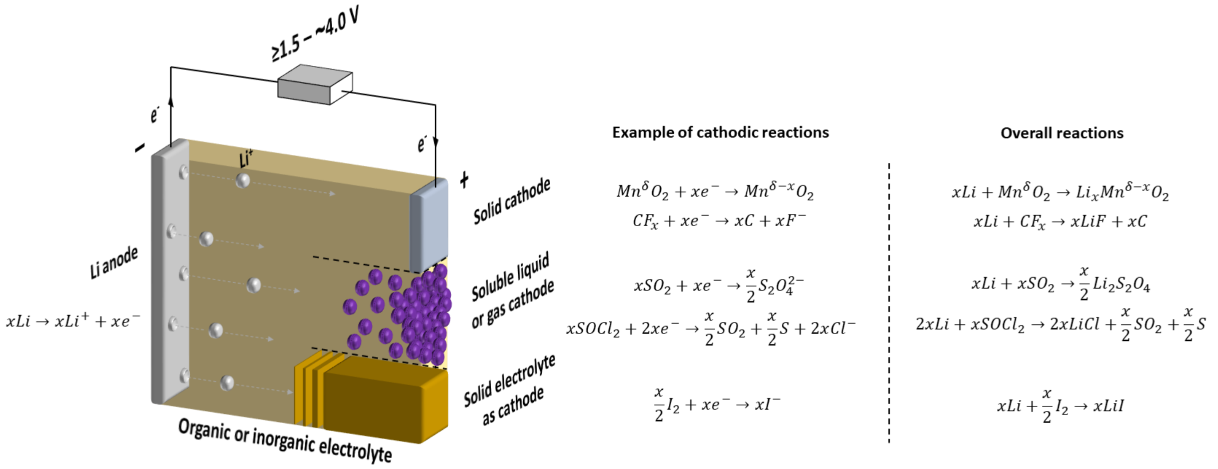

Figure 11: Lithium primary batteries common technologies and cell discharge mechanisms

Even though lithium was first isolated by electrolysis of lithium oxide in 1821 by William Thomas Brande[46], the bulk production by the same method but from molten lithium chloride salt by Robert Wilhelm Bunsen in 1855[27] opened the place for an extensive study of metallic lithium. It is in few decades later, in 1913, that lithium's electrochemical characteristics were observed by Gilbert Newton Lewis and Frederick George Keyes[47]. Nevertheless, for a hypothetical application of metal Li as an anode material, the use of aprotic organic solvents was one of the main concern to deal with. Jan Hajek published deposited a patent in 1949 entitled "Electrolyte for lightweight electrodes" (translated from the French "Electrolyte pour des électrodes de poids légers")[48] presenting aprotic organic and inorganic solvent and ionic salt combinations to reach 3.0 V of EMF and more. His patent is considered a pioneer work on the development of lithium primary batteries. Later on, William Sidney Harris presented his thesis 1958[49] showing the solubilities of diverse salts including lithium bromide LiBr, lithium chloride LiCl and lithium iodide LiI in various aprotic organic solvents (i.e. cyclic esters) which are ethylene carbonate, propylene carbonate, γ-butyrolactone and γ-valerolactone. Also very interesting, the electrodeposition of lithium metal from saturated LiBr salt provided a stable metal electrode in the used organic solvents. These different results led the following years in research of practical primary lithium cells using such kind of electrolyte solvent and ionic conducting salts.

One of the first lithium battery, the lithium/sulfur dioxide Li/SO_2 technology, was patented in 1969[50] and is currently one of the most developed providing very high energy density (~ 300 Wh/kg, 415 Wh/L). It belongs to the soluble cathode category (SO_2 cathode) and can provide high-rate capabilties with high current capacities and long shell/life at good working temperature range. Due to the use of SO_2, the internal pressure of the battery is very high (few 10^5 Pa) and is reducing upon discharge since it is consumed and forming a lithium dithionite $Li_2S_2O_4$ precipitate (Figure 11).

Generally, the cathode SO_2 is the limiting reactant since it can be blocked by this precipitation. Nevertheless, this one is also responsible for the durability of the battery since a film protective layer is formed on the lithium anode. As another example of a soluble cathode, the lithium/thionyl chloride Li/$SOCl_2$ – patented in 1969 by J-P. Gabano[51] - is considered as one of the most powerful primary battery technology (~ 590 Wh/kg, 1100 Wh/L) thanks to its high operational voltage window of 3.6 V. Thionyl chloride $SOCl_2$ not only serve as the active cathode material (with porous carbon substrate) but also as the electrolyte solvent in which an ion conducting lithium salt is dissolved (typically $LiAlCl_4$). Besides its excellent performance, $SOCl_2$-based soluble cathode are considered more dangerous than SO_2 technology. Indeed, the discharge products are SO_2 gas increasing the internal pressure of the cell and sulfur S that could react with the lithium anode into Li_2S through an exothermic reaction (ΔrH^o = -447 kJ/mol). However, they can operate in a long range of temperature due to the physical properties of $SOCl_2$ (m_p = -101 °C, b_p = 75.6 °C[26]).

As for the alkaline primary batteries, manganese dioxide was also considered as a solid cathode active material for the lithium technology. Indeed, the Li/MnO_2 battery firstly commercialized by Sanyo in 1976[52] – and now the most used primary battery – has attractive characteristics such as its voltage window superior to 3.0 V, high energy densities (~ 280 Wh/kg, >580 Wh/L), low cost of material and safety. The overall reaction mechanism consists on the intercalation of lithium cation inside the MnO_2 cathode into Li_xMnO_2 (Figure 11). The second solid cathode technology concerns the lithium/carbon monofluoride Li/CF_x in organic solvent patented in 1970 by Watanabe and Fukuda[53] from Panasonic. The CF_x is an intercalation compound in which the discharge product would be an intermediate compound graphitic carbon, Li^+ and F^- due to the intercalation of lithium cation inside the active cathode material[54]. LiF is also forming as a precipitate at the cathode during the discharge. The transition towards a graphitic carbon is accompanied with an increase in the electronic conductivity of the cathode, leading to enhance discharge efficiency. These Li/CF_x batteries can serve low-to-medium capacity rate compare to soluble cathodes, be manufactured in various cell types and still provide high energy densities (~250 Wh/kg, >630 Wh/L). Finally, the solid-electrolyte cathode material technology is well implemented for pacemakers, introduced with the lithium/iodine Li/I_2 cell in 1972[55] and still the only one produced nowadays. For such medical applications, a very long shelf life is required with a low-rate operation condition. Iodine I_2 and poly(2-vinylpyridine) (PVP, organic donor and complexing agent) are mixed together to cover up the lithium anode and in a typical discharge, lithium iodide LiI is formed acting as a separator between the cathode and the anode (discharging causes a progressively increase on the thickness and hence internal resistance) but also as the solid-electrolyte.

- Secondary batteries (or rechargeable batteries)

In parallel with the development of the primary batteries in the 19th century, the consideration for rechargeable batteries were already in the minds of scientists of that time[56]. Prior to the invention of the first secondary batteries/accumulators, it is important to note that thermodynamically the storage of energy is fundamentally non-spontaneous. In other words, energy has to be provided if one wants to recharge a battery (spontaneous system). For batteries, the spontaneous reaction is referred to the discharge mechanism occurring between a reduction half-reaction at the cathode (or positive electrode) and an oxidation half-reaction at the anode (or negative electrode). Hence, energy is demanded – typically electrical energy – to recharge a battery by reversing these reactions and providing available chemical energy. This conversion between chemical energy to electrical energy, and *vice-versa*, is at the core of rechargeable batteries research.

Gaston Planté introduced the very-first rechargeable cell in 1859 (Figure 12 left) with the famously known lead-acid batteries [57]. The architecture relies on the corrosion of a lead Pb plate into the positive active electrode lead dioxide PbO_2 in an aqueous sulfuric acid H_2SO_4 solution electrolyte and a porous surfaced Pb plate as the negative electrode (Figure 12 right). Camille Alphonse Faure improved the technology starting from 1880[58] and leading to the industrial development of the lead-acid battery thanks to further of his work[59]. The positive electrode constituted of a lead foil was improved by pasting or electroplating an active lead-based material, such as lead oxide directly, and covered with a porous inert surface to main the active composition onto the plate. Gladstone and Tribe established in 1882[60] the chemistry inside the lead-acid battery involving a double sulfate theory with lead sulfate production at each electrode during discharge, experimentally proven later on by Hamer and Harned in 1935[61]. The chemistry entails bond breaking and creation at each cycle with the $PbO_2/PbSO_4$ and $PbSO_4/Pb$ couples accompanied by the solvent consumption during charging and the solute (H_2SO_4) during discharge. The lead-acid battery can achieve 2.0 V of tension – surpassing the water stability domain – due to high overpotentials. One major drawback of such accumulator is the production of the lead sulfate insulating salt making difficult the battery recharge after a quasi-fully discharge state.

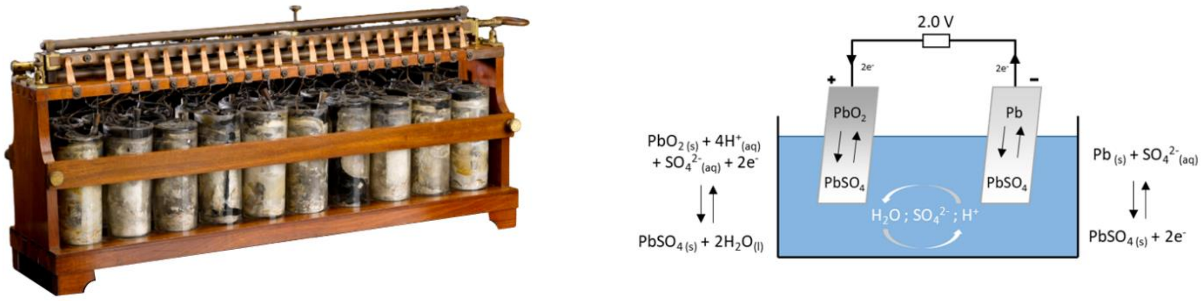

Figure 12: Initially designed lead-acid battery by Gaston Planté in the early 1860's (left)[62]; Charge-discharge mechanisms of a lead-acid battery

Nowadays, approximately half of the automobile vehicles are still equipped of lead-acid batteries due to their ease of manufacture in different size designs and good high to low-rate capability, electrical efficiency, and relatively high operating voltage in aqueous media (~ 2.0 V). However, they lack in terms of energy densities (~30-40 Wh/kg) and low-to-moderate cyclability (ca. <1500 cycles for traditional models and up to few thousands with the modern ones). The limiting cycling efficiency and low reversibility is explained by the high structural and crystallographic tensions occurring during each cycle. Indeed, the reactions are reconstructive which means that bonds are broken and recreated during charge and discharge. Hence, new electrode materials that could handle such reaction without processing to high constraints during charge/discharge mechanisms are needed.

The next challenge is using an electrode material that would have limited constraints during redox transitions. For such purpose, nickel in an oxidized form match the requirements. More precisely, NiOOH/Ni(OH)$_2$ electrode gives rise to intercalation reaction in which protons are reversibly inserted/extracted from the stable lamellar structure with no Ni-O bonds breaking. Waldemar Jungner established the first nickel technology in 1899[63], known as the nickel-cadmium Ni-Cd accumulator. The working operation voltage is set to the water stability domain of ~1.2 V with a nickel oxyhydroxide NiOOH/nickel hydroxide Ni(OH)$_2$ couple at the positive electrode and a metallic cadmium Cd/cadmium hydroxide Cd(OH)$_2$ couple at the negative electrode in an alkaline electrolyte, usually KOH (Figure 13). As stated previously, the nickel oxide-based positive electrode is a lamellar structure material that reversibly (de-)intercalate protons when undergoing redox transitions between the NiOOH (Ni^{3+}) and Ni(OH)$_2$ (Ni^{2+}) phase improving the electrode stability upon cycling (> 2000 cycle). Nevertheless, the cadmium-based negative electrode material undergoes a highly reconstructive reaction between the Cd^0 and Cd(OH)$_2$ (Cd^{2+}) phases, being the limiting factor of an ever more prolonged cyclability. Up to ~35-60 Wh/kg energy density and ~460 W/kg of power density can be reached with the vented architecture.

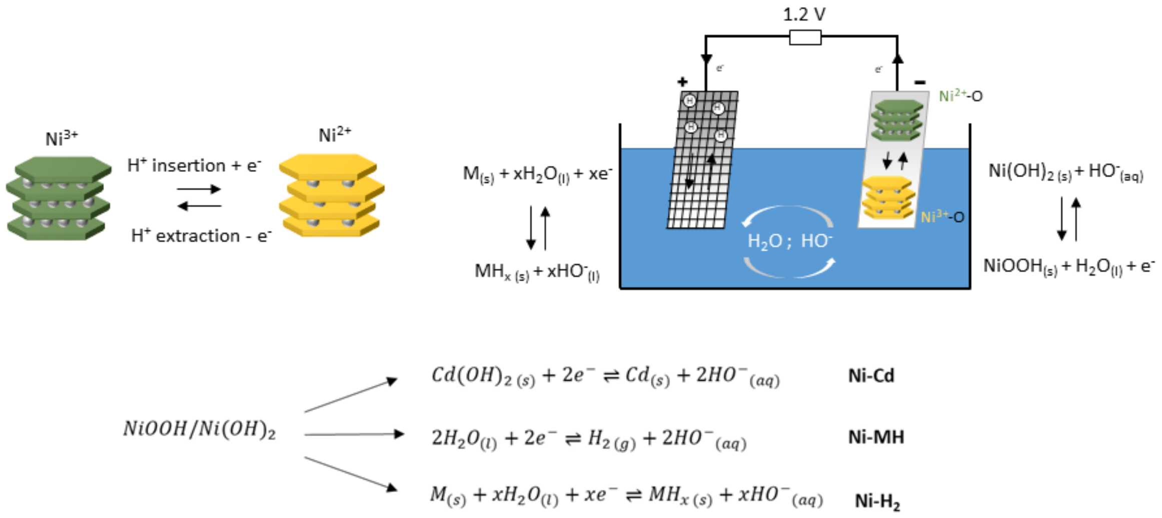

Figure 13: Representation of Ni-based oxide intercalation-type material with Ni^{3+}/Ni^{2+} redox transitions and its application in Ni-Cd, Ni-MH and Ni-H_2 technologies

The second most known nickel technology battery is the nickel-metal hydride Ni-MH developed in the 1970-1980's notably between Phillips laboratories and the French Research National Center (CNRS) .In 1987, Willems and Buschow demonstrated the efficient hydrogen storage in $LaNi_5$-based alloys[64] which led the to a faster development. Indeed, Johnson Control Inc. commercialized the first Ni-MH battery in 1989. Using also an alkaline electrolyte and 1.2 V of voltage window, the positive electrode is still based on the NiOOH/$Ni(OH)_2$ couple but the negative electrode is based on a metal hydride MH_x/metal alloy M couple. Unlike the cadmium electrode, the MH_x/M reaction mechanism corresponds to a hydrogen intercalation leading to better stability upon charge/discharge cycles. Hence, the Ni-MH technology benefits from both electrodes intercalation reaction enhancing strongly the battery shelf life. In addition, hydridable metal alloys provides higher energy density than lead-acid and Ni-Cd batteries due to the lower molar mass compared to Cd and Pb (up to ~ 300 Wh/L). These batteries are still highly employed and commercialized nowadays. A third nickel technology would be the nickel-hydrogen Ni-H_2 battery already prototypes and discovered before the Ni-MH batteries. In fact, works realized on Ni-H_2 directly impacted and led to research on nickel-metal hydrides. Still using alkaline electrolyte, the technology is a combination of a rechargeable battery and a fuel cell by using a nickel oxide positive electrode and a platinum negative electrode (also referred to as hydrogen electrode). Similarly to technologies cited above, the nickel oxide electrode will (de-)intercalate protons upon charge/discharge cycles based on an intercalation half-reaction mechanism. On the other hand, hydrogen H_2 is oxidized at the surface of the catalytic platinum electrode surface into H_2O during discharge whereas water electrolysis occurs during charging with the formation of hydrogen and HO^-. Hence, the concentration in alkaline solute and water remains unchanged within the cell. The cell can also be safely overcharged with the production of oxygen O_2 at the positive nickel-based electrode with a very fast recombination of O_2 to HO^- at the negative platinum electrode. Continuous overcharge can then be provided without change in neither solute concentration nor water quantity while keeping away from thermal runaways. Interestingly, the cell can also operate in reversal mode with two different precharge modes. Hydrogen precharge at the negative electrode with an excess of H_2 in a fully discharged cell such that the cell capacity is not H_2-limited or, nickel positive electrode precharge with a deficit in H_2 in a fully discharged cell such that the cell capacity is H_2-limited[65]. The main advantages of the Ni-H_2 battery are high energy density (~60 Wh/kg) and very long cycling and lifetime (>40,000 cycles, >15 years); but it has a high cost of production (i.e. Pt electrode) and low volumetric energy density (~20 Wh/L). These reasons make them usable for specific applications such as for satellites in orbit that requires very long lifetime.

The well-implemented Ni battery technologies were lacking of energy densities due to the water stability domain of ~1.2 V. Therefore, to increase the energy density of batteries newer electrolytes with extended voltage window are needed but also the use of other elements/materials that would allow higher theoretical capacities. Hence, the half-cell potentials at the cathode and anode dictate the theoretical voltage of the cell. Lithium has the highest reducing potential ($E^o = -3.04$ V) and is then considered as the most electropositive element (i.e. highest capacity to donate an electron to form a cation). The high reducing potential of lithium makes it very advantageous as an anode material and for intercalation of Li^+ ions in an intercalation-type anode material during the charging mechanism. This intrinsic property and the molar mass/density are proper to each element and is the reason why lithium-based technology will always remain more performant compared to other element-based batteries such as sodium. Indeed, theoretical capacities can be calculated according to atomic/molecular weight of the element/compound, its related standard reduction potential, valence change and density. From this data, electrochemical equivalents Z (in g/Ah, Ah/g or Ah/cm^3) can be obtained following the equation:

$$Z = \frac{M}{q} = \frac{M}{i \cdot t} \rightarrow \frac{M}{n \cdot F} \qquad (2)$$

with M the molar mass, q the charge, i the current passed for a time t, n the number of electron involved in the reaction and F the Faraday's constant. The electrochemical equivalent of lithium is Z_{Li} = 3860 mAh/g (or 0.259 g/Ah, or 2.06 Ah/cm^3) and this value allow to obtain the theoretical capacity Q_{th} with the theoretical voltage window by V_{th} considering the voltage difference between the cathodic and anodic reaction:

$$E_{th} = Q_{th} \cdot V_{th} \qquad (3)$$

Coupled to a positive cathode material, around ≥ 3.0 V can be considered giving a starting approximated theoretical energy density of 11.58 Wh/kg. Thanks to these very advantageous properties of lithium, Li-based primary batteries were firstly developed in the 1960's as described previously. The use of aprotic organic electrolyte solvents with a conductive salt is mandatory due to metal lithium high reactivity towards humidity. The successful application of lithium anodes for primary batteries immediately aroused the interest for its usage in rechargeable device. With the development of intercalation-type oxide and chalcogenide cathode materials, metal lithium is considered as anode material with the discharging process involving intercalation of Li^+ into the host cathode material and with the charging process considering lithium ion reduction (or plating) at the lithium anode. Researches were mainly focused on reversible cathode rather than anode material since it was believed that lithium would simply plate back during the charging process. Two major breakthroughs led to development of lithium secondary batteries. The first pioneer works were proposed by Stanley Whittingham in 1976[66] using titanium disulfide TiS_2 as an intercalation-type cathode material to reversibly store and deliver Li^+ using a metal lithium anode in a $LiClO_4$ containing dimethoxyethane and tetrahydrofuran solvent mixture electrolytes. Later on in 1978, Whittingham published a more complete work on other intercalation materials, especially metal dichalcogenides[67]. The second breakthrough – with an industrial scope – is the patent deposited by Exxon Company in 1978 with metal lithium at the anode and cathode mixture of TiS_2 and aluminum Al[68]. This led in the 1970's-1980's to the first commercialized lithium secondary batteries by Exxon Company (TiS_2 cathode, USA) and Moli Energy (MoS_2, Canada). In parallel, the works done by Peter V. Wright in the 1970's on ionic conductive polymer oxides (poly(ethylene) oxide PEO complexes)[69,70] led to the implementation of those in battery technologies with recognized works from Michel Armand starting from 1978[71,72] with Li/PEO electrolyte/V_2O_5 battery. The secondary lithium batteries from Exxon and mostly Molicel were commercialized in the 1980's and used in many cellphones. In August 1989, an unfortunate accident from the cellphone of a Japanese customer that light up and causes burns. The reason behind was the internal short circuit from the lithium plating on the anode. More specifically, an ionic conductive passivation layer occurring from the lithium reactivity with the electrolyte – called the solid electrolyte interphase SEI – provokes irregular lithium deposition at the anode upon charging process. Lithium dendrites formation and growth can result in a short circuit of the cell that could lead to very exothermic reactions, thermal runaway and incidents related to those issues. After this accident, all the batteries and cellphones were taken back leading to the halt of sales, suspension of shares trade and put the company into sale[73].

The use of lithium metal anode as described was not viable for a secondary battery usage and safer options were rightly investigated among the scientific community and battery tech companies. Among the proposed options, either novel electrolytes enabling the dendrite-free deposition at a lithium metal anode or the replacement of lithium metal anode by another anode material preventing the same plating issue previously stated. An ionic conductive polymer as electrolyte, researched extensively by Michel Armand as mentioned, could be a promising solution. Few technologies were developed based on the Li/PEO/V_2O_5 but never reached the large-scale commercialization of such batteries due to the ongoing fears and unsolved issues of lithium metal anodes. On the other hand, the research on another reversible intercalation-type cathode material attracted most of the intention. The concept would rely on the intercalation of the lithium contained in the cathode into the anode material host during the charging and reversed during the discharge. The performance and reactions occurring within the battery cell would then depends on xLi^+ equivalents being intercalated. These kind of systems where only specific ionic charge carrier – here the lithium ion – is moved or "rocked" within electrolyte between the cathode and the anode are referred to rocking chair batteries RCBs. Concerning the first lithium ion cathode material, the $LiCoO_2$ (LCO) lamellar oxide brought into light by John B. Goodenough in 1980[74] and is still widely nowadays used either for fundamental research scope or industries. In the same moments, $LiMn_2O_4$ (LMO) was also investigated in 1983[75]-1984[76] by Michael M. Thackeray and J. B. Goodenough as an alternative to cobalt use. Manganese is more abundant, cheaper and less toxic compared to cobalt and $LiMn_2O_4$ provides extended thermal stability at the expense of manganese dissolution. Even though lithium ions can intercalate reversibly and maintain the structural integrity of the cubic spinel phase of $Li_xMn_2O_4$ for the $0 \leq x \leq 1$ lithium window, further intercalation ($1 < x \leq 2$) around ~3.0 V leads to Jahn-Teller distortion with the transition to Mn^{3+} and tetragonal phase. The extra electron occupying an e_g orbital is responsible to the crystal expansion and change in volume, leading to an electronic percolation loss within the electrode. In addtition, disproportionation of Mn^{3+} to Mn^{4+} and Mn^{2+} can provoke the dissolution of Mn^{2+} due to traces of hydrofluoric acid HF formed by side reaction of the lithium salt ($LiPF_6$) and water traces (ppm levels is sufficient for it to happen)[77]. To note $Li_{1-x}CoO_2$ also lack of stability due to a very high repulsion of layers when $x<0.5$ and further development will arise in the following years by implement cationic substitution. High voltage stability of LCO would enable higher energy density with extended delithiation ($x>0.5$), to reach the higher theoretical capacity around 270 mAh/g (complete delithiation $x=1$) instead of the usual ~140 mAh/g for approximately half lithium disinsertion. To be more precise, starting from $x=0.5$, LCO lattice distortion occurs with phase transition from the hexagonal to monoclinic phase[78]. Moreover, LCO in a profound discharged state (i.e. lithium content tending to zero) can lead to a high exothermic reaction with the production of cobalt spinel oxide Co_3O_4 and oxygen leading to thermal runaway with reaction with the electrolye[79]. This issue can occur at temperature closed to 200°C.

For the anode material, carbon materials were the most interesting, especially graphitized carbons with a high theoretical reversible capacity of 372 mAh/g considering the uptake of one lithium ion for a six-carbon atom ring:

$$xLi + + xe^- + C_6 \rightleftharpoons Li_xC_6 \qquad (4)$$

Graphite is the major candidate for intercalation-type anode due its layered structure and was used for lithiation in a graphite host structure in organic electrolyte upon a applied voltage by Besenhard and Fritz for the first time in 1974[80]. By the time, organic electrolyte decomposition was already an encountered issue that could lead to lithium plating, which must be avoided. This formation of an insulating but ionic conductive passivation layer will named as the solid electrolyte interface (SEI) few years later in 1979[81]. This passivation layer is due to non-desired non-aqueous reduction since most of the usable and investigated non-aqueous electrolyte lowest unoccupied molecular orbitals (LUMOs) have a lower potential than lithium ion reduction[82]. More precisely, even though the calculated HOMO/LUMO levels of the pure organic solvent are at higher/lower levels, respectively, the electrolyte is mixture including lithium salt impacting these levels. The LUMO levels of electrolyte of common carbonates decrease with lithium ion addition essentially due to Li^+ interaction with the localized electron of the carbonate group solvent rendering the electrolyte thermodynamically less stable against its electrochemical reduction[83]. Concerning the HOMO levels, they can be increased due to the interaction of the salt anion and pure organic solvent (i.e. proton transfer) leading to less stable electrochemical oxidation of the electrolyte in this case. The presence of impurities and additives would also affect these levels. Recent work would recommend using electrolyte potentials (i.e. Gibbs free energy) instead of the HUMO/LUMO levels of solvents since they do not take into consideration the previously stated interactions (and with salt ions) that would overestimate the electrolyte stability neglecting H^- and F^- transfer based on electrolyte decomposition[83,84]. A schematic illustration is presented in Figure 14 (left). The large SEI layer drove concerns as well with the creation of large cell impedance limiting the energy efficiency of these cells. More precisely, the works done correlated the graphitization degree of carbonaceous materials and their capacity while also reporting the higher instability of the SEI (mostly formed by using propylene carbonate PC electrolyte). However, PC could intercalate as well within the graphite layers causing an exfoliation of the layers and hence, resulting in poorer stability of the cell at the anode. Akira Yoshino, working at the Asahi Kasei Corporation, implanted a petroleum coke soft carbon anode coupled with LCO cathode in a PC-based electrolyte with $LiClO_4$ lithium salt, which showed high cyclability and stability with a reversible capacity lower than the theoretical capacity (~180 mAh/g)[85,86]. This cell technology is considered the first commercially available lithium-ion battery distributed by Sony in 1991. The higher stability during cycling on soft/hard carbons as anode materials is due to the larger interlayer spacing in those carbons compared to graphite would limit the contraction/expansion to layers (i.e. increased stability) as well as the carbon defects that would "stack" stronger the graphitic domains between them[87]. Later on, hard carbon was used as a replacement to extend the potential window (i.e. higher energy density) due to lower interlayer spacing than soft carbons and better stability at expense of a large first cycling irreversibility[88]. Graphite anode is reconsidered as anode material to possibly increase the capacity towards the theoretical value of 372 mAh/g and having less sloped charge/discharge plateaus. To solve the issue of stability caused by PC intercalation within the layers, a mixture of propylene carbonate and ethylene carbonate (EC) was used[87]. The latter compound did not intercalate but could not be used alone as its melting point is relatively high (~35-39°C). As a result, graphite was introduced in the commercial cells with a PC:EC mixture solvent electrolyte between 1995-1997, proving higher capacities and formation of SEI layer mostly produced during the very-first cycle and stable over time. In fact, without a stable passivation layer (SEI) during cycling caused by the non-aqueous electrolyte reduction, the stability of the system would be hampered. An improved electrolyte composition based on an ethylene carbonate and dimethyl carbonate (DMC) mixture with 1M $LiPF_6$ salt with higher oxidation stability – especially at higher temperature – with an LMO cathode was proposed by Guyomard and Tarascon in 1993[89]. This electrolyte formulation is nowadays widely used in commercial application with some slight changes in choice of organic solvents but respecting a mixture of linear and cycling carbonates in $LiPF_6$. The main requirements and properties for the electrolyte solvents formulation are a high dielectric constant ε for charge separation of the lithium salt, low viscosity η, avoiding high vapor pressure, wide temperature range during operation and inert for the constituents of the cell. Cyclic carbonates account for high dielectric constant and low vapor pressure but at the expense of a high viscosity. For this reason, linear carbonates are added for synergetic effects thanks to their low viscosity but cannot be used alone (low dielectric constant and high vapor pressure). Hence, a usual mixture of EC:PC:DMC is used to provide all the requirements and enable optimum working conditions and salt ions conductivity. The choice of the lithium salt is based according to dissociation in the electrolyte solvents, conductivity, ion transport number, anion stability during high oxidative potential (i.e. > 5V), non-toxic and inert for the diverse constituents of the cell. For these reasons, $LiPF_6$ is the quasi-only used lithium salt.

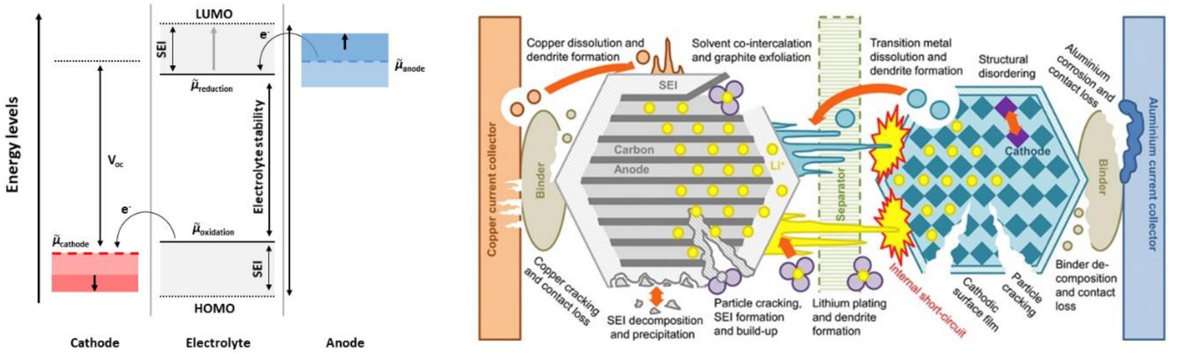

Figure 14: Energy levels representation inside a lithium-ion battery (left) ; Representation of various side reactions and degradation occurring inside a lithium-ion cell[90](right)

After years of technology maturing and improvement, graphite is the predominant carbonaceous anode material used in nowadays lithium-ion batteries. However, lithium plating is still occurring with one reason of the overpotential at fast charging rates. In those cases, the anode graphite overpotential results in a more negative electrode potential, hence lower than lithium deposition reaction potential. Lithium plating is then kinetically favorable when the graphite electrode potential is getting closer to the lithium deposition reaction potential[91]. The graphite electrode overpotential main causes are solid-state diffusion of lithium within the graphite lattice, mass transfer and charge transfer limitations[92]. From a general point of view, many side reactions can occur within a Li-ion battery cell involving more or less all the components, as the active and the non-active materials[90]. Examples of side reactions impeding a proper working of a lithium-ion batteries – and could lead to accidents – could be the copper current collector dissolution and dendrite formation, its cracking, aluminum current collector corrosion, binder decomposition, lithium plating and transition metal dissolution from the cathode resulting in dendrites formation at the anode or even particles cracking in a general manner (Figure 14 right).

Oxide-based cathode materials are widely investigated as possible replacement to $LiCoO_2$, mostly due to cobalt scarcity, cost, toxicity, geopolitical tensions and humanitarian disaster (i.e. cobalt mines in Congo[93]). As mentioned previously, $LiMn_2O_4$ (LMO) – a 3D spinel structural material – was also discovered and investigated as cathode electrode material. LMO presents the advantage of low toxicity, low cost, abundancy and higher thermal stability compared to LCO. Its theoretical capacity (148 mAh/g) could not be totally achieved and sustained through cycling for reasons stated previously (i.e. Mn^{3+} disproportionation, Mn^{2+} dissolution and possible Mn deposition at the anode) and illustrated in Figure 15 (left)[94]. More precisely, some research works in the 1990's tried to demonstrate the structural composition of $LiMn_2O_4$ and cycling stability[95,96]. It was explained with further work that the oxygen vacancies in the crystal structure induced by difference in synthesis conditions (i.e. low oxygen partial pressure and quenched cooling down synthesis leads to higher oxygen vacancies) give rise to different phases[97]. Indeed, the oxygen deficient obtained compound seen its potential for oxygen anion reintroduction in the structure limited, which turns from cubic to irreversible tetragonal phase transition (i.e. less cycling stability) for temperature higher than room temperature. Strategies exist to maintain oxygen stoichiometry and structural integrity upon cycling such as cation/anionic doping. By introducing divalent/trivalent cations with similar size to Mn^{3+} cation inside the structure, approximately the same bonding energy than Mn-O, a higher amount of Mn^{4+} is expected to increase the structural stability by moving from the Mn^{4+}/Mn^{3+} in initial stoichiometric structure[94]. For this purpose, magnesium Mg and aluminum Al are commonly used doping cations to suppress the Jahn-Teller induced volume expansion. Lithium excess is also a considered approach to improve the structural stability of LMO cathodes. Anion doping could help solving Mn migration by decreasing the oxygen vacancies. A schematic illustration in Figure 15 (right) shows how the different doping strategies can be adopted for enhancing LMO stability.

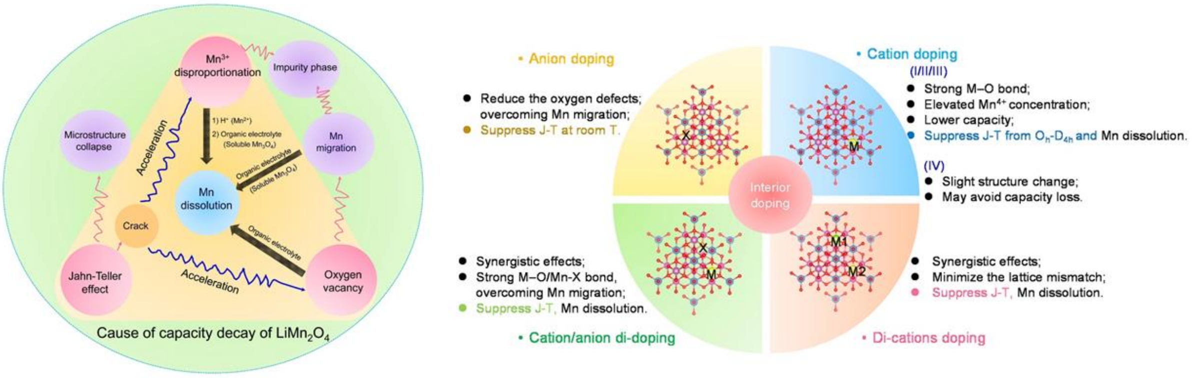

Figure 15: Reasons for LMO cathode stability and capacity fade (left)[94] ; LMO doping strategies to enhance cathode stability (right)[94]

As similar layered structure to $LiCoO_2$, Ni-based layered oxides were considering promising – especially $LiNiO_2$ (LNO) – due to economic advantage for similar theoretical capacity (275 mAh/g for one lithium deintercalation). LNO lacked several requirements and showed few technical problematics. The synthesis of a pure stoichiometric $LiNiO_2$ is complicated and mostly result in additional nickel ions within the interslab (i.e. lithium layer) at the expense of Li^{+}[98]. However, relatively close stoichiometric LNO synthesis can still be achieved[99]. However, one of the main issue results in the cation mixing with Ni^{2+} irreversibly substituting to Li^+ sites because of their quasi-similar size causing severe structural instability and also hindering lithium diffusion[100]. Thermal stability of LNO is another major drawback due to random nickel and lithium cations mixing around 200°C causing an exothermic reaction into a disordered rock-salt structure with Ni^{3+} more easily reduced than Co^{3+} as shown with both LCO and LNO decomposition reaction by Yamada[101]. Strategies to improve $LiNiO_2$ thermal/structural stability and overall performance were explored with a special regard to cation substitution to form binary oxides. Manganese being a great transition metal substitute, binary Ni-Mn oxides could show interesting features compared to pure LNO while expecting to show similar capacities. Hence, $LiNi_{1-x}Mn_xO_2$ cathodes (NMO) were synthesized – commonly $LiNi_{0.5}Mn_{0.5}O_2$ (Ni^{2+}/Mn^{4+}) – and showed improved thermal stability as well as cyclability compared to LNO but at the expense of lower reversible specific capacity[102]. Ni^{2+} is acting as redox active center mainly responsible for the high delithiation capacity and Mn^{4+} for maintaining structural stability. Aluminum is another cheaper and less toxic element used for cation substitution. Synthesis and characterization of $LiNi_{1-x}Al_xO_2$ revealed that no phase transition was observed during in the first range of delithiation, which was attributed to monoclinic phase change for LNO (i.e. from cooperative Ni^{3+} low-spin Jahn-Teller effect), in addition to the conservation of interlayer spacing for further lithium extraction[103]. The fully charged state acting as an electronic insulator would prevent thermal runaway to occur, so improving the safety, but at the expense of polarization. It was also found that 10% of aluminum substitution would be enough to prevent phase transitions but the cathode would still see a diminished reversible capacity (~100 mAh/g) due to some Ni^{2+} migration in the interslab[104]. Further works with nickel and cobalt mixing forming $LiNi_{1-x}Co_xO_2$ shows improved structural stability due to the smaller size of Co^{3+} hindering Ni^{3+} migration in the interslab and still proving high capacities with a cobalt percentage less than 30% up to 20%[105]. Unfortunately, these materials still suffer from thermal issues and negatively affect their safe use. Ternary oxides with a mix of the previously cited cations could then lead to synergetic effects and improving thermal and structural stability of LNO and its performances (i.e. high voltage vs. Li^+/Li, high and reversible capacity). One of the first case is the so-called NMC cathode composed of a Nickel-Manganese-Cobalt mixture with a generic formula being $LiNi_{1-x-y}Mn_xCo_yO_2$. Generally, this type of cathode can possess various ratios of Ni-Mn-Co directly impacting the materials characteristics. It has been demonstrated that the Ni is responsible for higher discharge capacities being the active redox center with consecutive Ni^{2+} oxidation up to the Ni^{4+} state. Manganese in its Mn^{4+} (non-electrochemically active) would preserve structural stability while lowering the cost of cathode production. Cobalt in its Co^{3+} obtained after Ni^{3+} oxidation to Ni^{2+} would prevent the migration of the latter within the lithium-containing interslab[77]. Generally, the attractive Ni-rich NMC cathodes due to their higher content Ni – that would provide higher capacities – present the same drawbacks as for LNO and LCO which are low thermal/structural stability and some lower capacity retention. It was found that higher nickel content is subject to increase oxygen release and hence reaction with the electrolyte creating safety issues[106]. Hence, the choice of NMC with different molar composition is essential according to the usage with a decision between high capacities and thermal/structural stability as illustrated in Figure 16 (left)[107]. NMC –especially NMC 333 ($LiNi_{1/3}Mn_{1/3}Co_{1/3}O_2$) for better safety and sometimes blended with LMO – with a one of the most commercialized cathode materials nowadays. Another ternary oxide consists in the composition of Nickel-Cobalt-Aluminum (NCA), $LiNi_{1-x-y}Co_xAl_yO_2$. The aluminum had the effect of improving the thermal safety as stated previously with

$LiNi_{1-x}Al_xO_2$ materials. As with the latter cathode, a high content of Al would result in diminished capacity as well as hindered lithium ion diffusion within the material (Figure 16 right[108]). Hence, NCA compounds would often give high content in nickel and cobalt with improved structural stability (i.e. cobalt addition) and high capacities but not a very efficient thermal runaway prevention.

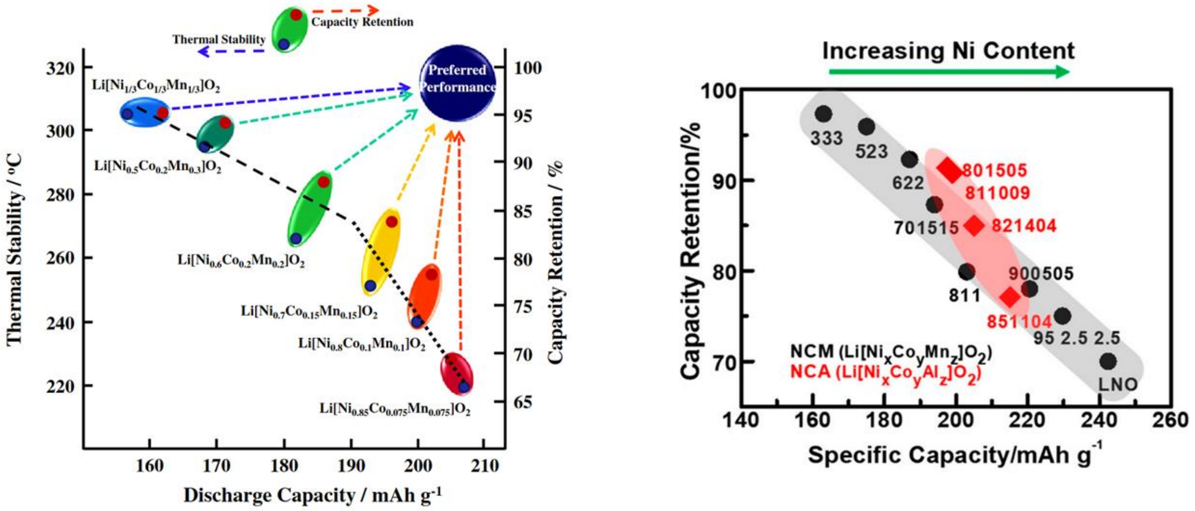

Figure 16: Composition variation of NMC and its effect on thermal stability, discharge capacity and capacity retention (left)[107] ; Composition variation of NMC and NCA on the capacity retention and specific capacitance (right)[108]

Besides layered and spinel structures, olivine-type materials – and more precisely here, phospho-olivines – represent another class of cathodes. Olivine-type cathodes can be defined as the following formula $LiMPO_4$ with M commonly a transition metal among Fe, Mn, Ni and Co. The choice of PO_4^{3-} polyanion choice compared to others such as sulfate SO_4^{2-}, arsenate AsO_4^{3-}, molybdate MoO_4^{2-} or tungstate WO_4^{2-} was to lower the energy level of the transition metal redox couple, leading to higher voltage window vs. Li^+/Li. This is explained by the oxygen anions O^{2-} seeing its electrons strongly polarized with the strong P-O covalent bond, inducing a weaker binding energy with transition metal cation and hence lowering the latter redox potential. A. K. Padhi demonstrated in 1997 with various phospho-olivine cathode ($LiMPO_4$ with M = Fe, Mn, Co and Ni) the difficulty to reversibly de-/intercalate lithium for the $LiMnPO_4$, $LiCoPO_4$ and $LiNiPO_4$ structures but successful for $LiFePO_4$ which will be referred as LFP[109]. The latter can operate up to approximately 3.5 V vs. Li^+/Li with a flat and stable discharge/charge plateau (theoretical capacity ~170 mAh/g) due to its two-phase lithiation process. In addition, the strong covalent bond within the polyanion impedes oxygen formation and the low heat generation at high temperature decomposition for LFP, shows its advantages for higher safety cells[77,110]. However, the low electronic conductivity of bulk LFP as well as slow lithium ion diffusion result in capacity loss at high current rates. These issues can be solved thanks to a conductive carbon coating around the LFP particles and reducing its size to nanoparticles to shorten the lithium ion diffusion length (i.e. improve Li^+ diffusion) and improving the percolation network. Hence, nanosized and conductive-carbon coated $LiFePO_4$ allowed for high-power rechargeable batteries. As illustrated in Figure 17, the most commonly used and studied cathode materials are represented by three main classes constituted of layered oxides $Li_{1-x-y}M_xM'_yO_2$, spinels $LiM_{2-x}M'_xO_4$ and phospho-olivines $LiM_{1-x}M'_xPO_4$. Layered oxides – Ni and Li-rich NMC, NCA or $LiMn_{1.5}Ni_{0.5}O_4$ more recently at the research scale – are very used and promising for high energy density use such in electric vehicles due their high voltage operation window and capacity (> 4 V, up to ~200 mAh/g). Their main drawbacks lays in terms of structural stability upon cycling, oxygen release, thermal stability and use of cobalt. Spinel oxides could also offer a good alternative to layered oxides with Mn-based materials such as LMO with safer use and using cheaper, non-toxic elements very useful for cost-sensitive applications. However, issues regarding capacity loss and retention upon cycling – more pronounced at raised temperature – diminish its attractiveness. Phospho-olivines such as LFP are very interesting due to their high safety, good capacity performance and cyclability. Due to their low operating voltage ($LiFePO_4$), this cathode technology is suited nowadays for low-to-moderate energy density applications requiring high safety.

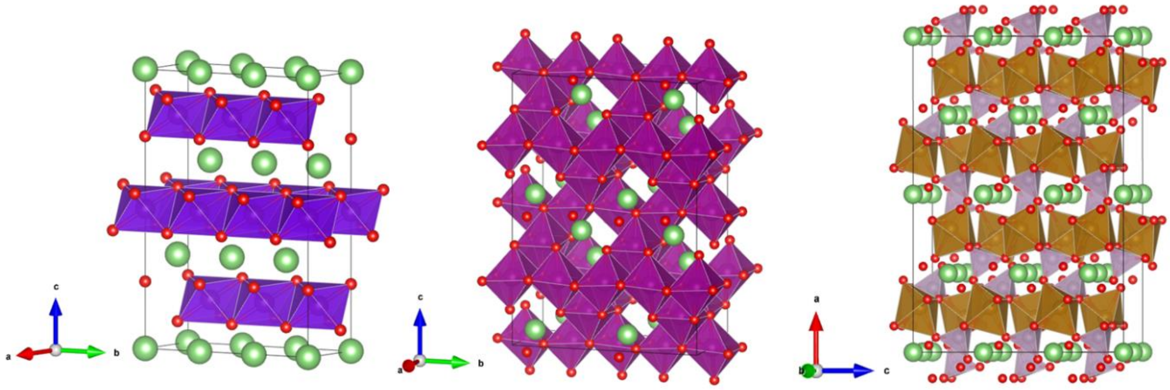

Layered oxides $Li_{1-x-y}M_xM'_yO_2$
M = Co, Ni
M' = Al, Mn, Fe, Ti, Mg, Cu, Ga, B

Spinels $LiM_{2-x}M'_xO_4$
M = Mn, Co, Ni
M' = Li, Ni, Co, Mg, Al, Zn Cu, Ti, Cr

Phospho-olivines $LiM_{1-x}M'_xPO_4$
M = Fe, Co, Ni
M' = Mn, Co, Ni, V

Figure 17: Crystallographic structure representations of layered oxides (left); spinels (middle); and phospho-olivines (right)

Other than graphitic carbonaceous materials, different materials are also investigated as anode materials. One of the best example and already commercialized is the case of lithium titanate oxide LTO $Li_{4/3}Ti_{5/3}O_4$ (or $Li_{1+x}[Li_{1/3}Ti_{5/3}]O_4$ with $0 \leq x \leq 1$), a spinel-type anode discovered in the late 1980's[111]/early 1990's[103,112]. With a theoretical capacity of 175 mAh/g with a higher lithium intercalation potential (~1.5 V vs. Li^+/Li) than usual carbonaceous anode materials, does not seem interesting from an energy density point of view but present quite other advantageous properties. Indeed, the higher potential provided by LTO would prevent the risk of lithium plating/dendritic growth and an SEI formation which would imply a decrease in capacity after the first cycle as well as a slower lithium ion diffusion. Furthermore, the zero-strain in structure during cycling showed by Ohzuku[103] with a very flat charge/discharge plateau around 1.55 V bring high cyclability (≥ 10 000 cycles) with almost perfect coulombic efficiency (i.e. quasi 100%) and suitable operation at high current rates. LTO also has a non-negligible drawback, which is its low electrical conductivity (~10^{-8}-10^{-7} S·cm^{-1})[113]. The main strategies consist in nanosizing the particles to reduce lithium ions and electrons pathways within the LTO lattice, coating with a conducting agent (carbon or metal-based materials) around the particles or even ion doping (i.e. variation in energy level and electron density distribution). Overcoming these issues, LTO was and still is a successful implementation in lithium-ion rechargeable batteries bringing high safety, long life range and cyclability, and high power.

Interestingly, two other kind of anode materials based on conversion and alloying reactions are studied since they could offer very high capacities (hundreds of mAh/g up to few thousands) and especially way higher volumetric capacities compared to graphite. Conversion reaction for lithium-ion batteries usually implies the use of a transition metal oxide (e.g. Fe, Co, Ni, Cu or Mn) that will be reversibly reduced to its metallic state within the co-formed lithium oxide Li_2O amorphous structure as depicted on the Figure 18 (left). In a more general way, the conversion reaction can be applied to other alkali metals such as sodium Na or potassium K and diverse anions instead of oxygen O (e.g. N, P, S, F, etc…). Important pioneer work from Poizot in 2000 described the use of Co, Ni and Fe oxide nanoparticles as anode materials demonstrating very high capacities[114]. CoO nanoparticles were reversibly reduced to very few nanometer sized metal particles (~1-5 nm) accompanied with the reversible formation of amorphous Li_2O. Up to ~700 mAh/g of capacity was observed for a hundred of cycle keeping almost 100% of coulombic efficiency.

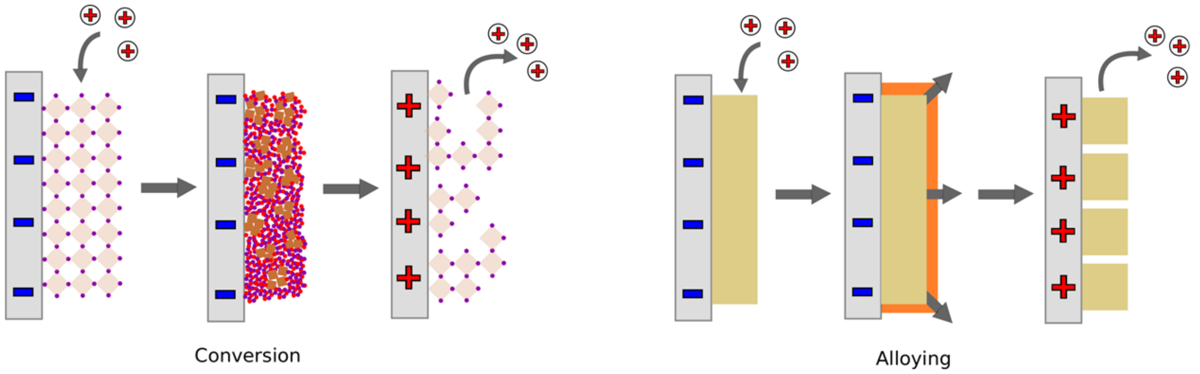

$$M_xO_y + 2yLi^+ + 2ye^- \rightleftharpoons xM^0 + yLi_2O$$

$$M^0 + yLi^+ + ye^- \rightleftharpoons Li_yM$$

Figure 18: Mechanism representations for conversion-type (left); and alloying-type reactions (right)

The reversible formation and decomposition upon cycling of the transition metal oxide/transition metal and Li/Li_2O was confirmed later on[115] by X-ray photoelectron spectroscopy (XPS), also revealing the formation of an inorganic/organic layers composed respectively of lithium carbonate Li_2CO_3/alkyl carbonates mainly and poly(ethylene oxide) oligomers. In addition, *in situ* transmission electron microscopy (TEM) on a porous cobalt oxide spinel Co_3O_4 nanoplates embedded on graphene allowed to observe clearly the conversion of the oxide into Co nanograins (~1-3 nm) within a Li_2O matrix (few nanometer layer shell) during lithiation[116]. It showed that Co nanograins reversibly oxidized to CoO – and not Co_3O_4 – upon subsequent delithiation (explaining the loss of capacity after the first cycle) with thinned but still remaining Li_2O layer. A clear volume expansion can be seen upon lithiation but minimized due to porous structure of the nanoplates accommodating it. Note that the metal nanograins would provide good electronic conductivity within the Li_2O matrix while the latter enabling lithium ion diffusion as for the SEI. The metal nanograin-percolating network would also represent a source of locally available electron within the Li_2O matrix to ensure its reversible reaction. Hence, the diffusion and mobility of the transition metal cations is an important parameter to take into account since it affects directly the size of metal nanograins as well as their isolation/displacement within the matrix. Higher mobility cations could result in bigger and isolated nanograins negatively impacting the electronic percolation network and thus, the reversibility of the Li_2O formation[12]. This was notably observed in the case of iron and copper fluorides, the latter resulting in bigger metal grains and more isolated ones diminishing the reversible formation of lithium fluoride LiF[117]. A study from Wang *et al.* in 2012 brought some light about the conversion mechanisms occurring with an iron fluoride FeF_2 anode materials[118]. Lithium ions migrate very fast to the particle surface with a slower diffusion within the bulk of the material due to complex transport dynamics of the various ions and the electrons within the multiple-phase mixture composed of insulating and metallic phases. The lithiation would then be surface, or interphase-driven to be more precise, with the major fluorine transport happening at the interface with parallel growth of a two-phase LiF and Fe mixture. A layer-by-layer propagation conversion reaction is then occurring with a local near-surface lithium diffusion with supersaturation of the layer leading to phase separation/decomposition due to no thermodynamic barrier to phase separation into new phases without nucleation. This decomposition process refers to spinodal decomposition. Hence, iron nanoparticles along with a three-phase Fe-LiF-FeF_2 interphases are created. Other studies, on NiO nanosheets[119], confirmed the heterogeneous phase conversion at the interface with the formation of a nanoporous metallic framework inhibiting pulverization and the maintain of the primary structure integrity, revealing the more complex reduction of the transition metal in not a simple interconnected or discrete nanoparticles or amorphous domains. This observed electron-diffusive nanoporous network would then be interesting for high-rate applications.

The properties and performance are dependent on the composition choice of the conversion-type materials and its structure. For the aforementioned observations, nanostructuration of materials for conversion-type reaction is of main importance the latter proven to be an interphase-driven process. As well as shortening the lithium diffusion path for enhancing high-rate capabilities and increasing the number of accessible active sites (i.e. increased capacities), reduction to the nanoscale allow a better resistance towards volume expansion and add solutions to its related issues[120]. The hysteresis voltage - which was originally thought as a major drawback for practical application - could be explained by the various reaction processes occurring upon lithiation/delithiation, therefore being intrinsic to the type of material, composition and structure[12]. However, at the nanometer scale the reactivity tends to increase with the surface area as it can be seen with a continuous electrolyte decomposition, which is partially reversible. Indeed, the capacity increase at low potential during lithiation and high potential during delithiation is due to this partial electrolyte decomposition and not the effect of negligible interfacial storage (i.e. surface storage) with volume changes[121]. To be more precise, the dissolution of the inorganic outer layer of the anodic electrolyte interphase (AEI) – in similarity to term of SEI – mainly composed of Li_2CO_3 is responsible for the partial electrolyte dissolution[122], which was efficiently dissolved after the delithiation but seen a residual increasing layer with the increase charge/discharge cycles. The anion nature coupled to the transition metal has a direct impact on the voltage hysteresis with a decrease in the latter (i.e. increased energy efficiency) for a decrease in the polarizability of the anion ($H<P<N<S<O<F$)[123] as it was observed in the case magnesium hydride (MgH_2). However, many drawbacks impede the use of such anode in practical commercial batteries[124]. The reorganization induced by the strong bond construction and reconstruction could lead to dispersion of particles and loss a percolation network (contact loss), lowering the electronic conductivity, is one of the issue that have to solved. Tremendous efforts are existing nowadays to improve the stability and overall performance of conversion-type anodes for practical and commercial application but is still at the laboratory scale.

Alloying-type reaction is the other very promising process for anode materials since very high capacities can be obtained (> 1000 mAh/g and thousands of mAh/cm^3). Lithium can form an alloy through with some metal atomic framework involving bond breaking of the latter material to host lithium. As a result, higher amount of lithium per mole of host material could be achieved (i.e. more electrons) at the price of very high structural change and volume expansion[125]. One of the first material studied was the case of a tin-based amorphous oxide in 1997 by Idota *et al.*[126] which show a high first cycle capacity up to 1030 mAh/g (equivalent of 8 moles of lithium per tin-based amorphous oxide) for 1.2 V voltage window but decrease to ~650 mAh/g for subsequent cycles by keeping a nearly 100% coulombic efficiency. Other elements than tin Sn appear quickly more attractive. The best example is the one of silicon Si which could intercalate up to 4.4 mole of lithium with its lithiated $Li_{22}Si_5$ state[127] (or $Li_{4.4}Si$) leading to a theoretical ~4200 mAh/g gravimetric capacity and more impressively ~9779 mAh/cm^3. Unfortunately, the alloying-type anodes experience very high volume expansion, up to 310% in the case of Si and 260% for Sn, resulting in high strain breaking the particles[128]. This is the main reason for the heavy loss capacity for such systems with electrical contact loss, accentuated with higher reactivity with the electrolyte as the volume is expended. The principal issues are depicted in Figure 19 (left)[129]. Solutions to maintain the structural integrity, reduce the mechanical fractures and avoid possible undesired side reactions are of a main concern. Nanostructuring was then the major strategy to improve the stability of silicon-based anodes. One of the most impressive research was the formation of silicon crystalline nanowires with an average diameter (about 89 nm of diameter) that were able to reach the theoretical capacity value of Si at the first cycle with lower loss during the subsequent cycles[130]. These better performances for Si anodes were attributed to the nanowire architecture – grown on a conductive nickel current conductor – with small diameter size for better accommodation of high volume expansion preventing mechanical fractures; direct growth on the current collector for the use of all silicon as active sites; and efficient charge transport due to one-dimensional electronic pathway. Extensive research is currently done to correct the main drawbacks of silicon anodes and after many years of development, silicon-based anodes are believed to be very close to large-scale production and implementation in post lithium ion batteries[131]. Interesting to note, combining conversion and alloying reactions represent also a good alternative to obtain improved stability and performance in the case anode materials for which many works are being done (Figure 19 right[12]). One brief example would be the conversion/alloying materials (CAMs) which combine a classical transition metal material for conversion reaction with a cation dopant which will alloy with lithium. This has the effect of increasing the capacity as well as lowering the potential (i.e. increased voltage window for a full cell) thanks to the alloying-type metal. The two reaction mechanisms would take place with the formation of the lithium oxide matrix embedding the nanosized transition metal electron-conductive percolating network while ensuring the nanocrystallinity of the alloying element. The latter reacting at lower potential than the conversion reaction and maintaining a limited volume expansion and decrease voltage hysteresis[12].

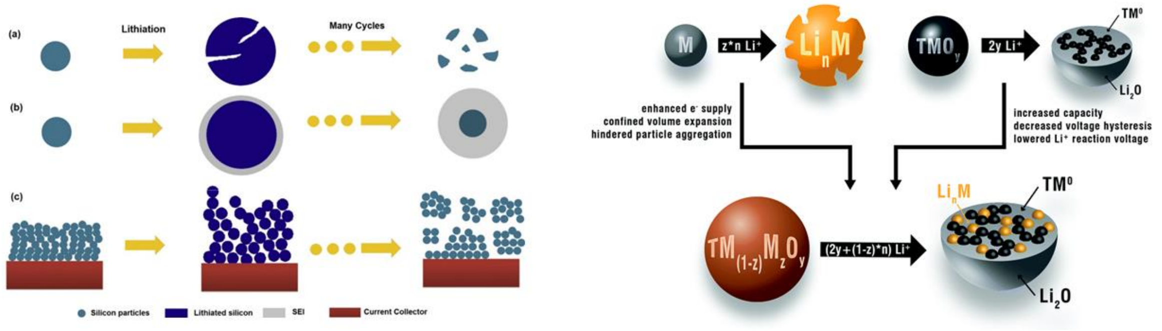

Figure 19: Representation of the main issues with Si anodes with material pulverization (a), electrolyte decomposition and continuous SEI growth (b) and volume expansion/morphology change (c) (left)[129]; Potential benefits of combining conversion- and alloying-type reactions (right)[12]

- Supercapacitors

Supercapacitors represent the other most known electrochemical energy storage besides batteries. Compared to the latter, the electrical energy is stored in a different way that is at the foundation of the specific properties of supercapacitors mostly famous for their very high specific power (i.e. capability to store and deliver electricity very rapidly, ~10 kW/kg) and high stability with almost no performance loss after hundreds of thousands of cycles. This is explained by the non-Faradaic electrostatic force-based energy storage mechanism with the anions and cations contained in the electrolyte on either sides of the positive and negative electrodes - separated by a porous membrane – creating a so-called electrochemical double-layer (EDL)[132]. Charges are stored at the surface of the electrodes and the capacitance (i.e. charge stored when a difference of potential is applied between the electrodes) and directly dependent on the accessible surface area of the active material, the distance between the ion and the electrode surface, and the dielectric constant of the electrolyte used. This charge storage capacitance is referred to the electrochemical double-layer capacitance (EDLC). The capacitance can be expressed by the following formula[5]:

$$C_{DL} = \frac{A \cdot \varepsilon_0 \cdot \varepsilon_r}{d} \tag{5}$$

with C_{DL} the double-layer capacitance (in Farad, F), A the accessible surface area of the electrode (in square meter, m^2), d the ion-electrode surface distance (in meter, m), ε_0 the vacuum permittivity ($8.854 \cdot 10^{-12}$ F/m) and ε_r the electrolyte's dielectric constant (dimensionless). In a more general manner, the capacitance can be defined as the charges stored Q (in Coulombs, C) over the applied voltage between the two electrodes V or ΔV (in volt, V) and can be determined from either cyclic voltammetry (C_{CV}) or galvanostatic charge-discharge (GCD) test at constant current (C_{GCD}) with these following formulas[133–135]:

$$C_{CV} = \int_{V_1}^{V_2} \frac{I \cdot dV}{(V_2 - V_1) \cdot \vartheta} \tag{6}$$

by considering the "discharge" part of the CV (i.e. the negative area), with I the discharge current (in ampere, A), dV the infinitesimal voltage change (in volt, V), V_1 and V_2 the lower and upper potential limits (in volt, V) and ϑ the scan rate (V/s), or:

$$C_{CV} = \int_{0}^{V_{OV}} \frac{I \cdot dV}{2V_{OV} \cdot \vartheta} \tag{7}$$

with V_{OV} the operating voltage (i.e. ΔV = $2V_{OV}$, in volt, V). With GCD, the formula would be:

$$C_{GCD} = \frac{I \cdot \Delta t}{\Delta V} \tag{8}$$

with Δt the discharge time (in second, s), I the applied discharge current and ΔV the voltage window (in volt, V). It a not ideal linear case, the capacitance can be obtained from the area under the discharge curve with:

$$C_{GCD} = \int_0^{t_d} \frac{I \cdot dt}{\Delta V} \tag{9}$$

with t_d the discharge time (in second, s).

Usually, the capacitance is normalized by the mass of the electrode (F/g), its volume (F/cm^3) or its surface area (F/cm^2). The capacitance rising from the electrochemical charge storage is typically ranging about $C_{DL} \approx$ 10-30 µF/cm^2, underlining the need for very high specific surface area materials. In that sense, carbon materials and especially activated carbons with very high specific surface area (> 1000 m^2/g) are thought to be the main interesting electrode materials for supercapacitor applications (Figure 20).

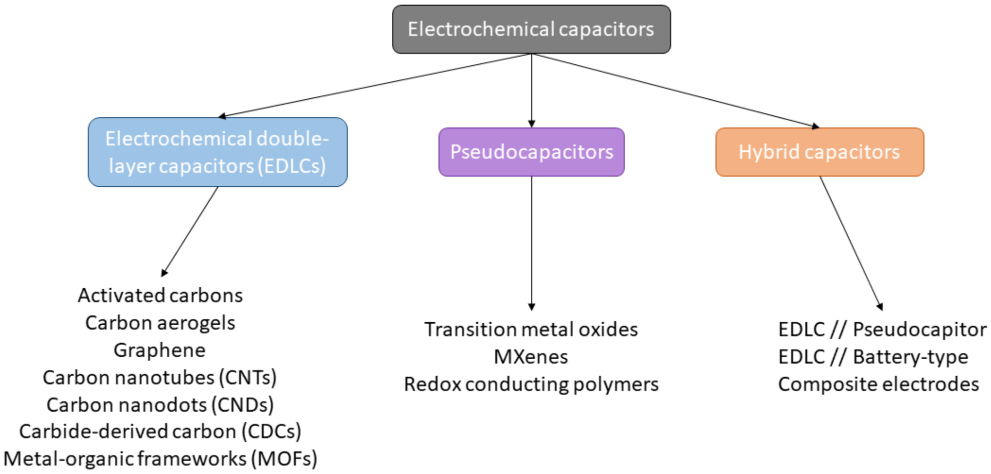

Figure 20: Electrochemical capacitors and their different types

Additionally to EDLCs, electrochemical capacitors based on pseudocapacitance are presented as complementary technologies. Pseudocapacitance refers to the electrosorption of species from the electrode/electrolyte interface through redox reactions at the surface of various transition metal oxides for instance (e.g. ruthenium oxide(IV) RuO_2, Figure 20)[132]. The phenomenon is then related to interfacial electron transfer and is considered Faradaic in origin, which is not the case of classical charge storage through double-layer capacitance with electrostatic interactions (i.e. non-Faradaic). A direct electron transfer occurs across the double-layer into surface redox or in some ion intercalation processes as in battery-like electrodes but due to thermodynamics and kinetics reasons, the capacitance phenomena can be ascribed as reversible and fast surface similar to adsorption/desorption. Hence, an almost quasi-linear dependence can defined between the on the surface coverage/redox/intercalation process (i.e. extent of reaction) and the applied potential[132]. Detailed starting from simple chemisorbed species/ions A onto a metal surface M:

$$\begin{array}{ccccccc} M & + & A^{\mp} & \mp & e^{-} & \underset{k_{-1}}{\overset{k_1}{\rightleftharpoons}} & MA_{ads} \\ 1-\theta_A & & c_A^{\mp} & & V & & \theta_A \end{array}$$

with MA_{ads} the metal-adsorbate species.

B. E. Conway and H. Angerstein-Kozlowska[136] gave a relation between the potential applied V and the surface coverage of the A species θ_A by a monolayer ($0 < \theta_A < 1$) assuming a Langmuir-type electrosorption isotherm and a one-electron process at the thermodynamic equilibrium:

$$\frac{\theta_A}{1-\theta_A} = K_1 c_A^{\mp} e^{\pm VF/RT} \qquad (10)$$

with $K_1 = \frac{k_1}{k_{-1}}$ the adsorption-to-desorption equilibrium constant (comprising the exponential term for the standard potential V_0), $c_A^{\mp}$ the concentration of $A^{\mp}$ species, V the electrode potential (in volt, V), F the Faraday constant (96 485 C/mol), R the ideal gas constant (8.314 J/(K·mol)) and T the temperature (in Kelvin, K),

where $\theta_A = \frac{K_1 \cdot c_A^{\mp} \cdot e^{\pm VF/RT}}{1 + K_1 \cdot c_A^{\mp} \cdot e^{\pm VF/RT}}$ for the Langmuir-type electrosorption isotherm.

From this, a kinetic equation of the net current density j (in A/cm^2) passing through the metal surface M can be defined as[136]:

$$j = q \cdot \frac{d\theta_A}{dt} = q \cdot k_1 \cdot c_A^{\mp} \cdot (1-\theta_A) \cdot e^{\pm\frac{\beta VF}{RT}} - q \cdot k_{-1} \cdot \theta_A \cdot e^{\mp(1-\beta)VF/RT} \qquad (11)$$

with β the Brønsted barrier symmetry factor (usually ≈ 0.5), directly affecting the exponential activation energy contributions. A maximum of current density is obtained for a surface coverage of θ_A=0.5 for a reversible adsorption-desorption process.

An analogy can be directly made with Nernst equation[13]:

$$E = E^0 + \frac{RT}{F} \ln\left(\frac{[Ox]^{\nu_{ox}}}{[Red]^{\nu_{red}}}\right) \qquad (12)$$

Considering that at the equilibrium state (i.e. rate of adsorption r_{ads} = rate of desorption r_{des}):

with $r_{ads} = k_1 \cdot [M] \cdot c_A^{\mp} \cdot e^{\pm VF/RT}$, and $[Ox] \equiv c_A^{\mp}$ (13)

and $r_{des} = k_{-1} \cdot [MA_{ads}]$, and $[Red] \equiv [MA_{ads}]$ (14)

$$E = E^0 + \frac{RT}{F}\ln\left(\frac{c_A^{\mp}}{[MA_{ads}]}\right) \tag{15}$$

That could be rewritten as:

$$E = E^0 + \frac{RT}{F}\ln\left(\frac{\frac{c_A^{\mp}}{c_A^{\mp}+[MA_{ads}]}}{1-\frac{c_A^{\mp}}{c_A^{\mp}+[MA_{ads}]}}\right) \tag{16}$$

with $\theta_A = \frac{c_A^{\mp}}{c_A^{\mp}+[MA_{ads}]}$ (17)

giving the following generalized equation for adsorption pseudocapacitance:

$$E \approx E^0 + \frac{RT}{F}\ln\left(\frac{\theta_A}{1-\theta_A}\right) \tag{18}$$

Considering that the extent of reaction – the coverage θ_A here – and assuming a complete monolayer with a required charge q, the coverage can be differentiated according to the electrode potential and giving rise to the pseudocapacitance C_ϕ:

$$C_\phi = q \cdot \frac{d\theta_A}{dV} = q \cdot \frac{F}{RT} \cdot \frac{K_1 \cdot c_A^{\mp} \cdot e^{\pm\frac{VF}{RT}}}{\left(1+K_1 \cdot c_A^{\mp} \cdot e^{\pm\frac{VF}{RT}}\right)^2} = q \cdot \frac{F}{RT} \cdot \theta_A \cdot (1-\theta_A) \tag{19}$$

However, the Langmuir isotherm do not take into consideration the often perceived broad distribution of the pseudocapacitance over the potential range. One factor reducing the steepness of an ideal Langmuir isotherm is due to the successive stages of adsorption/desorption of the adsorbates over the potential range and coverage. This phenomenon is well seen on platinum[137] or ruthenium(IV) oxide[132] where successive peaks can overlap with quasi-similar C_ϕ for each peak but increase overall charge accumulation. The second parameter that should be taken into account and exist in the Frumkin isotherm is the introduction of a lateral interaction parameter g between the adsorbates on the adsorbent surface. This parameter can be either attractive ($g > 0$) or repulsive ($g < 0$) and be introduced in the exponential activation energy contribution:

$$\frac{\theta_A}{1-\theta_A} = K_1 c_A^{\mp} e^{\pm\left(\frac{VF}{RT}-g\theta\right)} \tag{20}$$

and in the same way:

$$C_\phi = q \cdot \frac{F}{RT} \cdot \frac{\theta_A \cdot (1-\theta_A)}{1+g \cdot \theta_A \cdot (1-\theta_A)} \tag{21}$$

Generally, the surface adsorption phenomena can be replaced by the ion occupancy in the lattice X for intercalation-type pseudocapacitance or the oxidant and reductant concentration for surface redox pseudocapacitance. Noted that for adsorption pseudocapacitance, the double-layer contribution can be superior or equal to the Faradaic contribution, giving a cyclic voltammetry signal with almost invisible redox peak appearance[138]. Attention should be devoted to the fact that, as defined by Conway, the surface redox pseudocapacitance must show fast and reversible redox reactions (with no mass transfer limitations) for an extended time scale with no significant phase transformation (≠ batteries). However, as the research field evolves, the definition of pseudocapacitance tends also to do it. Some "strict" definition arose due to the fact of the overused of the "capacitance" term for the use battery-like materials, where the term "capacity" is more correct, proposing to only defines pseudocapacitance for materials exhibiting quasi-linear capacitance dependence over a large potential scale[139]. However, such quasi-linear signature can be seen for battery-like materials with an intercalation-based storage mechanism when their particle size is decreased to nanometer scale and/or thin film. This is explained by the significant decrease in the diffusion length of ions in those materials, which is way lower than the diffusion time and coefficient, leading to high power applications as well. Proposition to define such effect as "extrinsic" pseudocapacitance due to the capacitive signature at nanosize compared to classical "intrinsic" pseudocapacitance materials showing capacitive signature at the bulk too[140]. Nevertheless, the intercalation mechanism in batteries with nanostructured materials and intercalation-type pseudocapacitive materials underlines the difficulty of proposing clear definition with established barriers. Recent advances made with machine-learning methods and artificial intelligence (AI) present emerging tools to classify the type of storage mechanism, thus distinguishing between pseudocapacitors and batteries in complex identification cases[141] (Figure 21 left). This method would allow to predict the EES type thanks to a trained dataset comprised of different battery-like and (pseudo)capacitive materials ranging from easy-to-difficult identification and giving a "grade" to the tested input CV or GCD curve as a "capacitive tendency" from 0% to 100% (Figure 21 right).

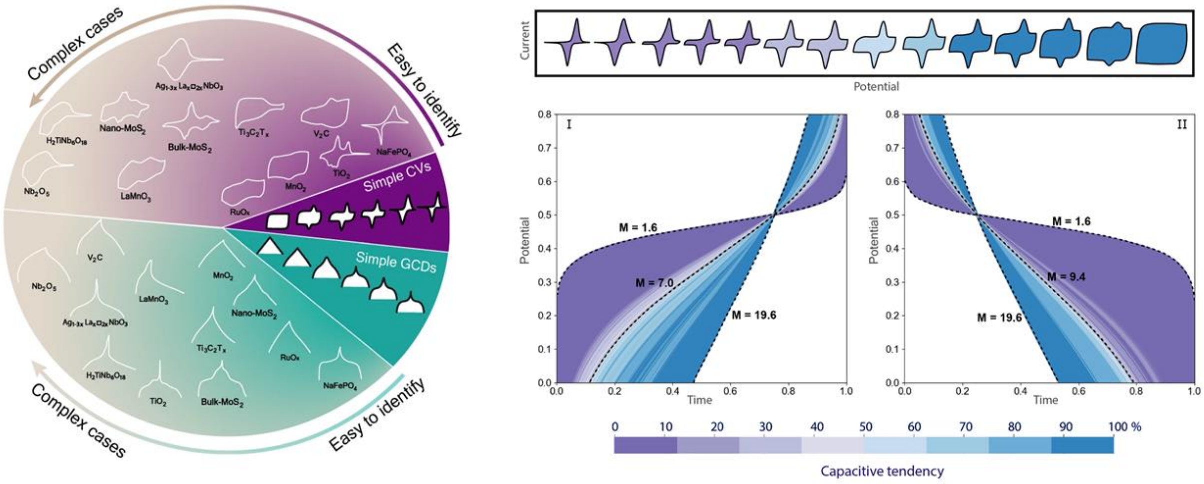

Figure 21: Schematic representation of CV and GCD curved of various battery and pseudocapacitive materials from easy to complex identification of their type (left); Representative CV and GCD curves to address a capacitive tendency (right)[141]

Furthermore, a continuum can be drawn between a pure non-Faradaic electrochemical double-layer charge storage and Faradaic battery-like charge storage. The degree of confinement of the inserted ion can be represented as the determining factor influencing the charge storage mechanism. The confinement can ascribed by the solvation degree of the ion entering the host material with an increase in the ion-host interaction with the partial-to-complete desolvation and intrinsic increase in the electron transfer. Hence, research on the fundamental charge storage mechanisms in EESDs is essential in designing high performance electrode materials in adequacy with the requested need.

Apart from EDL-based capacitors, pseudocapacitors or batteries, hybrid technologies can be designed to obtain complementary advantages of each different type of electrode storage mechanism. One could think about employing a fast charge/discharge capability electrode with a high capacity electrode to obtain a technology between a supercapacitor and a battery (i.e. higher power density than a regular battery and higher energy density than a regular supercapacitor, Figure 22[142]). Three main architectures of hybrid systems exist (Figure 20): (i) EDLC // Pseudocapacitor; (ii) EDLC // Battery-like and; (iii) composite electrodes. The former design which is also referred as an “asymmetric” supercapacitor compared to classical “symmetric” supercapacitor (i.e. ELDC // EDLC) usually combining a carbon-based ELDC-type electrode and a TMO-based pseudocapacitor-type electrode. This configuration usually allows to extend the voltage window due to the different potential stability of each electrode. The second type of configuration rely on the use of a fast double-layer charge storage mechanism of a carbonaceous electrode coupled to a battery-like electrode. The idea with this kind of design is to take advantage of the fast charge/discharge rates offered by the ELDC-type carbon electrode (i.e. high power density) and the high capacity offered by the use of an intercalation-type battery electrode (i.e. high energy density). In this category, known examples can be cited such as lithium-ion capacitors (LICs) or even sodium-ion capacitors (NICs). The latter case is based on the use of composite materials typically mixing a carbonaceous material, transition metal oxides and/or conductive polymers. The latter technology directly mix within the electrode different charge storage mechanisms and supporting materials for additional and beneficial effects on the performance. A section dedicated to hybrid supercapacitors/batteries will be hold latter in the introduction (I.b.iii.) giving more details.

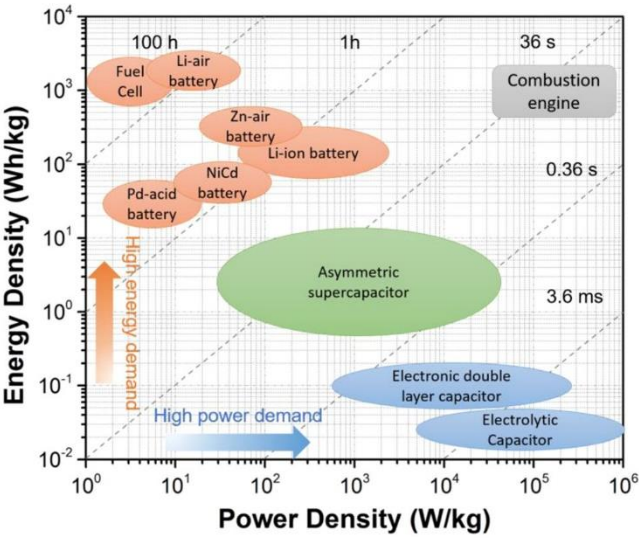

Figure 22: Ragone plot putting into perspectives the place of asymmetric supercapacitors compared to other classical EESDs[142]. Here the authors comprise hybrid and asymmetric supercapacitors by only taking into consideration electrodes with two different charge storage mechanisms

- <u>Carbon-based supercapacitors</u>

The very first patent for what is known as a supercapacitor nowadays was attributed in 1957 to Howard I Becker at General Electric Co. entitled “Low voltage electrolytic capacitor”[143]. The technology was based on cells connected in series, with each cell composed of two porous carbon electrodes separated in an NH_4Cl (“salammoniac”) or an aqueous sulfuric acid electrolyte in an insulating material-based container (Figure 23 left). The active carbon electrodes were made of sticks of fired tar lampblack. It is in 1966 with a patent from the Standard Oil Company (SOHIO) by R.A. Rightmire that a second activity interest for high surface area carbon to store electricity at the electrochemical double-layer appeared[144]. High surface area carbon electrodes were made out of black or coconut charcoal and then separated in a cell with a 9M sulfuric acid electrolyte. Note that SOHIO also may tests in organic electrolyte containing tetraalkylammonium (TEA) salt[132]. The aqueous electrolyte-based formula was developed further using carbon paste electrodes and assembled in disc-shaped cell in 1970[145] and the Nippon electronic Company commercialized the first known trademarked “SuperCapacitor” the following year. Pinnacle Research Institute released in 1982 a high power with low internal resistance electrochemical capacitor for military applications. It the first utilization of the “Ultracapacitor” term which is also slightly used to refer to nowadays electrochemical capacitor[146]. The concept was based on the use of mixed oxides – precisely ruthenium dioxide – in acidic aqueous medium that presented pseudocapacitance effect to store charges[132]. However, the very high cost of ruthenium oxide impedes its wide commercialization despite its very high performance. Naturally, carbon materials appear as the best candidate for supercapacitor applications. Matsuhita Electric Industrial, nowadays called Panasonic Corporation, were commercializing carbon-based electrochemical double-layer capacitors in organic electrolytes since the 1990’s. In the same decade, Maxwell Company designed their electrochemical capacitors under the appellation and provide high power devices for a wide range working temperature (Figure 23 middle)[146,147]. Their technologies are well implemented nowadays and is one the leader in the market with Panasonic, Murata (acquired by CAP-XX), Eaton and more recently Skeleton Technologies (Figure 23 right). Carbon materials for supercapacitor applications represent then an important market and diverse technologies exist. A synthetic approach to present these various designs and architectures would be done according to the dimensionality of the carbon materials: from 0D to 3D.

Figure 23: First design of an electrochemical capacitor by Becker (left)[143]; DuraBlue, XP and Strandard Series ultracapacitors from Maxwell (middle)[147]; Ultrathin prismatic supercapacitor from CAP-XX/Murata (right)[148]

Among the 0D-carbons, mainly three different varieties of carbon under the names of carbon nano-onions (CNOs), onion-like carbons (OLCs) carbon nanodots (CNDs) or quantum dots. As their name indicate it, CNOs or OLCs are conductive spherical carbon materials with a concentric gradient of graphitic “shells” or layers ($d_{interlayer}$ = 0.335 nm, Figure 24 left)[149]. These structures are also related to the fullerene C_{60} family (i.e. multi-walled fullerenes) or also called “buckyballs” due to their spherical/polyhedral structure. Hence, the different layers are composed of 6-ring and 5-ring carbons with sp^2 hybridized carbon atoms to enclose the spherical structure, obeying to Euler’s law[150,151]. Some defects and holes can occur leading to quasi-spherical particles with the creation of extra pentagons for each heptagons (positive curvature) and vice versa (negative curvature) leading to an amorphous (non-symmetric) or crystalline phase (symmetric)[151]. To create such concentric layers, the following equation can be used to estimate the number of carbon atoms $C_x(n)$ of the n^th layer[152]:

$$C_{x(n)} = C_{60} \cdot n \qquad (22)$$

CNOs have a size of ca. tens of nanometers and exhibit very high electronic conductivity with the π-conjugated shells. They can be obtain from diverse types of synthesis (electron-beam irradiation, arc-discharge, chemical vapor deposition CVD, pyrolysis) with the most commonly used being vacuum annealing or detonation from nanodiamonds providing a very high yield of CNOs[153,154]. Their non-porous structure showing relatively low SSA compared to porous activate carbons (<600 m^2/g) limit greatly their performance as EDL capacitors (~30-50 F/g) but, with their highly conductive external layer accessible for electrolyte ions, high current rates are achievable[5,155]. As presented, 0D carbon nano-onions do not present interesting characteristics for high performance supercapacitors. However, they could be employed as conductive agent and support for composite materials exhibiting low electronic conductivity. Furthermore, CNOs can be functionalized with organic functional groups[156] which could increase their charge storage ability thanks to additional pseudocapacitance phenomena. Indeed, oxygen or nitrogen functional group doping could affect impressively the carbon materials as it will be described later on. Carbon nanodots (CNDs) or carbon quantum dots (CQDs) refer to small spherical carbon particle with size lower than 20 nm and exhibiting fluorescence and high electrical conductivity[157–159]. Thanks to their very small size (i.e. high surface area), fast electron transfer properties and easy scalability from biomass and waste, CNDs appear interesting for various application including energy storage[159]. According to their core, carbon nanodots can be classified into three main categories[158,160] (Figure 24 right). One is graphene quantum dots (GQDs) which can be subdivided into single-layer graphene quantum dots (s-GQDs) and multi-layer graphene quantum dots (m-GQDs). The second category would be the simple carbon quantum dots (CQDs) of simple quasi-spherical shape with no particular phase but composed of sp^2-hybridized domains explaining their high electronic conductivity. The last is the polymer dots (PDs) composed of cross-linked linear polymeric chains (or monomer). For small size below 5 nm, capacitance as high as 300 F/g can be achieved[161]. As for the CNOs, their limited accessible surface area limits their usage but different approaches are investigated using heteroatom doping with functional group[162] or formation of composites with battery-like materials[163,164].

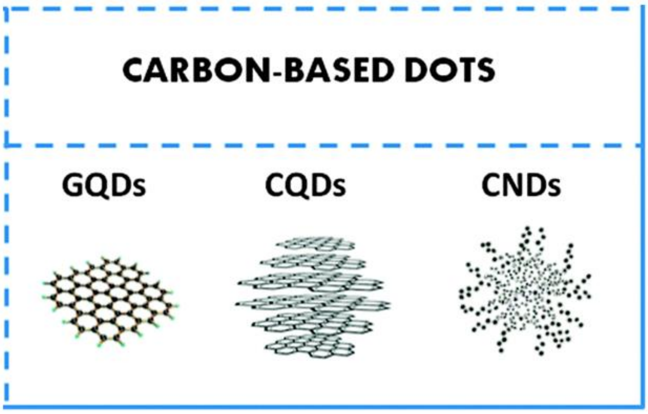

Figure 24: High resolution transmission electron microscopy image of a carbon nano-onion (left)[149]; Different kinds of carbon-based dots (right)[160]

Carbon nanotubes (CNTs) and carbon nanofibers (CNFs) constitutes the main one-dimensional carbon architectures. CNTs – firstly described in 1991 by Sumio Iijima[165] – can be regarded as a graphene sheet wrapped to form a tube. Hence, different types of CNTs can exist and exhibiting different properties. They can either be single-walled (SWCNTs) or multi-walled (MWCNTs), the latter being a concentric structure of SWCNTs with a diameter up to ca. 50 nm[166]. CNTs can be obtained through various methods such as CVD, laser ablation process or by arc-discharge technique[167]. Important to mention, even if a conductive semi-metal graphene layer is considered to described the CNTs morphologies, according to the chirality of the tube, the latter can show behavior of a metal or semi-conductor (Figure 25 left). The chirality is described with a chiral vector $\vec{C}$ as:

$$\vec{C} = n\overrightarrow{a_1} + m\overrightarrow{a_2} \tag{23}$$

with $\overrightarrow{a_1}$ and $\overrightarrow{a_2}$ the unit cell vectors of the graphene lattice and n, m their respective integers[168]. Two limiting geometrical structures exist: the zig-zag structure with $\vec{C}_{zig-zag}$ (n,0) and the arm-chair structure with $\vec{C}_{zig-zag}$ (n,n). Considering only one side of a graphene layer, a SWCNT would have a SSA of 1315 m^2/g but in close bundle pack where each tube would be stacked, the accessible SSA can drop to 751 m^2/g for a small pack of seven SWCNT where six tubes surround the centered tube[169]. This number can decrease down to 151 m^2/g for 217 SWCNTs pack. For the most commonly produced MWCNTs, the SSA varies between 680-850 m^2/g (composed of two walls) to roughly 50 m^2/g (40 walls, 35 nm of diameter). As for CNOs, the limited accessible surface area (mainly mesopores) for charge storage hinders their use as high performance materials, with their inner pore not contributing due to unfavored electrolyte ion diffusion. However, their high conductivity and their exclusively accessible external SSA make them good candidates for very high power applications. Similarly to CNOs, functionalization of their surface with oxygen or nitrogen functional groups represent a viable strategy to increase the SSA as well as their wettability in aqueous electrolyte and to enhance capacitance with pseudocapacitance participation. Since their morphology is tunable and presenting advantageous properties such as high conductivity and mechanical resistance to cite only, CNTs are widely studied as support for composite materials[170]. Indeed, metal oxides presenting pseudocapacitive or battery-like behavior or even conducting polymers (Figure 25 right[171]) can grafted onto the external walls to ensure electronic conductivity among all the grafted particles. The heteroatom doping can also facilitate the synthesis of composites thanks to the creation of adsorption sites for the metal precursors.

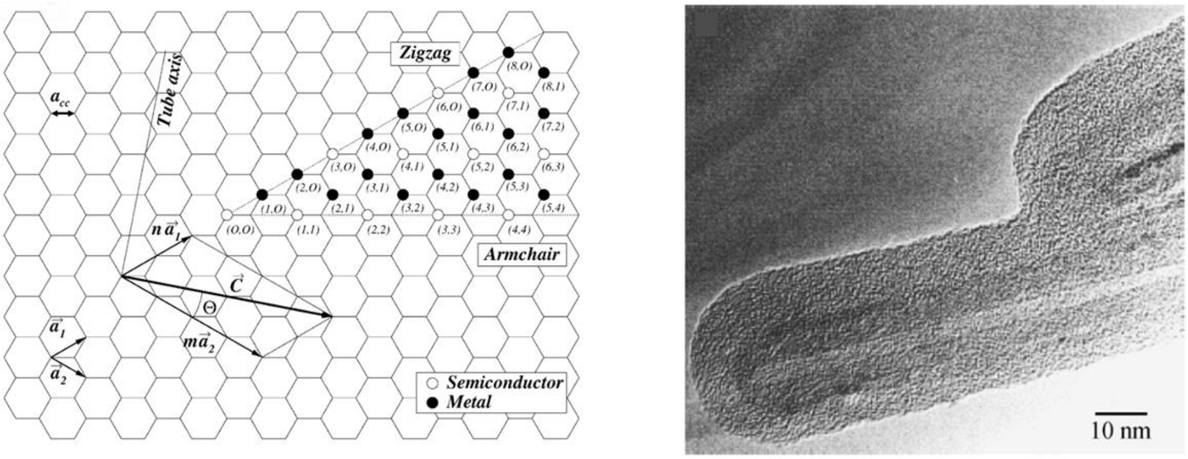

Figure 25: Impact of graphene sheet rolling on the final geometry of the CNTs (left)[168]; CNTs coated with a conductive polypyrrole polymer (right)[171]

Two-dimensional (nano)materials are receiving a great enthusiasm due to their high surface-to-volume ratio, high theoretical volumetric capacitances and possibility of fast kinetics and transports of ions especially under nanofluid confinement[172]. Graphene is single layer atom of carbon arranged in hexagons with sp^2-hybridization. Konstantin S. Novoselov and Andre K. Geim experimentally discovered this material in the form of bilayer in 2004 by exfoliating graphite with a scotch tape[173]. Graphene gave high electronic in-plane conductivity and is explained by the sp^2 carbon hybridized lattice proving a delocalized electron cloud from either side of the graphene layer. In addition, graphene has very high mechanical stability with Young modulus (measure of compressive stiffness by lengthwise-applied force) of 1.0 terapascals (1 TPa = 10^{12} Pa) and intrinsic strength or break stress of 130 GPa[174]. Different synthetic ways exist and were developed to produce from either top-down approach or bottom-up approach. The Figure 26 sums up all the various methods to obtain graphene[175]. The top-down approach consist by producing graphene starting from a bulkier precursor being graphite (i.e. stack of multiple graphene layers). Exfoliation methods compose the main methods either mechanically, (electro)chemically or sonochemically. The mechanical exfoliation of graphite into graphene (mono-, bi- or few-layers) can be done according to the use of normal or shear forces. The normal force refers to the peeling of layers as done historically while mentioning the "scotch tape" method[173] or by advanced cleavage method such as ultrasharp wedge of single crystal diamond to "peel" few-layers graphene of tens of nanometer thickness[176]. Shear force method using essentially ball-milling is viable technique not only to exfoliate graphite but also to functionalize it or creating composite materials. This technique is based on the high energy impact liberated during the grinding process with balls. This method provide relatively good quality graphene due to low processing with quasi no negative environmental impact but requires advanced peeling tools to exfoliate qualitatively the layers, time consuming and is not scalable for large production. Chemical exfoliation consists in the use of strong oxidative agent to oxidize graphite to graphite oxide in aqueous solvent followed by the easy exfoliation thanks to the hydrophilic polar groups on the graphite oxide surface. The exfoliation results in the dispersion of graphene oxide (GO) in aqueous solvent. Historically, graphite oxide was initially produced in 1859 by Benjamin C. Brodie[177] using a mixture of graphite and potassium chlorate $KClO_3$ with fuming nitric acid HNO_3 during several days with four oxidation steps before a washing step with water to obtain a suspension. In 1898, L. Staudenmaier modified Brodie's method using a sulfuric acid and fuming nitric acid mixture with the addition in smaller parts, avoiding the several oxidation steps of Brodie[178]. Later on in 1937, Ulrich Hofmann elaborated another method by simply using non-fuming nitric acid[179]. In 1958, William S. Hummers Jr. and Richard E. Offeman presented one of the most utilized and known method for a safer GO synthesis by avoiding the use of nitric acid and adding potassium permanganate as an oxidizing agent and sodium nitrate[180]. Nowadays, modified and improved methods exist to ensure proper safety and ease of synthesis procedure[181]. For the reduction of graphene oxide to reduced graphene oxide (rGO) – which is a more conductive GO with fewer oxygen moieties and higher C/O ratio – chemical reduction or temperature annealing methods are commonly employed. Chemical reduction implied the use of chemical reducing agents such sodium borohydride $NaBH_4$ or hydrazine N_2H_4 for the most used[182]. While chemical agents can be very efficient and useful, they can also be very toxic and harmful. Thermal annealing of GO consist in removing oxygen moieties by a thermal treatment but at the expanse of high temperature use or long-time annealing, risk of material expansion and cracking and compatibility in the case of substrate usage[183]. Chemical oxidation-reduction route provides generally high yields and ease of scalability with qualitative graphene-like materials (rGO) but suffer from its cost (high number of chemicals) and processing with many steps. Sonochemical exfoliation in liquid phase is another exfoliation technique based on the creation of ultrasounds to create micrometer-sized bubbles producing shear forces and cavitation while collapsing to exfoliate graphite layer in solution without the use of oxidative agent[184]. This method is convenient in regard to the chemical oxidation-reduction route by preventing the formation oxygen moieties and keeping "pristine" graphene layers with low defects. Graphite is generally exfoliated in organic solvents (i.e. N-methyl-2-pyrrolidone, NMP) which can be toxic. In addition, despite the scalability of the process producing high-quality graphene and the requirement of less processing, the yield of obtained graphene is not very high and requires additional centrifugation cycles to separate the sheets. Interestingly, modified method using the addition of surfactants can be used to exfoliate the graphene in aqueous solution but present the particularity of keeping the surfactant on the material with some difficulty to remove them while keeping a low defect graphene. Nevertheless, the presence of surfactants prevent the restacking of the graphene layers of the mostly obtained few-layer graphene (FLG) while using non-toxic and biocompatible source of surfactants and solvents[16].

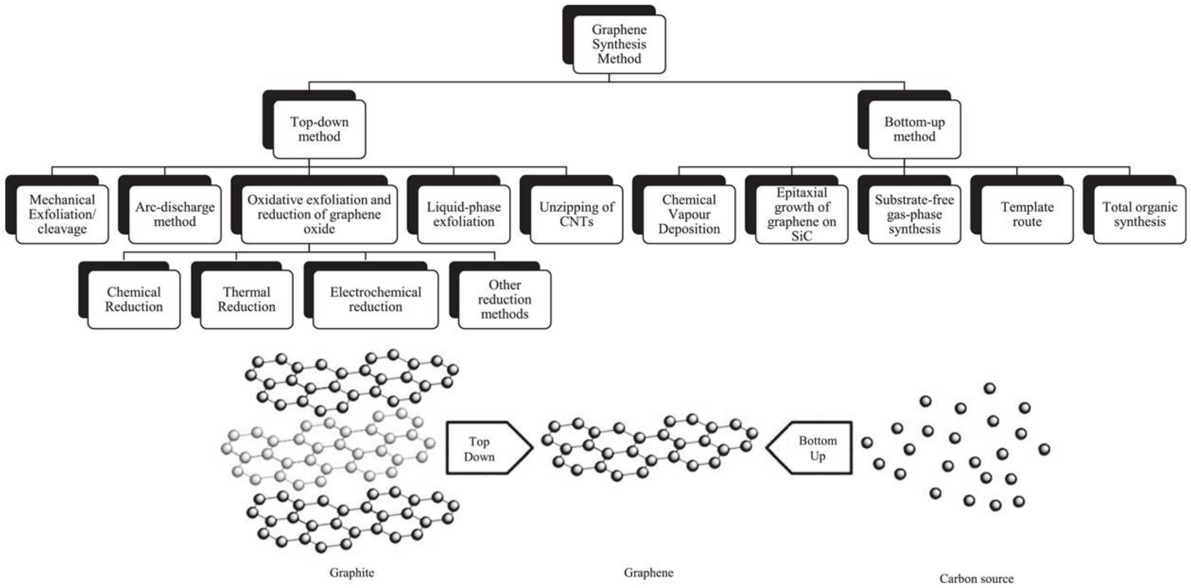

Figure 26: Various graphene synthesis methods decomposed into top-down and bottom-up approaches[175]

Concerning top-down approach, two main methods stand out from the crowd which are epitaxial growth on substrate and chemical vapor deposition. Epitaxial growth onto a crystalline silicon carbide SiC film substrate of graphene is one the most praised method to produce high quality single-layer graphene sheet that could be used as it is for electronic measurements and applications[175,185]. Firstly reported in 2009 by Konstantin V. Emtsev[186], graphitization onto the surface occurs via the silicon sublimation of SiC under high temperature annealing (> 1000°C) and ultra-high vacuum (UHV). Graphene can grow on both Si-rich (0001) and C-rich $(000\overline{1})$ giving rise to different electronic properties. The latter shows enhanced electronic conductivity similar to graphene monolayer due to rotation fault stacking of graphene bilayers with enhanced electronic decoupling (i.e. lower interlayer coupling)[187] compared to classical Bernal bilayer stacking ($(6\sqrt{3} \times 6\sqrt{3})R30°$ unit cell reconstruction onto SiC (0001) face)[188]. CVD is the other preferred bottom-up approach method for graphene growth. It relies on the high temperature decomposition of hydrocarbon gases (e.g. methane CH_4, ethylene C_2H_4, etc…) and graphene layer growth on a metal catalytic surface (e.g. Cu). Depending on the type of reaction, graphene monolayer can be form or few-layer graphene with very low defect density. Growth on copper film occurs via a surface catalyzed reaction where once the Cu surface is covered with a monolayer, no further growth can occur[189]. On the other most studied metal, nickel, growth occur via a segregation mechanism where graphene layers are formed due to the carbon resurface during cooling from its initial dissolution in the bulk metal at high temperature[190]. CVD method allow the obtention of high quality graphene and monolayers but at high cost and catalyst purification steps.

The theoretical specific surface area of single graphene sheet is about 2630 m^2/g which can provide ca. 21 µF/cm^2 of surface capacitance or ca. 550 F/g of gravimetric capacitance if all the surface (without defect) could contribute to the charge storage[191]. These presented properties already make graphene an outstanding candidate for energy storage application. However, two of the major drawbacks of graphene consist on its tendency to π-(re)stacking of the layers diminishing drastically the accessible surface area and the large-scale production of defect-free single layer graphene. Diverse strategies exist to improve graphene-based materials performances. One consists in preventing the restacking of graphene layers by introducing surfactants[192], spacers[193] or molecular pillars[194,195]. Molecular surfactants such as tetrabutylammonium hydroxide (TBAOH) intercalated between graphene oxide ($d_{interlayer}$ = 2.2 nm) and subsequent reduced graphene oxide after hydrazine assisted reduction ($d_{interlayer}$ = 0.39 nm) show the stabilization of such structure by preventing their restacking[192]. Besides the stabilization, the surfactants are thought to enhance the wettability of the electrodes with the electrolyte. The rGO with intercalated TBAOH showed specific capacitance values of 194 F/g in 2M H_2SO_4 (1V window) and 144 F/g in ionic liquid 1-butyl-3-methylimidazolium tetrafluoroborate ($BMIMBF_4$, 4V window) at 1 A/g of charging rate. Interestingly, one could think about applying researches done on graphene oxide-based membranes with tunable interlayer distance thanks to the intercalation of cations (Li^+, Na^+, K^+, Ca^{2+}, Mg^{2+})[193,196] for supercapacitor applications. Similarly, molecular pillars can be used as spacers to tune the interlayer distance and preventing the restacking of layers[194,197,198]. This method involves the functionalization and cross-linking of graphene oxide with alkyl diamines chains with subsequent chemical reduction to functionalized rGO (Figure 27 top)[197]. Hence, ion sieving during intercalation upon charge storage according to their size is possible while tuning ion transport mechanism (Figure 27 bottom)[194]. These sieving and pillaring methods are also serving fundamental research purposes to enlighten electrochemical charge storage under nanoconfinement[199,200]. Besides these methods, different approaches exist as well to enhance the capacitance of graphene-based materials via functionalization and N-doping. The latter has revealed greater performance than graphene in aqueous or organic electrolyte by a factor four (up to 280 F/g) thanks to pyridinic, pyrrolic and quaternary nitrogen functionalization[201]. Similarly to activation of carbon sources to produce high surface area activated carbon, KOH-assisted thermochemical activation can be used on graphene oxide to produce microporous activated and exfoliated rGO[202]. Such material exhibited SSA as high as 3100 m^2/g, high electronic conductivity (~ 500 S/cm, measured on powder), high C/O ratio, very low hydrogen amount, absence of dangling bonds and specific capacitance about 200 F/g in neat ethyl-methylimidazolium bis(trifluormethylsulfonyl)imide (EMIM TFSI) ionic liquid electrolyte (3.5V window). As for the previously mentioned carbon allotropes, graphene-based materials can be used as conducting supporting materials for composites with transition metal oxides or even conducting polymers. Many examples account for the use of MnO_2 active material with specific capacitance above 210 F/g at 0.2 A/g[203], with Fe_3O_4/rGO composites showing ~160 F/g at 0.5 A/g[204] or with graphene/polyaniline nanofiber composites providing up to 480 F/g of specific capacitance at 0.1 A/g charging rate[205].

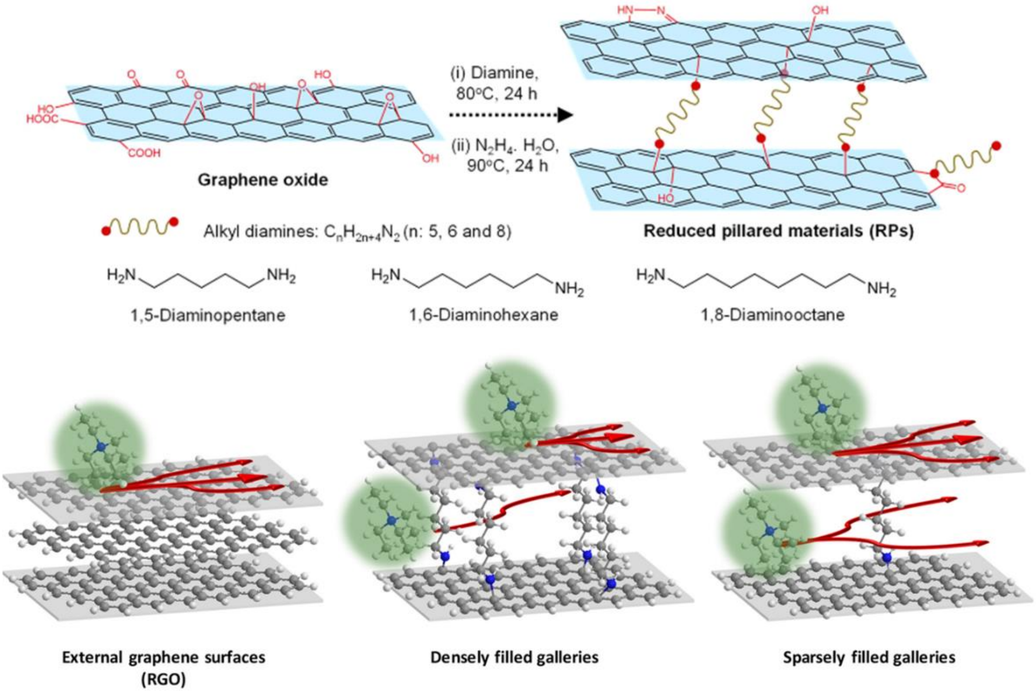

Figure 27: GO functionalization and cross-linking with alkyl diamines followed by hydrazine reduction (top)[197]; Difference in ion transport according to the functionalization of rGO by pillars (bottom)[194]

The most studied carbon form for supercapacitor applications is without surprise the 3D-carbon materials due to their historical anchor, ease of production from various carbon sources and very high SSA (> 2000 m^2/g). Among these 3D carbons, the main studied ones are activated carbons (ACs) and carbide-derived carbons (CDCs). Activated carbons are mainly used for industrial supercapacitor applications using coconut shell wastes as carbon source, proving high surface area (> 2400 m^2/g)[206,207]. ACs provide the advantages of being produced from many sorts of biomass and carbon-rich wastes, with high SSA, good electronic conductivity thanks to the presence of high content in sp^2-hybridized carbons at relatively low cost of production. The “activation” of the carbon source is done either physically or chemically. The physical activation refers to the use of first step of pyrolysis under inert atmosphere to remove most of organic volatile impurities before the high temperature (~400-1200°C) annealing under oxidizing gaseous environment (steam, air, CO_2, etc…)[208]. The chemical or thermochemical activation process relies on the use of chemical oxidizing agent (KOH, NaOH, LiOH,

$ZnCl_2$, $MgCl_2$, H_3PO_4, etc…) at usually lower temperatures than physical activation process (400-900°C), involving one step or two in the case pre-treatment of the carbon-source, better yield, high SSA (> 3000 m^2/g) with high proportion and control of micropores diameter, volume and distribution and presence of meso- and macropores (Figure 28 left). The latter method depends a lot on the choice of carbon precursors, activation agent and pyrolysis temperature to tailor the physicochemical properties of the obtained activated carbon[209]. AC powders is widely used in industry for ELDC electrodes for direct supercapacitors production (Maxwell, NEC, Panasonic, etc…), for fundamental research purposes using ACs with narrow micropore size distribution to study its influence on the electrochemical performances (Kuraray Co. LTD) or for direct application related use (NORIT, Cabot). Thermochemically activated ACs are mostly studied due to their tunability in their structure and microporosity (high SSA and PSD) giving rise to specific capacitances superior to 200 F/g in organic electrolyte or up to 300 F/g in aqueous electrolytes[5,208].

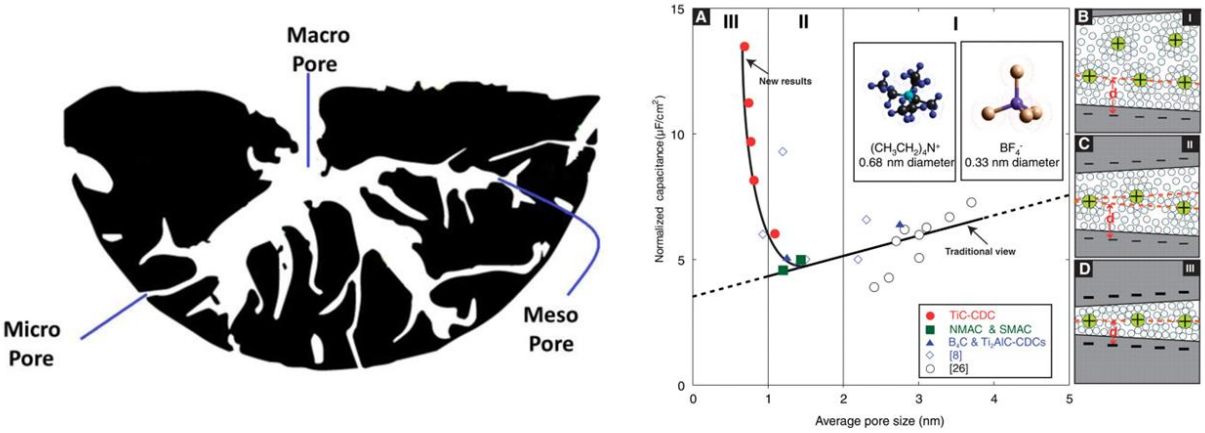

Figure 28: Different types of pores present in an activated carbon (left)[210]; Pore size influence of the capacitance in finely-tuned CDCs (right)[211]

Carbide-derived carbons (CDCs) are also 3D carbon offering high SSA (> 1000 m^2/g) due to selective etching of metals from metal carbides such as titanium carbide TiC or silicon SiC through chlorination at different temperatures[212]. The main advantage of CDCs is the control allowed on the pore size distribution in the micropore region according to the synthesis conditions. It was particularly considered as a breakthrough in 2006 when Chmiola *et al.* finely-tuned the PSD of TiC-derived carbons with chlorination from 500°C to 1000°C giving pore size from 0.6 to 2.25 nm[211]. This study revealed the anomalous increase in capacitance in pores smaller than the solvated ions size, which was a change from the traditional view on ion storage in pores (Figure 28 right). It underlined the effective partial desolvation of ions entering pores smaller than their fully hydration shell size, further confirmed by electrochemical quartz crystal microbalance (EQCM)[213]. CDCs can be performant and show capacitance higher than 140 F/g in organic electrolyte and higher than 200-250 F/g in aqueous electrolytes[214] but they are mostly used for fundamental studies compared to large scale applications of activated carbon-based electrodes.

Organic electrolytes such as acetonitrile (AN) or propylene carbonate (PC) with quaternary ammonium salts are usually used and preferred due to their high voltage window (2.7-2.8 V) than aqueous electrolyte (~1 V) proving higher energy density[215]. However, the organic electrolytes lack of ionic conductivity compared to water-based ones (ε_{AN}, ε_{PC} and η_{AN}, $\eta_{PC} < \varepsilon_{water}$ and η_{water}) and are less safe due to lower thermal stability and risk of flammability. Electrolytes using acetonitrile usually show higher ionic conductivity and lower viscosity compared to propylene carbonate-based ones but the latter is considered less toxic, safer and slightly higher operating voltage window[215]. Ionic liquids (ILs, pure liquid salt composed only of cations and anions) can be considered a promising candidate for next generation supercapacitors due their very low vapor pressure (almost negligible), high stability, > 3 V voltage window and inflammability[215,216]. In addition, since ILs are only composed of cation and anions, they constitute very useful tools for fundamental research on charge storage mechanism[211,213,217]. Strategies to increase capacitance and power density of activated carbons with nitrogen and oxygen doping will be presented later, in the scope of this PhD research study.

- Transition metal oxide-based pseudocapacitors

As described previously, the pseudocapacitance phenomena arises from the fast and reversible charge storage/delivery of ions via surface adsorption, surface redox reaction or intercalation-type pseudocapacitance. The term “pseudo-capacity” was introduced in 1941 by D.C. Grahame to describe the excess of capacity from the reversible electroreduction of ion at the surface of mercury which was not characterized by a classical electrochemical double-layer[218]. Later on, B.E. Conway and E. Gileadi theorized the kinetic theory of pseudocapacitance in link with the surface coverage that can be seen on metallic surface such as proton and oxygen adsorption onto platinum surface[219]. The concept of pseudocapacitance at this time was linked to the underpotential deposition (upd) is an electrodeposition method which refers to the monolayer deposition of a metal species onto the surface of another foreign metal substrate at potentials higher than the equilibrium Nernst potential than for the reductive deposition of the same metal substrate[220]. However, even though the upd refers to highly reversible charge transfer, they are not applied on broader potential window accompanied with low overall charge as initially intended by Conway for application in energy storage systems with the term pseudocapacitance[13]. The first pseudocapacitance study with transition metal oxide was offered in 1971 by Sergio Trasatti and Giovanni Buzzanca for ruthenium(IV) oxide RuO_2 thin films in sulfuric acid[221]. RuO_2 attracted much interest since then as one of the first pseudocapacitive materials showing very specific capacitance. The rectangular capacitive signature of RuO_2 thin films was attributed to fast and reversible surface redox reactions with protons[222]:

$$RuO_x(OH)_y + \delta H^+ + \delta e^- \rightleftharpoons RuO_{x-\delta}(OH)_{y+\delta} \tag{24}$$

A comparison was done between acidic and alkaline media with a study on the charge stored at the "outer" and "inner" surface of the electrodes. It also emphasized a faster Grotthus mechanism diffusion of protons in the inner surface active sites in acidic media underlying a pH-function accessibility if surface regions whereas the charge accumulation at the outer surface occurs without hindrance[222]. Another study in 1995 by Zheng, Cygan and Jow[223] underlined the effect of hydration of the $RuO_2{\cdot}xH_2O$ particles when switched from amorphous phase to highly crystalline phase through temperature annealing. The proton intercalation is fastened in hydrated amorphous $RuO_2{\cdot}xH_2O$ phases and not in crystalline phases which exhibited a rectangular-like CV signature (Figure 29a) with high electronic conductivity and capacitances as high as 768 F/g in H_2SO_4 for a $RuO_2{\cdot}0.5H_2O$ phase. In 2002, Dmowski and Egami studied by X-ray diffraction and atomic pair density function (PDF) the local atomic structure and conduction mechanism of hydrated $RuO_2{\cdot}xH_2O$ in function of the hydration level ($0.02 \leq x \leq 0.84$) thanks to thermal annealing[224]. They revealed that the $RuO_2{\cdot}xH_2O$ is not a pure amorphous material nor a mixture of amorphous/crystalline grains but a composite of anhydrous rutile-like RuO_2 nanocrystals with metallic conductivity separated with structural water (chemisorbed or physisorbed) along the grain boundaries facilitating the proton transport. A maximum of 850 F/g for a hydrated $RuO_2{\cdot}0.58H_2O$ was found. Complementary worked realized with small-angle X-ray scattering (SAXS) analyzed the correlation between nanostructuration and water content within $RuO_2{\cdot}xH_2O$ at subnano- to nanoscale[225]. SAXS allowed revealing the hierarchical nanostructure of $RuO_2{\cdot}xH_2O$ nanoagregates in confined water and proper representation of the specific surface area in function of the annealing temperature (Figure 29b). It revealed that the high capacitance obtained after 130°C annealing was due to densified loose aggregates with the same primary particles size compared to the original sample, with a significant higher accessible surface area (i.e. higher capacitance) and slight loss of confined water content (Figure 29c). Further annealing encouraged grain growth with formation of larger particles and continuous loss of water content. Also, pseudocapacitance represented approximately 70% of the total measured capacitance, the rest 30% coming double-layer capacitance (Figure 28d). Hence, the charge storage and capacitance of hydrous ruthenium(IV) oxide is dictated by the outer accessible surface sites and not by the inner bulk of particles, facilitated by the fast proton transfer between nanodomains by a Grotthus-like transport in the confined water environment. Unfortunately, even though ruthenium dioxide seems like an ideal material for supercapacitor applications, the very high cost of ruthenium drastically hinders its large-scale commercialization. Nevertheless, $RuO_2{\cdot}xH_2O$ is still an interesting materials for the study of charge storage mechanism in fundamental research. Implementing RuO_2-based composites with cheap conductive polymers/carbons, supporting materials to avoid agglomeration and improve stability, and reducing the content of ruthenium to lower the cost of production is still at core of many works to reach possible large-scale industrialization[226].

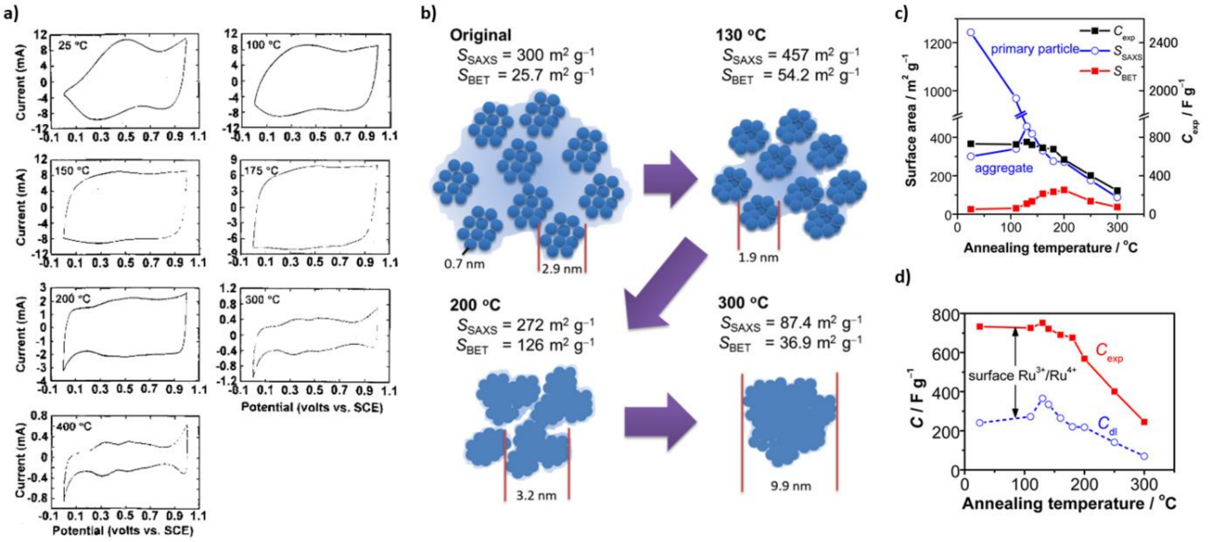

Figure 29: CV evolution of $RuO_2{\cdot}xH_2O$ in function of the annealing temperature (a)[223]; Representation of $RuO_2{\cdot}xH_2O$ nanodomains and particles with their SAXS or BET N_2 adsorption-desorption specific surface area according to their annealing temperature (b)[225]; Correlation between the SSA obtained by SAXS and BET N_2 adsorption-desorption, annealing temperature and specific capacitance (c); Deconvolution of the double-layer capacitance from the experimentally measured total capacitance (d).

As another alternative material at low cost, low toxicity and relatively high abundancy, manganese dioxide MnO_2 is envisaged for pseudocapacitors. It is in 1999 H. Y; Lee and J. B. Goodenough presented their work on amorphous $MnO_2{\cdot}nH_2O$ in neutral 2M KCl aqueous electrolyte showing clear capacitive signature on a 1.2V potential window[227]. The reported material showed capacitance value up to 203 F/g with very stable cyclability. The prepared amorphous-MnO_2 material by mixing two manganese precursors ($KMnO_4$ and Mn(II) acetate) in deionized water for 6 hours. Due to the poor electronic conductivity of the material, mixing with relatively high content of carbon conductive agent (ca. 25% in mass) is required to ensure proper signals and performance. The as-tested electrode in neutral 2M KCl shows a short-circuit release rate faster than amorphous-RuO_2 in acidic 5.3M H_2SO_4. The faster proton mobility in acidic media compared to K^+ in neutral media underlies the fact the discharge rate not only depend on mobility of the stored ion but also on the desorption/diffusion of the latter from the active material surface. Works performed in NaCl and LiCl electrolyte approved this hypothesis with Na^+ and Li^+ having bigger hydration shell that K^+ (Figure 30 left). Slower kinetics ($Li^+ < Na^+ < K^+$) was indeed observed at the two end potentials for these two electrolytes compared to KCl. This study emphasizes the concept of ion partial desolvation while entering the active material lattice leading to slower kinetics with bigger hydration shell. Later on, the first asymmetric supercapacitor based on amorphous-MnO_2 and activated carbon appeared with operating voltage window of 2V in KCl neutral electrolyte, fast power rates, high cyclability and energy densities similar to those of ruthenium(IV) oxide symmetric capacitor[228]. Different amorphous and crystalline MnO_2 phases were also tested in mild 0.1M K_2SO_4 electrolyte to assess the influence of crystallinity, nanostructuring order and surface area on the observed electrochemical measurements[229]. Amorphous samples presented broad specific capacitances that might originate from surface and bulk contributions while reaching maximum performance around 200 F/g. The latter value did not further increased with the specific surface area which is a limiting factor for amorphous materials. As for crystalline phases, the observed performance depends highly on the crystalline structure of the phase, for instance insertion pathways of ions inside the dimensional tunnels. "Opened" 2D tunnels offered by birnessite δ-MnO_2 provided high capacitances in comparison to their specific surface area while 1D tunnel structure of pyrolusite β-MnO_2 or nsutite γ-MnO_2 showed limited pseudofaradaic surface capacitance with potential size of tunnels limiting the cation insertion. λ-MnO_2 with 3D tunnel structure showed an intermediate behavior compared to 2D and 1D tunnel structures. This specific surface area proposed limitation on capacitance can be argued to be due to ionic conductivity of the so-obtained microstructures of amorphous phases rather than solely to specific surface area. Indeed, charge storage in MnO_2 is mostly Faradaic in essence and the ionic conductivity, related to the crystallographic microstructure, is at the core of H^+ and/or alkali cations (de-)insertion[230]. The charge storage mechanism of an amorphous- MnO_2 was presented with the influence of the charge storage efficiency according to the film thickness[231]. The thinner film deposited onto a platinum surface exhibited a quasi-similar specific capacitance in accordance with the theoretical value for a one-electron process (i.e. 1370 F/g) which was significantly lower for a thicker film. The X-ray photoelectron spectroscopy (XPS) results highlighted the evolution of the Mn 3s and O 1s peaks with the oxidation change of manganese (+III and +IV), and the involvement of Na^+ but also protons (to account for the lack of charge compensation upon Mn^{4+} reduction). The thicker film did not show practical changes in relation with the manganese evolution state. It is then ascribed that only thin layers are involved in redox processes, underlying the surface dominated importance for electrochemical activity of MnO_2 for energy storage whereas thick/bulk particles will only participate through non-Faradaic process. The charge storage mechanism seems in accordance with the following one of cation C^+ at the surface of MnO_2:

$$(MnO_2)_{surface} + C^+ + e^- \rightleftarrows (MnO_2^- C^+)_{surface} \qquad (25)$$

Raman spectroscopy measurements gave additional insights on the understanding of the pseudocapacitive behavior of MnO_2. *In situ* Raman spectroscopy done Hsu *et al.* in 2011 abled to acknowledge the structural evolution of birnessite nanosheets in Na_2SO_4 electrolyte with reversible hexagonal (Na^+ deintercalated) – monoclinic (Na^+ intercalated with water molecule replacement) phase change[232]. The observation revealed the shift in MnO_6 layer distance next to each other with a slight interlayer decrease during Na^+ intercalation. Sodium cation is then responsible for the pseudocapacitive behavior of birnessite with balance of the manganese valence state. Electrochemical impedance spectroscopy (EIS) also revealed that upon intercalation of Na^+, further intercalation is hindered by the interlayer distance decreasing and lower the Na^+ available sites. Diffusion of the cation becomes more and more limited and shortened with an increasing charge-transfer resistance.

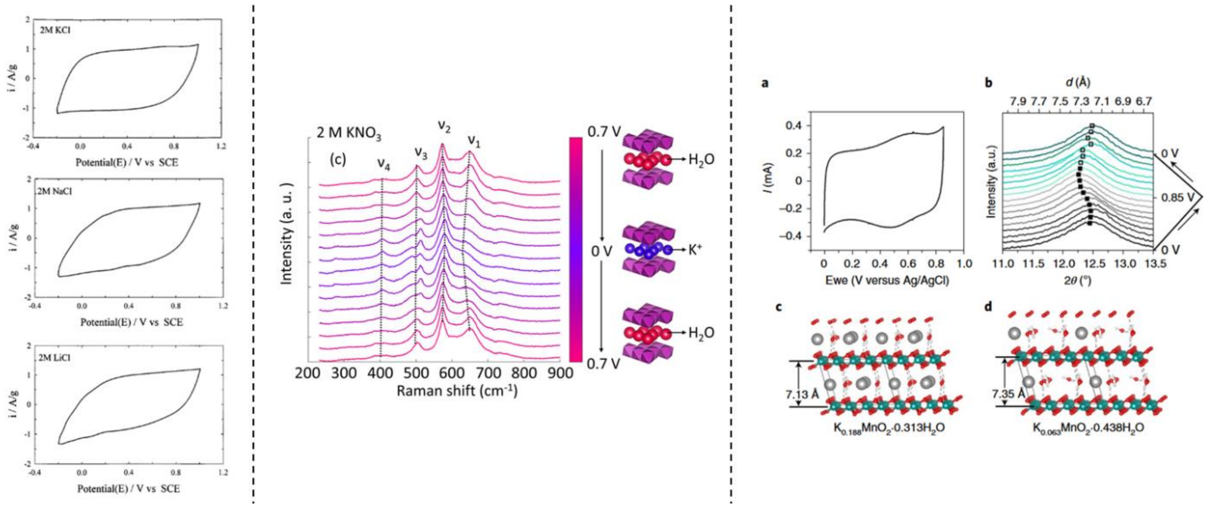

Figure 30: CVs of amorphous-MnO_2 performed in KCl, NaCl, and LiCl electrolytes (left)[227]; Variation of Raman bands of birnessite in KNO_3 electrolyte[233] (middle); CV of birnessite in K_2SO_4 electrolyte (a), change in the (001) 2Theta angle upon potential cycling showing the interlaying spacing evolution (b), and the DFT structures of birnessite before (c) after K^+ deintercalation (d)[234].

Another *operando* Raman study evoked the cation-size effect – already mentioned previously in older study – with the intercalation of Li^+, Na^+ and K^+ and their relative structural difference with the charge storage behavior[233]. All of these three cations involved pseudocapacitive behavior of the MnO_2 thin film but with different electrochemical performance, especially the cycling stability. K^+ showed the most stable cyclability whereas Li^+ showed the lowest stability. This is explained by the stronger structural changes brought back by the insertion/deinsertion of smaller cations. When oxidation of the Mn is gradually lowered (cathodic scan), more cations is intercalated with replacement of larger water molecules in size compared to the cation that would lead to shrinkage of the interlayer spacing (i.e. increased electrostatic interaction and less steric hindrance) as seen for K^+ in Figure 30 middle. In addition, charge-discharge curves and EIS measurements show that for smaller cations (i.e. Li^+) higher capacitance and higher capability rate. The latter is explained by the faster diffusion of smaller cations within the interlayer supported by lower cell resistance and higher frequency shift from the diffusion region (mid-frequency part) to the capacitive storage (low-frequency part). Yang *et al.* observed by *operando* Raman spectroscopy that no proton insertion was involved during Na^+ intercalation, the latter being sufficient for charge compensation of Mn oxidation state change[235]. DFT calculations emphasized as well the less thermodynamically favorable proton adsorption due to the stronger sodium cation adsorption energy. The interlayer spacing change during cation insertion is also monitored by X-ray diffraction (XRD) and seen on various manganese dioxide allotropes[236]. A recent study clarified the effect of interlayer confinement and hydration level of birnessite by *ex situ* XRD, electrochemical quartz crystal microbalance (EQCM), *in situ* Raman spectroscopy, *operando* atomic force dilatometry supported by atomic-scale simulations using density functional theory (DFT)[234]. It reveals that potassium cation intercalated within the hydrated interlayer of birnessite causing very low structural changes and at the origin of the capacitive behavior (Figure 30 right). K^+ inters right in the middle of hydrated interlayer by losing about half of its hydration shell but still showing a relatively large distance between the K^+ and coordinating oxygen of MnO_2. Hence, the structural water within the hydrated birnessite layer plays an important role by increasing the previously mentioned K^+-oxide distance. Manganese oxide-based materials are a very promising class of material for supercapacitor applications. Thus, many researched focus on creating hybrid technologies, composites with carbon-based materials and various doping strategies to correct the electronic conductivity problem, stability, low potential window application and overall performances[237].

The other type of pseudocapacitance phenomena is the so-called intercalation-type pseudocapacitance which involves the fast and reversible intercalation of ion within the lattice of the host material. B. E. Conway describe the lithium ion intercalation in layered sulfides (e.g. TiS_2, MoS_2) and oxides (e.g. CoO_2) battery materials introducing the term of “quasi-two dimensional sorption”[238]. One of the first considered intercalation-type pseudocapacitive material was introduced by M. Zukalová *et al.* in 2004 which consist on a pure-phase monoclinic bronze titanium oxide TiO_2(B) nanofibers[239]. This material showed no solid-state diffusion limitation over lithium ion intercalation – between 0.1 and 2 mV/s of scan rates (Figure 31 left) – within parallel channels perpendicular to the (010) face in organic electrolyte and a pair of reversible peaks ca. 1.5 V and 1.6 V vs. Li^+/Li. The bulk anatase phase TiO_2 is however not showing any significant pseudocapacitive behavior but rather a classical intercalation-type storage mechanism. Study on nanostructured anatase particles ranging from 30 nm to 7 nm revealed the significant pseudocapacitive participation for charge storage when the particle size is decreased < 10 nm (Figure 31 middle)[240]. Important result highlights the decrease in lithium ion intercalation charge storage process (i.e. Faradaic battery-like mechanism) as the particle gets smaller but the pseudocapacitive contribution over-compensate this loss and allow higher overall specific capacitance. Thermodynamic studies derived from first-principle DFT allowed to show that TiO_2(B) phase could intercalate Li^+ up to Li/Ti ratio of 1.25 and thus having a higher theoretical specific capacitance than a classical one-electron process than for one unit of TiO_2 (419 mAh/g vs. 335 mAh/g), with lithium occupying A1, A2, C and C’ sites[241].

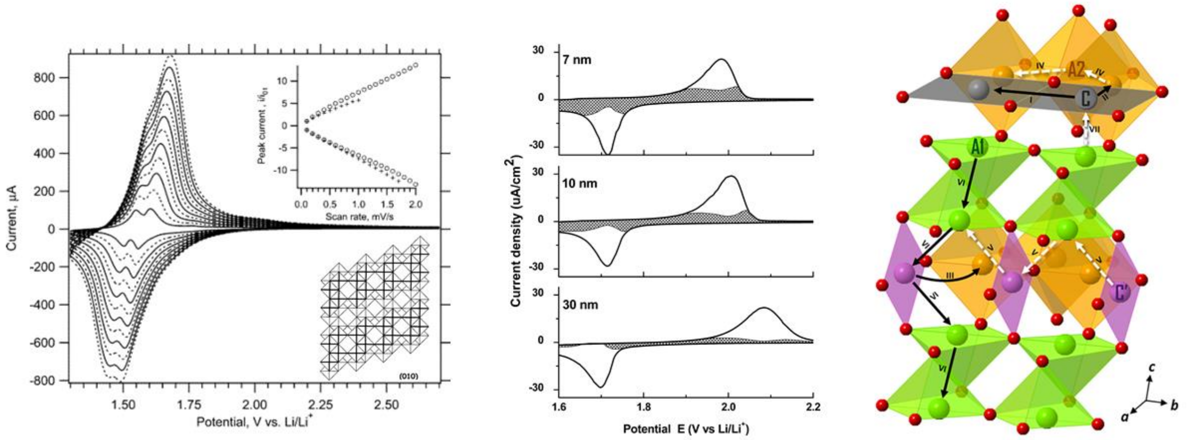

Figure 31: CVs of TiO_2(B) with no solid-state diffusion limit at 0.1 to 2 mV/s scan rate (left)[239]; Anatase phase showing high pseudocapacitive contribution for nanoparticles below < 10 nm (middle)[240]; Structural representation of TiO_2(B) with the different Li^+ migration pathways from site to site (black arrow: probable; white arrow: improbable)[242]

Besides the morphology dependency, the lithium content dictates its own transport and kinetics through various pathways in nanoparticles[242]. For lithium content of $x < 0.25$ (considering Li_xTiO_2), Li^+ migrates rapidly with association to pseudocapacitive phenomena through the most favorable thermodynamic pathway along the *b*-channel through C site hoping via C' followed from C to A2 site which is also energetically low. When half of A2 sites are fulfilled (i.e. $x = 0.25$), C site destabilization occurs with repulsive interactions (i.e. Li^+ repulsions in A2 sites) which changes the diffusion pathway from C' site to A2 site occurring in a two-step process. The latter is diffusion-controlled with higher diffusion energy barriers most probably causing Li^+ trapping into A2 sites up to $x = 0.5$. Further lithiation up to $x = 0.75$ occurs via C' two-step fulfilling, which is kinetically fast. After that, migration towards A1 sites happen via a diffusion-controlled solid-solution reaction. Hence, TiO_2(B) show a pseudocapacitive behavior associated with fast diffusion kinetics thanks to half of A2 sites fulfillment via C site hoping in prior and then C' sites. Further A2 and A1 filling is diffusion-limited and can be observed in nanostructured particles, requiring morphological adaptation to reduce their kinetic diffusion energy barriers for fast Li^+ transport.

A second material attracted the attention for pseudocapacitive application, which was niobium pentoxide Nb_2O_5. First capacitive-like behavior with Li^+ pseudocapacitive intercalation was observed in the orthorhombic *T*-Nb_2O_5 phase in 2010 with high surface area mesoporous oriented layered nanodomains (Figure 32 left)[243]. It was only hypothesized that these fast kinetic results were due to the nanostructuring of the particles with preferred orientation of the layers. It was later confirmed that this Li^+ intercalation pseudocapacitive feature was intrinsic to the material[244]. High capacitance at fast charge/discharge rates (ca. 450 F/g for 12s charging time) were found while exhibiting fast Li^+ intercalation kinetics for *T*-Nb_2O_5 aerogel, but also for the pseudohexagonal *TT*-Nb_2O_5 phase (Figure 32 left). Preferential crystallographic pathways for fast Li^+ transport is thought to be at the core of the fast and reversible pseudocapacitance of *T*-Nb_2O_5 within the (001) and (118) planes , with cation size-exclusion study (i.e. in $LiClO_4$- and $NaClO_4$-based electrolytes) confirming the pseudocapacitive charge storage (i.e. only ELD capacitance with Na^+). Further kinetics study performed by same researchers the following year, showed the surface-controlled dominated regime up to 20 mV/s of scan rate while diffusion-controlled process above 50 mV/s with solid-state diffusion limitations started to appear[245]. This study also enlightened the gradual oxidation of Nb^{5+} to Nb^{4+} upon lithium intercalation via a two-step intercalation process with the use of advanced *in situ* X-ray absorption spectroscopy (XAS) and FT-extended X-ray absorption fine structure (EXAFS). Use of in-depth characterization tools such as $^{6/7}Li$ solid-state NMR (ssNMR) revealed the inherent pseudocapacitive behavior to not only nanocrystalline *T*-Nb_2O_5 and *TT*-Nb_2O_5 but also to the bulk micrometer-sized particles[246]. *T*-Nb_2O_5 was described as framework alternating layers of bridging oxygen pillars along the *c*-axis and Nb-O polygons with relatively large interlayer distance (ca. 0.39 nm). This structuration and the very low kinetic activation barrier for lithium diffusion (between 60 to 100 meV) are considered to be at the origin of the very fast Li^+ mobility with minimized structural strains. The insulating nature of Nb^{5+} compared to conducting Nb^{4+} upon lithiation might be the main reason for extended high-rate use. *In situ* XRD experiments emphasized the Li^+ fast and reversible intercalation pseudocapacitance in the bulk material in one- phase process up to x = 1.8 with interlayer spacing shifting from 3.93 Å to 4.02 Å upon lithiation intercalation and Nb^{5+} to Nb^{4+} reduction[140]. Hence, it confirmed the highly favorable pathways from the {001} planes of the structure. In-depth analysis with *operando* Raman spectroscopy underlined the Li^+ intercalation and location within *4g* atomic layers between bridging oxygen of neighboring *4h* layers. Fast lithium diffusion occurs via two-path (i.e. coordination with six oxygen atoms for the path A, and seven atoms for the path B) mainly due to low-hindrance and large void between *4h* (Figure 32 right).

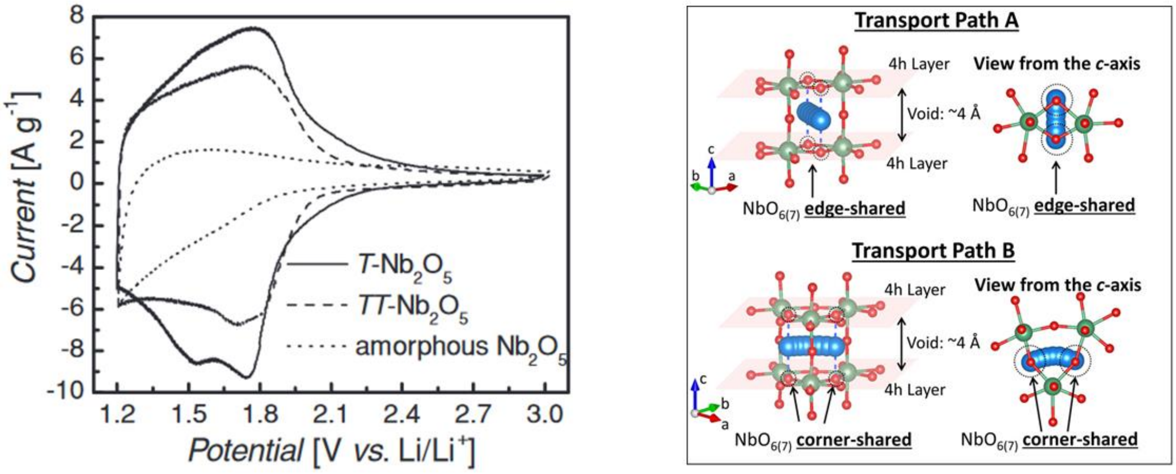

Figure 32: CVs of T-Nb_2O_5, TT-Nb_2O_5 and amorphous showing the high pseudocapacitive signal offered by fast and reversible Li^+ intercalation in titania bronze phases (left)[243]*; Transport pathways A and B proposed for the pseudocapacitive lithium intercalation within T-Nb_2O_5 (right)*[247]

- Nanostructuring of electrode materials in EESDs

As another aspect but nonetheless very interesting, is the case of achieving "extrinsic" pseudocapacitance and fast charge/discharge rates by nanosizing some intercalation-type materials such as transition metal oxides. This can be addressed by some thermodynamics and kinetics fundamentals upon particle size decrease at the nanoscale. In a lithium-ion battery, the driving force of the cell depends on the Gibbs free energy of the lithium intercalation from the anode to the cathode $\Delta_r G$ (in J/mol), which can be defined as:

$$E_{cell} = -\frac{\Delta_r G}{z_r \cdot F} \tag{26}$$

with E_{cell} the equilibrium potential or cell voltage (in volt, V), z_r the number of electron involved in the reaction and F the Faraday constant (96 845 C/mol or J/V/mole of electron). The charging process in such system is directly dependent on the evolution of the chemical potential of lithium μ_{Li} going from the anode to the cathode (i.e. increase in μ_{Li})[248]. Hence, the cell voltage is determined by the chemical potential of μ_{Li}. The latter can be described by the sum of the electrochemical potential (i.e. chemical potential added with a $z_i F\phi$ term) of lithium ion $\tilde{\mu}_{Li^+}$ and the one of electrons as $\tilde{\mu}_{e^-}$ at equilibrium:

$$Li \rightleftarrows Li^+ + e^- \tag{27}$$

$$\tilde{\mu}_{Li} = \tilde{\mu}_{Li^+} + \tilde{\mu}_{e^-} = \mu_{Li} + z_{Li}F\phi = \mu_{Li} \tag{28}$$

with ϕ the local electrostatic potential difference. Since lithium is a neutral component (z_{Li} = 0), its chemical potential equals its electrochemical potential. The electrochemical potentials of the electrons between two points - here, the two electrodes with local chemical equilibrium with Li, Li^+ and e^- and hence quasi-identical chemically with high electronic concentration - refer to the difference in the Fermi potentials and is equal to the electric voltage times the Faraday constant (i.e. charge per mole of electrons). Due to no Li$^+$ flux in the electrolyte at equilibrium (i.e. $j_{Li+} = 0$) and since the Li$^+$ conductivity is not zero (σ_{Li+}), the gradients in the (electro)chemical potentials of lithium ion is considered null. Hence, one could write:

$$\Delta\tilde{\mu}_{e^-} = \tilde{\mu}_{e^-_{cathode}} - \tilde{\mu}_{e^-_{anode}} = \mu_{Li_{cathode}} - \mu_{Li_{anode}} = \Delta\mu_{Li} \tag{29}$$

and considering that it is a pure one-electron process,

$$E_{cell} = -\frac{\tilde{\mu}_{e^-_{cathode}} - \tilde{\mu}_{e^-_{anode}}}{F} = -\frac{\mu_{Li_{cathode}} - \mu_{Li_{anode}}}{F} \tag{30}$$

From the rewritten differences in the electrochemical potentials of electrons and lithium in the cathode and anode, a clearer equilibrium equation can be defined as follow:

$$Li_{cathode} + e^-_{anode} \rightleftarrows Li_{anode} + e^-_{cathode} \tag{31}$$

However, even though electrochemical equilibrium cell is here ascribed by the local electrode equilibrium, only the ions are really considered at equilibrium when no voltage difference is applied. Considering this and the fact the studied reactions in research for TMO involves the understanding of lithium intercalation in the bulk of the cathode vs. a lithium metal pseudo-reference electrode, the equation of reaction can be transformed to:

$$Li \rightleftarrows Li_{cathode} \tag{32}$$

Since in most TMOs can be considered as ionic materials, lithium is at least partially ionized and gives simplified and clear equation as:

$$Li \rightleftarrows Li_{cathode} + e^-_{cathode} \tag{33}$$

with,

$$\mu_{Li} = \mu_{Li^+_{cathode}} + \mu_{e^-_{cathode}} \tag{34}$$

For understanding the effect on nanostructuration, one can regard the change applied to the chemical potential of lithium. Indeed, nanostructuration implies high surface-to-volume ration with increased capillary pressure on the particle surface. Wulff-shaped nanocrystals in equilibrium state with neglected surface stress can be used to analyze the impacts. For this nanoparticles, the increase capillary pressure is directly given by two times the surface tension γ_S (averaged to area of the given surface of the plane) by the distance of the plane from its origin r_S (also averaged by the plane surface). This effect gives to an excess of chemical potential μ_{Li}^{ex} not negligible at nanosized, noted as:

$$\mu_{Li}^{ex} = 2\frac{\gamma_s}{r_s}\nu_{Li} \tag{35}$$

with ν_{Li} the partial molar volume of lithium. This can be applied to point-defects as well with $\nu_{d,Li}$. The chemical potential of lithium can then be decomposed according to the bulk and surface contributions in function of the averaged distance r_s:

$$\mu_{Li} = \mu_{Li}^{\infty}(r \to \infty) + \mu_{Li}^{ex} = \mu_{Li}^{\infty}(r \to \infty) + 2\frac{\gamma_s}{r_s}\nu_{Li} \tag{36}$$

The observed redox transition peaks in a typical intercalation-type materials is then depending on the size of the particle. Indeed, if all the chemical potentials of the different phases involved during the redox transition-accompanied lithium intercalation are considered, then the observed peak can shift non negligibly when high capillary pressure is exercised on the lithium with nanosized intercalation-type particles. This effect is in this case responsible for plateau-to-sloppy transition, even more pronounced when a larger dispersion of crystallite sizes and shapes are present (i.e. broader redox potential distribution at the macroscopic level)[249]. In addition, this nanosizing can also affect the phase transition (e.g. α to β) occurring during intercalation-redox transition in TMOs battery materials[250]:

$$\Delta G_{\alpha\to\beta} = \Delta G_{\beta} - \Delta G_{\alpha} \tag{37}$$

For a small sized particle *i*, the surface energy term is not negligible and should be accounted with the bulk free energy contribution:

$$\Delta G_i = G_{v,i} + \gamma_{sn,i} \tag{38}$$

with G_v the bulk or volume free energy and $\gamma_{sn,i}$ the surface energy normalized by the surface area of the particle. Additionally, one should also consider the free energy for the creation of an interphase between the nucleus of β and the matrix of α – noted as ΔG_{int} –, the free energy associated with strain creations upon nucleation of a new phase – as ΔG_{strain} – and the free energy linked to atoms to pass through the created interface, ΔG_d. The factors that are highly dependent on the particle size are the surface energy and the strain free energy that will directly influence the driving for phase transition. In other words, increased surface area will lead to higher surface tension, then directly affecting the free energy of phase transition. The strain created by the formation of nucleus is related to the density of the new phase but also to the capillary pressure exercised on these crystallites. A positive volume change will increase this strain energy while a lower will reduce it. If strain energy might increase for a given phase change, it would imply an increase in one of the energy barriers to the transformation and thus, tend to inhibit the transformation. As a notable example, molybdenum dioxide MoO_2 used for intercalation-type energy storage in Li-ion battery sees its phase transition from the monoclinic phase to the orthorhombic phase suppressed with 15 nm-sized crystals (Figure 33)[251]. These MoO_2 nanoparticles exhibited a pseudocapacitive behavior with improved kinetics and a slopping voltage signal, leading to higher storage performance, capacity improvement at high charge/discharge rate, better stability of the material and lower voltage hysteresis. Besides possible reduction of the diffusion length while nanosizing the particle (i.e. improved diffusion kinetics), the preservation of the monoclinic phase might reduce the strain creation, improving the overall stability, but also to preserve the Li^+ fast diffusion tunnels.

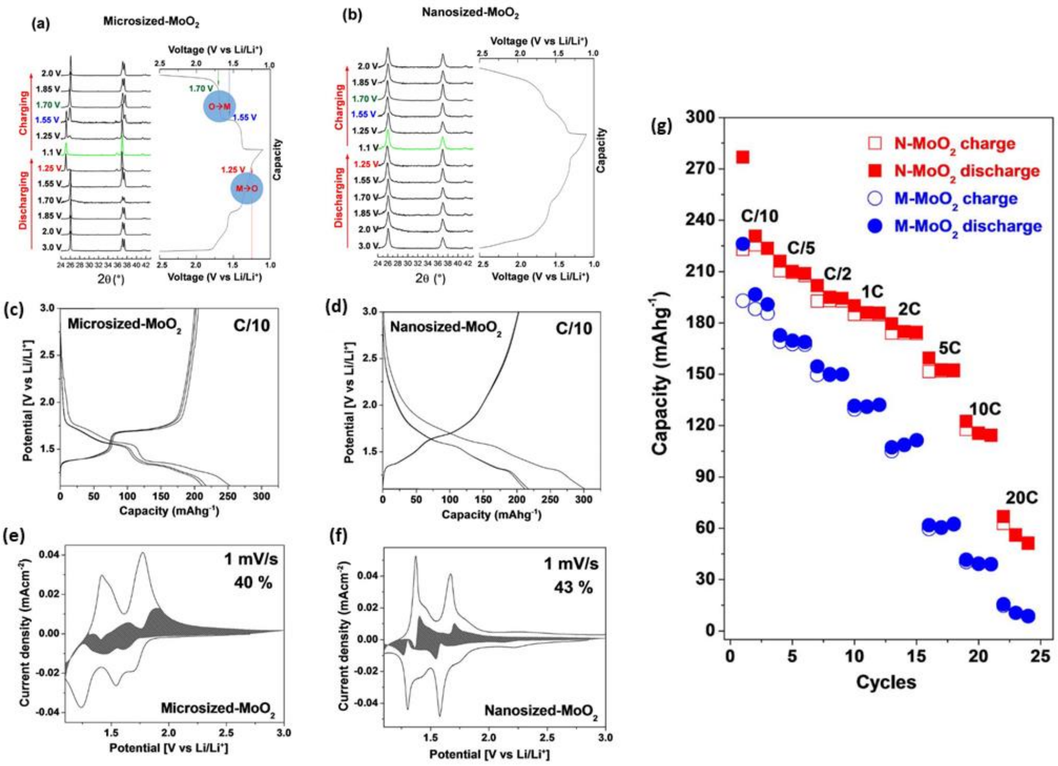

Figure 33: Ex situ XRD realized on microsized (a) and nanosized MoO_2 in accordance with their respective galvanostatic charge/discharge curves showing phase transition or not; GCD curves of the micro- (c) and nano-MoO_2 at C/10 rate; and their respective CVs at 1 mV/s (e and f); Plot showing the increased capacities at different charge/discharge rates for the nano-MoO_2 compared to its microsized form[251]

Concerning the kinetics, nanosizing of the electrode appears to be a promising to achieve high rates for intercalation battery materials. In a LiB, three main kinetic movement of lithium ions exist with: (i) the ion transport within the ionically conductive electrolyte; (ii) its transfer at the electrolyte/electrode interface and; (iii) its diffusion within the host electrode lattice for intercalation in the active sites accompanied by electron diffusion as well. These phenomena and their principle parameters are showed in the Figure 34[252]. What appears fundamental is the change in the diffusion length L within the electrode is directly related to lithium ions flux inversely. If the electrode size is significantly decrease from micrometer (10^{-6} m) to nanometer size (10^{-9}), the diffusion length is shorten by a factor thousand and the diffusion time t_d is proportional to the square of this length. For micrometer sized intercalation-type TMO particles, the process is said to be diffusion-controlled since the diffusion length is longer than the root of the diffusion time (times the diffusion coefficient D) for a given cycling rate. However, drastic diminution of this diffusion length tends to give a surface-controlled process since now the diffusion time is largely smaller:

$$L < \sqrt{t_d \cdot D} \tag{39}$$

This effect was shown in different research works, such as the one with anatase TiO_2 (Figure 31 middle)[240]. As the size of particles diminished from 30 nm to 7 nm, a higher surface-controlled contribution is observed, leading to higher performance at faster cycling rates. Another example would be the dispersion of nanoscale particles of TiO_2(B) (~ 5 nm) onto MWCNTs which show improved performance even at very high cycling rate (ca. 235 mAh/g at 300C rate)[253].

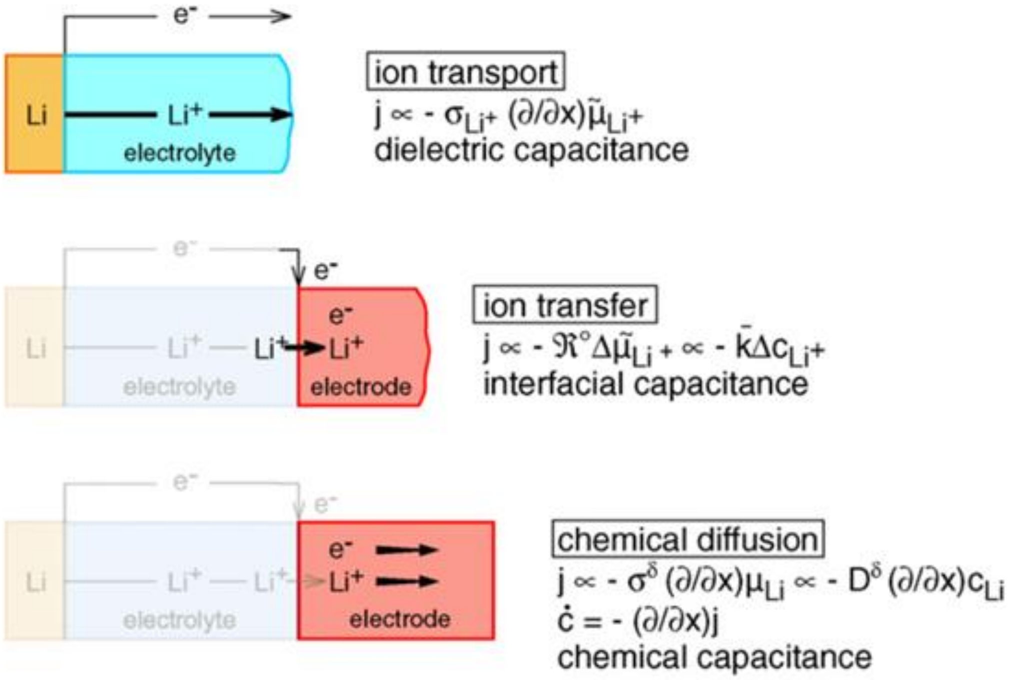

Figure 34: Schematic representation of lithium ion transport within the electrolyte towards the electrolyte/electrode interface for ion transfer prior to diffusion within the host lattice[252]

Before switching to hybrid technologies, it is worth to mention that researchers investigate the use of “greener” transition metal elements for their application in EESDs. Manganese and iron elements are considered promising in that sense, with profound studies on various Mn- and Fe-oxides. Spinel Mn_3O_4 represent another interesting manganese oxide material for such applications. The latter will be discussed later as the scope of this research study alongside iron-based materials such as Fe_3O_4.

- Hybrid technologies
    - Hybrid supercapacitors/batteries

When referred to supercapacitors, the most common and firstly designed type consist of two identical positive and negative electrodes made of porous carbons. This design is then called “symmetrical supercapacitor”. In a general manner, the positive and negative electrode possess the same type of charge storage mechanism, such as EDLC//EDLC. The positive and negative electrodes in a typical 2-electrode cell – the more comparable to a real commercialized supercapacitor to study performance metrics – must provide charge balance for optimal use. Both electrodes should respect the following equality:

$$Q_{positive} = Q_{negative} \tag{40}$$

$$m_{positive} \cdot C_{positive} \cdot \Delta E_{positive} = m_{negative} \cdot C_{negative} \cdot \Delta E_{negative} \tag{41}$$

Since in symmetric configuration both electrodes are identical (i.e. same potential window and capacitance), they should also have the same mass. Therefore, the potential window stability tested in a 3-electrode setup to study the active materials behavior more precisely can be directly implemented for 2-electrode cells (Figure 35[254]). For instance, symmetric supercapacitors using aqueous electrolyte are limited to ca. 1.2 V, which is limiting the energy density.

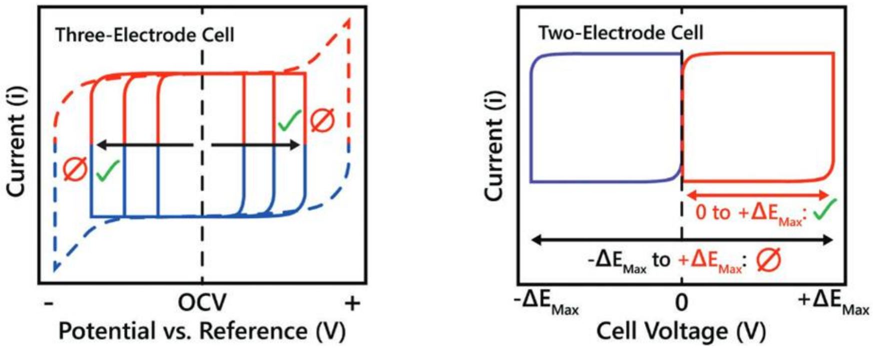

Figure 35: CV representation of an ELDC in a 3-electrode cell with proper voltage window without electrolyte reduction nor oxidation (left); Same electrodes configuration in a 2-electrode cell showing the voltage of each electrolyte and the correct potential window (right)[254]

It is from this potential limitation that the idea of using asymmetric architecture becomes interesting. Indeed, where the potential window in aqueous symmetric supercapacitors would be around 1.2 V, it can be increased around 2.0 V in asymmetric cells. More generally speaking, the operating voltage window of a cell will depend on the nature of the used electrolyte and its potential stability, the potential range of the electrodes in this same electrolyte and, the occurrence or not of a passivation layer the surface of the electrodes[142]. The first point is the major concern for every type of electrochemical measurements. The decomposition of the electrolyte at high potential (oxidation) or low potential (reduction) will determine the range of potential that can be achieved and hence, the stability domain. In the case of water, this is determined by the oxygen evolution reaction (OER) for the oxidation step and by the hydrogen evolution reaction (HER) at the reduction step. The second point refers to the potential stability range of the active material in this same electrolyte without involving harsh decomposition/deterioration of the electrode material. The last point concerns the presence of a passivation layer at the electrode, which would affect the electrolyte oxidation/reduction kinetics and provide enhanced potential window stability domain. Furthermore, combining a negative electrode with potential range located at low potentials and a positive electrode with potential range in the high potential region would theoretically allow an extended voltage window than each electrode used solely in symmetric configuration (Figure 36 a and b). Of course, one important note to take into consideration is to respect charge counterbalance. Since both electrodes are different, the masses of each electrode have to be calculated and adjusted according to their respective specific capacitances obtained in a 3-electrode cell setup.

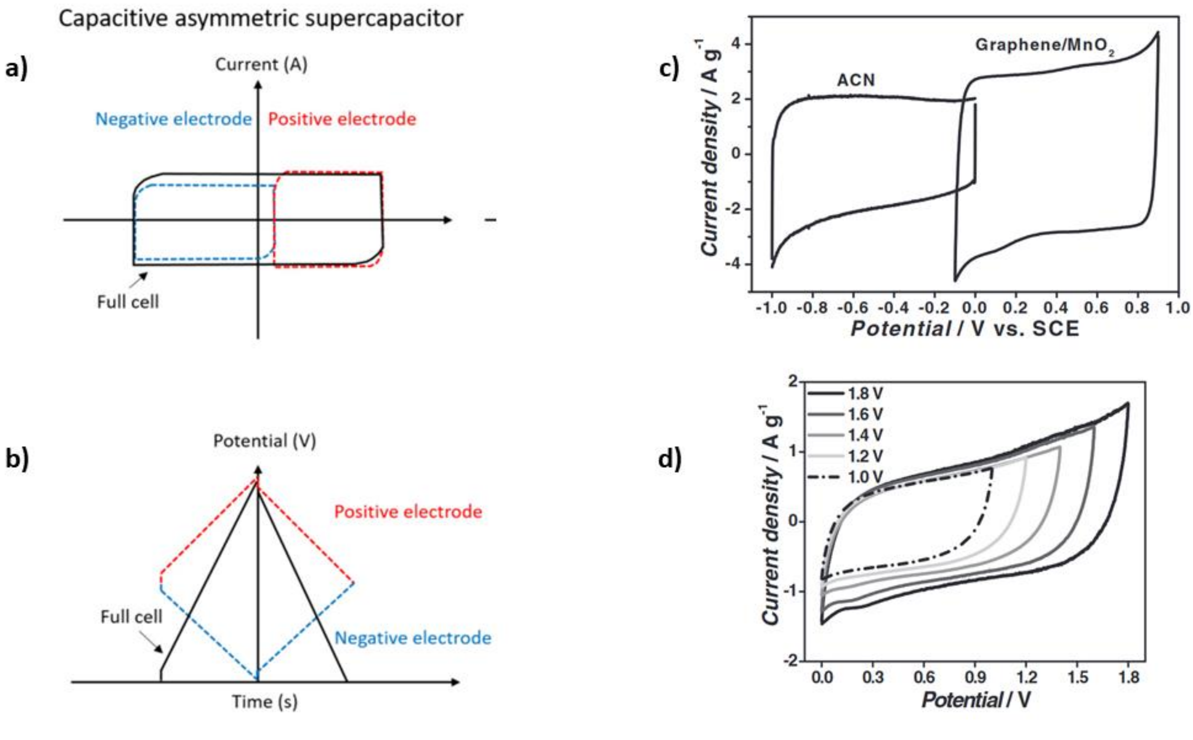

Figure 36: Representation of a full cell capacitive asymmetric supercapacitor showing the CV (a) and GCD deconvolution of the negative and positive electrodes (b)[142]*; Separated CVs at 10 mV/s of the negative activated carbon nanofibers electrode and the positive graphene/*MnO_2 *electrode (c), and the full cell CV for different potential windows (d)*[255]

As an example purpose, one previously cited example was the case of the first asymmetric cell using amorphous MnO_2 as a positive electrode and activated carbon as negative electrode in 1M KCl[228]. CVs at 10 mV/s of each electrode tested separately showed a 160 F/g from 0.0 V to 1.0 V vs. Ag/AgCl for MnO_2 and 210 F/g from -1.0 V to 0.6 V for the activated carbon. The asymmetric configuration's operating voltage was extended up to 2.0 V and a specific capacitance of 52 F/g (the specific capacitance of a capacitor is about 4 times lower than the specific capacitance of the electrode) was obtained for a charging rate of 0.25 A/g. Note that symmetric supercapacitor based on amorphous RuO_2 in aqueous acidic (ca. 1 V of potential window) media at this time reached 190 F/g with an energy density of 26.7 Wh/kg. However, this AC // MnO_2 configuration provided an energy density as high as 28.8 Wh/kg despite the low specific capacitance C of the cell. This is due to the extended voltage V by about ~1 V compared to the RuO_2 symmetric cell, which is translated by an energy density E_d multiplied by 4:

$$E_d = \frac{1}{2} C V^2 \tag{42}$$

Another example[255] using MnO_2 is shown by using a conductive composite made of graphene/MnO_2 as a positive electrode and activated carbon nanofibers as the negative electrode in 1M Na_2SO_4. While each material exhibited separately a ca. 1 V potential window in different ranges (Figure 36 c), the asymmetric cell showed a specific capacitance up to 63 F/g at 10 mV/s and 113.5 F/g at 1 mV/s for a 1.8 V voltage window (Figure 36 d). An energy density up to 51.1 Wh/kg - and a maximum power density of 198 kW/kg - were able to be reached for a MnO_2 asymmetric system, with an E_d almost doubled in about 10 years.

Use of conductive polymer composites showing pseudocapacitance charge storage mechanism and a EDL capacitor is also a good example of design variety for asymmetric supercapacitors. For instance, a positive electrode constituted of polyaniline (PANI)/sulfonated graphene nanosheets/carboxylated multiwalled carbon nanotubes and a negative electrode of activated graphene showed a potential window stability up to 1.6 V in 1M H_2SO_4 with an energy density of 20.5 Wh/kg at a 20 kW/kg power density[256]. Use of conductive polymer as active materials such as PANI in this case presents the advantages of low synthesis cost, high electronic conductivity and adaptability for flexible supercapacitive devices. One could also think about another configuration based on one side with a surface redox pseudocapacitive electrode material and on the other side, an intercalation-based pseudocapacitive electrode material. On this basis, MXene or also defined as a 2D transition metal carbide/nitride material, present interesting properties thanks to its unique structural composition. They are generally composed of a conductive carbide layer enveloped by two layers based on an early transition metal with oxygen, hydroxyl or fluoride surface functionalization, with pre-intercalated water[257,258]. These materials present metallic electronic conductivity, high hydrophilicity, surface redox active sites able of charge storage and fast storage thanks pre-intercalated water molecules[259]. For instance, a $Ti_3C_2T_x$ MXene (i.e. the most commonly prepared and studied) can show specific capacitance up to 310 F/g in sulfuric acid aqueous media thanks to fast proton intercalation pseudocapacitance[259]. However, their limited 1 V potential window cannot allow to obtain high energy densities in a symmetric assembly and emphasizes the need for an asymmetric configuration. Therefore, here is an example of combining a $Ti_3C_2T_x$ MXene as a negative electrode and RuO_2 as a positive electrode in acidic electrolyte (Figure 37 a)[260]. While the MXene present a proton intercalation pseudocapacitive charge storage, the RuO_2 will exhibit a surface-redox pseudocapacitive behavior. The full cell device voltage window was enhanced up to 1.5 V (Figure 37 b and c) with an energy density of 24 Wh/kg at very high power density (26 kW/kg).

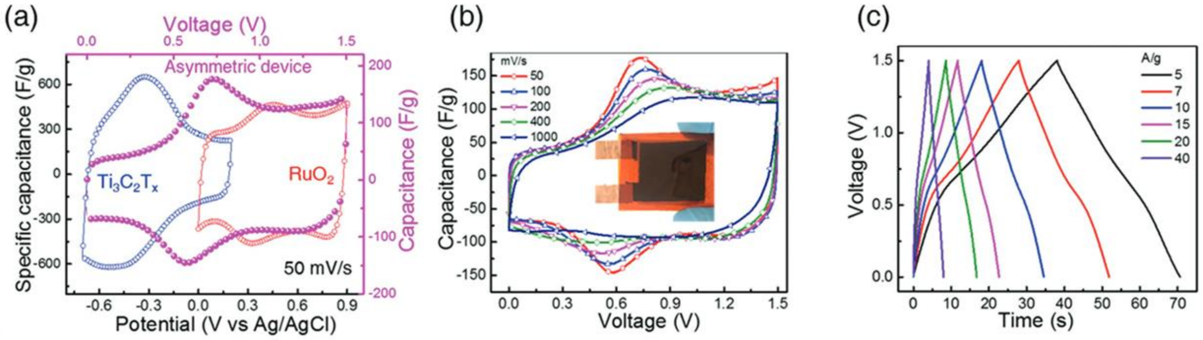

Figure 37: Separated CV signals of $Ti_3C_2T_x$ and RuO_2 superimposed with the one of asymmetric cell (a); Asymmetric cell CV signal at different scan rates (b); GCD curves of the full cell (c)[260]

Where all the above configurations possess the same charge storage mechanism, in the way that they are capacitive, they are solely referred to asymmetric capacitors. However, hybrid capacitors – which can be considered as a specific case of asymmetric configuration – refers to the use of different charge storage mechanism for each electrode. Hence, combining an EDLC electrode (e.g. porous activated carbon) and a battery-like electrode material (e.g. $Ni(OH)_2$) is an interesting design to match the advantages of both electrode (Figure 38 a and b). In other ways, a hybrid device could be at the intermediate of an EDLC and battery by reaching energy densities and power densities at the middle level of both technology. An representative example would be this study using a porous graphene capacitive electrode and a $Ni(OH)_2$/graphene composite as the battery-like electrode in alkaline media[261]. Each electrode was tested in prior separately in a 6M KOH electrolyte at different potential range (Figure 38 c and d). The $Ni(OH)_2$/graphene composite positive electrode showed a capacity up to 1735 F/g in a 0.55 V potential window according to the authors. However, when a battery-like material is considered, it is advisable to talk in terms of capacities (in mAh) and not capacitance (in F). This value would then be ca. 265 mAh/g. The porous graphene negative electrode present capacitance values up to 245 F/g for a 1.0 V potential range (i.e. 68 mAh/g). The hybrid full cell assembly (Figure 38 e) a maximum of ca. 218 F/g was reached for 1 mV/s of scan rate for 1.6 V extended voltage range (ca. 97 mAh/g). The full device exhibited a way higher energy density than the previously presented aqueous asymmetric capacitors with ca. 77.8 Wh/kg at 0.17 kW/kg of power density and even 13.5 Wh/kg at fast power of 15.2 kW/kg. This technology architecture is then viable and very attractive to obtain an in-between performant EESD.

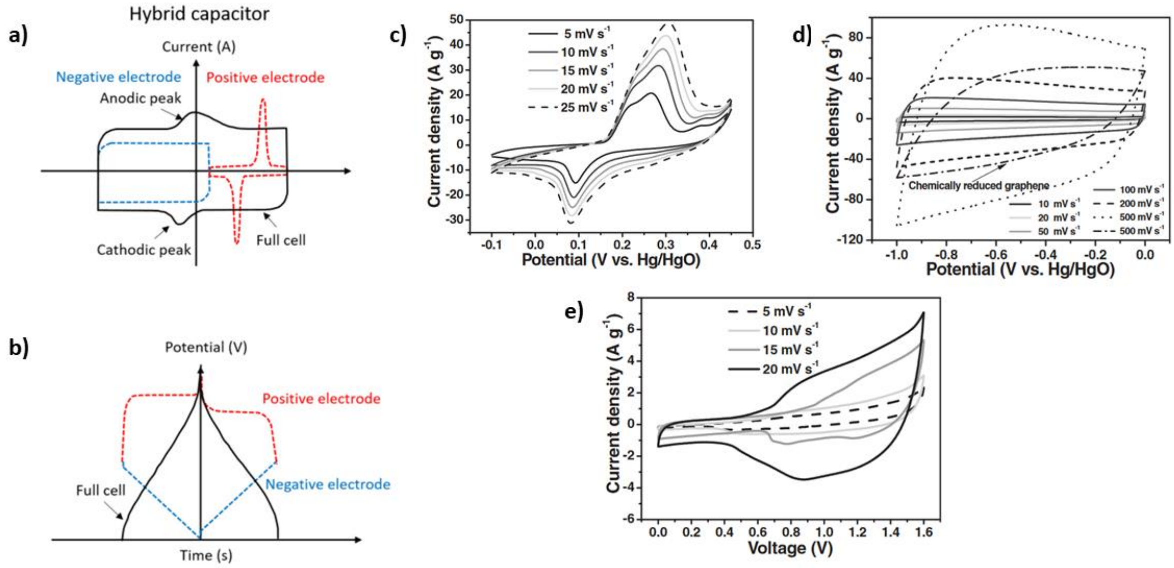

Figure 38: Representation of a full cell hybrid capacitor showing the CV (a) and GCD deconvolution of the negative capacitive electrode and the positive battery-like electrode (b)[142]; CV at different scan rate of the $Ni(OH)_2$ battery-like electrode (d); the one of the porous graphene capacitive electrode (d); and the CV of the hybrid full cell assembly (e)[261]

- <u>Lithium-ion capacitors</u>

Lithium-ion capacitor (LIC) is a specific kind of hybrid capacitor – also known as metal-ion capacitor – used in the specific case of lithium ion storage. The goal is to design a device sharing similarities between a lithium-ion reversible battery and an electrical double-layer capacitor. Indeed, a positive capacitive-like electrode (e.g. made of activated carbon) will store ion at its surface through electrostatic interactions (EDL), thus achieving high power densities. For such application, porous activated carbons are very interesting since they can offer very high surface area. Concerning the negative electrode, a battery-like anode is used which will store ions through a reversible intercalation mechanism (e.g. graphite) with high energy density. A typical all-carbon device is represented in Figure 39 using a porous activated carbon as the positive electrode and graphite as the negative electrode. One could think of many kinds of electrode associations depending on wished strong points of the full cell by privileging the energy density, power density, cost of production and/or cyclability for instance. Concerning the choice of capacitive electrodes, carbon-based materials are the most suitable ones (e.g. activated carbon, CNTs, carbon aerogels, graphene-like, etc…). For the battery-like electrodes, a plethora of choices exist with metallic/metalloid materials (e.g. Si on carbon), transition metal compounds (e.g. TiO_2, LTO, Nb_2O_5, etc…), polyanionic compounds (e.g. LFP) or even some carbonaceous materials (e.g. graphite or graphene-like, bio-mass derived soft/hard carbons, etc…)[262].

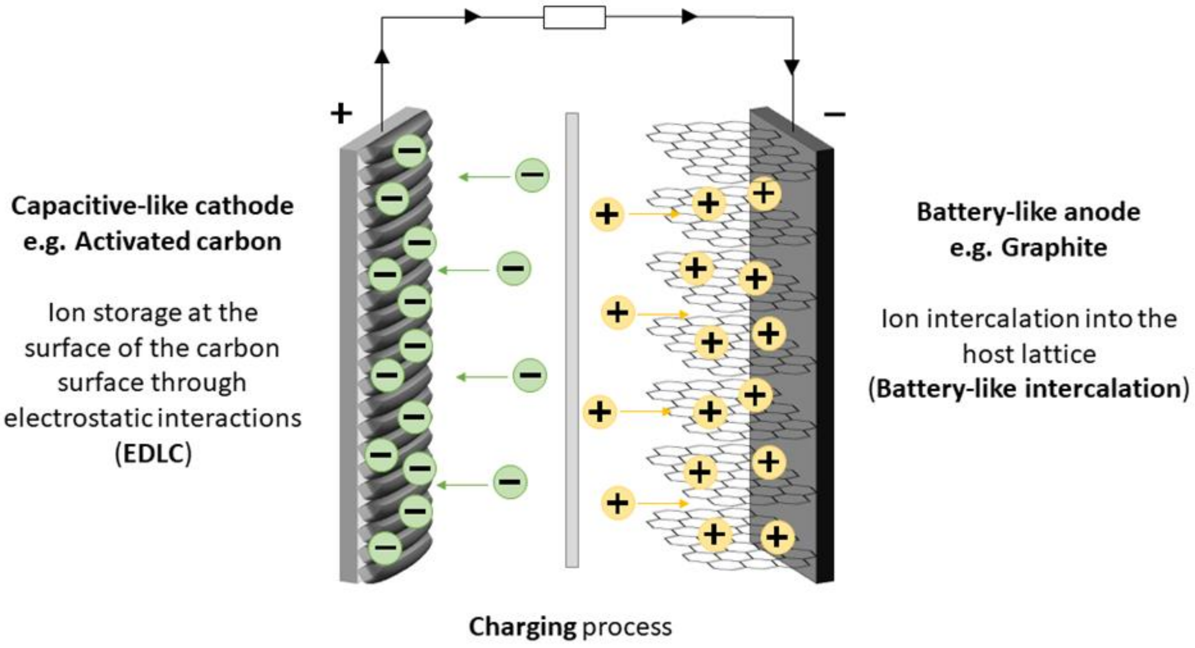

Figure 39: Representation of the charging process in an all-carbon lithium ion capacitor with an activated carbon cathode/positive electrode and a graphite anode/negative electrode

In concern of negative electrodes, the graphite system is very well known in the domain of LIBs and is more than suitable in LICs. Furthermore, its abundancy, physico-chemical properties and low cost makes it already very attractive fur such hybrid architecture. One study here provides the performance for a classical all-carbon LIC using an activated carbon // graphite assembly[263]. The tested activated carbon showed a capacity ca. 75 mAh/g using a 1M in $LiPF_6$ EC/DMC 1:1 electrolyte with a 2.0 V to 5.0 V potential window vs. Li^+/Li. The graphite electrode provided almost five times this value. The different behavior of each electrode can be seen from the deconvolution of the GCD signal into the positive and negative electrode signals (Figure 40 a). While charging the cell, the AC electrode will see its lithium ion removed from its surface to intercalate within the interlayers of the graphite sheets, and vice versa during the discharge process. Even though this cell could be applied up to 5.0 V and showing energy density as high as 145.8 Wh/kg, a 4.5 V voltage window allow a significantly higher cyclability (85% after 10 000 cycles) at a 103.8 Wh/kg energy density and a 10 kW/kg of maximum power density. From the Ragone plot comparing the hybrid and symmetric designs (Figure 40 b), it is demonstrated that above a 10 seconds working range of the devices, the hybrid architecture is clearly superior with almost a factor 15.

Alternatively, transition metal compounds can be used as anodes for LIC. A work described the use of porous TiO_2 hollow microspheres enveloped by graphene nanosheets (negative electrode) and graphene nanosheets (positive electrode). Here, the TiO_2 composites battery-like materials is used as a negative electrode while the capacitive electrode – graphene nanosheets – is the positive one (Figure 40 c)[264]. This emphasizes the various and liberty offered on choosing the electrode materials configuration for the hybrid system. The device exhibited 72 Wh/kg at 300 W/kg, which is more than twice the energy density obtained for symmetric assembly (30 Wh/kg). To cite another material, orthorhombic Nb_2O_5 can also be used to design a flexible hybrid assembly as negative electrode with a classic commercial activated carbon as the positive capacitive electrode[265]. Furthermore, single crystals nanorods of Nb_2O_5 were formed as a film that ensure fast electronic conduction and lithium ion diffusion within the pores accentuated by a reduced diffusion length offered this nanostructure. This flexible hybrid cell provided high energy densities ca. 96 Wh/kg and maximum power densities about 5.3 kW/kg with maintained performance even when the flexible capacitor is bended severely (30° to 180°, Figure 40 d).

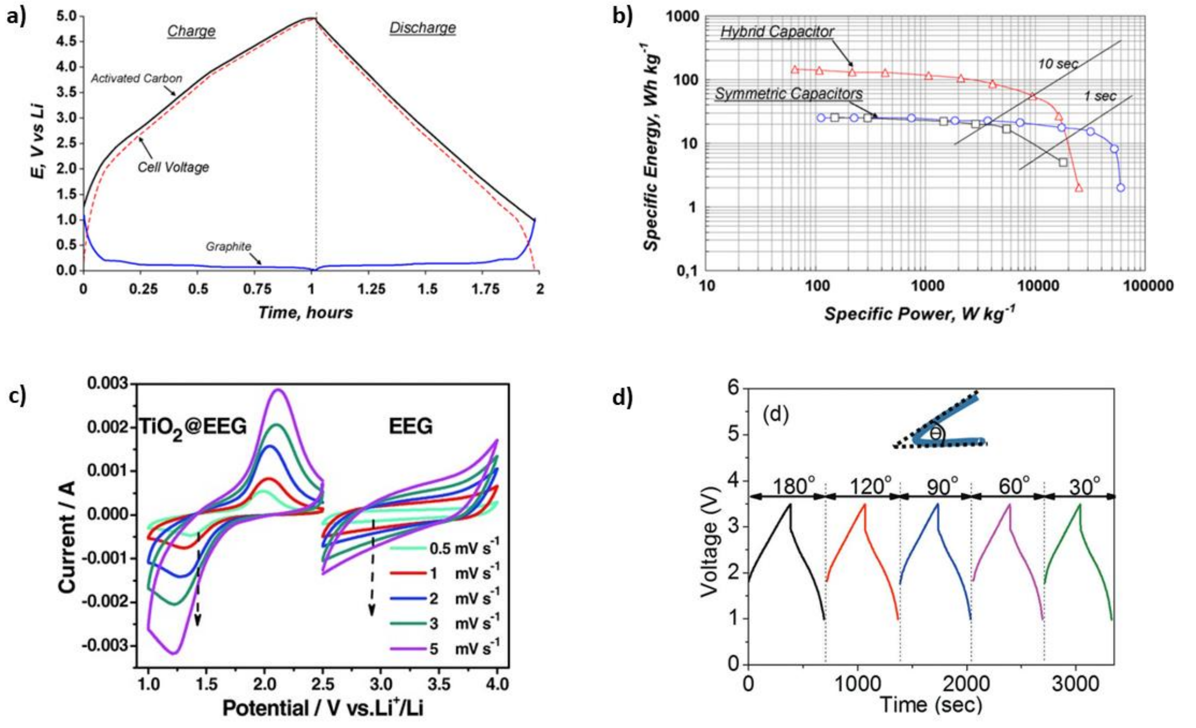

Figure 40: GCD curve showing the hybrid AC/Graphite cell at a current rate C in 1M LiPF6 in EC/DMC 1:1 (a); and the Ragone plot comparing the hybrid and symmetric capacitors (b)[263]*; Separated CVs of the porous TiO_2 hollow microspheres embedded in graphene nanosheets (TiO_2@EEG) as negative electrode and graphene nanosheets (EEG) as positive electrode (c)*[264]*; GCD curves of the flexible hybrid cell at different bending angles (d)*[265]

- Scope of this research work
    - N-doped Activated Carbons for supercapacitors

Nowadays, activated carbons can reach SSA even higher than 3000 m^2/g which make them very attractive in that sense. Nevertheless, it was also found that the pore size – especially the micropores (d<2nm) – in carbide-derived carbon (CDC) has an important effect on the charge storage mechanism. Indeed, pore size matching the relative size of the ions tends to an increase in the capacitance accompanied by the partial desolvation of the cation/anion entering the pore, lowering in a way the distance to electrode surface[211]. Besides pore size, other parameters can also influence charge storage mechanism in carbon-based supercapacitors. The simple electrode-electrolyte interface at the open circuit potential (i.e. no voltage is applied) is adding more complexity with the possibility of the pores being already filled with electrolyte ions/solvent (i.e. ionophilic pore) or empty (i.e. ionophobic pore)[266]. The local environment of the pores (size, volume, shape, degree of confinement, disorders…) is then a direct factor to understand and monitor the charge storage. The potential of zero charge is another parameter often looked at and used to ascribe the dynamics of ions during the charge/discharge processes using electrochemical quartz crystal microbalance (EQCM)[266–268]. A new study underlined by solid-state nuclear magnetic resonance (ssNMR) marks the importance of disorders in nanoporous carbons which would determine the achieved capacitance and not strictly their pore size[269].

Summing up, designing porous conductive carbons with high surface area with some disorder degree in their pores seems like an aim to achieve high capacitance. In addition, surface functionalization of carbon materials with oxygen and nitrogen functional groups can be beneficial to improve their overall performance. Doping with heteroatoms – most commonly oxygen and nitrogen – can affect diverse properties of the N/O-doped carbon materials as illustratively described from Figure 41[270].

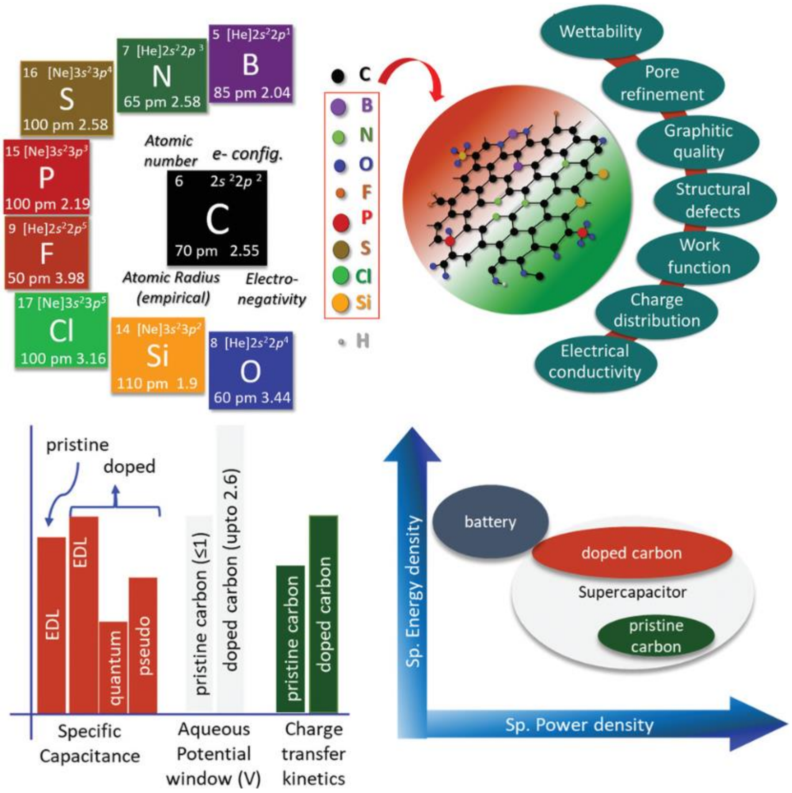

Figure 41: Influence of heteroatom doping on carbon materials for supercapacitor applications[270]

The accessible SSA can be increased by a substantial amount from carbon atom loss in the lattice. This is due to oxygen/nitrogen containing functional group formation leading to micropore creation. However, a higher degree of functionalization can induce the collapse of these micropores into mesopores (2 nm < d < 50 nm) and then a decrease of SSA. Besides that, the electronic conductivity of the carbonaceous material can be heavily impacted and will depend of the specific functional groups attached. For example, positively charged graphitic N or quaternary N (N-Q) or oxidized pyridinic groups possess an extra lone pair of electrons that participate to the π-conjugated electrons delocalization improving the electronic conductivity. Negatively charged pyrrolic or pyridinic nitrogen – mostly located on the edges or defect sites – improve the electronic charge density and charge transfer kinetics[270–272]. Nitrogen doping is usually preferred for enhancing electronic conductivity and charge density to oxygen for these reasons. Nevertheless, a high amount of doping can have a counter effect by increasing the ratio of sp^3/sp^2 hybridized carbon ratio, hindering the electronic delocalization then the overall electronic conductivity. The latter is a very important parameter for high power capabilities since the power density is inversely proportional to the equivalent series resistance:

$$P_{max} = \frac{E_{max}^2}{4 \cdot R_{ESR}} \qquad (43)$$

with P_{max} the maximum power achievable (in watt, W), E_{max} the operating voltage (in volt, V) and R_{ESR} the equivalent series resistance (in ohm, Ω). To add precision, the electronic properties of the doped carbons are determined by their energy band and relative band gaps with the introduction of an *n-type* and/or *p-type* doping element. Nitrogen is considered as an *n-type* dopant or electron-donor that will shift the Fermi level E_F towards higher energy levels in the conduction band accompanied by a reduction in the work function and increase charge carriers from extra electrons[273]. Oxygen is, however, considered as a *p-type* dopant or electron-acceptor that will shift the Fermi level towards lower energy levels in the valence band accompanied by an increase in the work function and charge carriers from the created “holes”. Another property to take into account is the wettability of the electrode, which transcripts as the efficient electrolyte diffusion within the whole materials including the pores. This will induce an efficient ionic diffusion within the porous structure carbon to access all the available surface active sites, fast diffusion and transport for at high current rates or simply reduce the internal resistance of the cell. The main contributing factor in a carbon material would be the presence of polar groups.

First of all, oxygen functional groups will be more or less always present within the carbonaceous materials due to synthesis conditions (i.e. oxidative environment) or simply the choice of the carbon source (e.g. bio-mass waste, organic carbon compounds)[270,274]. They can affect the obtained carbonaceous materials structure, conductivity, wettability and electrochemical performances. Indeed, as briefly said before, introduction of functional groups leads to the creation/increase of micropore domains and hence the specific surface area. However, the further increase in these domains would lead to the collapsing of micropores and creation of mesopores and/or macropores (i.e. decrease in the SSA). The rupture in the sp^2-C bonds can lead to loss in electronic conduction pathway with loss of overall conductivity and increase of cell impedance. Depending on the functional groups and their percentages, the energy levels and band gaps of the carbonaceous materials is affected by a *p*-type doping as previously mentioned. Oxygen functional groups will however tend to reduce the electronic conductivity of the material. Concerning the wettability, it will depend on the polarity of the groups attached. Hydrophilic groups (e.g. hydroxyl, epoxy, carboxyl) can act as actives sites that will increase the interaction between the carbon matrix and the electrolyte ions. Hydroxyl, carbonyl and quinone groups – which are CO-type decomposed groups known to be more stable than the CO_2-types – are most likely to give a positive contribution to the capacitance of the materials via the participation of pseudocapacitance phenomena[275]. Indeed, carbonyl and quinone groups can undergo reversible reactions such as with protons (Figure 42 a) in acidic media achieving extra pseudocapacitance. Carboxyl and phenols groups, which are more acidic sites, can be beneficial on the other hand in basic media by reacting with hydroxide ions (Figure 42 b)[276]. Strategies exist then in order to introduce electrochemically in control manner the oxidation level of the carbon materials and tune its capacitive/pseudocapacitive behavior (Figure 42 c)[277]. Nevertheless, over-functionalization can be detrimental not only for the electronic conductivity and decrease in capacitance can also be observed due to the clogging of the pores. These effects can be due to the presence of carboxylic groups around the entry of the micropores creating steric hindrance, diminish the electronic conductivity due to sp^2-C pathway rupture and increased leakage currents. A team developed an approach to create cyclic ether-functionalized carbon material and compare it with a carboxyl-functionalized one[278]. The cyclic groups functionalization while preserving the carbon sp^2 hybridization allowed to increased performance due to lower steric hindrance within the micropores (i.e. hydrated ion accommodation), lower leakage currents and higher electronic conductivity (Figure 42 d). Oxygen functionalization is then an interesting strategy to tune the properties and increase the overall performance of carbonaceous electrodes. This can notably be done by inducing positive pseudocapacitance effects, improved wettability for the insertion of ions within the micropores and change in the surface structure of the carbon materials. However, current leakages are very common even though improvement could be done by achieving specific functional groups linkage (i.e. cyclic ether). This effect can also be accompanied by some voltage drop, steric hindrance of micropores, decrease in electronic conductivity, electrolyte decomposition with the presence of active sites and oxidation/corrosion of the carbon severely reducing its span life and performance on the long term.

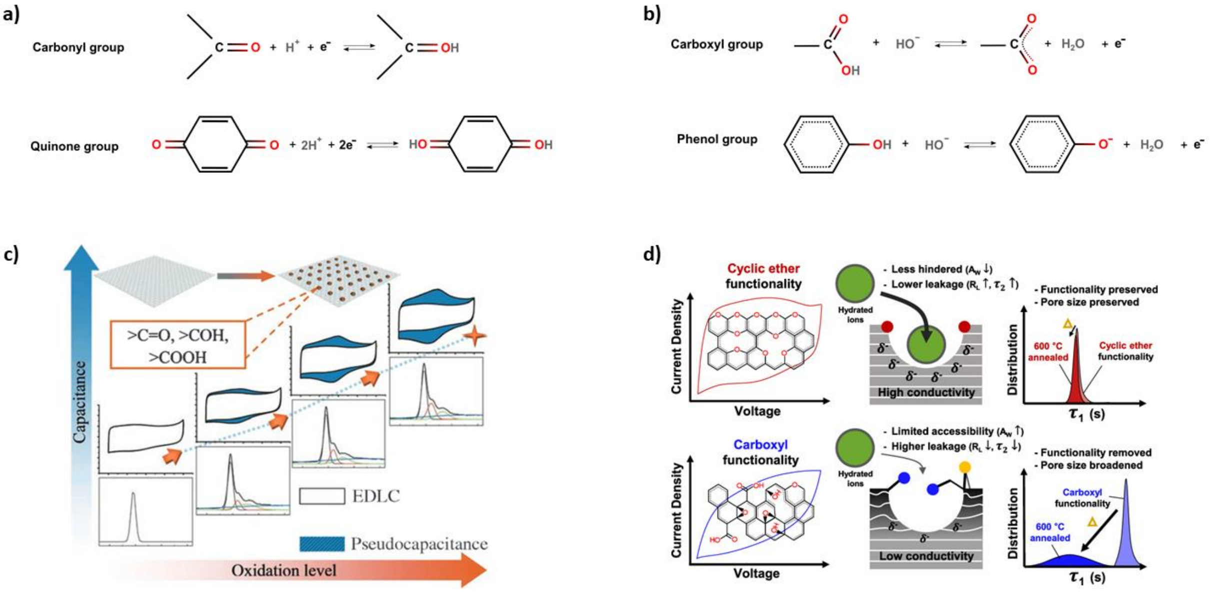

Figure 42: Carbonyl and quinone groups protonation reactions in acidic media (a); Carboxyl and phenol groups reactions with hydroxide anions in alkaline media (b); Increase in pseudocapacitance during electrochemical oxidation of the carbon materials (c)[277]; Difference in performance and properties of a cyclic ether-functionalized carbon and a carboxyl-functionalized carbon (d)[278]

Nitrogen doping – a kind of a *n*-doping strategy – can have beneficial impacts on carbonaceous materials. Effect on the electronic conductivity is outlined previously and is not the only advantage of attaching nitrogen functional groups. Concerning the latter point, various N-groups exist and can be present on the carbon matrix such as amides C-N$_2$H, (aromatic) amines Ar-N$_2$H, pyridine (N-6), pyrrolic-N or pyridine-N (N-5), quaternary and/or graphitic nitrogen (Q-N), oxidized pyridinic N (N-X), nitrogen oxides (N-O$_x$) or even lactam group (HN-C=O) as seen in Figure 43a[270,271]. Some groups are more stable than the others and their presence on the carbon matrix will mostly depend on the synthesis conditions (i.e. choice of precursors, doping agents, method of synthesis/doping, temperature if pyrolysis, energy brought to the reaction, etc…). As for oxygen functional groups, the polarity induced by the nitrogen functional group will influence the wettability of materials and its pores. For instance, the pyridinic-N and pyrrolic-N can have larger dipole moments – especially when they are negatively charged - and have a positive effect on the wettability of the electrolyte ions. These two groups can also participate to improved charge storage thanks to surface redox pseudocapacitance in either acidic or alkaline media. Example and proposed redox reactions are proposed for these groups in acidic media[279] in Figure 43b in addition to pyridone-N group. Pyridinic-N and pyrrolic-N groups pseudocapacitance is surface-redox process driven by the reaction with protons and thus is limited in alkaline media. However, aromatic amine groups can participate to additional charge storage in alkaline media and improve the charge transfer reaction[280]. The role of pyrrolic-N effect is notably investigated and is confirmed to positive contributes to the charge storage thanks to the synthesis of a single-site pyrrolic-

N doping on a *sp*^{2}-carbon matrix materials[281]. Nitrogen doping is then an interesting strategy to develop high performance carbonaceous materials. However, further understanding on the role of the various nitrogen functional groups are needed to ensure improved performance on the N-doped carbon materials development.

Hence, one scope of this thesis research is to further investigate the effect of N-doping of a model carbon source precursors by varying the synthesis conditions and provide high performance electrode for applications in supercapacitors.

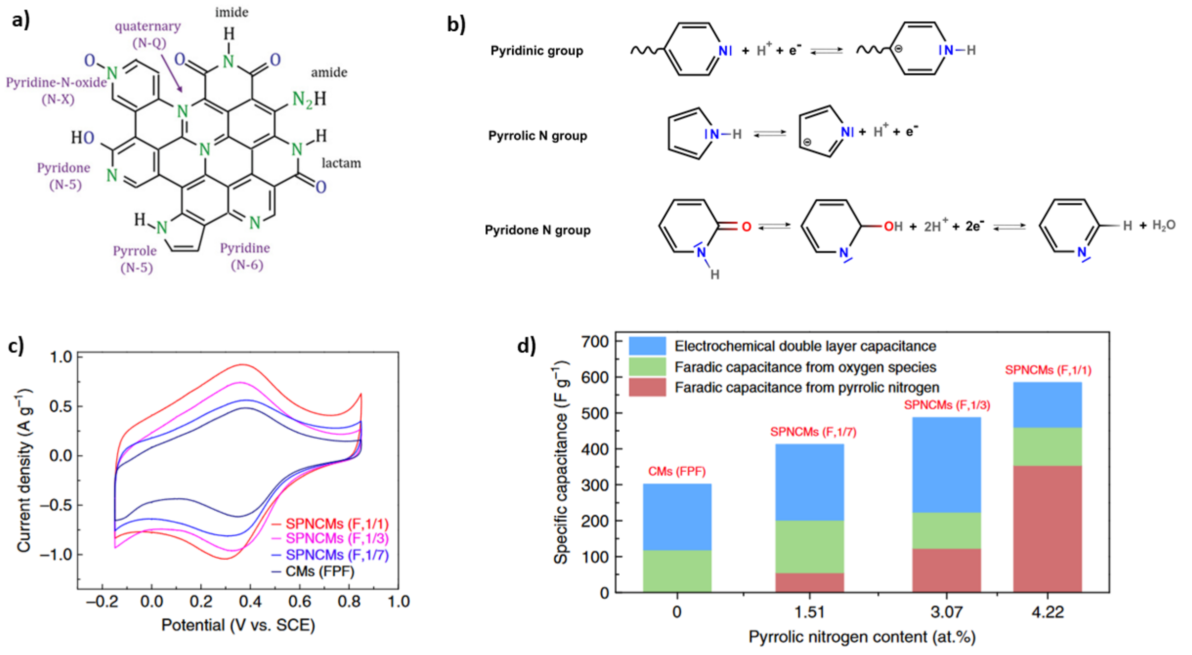

Figure 43: Representation of a carbon matrix with various nitrogen functional groups (a)[270]; Redox reactions of pyridinic-N, pyrrolic-N and pyridone-N groups in acidic media (b); CV of carbonaceous materials with single-site pyrrolic-N groups attached with different precursor ratios (SPNCMs) and comparison with absence of nitrogen dopant (CMs) (c); Different contributions to the capacitance of these materials according to the content in pyrrolic-N (d)[281]

- Manganese and Iron-based TMO nanoparticles for pseudocapacitors and batteries

Manganese oxides are presented as a greener alternative materials in different sectors including the one of electrochemical energy storage. In the latter application, it is particularly used as presented in the beginning for primary batteries with specific manganese dioxide phases, in lithium-ion batteries with spinel-type $LiMn_2O_4$ or even supercapacitors with birnessite layered MnO_2. The Figure 44 depicts the most common manganese oxide crystallographic phases. Layered MnO_2 is widely studied for supercapacitor applications. Spinel Mn_3O_4 is however also considered as a promising phase for the same applications showing an increase research interest. The Hausmannite Mn_3O_4 phase possesses a theoretical specific capacitance of 1370 F/g, which could provide highly performant supercapacitors. Its abundancy, lower cost and toxicity render it very attractive as an alternative to ruthenium oxide. However, its low electronic conductivity impedes its direct application and necessitates mixing with relative amount conductive agent and/or preparation of composite materials. Works have been realized on the application of such Mn_3O_4 as nanoparticles. Notably, its charge storage mechanism was studied in a sodium sulfate neutral electrolyte[282]. The experiments realized with EQCM and X-ray absorption spectroscopy revealed the insertion of sodium cation Na^+ at the negative electrode with the formation of $Na_\delta MnO_x \cdot nH_2O$ starting from the first charging cycle followed by subsequent surface-redox driven storage mechanism accompanied with the diminution of the average oxidation state of Mn from +2.67 to +2.38. The charge storage mechanism is represented as followed:

$$Mn_3O_4 \overset{1^{st}\ charge}{\rightleftharpoons} Na_\delta MnO_x \cdot nH_2O \tag{44}$$

$$Na_\delta MnO_x \cdot nH_2O \rightleftarrows MnO_x \cdot nH_2O + \delta Na^+ + \delta e^- \tag{45}$$

At the positive electrode, the charge storage is accompanied with the insertion of sulfate anion SO_4^{2-}. As for application for lithium-ion batteries, Jahn-Teller distortion and crystal expansion influence the stability of the spinel oxide with an overall decrease of the oxidation state to +2.43 (positive electrode) and +2.38 (negative electrode) due to Mn^{2+} extraction and dissolution into the electrolyte. Nevertheless, the symmetric assembly of these Mn_3O_4 nanofibers exhibited energy density up to 37.4 Wh/kg and maximum power density of 11.1 kW/kg (Figure 45 a and b).

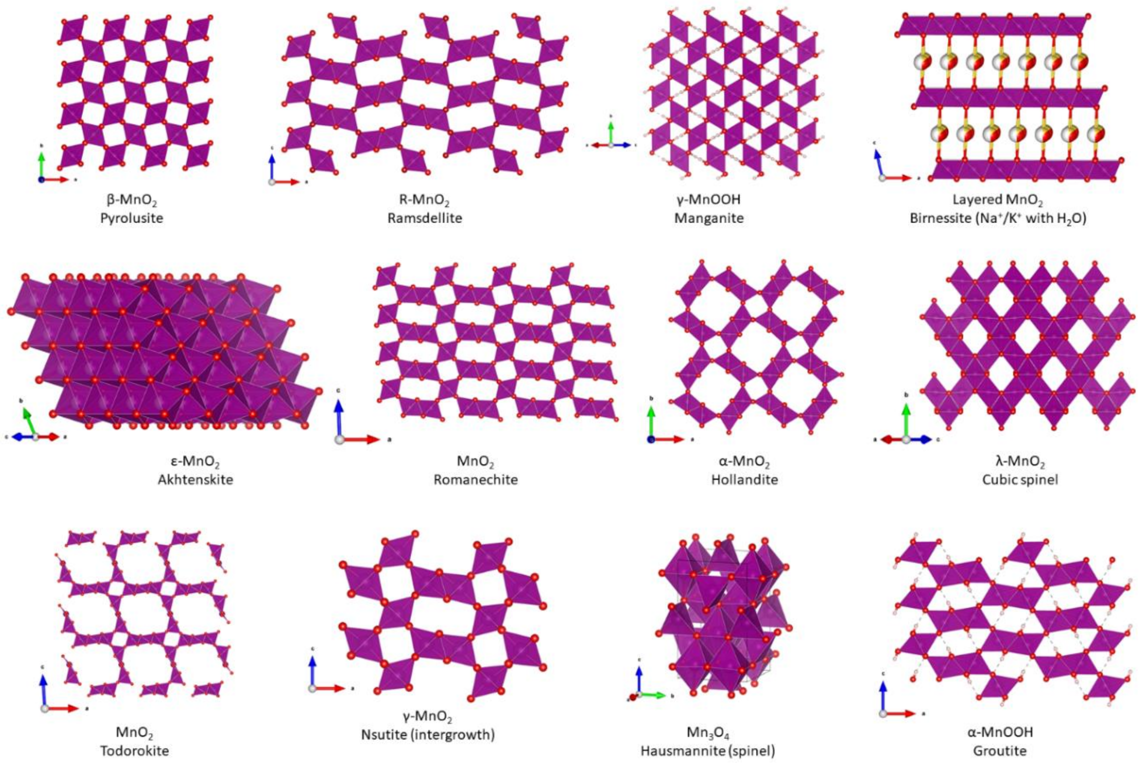

Figure 44: Presented variety of manganese oxide phases with their crystallographic representations

As an example of composite materials, graphene can be grafted to Mn_3O_4 particles to enhance its overall stability during cycling test and electronic conductivity due to the conductive behavior of graphene. A work reported by Lee *et al.* in 2012 show the synthesis of Mn_3O_4 nanorods onto graphene to form a composite materials (Figure 45 c)[283]. The composite showed clear increase in performances as supercapacitor electrodes in 1M Na_2SO_4 electrolyte with an almost 4-fold enhanced specific capacitance compared to pristine Mn_3O_4 (Figure 4 d). In addition, the electrode's stability remained at 100% even after 10 000 cycles realized at 5 A/g whereas Mn_3O_4 show decline even after few hundreds of cycles. These improved performance could be notably explained by the electronic conductive character of graphene decrease the overall resistance allowing faster surface-redox reactions and inhibiting the Mn_3O_4 particles aggregation.

The performance of electrode materials as supercapacitors depends heavily on the overall structural properties of it, its morphology, crystallinity, porosity, SSA and deposit thickness/loading. Mn_3O_4 being studied less than MnO_2 or even MnO, some research focuses have to be dedicated to fully exploit the high theoretical capacitance of the Hausmannite spinel.

Thus, another scope of this research work is to elaborate and produced Mn_3O_4 nanoparticles via various structural properties and innovative synthesis approach to bring better insight on its application in supercapacitors. Concerning the synthesis approach, a focus will be given to solution combustion synthesis (SCS). This process allow the synthesis of various TMO (nano)particles through a very fast self-propagated exothermic reaction liberating high amount of heat and gas which could lead to the creation of porosity[11]. A profound study will be held to understand the synthesis insight and influence of the formation of Mn_3O_4 nanoparticles and its structural/electrochemical properties as supercapacitor electrode materials.

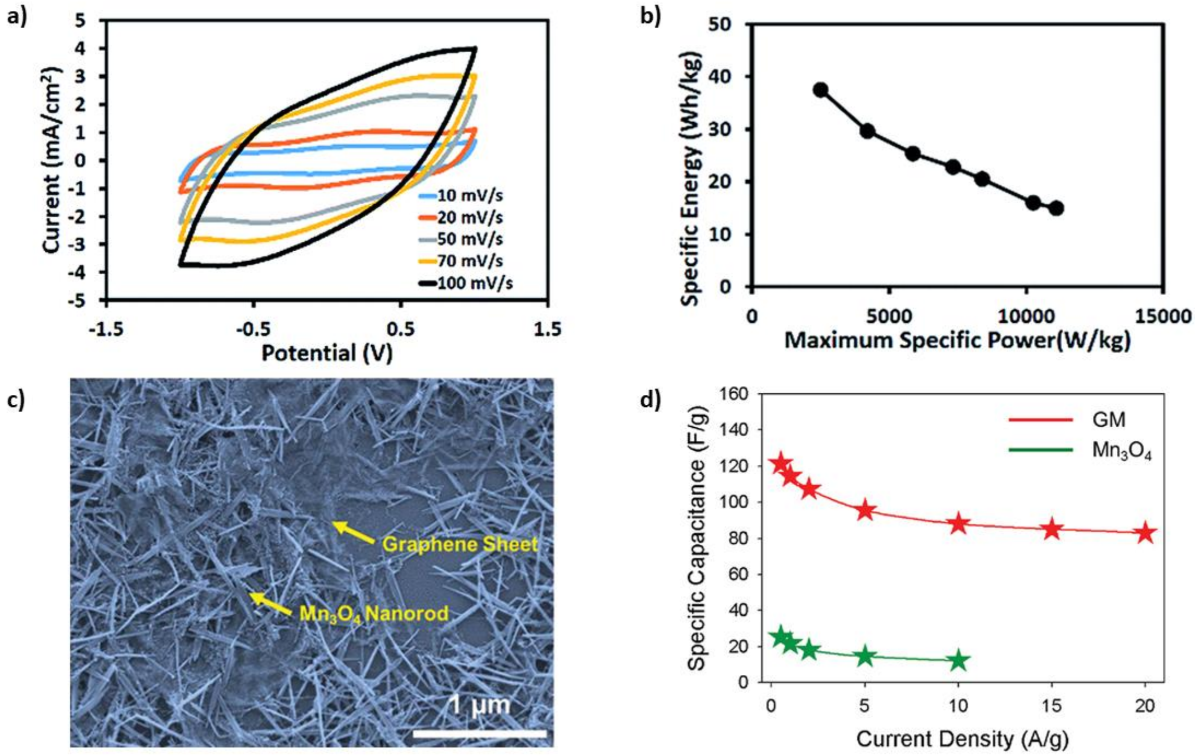

Figure 45: CV realized at different scan rate of a symmetric Mn_3O_4 supercapacitor cell (a); and the related Ragone plot (b)[282]; SEM image of the Mn_3O_4 nanorods/graphene composites (c) and its specific capacitance as electrode materials at different charging rate compared to pristine Mn_3O_4 (d)[283]

Iron oxide materials are another interesting candidates for greener electrode materials for EESDs. They could be applied for supercapacitors as well as for lithium-ion batteries as an anode materials. In the same line as Mn_3O_4, another spinel will be chosen for alternative, which is the magnetite Fe_3O_4. Theoretically, this material can provide a very high specific capacitance of ca. 2300 F/g, considering that two Fe^{3+} and one Fe^{2+} are considered undergoing complete reduction with an 8 electrons process. Early works realized by Wu *et al.* recorded the high specific capacitance of 510 F/g in 1M sodium sulfite Na_2SO_3 electrolyte with 1.2 V potential range[284]. After realizing test in various electrolytes, it was found that sodium sulfite provided the highest capacitance values thanks to surface redox reaction with sulfite anions insertions as given by two possible charge storage mechanism, as follow:

$$FeO + SO_3^{2-} \rightleftharpoons FeSO_4 + 2e^- \tag{46}$$

$$2Fe^{II}O + SO_3^{2-} \rightleftarrows (Fe^{III}O)^+SO_3^{2-}(Fe^{III}O)^+ + 2e^- \tag{47}$$

Works realized few years later with the help of EQCM and XPS attributed more precisely the charge storage mechanism in these various electrolytes (Figure 46 a)[285]. The high capacitances obtained in the case of sodium sulfite electrolyte is due to the pseudocapacitive behavior accompanied with the oxidation and reduction of the SO_3^{2-} anion adsorbed specifically, undergoing multiple-electron driven processes. As stated previously, structure and morphology of Fe_3O_4 will impact as well its electrochemical properties. Hence, nanosizing and structural engineering appear primordial to achieve highly performant iron oxide-based electrode materials for supercapacitors but also for conversion-type anodes in Li-ion batteries. For instance, high surface area Fe_3O_4 particles (SSA = 165 m^2/g) via hydrothermal synthesis showed capacitances as high as ca. 208 F/g with excellent stability of 100% after 2000 cycles[286] (Figure 46 b). As for lithium-ion batteries, interesting research was done and showed by Taberna *et al.* on Fe_3O_4 nanorods obtained through direct electrodeposition on Cu-based current collector nanorods, itself grown with an anodized alumina oxide (AAO) membrane (Figure 46 c)[287]. The 1D morphology of these particles and growth on the current collector allowed very high capacity retention even at fast charging rate (Figure 46 d). Up to 80% of the highest capacity (at C/32 rate) was achieved at an 8C charging rate. As a scope of research, engineering of structural Fe_3O_4 nanoparticles will be done to achieve high performance electrode materials for applications in supercapacitors and LIB as conversion-type anode. For such goals, the use of another synthesis approach will be elaborated which the use of the polyol method to order and control the morphological structure and growth of iron-oxide particles. Composite materials will be studied as well, notably with the use graphene-like materials to enhance the electronic conductivity of the electrode and improve its stability due to hindered particle aggregations.

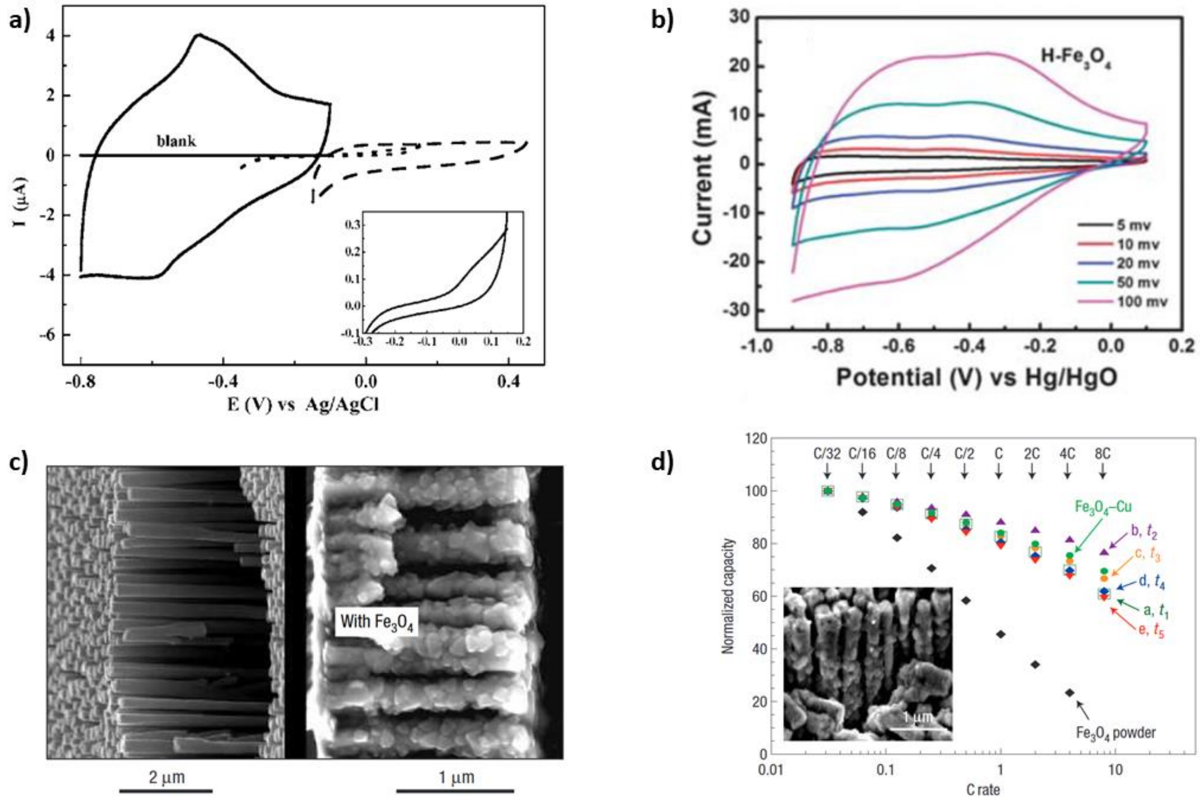

Figure 46: CV of Fe_3O_4 electrode materials realized in 1M Na_2SO_3 (solid line), Na_2SO_4 (dashed line) and KOH (dotted line) (a)[285], CV of high SSA prepared Fe_3O_4 nanoparticles in sodium sulfite electrolyte at different scan rate (b)[286]; SEM images of Cu nanorods and Fe_3O_4 grown on Cu nanorods (c); Capacity of such electrode material at different C rate (d)[287]

Objectives of research

As stated in the overall introduction, electrochemical energy storage devices (EESDs) development constitutes one of the major objectives of our century to bring accessible and sufficiently performant electricity storage/delivering tools for a wide variety of applications. Emphasized by global warming issues, need of electricity accessibility for the global population, scarcity and toxicity of essential elements constituting the EESDs, more performant and "greener" devices are required using more abundant and low toxic elements. For such reasons, this work will focus on the development of electrode materials for supercapacitor and rechargeable lithium-ion battery applications using three main elements which are carbon, manganese and iron.

Carbon materials, especially activated carbons (ACs), are representing a major part in the construction of supercapacitor electrodes. Their high abundancy, ease and possibility of structural/properties modulation by the choice of synthesis and modification of its parameters allow to obtain ACs with different characteristics including high specific surface area, modulation of macro-, meso- and micropores, or even its doping by heteroatoms. In addition, ACs can be obtained from a quasi-unlimited source of carbonaceous precursors, allowing to use relevant bioproducts for a "greener" approach. Therefore, this work will focus on the synthesis of activated carbons with high specific surface area starting from an abundant bioproduct source of carbon free of nitrogen heteroatom – i.e. sucrose – and then studying the effect of the addition of a N-doping agent, the ammonium citrate, on the characteristics of the obtained ACs by a classical thermochemical activation process assisted by KOH. The subsequent objective is to enlighten the role of the various functional groups attached to the carbon and how they affect the electrochemical performances such as the presence of surface-redox N-functional groups that could enhance the measured capacitance by an additional pseudocapacitive phenomena. Not only focusing on the obtention of performant materials and the role of dopant, development on characterization techniques for obtention in-depth and complementary information of the materials structural characteristics and charge mechanisms is essential as well. Therefore, electrochemical impedance spectroscopy with a simplified geometrical model is also studied to allow an easy but nonetheless very informative method to analyze the properties of various carbon material showing different characteristics.

Transition metal oxides represent another category of promising candidate for applications not only for supercapacitors but also for lithium-ion batteries. As mentioned previously, manganese-based materials are shown to be promising candidates for these applications with substantial greener approach. Manganese oxide, and more precisely spinel Mn_3O_4, will be studied in this research work for its application as supercapacitor electrode materials which would provide high capacitance thanks to surface-redox driven pseudocapacitance. Obtention of nanomaterials with high number of electrochemical active site and maximized interface with the electrolyte ions is then essential for high performance. Solution combustion synthesis (SCS) which is self-propagating exothermic reaction will be used to form this manganese oxide. This synthesis method is quite complex and involves the formation of many gaseous byproducts as well. Therefore, not only the proper role of manganese oxide performance and electrochemical characteristics will be studied but also the formation mechanism of such manganese oxide Mn_3O_4 phase by SCS with *in situ* characterization tool which was not referenced before. Hence, manganese oxide spinel will be prepared by using different reactant mixtures (i.e. different fuels and addition of complexing agent), analyzing the formation of various products by *in situ* temperature-dependent diffuse reflectance infrared by Fourier transform spectroscopy (TD-DRIFTS). The obtained manganese oxides with different structural characteristics will be studied then by electrochemistry and will be compared according to their differences in structural properties.

The other element which will put on show for this project work will be the iron element, and more precisely its spinel polymorph Fe_3O_4 as supercapacitor electrode material but also as conversion-type anode electrode. As for manganese, iron is also a relatively very abundant element, easily recyclable and can be extracted without involving as much environmental and humanly questionable methods as for more precious element (e.g. cobalt). The Fe_3O_4 can perform theoretically up to ca. 924

mAh/g of capacity considering an 8 electron process where the iron elements (Fe^{2+} and Fe^{3+}) would go to complete reduction. Thus, this material is one of the most promising candidate for greener EESDs. The obtention of nanoparticles is as much important as for the manganese oxides as explained above for supercapacitors involving pseudocapacitive type of charge storage mechanism. For conversion-type anode, the electrode materials undergo high volume expansion (up to 300%) and structural engineering is considered to accommodate this expansion during lithium insertion and phase changes. Polyol synthesis method will be used to obtain hollow raspberry-shape nanoparticles (RSNs) to answer those purposes. In addition, composite materials using few-layer graphene will be done to improve to electrode cyclability and reversibility of the conversion reaction. Indeed, the electronically conductive few-layer graphene (FLG) would relatively prevent an electronic and spatial isolation of subsequent metallic iron phase obtained from the complete reduction of iron cations, anchored on the conductive layers of FLG. The composite synthesis might also interfere with the structural characteristics of the RSNs and their impacts will be investigated on their electrochemical results.

Chapter 1: N-doped Activated Carbons for supercapacitors

Nitrogen doping for highly performant supercapacitors

- **Abstract**

Porous carbon electrode materials are utilized in supercapacitors with very fast charge/discharge and high stability upon cycling thanks to their electrostatic charge storage mechanism. Further enhancement of the performance of such materials can be achieved by doping them with heteroatoms which altering the kinetics of charge/discharge of the adsorbed species and result in pseudocapacitance phenomena. Here, microporous N-doped activated carbons were synthesized by thermochemical activation process. The structure and composition of the final material are adjusted by tuning the synthesis conditions and the choice of precursor molecules. In particular, N-doped activated carbon with controlled specific surface area in the range of 556-1534 m^2/g has been prepared by KOH-activation of sucrose / ammonium citrate mixture. By adjusting the composition of precursors, N-doping was varied between ca. 1.5 to 7.3 atomic percentage. The role of the components and synthesis conditions on the composition and structure of final product has been evaluated. The N-doped activated carbon with optimized structure and composition has demonstrated an outstanding performance as electrode materials for aqueous electrolyte supercapacitors. The specific capacitance measured in 3-electrode cell with 0.75 mg/cm^2 loading of optimized activated carbon in 1M H_2SO_4 changed from 359 F/g at 0.5 A/g charging rate to 243 F/g at 20 A/g. Less than 0.01% of capacitance loss has been detected after 1000 charging/discharging cycles.

- **Introduction**

Supercapacitors are the type of Electrochemical Energy Storage Devices (EESD), with performance characteristics complementary to batteries. Namely, in comparison to Li-ion batteries, supercapacitors are characterized by high power density and charging cyclability, but lower energy density[288,289]. Carbon materials are among the most commonly used electrode materials for supercapacitors, in particular in electrical double layer capacitors (EDLC), relying on the charging of interfacial electrical double layer as a mechanism of charge storage. The advantages of carbon materials are their high electrical conductivity, electrochemical stability, and controlled variability of materials structure and composition [290]. Carbon materials can be synthesized with wide variety of structures [291,292]: from 0D (carbon nanodots and carbon quantum dots [293]), to 1D (carbon nanotubes and nanofibers), 2D (graphene-type carbons [294]), to numerous porous 3D carbons, for example activated carbons (AC). For EDLC electrodes the carbon materials with high specific surface area (SSA) are of high interest, AC in particular [295].

AC is the group of carbon materials with outstandingly high specific surface area (SSA), close to the theoretical maximum of SSA for closely packed sp^2-carbon sheet (single graphene layer) of 2680 m^2/g. Considering the typical value of surface-specific interfacial capacitance of carbon materials $C_s \approx$ 5-10 µF/cm^2 [296], one may expect the mass specific capacitance of carbon electrodes in the range $C_g \approx$ 150-300 F/g. High SSA is provided by open porous structure of AC with predominant contribution of micropores (diameter $d < 2$ nm). The porous structure is formed by thermal or thermochemical activation of carbon precursors at high temperature (600-900 °C) under inert atmosphere. As it has been thoroughly discussed in a number of reviews from the recent decade [297–301], AC materials can be prepared from the wide range of carbon-rich precursors, including relatively cheap and abundant bio-wastes (domestic, agricultural, or agro-industrial). The electrochemical characteristics of AC materials, in particular their specific capacitance and stability, are influenced by the properties of AC, namely its chemical composition, SSA and porosity, and electrical conductivity. These properties are strongly varied depending on the choice of precursor and preparation conditions, which have to be optimized for the case of each particular type of precursors. The bio-sourced precursors have a complex composition, mostly containing sugars (sucrose and polysaccharides), cellulose, hemicellulose, and lignin [297,302]. In order to understand the correlation between the properties of AC and the conditions of its preparation, a simple chemically pure precursor model is used, such as glucose, sucrose, or cellulose. In particular, sucrose has been used as a precursor for the AC electrode materials for electrocatalysis [303] and EDLC supercapacitors [300]. It has been demonstrated [304] that AC materials with high SSA > 2000 m^2/g can be prepared by the KOH thermochemical activation of sucrose under inert atmosphere.

This work present a two-step synthesis of N-doped activated carbon (ACN) prepared by conventional approach with thermochemical activation by KOH as the final step. We intended to study the influence of addition of ammonium citrate to the sucrose precursor on the properties of a final AC material. Citric acid is known to efficiently catalyze the hydrothermal carbonization of bio-waste precursors [305–307] through esterification reaction with carbohydrates [308]. By using ammonium salt of citric acid we intended to introduce N-heteroatoms into the carbon matrix of the final AC material. N-doped carbon materials are intensively studied as electrode materials for energy storage devices, namely Li-S and Li-ion batteries [309]. A systematic increase of the capacitance of carbon electrodes of supercapacitors with an increase in N-content (in the range 2-7 at.%) in various electrolytes has been demonstrated [310,311]. Outstanding mass specific capacitance above 800 F/g has been reported for N-doped mesoporous carbon prepared by hard template method [312]. However the variety of the nature of N-heteroatoms imbedded into carbon structure complicates the general prediction of an optimal composition of N-doped carbon. In the present work we demonstrate that using ammonium citrate and sucrose as initial precursors, N-doped AC materials with high SSA and performance as EDLC electrodes can be obtained. The origins of high capacitance and the role of different components of the synthesis are evaluated and discussed.

- **Materials and Methods**
    - Synthesis of N-dopes activated carbon (ACN)

10 g of D(+)-Sucrose $C_{12}H_{22}O_{11}$ (Acros Organics, 99+% purity for analysis, CAS: 57-50-1) has been mixed with 10 g of anhydrous ammonium citrate tribasic $(NH_4)_3Cit$ (Sigma, ≥ 97% purity, CAS: 3458-72-8), and finely grinded in a coffee grinder. The solid powder was then put into an oven at 160 °C in air for 4 h. The resulting solid intermediate was grinded once again and mixed with a concentrated aqueous solution containing 10 g of KOH (Acros Organics, extra pure, ca. 85%, flakes, CAS: 1310-58-3). The slurry mixture was dried again at 160 °C for 4h. Dried KOH-impregnated intermediate was loaded into a tubular reactor kept under Ar flow (10 ccm/min). The temperature was raised to the annealing temperature of 700 °C/800 °C/900 °C with a 10° C/min ramp, and then kept at the set temperature for 1h. The product was then left to cool down under the flow of Ar. The final product was washed with 2M HCl and ultrapure water, filtered, and dried in the oven overnight at 80 °C. The reference samples were also synthesized by using 10 g of pure sucrose without any other additive, and 10 g of sucrose and 10 g of citric acid (Chem-Lab, 99.5-101%, CAS: 5949-29-1). All other conditions of synthesis were the same as described above. All aqueous solutions in this work were prepared by using ultrapure water (18.2 Mohm·cm, TOC < 2 ppb) produced by UltraAnalytique Veolia device.

- Physicochemical characterization of ACN

SEM measurements were done using a Zeiss 2600F microscope with a resolution of 5 nm. The carbon samples were deposited on a conductive carbon tape. XRD measurements were performed by Bruker D-8 Advance diffractometer with Cu Kα source (λ = 1.54184 Å). ATR-FTIR measurements were done by ThermoFisher IR spectrometer equipped by ATR Smart Orbit setup. BET measurements were done using ASAP 2420 Micrometric analyzer measuring N_2 physisorption isotherm at 77 K after degassing the samples at 150 °C for 12 h. Raman spectra were recorded using LabRAM HORIBA ARAMIS spectrometer with CDD detector and laser line from 532 nm / 100 mW (YAG) Laser Quantum MPC600 PSU. XPS measurements were done using Multilab 2000 Thermoelectron spectrometer with Al Kα source (λ = 1486.6 eV). For 2-point conductivity measurements a controlled amount of power was placed in a vertical narrow calibrated glass tube (inner diameter d = 0.61 cm). The lower end of the tube was blocked by Cu foil. The powder was blocked in the tube from above by another glass rod with Cu contact at the end (d ≈ 0.61 cm). Thus, the cross-section of the contact was $A = \frac{1}{4}\pi d^2 = 0.29\ cm^2$. No extra pressure was applied on the power except the weight of the glass rod (8.1 g). The volume of the powder V between 2 contacts was precisely measured. Conductivity of the powder was measured by

Ohm’s law by passing a constant current and measuring voltage between two Cu contacts. The dependence of conductivity on frequency was measured by measuring impedance between 2 contacts by applying 7 mV voltage modulation with frequencies f from 10^6 to 10^{-1} Hz.

- **Electrochemical measurements**
  - Preparation of electrodes

Ink preparation

Inks are prepared by adding a desired amount of active material in a glass vial and the required volume of MilliQ water (resistivity of 18.2 MΩ·cm at 25 °C, Total of organic compound (TOC) ≤ 1 ppb) to obtain a 2 g/L concentrated ink. All the inks were prepared by usually weighting 10.0 mg of activated carbon powder in the vial and adding 5000 µL of MilliQ water with a 0.5 – 5.0 mL micropipette. The ink is then shaken and sonicated in an ultrasonication bath for 20 minutes.

Ink deposition on glassy carbon rod

The active material was deposited by drop casting onto the surface of a glassy carbon rod electrode of 6 mm radius. The total deposited volume of ink is 75 µL divided by 5 deposition step of 15 µL in which the electrode is dried for 10 minutes in an oven programmed at 80 °C between each step. The loading of active material is approximated to 0.75 mg/cm^2. A final deposition of 15 µL Nafion 0.5 wt. % in mixture of lower aliphatic alcohols and water was added and dried to act as a binder.

3-electrode cell set-up

A 3-electrode cell inside a Faraday cage is used for the electrochemical tests. A 100mL 1M H_2SO_4 electrolyte is poured in the cell followed by the addition of a platinum wire with a coil end counter electrode in the compartment separated by a fritted and a mercury/mercurous sulfate electrode (MSE) in saturated K_2SO_4 in the compartment separated by Luggin capillary. The solution in the cell is then purged for at least 30 minutes under N_2 gas. The glassy carbon rod electrode with active material – the working electrode - is placed in a holder and then placed inside the electrochemical cell in order to only have a contact with the surface of the electrode. The N_2 gas is flushing above the electrolyte to keep a controlled atmosphere without O_2. The electrodes are connected to a SP-300 potentiostat from BioLogic.

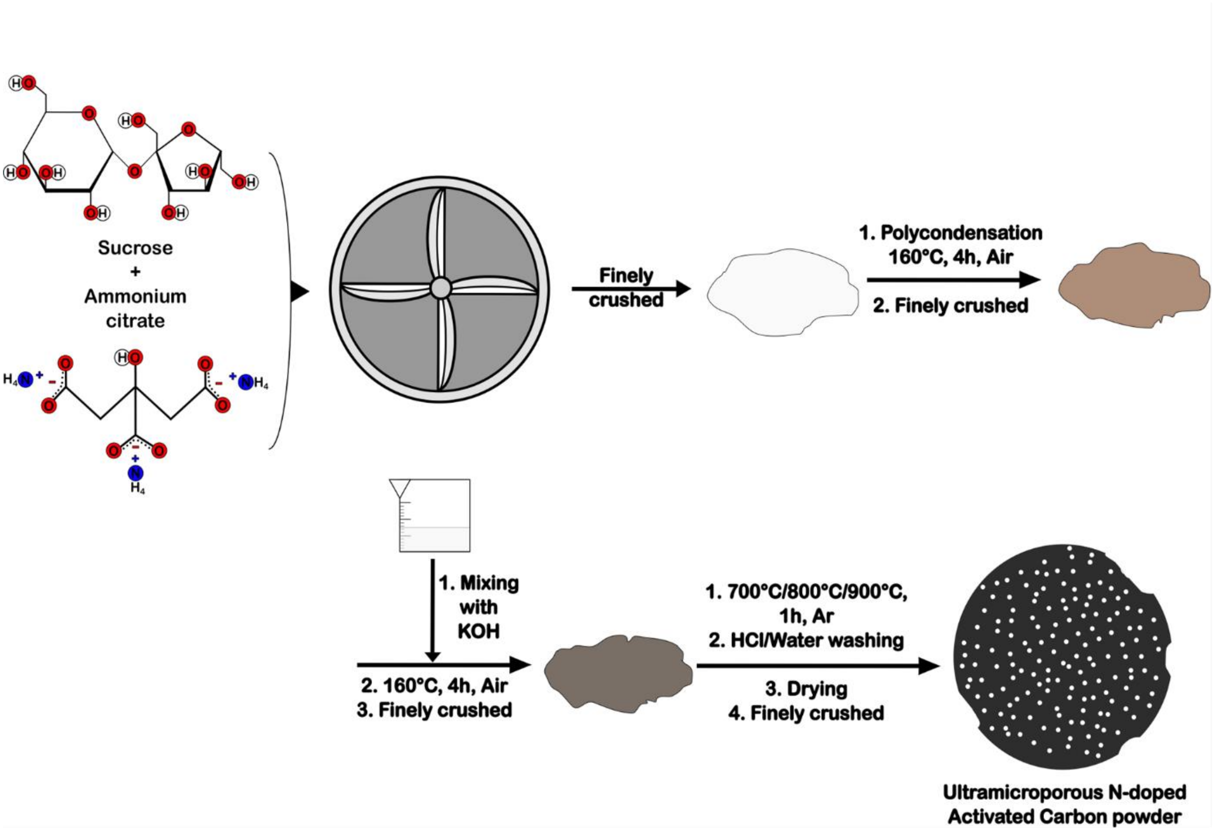

Figure 47: The scheme of two-step synthesis of ACN samples.

- **Results**
    - Synthesis of ACN samples

The Figure 47 summarizes the different synthesis steps, i.e. precursors nature and temperature, for the preparation of ACN samples. The synthesis was carried out through a two steps process: polycondensation at 160 ^{o}C in air for 4 h, and thermochemical activation by KOH at various temperatures under Ar for 1 h. The samples synthesized by this process are denoted as ACN-xxx, where xxx is the temperature of the activation step. For comparison, two other samples were synthesized, differentiating from ACN samples only by the composition of the precursors. Namely, ACS-800 sample was synthesized from pure sucrose, and ACC-800 sample was synthesized from sucrose and citric acid with 1:1 molar mixture. Both these samples were activated by KOH at 800 ^{o}C under inert atmosphere.

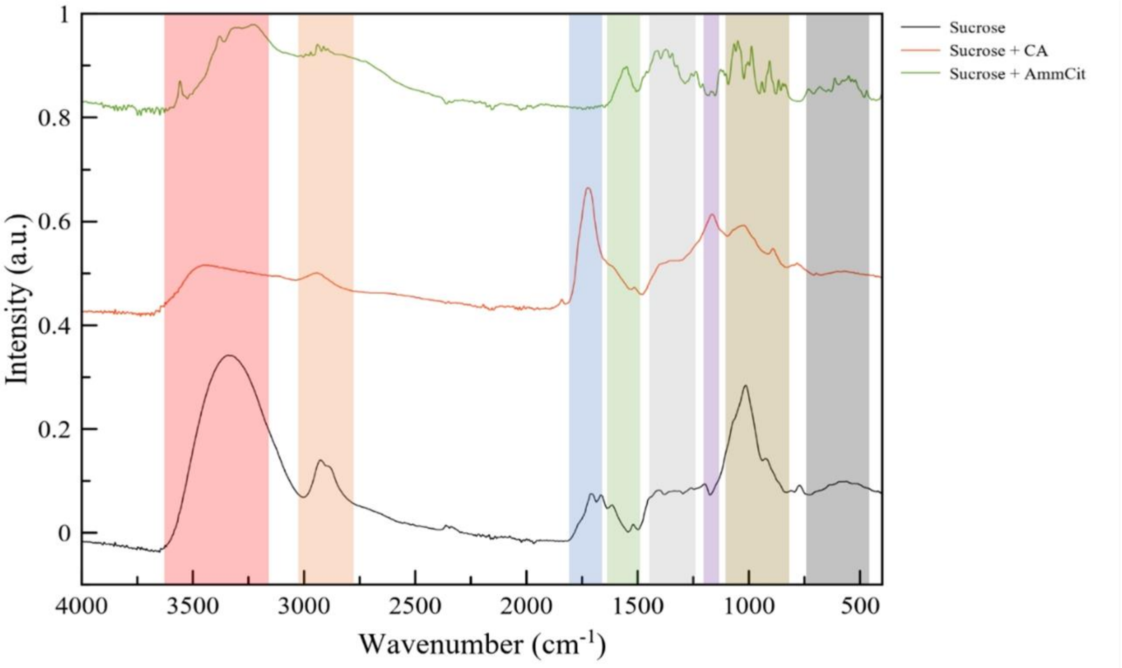

Figure 48: ATR-FTIR spectra of intermediate products prepared by polycondensation of precursors mixture at 160 °C.

Polycondensation of precursors results in foam-like dark solid intermediate product. The ATR-FTIR spectra of solid intermediates prepared are shown in Fig. 48. The proposed composition of polycondensation intermediates are given in Fig. 49.

The thermal transformation of sucrose close to its melting temperature (186 °C) results in its partial decomposition with the formation of glucose and fructose, and its polycondensation with formation of a mixture of oligo- and polysaccharides[313]. Indeed, the IR spectra of the product of sucrose polycondensation (1st step of the synthesis), Fig. 48, shows strong ν_{OH} band centered at around 3340 cm^{-1}, doubled peak of ν_{C-H} at around 2930 cm^{-1}, and the set of peaks in the 1200-1400 cm^{-1} range, which are attributed to ν_{C-O-C} stretching. The set of peaks in the range 1600-1780 cm^{-1} can be attributed to $\nu_{C=O}$ and $\nu_{C=C}$ stretching and associated to the formation of 5-hydroxymethylfurfural (5-HMF), one of the byproducts of sucrose polycondensation[314].

Addition of citric acid to sucrose during its thermal treatment has a strong influence on the process of sucrose decomposition and polycondensation. It has been proposed[315,316] that citric acid acts as a catalyst of sucrose hydrolysis at temperatures close to 100 °C, accelerating the formation of glucose and fructose, as well as 5-HMF, which, in terms, triggers the formation of oligosacharides already at 100 °C. Further increase of the synthesis temperature to 170 °C results in esterification reaction between alcohol group of saccharides and carboxylic group of citric acid. This process results in cross-linking of polysaccharides chains and formation of strong adhesive solid[315,316]. In the IR spectrum (Fig. 48) one can observe a strong band at 1720 cm^{-1} which can be attributed to $\nu_{C=O}$ stretching in ester and, perhaps, carbonyl fragments. Strong band appears at 1165 cm^{-1} is attributed to $\nu_{RC-O-CR}$ stretching in aliphatic ether fragments, while peaks related to the presence of alcohol groups

(ν_{OH} at 3400 cm^{-1} and $\nu_{C\text{-}OH}$ at 1020 cm^{-1}) are significantly weaker than in the case of the product of pure sucrose polycondensation.

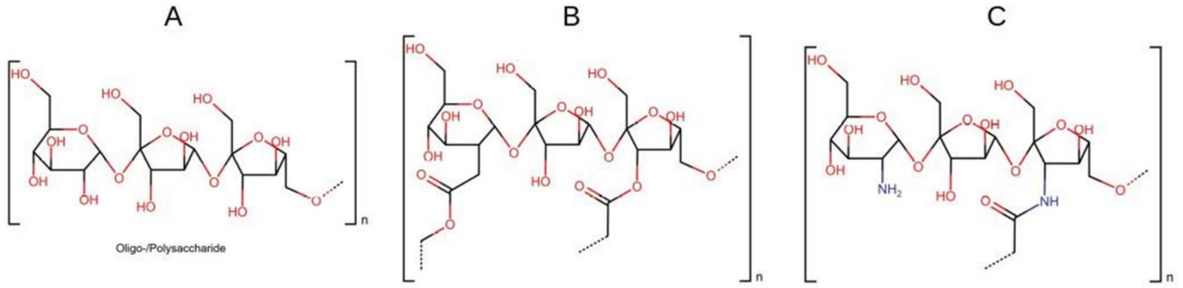

Figure 49: Proposed structure of intermediates formed by polycondensation of sucrose (A), sucrose-citric acid (B), and sucrose-ammonium citrate (C).

The IR spectra of polycondensation intermediate produced from sucrose and ammonium citrate mixture shows several differences comparing to one from sucrose and citric acid intermediate. The peaks related to alcohol groups (ν_{OH} at 3400 cm^{-1} and $\nu_{C\text{-}OH}$ at 1020 cm^{-1}) are much weaker in the case of sucrose - ammonium citrate mixture. Also, in this case, new IR bands are observed: strong and broad band centered at 3210 cm^{-1}, and a peak at 1350 cm^{-1}, as well as a broad shoulder at 1580 cm^{-1}. These bands can be attributed to $\nu_{N\text{-}H}$ and $\nu_{C\text{-}N}$, and $\delta_{H\text{-}N\text{-}H}$ in primary amines/amides correspondingly, indicating that ammonium is at least partially transformed to amine/amides (primary or secondary) in polycondensation products (Fig. 49C). We note that the vibrations $\nu_{N\text{-}H}$ and $\delta_{H\text{-}N\text{-}H}$ in ammonium citrate are also detected close to the peaks observed in polycondensation product, and, thus, the presence of ammonium in the product cannot be excluded.

After thorough grounding of polycondensation product, it was mixed with KOH solution and then dried at 160 °C in air. This procedure is expected to eliminate any remaining ammonium salt within the polycondensation product via formation of gaseous ammoniac. The dried product was again grounded and then pyrolyzed at 700 °C, 800 °C, or 900 °C in Ar for thermochemical activation of the carbon.

The structure and composition of these prepared samples was characterized as described in the next section. The synthesis conditions and some characteristics of the studied samples are summarized in Table 1.

Table 1: Summary of the conditions of samples AC samples studied in the work, and some of their characteristics.

Sample name	**Precursors**	**Activation temperature, °C**	***SSA*, m^2/g**	***x*(O), *x*(N), at.%**	***ρ*, kOhm. cm**	***Cg*, F/g (2A/g, 1 M H_2SO_4)**
ACS-800	Sucrose	800	10	30.4 / -	0.61	3
ACC-800	Sucrose + Citric acid	800	130	15.9 / -	0.30	75
ACN-700	Sucrose + $(NH_4)_3$Cit	700	271	11.8 / 7.3	19.5	44
ACN-800	Sucrose + $(NH_4)_3$Cit	800	776	10.8 / 3.3	0.19	321
ACN-900	Sucrose + $(NH_4)_3$Cit	900	1379	8.6 / 1.5	0.009	208

- Physicochemical characterization of AC samples

Typical SEM images of the ACN samples are given in Figure 50. The SEM images demonstrate irregular porous structure typical for AC materials. No clear difference in the structure of samples activated at different temperatures was detected. Also, we did not detect any visible difference in terms of structures between ACN and ACC-800 sample, prepared from sucrose and citric acid mixture. The SEM resolution allows only evidencing the presence of macropores. For more detailed understanding of the porosity of the sample BET study has been done (see Fig. 51).

The increase in the activation temperature results in an increase in specific surface area (SSA) of the as-synthesized ACN samples. High SSA values and diameter distribution demonstrates the formation of large contribution of micropores with $d \leq 2$ nm, that is confirmed by the Type I of observed isotherm. In the case of ACN-800 we also observed the formation of small amount of mesopores with $d \approx 10\text{-}20$ nm can be observed, while for ACN-900 sample the distribution of the sizes of mesopore is much broader. However, the contribution of mesopores is very low as attested by the absence of hysteresis of the isotherms.

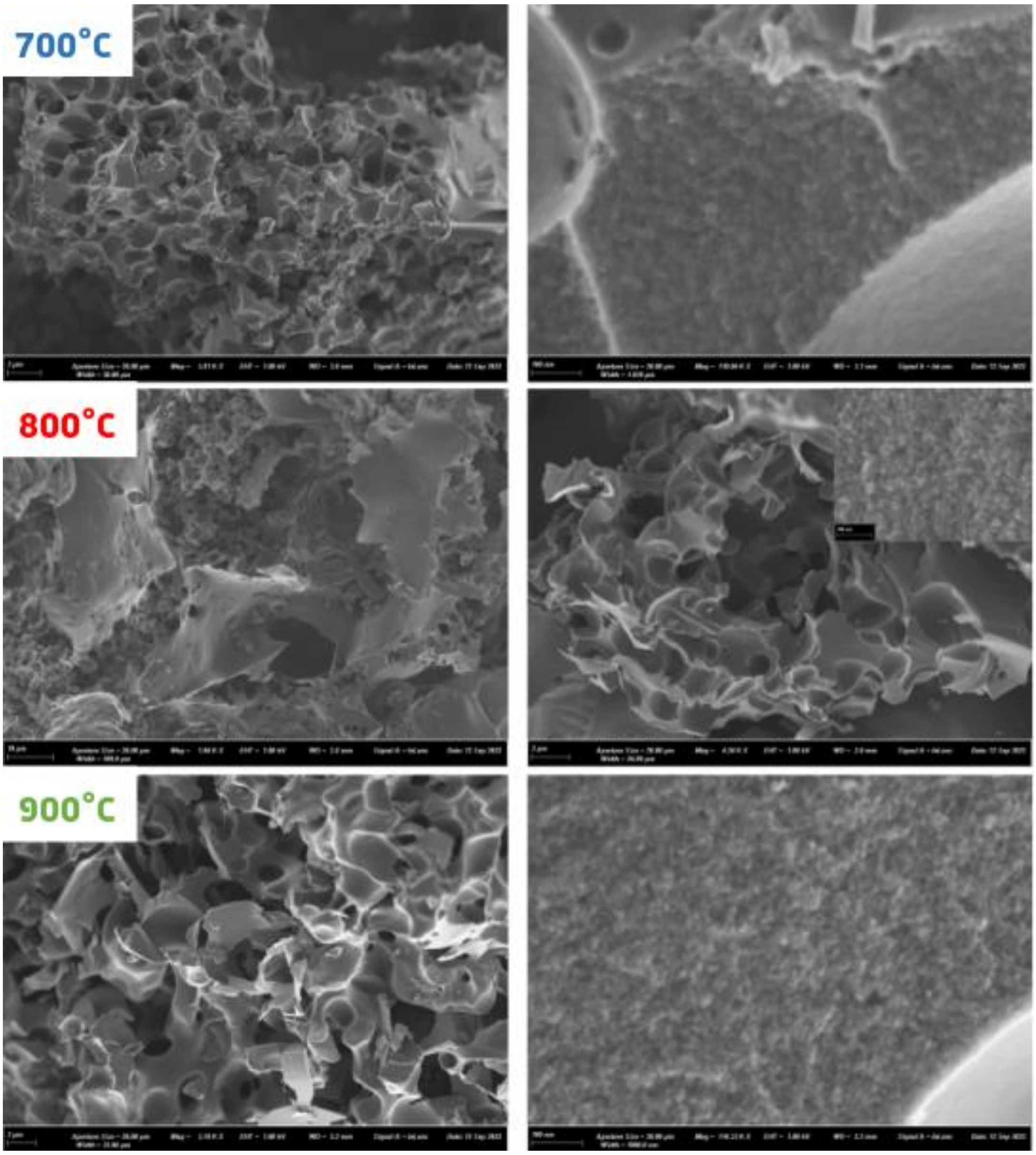

Figure 50: Typical SEM images of ACN-700 (A), ACN-800 (B) and ACN-900 (C) samples.

In general these results are in agreement with studies of porous structure of bio-char derived activated carbon on activation temperature[304,317]: an increase in activation temperature at least up to 800 °C results in a higher BET surface area of the sample due to the opening of micropores formed at lower temperature. An increase of activation temperature above 700 °C results in general widening of pores: the relative contribution of ultramicropores (diameter $d \approx 0.3\text{-}0.4$ nm) decreases with higher temperature and longer activation time, while relative contribution of micropores with $d \approx 0.8\text{-}2.0$ nm increases[317]. The BET surface area of ACN-800 sample is significantly higher than that of ACC-800 (sucrose + citric acid). It shows that thermal decomposition of cross-linked product of polycondensation of sucrose and ammonium citrate addition, results in more porous structure than in the case of sucrose and citric acid, demonstrating the effect of the presence of N-containing groups in polycondensation intermediate.

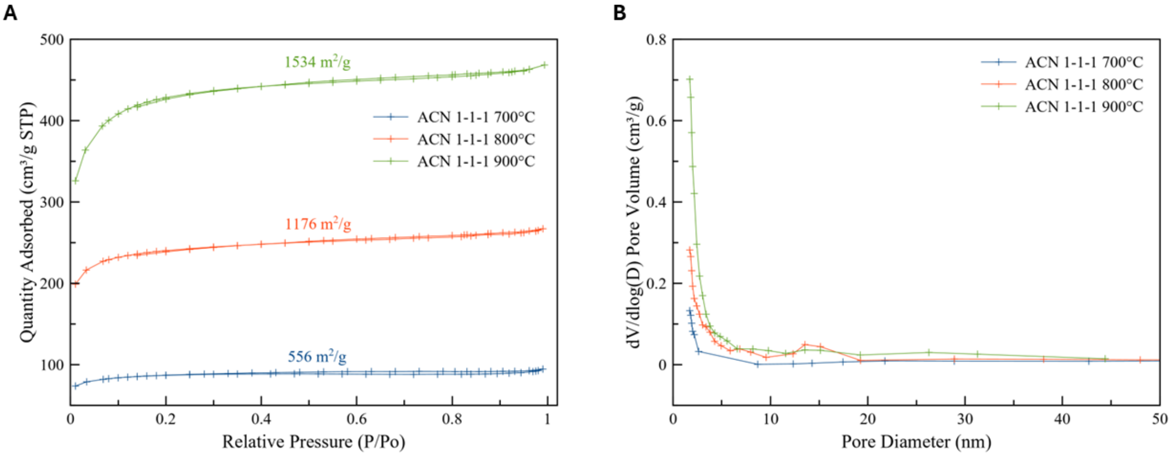

Figure 51: BET isotherms (A) and pore diameter distribution (B) of ACN samples

Figure 52 shows N*1s* XPS spectra of ACN samples after KOH activation. Deconvolution of N*1s* XPS spectra of ACN samples demonstrates that N-heteroatoms are incorporated to carbon structure in various forms: pyrrolic N, pyridinic, amines/amides, quaternary N (Q-N), and NO_x. Due to the variety of the types of N-heteroatoms, there is certain incertitude in peaks deconvolution, making difficult the precise analysis of the ratio of different types. However, certain qualitative conclusions can be drawn, as described below.

N-pyrrolic is the predominant type of N-heteroatoms, and its ratio slightly decreases with activation temperature. Also, the ratio of remaining amine/amide-N slightly decreases, while the ratio of more thermally stable N-pyridinic and, perhaps Q-N, increases. In general, as the activation temperature increases, the concentration of heteroatoms (N and O) is decreasing. The pyrolysis of polycondensation intermediate results in a decomposition of N- and O-containing functional groups, which starts at ca. 600 °C[318]. The decomposition results in the formation of gaseous products, such as CO_2 and NH_3 and/or NO_x. Formation of gaseous products is one of the processes responsible for the development of open porous structure of the final carbon product. In particular, formation of ammonia via decomposition of amine/amide groups of polycondensation intermediate results in higher BET surface area due to chemical etching of carbon by gaseous ammonia, which above 700 °C reacts with carboxylic groups and carbon skeleton forming more thermally stable pyrrolic, pyridinic, and Q-nitrogen groups[319,320]. Indeed, XPS results show that ACN-800 sample is more reduced (contains less oxygen) comparing to ACS-800 and ACC-800 prepared without using N-containing precursors. Certain ratio of amine/amide N-heteroatoms remains even at 900 °C, even though this ratio is, as expected, decreases with temperature due to transformation of amines and amides to more stable forms of N-heteroatoms.

XPS N1s for ACN 700°C

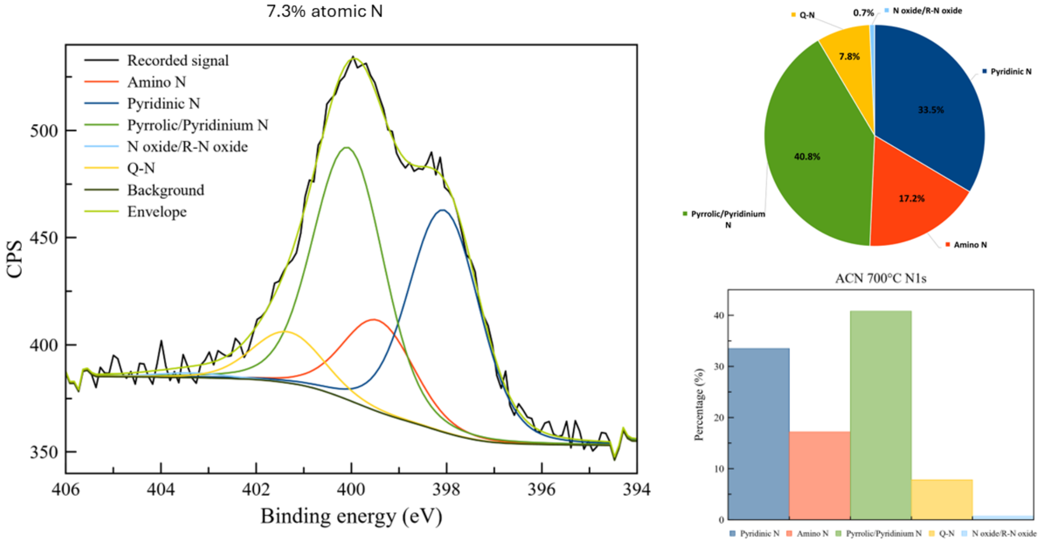

XPS N1s for ACN 800°C

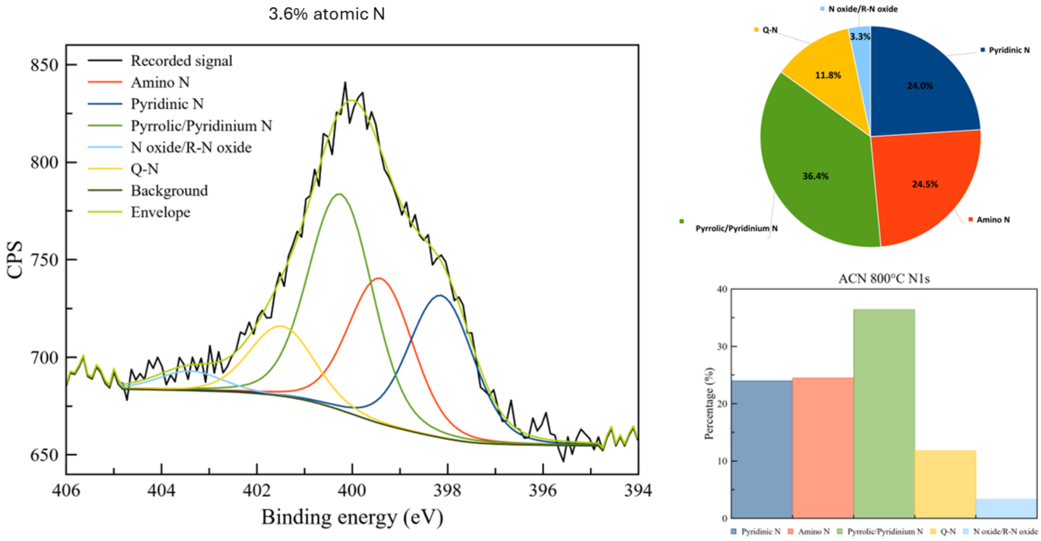

XPS N1s for ACN 900°C

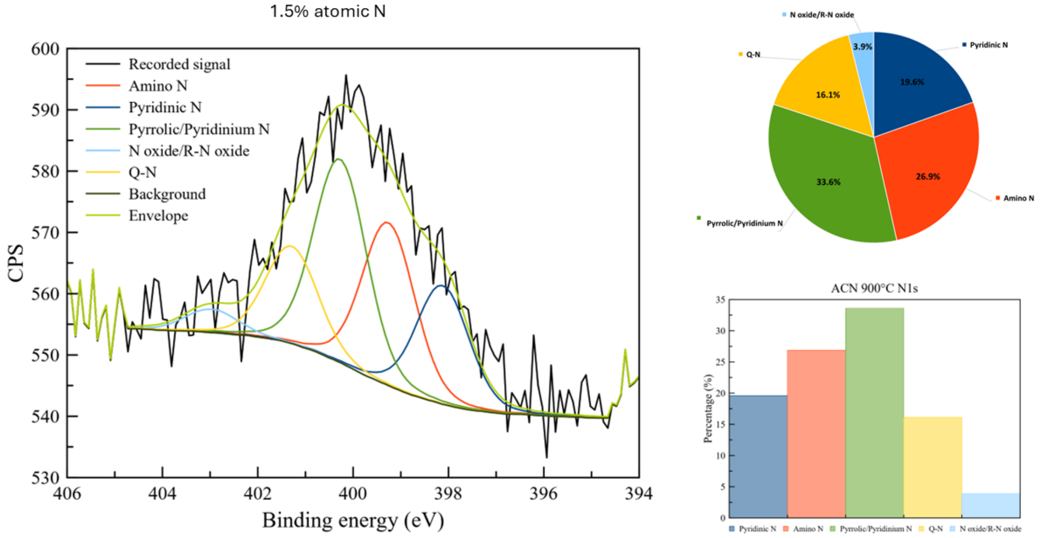

Figure 52: N1s-XPS spectra of ACN samples with peak deconvolution

The decomposition of N- and O-containing functional groups results in formation of unsaturated C-C bonds, i.e. in increase in relative population of *sp*^{2}-carbon, and in graphitization of remaining carbon structure. The Raman spectra of ACN and ACC-800 and ACS-800 samples show D- and G-band at 1344 and 1593 cm^{-1} correspondingly (Fig. 53) which is usual for disordered graphitic structures. The full width at half maximum (FWHM) values of G-band for ACN-700, ACN-800, and ACN-900 samples are accounted for 117, 103, and 81 cm^{-1}, demonstrating a systematic decrease in the FWHM with an increase in activation temperature. It has been shown that G-band FWHM is inversely proportional to average size of ordered *sp*^{2}-domain L_a,[321,322]. Using the empirical correlation equation for pyrolyzed nanographites[322], the L_a of ACN-700, ACN-800, and ACN-900 can be estimated as 4.2 nm, 4.9 nm, and 6.4 nm correspondingly, i.e. 10-20 graphitic layers. Thus one can conclude that the L_a of ACN samples is slightly increasing with an increase in activation temperature. The values of FWHM of ACS-800, ACC-800, and ACN-800 samples are close, indicating that the activation temperature is a determining factor for the size of *sp*^{2}-domains.

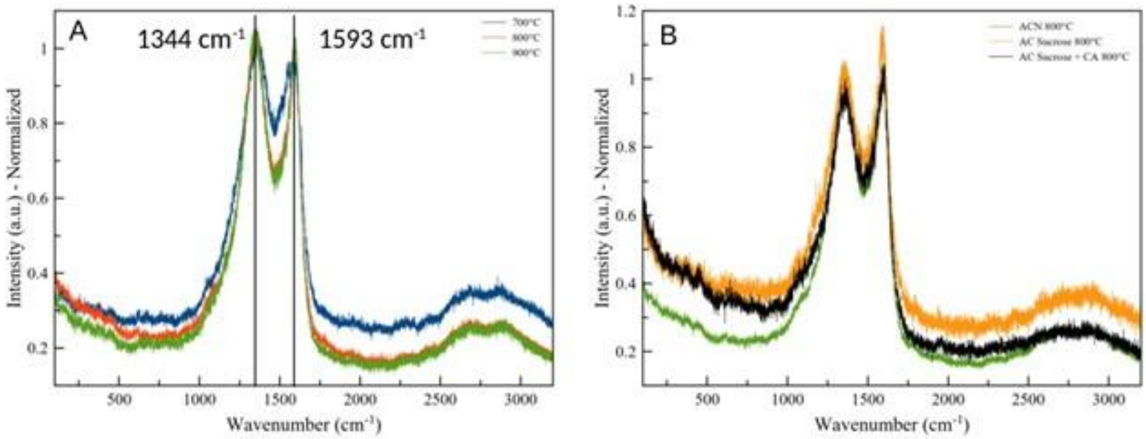

Figure 53: Raman spectra of ACN samples (A) and ACN-800, ACC-800, and ACS-800 samples (B).

Two-point conductivity of ACN samples increases approximately by 2 orders of magnitude with every 100 °C increase of activation temperature. The resistivity of ACN-700 sample ρ ≈ 19.5 kOhm.cm is close to the typical one for activated carbons. The resistivity of samples ACN-800 and ACN-900 are 194 and 9.2 Ohm.cm, correspondingly. For all 3 samples the value of resistivity was found to be frequency-independent in the range 10^{-2}-10^{6} Hz. It suggests that for ACN-700 sample the electron transport via direct continuous pathway is the predominant conductivity mechanism, while contribution of other mechanisms (electrons hopping and tunneling between carbon clusters, interfacial polarization) are negligible[318]. Relatively high resistivity of ACN-700 sample can be explained by the small concentration and narrow size of continuous electron pathways, which is in agreement with above assumption of smaller L_a of ACN-700 sample. Considering that the estimated size of *sp*^{2} domains in ACN-800 sample is only slightly larger than that of ACN-700, the strong increase of conductivity with activation temperature could be related to the strong increase in the concentration of ordered sp^2 domains.

The conductivity of ACS-800, ACC-800, and ACN-800 samples is in good correlation with reduction state of the carbon, as characterized by x(O) at.%. One may argue that the decomposition of O-containing fragments of polycondensation intermediates and formation of C-C unsaturated bonds is the main mechanism of appearance of sp^2-domains, which are in turns responsible for electronic conductivity. Transformation of N-amine/amide and N-pyrrolic to N-pyridinic and Q-N may also be expected to increase conductivity, as in the last two forms N-heteroatoms are included to π-electrons conjugated network. Also, the thermal decomposition of an intermediate with N-heteroatoms results in more reduced carbon state, and, as a result, with higher conductivity.

- Electrochemical properties of AC samples

Figure 54A shows the stable CV curves of ACN samples measured in 1 M H_2SO_4 at 20 mV/s. The CV curves of ACN-800 and ACN-900 samples contain a pair of broad reversible redox peaks centered around 0.70-0.80 V *vs.* RHE, conventionally attributed to reversible surface redox transition of O-containing groups (quinone-hydroquinone type[295]), and/or N-containing groups (for example N-pyrrolic) (Fig.7). The integral mass specific capacitance calculated from the CV curves measured at 20 mV/s is 55 F/g, 284 F/g, and 197 F/g for ACN-700, ACN-800, and ACN-900 samples, correspondingly.

It is most surprising to observe that the capacitance of ACN-900 sample is ca. 30% smaller comparing to ACN-800 sample, despite nearly twice as higher SSA of the former. The SSA of the carbon samples can be used to estimate the corresponding specific surface capacitance C_s, which for the studied samples was 6, 27, and 13 μF/cm^2 for ACN-700, ACN-800, and ACN-900. The values of C_s for ACN-700 and ACN-900 are just slightly higher than $C_s \approx$ 5-10 μF/cm^2, expected for 3D carbon electrodes with high SSA[296], while the value of C_s of ACN-800 sample is few times higher: one would expect the value $C_g \approx$ 141 F/g for pure double-layer capacitance for carbon electrode with SSA = 1176 m^2/g and with a corresponding $C_s \approx$ 10-12 μF/cm^2.

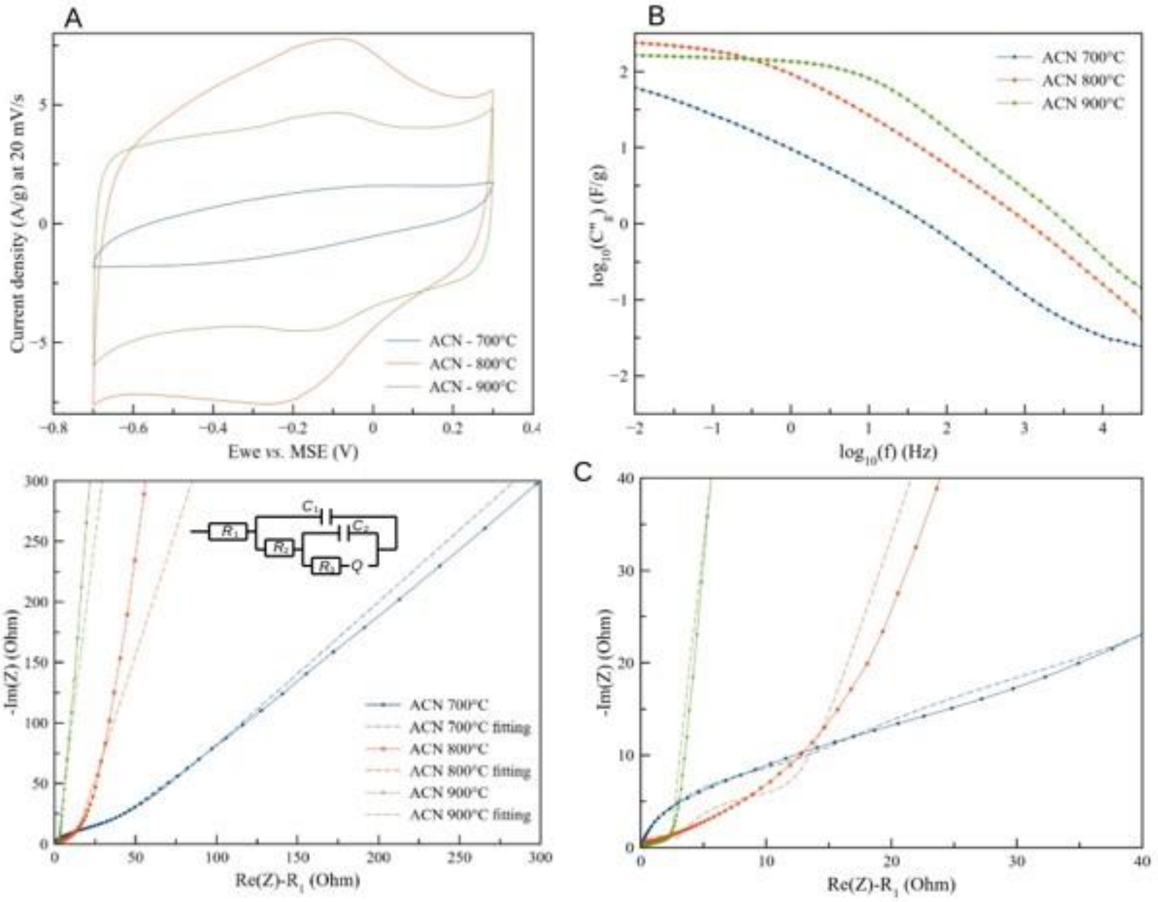

Figure 54: Electrochemical characterization of ACN samples in 1M H2SO4. Stable CVs at 20 mV/s (A); frequency dependence of a capacitive component of total impedance C" (B); Nyquist plots of impedance (C) (right side graph is a zoom of the left side plots).

One may argue that additional contribution to interfacial capacitance can be attributed to pseudocapacitance related to the redox transitions of N-heteroatoms. As mentioned earlier, nearly linear increase of C_g with x(N)%at. was reported for PAN-derived carbons[311], and attributed to pseudocapacitance reaction involving N-pyridinic. Outstandingly high mass specific capacitance $C_g >$ 800 F/g (in H_2SO_4 at 1 A/g) was reported for N-doped mesoporous carbon, and explained by redox reactions involving pyrrolic and pyridinic N-heteroatoms[312]. These redox reactions result in exchange of 1 H^+ between carbon electrode and electrolyte, and, thus, contribute the charge of 1 e^- per 1 N-heteroatom (Fig. 55). The additional mass specific capacitance contribution related to pseudocapacitance reaction involving N-heteroatoms $C_{N\text{-}PS}$ (in F/g) for 1V range can be estimated as:

$$C_{N-PS} = \frac{F \cdot x_N}{M_C} = x_N \cdot 8041 \qquad (1)$$

where x_N is an atomic ratio of N-heteroatoms active in pseudocapacitance reaction.

In order to evaluate the nature of active N-heteroatoms it is useful to compare the oxidation potentials of various N-containing organic aromatic molecules, see Table 2. The comparison of oxidation potential of aniline, pyrrole, and pyridine shows that N-amine and N-pyrrolic heteroatoms can be oxidized at lower potentials and thus, are more probably to contribute to pseudocapacitance than N-pyridinic.

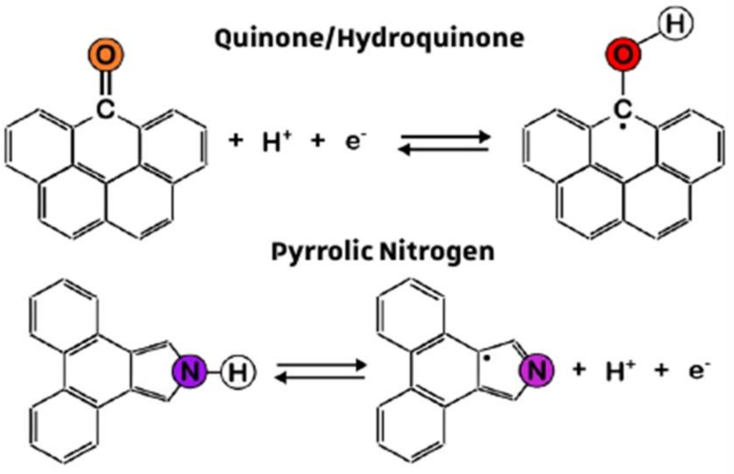

Figure 55: Surface redox reactions responsible for surface fast pseudocapacitance phenomena in ACN-800 and ACN-900 samples.

Table 2: *Selected N-containing aromatic organic molecules and the redox potential of their oxidation, estimated as $E_{1/2}$ of oxidation wave, V SCE* [323],[324]

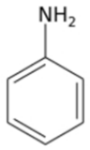 1.14 V Aniline	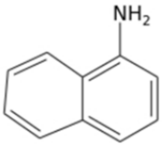 0.88 V 1-Naphtylamine	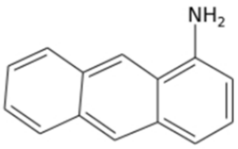 0.75 V 1-Aminoanthracene
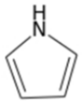 1.24 V Pyrrole	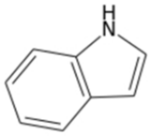 1.16 V 1H-Indole	
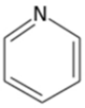 2.26 V Pyrridine	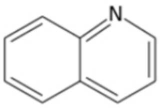 2.14 V Quinoline	

Considering that for ACN-800 sample the total ratio of N-heteroatoms is 3.3 at.%, and ca. 71% of these atoms are N-amine or N-pyrrolic, x_N = 2.34%, and $C_{N\text{-}PS}$ = 188 F/g for this sample, which can well account for the difference between C_g (284 F/g) and expected double layer capacitance (141 F/g). On the other hand, ACN-900 contains 1.5at.% of N-heteroatoms, only 58% of which are N-amine or N-pyrrolic, and, thus, x_N=0.87%, and $C_{N\text{-}PS}$=70 F/g, significantly lower comparing to ACN-800.

However, one still has to explain the low capacitance of ACN-700 sample, which has more than double total x(N) comparing to ACN-800, 74% of which are N-amine and N-pyrrolic, and yet lower C_s value. According the measurements of conductivity, ACN-700 sample has significantly lower concentration of ordered graphitic domains. We may speculate that only N-heteroatoms incorporated to graphitic domains are capable to contribute to pseudocapacitance phenomena. N-heteroatoms of disordered carbon structure are arguably inactive either due to the lack of the possibility of stabilizing the extra charge added by redox transition. Indeed, comparison of oxidation potentials of aniline, 1-naphtylamine, and 1-aminoantracene (Table 2), clearly shows that addition of an aromatic ring to the conjugated π-electron network facilitates oxidation of amine. The same trend can be seen by comparison of oxidation potentials of pyrrole and 1H-indole, and pyridine and quinoline. Thus, it is reasonable to suggest that N-heteroatoms included into extended conjugated π-electron network (conductive graphitic domain) is more active in pseudocapacitance phenomenon than isolated N-heteroatoms.

Summing up, we suggest that the high pseudocapacitance of carbon requires simultaneous high content of both graphitic domains and N-pyrrolic heteroatoms, like N-doped mesoporous carbons in ref.[312], or, in a lesser extent, sample ACN-800 in the present study. For the preparation of N-doped AC materials, 800° C appears to be an optimal activation temperature, as in the products of activation at lower temperature, the majority of N-heteroatoms are not linked to the conductive graphitic domains, and at higher temperature N-heteroatoms are gradually transformed to less active N-pyridinic and Q-N heteroatoms.

Impedance spectroscopy is a valuable tool to have a deeper insight on the dependence of interfacial capacitance on the rate of charging of the interface. The Nyquist plots of ACN samples are shown in Fig. 54C. The observed curves can be qualitatively fitted by an equivalent circuit depicted in the inset. It must be noted that this equivalent circuit serves only for qualitative explanation of the impedance behavior and for the comparison between similar carbon materials. The impedance of complex porous system is properly described by models based on transmission line concept[325]. This circuit in Fig. 54C can be interpreted as follows: R_1 is a resistance of the electrolyte, C_1 is the interfacial capacitance of the outer surface of carbon deposit, C_2 is the interfacial capacitance of the surface of large open pores easily accessible for the electrolyte, R_2 is the resistance of the electrolyte inside of these pores, R_3-Q is an impedance of smaller pores, which are the branches of the bigger open pores. Q is a constant phase element (CPE) with a as the CPE constant. In the case of the impedance of a pore, the value of a depends on the relative values of the length of small pores l_p and AC penetration depth λ, namely $a = 0.5$ for $l_p > \lambda$, and $a \approx 1$ for $l_p < \lambda$. The value of λ can be estimated by equation 2 [9]:

$$\lambda = \frac{1}{2}\sqrt{\frac{\delta \cdot d_p}{2\omega \cdot C_s}} \tag{2}$$

where σ is the conductivity of the electrolyte, d_p is the pore diameter, $\omega = 2\pi f$ is angular frequency, and C_s is surface specific capacitance. According to equation 3, for thinner pores, the modulation penetration depth is shorter, and the pore-specific impedance (*i.e.* $a = 0.5$) is observed already at lower modulation frequencies. The parameters of the fitting of experimental Nyquist diagrams are given in Table 3.

Table 3: *Parameters of the fit of Nyquist diagrams by equivalent circuit in Fig. 54C*

Sample	R_1, Ohm	C_1, mF	R_2, Ohm	C_2, mF	R_3, Ohm	Q^{1-a}, $(\mathrm{mF})^{1-a}$	a
ACN-700	2.4	0.022	18.2	0.113	26.8	2.35	0.55
ACN-800	2.0	0.129	3.04	3.55	12.5	20.8	0.85
ACN-900	4.5	0.146	0.92	3.67	1.99	18.1	0.96

The EIS diagrams of ACN-900 can be well fitted by circuit depicted in Fig. 7 with $a = 0.9$. It demonstrates the open porous structure of the sample with wide and short pores, easily accessible for electrolyte for whole range of utilized frequencies. Also, the value of capacitive component of total impedance C'':

$$C'' = -\frac{1}{Im(Z)\cdot\omega} \tag{3}$$

where Z is a total impedance remains nearly constant up to intermediate range of frequencies $f \approx 10$ Hz (Fig.54B). At higher frequencies the decrease with the slope -1 of log C'' - log f is observed, which is an indication of the influence of resistance of the electrolyte in pores. In contrast to ACN-900, the EIS diagrams of ACN-700 can be fitted only with $a = 0.5$, demonstrating that the narrow pores are longer, and $l_p > \lambda$ even for low frequency (0.1 Hz). In the case of ACN-800, the best fit was obtained with $a = 0.90$; However, it appears that the fit is not correct at low frequencies range, as AC penetration depth is getting deeper, and narrower and longer pores are engaged to the charge storage. The fit for ACN-800 sample is only possible assuming the value of a varying with applied frequency, which is an indication of the non-uniform size of the pores. The C'' component decrease observed already at low frequencies with the slope ca. -0.75, indicating the limitation related to both resistance of electrolyte, and AC penetration depth dependence of frequency. More detailed impedance study of electrochemical properties of ACN-800 electrode material is discussed in the sub-section “Impedance spectroscopy study…” of this chapter.

Summing up, EIS analysis confirms the assumption of the fact that the diameter of the pores is increasing as activation temperature increases (from ACN-700 to ACN-900), and thus the pores are getting more open, facilitating the accessibility of electrolyte (lower R_2 and R_3), and penetration of AC-signal.

Fig. 56A shows the dependence of mass specific capacitance of ACN samples on the number of charge/discharge cycles applied at 2 A/g. All samples demonstrated excellent stability within the

1000 cycles. It is important to note that the capacitance of ACN-900 sample significantly increased in the first hundred charging cycles. This increase in capacitance can be attributed to improving accessibility of inner pore volumes of ACN-900 by potential cycling. Indeed, the surface ACN-900 sample is most reduced, comparing to other ACN samples, and, arguably, less hydrophilic. Also, the surface of ordered graphitic domains, of which ACN-900 has the highest content, is hydrophobic. Thus, originally the volume of micropores of ACN-900 can be less accessible comparing to other ACN samples, despite larger average diameter, suggested earlier. However, periodic oxidative polarization of carbon electrode results in the partial oxidation of carbon surface, its improved hydrophilicity, and better accessibility of pores. We note that the impedance measurements discussed above were performed after the stability tests done by 1000 charge/discharge cycles.

Fig. 56B shows the dependence of specific capacitance on charging rate. These measurements were also performed after 1000 charging cycles. As expected, all samples demonstrated a decrease in specific capacitance, as the charging rate increases from 0.5 A/g to 20 A/g. However, the loss of capacitance systematically depends on the activation temperature: it is 93%, 32%, and 19.5% for ACN-700, ACN-800, and ACN-900 correspondingly. This observation is in agreement with assumption of wider pores of ACN-900 sample, and their easier accessibility for electrolyte species, comparing to ACN-800, and ACN-700 samples.

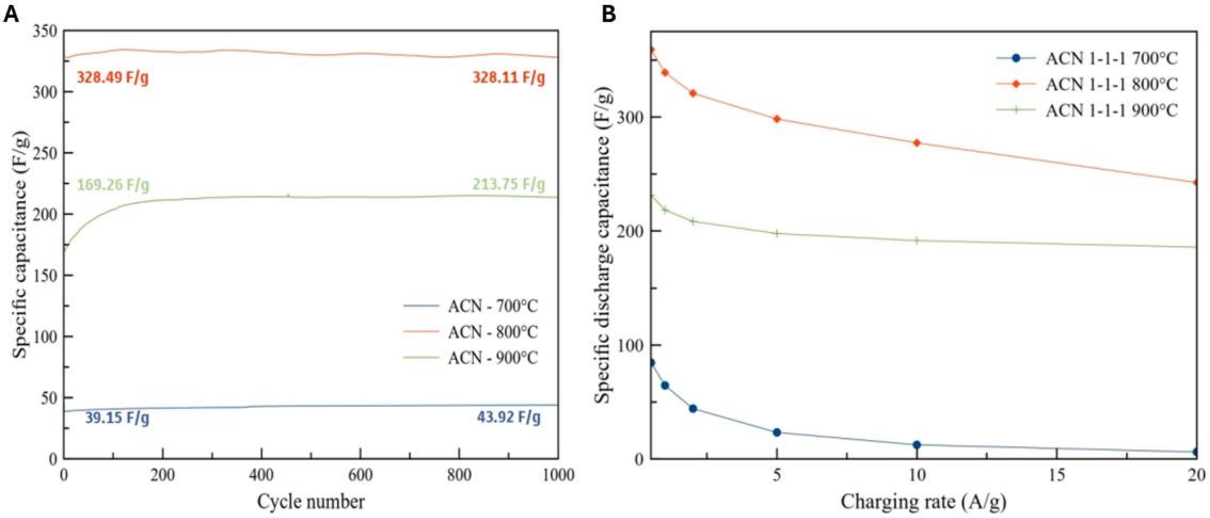

Figure 56: Evolution of specific capacitance with cycling at 2 A/g (A); dependence of specific capacitance on the rate of charge/discharge, measured in 1M H_2SO_4 (B).

- **Discussion**

Addition of ammonium citrate to sucrose precursor for the synthesis of activated carbon results in a significant change in the structure and properties of the final product. The cross-linked polycondensation intermediate formed from ammonium citrate and sucrose (Fig. 49C) contains amide and imide groups, which are decomposed above 600 °C[326] nitrogen groups and formation of more stable aromatic N-containing fragments of carbon matrix. These phenomena results in significantly higher surface area of ACN-800 synthesized with ammonium citrate comparing to ACC-800, synthesized with citric acid additive. Besides, ACN-800 has lower oxygen content x(O), and higher electrical conductivity. Increase in activation temperature results in a decrease in remaining content of N-heteroatoms.

All synthesized AC samples are electrically conductive, demonstrating constant electrical resistance in the frequency range 10^{-1}-10^6 Hz. This is an indication that already after activation at 700 °C the continuous network of conductive *sp*^{2}-carbon domains is developed. Increase in the activation temperature from 700 to 800 and to 900 °C results in ca. 100-times increase in conductivity of carbon samples. The FWHM of Raman spectra G-band of these samples indicates an slight increase in the average size of ordered graphitic domains, however, the main factor responsible for strong increase in conductivity is assumed to be a strong increase in the concentration of ordered graphitic domains with activation temperature. It is important to note that the estimated size of these domains remains relatively small so that no graphitic domains are detected by XRD, and thus even after activation at 900 °C the final structure can be characterized as a disordered graphitic structure.

The samples prepared from sucrose and ammonium citrate mixture after activation at 800 and 900 °C (ACN-800 and ACN-900) demonstrate excellent properties as EDLC electrode materials. In particular, ACN-800 sample demonstrate very high mass- and surface-specific capacitances, C_g = 320 F/g and C_s = 27 μF/cm^2 correspondingly in 1M H_2SO_4 at 2 A/g. Such unusually high C_s value is arguably related to the combination of 2 factors: the presence of relatively high surface concentration of N-pyrrolic heteroatoms, responsible for fast redox surface transitions (Fig. 56), and high concentration of ordered small graphitic domains, facilitating the redox reactions. The lower content of both graphitic domains (ACN-700 sample) and N-pyrrolic heteroatoms (ACN-900 sample) resulted in lower specific capacitance.

It has to be mentioned that outstandingly high capacitance (≈ 600 F/g) in concentrated H_2SO_4 has been observed for AC CHI900-20, with no N-heteroatoms and predominantly amorphous structure [327]. The observed capacitance was attributed to the intercalation of H^+ to the extent of formation of stoichiometric C_6H composition. However, this process was strongly limited by the kinetic of charge transfer and solid state diffusion of H^+, and high intercalation extent required several hours of charging.

In order to evaluate the contribution of a mass transport controlled processes into the charge capacitance, the CVs of ACN-800 were measured with different potential sweep rates from 1000 to 0.5 mV/s (Fig. 57A,B). The dependence of CV currents on sweep rate is close to linear at list for not very high rate $\omega < 200$ mVs/ (Fig. 57C), demonstrating negligible contribution of mass transport controlled processes to the charge of CV curves at these conditions. At higher sweep rates the dependence deviates from linear as the time of single sweep becomes comparable with RC constant of the cell (ca. 0.5 s). Following the deconvolution method suggested earlier[312], the fast charging contribution to capacitance C_{DL} was estimated by extrapolating $C(\omega)$ vs. $\omega^{-1/2}$ dependence to $\omega \rightarrow \infty$ ($\omega^{-1/2} \rightarrow 0$), see Fig. 57D:

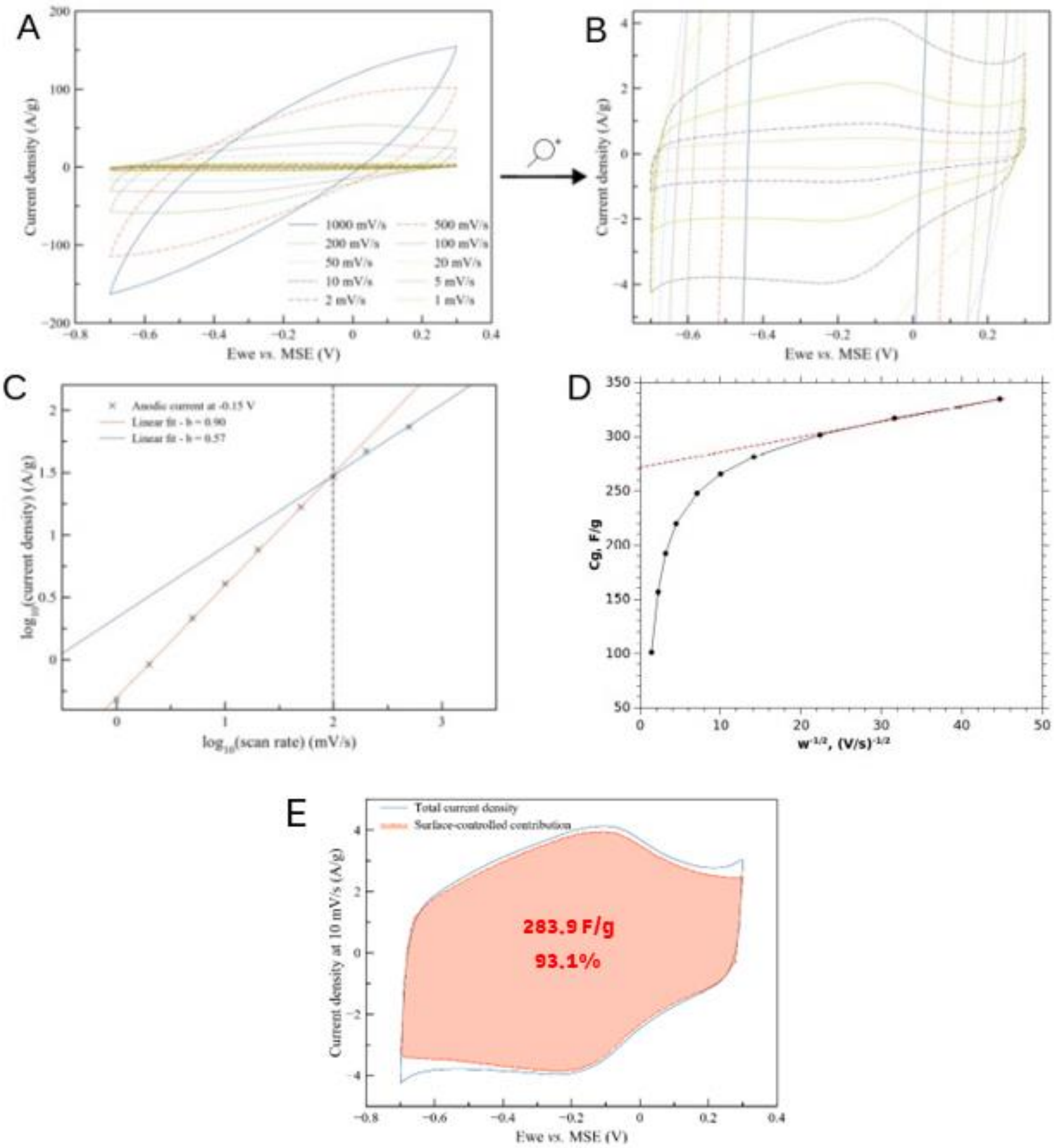

Figure 57: CV curves of ACN-800 sample in 1M H_2SO_4 measured at different sweep rates (A,B); dependence of CV current at direct sweep at -0.15V vs. MSE on sweep rate (C); dependence of integrated mass specific capacitance on $w^{-1/2}$ (D).

$$C(\omega) = C_{DL} + k\omega^{-\frac{1}{2}} \tag{4}$$

Thus, by estimating that the capacitance related to fast charging is ca. 93% of the total capacitance measured at 10 mV/s (Figure 57E), which confirming negligible contribution of any mass transport controlled process to charge capacitance at these conditions. We can conclude that the kinetics of pseudocapacitance reaction involving H^+ addition/elimination from carbon network is strongly facilitated by the presence of N-heteroatoms.

Increase in the activation temperature from 800 to 900 °C results in the widening of the pores and better accessibility of the pores for electrolyte species, and lower pores resistance. The full accessibility of pores inner volume requires few hundreds of potential cycling in order to improve the hydrophilicity of carbon surface, which is too reduced and too hydrophobic after thermochemical activation at 900 °C. After the cycling, the easy accessibility of pores inner volume of ACN-900 is indicated by lower decrease of capacitance when charging rate is increased from 0.5 A/g to 20 A/g, and by the results of the fitting of EIS spectra. For ACN-900 sample the EIS diagram qualitatively described by the model, assuming that all pores are available for charge storage even at high charging rates (high modulation frequencies *f*). On the other hand, ACN-700 sample demonstrated strongest decrease in capacitance with an increase in charging rate, and the capacitance is limited by the depth of penetration of potential modulation even at low charging rates (low frequencies). ACN-800 sample also shows stronger dependence of capacitance on charging rate. Nevertheless, this sample demonstrates the highest specific capacitance in the wide range of charging currents due to the simultaneously relatively high content of N-pyrrolic heteroatoms and ordered graphitic domains.

- **Conclusion**

The two-step synthesis process of activated carbon from sucrose and nitrogen-containing sources is a conventional strategy of AC preparation, involving polycondensation and thermochemical activation. We have demonstrated that addition of ammonium citrate to sucrose has a strong influence on the structure and composition of resulting AC material, and on its electrochemical properties. The N-doped AC with electrochemical properties offering high performance as an EDLC electrode material has been synthesized. In particular ACN-800 sample, prepared by activation at 800 °C, demonstrated mass specific capacitance of 320 F/g at 2A/g in 1M H_2SO_4. This sample demonstrates higher capacitance than the sample ACN-900, prepared by activation at 900 °C, despite significantly lower SSA of the former. We attributed higher capacitance of ACN-800 sample to the higher content of N-heteroatoms, in particular N-pyrrolic and N-amine heteroatoms. Comparison of redox potentials of N-containing organic aromatic compounds allows to argue that these types of N-heteroatoms are more active in redox pseudocapacitive reaction than N-pyridinic and Q-N heteroatoms, the ratio of which is increasing with activation temperature. On the other hand, low capacitance of ACN-700 sample, prepared by activation at 700°C, and which also contains high ratio of N-pyrrolic and N-amine heteroatoms, points to the suggestion that only N-heteroatoms included into the ordered graphitic domains are active in the pseudocapacitance phenomena. The latter can be explained by facilitated stabilization of an extra charge by conjugated π-electrons network of graphitic domain.

The improvement of the performance of N-doped AC electrode materials, prepared by described 2-step thermal activation method can arguably be achieved by further optimization of the synthesis conditions. In particular, the ratio between ammonium citrate and sucrose precursor is expected to have an influence on the atomic ratio of N-heteroatoms in the resulting AC material. The study of electrochemical properties of ACN materials in organic electrolytes is expected to demonstrate the influence of the hydrophilicity/hydrophobicity of the materials on their electrochemical properties. Finally, a detailed analysis of electrochemical impedance of ACN electrode materials with variable electrode loading will provide better understanding of the influence of carbon porosity on its electrochemical performance. These studies are currently performed as a follow-up of the present work.

Fluorination as a mean to modify activated carbon properties for supercapacitor applications

- **Abstract**

Fluorination using xenon difluoride on N-doped activated carbons was chosen to investigate the probable role of fluor doping on already N-doped compounds and reveal its impact on the structural properties and performance as supercapacitor electrode materials. Fluorination at low level on a more disordered ACN-800 allowed to reduce the number of dangling bonds but at the expense of materials conductivity, hindering its performance as electrode material. On a more ordered ACN-900 material, fluorination was easier to achieve and allowed a slight increase in the performance due to probable increase in pore wettability and accessibility for the electrolyte while not affecting drastically an already more conductive sp^2-carbon matrix. Nevertheless, high amount of fluorination would have negative effect on both samples with a profound deterioration of the conductive matrix of the activated carbons.

- **Introduction**

Carbon-based materials are widely used in energy storage applications as electrode materials or even additives due to their various modulable properties. They are widely employed as electrode materials for supercapacitor applications with the use of high-SSA porous activated carbons (AC). As discussed above, an interesting strategy to enhance the performance of such electrodes would be to add pseudocapacitive moieties with the presence of O-/N-heteroatoms. It was shown with the synthetized N-doped activated carbons (ACN) that N-pyrrolic and pyridinic groups, as well as quinone groups, abled to increase the overall capacitance with extra proton/electron exchange due to additional surface-redox reactions. Doping with O-/N-heteroatoms showed promising results already. However, fluorination is less regarded as an alternative doping element strategy. We have attempted to analyze the possible effects of fluorination of ACN materials on the properties of these carbons.

- **Materials and Methods**
  - Synthesis of N-dopes activated carbon (ACN)

The synthesis of the used N-doped activated carbons is identical to the one described previously. 10 g of D(+)-Sucrose $C_{12}H_{22}O_{11}$ (Acros Organics, 99+% purity for analysis, CAS: 57-50-1) has been mixed with 10 g of anhydrous ammonium citrate tribasic $(NH_4)_3Cit$ (Sigma, ≥ 97% purity, CAS: 3458-72-8), and finely grinded in a coffee grinder. The solid powder was then put into an oven at 160 °C in air for 4 h. The resulting solid intermediate was grinded once again and mixed with a concentrated aqueous solution containing 10 g of KOH (Acros Organics, extra pure, ca. 85%, flakes, CAS: 1310-58-3). The slurry mixture was dried again at 160 °C for 4h. Dried KOH-impregnated intermediate was loaded into a tubular reactor kept under Ar flow (10 ccm/min). The temperature was raised to the annealing temperature of 800 °C and 900 °C with a 10° C/min ramp, and then kept at the set temperature for 1h. The product was then left to cool down under the flow of Ar. The final product was washed with 2M HCl and ultrapure water, filtered, and dried in the oven overnight at 80 °C. The reference samples were also synthesized by using 10 g of pure sucrose without any other additive, and 10 g of sucrose and 10 g of citric acid (Chem-Lab, 99.5-101%, CAS: 5949-29-1). All other conditions of synthesis were the same as described above. All aqueous solutions in this work were prepared by using ultrapure water (18.2 Mohm·cm, TOC < 2 ppb) produced by UltraAnalytique Veolia device.

  - Fluorination of activated carbons

Important to note that the fluorination of the materials were realized by Dr. Batiste Clavier from the Institut de Chimie de Clermont-Ferrand, partner of this global research project under the supervision of Dr. Katia Guérin Araujo da Silva (team leader) and Dr. Malika El Ghozzi (project responsible). Xenon difluoride XeF_2 is a volatile solid at room temperature. It is highly reactive with ambient humidity, releasing HF vapors. Fluorination of activated carbons (ACN-800 and ACN-900) with this fluorinating agent took place in a sealed 30 mL Teflon reactor, prepared in an argon glovebox. In a typical experiment, ACN is weighed and introduced into the Teflon reactor. Then, a quantity of XeF_2 corresponding to a fluorine to manganese ratio of 0.10 was weighed into an alumina crucible of 500 µL volume before being introduced into the Teflon reactor. The Teflon reactor was sealed and removed from the glove box before being placed in an oven at 120 °C for 16 hours. Once the reaction is complete, the reactor is returned to the glovebox and opened to recover the sample.

The rate of fluorination of the activated carbons was determined using a specific fluoride ion electrode. The protocol is as follows. Approximately 10 mg of compound is accurately weighed and then introduced into a Teflon reactor. Next, 20% acetic acid solution is added. The reactors are stirred at room temperature for 15 minutes, then introduced into a microwave mineralizer. Digestion takes place at 190 °C for 1 hour, allowing complete dissolution of the sample. The choice of acid is crucial to minimize the formation of HF (pKa HF/F^- = 3.2), which can be released and distort measurements by underestimating fluoride ion concentration. Once mineralization is complete, 5 mL of the solution is diluted in a 50 mL flask, then 25 mL of this solution is withdrawn into a polyethylene vial. Ionic strength buffer is added, and the mixture is stirred for 30 min. The fluoride ion concentration is determined by pre-calibrating the fluoride electrode with standard solutions. The fluorination rate can then be calculated for each fluorinated oxide.

- Physicochemical characterization of ACN

ATR-FTIR measurements were done by ThermoFisher IR spectrometer equipped by ATR Smart Orbit setup. XPS measurements were done using Multilab 2000 Thermoelectron spectrometer with Al Kα source (λ = 1486.6 eV). Electron paramagnetic resonance (EPR) spectrums were recoded using a double-cavity Bruker ER041XG EPR spectrometer. The recording conditions were 200-6200 G, three scans of 100 seconds each and 40 dB (0.02 mW).

- **Electrochemical measurements**
    - Preparation of electrodes

Ink preparation

Inks are prepared by adding a desired amount of active material in a glass vial and the required volume of MilliQ water (resistivity of 18.2 MΩ·cm at 25 °C, Total of organic compound (TOC) ≤ 1 ppb) to obtain a 2 g/L concentrated ink. All the inks were prepared by usually weighting 10.0 mg of activated carbon powder in the vial and adding 5000 µL of MilliQ water with a 0.5 – 5.0 mL micropipette. The ink is then shaken and sonicated in an ultrasonication bath for 20 minutes.

Ink deposition on glassy carbon rod

The active material was deposited by drop casting onto the surface of a glassy carbon rod electrode of 6 mm radius. The total deposited volume of ink is 75 µL divided by 5 deposition step of 15 µL in which the electrode is dried for 10 minutes in an oven programmed at 80 °C between each step.

The loading of active material is approximated to 0.75 mg/cm^2. A final deposition of 15 µL Nafion 0.5 wt. % in mixture of lower aliphatic alcohols and water was added and dried to act as a binder.

3-electrode cell set-up

A 3-electrode cell inside a Faraday cage is used for the electrochemical tests. A 100mL 1M H_2SO_4 electrolyte is poured in the cell followed by the addition of a platinum wire with a coil end counter electrode in the compartment separated by a fritted and a mercury/mercurous sulfate electrode (MSE) in saturated K_2SO_4 in the compartment separated by Luggin capillary. The solution in the cell is then purged for at least 30 minutes under N_2 gas. The glassy carbon rod electrode with active material – the working electrode - is placed in a holder and then placed inside the electrochemical cell in order to only have a contact with the surface of the electrode. The N_2 gas is flushing above the electrolyte to keep a controlled atmosphere without O_2. The electrodes are connected to a SP-300 potentiostat from BioLogic.

- **Results**

The EPR spectrums recorded for ACN-800°C (Fig. 58A) and ACN-900°C (Fig. 58B) at different fluorination levels. The written fluorination percentage is based on the molar mass of the compounds considering carbon and xenon difluoride when the fluorination is realized within the fluorination oven. Hence, the experimental atomic percentage of each element is obtained through XPS analysis. From the EPR spectrum of "pure" ACN-800 and ACN-900 without fluorination, the EPR intensity is clearly higher for the compound pyrolyzed at 800°C than at 900°C. For 5% and 10 %F of fluorination, the intensity of the EPR signals for ACN–800 is reduced but highly increased, higher than for the bare sample, for 25% F. Concerning ACN-900, no real change was observed for a 5% and 10%F. Nevertheless, a 25%F level shows a drastic increase in the EPR intensity.

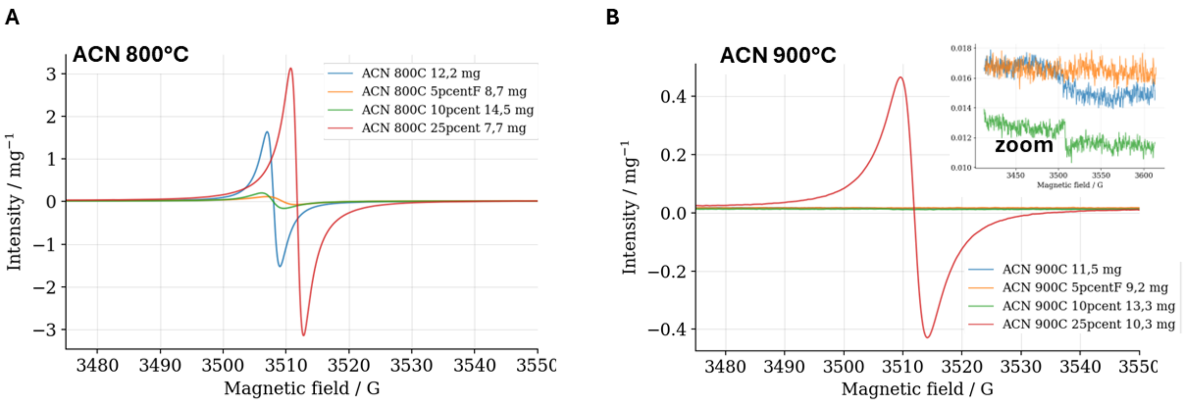

Figure 58: EPR spectra at different fluorination levels of ACN-800°C (A) and ACN-900°C (B)

The FTIR-ATR spectra of the ACN-800°C and ACN-900°C with different %F are presented in Fig. 59A and 59B respectively. Main contributions are given by the four different bond stretching frequencies: ν(C-F) weak at ~1050 cm^{-1}; ν(C-F) strong at ~1200 cm^{-1}; ν(C=C) ~ 1600 cm^{-1} and; ν(C=O) ~ 1750 cm^{-1}. Intensity of the ν(C-F) peaks in ACN-900°C upon fluorination is more marked at than for the 800°C. In each case at 25%F, strong variations of peak intensities appear with noticeable ν(C=O) peak increase.

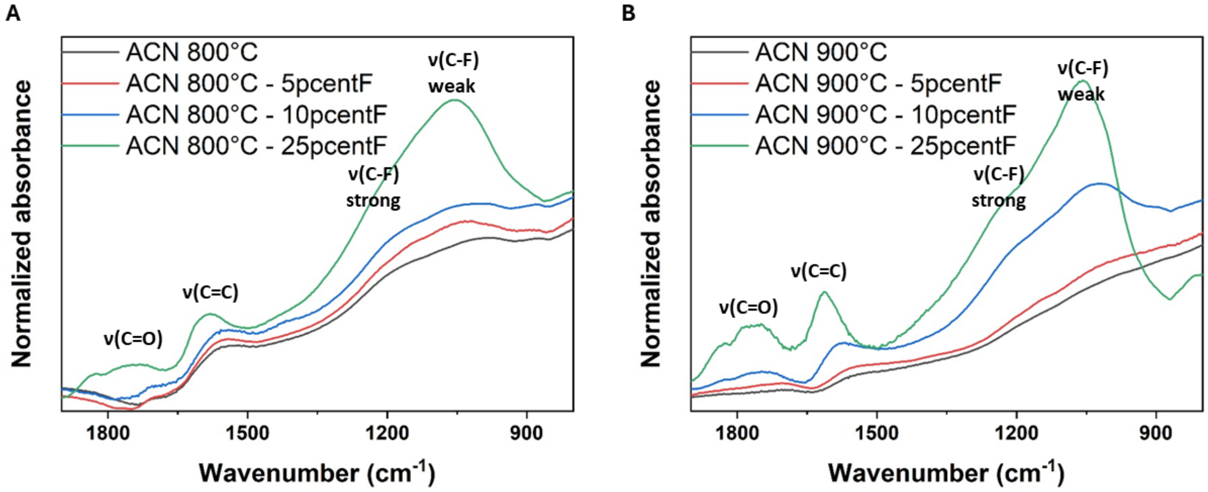

Figure 59: FTIR-IR recorded spectra of ACN-800°C (A) and ACN-900°C (B) at different fluorination levels

XPS data shown for ACN-800 and ACN-900 in the following Table 4. From these values, it can be seen for the ACN-800 sample that the 5-10%F fluorination would only give a 0.6-0.7% F atomic percentage and higher amount of oxygen species. At 25%F, an important increase to 9.2 at.%F is seen with slight diminution in the N and more pronounced decrease of C at.%. For the ACN-900 sample, the N content remain more or less constant over the different %F level. However, the 10%F sample shows an atomic percentage of 6.5% in F and about 14.5% for the 25%F sample. Unfortunately, low quality of the XPS spectra acquisition for the fluorinated samples could not allow an in-depth analysis and precise deconvolution of elements.

Table 4: *Atomic percentage of C, O, N and F elements obtained from XPS data for ACN-800 and ACN-900 samples at different fluorination levels*

	ACN-800	ACN-800 5%F	ACN-800 10%F	ACN-800 25%F
C	85.9%	82.3%	82.7%	77.0%
O	10.8%	12.7%	12.8%	11.3%
N	3.3%	4.3	3.9%	2.5%
F	0.0%	0.7%	0.6%	9.2%
	ACN-900	ACN-900 5%F	ACN-900 10%F	ACN-900 25%F
C	89.9%	85.8%	83.9%	74.0%
O	8.6%	11.6%	8.2%	10.4%

N	1.5%	1.0%	1.4%	1.1%
F	0.0%	1.6%	6.5%	14.5%

Electrochemical measurements realized in 1M H_2SO_4 of each samples are depicted in Fig. 60. Cyclic voltamogramms at 20 mV/s of ACN-800 and ACN-900 samples at different fluorination level are in Fig. A and B respectively. Galvanostatic charging with potential limitations (GCPL) at constant charging rate of 2 A/g for 1000 cycles and at various charging rates (20 A/g – 0.5 A/g) in Fig. C,D and Fig. E,F respectively. These figures show that in the case of ACN-800°C, fluorination has negative impact with a net reduce in specific capacitance but keeping 100% of retention. It can be seen from the CV shape that increase in %F might induce an increase in the electrode resistivity. Concerning the ACN-900°C sample, the 10%F show a very slight increase in the specific capacitance while the 25%F show a performance diminution.

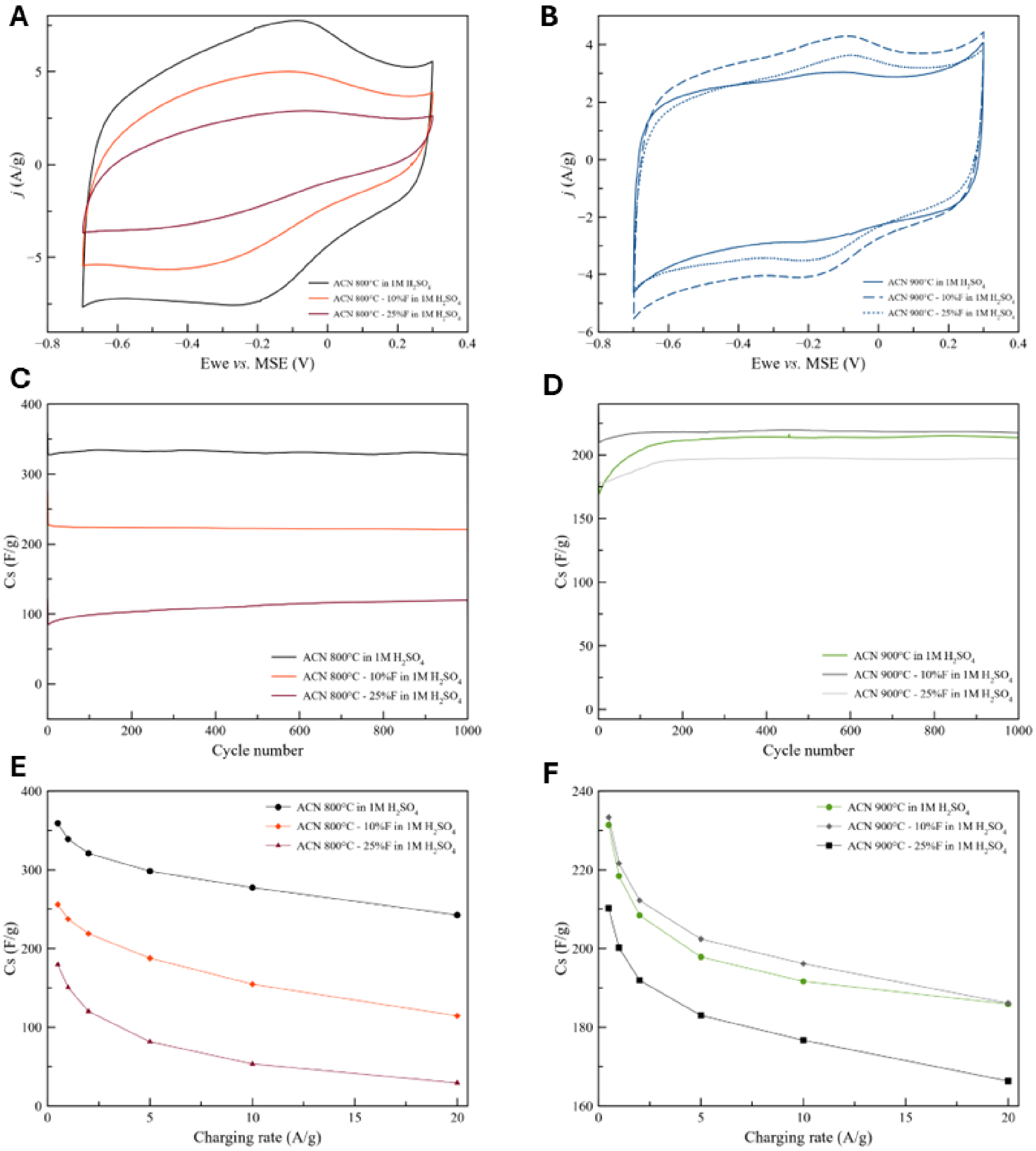

Figure 60: CV at 20 mV/s in 1M H_2SO_4 (A, B), GCPL curves at 2 A/g (C, D) and at various charging-rate (E, F) for ACN-800°C and ACN-900°C at different %F level respectively.

- **Discussion**

From all the performed characterization, different impact on the properties of the activated carbons can be observed. EPR results show, as expected, that a higher pyrolysis temperature for the carbon materials implies a higher structural order with a lower presence of dangling bonds (lower EPR intensity). A lower level of fluorination (5-10%) will reduce the amount of dangling bonds where the fluor atoms will “fill in” them. This especially seen for the 800°C sample presenting initially a higher degree of disorder/dangling bonds than for the sample heated at 900°C. For the latter, only a very slight change was seen for the 5-10%F signal. In both samples, a fluorination at 25%F is countereffecting with an increase in the EPR signals, meaning the creation higher disorder in the structure even more pronounced for the ACN-800°C sample.

The FTIR-ATR spectra show that the 900°C sample gets more easily fluorinated with more marked ν(C-F) peak intensity variation upon 5%, 10% and 25%F than for 800°C. It indicates a easier fluorination for the 900°C for low degree of fluorination. This is also in adequation with the XPS data where for the 5%F ACN-800°C sample, almost no fluorination was detected (<1 at.%F) whereas ca. 6.5 at.% was observed for the 900°C pyrolyzed activated carbon. Upon high degree of fluor treatment, high increase in the ν(C=O) peak signal appears. The C=O bond increase implies a deterioration of the carbon material with rupture of the *sp*^{2}-carbon electron conductive matrix. This is also seen with a rise of the at.%O/at.%C ratio with the XPS data. The loss of conductivity can also be observed through the CV shape of the ACN-800°C material with marked resistive shape of the curve (i.e. tilted).

Concerning electrochemical measurements, cyclic voltammetry curves for the ACN-800°C electrode material show a clear diminution in the curve area/normalized current upon fluorination. The same diminution can be seen as a loss in the measured specific capacitance during charge/discharge cycling at constant and various charging rate. The negative impact of fluorination on this sample could be explained by a loss in the electronic conductivity of the material (increase in the O/C ratio, loss of *sp*^{2}-carbon core upon fluor attachment) directly seen on the CV curve shape. Since at 10%F the atomic nitrogen content did not evolve and a slight increase in the ν(C=O) peak signal is observed, the increase in the materials resistance would explain the performance loss. An interesting point coming from EPR data would be that ordering of the materials (i.e. decrease in the number of dangling bonds) would have a detrimental effect on the performance of the electrode material. Nevertheless, fluorination for the ACN-800°C sample had a diminution of the performance with no visible properties improvement. However, the result on ACN-900°C sample show a very slight improvement on the 10%F sample on the electrode material and a clear decrease for the 25%F. The latter was also seen for the ACN-800°C, explained by the deterioration of the material by an intense fluorination where fluorination attacks the carbon structure, creating defects, diminishing the *sp*^{2}-core structure integrity and further attacking the O-/N-functional groups (i.e. loss in pseudocapacitance). It is not clear on how the 10%F could have benefited the performance of the ACN-900°C material. Some hypothesis could be given such as the opening of close pores through the fluorination process and/or the increase in wettability of the pores with the attachment of fluor atoms in an already existing more ordered and more conductive activated carbon matrix.

- **Conclusion**

Fluorination with XeF_2 at different level was performed on two N-doped activated carbons: ACN-800°C and ACN-900°C. Physico-chemical characterization and electrochemical measurements of electrode materials for supercapacitor applications revealed that low level fluorination allowed to reduce the number of dangling bonds on the structure of disordered activated carbon pyrolyzed at low-to-moderate temperatures. However, the damage on the conductive core of the carbon matrix and the functional groups of such carbon induced a diminution of the electrode materials performance due increase in materials resistance, probable defects creation and loss of electrochemically active N-heteroatoms. On more ordered and conductive carbons synthesized at higher temperatures, low level of fluorination could slightly improve the materials performance either by improving the wettability of the pores and also open the closed/non-accessible ones prior to the fluor treatment.

Electrochemical impedance spectroscopy: Transmission line model of impedance as an *in situ* characterization tool of porous electrode materials

- **Abstract**

The analysis of the frequency dependence of complex capacitance of a porous electrode material allows to in situ characterize its porous structure, and, in particular, the conditions of the polarization of an electrochemical interface inside the pores. The complex capacitance is directly calculated from the measured impedance, corrected for electrolyte serial resistance. In order to analyze the capacitance, we utilized a simplified geometric model of porous electrode materials assuming three generations of hierarchical (i.e. consecutive) branching pores. The model has been validated by fitting the impedance results for varied loadings of an electrode material, ensuring that only the parameters related to the electrode thickness are varied, while geometric parameters of the inner pores are nearly independent on the loadings. The model has been applied for three porous carbon materials, namely, Cabot Vulcan XC-72, AC Norit-732, and home-made activate carbon ACN-800. The complex capacitance dependence on frequency reflects the difference in porous structure of these materials, namely the average pore size and length, and branching factors, in a good agreement with the results of ex situ porosimetry by gas adsorption-desorption and SEM studies. In particular, this analysis allows to evaluate the accessible surface area of the electrode material, and explain the dependence of the polarization of the interface within the pores on the rate of potential modulation.

- **Introduction**

Porous electrode materials are widely utilized in various applications for electrochemical energy conversion, such as electrolyzers and fuel cells, and energy storage, such as batteries and supercapacitors. The geometry of pores, namely the distribution of their size and length, their interconnection, and their shape are key structural factors determining the conditions of mass transport and electrolyte accessibility within the material, as well as potential modulation conditions, and thus influencing the efficiency of the material as a catalytic support or as an energy storage media.

Generally, the porosity of electrode materials is characterized by *ex situ* methods, most commonly by gas (N_2, CO_2) adsorption-desorption and BET analysis of their isotherms. The accuracy of this characterization is limited by the assumptions of BET adsorption model. Nevertheless, the combination of BET analysis of adsorption data for various gas probes and DFT-based adsorption models allows to accurately determine specific surface area (SSA) and pore size distributions of carbon materials [328]. However, the surface area of a carbon electrode, accessible for an electrolyte, so-called electrochemical surface area (ECSA), can significantly differ from SSA due to the hydrophilic/hydrophobic character of carbon surface: the repulsive interaction between solvent and electrode surface may restrict an access of the electrolyte to narrow pores. The variation of the potential of carbon/electrolyte interface may results in a chemical modification of carbon surface, changing its hydrophilic/hydrophobic character and, hence, the accessibility of an electrolyte. Thus, the value of ESCA may be changing during the electrochemical measurements. An extreme example of such electrochemical modification of carbon surface composition is a covalent bonding of various aromatic radicals to a polished carbon surface achieved by a potentiodynamic electrolysis of diazonium salts. It has been demonstrated that such modifications result in a strong change of carbon interfacial properties, namely in the kinetics of oxygen electroreduction [329]. Thus, it is desirable to have an *in situ* electrochemical tool of a characterization of the porosity and ECSA of porous electrodes utilized as electrocatalysts or energy storage media.

The problem related to the understanding of electrochemical properties of porous electrode materials is that the response of the electrochemical interface inside of the porous material to the potential (or current) modulation varies depending on the position of the interface inside the pore. It creates non-uniform local conditions of interfacial potential within the single pore, and, consequently, inside the material. The response of the electrochemical interface to the potential modulation is characterized by local surface specific interfacial impedance Z_c (Ohm·m^2), which is, for example, in the absence of interfacial charge transfer is determined by surface specific interfacial capacitance C_s (F/m^2). The impedance spectroscopy is a versatile tool of the study of electrochemical electrode/electrolyte interface, intensively employed in the studies of the mechanism of interfacial processes (electrocatalytic reactions, corrosion) and in the characterization of electrode materials [330]. In the absence of redox reaction limited by bulk mass transport, the impedance of a porous electrode material, Z_{em}, consists predominantly a resistance of electrolyte (bulk R_Ω and within the pores) and interfacial capacitance. In a cornerstone set of works, DeLevi demonstrated [7,8] that the response to the potential modulation of an interface inside a single semi-infinite pore can be well described by a transmission line model. The solution of this model can be expressed by the equation of the impedance of a single pore as follows:

$$Z_p = \sqrt{R_s Z_s} \coth \sqrt{\frac{R_s}{Z_s}} = \sqrt{\frac{Z_c \rho}{2\pi^2 r^3}} \coth(l \sqrt{\frac{2\rho}{Z_c r}}) \qquad (1)$$

Here R_s and Z_s are the total resistance of an electrolyte and total interfacial impedance inside the pore (in Ohm), ρ is the resistivity of an electrolyte (in Ohm·m), r and l are the size (radius) and the length of the pore. Two main conclusions drawn from the equation (1) are following. First, the amplitude of the interfacial potential modulation response decreases with an increase of the distance from the pore opening as 1/coth function. One can define the characteristic distance of a propagation of potential modulation signal, or "modulation penetration depth" λ from the argument under the *coth* function in equation (1), as follows (in the absence of interfacial charge transfer):

$$\lambda = \frac{1}{2} \sqrt{\frac{Z_c r}{2\rho}} = \frac{1}{2} \sqrt{\frac{r}{4\pi \rho f C_s}} \qquad (2)$$

Here f is the frequency of potential modulation. The value of λ depends on the potential modulation rate, as expressed by modulation frequency f. For very fast modulation, $\lambda \approx 0$, and only an interface at the opening of the pore is polarized. While for sufficiently slow modulation, λ»l, and the potential of the interface inside the pore is distributed uniformly. Second, the phase angle of Z_p is a half of that of Z_c. For example above, if Z_c is determined only by C_s, its phase angle is 90°, and phase angle of Z_p is 45°.

The applicability of a simple solution of DeLevi for more realistic cases of pores with finite length and in the presence of electrolyte resistance outside of the porous layer, R_Ω (assumed to be 0 in the work of De Levi) has been debated. In a recent detailed analysis, combining both analytical solution with proper boundary conditions, and numerical simulation, Pedersen *et al.* [331] demonstrated that simply adding R_Ω to Z_p (as a serial connection) yields correct results for the pores with aspect ratio l/r»5, while for shorter pores the deviation is predicted, for example, manifesting as phase angle above 45°.

During the decades after the work of DeLevi, TLM models of Z_{em} has been intensively utilized to characterize the electrochemical properties of porous electrodes. It has been shown [332] that the analysis of frequency dependence of complex capacitance of the electrode, C_z, calculated from Z_{em} is very useful tool of characterizing the porous structure of the electrode. For example to evaluate the dependence of the impedance of an electrode on the shape of pores [9], or on the width of pore size distribution [10]. It has been shown [332], that the analysis of frequency dependence of complex capacitance of the electrode, C_z, calculated from electrochemical impedance is very useful tool of characterizing the porous structure of the electrode. The complex capacitance C_z of electrode material can be calculated from measured electrode impedance Z, corrected by R_Ω value, by the following equations:

$$C_z = \mathrm{Im}(C_z) + j\mathrm{Re}(C_z)$$
$$\mathrm{Re}(C_z) = \frac{\mathrm{Im}(Z)}{j\omega|(Z-R_\Omega)|^2}; \mathrm{Im}(C_z) = -\frac{\mathrm{Re}(Z)-R_\Omega}{j\omega|(Z-R_\Omega)|^2}; \tag{3}$$

The real component of C_z, $\mathrm{Re}(C_z)$ is measurable interfacial capacitance of porous electrode material, proportional to ESCA, and can be used for estimation of ESCA:

$$\mathrm{ECSA} = \frac{\mathrm{Re}(C_z)}{C_S \cdot \mathrm{SSA}} \tag{4}$$

The advantage of C_z determination from impedance spectroscopy is that it returns the value of ECSA of an interface polarized under the different potential modulation rates, characterized by modulation frequency f. Under the conditions of $\lambda \gg l$, the value of ECSA corresponds to the total surface area of an electrochemical interface.

The value of $\mathrm{Im}(C_z)$ is a characteristic of a capacitance losses due to the resistive component of the impedance of porous electrode material. It is expected to be 0 for very fast potential modulation (high f limit), when the interface inside the pores cannot be polarized, and the $|C_z|$ is 0; it is also decreasing to 0 for slow potential modulation rates (low f limit), when the resistance of electrolyte in pores is negligible comparing to capacitive impedance, and the total of the interface inside the pores is uniformly polarized. The position of a maximum of $\mathrm{Im}(C_z)$ dependence of f indicates the characteristic time response of the interface to potential modulation, and its width is correlated to the dispersion in “penetrability” parameter α_0, defined in as follow:

$$\alpha_0 = \frac{1}{2}\sqrt{\frac{r}{\rho C_S l^2}} \tag{5}$$

Thus, the width of the peak of $\mathrm{Im}(C_z)$ is correlated with the dispersion of $\sqrt{r}/l$ geometric parameter of pores. Reasonable correlation has been found between the average pores size and its dispersion determined from N_2 adsorption-desorption and complex capacitance dependence on modulation frequency for electrode materials with different porosities [332,333], introducing the concept of an « electrochemical porosimetry ».

More complex geometric models of hierarchical pore structure incorporating TLM description of a single pore impedance have also been developed [334,335], allowing qualitative description of a complex impedance response. Huang *et al.* [336] utilized DeLevi solution to model an impedance of the deposits of porous carbon with varied thicknesses. In their study, the interfacial impedance of the porous layer was approximated by the impedance of inner pores of the carbon particles, neglecting the outer surface of the particles. They have demonstrated that the 6-fold increase in the layer thickness results in the 38-fold increase in the characteristic times response of the interface to potential modulation. Itagaki *et al.* [335] utilized the fractal model of branching pores and demonstrated that branching, or formation of interconnected pores network, results in further decrease in apparent phase angle below 45°, expected for the arrays of isolated pore.

One of the difficulties in the development of the models of hierarchical pores is the large amount of model geometric parameters utilized, such as size and length of each generation of pores, and branching factors. Eikerling *et al.* [334] isolated a limited number of a combination various structural factors, such as the ratio of sizes of pores in different generations and branching factors, in order to propose a simplified but consistent model of multi-level hierarchical porous carbon. The authors demonstrated that the geometric parameters of macropores of porous carbon, mostly formed by inter-agglomerated spaces can be relatively well separated from the parameters of meso- and micro-inner pores of agglomerates. This is due to the predominant contribution of the latters into the interfacial surface area of carbon materials with moderate or high SSA, and significant difference in characteristic time of modulation response of macro- and inner pores. The model developed in ref. [337] allowed to suggest the routes to the design of a porous carbon structure for electrode materials with high charge capacitance.

It is obvious that it is not possible to suggest the geometrical model precisely describing the real structure of porous electrode materials: such model would have too many interconnected parameters, which results in strong incertitude of their determination. In this work we propose two-fold strategy in order to develop simplified but consistent geometric model or porous electrode materials, applicable to model electrochemical properties of porous materials with wide variety of porosity. First, the geometric model should be consistent with the variety of structural parameters determined by *ex situ* methods, namely with BET-determined SSA, volume of pores, micropores, and surface relative contribution of pores and micropores. Second, the model should be consistent with electrochemical data obtained for varied thickness of porous electrodes, using the same parameters for the geometry of inner pores, and adjusted parameters of macro-pores. In order to test the model, we choose three porous carbon materials with different porosities: predominantly mesoporous XC-72

Vulcan, meso- and microporous AC Norit, and predominantly ultramicroporous home-made ACN-800. The geometric parameters of these carbon materials are given in Table 5.

Table 5: *Geometrical information on the used carbons*

	SSA, m^2/g	V_p, cm^3/g	V_{mp}, cm^3/g	A_{mp}, m^2/g
XC-72	226	0.312	0.036	75
AC Norit	732	0.675	0.175	362
ACN-800°C	1176	0.594	0.520	970

- **Materials and methods**
    - Materials

Commercial carbon materials, namely Vulcan XC-72 © Cabot and AC Norit have been used as received. The home-made N-doped activated carbon ACN-800 has been prepared according to the synthesis route described previously [6].

For the preparation of the electrode, a carbon powder has been dispersed in water to make an ink containing 2 g/L of carbon. Next, a 15 µL of the ink was drop-casted on 0.2 cm^2 surface of polished glassy carbon substrate, and dried at 70°C for 10 min in air. This step has been repeated few times in order to achieve necessary loading of carbon materials, which was varied from 0.15 to 0.75 mg/cm^2.

The 1M H_2SO_4 electrolyte was prepared by using ACS grade 99.8% H_2SO_4 and ultrapure water (UltraAnalytique Veolia, TOC<1 ppb, 18.2 MOhm·cm).

- Electrochemical measurements

The measurements were performed in a 3-electrode cell with mercury/mercury sulfate (MSE) reference electrode and Pt gauze counter electrode. The experiments were done in N_2-purged electrolyte under the constant flow of N_2 above the solution. The cell was connected to SP-300 Bio-Logic potentiostat equipped by impedance module. The impedance measurements were done in the frequency range from 0.1 Hz to 10 kHz with 5 mV RMS amplitude.

- **Materials characterization**

Besides electrochemical measurements and scanning electron microcopy imaging, the main characterization tool used for the three carbonaceous samples relies on nitrogen N2 gas adsorption-desorption technique. The characterization was done using an ASAP 2420 analyzer from Micromeritics. First, approximately 100 mg of each sample were placed in adapted tubes and were degased at 150°C for 12 hours. After that, the samples were analyzed for nitrogen N_2 physisorption. The obtained isotherms are presented in the Supplementary Information 1 and principal materials characteristics such as the specific surface area (SSA), total volume of their pores V_p, their micropores V_{mp} and the surface area provided my these micropores A_{mp} are present in Table 5. The isotherms are of type-IV according to the IUPAC classification. BET analysis allowed to obtained the surface area related values, BJH analysis for the characteristics related to the pore size distribution and Non-local DFT (NLDFT) porosity distribution using a N_2 at 77K on carbon slit pores operated by the MicroActive analysis software to obtain more accurate volume and area values of pores.

- **Model description**
  - Geometric model

The model structure of a porous layer is depicted in Fig. 61. We assume that the layer is composed of micrometric particles forming vertically aligned agglomerates. The expected size of these agglomerates is few tens up to few hundreds of nm, and thus these agglomerates forms the first level of pores, which are referred to as « macropores » with average size r_1 and length l_1. Inside these particles the pores of the second level are formed, with expected size from few nm to few tens of nm, and thus referred to as « mesopores », with average size r_2 and length l_2. Each of macropores is branched into in average r_{21} mesopores, which are randomly and uniformly distributed over the inner surface of the macropore. In its own turn, each mesopore is branched into r_{32} of pores of 3rd level (Fig.61B), referred to as « micropores », with average size r_3 and length l_3. The parameters r_{21} and r_{32} are called « branching factors ».

In order to minimize the number of unknown parameters, we assume that l_1 can be approximated by the thickness of the deposit, which is calculated from the eq.6.

$$l_1 = \frac{m_d}{\rho_c A_g} \tag{6}$$

where m_d is the mass of the deposit (g), ρ_c is the volumetric density of porous material (g/m^3), and A_g is the geometric surface area of substrate ($2 \cdot 10^{-3}$ m^2). The parameters r_1, r_2, r_3, l_2 and l_3, as well as branching factor r_{32} are fitting parameters. From these parameters, the values of A_1, A_2, A_3, and V_1, V_2, and V_3, *i.e.* the surface of walls and the volume of a single pore of 1st, 2nd, and 3rd level respectively, are calculated. This allows to calculate the total number of macropores N_1, and branching factor r_{21} by the following equations.

$$r_{21} = \frac{(m_d \cdot SSA - A_g) \cdot V_1 - 2\pi r_1 l_1 m_d \sigma_c}{m_d \sigma_c (A_2 + r_{32} A_3 - \pi r_2^2) - (V_2 + r_{32} V_3) \cdot (m_d \cdot SSA - A_g)} \quad (7)$$

$$N_1 = \frac{m_d \cdot SSA}{A_1 + r_{21} A_2 + r_{21} r_{32} A_3} \quad (8)$$

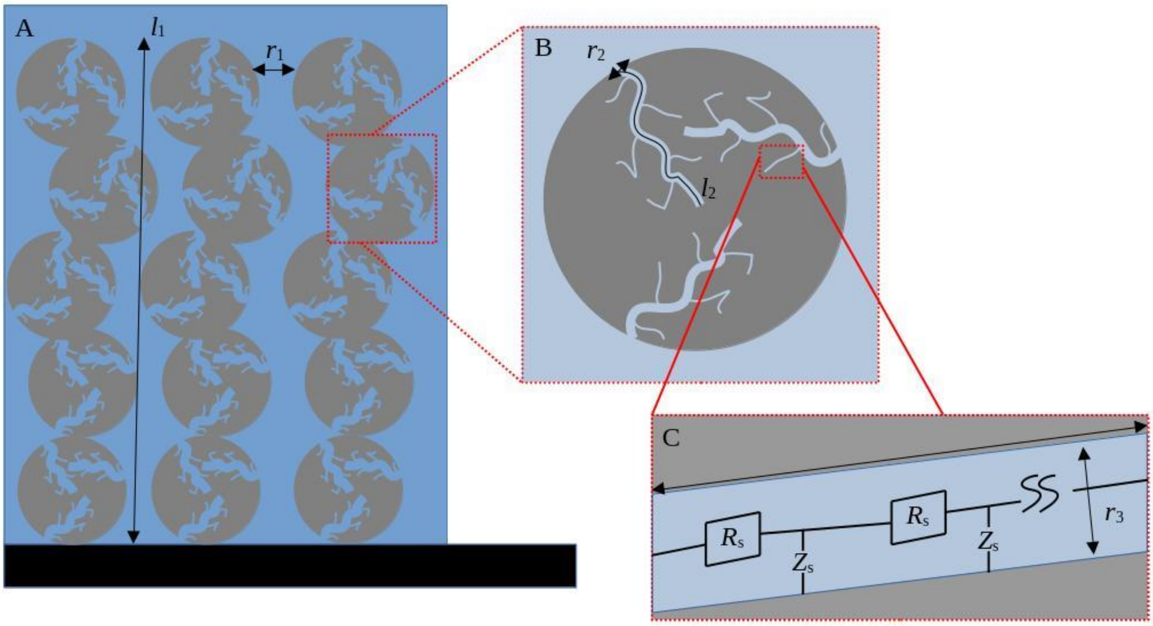

Figure 61: The diagram representing the model structure of a porous layer, consisting of vertically oriented agglomerates of particles, separated by macropores (A); the particles contains mesopores branching to micropores (B); the impedance of a single pore is modelled by a transmission line (C).

In the equations above, is volume expansion factor, showing how much bigger is the volume of porous carbon with density ρ_C comparing to compact carbon (no porosity) with density ρ_G. For the calculations below the density of graphite was used for ρ_G, namely $\rho_G = 2.1 \cdot 10^6$ g·m^{-3}.

Using equations (6)-(8), the volume of inner pores V_p and micropores V_{mp} are calculated as follows:

$$V_p = \frac{N_1 (r_{21} V_2 + r_{21} r_{32} V_3)}{m_d} \quad (9)$$

$$V_{mp} = \frac{N_1 r_{21} r_{32} V_3}{m_d} \quad (10)$$

- Transmission line model of the impedance of porous deposit

The model of an impedance of carbon porous material is represented by the set of equivalent circuits, depicted in Fig.62.

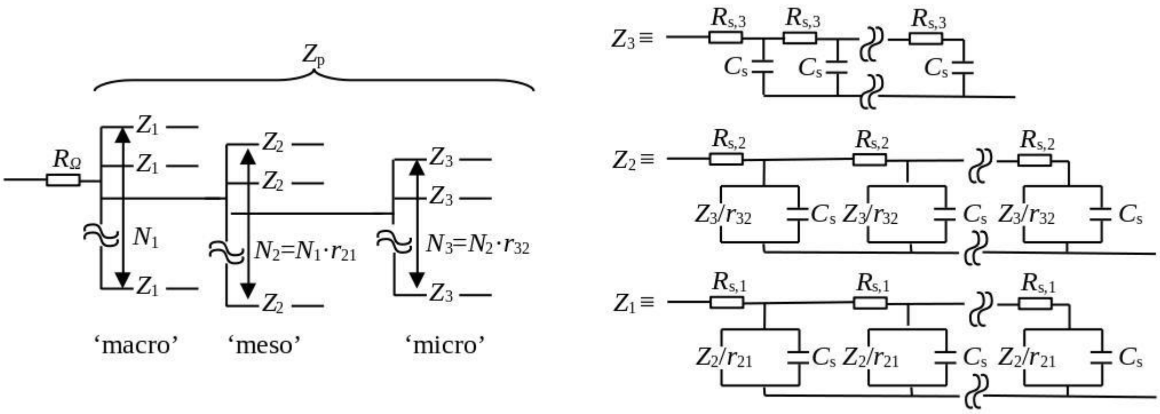

Figure 62: Diagrams representing the equivalent circuits utilized in the model of an impedance of porous carbon materials

The impedances Z_1, Z_2, and Z_3 correspond to the impedance of a single pore of *i*-th level, Z_i, and are calculated by De Levie equation, similar to eq.1.

$$Z_i = \sqrt{R_{s,i} Z_{s,i}} \coth\sqrt{\frac{R_{s,i}}{Z_{s,i}}} \tag{11}$$

Here $R_{s,i}$, and $Z_{s,i}$ are length-specific resistance and the interfacial impedance (in Ohm) of a segment of *i*-th level pore.

$R_{s,i}$ is calculated as follows:

$$R_{s,i} = \frac{\rho_e l_i}{\pi r_i^2} \tag{12}$$

Here ρ_e is the resistivity of an electrolyte (in Ohm·m).

For a single micropore (3rd level pore), $Z_{s,3}$ is calculated as an impedance of a constant phase element (CPE) by the following equations:

$$Z_{s,3} = \frac{Z_C}{2\pi r_3 l_3} \tag{13}$$

$$Z_C = \frac{1}{C_s (j\omega)^\alpha} \tag{14}$$

where C_s is surface-specific capacitance of electrode/electrolyte interface (in F·m^{-2}). Eq. 10 shows that the micropores are not branching, and its interfacial impedance depends only on interfacial capacitance C_s.

In contrast to a pore of 3rd level, the pores of 1st and 2nd level are branching, and the impedance of branches is contributing to the impedance of "parent" pore. Thus, the impedance $Z_{s,2}$, and $Z_{s,1}$ are calculated with two contributions:

$$\frac{1}{Z_{s,2}} = \frac{2\pi r_2 l_2(1-e_{32})}{Z_c} + \frac{r_{32}}{Z_3} \tag{15}$$

$$\frac{1}{Z_{s,1}} = \frac{2\pi r_1 l_1(1-e_{21})}{Z_c} + \frac{r_{21}}{Z_2} \tag{16}$$

$$e_{32} = \frac{r_{32} r_3^2}{2 r_2 l_2}, e_{21} = \frac{r_{21} r_2^2}{2 r_1 l_1} \tag{17}$$

here e_{21} and e_{32} are the ratio of the surface of pores of 1st and 2nd level occupied by the openings of the pores of next level (2nd and 3rd) correspondingly.

The impedance of the deposit of porous electrode material, Z is calculated by the following equation.

$$Z = Z_t - R_\Omega = \frac{1}{\frac{A_g(1-e_{01})}{Z_c} + \frac{N_1}{Z_1}} \tag{18}$$

$$e_{01} = \frac{N_1 \pi r_1^2}{A_g} \tag{19}$$

Here Z_t is the measured impedance, consisting of the impedance of working electrode, Z, and bulk electrolyte resistance R_Ω.

- Fitting workflow

As mentioned in 3.1., the model has the following fitting parameters : r_1, r_2, r_3, l_2, l_3, and r_{32}. The values of SSA measured from BET were taken for initial guess of ECSA value, C_s=5 µF·cm^{-2} = 5·10^{-2} F·m^{-2} for specific surface capacitance, and α=0.99 for CPE constant.

The fitting quality was evaluated by analyzing three types of Bode plots, and Nyquist plot. Namely, Bode plots of log $|Z|$, phase angle φ, Re(C_z), and Im(C_z) vs. log f were plotted using experimental and modeled data. The components of surface-specific complex capacitance C_z were calculated using Z_t values as follows:

$$\mathrm{Re}(C_z) = \frac{-\mathrm{Im}(Z)}{j\omega \mathrm{ESCA}|Z|^2}; \mathrm{Im}(C_s) = \frac{\mathrm{Re}(Z)}{j\omega \mathrm{ESCA}|Z|^2} \quad (20)$$

The fitting parameters were adjusted in order to reach the best agreement with experimental structural parameters determined from *ex situ* methods, and with the all three types of Bode plots. It must be highlighted that the full agreement with all aforementioned experimental data could not have been achieved due to certain simplification of pores geometry allowed in the model, for example the same size all pores of one generation.

- **Results and discussion**

The geometric parameters of carbon deposits are summarized in Table 6. All these parameters, except branching factor r_{21}, are adjusted during the fitting. The factor r_{21} is calculated by eq. 7. We detected a strong incertitude in parameter r_1: the fitting quality is barely sensitive to a strong changes in this parameter. It may be related to the weak influence of the geometry of macropores on the impedance of porous layer due to a moderate contribution into the overall surface area of an interface. This, we choose to fix the parameter r_1 manually at the same value of 100 nm for all studied materials.

Table 6: *Fitted geometric parameters*

	r_1, nm	r_2, nm	r_3, nm	l_1, µm	l_2, nm	l_3, nm	r_{21}	r_{32}
XC-72, 0.15 mg/cm^2	100	39	1.0	7.5	30	10	114	550
XC-72, 0.45 mg/cm^2	100	43	1.05	22.5	30	10	288	550
XC-72, 0.75 mg/cm^2	100	34	0.87	37.5	30	10	781	550
AC-Norit, 0.75 mg/cm^2	100	81	0.85	15	30	40	424	2600
ACN-800, 0.75 mg/cm^2	100	8	0.90	15	1000	4500	1.4	15000

ACN-800, 0.75 mg/cm^2, after 1000 cycles	100	8	0.90	15	1000	3800	1.5	15000

From the fitted geometric parameters of carbon materials, the integral characteristics, such as A_p, V_p, and V_{mp} were calculated for direct comparison with the results of gas adsorption-desorption analysis. If the strong discrepancy was observed, the fitting procedure was started again with adjusted sets of initial guess parameters, until the agreement with *ex situ* results was achieved. The characteristics of carbon materials.

Table 7: *Properties of carbon deposits obtained from fitting*

	ECSA, m^2/g	C_s, μF/cm^2	e_{01}	e_{12}	e_{32}	γ_s	γ_V	V_p, cm^3/g	V_{mp}, cm^3/g	A_p, m^2/g
XC-72, 0.15 mg/cm^2	170	5.0	0.842	0.11	0.235	2.01	1.08	0.327	0.035	74
XC-72, 0.45 mg/cm^2	160	5.0	0.839	0.18	0.235	3.71	1.23	0.331	0.033	65
XC-72, 0.75 mg/cm^2	185	5.0	0.837	0.12	0.204	2.21	1.08	0.338	0.036	87
AC-Norit, 0.75 mg/cm^2	460	5.0	0.431	0.93	0.387	26.6	1.77	0.663	0.183	435
ACN-800, 0.75 mg/cm^2	1176	13.0	0.502	$3.03\cdot10^{-5}$	0.759	57.2	1.51	0.521	0.520	1156
ACN-800, 0.75 mg/cm^2, after 1000 cycles	1176	14.5	0.531	$3.22\cdot10^{-5}$	0.60	46.6	1.37	0.464	0.462	1154

The CV curves of XC-72 deposits with different loadings are shown in Fig.63. The shape of the CV curves is typical for capacitive electrochemical response with very slight dependence of interfacial capacitance on the applied potential. A pair of weak and broad CV peaks around -0.1 V MSE is related to redox transition of oxygen containing surface groups, conventionally assigned to quinone/hydroquinone transition. In the studied range of loadings 0.15-0.75 mg/cm^2, the mass-specific CV currents show no dependence on loading: slight deviation of curves in is related to the incertitude in the exact mass of deposited material.

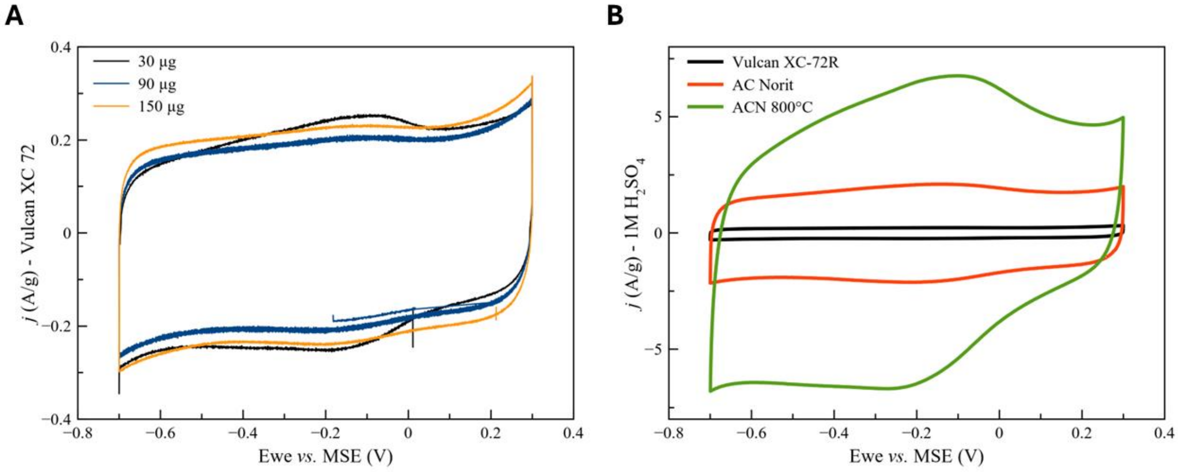

Figure 63: CV curves of XC-72 carbon electrodes with 3 loadings 0.15, 0.45, and 0.75 mg/cm^2 (A) and three different carbons with loading 0.75 mg/cm^2, recorded in 1M H_2SO_4 at 20 mVs/s

- Various loadings of Vulcan XC-72

Fig.63 shows the impedance results obtained with various loading of Vulcan XC-72 carbon, as the dots, and the results of the fitting of experimental data as lines.

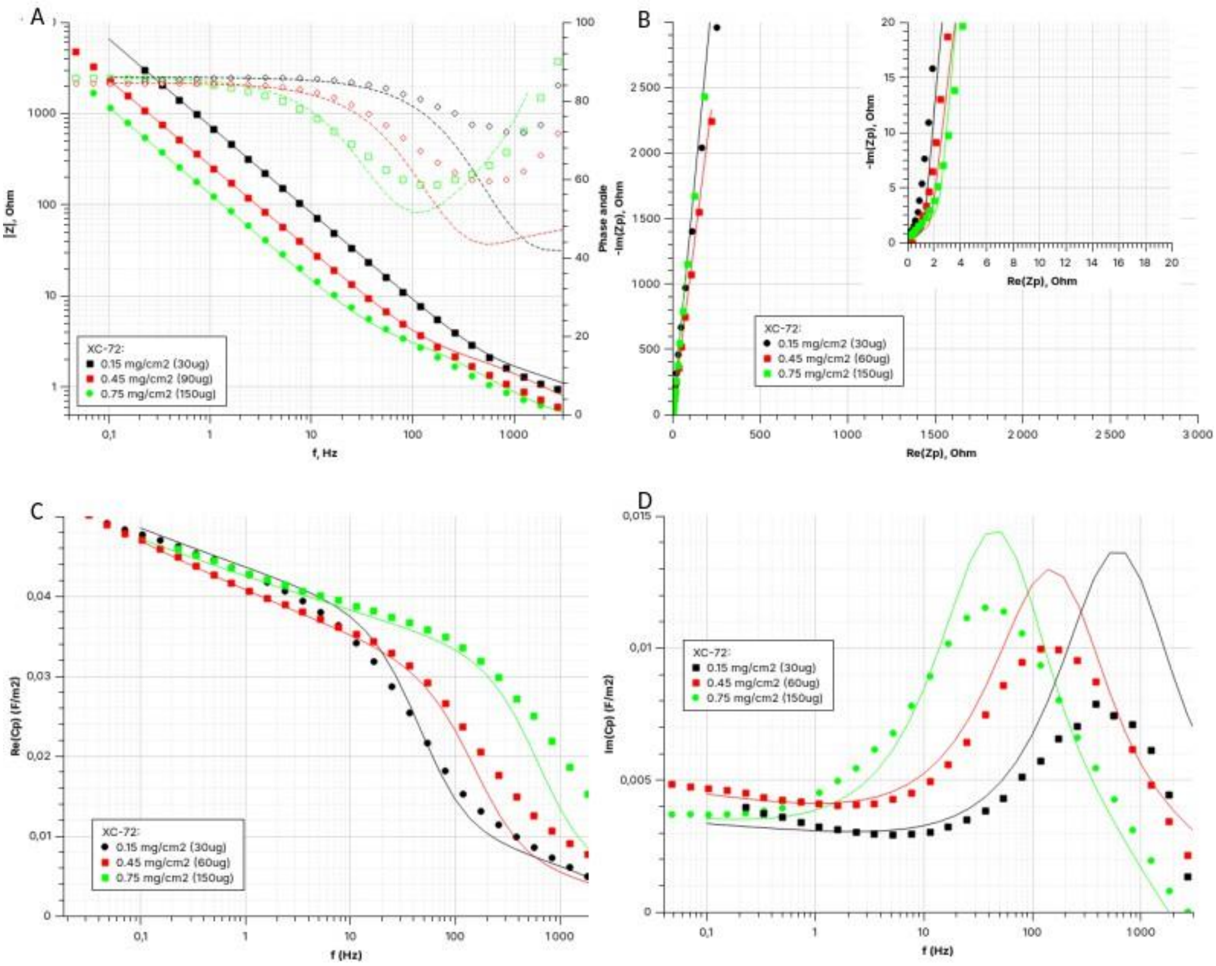

Figure 64: EIS data, modelled (lines) and experimental (dots) for XC-72 carbon electrode with various loadings in 1M H_2SO_4

The behavior of Bode and Nyquist plots for XC-72 deposits (Fig.64A and 64B respectively) is close to one expected for a porous electrode in the absence of any interfacial faradaic reaction. Namely, for $f \to \infty$, $Z_t \to R_\Omega$, and $Z \to 0$; thus, $\phi \to 0$, and $\mathrm{Re}(C_z) \to 0$, $\mathrm{Im}(C_z) \to 0$, *i.e.* for very high modulation frequency (very fast polarization), the impedance is totally determined by bulk electrolyte resistance, while $\lambda \to 0$, and electrode/electrolyte interface inside the pores cannot be polarized. On the other hand, as $f \to 0$, and $\lambda \gg L_p$, and the impedance of electrode material Z is predominantly determined by $C_s \cdot$ESCA; thus $\phi \to 90°$, $\mathrm{Re}(C_z) \to C_s$, and $\mathrm{Im}(C_z) \to 0$ (ref.[332]). The Bode plots of $\mathrm{Im}(C_z)$ show a maximum at a certain frequency f_{max}, which, according to ref. [332] correspond to a reciprocal characteristic time of a response of porous electrode material.

Good consistency between model and experimental data for various loadings of porous carbon has been achieved predominantly by the adjustment of the length of macropores, thus validating the approach proposed in the model (Table 6). The branching factor r_{21} is also increasing with an increase of carbon loading, according to eq. 7, while all other parameters of the geometry of carbon deposit remains similar for loadings varied in the range from 0.15 to 0.75 mg/cm^2.

Both experimental and model data demonstrate a deviation from ideal capacitor behavior at low frequencies. The value of phase angle in this frequency range for XC-72 is 86-87°, indicating non-ideal capacitive behavior, which is taking into account by using CPE power constant $\alpha=0.955$ (see eq. 14). The deviation from ideal capacitive behavior in the case of flat electrochemical interface is related to the inhomogeniety of the properties of interface [338,339]. In the case of porous electrodes, the distribution of size of macropores is another factor resulting in non-ideal capacitive behavior at low frequencies [340].

As expected, the measured surface specific capacitance, Re(C_z) is increasing with frequency decrease (Fig.63C) due to an increase in potential modulation depth λ, according to eq. 2. At the same time, the Im(C_z) contribution passes through maximum at f_{max}, the position of which shifts to lower frequencies as the thickness of porous layer increases (Fig.64D). This is an indication that the average response time of porous electrode to potential modulation increases with the thickness of electrode increase: it is remarkable that 5-fold increase in the thickness of the layer (from 0.15 to 0.75 mg/cm^2 loading) results in nearly 15-fold increase in the response time (from 1.63 ms to 22.5 ms). Qualitatively these results are in good agreement with the modeling results reported in ref. [336].

For $f \ll f_{max}$, the condition $\lambda \gg L_p$ is expected (i.e. modulation penetration depth is much longer than the maximal pore length), and the complex capacitance C_z of all loadings of carbon is approximately the same. We note that in this frequency range, the value of Im(C_z) is not dropping down to zero, in contrast to prediction of a simpler models of Jang and Oh [332]. We tentatively explain this discrepancy by the fact that our model suggests branching of mesopores into micropores, thus assuming the continuous variation of total length of micropores.

The presented geometrical model of the deposit of porous material is oversimplification of its real complex structure. In particular, the distribution in size and length of pores of different levels is neglected in order to decrease the number of fitting parameters. However, the fact that the deposits with various loadings can be well fitted by the model with similar geometric parameters validates the consistency of proposed geometric model. Due to oversimplification, the geometric parameters of the pores should not be taken as exact characteristics. Nevertheless, the model allows to estimate the integral characteristics of the layer, such as ECSA.

Since the capacitance electrode/electrolyte interface is proportional to its surface area, the capacitance measurements can be used as a method of ESCA evaluation. According to Trasatti and Petrii, the main limitation of this method is related to an incertitude in the value of surface-specific interfacial capacitance C_s, which for carbon electrodes depends on both their surface composition and their porous structure [341]. By analyzing the literature reported data, Ji *et al.* [342] observed that the surface specific capacitance of carbon electrodes decreases as BET-determined SSA increases above ca. 1000 m^2/g. The authors argued that this correlation is related to the overestimation of SSA by standard BET analysis, while for stacked graphite electrode, the $C_s \approx 5$ µF/cm^2 is expected. It has been confirmed by analysis of even larger set of literature data by Lobato *et al.* [328] that most of the data reporting SSA from BET measurements above ca. 1600 m^2/g are overestimated, while when SSA values are corrected by using other methods, the linear dependence of mass-specific surface capacitance and SSA is observed in both aqueous and organic electrolytes. The value of C_s for pristine (i.e. no O,N-heteroatoms) carbon surface is still disputed: [342,343] Jäckel *et al*. demonstrated [344] that an increase in C_s up to 25 µF/cm^2 for ultramicroporous carbons with average pores size below 1 nm can be observed, related to partial distortion of solvation shell of electrolyte ions. Nevertheless, the values of C_s in the range of 5-10 µF/cm^2 is generally expected for porous non-doped carbons, including ultramicroporous carbon materials [343,345], providing that the SSA is correctly determined by using the set of complementary methods.

For all loadings of XC-72 the fitting requires the value of ECSA≈172±13 m^2/g, lower than SSA=236 m^2/g determined by N_2 adsorption. We note that the same fit can be also achieved by using ECSA value equal to SSA, but assuming lower C_s; however, the assumption of C_s lower than 5 µF/cm^2 for carbon surface is not reasonable. On the other hand, lower values of ECSA comparing to SSA can be explained by electrolyte inaccessibility of pores with certain size or surface composition.

The other important characteristic parameters estimated by the model is the ratio of pores surface occupied by the openings of next level pores (e_{01}, e_{12}, e_{23} for macro-, meso-, and micropores respectively), Table 7. In the case of XC-72, the obtained fitted values demonstrate low degree of pores ramification: only 14±4 % of the surface of macropores is occupied by the opening of mesopores, and 23±3 % of surface of mesopores is occupied by the openings of micropores.

In order to further characterize the effect of pores branching we propose to use surface- and volume-enhancement factors, γ_s and γ_V, which were calculated by the following equations.

$$\gamma_A = \frac{A_1 + r_{21}A_2 + r_{21}r_{32}A_3}{A_1 + A_2 + A_3}; \gamma_V = \frac{V_1 + r_{21}V_2 + r_{21}r_{32}V_3}{V_1 + V_2 + V_3} \qquad (21)$$

These parameters characterizes the factor by which surface area and inner volume of pores is increased due to the branching of the pores. For electrochemical applications, such as electrocatalysis and energy storage, the structures with high γ_A should be more favorable due to increased interfacial surface area. At the same time, low γ_V should be preferred, as high value of γ_V signifies increased volume of electrode material. As mentioned above, XC-72 is characterized by low degree of pores ramification, and by moderate values of the enhancement factors of both surface (γ_A=2.6±1.1) and volume (γ_V=1.1±0.1) of pores. XC-72 can be characterized as "mesoporous" carbon, as micropores contribute only ca. 10±1% to total pores volume and 45±2% to total pores surface (see Table 5).

Summing up, the fitting of the impedance data for XC-72 deposits with various loadings allowed to validate the geometric model of the layer and estimated the integral geometric characteristics of the material, such as ECSA, ratio of pores opening on the surface of pores, and surface and volume enhancement, related to pores branching. As the next step, the model is applied for the deposits of carbon materials with different porosity.

- Impedance of XC-72, AC-Norit, and ACN-800 carbon materials

For all three carbon materials studied the consistency of the model was verified by fitting of the impedance for various loadings in the range from 0.15 to 0.75 mg/cm², and ensuring that the fitting is possible with the similar set of geometric parameters, as it is discussed for the case of XC-72 in the previous section. Below only the results for 0.75 mg/cm² loading are compared.

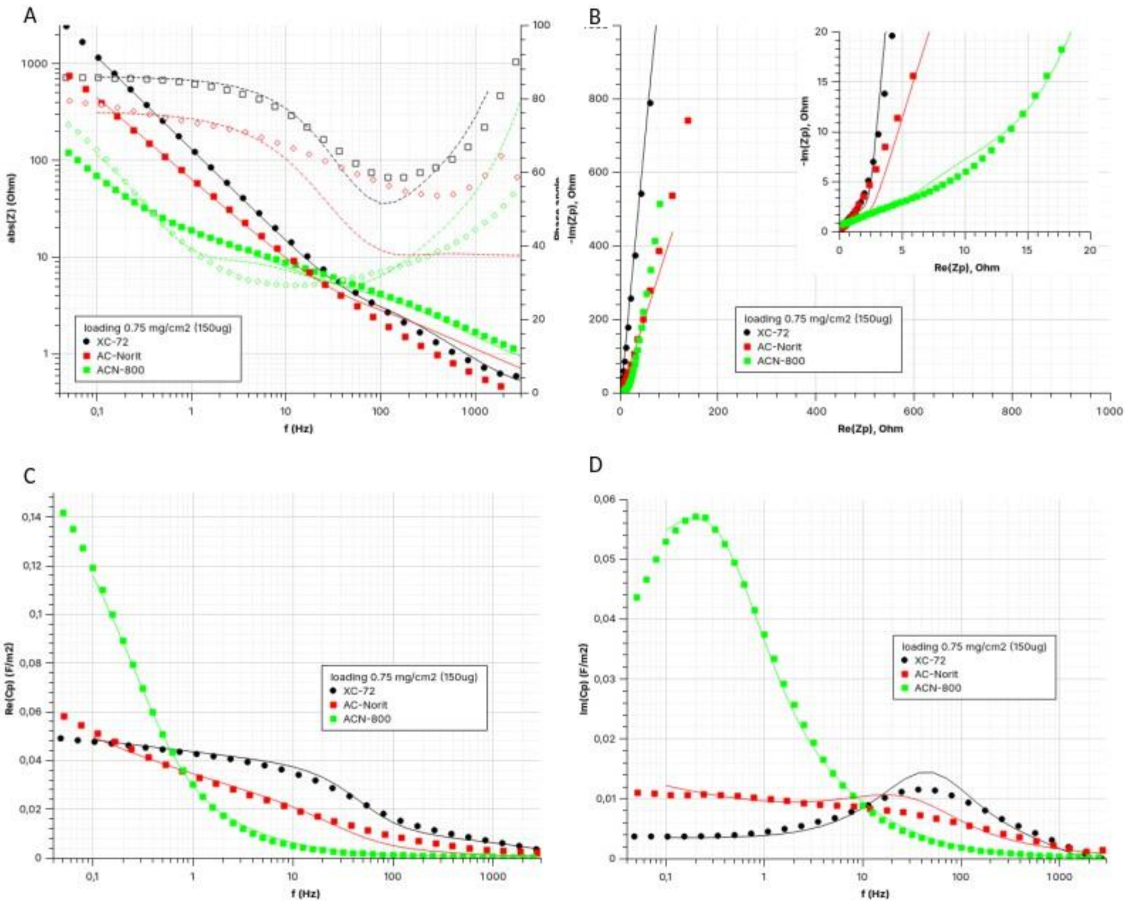

Figure 65: Impedance Bode and Nyquist plots for 0.75 μg/cm² deposits of various carbon materials

Fig. 65 demonstrated noticeable difference in the impedance spectra of various carbon materials, related to the differences in their porous structure. Nevertheless, the 3-level geometrical model of the porous material allows to well fit the gas adsorption-desorption and electrochemical characteristics of all materials in this study.

The behavior of the impedance spectra of AC-Norit and ACN-800 at low frequencies points to relatively low power constant of CPE, α=0.85. This value is significantly lower comparing to XC-72 (α=0.955), and cannot be explained only by surface microroughness or local inhomogeneities. In the case of porous electrodes, the distribution of size of macropores is another factor contributing in non-ideal capacitive behavior at low frequencies. Thus, low α values of AC-Norit and ACN-800 are related to stronger influence of inner pores on impedance and to the wider distribution in pores size.

As we have mentioned above, the effect of inhomogeneities in pore length is enhanced in the case of pore branching and forming interconnected pore network. Indeed, comparing to XC-72, for both AC-Norit and ACN-800 the stronger branching of mesopores to micropores is suggested by the model. Also, the micropores for AC-Norit and especially ACN-800 are significantly longer, forming an extensive network of interconnected micropores. In the case of AC-Norit, mesopores are larger than those of XC-72, while for ACN-800 the narrower mesopores are suggested by the model. In summary, the suggested structure of carbon particles for each of studied carbon materials are depicted in Fig.66.

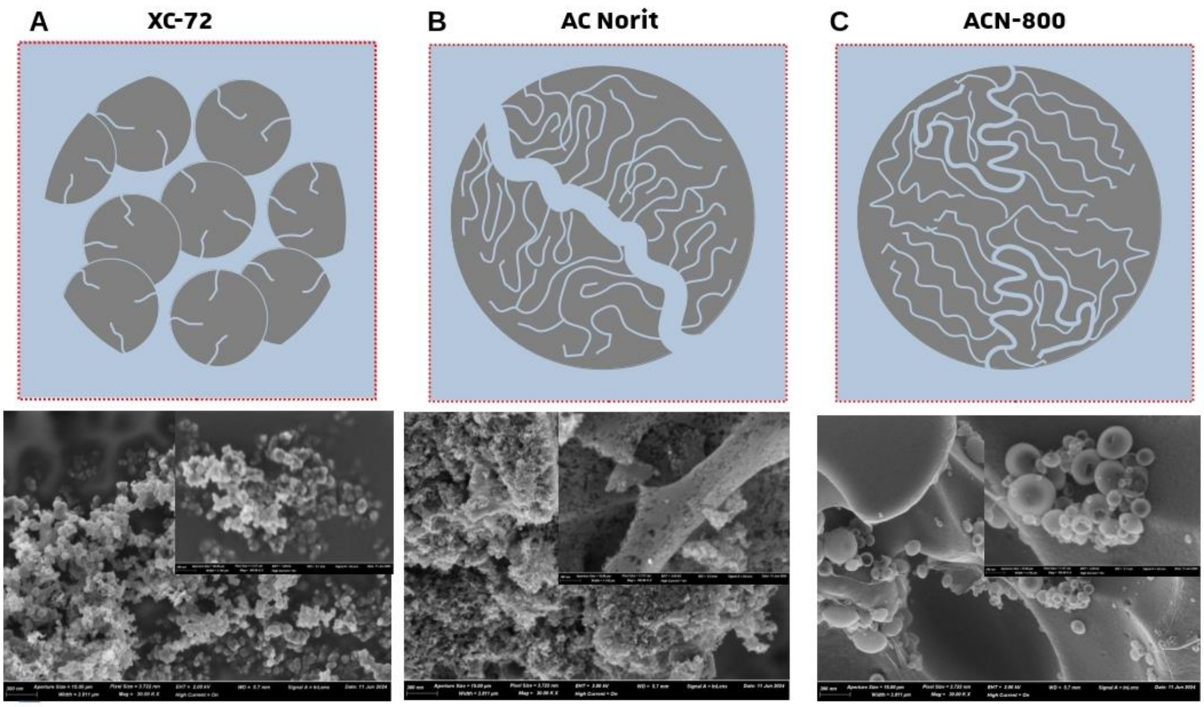

Figure 66: Schematic depiction of the geometry of carbon particles for various carbons, as suggested by the impedance model (above), and corresponding SEM images (below)

SEM images of XC-72 demonstrated relatively regular structure of carbon, consisting of small particles with 20-40 nm size, forming long blocks of several hundreds of nm size. The contribution of micropores into the total pore volume, as measured from CO_2 and N_2 adsorption, is ca. 10%, which is relatively small. Thus, most of mesopores are formed by the walls of the blocks of carbon particles.

In the case of AC-Norit the larger blocks of several hundreds of nm are observed, with less regularity in their sizes (Fig.65B). The larger blocks form mesopores of larger size, comparing to XC-72, as predicted by the impedance model. On the other hand, inside the particles constituting these blocks, a network of long interconnected micropores is formed. In AC-Norit the contribution of micropores to total volume of pores is 25.9% as measured by N_2/CO_2 adsorption-desorption, and 27.6% as given by the geometric model of impedance, and is more than two times higher comparing to XC-72. Moreover, the model suggest that ca. 94% of inner pore surface of AC-Norit is due to micropores, in contrast to ca. 45% of XC-72.

Figs. 65C and 65D shows the difference in the dependencies of complex capacitance C_z on frequency f for XC-72 and AC-Norit. Namely, in the case of AC-Norit, the Re(C_z) continues to increase with a decrease in frequency even at low frequencies $f \approx 0.1$ Hz. Also, the peak of Im(C_z) is very broad, and no clear indication of a decrease at low frequencies is detected. According to the authors of ref. [332], the width of the peak of Im(C_z) is correlated with the width of the dispersion of pores penetrability, which is the parameter related to the ratio of pores size and length. The strong branching of AC-Norit pores is reflected in the values of enhancement factors $\gamma_s=27$ and $\gamma_V=1.8$, significantly bigger comparing to XC-72.

This behavior can be interpreted as a result of stronger branching of mesopores into the smaller and longer micropores, which creates strong dispersion in the total length of these pores. One can note that, according to fitting results, more than 38% of mesopore walls of AC-Norit are occupied by the openings of micropores, comparing to 22% in the case of XC-72.

Both the structure of ACN-800, as seen by SEM images and the results of the fitting of impedance (Fig.65C) are very different comparing to XC-72 and AC-Norit. The most striking difference is significantly higher contribution of the volume of micropores to total volume pores: 87.5% according to N_2/CO_2 adsorption-desorption data, or 99.8% as predicted by the model. In the case of ACN-800, the model suggests existence of very few and narrow mesopores which are strongly branched into the numerous and long micropores. This structure can be interpreted as the ensemble of large blocks of carbon (larger than in the case of XC-72 and AC-Norit), forming very few mesopores between them, while inner structure of these blocks consists of a well-developed network of long interconnected micropores. This interpretation is consistent with SEM observation, bearing in mind that the micropores are too small to be detected by SEM.

It is noteworthy that assuming the value of $C_s=5$ µF/cm^2, which can be considered as a reasonable estimation for high surface area carbon materials [341,342], the ECSA predicted by model for XC-72 and AC-Norit is well below the value of SSA assessed from BET modeling of N_2 adsorption-desorption. On the other hand, in the case of ACN-800, the model assumes ECSA to be the same as SSA, and even in this case higher values of surface-specific capacitance C_s=13-15 µF/cm^2 have to be assumed. In the model, the influence of ECSA and C_s cannot be separated, i.e. an increase in ECSA can be set off by a decrease in C_s, and, thus, it is impossible to obtain exact values of these parameters from impedance modeling. However, the value of $C_s=5$ µF/cm^2 is a reasonable minimal value of C_s, and thus the results of impedance modeling are clearly showing that the ECSA is lower than SSA for XC-72 and AC-Norit, which is an indication of limited accessibility of pores of these carbon materials for an electrolyte. On the other hand, the reasonable upper limit for ESCA is SSA measured by gas adsorption, indicating high accessibility of pores in the case of ACN-800 and higher C_s values comparing to other carbons. These conclusions are in agreement with the results of the study of electrochemical properties of ACN-800 (ref.[6]), for which high mass- and surface-specific capacitances (C_g=320 F/g, C_s=27 μF/cm^2 in 1M H_2SO_4 at 2 A/g charging rate) have been reported, and explained by the positive influence of in-plane graphitization and N-doping of this activated carbon.

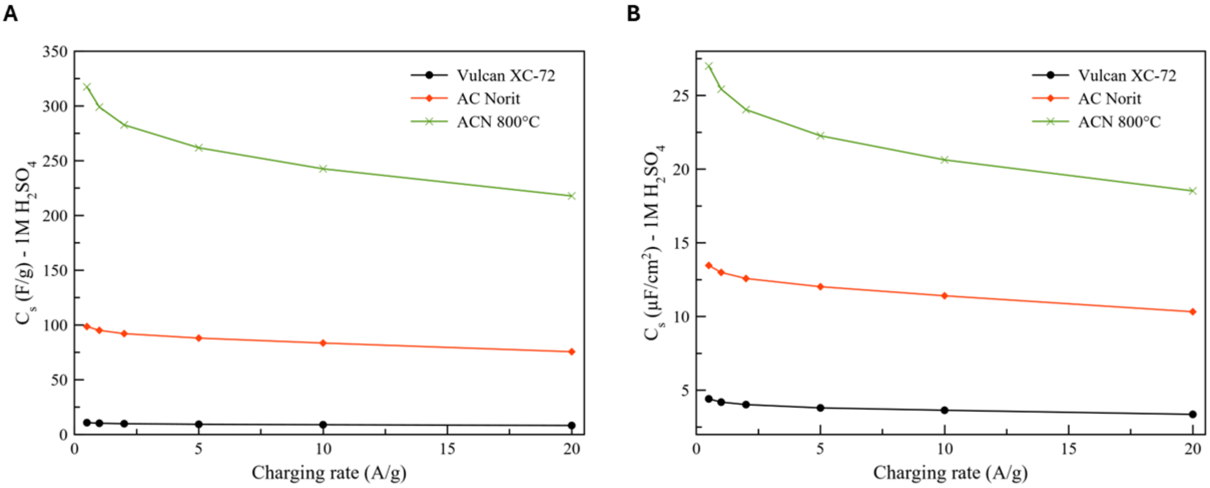

Figure 67: GCPL curves of the three different carbons at different charging rates with the capacitance normalized to the mass (A) and to the measured SSA (B)

The difference in structures of ACN-800 and other carbons is reflected in the dependence of complex capacitance on modulation frequency (Fig.65C and 65D). Re(C_z) strongly decreases with an increase in f, while Im(C_z) has a distinct peak at much lower frequencies comparing to XC-72, indicating much slower characteristic response time to potential modulation in the case of ACN-800 comparing to XC-72 (ca. 5 s and ca. 22 ms respectively). It is in agreement with stronger decrease of integral charge capacitance of ACN-800 comparing to AC-Norit and XC-72, as measured by galvanostatic charging with the rate increasing from 1 A/g to 20 A/g (Fig. 67A,B). Slower response to potential modulation in the case of ACN-800 is attributed to predominant contribution of long micropores to the interfacial surface area.

- **Conclusions**

The impedance measurements, in particular, the analysis of a dependence of complex capacitance on modulation frequency, provided the *in situ* characterization of the structure of porous carbon electrode materials. For this, the simplified geometric model assuming three levels of hierarchical pores have been applied to fit impedance data for varied loadings of a material. The impedance of each individual pore was approximated by transmission line model, taking into account the interfacial impedance of the pore and a contribution from its branching to the pores of next generation. The DeLevi solution for the impedance of TLM of an individual pore has been utilized.

The model has been validated by the fact that the fit has been achieved for varied loadings with the same parameters of inner pores (« meso »-, and « micro »-pores), while only length of the macropores within the deposit was adjusted. The quality of the fit has been evaluated by comparison of the fitted results with both electrochemical impedance data and the results of the structural characterization by *ex situ* gas adsorption-desorption, namely with the ratio of volume of micropores to the total pore volume, and with the ratio of pores surface area to the total specific surface area of the material. Even though simplified geometric model does not allow to determine precisely the geometric parameters of the pores, it provides useful in situ characteristics of the accessibility and polarizability of the interface inside of the porous electrode layer, as it is summarized below for each of the studied material.

1. Carbon Vulcan XC-72: The estimated ESCA of XC-72 is 172 m^2/g, and below the SSA measured by N_2 adsorption (236 m^2/g). The inner pores contribute ca. 7 % to the total pore volume of the electrode deposit, but more than 60 % to the interfacial surface area, of which ca. 45 % is due to the micropores. The inner pores are relatively short (up to few tens of nm), and are readily polarized, e.g. for 75 $\mu g/cm^2$ loading the threshold frequency is estimated by the position of maximum of Im(C_z) as 45.2 Hz, or 22 ms characteristic time response. At slower potential modulation only minor change in Re(C_z) is observed, both in impedance and galvanostatic charging, confirming the uniform potential modulation of the interface within the pores. SEM images of XC-72 demonstrate that it consists of relatively small particles of few tens of nm coalesced into the larger agglomerates, forming network of mesopores branching into the inner meso- and micropores (non-detectable by SEM), in agreement with the geometry of pores suggested by impedance fitting.
2. AC-Norit: The estimated ESCA of AC-Norit is 460 m^2/g, which is significantly lower than its SSA value of 732 m^2/g. The inner pores contribute ca. 36 % to the total pore volume of the deposit, and ca. 99 % of the total surface area, of which ca. 94 % is due to the micropores. The micropores of AC-Norit are in average narrower and longer than those of XC-72, which may result in their more restricted accessibility for electrolyte species, and, thus, lower values of ESCA relative to SSA. Since most of the interface surface area is located within the micropores, their polarizability is determining the electrochemical properties of the AC-Norit material. The micropores pores are forming the interconnected network, making the determination of the threshold frequency complicated. However, the values of Re(C_z) are continuously increasing even at the low frequencies. Altogether, the behavior of both Re(C_z) and Im(C_z) indicates that non-uniform conditions of the potential modulation of the interface in the inner pores of AC-Norit even at the low frequencies. The SEM images of AC-Norit demonstrated that the particles

of carbon are coalesced into the bigger blocks with stronger dispersion in sizes, comparing to XC-72.

3. ACN-800: Most of the interface (more than 98 %) of ACN-800 is located within the narrow and long micropores, which are presumably well accessible for electrolyte species, providing ESCA similar to SSA. Narrow and long mesopores of ACN-800 are strongly branched into the long micropores, forming, similarly to AC-Norit, a network of interconnected pores. However, the potential modulation conditions of the interface within the pores is more uniform, as indicated by clear maximum in Im(C_z) at low threshold frequency at 0.2 Hz. It may be interpreted as an indication of a narrower dispersion in sizes of micropores of ACN-800 comparing to AC-Norit. SEM images show that ACN-800 is a carbon material consisted of large foils or sheets containing large macropores, while meso- or micropores are barely detectable. One must assume that most of the pores are the inner pores inside of these sheets with lengths of several hundreds of nm up to few µm, i.e. comparable with the size of the sheets. The accessibility of these pores is related to the functionalization of the surface of carbon by chemical groups containing O- and N-heteroatoms (ref. [6]). Despite the accessibility of the pores for electrolyte species, due to the length of micropores, the polarization conditions are not uniform even at low potential modulation frequencies, resulting in the continuous growth of Re(C_z).

In general, analysis of complex capacitance dependence on potential modulation frequency provides an important *in situ* tool of the characterization of porous structure of electrode materials. The simplified model will be further extended in the following studies, taking into account the dispersion in the sizes of the pores. The model is useful for the comparison with the results of *ex situ* characterization, in particular by gas adsorption. This comparison allows to evaluate the accessibility of the electrochemical interface for electrolyte species and the conditions of the potential modulation of the electrochemical interface at various potential modulation rates.

- **Overview**

The development of performant supercapacitors is essential to maintain the needs in energy storage devices. In this first work, it was shown that doping activated carbons with nitrogen functional groups appear as a promising strategy to enhance the performance of the electrode by surface-redox driven process bringing additional pseudocapacitance effect. It was demonstrated that not only this strategy can provide higher performance than materials having higher specific surface area, enlightening the limit of pure electrochemical double-layer capacitors and needs in further charge storage mechanisms that could be brought by pseudocapacitance. The study of the latter phenomena is even more interesting considering the use of transition metal oxides with reversible and fast surface-redox driven storage processes. This will be emphasized in the following two chapters using Mn_3O_4 and Fe_3O_4. Hence, the search in better and greener supercapacitor electrodes should be investigated not only for carbon materials but also other category of materials with TMOs.

In addition, electrochemical impedance spectroscopy is once more seen as an interesting and complementary tool to assess the structural properties of electrodes and their charge storage process by the potential modulation. This work on carbon materials with a simplified geometrical model could also be applied for other materials such as TMOs. This could allow a better understanding of the pseudocapacitance charge storage mechanism in link with the structural characteristics of the active materials in the electrode. Hence, work performed on carbon materials for supercapacitor electrodes should be considered complementary to the work of on other materials type involving similarities but also differences in their charge storage mechanism to enlarge the view and knowledge of EESDs. All these complementary works are essential to better understand and design EESDs electrodes.

Chapter 2: Solution Combustion Synthesis for MnO_x as pseudocapacitor electrode materials

Abstract

Solution combustion synthesis (SCS) is often utilized to prepare crystalline nanoparticles of transition metal oxides, in particular Mn oxides. The structure and composition of the final product depend on the conditions of the synthesis, in particular on the composition of metal precursors, its molar ratio to the fuel component, and the mode of heating. In the present work the study of chemical phenomena which may occur in the during SCS process has been studied for the conventional nitrate-glycine synthesis of Mn oxide, as well as for nitrate-citrate-glycine and nitrate-citrate-urea synthesis. In the case of nitrate-glycine synthesis, formation of a weak complex of Mn(II) and glycine provides the conditions of instantaneous SCS reaction upon heating, resulting in only weak sintering of final oxide nanoparticles. However, partial hydrolysis of Mn precursor during slow solvent evaporation results in formation of mixture of oxides, namely MnO and Mn_3O_4. Formation of MnO is completely suppressed in the presence of ammonium citrate in the initial mixture, and pure Mn_3O_4 phase is obtained. SCS reaction in this case is slower, resulting in stronger sintering of the nanoparticles. The study of electrochemical properties of synthesized oxides demonstrated that the SCS with nitrate-citrate-urea mixture provides the highest charge capacitance in 1M NaOH: 130 F/g at 2 A/g. Impedance characterization of materials allowed to propose tentative mechanism of degradation of electrode materials during the galvanostatic cycling.

Introduction

Transition metal oxides (TMO) are one of the main classes of materials used as electrodes in electrochemical energy storage devices (EESD), in particular in batteries [346,347], and pseudocapacitors [348]. Manganese oxides are historically among the most studied electrode materials for EESD [346,349,350]. In particular, spinel manganese oxide Mn_3O_4 have been intensively studied in the recent years as a promising electrode materials for pseudocapacitors [351–353] and anodes of Li-ion batteries [354,355]. The electrochemical properties of manganese oxides can be adjusted by tuning its composition, by partially or totally replacing one of the cations [350]. Dosaev *et al.* [356] have prepared a series of AMn_2O_4 substituted spinels with A=Li, Mg, Cd, thus controllably varying unit cell parameters and the oxidation state of Mn from +2.5 (in Mn_3O_4) to +3.5 (in $LiMn_2O_4$). They have observed a systematic dependence of the electrocatalytic activity of prepared oxides on the oxidation state of Mn.

Solution combustion synthesis (SCS) is known for decades as a low cost, low energy intake and versatile method of preparation of binary and mixed oxides [357,358], such as aluminates [359], chromates [360], manganates [361]. The method allows preparation of well-crystallized mesoporous oxide powders, consisting of particles within the size range from few tens nm to few µm. In SCS, the metal precursor salt, which is most commonly a nitrate, is dissolved in a solution with the fuel component, the most common of which are glycine, urea, sucrose, or citric acid [362]. The solvent is then evaporated until the fuel is ignited at relatively low temperature (100-200 °C), generating heat and resulting in fast decomposition of metal salt. Self-propagating character of the process ensures relatively short reaction time and uniform conditions of the reaction. Decomposition of both nitrates and fuels resulted in the formation of large amount of gaseous products, allowing the heat to be rapidly dissipated, minimizing sintering of solid products.

The main challenge of the SCS is to ensure a control on the morphology and composition of resulting oxide materials due to the complexity of the processes occurring during the synthesis in a short reaction time. In most common version of SCS the nitrates and glycine are used as precursor and fuel correspondingly, and the stoichiometric reactions of their decomposition are often expressed as simple reactions in equations 1 and 2.

$$M(NO_3)_x \rightarrow MO_{\frac{x}{2}} + \frac{x}{2}N_2 + \frac{3x}{2}O_2 \qquad (1)$$

$$4\,C_2H_5NO_2 + 9\,O_2 \rightarrow 5\,H_2O + 4\,CO_2 + N_2 \qquad (2)$$

The overall stoichiometric equation for the mixture containing nitrate and glycine in the molar ratio of φ in equation 3.

$$M(NO_3)_x + \left(\frac{5}{9}\phi x\right) C_2H_5NO_2 + \left(\frac{5}{4}(\phi - 1)x\right) O_2 \rightarrow MO_{\frac{x}{2}} + \left(\frac{25}{18}\phi x\right) H_2O + x\left(\frac{5}{18}\phi + \frac{1}{2}\right) N_2 + \left(\frac{10}{9}\phi x\right) CO_2 \qquad (3)$$

The above equations are often used for categorizing the composition of initial system as fuel lean (φ<1), or fuel rich (φ>1) mixtures. In particular, when φ=1, the amount of oxygen consumed by glycine combustion is supposed to be equivalent to amount of oxygen produced by nitrate decomposition. In this case no oxygen depletion is expected in the reaction media even despite the escape of large amount of hot gaseous products of decomposition.

However, it is also well recognized that the reactions (1) and (2) are oversimplifications of the complex mechanism of decomposition reactions occurring at high temperature of SCS synthesis. Some of the reactions which may occur during the SCS process with $Mn(NO_3)_2$ are listed in Table 8.

Table 8: *Decomposition reaction that may occur in the course SCS synthesis with $Mn(NO_3)_2$ and various fuels*

Component	Reactions	Conditions	Heat effect, kJ/mol	Reference
Mn(II) nitrate, $Mn(NO_3)_2$	$Mn(NO_3)_2 \rightarrow [MnONO_3] + NO_2 \rightarrow MnO_2 + 2NO_2$	ca.240 °C	155±12	363,364
	$MnO_2 \rightarrow Mn_2O_3$	560-570 °C	≈24	
	$Mn_2O_3 \rightarrow Mn_3O_4$	above 800 °C		
Glycine, $C_2H_5NO_2$	$4C_2H_5NO_2 + 9O_2 \rightarrow 5H_2O + 4CO_2 + N_2$	210 °C	-972.98±0.12	365
	$4C_2H_5NO_2 \rightarrow 6H_2O + 2NH_3 + 6C + 2HNCO$	250 °C, no O_2	-528	366

Table 8 does not list all possible reactions and processes occurring during SCS. In particular, formation of metal complexes with fuel components, for example complexes of Mn with glycine [367] may occur during the evaporation of solvent, and result in change in ignition and adiabatic temperatures for the SCS process. The intermediate and final products of decomposition reactions may undergo phase transitions, also resulting in changes in reaction heat.

In numerous studies the analysis of thermodynamic effects of SCS reaction is done by calculating adiabatic temperature T_{ad} from energy balance equation, taking into account enthalpies of decomposition reactions and phase transitions, and heat loss due to the escape of hot gaseous products [362,368]. This analysis gives valuable qualitative predictions of the dependence of T_{ad} on the composition of initial SCS mixture. However, the maximal temperature detected in SCS process T_{max} is systematically higher than predicted T_{ad} values due to (i) uncertainty in thermodynamic parameters of reagents and intermediates of SCS processes and (ii) limitations in modelling of heat dissipation during fast SCS reactions. In order to better understand the nature of SCS processes and being able to adjust the conditions to synthesize the materials with desired structure and composition, a combination of thermodynamic analysis and detailed experimental studies is the necessary.

Table 9 summarizes recent studies of SCS synthesis of Mn oxides.

Table 9: *Overview of studies of SCS synthesis of Mn oxides*

Precursor	Fuel	Product	Conditions	Ref.
$Mn(NO_3)_2$	Glycine	ε-MnO_2, 23 m^2/g	Heating plate evaporation/ignition; $\phi=0.5$;	369
		ε-MnO_2, 43 m^2/g	$\phi=2.0$; higher ϕ results in better crystallinity	
$Mn(NO_3)_2$	Glyoxalic acid	$Mn_3O_4+Mn_2O_3$, 43 m^2/g	Oven heating up to 120°C (1h ramp, 1h hold), then annealing at 350°C for 4h	370
	Ketoglutaric acid	$Mn_2O_3+Mn_3O_4$, 23 m^2/g		
$Mn(NO_3)_2$	Glycine	Mn_2O_3; 43 m^2/g, 21±4 nm	Oven heating at 600°C for 20 min; $\phi=0.5$	371
		Mn_3O_4; 46 m^2/g, 17±3 nm	500°C, 30 min; $\phi=2$	
		$Mn_2O_3+MnO_2$; 47 m^2/g	350°C, 120 min, $\phi=2$	
$Mn(NO_3)_2$	Glycine	Mn_3O_4; 32 m^2/g	Slow evaporation in air, then heating plate ignition at 350°C.	372,373
		Mn_3O_4/C; 5-35 nm	+ *x*% of Vulcan	
$MnAc_2$	Ethanol	Mn_3O_4(85%)+MnO(15%)	Flame ignition of ethanol	374
$Mn(NO_3)_2$	Citric acid	MnO_2, 6.3 m^2/g	Oven evaporation at 150°C for 5h, then annealing at 400°C for 3h in air; $\phi=0$	375
		$Mn_3O_4+Mn_2O_3$, 15.3 m^2/g	$\phi=0.5$	
		Mn_3O_4, 31.7 m^2/g	$\phi=1$	
		Mn_2O_3, 55.1 m^2/g	$\phi=2$	
		$Mn_3O_4+Mn_2O_3$, 38.2 m^2/g	$\phi=4$	
$Mn(NO_3)_2$	Urea	68%MnO_2+32%Mn_2O_3, 7.5 m^2/g	330°C evaporation/ignition in oven $\phi=0.2$	376
		32%MnO_2+68%Mn_2O_3	$\phi=0.3$	
		22%MnO_2+78%Mn_2O_3	$\phi=0.4$	
		Mn_2O_3, 68±12 nm	$\phi=1.0$	
		65%Mn_3O_4+35%MnO	$\phi=2.0$	
	Glycine	Mn_2O_3	$\phi=0.2$	
		Mn_2O_3	$\phi=0.3$	
		Mn_2O_3	$\phi=0.5$	

		Mn_3O_4	ϕ=1.0	
		Mn_3O_4	ϕ=2.0	

From Table 9 it is clear that the composition and the structure of the final oxide product strongly depends on the conditions of SCS. Namely, the determining composition parameters are the composition of initial mixture, heating ramp, duration, and temperature.

The goal of the present work is to understand better the processes occurring during the SCS synthesis, how they can be controlled, and how they influence the structure of the resulting oxides as well as their electrochemical properties as supercapacitor electrode materials.

- **Materials and Methods**
    - Synthesis of Mn oxides

Different synthesis of manganese oxides were performed by varying the fuel-to-precursor ratio as well as the addition or not of a ligand as listed in the following Table 10. The nitrogen adsorption-desorption isotherms of the compounds are presented in the Supplementary Information 2.

Table 10: *Composition of initial mixtures*

Name	Mn precursor	Fuel	XRD attribution	Properties
N-G-0.5	$Mn(NO_3)_2$	Glycine, ϕ=0.50	Mn_2O_3 + [Mn_3O_4][1]	23-26 nm(2), 17 m^2/g
N-G-0.75	$Mn(NO_3)_2$	Glycine, ϕ=0.75	Mn_2O_3 + Mn_3O_4	18-27 nm, 4 m^2/g
N-G-1.0	$Mn(NO_3)_2$	Glycine, ϕ=1.00	Mn_3O_4 + [MnO]	19-22 nm, 40 m^2/g
N-G-1.25	$Mn(NO_3)_2$	Glycine, ϕ=1.25	Mn_3O_4 + [MnO]	19-20 nm, 18 m^2/g
N-G-1.5	$Mn(NO_3)_2$	Glycine, ϕ=1.50	Mn_3O_4 + [MnO]	20-22 nm, 14 m^2/g
N-AC-1.0	$Mn(NO_3)_2$	$(NH_4)_3$Cit	Mn_2O_3	20-22 nm, 14 m^2/g
N-AC-G-1.0	$Mn(NO_3)_2$	$(NH_4)_3$Cit+glycine	Mn_3O_4	11.3 nm, 24 m^2/g
N-AC-U-1.0	$Mn(NO_3)_2$	$(NH_4)_3$Cit+urea	Mn_3O_4	9.3nm, 35 m^2/g

---

[1] In square brackets a minor product is depicted

(2) Estimated from XRD

Manganese nitrate tetrahydrate $Mn(NO_3)_2{\cdot}4H_2O$ from Fischer Scientific (CAS: 20694-39-7, ≥97.5% purity, analytical) is used as the precursor, source of manganese and nitrate. The fuels are, from Thermo Scientific Chemicals, glycine (CAS: 56-40-6, 99% purity) and urea (CAS: 57-13-6, 99% purity, ACS reagent). The additional ligand is anhydrous ammonium citrate tribasic $(NH_4)_3Cit$ (Sigma, ≥ 97% purity, CAS: 3458-72-8). Depending on the mixture, the reactants are added in a 250 mL Erlenmeyer flask with 10 mL of ultrapure water (18.2 Mohm·cm, TOC < 1 ppb) produced by UltraAnalytique Veolia device. The mixture is agitated for approximately 10 minutes until dissolution of all remaining crystals, followed by a 20 min sonication bath treatment. The Erlenmeyer flask is then placed in an oven at 80°C for 48h for a slow evaporation of the water solvent to obtain a dried xerogel. For the synthesis, the Erlenmeyer flask is placed on an already heated plate at 350°C to undergo auto-ignition. The self-propagating combustion is usually done in 30-60s accompanied by gas evaporation. After letting the flasks to cool down, ultrapure water is added and another step of sonication bath is performed for 5 min to disperse all the obtain particles. The dispersion is then filter and washed using water. Finally, the powder is dried overnight at 80°C prior to characterization. The obtained powder generally yields at 90% according a theoretical 1.0 g of desired phase product (i.e. Mn_3O_4).

- Physicochemical characterization of manganese oxides

SEM measurements were done using a Zeiss 2600F microscope with a resolution of 5 nm. The carbon samples were deposited on a conductive carbon tape. XRD measurements were performed by Bruker D-8 Advance diffractometer with Cu Kα source (λ = 1.54184 Å). ATR-FTIR measurements were done by ThermoFisher IR spectrometer equipped by ATR Smart Orbit setup. BET measurements were done using ASAP 2420 Micrometric analyzer measuring N_2 physisorption isotherm at 77 K after degassing the samples at 150 °C for 12 h. Raman spectra were recorded using LabRAM HORIBA ARAMIS spectrometer with CDD detector and laser line from 532 nm / 100 mW (YAG) Laser Quantum MPC600 PSU. XPS measurements were done using Multilab 2000 Thermoelectron spectrometer with Al Kα source (λ = 1486.6 eV). Thermogravimetric analysis (TGA) was performed with Q 5000 TA Instrument under air using platinum crucibles from room temperature to 800-900°C with 5°C/min ramp. Temperature-Dependent Diffuse Reflectance Infrared Fourier Transform Spectroscopy (TD-DRIFTS) was performed thanks to Vertex 70 Bruker IR spectrometer (4000 cm^{-1} to 600 cm^{-1}) equipped with a one-pot sample compartment. The setup is equipped with a homemade chamber (ca. 7 mL of volume) for temperature-controlled analyses with ZnSe windows and a Praying Mantis ™ diffuse reflectance accessory from Harrick. The samples were diluted with KBr prior to analysis in the holder and purged with helium first. Then, the tests were conducted with air flow (5 mL/min) with heating ramp of 2°C/min up to maximum 440°C.

- Electrochemical measurements

Ink preparation

First, a certain amount of oxide powder (active material), Vulcan XC-72 (conductive agent) and Nafion 0.5wt% (binder) is considered and all the products are weighted to obtain a 70:25:5 ratio respectively. The active material and conductive agent are mixed together in an agate mortar. Inks are prepared by adding a desired amount of the prepared mixture in a glass vial and the required volume of MilliQ water (resistivity of 18.2 MΩ·cm at 25 °C, Total of organic compound (TOC) ≤ 1 ppb) and Nafion 0.5wt% to obtain a 2 g/L concentrated ink. The ink is then shaken and sonicated in an ultrasonication bath for 20 minutes.

Ink deposition on glassy carbon rod

The active material was deposited by drop casting onto the surface of a glassy carbon rod electrode of 6 mm radius. The total deposited volume of ink is 75 µL divided by 5 deposition step of 15 µL in which the electrode is dried for 10 minutes in an oven programmed at 80 °C between each step. The loading of active material is approximated to 0.75 mg/cm^2. A final deposition of 15 µL Nafion 0.5 wt.% in mixture of lower aliphatic alcohols and water was added and dried to act as a binder.

3-electrode cell set-up

A 3-electrode cell inside a Faraday cage is used for the electrochemical tests. A 100mL 1M NaOH electrolyte is poured in the cell followed by the addition of a platinum wire with a coil end counter electrode in the compartment separated by a fritted and a mercury/mercurous oxide electrode (Hg/HgO) in 1M NaOH internal solution in the compartment separated by Luggin capillary. The solution in the cell is then purged for at least 30 minutes under N_2 gas. The glassy carbon rod electrode with active material – the working electrode - is placed in a holder and then placed inside the electrochemical cell in order to only have a contact with the surface of the electrode. The N_2 gas is flushing above the electrolyte to keep a controlled atmosphere without O_2. The electrodes are connected to a SP-300 potentiostat from BioLogic.

- **Results**
  - Nitrate-glycine synthesis

FTIR and TGA analysis of decomposition processes

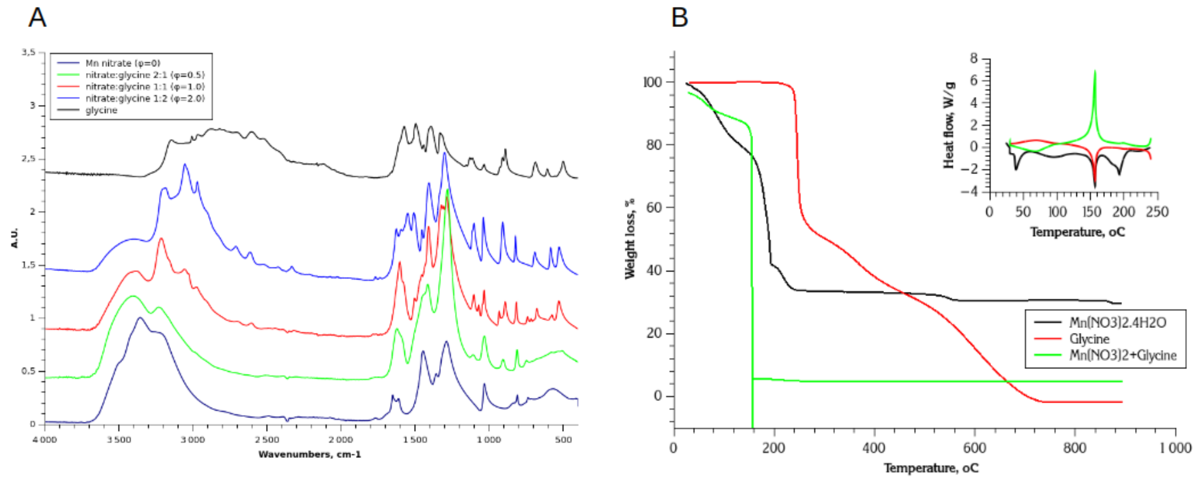

Figure 68: ATR-FTIR spectra of dried precursors $Mn(NO_3)_3{\cdot}4H_2O$ and Glycine, and their mixture with different ratios (A) ; TGA curves of in-air decomposition of Mn nitrate, Glycine, and their dried mixture (B), inset is the heat flow resulting from decomposition reaction.

Fig. 68 shows ATR-FTIR spectra of selected solid products at ambient temperature : the Mn(II) nitrate, Glycine, and their mixtures with different molar ratio ϕ. The solids were prepared by complete evaporation of water from their aqueous solutions at 80°C for 48h. The attribution of the main IR bands is given in Table 11. In general, the spectra are in agreement with the structure of hydrated $Mn(NO_3)_2$ [377] and zwitterion solid glycine [378,379], as reported in the literature. Noticeably, FTIR spectrum of $Mn(NO_3)_2.4H_2O$ shows a complex ν_{OH} band in 3200-3600 cm^{-1} region, containing several contributions. In symmetrical octahedral structure of $Mn(NO_3)_2.4H_2O$ complex the position of all water molecules is equivalent [380]. Thus, the complex nature of ν_{OH} band is due to a different coordination energy of water ligand forming H-bonds between themselves and with nitrate ligand. In particular sharp ν_{OH} band at ≈3350 cm^{-1} can be attributed to H_2O ligands weakly coordinated by intermolecular hydrogen bonds, while broader band located at lower wavenumbers is associated with water ligand forming long-range order intermolecular H-bonded network.

Table 11: *IR peak attributions for the manganese nitrate – glycine mixture*

Precursor	IR band (position cm^{-1}, observation)[3]	Attribution
$Mn(NO_3)_2.4H_2O$	3430, st.br.	ν(OH)
	3185, s.	
	2736, m.	
	2147, m.	

---

[3] st. = strong, m. = medium, w = weak, br. = broad, s. = sharp, sh. = shoulder

	1762, st., s.	$\nu_1+\nu_4$
	1601, st., s.	$2\nu_2$
	1435, sh.	ν_3 (NO_3^-)
	1367, st.	ν_3 (NO_3^-)
	1055, st.	ν_1 (NO_3^-)
	826, st.	ν_2 (NO_3^-)
Glycine, NH_2CH_2COOH	3165, w, sh.	$\nu_a(NH_3^+)$
	2820, w	$\nu_s(CH)$
	2610,	$\nu_s(NH_3^+)$
	2120, m	$\nu_a(COO^-)+\tau(NH_3^+)$
	1604	$\nu_a(COO^-)$
	1510	$\delta_s(NH_3^+)$
	1412	$\nu_s(COO^-)$
	1330	$\delta(CH_2)+\delta(NH_2)$
	1110	$\rho(NH_3^+)$
	1030	tw.(NH_2)
	890	$\delta(NH_2)+\delta(CH_2)$
	690	$\rho(COO^-)$
	610	$\omega(COO^-)$

The IR spectrum of dried nitrate-glycine mixtures contains the similar IR bands of nitrate ligand (ν_1-ν_6) as Mn nitrate nearly at the same positions. The ν_{OH} band is gradually distorted as the ratio of glycine-to-nitrate ϕ increases : for $\phi=2$ relatively broad band centered at ≈3500 cm^{-1} is observed, indicating disruption of the network of H-bonded water ligands. On the other hand, the IR bands of glycine are modified and shifted in the presence of Mn(II) nitrate comparing to pure glycine. Most remarkable is the absence of the peaks of $\delta_s(NH_3^+)$ at 1510 cm^{-1} and $\rho(COO^-)$ at 610 cm^{-1}, and wider separation of peaks $\nu_a(COO^-)$, which shifts from 1604 cm^{-1} to 1633 cm^{-1}, and $\nu_s(COO^-)$, which shifts from 1412 cm^{-1} to 1390 cm^{-1}. We attribute these changes to the formation of Mn-Gly complex [381,382] after the drying step, which also have been previously suggested [383] as a part of a mechanism of Mn nitrate-glycine SCS. Considering the presence of non-modified IR peaks related to NO_3^- in the spectrum of the mixture, and stoichiometry between nitrate and glycine, one may tentatively suggest the formation of $[Mn(gly)(H_2O)_4](NO_3)_2$ or $[Mn(gly)(H_2O)_2](NO_3)_2$ complex after drying step. It is not possible to evaluate more exactly the composition of the dried solids based on only ATR-FTIR data.

TGA curves of in air decomposition of Mn nitrate - glycine mixture also differs from the curves of pure solids (Fig.68B). In order to have more detailed interpretation of the processes happening during these decomposition reactions we performed temperature dependent DRIFT analysis of the composition of Mn(II) nitrate, Glycine, and their dried mixture (Fig.69). The interpretation of DRIFT spectra is discussed below.

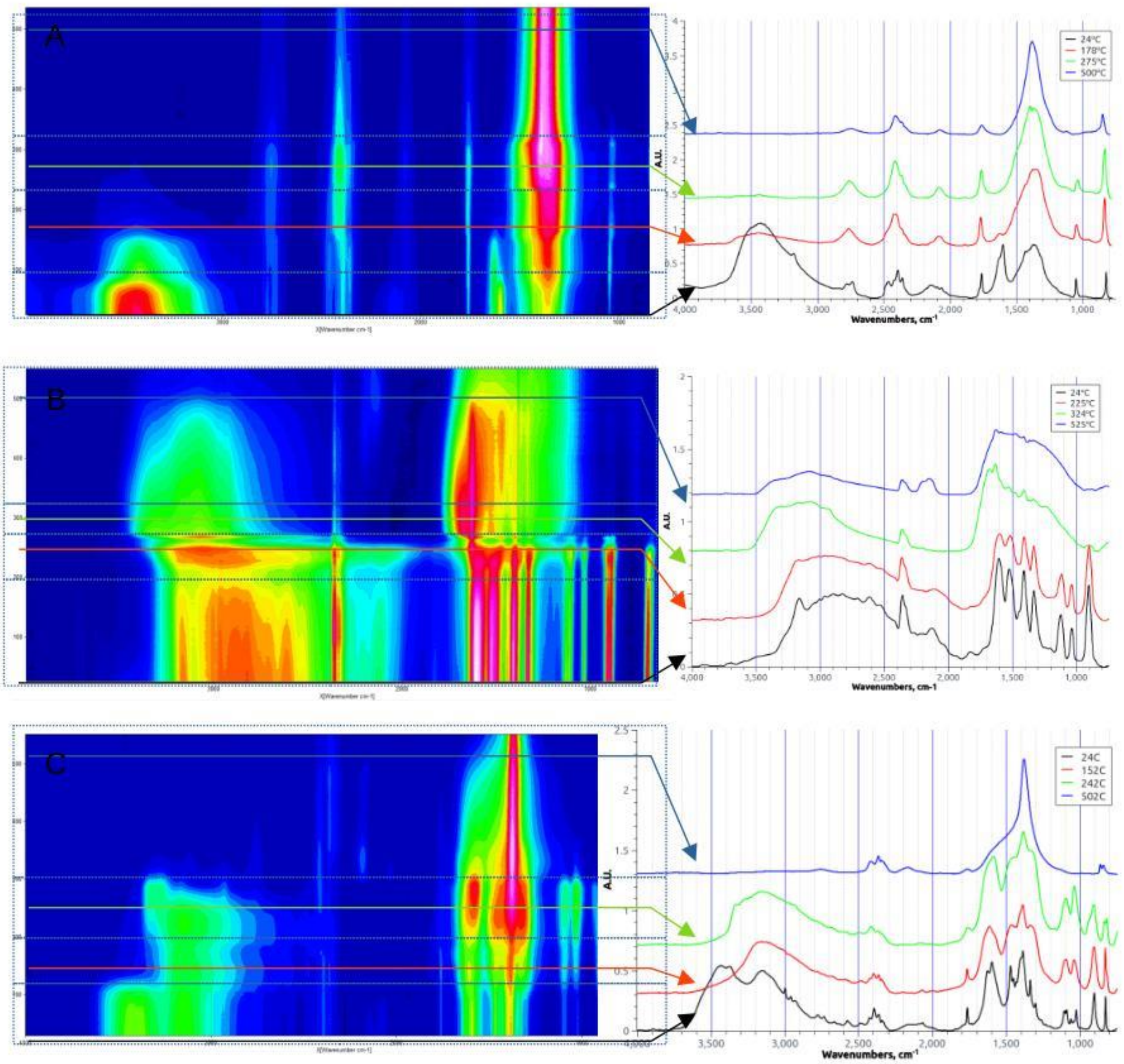

Figure 69: DRIFT spectra of $Mn(NO_3)_2$ (A), Glycine (B), and their dried 1-1 mixture (C); the arrows shows the temperature for which the slice spectra are shown at the right side.

Mn(II) nitrate (Fig.69A).

As TGA curve shows, in the range from ambient temperature to ca. 100-120 °C there is a gradual dehydration of $Mn(NO_3)_2.4H_2O$; the weight loss at 120 °C correspond to the loss of 2 molecules of H_2O par nitrate, i.e. formation of $Mn(NO_3)_2{\cdot}2H_2O$. The IR peaks of nitrate remaining nearly unchanged in this temperature range, while peaks of ν(OH) at 3400 cm^{-1} and δ(HOH) at 1650 cm^{-1} are gradually disappearing. In the range 120°C-180°C the weight loss is accelerating, reaching $Mn(NO_3)_2{\cdot}H_2O$ stoichiometry at 140-150 °C. At ca. 180 °C the weight loss correspond to anhydrous $Mn(NO_3)_2$; however, it is not possible to exactly evaluate the stoichiometry of remaining solid above 150 °C, because of the onset of low-temperature $Mn(NO_3)_2$ decomposition assisted by water evaporation [363]. In fact, anhydrous $Mn(NO_3)_2$ decomposes only at temperatures above 200 ^oC [363,384], while decomposition of hydrated complex starts at ≈150 ^oC.

The IR peaks related to nitrate are changing in the range 120-180 ^oC: the intensities of peaks $ν_1$-$ν_4$ in the range 1300-1600 cm^{-1} is decreasing, and the peaks are gradually transforming into a strong single IR peak centered around 1380 cm^{-1}. The latter peak remains relatively strong up to high temperature (above 500 ^oC). Similar changes in nitrate IR bands have been observed for alkaline metal nitrates above melting point [385], and explained by fusion of nitrate salt. The nitrate IR bands remaining even at high temperature have been observed before [386] and attributed to the remaining traces of nitrate, most probably, in a molten state. We note also that this strong band at 1500 cm^{-1} is absent in the ATR-FTIR spectra of final product after filtering, washing, and drying.

The weight of sample is stabilized at ca. 220 ^oC at the value of 35% of initial mass, corresponding to the formation of MnO_2. At t>550 ^oC there is additional 5% of weight loss indicating transformation of MnO_2 to Mn_2O_3. Reported results are agreement with reported studies of $Mn(NO_3)_2$ thermal decomposition [364,384,386]. The weight loss measured at transformation of dehydrated $Mn(NO_3)_2$ to MnO_2 allowed to suggest formation of unstable intermediate of oxonitrate $MnO_x(NO_3)_{2-x}$ at ca. 180 ^oC [364,386]. However, no direct experimental evidence of formation of this intermediate were ever reported. Neither presented DRIFT spectra also allow to claim or to reject the observation of oxonitrate intermediate.

It is important to note that the main gaseous products of hydrated $Mn(NO_3)_2$ decomposition at 180 ^oC are NO_2 and NO, and N_2O in a smaller quantities [386], while O_2 is produced in significantly smaller amounts comparing to nitrogen oxides. A noticeable amount of oxygen is formed around 500^oC and again above 600 ^oC due to transformation of MnO_2 first to Mn_2O_3 and then to Mn_3O_4. Nevertheless, the total amount of oxygen produced by Mn nitrate decomposition is smaller than stoichiometric. This is an important observation, considering that for the calculation of fuel-to-salt ratio ϕ is typically based on the assumption stoichiometric quantity of oxygen produced by decomposition of nitrate. Considering this uncertainty in the stoichiometry of O_2 production from nitrates decomposition it makes more sense to calculate the value of fuel-to-salt ratio ϕ simply as a molar ratio of nitrate and fuel precursors, rather than base it on the stoichiometry of reactions (R1)-(R3).

It is important to note that the thermodynamic analysis of thermal decomposition of $Mn(NO_3)_2$ demonstrated that dehydration of nitrate requires relatively low activation energy (ca. 60 kJ/mol), while decomposition nitrate have much higher activation barrier (210 kJ/mol).

Glycine (Fig.69B).

There are no changes in the structure of glycine below ca. 220 °C, as indicated by no weight losses in TGA, and no changes in DRIFT spectra. However, in the range 220-230 °C there is a significant weight loss of ca. 50%. In DRIFT spectra one observes new pair of peaks at 1640 cm^{-1} and 1680 cm^{-1}, and broad peak at 3300-3500 cm^{-1}, which can be attributed to ν(C=O) of primary and secondary amides, and ν(N-H) of amides. The analysis of gaseous products of glycine decomposition at temperature 220-230 °C demonstrated formation of NH_3 [365] as well as H_2O and CO_2, while liquid phase products various amides (formamide, acetamide, N-butylacetamide, n-butyramide and propionamide) and diones [366]. We propose that at *t*°>220°C, zwitterion structure of glycine is disrupted, and glycine is losing some of amino groups, producing gaseous ammonia while remaining amino groups are involved in formation of oligomeric amide-types intermediates [366].

At temperatures above 230°C one observes continuous weight loss which is completed at ca. 620 °C, when no solid residues are remaining. In DRIFT spectra in this temperature range one observes gradual decrease of all observed IR peaks. The strongest remaining peaks are detected in the range of 3000-3150 cm^{-1} (broad peak) and 1640 cm^{-1}. The appearance of these peaks is similar to the IR spectra of formamide and acetamide, and can be attributed to ν(N-H) and ν(C=O) in amides, thus confirming the formation of various amides as a products of glycine decomposition [365].

The amides and diones are the main products of glycine endothermic decomposition in oxygen-lean atmosphere [365,366].

It is noteworthy that the TGA behavior of dried glycine below 230 °C is the same in air, as observed in the present work, and under the N_2 [387]. The main difference occurs at higher temperatures: under N_2 the remaining weight is above 20% even at 900 °C, while it drops to 0% above 600 °C in air. Thus, the presented TGA and DRIFT data allow to suggest that the thermal decomposition of glycine in air also proceeds via first endothermic formation of amide-type intermediates, similarly to oxygen-lean atmosphere. However, in air these intermediates are eventually oxidized at temperatures above 230 °C, and totally decomposed above 600 °C.

Kinetic studies of glycine decomposition gave evidences that the first step (glycine to amides transformation) is a topochemical reaction, requiring formation of reaction nucleation sites, and certain incubation period, the length of which depends on the temperature [365]. After the induction period, the rapid growth of decomposition rate is observed, which may explain relatively sharp weight loss detected by TGA at 220 °C. Then the rate of decomposition is reaching the constant plateau, limited by the rate of reaction propagation. The second step of decomposition above 230 °C follows the kinetics of solid state thermal decomposition [387], and is characterized by relatively high activation energy (150-159 kJ/mol) [365,387].

Nitrate-glycine dried solid mixture (φ=1). Fig.69C.

Thermodynamic [388] and polarographic [389] studies suggested that Glycine forms relatively weak complexes with Mn^{2+}, comparing to other cations, such as Cu^{2+}, and Zn^{2+}. Above the temperature of dehydration, the Mn-Gly complexes are decomposing with products, similar to pure glycine. However, the temperature of dehydration of complexes may be somewhat higher than that of pure glycine [367].

In the temperature range from ambient to 170°C one observes slow weight loss of the mixture glycine-nitrate, simultaneous with strong decrease in intensity of ν(OH) broad peak at 3450-3600 cm^{-1}. One may suggest dehydration of the mixture in this temperature range, similar to one observed in the case of pure $Mn(NO_3)_2.4H_2O$. The weight loss at 170 °C is ca. 6%, corresponding to the loss of 1 H_2O entity of $[Mn(gly)(H_2O)_4](NO_3)_2$ (5.5%) or $[Mn(gly)(H_2O)_2](NO_3)_2$ (6.2%): the accuracy of our TGA measurements does not allow to distinguish between two possible compositions of dried solid mixture of nitrate-glycine.

At 170 °C very sharp weight loss is detected. This temperature is below the onset of decomposition of pure glycine (220 °C), suggesting the decomposition of glycine complex of Mn formed upon drying step. The weight loss during the decomposition of this complex is remarkably sharper than in the case of decomposition of pure nitrate or glycine, and points to auto-catalytic character of the decomposition. Contrary to the endothermic decomposition steps of pure Mn(II) nitrate and glycine, the decomposition of Mn glycine complex is exothermic (inset of Fig.68B), which may explain autocatalytic kinetics of the reaction. Alternatively, the products of initial decomposition of the complex, in particular ammonia and water vapor, may act as a catalyst of further decomposition of Mn glycine complex. In TGA curves the weight drop to ca. 5% of mass, which remains stable up to 600°C, and can be attributed to solid Mn oxide. The remaining mass is significantly lower than one expected for MnO_2 (29.6%) or Mn_3O_4 (26.0%), undoubtedly indicating the loss of solid products due to eruptive evolution of gas products of decomposition.

Interestingly, the DRIFT spectra do not demonstrate the same sharp changes. It may be related to the fact the DRIFT analysis is performed with the solids mixed with KBr as a mean to adjust the intensity of IR signals. Dilution of the solid mixture by a neutral component changes the conditions of reaction self-propagation. Another interesting point is that contrary to decomposition of pure glycine, no clear indication of formation of amide-related IR peaks (ν(N-H) at 3300-3500 cm^{-1}, and ν(C=O) at 1640-1680 cm^{-1}) during the decomposition of its complex with Mn(II) have been observed, indicating different mechanism of decomposition of pure glycine and glycine as a ligand in the complex with Mn(II).

Summing up the above evaluation of thermal decomposition of dried nitrate, glycine, and their mixture, one may suggest the following mechanism of SCS nitrate-glycine processes.

- During slow evaporation of solvent from nitrate and glycine mixed solution, the glycine complex of Mn(II) is formed, either $[Mn(gly)(H_2O)_2](NO_3)_2$, or $[Mn(gly)(H_2O)_4](NO_3)_2$. Formation of this complex ensures fine and uniform mixing of components of SCS mixture.
- The glycine complexes of Mn(II) are thermodynamically less stable than complexes of other transition metals [388,389] and easily decomposing upon heating [367]. The decomposition of this complex follows up its partial dehydration, and occurs at temperature 160-170 °C, which is below the decomposition of pure glycine (220 °C). It has been previously reported that decomposition of dried Mn nitrate-glycine mixture also occurs at lower temperature comparing to pure glycine under inert atmosphere [383].
- In comparison to a decomposition of pure nitrate and glycine, the first step of decomposition of dried mixture is fast, and results in formation of large amount of gas products. One may assume the "auto-catalytic" mechanism of glycine/nitrate decomposition with formation of glycine complex of Mn(II) as a catalytic intermediate. The fast kinetics of glycine-nitrate decomposition may be an indication of lowering of activation energy of this reaction, which is otherwise relatively high for both nitrate (210 kJ/mol) and glycine (155 kJ/mol) decompositions.

The observation of the SCS reaction also support the assumption of formation of complex intermediate. Indeed, dried mixture of components reacts instantaneously within first minute of the contact with heating plate at 350 °C and without any visible sign of phase transition. The only observation upon heating of dried mixture before ignition is formation of water vapor due to dehydration of complex. No liquid phase due to melting of $Mn(NO_3)_2$ (melting point t_f^o=37 °C) was observed.

- **Analysis of the products of SCS with nitrate-glycine mixture**

XRD diagrams of manganese oxides synthesized by nitrate-glycine SCS method are depicted in Fig. 3 for varied fuel-to-salt ϕ ratio. In the case of nitrate-glycine mixture, for all φ values, a mixture of oxides has been obtained. All oxides demonstrated typical mesoporous structure of partially agglomerated oxide nanoparticles with the size in the range 25-40 nm (Fig.70B).

At low $\varphi<1$, Mn_2O_3 is the main phase, while for $\varphi\geq1$, Mn_3O_4 + MnO mixture is formed. The same trend of formation of more reduced oxide for higher φ had been observed before [371,390].

According to Mn-O phase diagram [391], formation of more reduced oxides is thermodynamically preferable under the conditions of (i) higher temperatures and (ii) lower partial O_2 pressure, p_{O2}. In particular, at p_{O2}=1 bar, temperature range of thermodynamic stability of Mn oxides are following:

- MnO_2 :ambient to t°C < 461°C,
- Mn_2O_3: 461°C < t°C < 755°C,
- Mn_3O_4: 755°C < t°C < 1292°C,
- MnO: above 1292°C.

This temperature ranges are in full agreement with our TGA results (Fig. 68B) and study of slow thermal decomposition of $Mn(NO_3)_2.4H_2O$ in air: the main product of the decomposition up to ca. 485-500 °C is MnO_2, while at temperatures above 520° C oxide Mn_2O_3 is the main product [384].

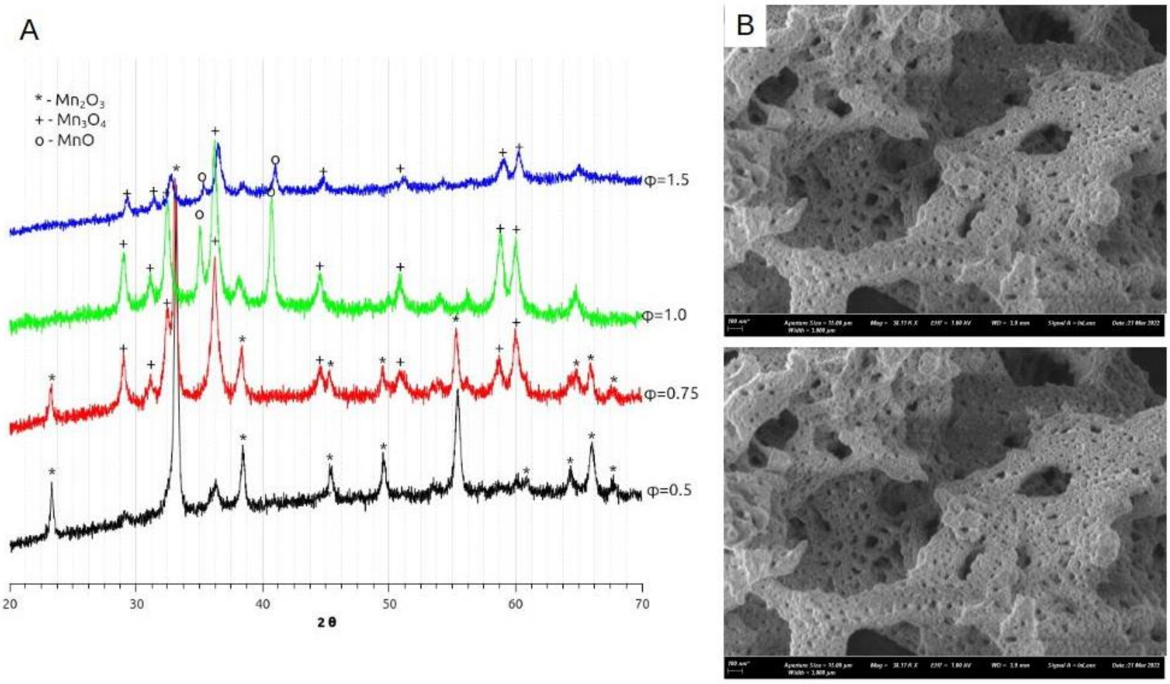

Figure 70: XRD diagrams of Mn oxides prepared by SCS with nitrate-glycine mixture with different fuel-to-salt ratio φ (A). Typical SEM images of Mn oxide prepared by SCS with 1:1 nitrate-glycine mixture (B).

As the decomposition of a fuel is a main source of heat generation during SCS, increase in φ is expected to result in higher reaction temperature. Thermodynamic models of SCS predicts that the adiabatic temperature, T_{ad} [376] is attained for stoichiometric quantities of nitrate/glycine are used, i.e. φ=0.89. Further increase in φ is expected to result in a slight decrease in SCS temperature due to stronger heat loss by escape of hot gaseous products, formed in bigger quantities from fuel than from nitrate decomposition. However, experimentally an increase in reaction temperature up to ϕ≈1 or even further is typically observed, while no decrease in synthesis temperature with increase in ϕ was detected. Thus, formation of Mn_2O_3 for low ϕ and Mn_3O_4 + MnO for ϕ≥1 can be explained by an increase in SCS temperature with higher content of glycine. It also may explain the decrease in BET surface area of oxide with increase in glycine content, which results in stronger sintering of oxide nanoparticles due to higher temperature of SCS reaction. In fact, the highest surface area of 40 m^2/g was obtained with MnOx-NG-1 oxide, resulting from the optimal conditions for heat generation.

Considering slow drying of the precursors mixture, and an instantaneous character of SCS process, one may expect uniform reaction conditions. Nevertheless, for all nitrate+glycine mixtures we always produced a mixture of oxides (see Table 10). In particular, for all $\phi \geq 1$, a mixture of Mn_3O_4 (predominant phase) and MnO (minor component) has been formed, in agreement with previous studies [383]. The formation of a mixture of products can be related to the following.

- The formation of mixture of oxides can be attributed to the partial reduction of Mn_3O_4 to MnO, indicating high temperature generated during the SCS decomposition reaction : at $p(O2)=1$ bar, MnO formation is detected only above 820 °C (Fig.68B). MnO remains a minor product due to effective evacuation of generated heat by formed gaseous products. However, in this case one would expect systematically higher content of MnO formed with higher ϕ value, which was not experimentally observed.
- The alternative explanation of formation of MnO as an SCS product is the precipitation of $Mn(OH)_2$ hydroxide due to the hydrolysis of Mn(II) nitrate during the solution evaporation. The pH of the solution of Mn(II) nitrate is slightly acidic (pH=4.6), both in the absence and in the presence of glycine, and thus no precipitation of $Mn(OH)_2$ ($pK_b=12.7$) is expected from nitrate solution. However, Mn(II) hydroxide may be precipitated during the evaporation of solvent due its much lower solubility comparing to nitrate (0.34 mg/100 mL and 118 g/100 mL respectively). The precipitated $Mn(OH)_2$ hydroxide is then decomposed during the SCS reaction to MnO. The latter is not oxidized to higher oxides due to the oxygen lean atmosphere within the SCS reaction.

It must be bear in mind that besides the composition of initial SCS mixture and ϕ ratio, other SCS conditions may strongly effect the T_{ad} and p_{O2}. Nitrate-glycine synthesis with very fast evaporation of solvent (in less than 20 min) on a heating plate resulted in formation of the same ε-MnO_2 oxide for both $\phi=0.5$, and $\phi=2.0$ [369]. On the other hand, the main product of nitrate-glycine SCS ($\phi=1.5$) with fast solvent evaporation in an oven at 500 °C is Mn_3O_4, while when slower evaporation is performed at lower temperature at 350 °C, the products are Mn_2O_3 and MnO_2 [371]. Thus, the temperature ramp, the rate of evaporation and the mode of heating (bottom heating on a heating plate or all-around inside an oven) are also the important conditions to bear in mind. It may be speculated that the slower evaporation of solvent favorizes hydrolysis of Mn precursor salt and precipitation of Mn hydroxide, resulting in the mixture of final oxide products.

- **SCS synthesis with ammonium citrate : nitrate-citrate, nitrate-citrate-glycine, and nitrate-citrate-urea synthesis**

Thermal stability studies with nitrate-citrate, nitrate-citrate-glycine, and nitrate-citrate-urea SCS mixtures

In order to better understand the role of formation of intermediate compounds and complexes during the drying step of SCS, we performed the similar study of SCS processes with Mn(II)-nitrate mixture with ammonia citrate as a complexing agent and a sole fuel, as well as in combination with glycine and urea as fuels. The study has been performed with 1-1-1 molar ratio mixtures of Mn nitrate, ammonia citrate, and an additional fuel.

Citrate is strong chelating anion and readily forms stable complexes with Mn(II) [392–395], thus preventing formation of hydroxide. Tri-basic ammonium citrate was chosen as the source of citrate ions due the fact that pH of its solution is close to 7, similar to glycine and urea solutions, ensuring comparable conditions of drying step. Also, the exchange of anions with Mn(II) in solution results in the formation of ammonium nitrate [396–398], which upon drying and heating decomposes with strong exothermic effect , thus favoring SCS conditions.

The pH of an aqueous solution of $(NH_4)_3Cit$ is close to 7, while the solution of $Mn(NO_3)_2$ and $(NH_4)_3Cit$ had pH=4.6. At this pH citrate is reported to form strong and stable complexes with Mn(II) salts [399]. The structure of complexes formed at slightly acidic pH is disputed: both monodentate complex $(NH_4)_4[Mn(Cit)_2]$ [392] and binuclear bidentate $(NH_4)_{2n}[Mn_2(HCit)_2(H_2O)_2]_n$ [393] were suggested as based on XRD and FTIR characterization. At higher pH=7.0-8.0 mononuclear complex of Mn(III), namely $(NH_4)_5[Mn(Cit)_2].2H_2O$ is formed due to simultaneous reaction with dissolved oxygen [392].

Fig. 71A shows the FTIR spectra of dried $Mn(NO)_3$, $(NH_4)_3Cit$, and their mixtures with glycine and urea. The FTIR spectra of $(NH_4)_3Cit$ are in agreement with literature, namely characteristic broad IR band of carbonyl ν(O-H) at ca. 3200 cm^{-1}, broad ν(N-H) at 2700 cm^{-1}, a pair of bands of $\nu_s(COO^-)$ at 1400 cm^{-1} and $\nu_a(COO^-)$ at 1575 cm^{-1}, ν(C-OH) at 1260 cm^{-1}. In the case of Mn nitrate - citrate dried mixture, one observes an additional strong and broad ν(O-H) band related to water ligand presence. One may also notice a stronger separation between the centers of bands of $\nu_s(COO^-)$ at 1390 cm^{-1} and $\nu_a(COO^-)$ at 1610 cm^{-1}, which can be explained by stronger coordination of citrate to manganese. On the other hand, these bands have clearly more contributions comparing to pure $(NH_4)_3Cit$, which may be an indication of various form of coordination of citrate with Mn, for example co-existence of both mono- and bidentate citrate in the dried mixture. This non-uniformity can be anticipated, considering that the structure of the complex depends on both metal-ligand ratio and pH of solutions, which can be changing during the evaporation of solvent. The appearance of small sharp band at 1750 cm^{-1} in the case of Mn(II) nitrate and citrate mixture can be attributed to ν(C=O) stretching vibration, related to partial protonation of citrate and formation in slightly acidic solution of Mn nitrate: for citric acid pK_{a1} = 3.18, pK_{a2} = 4.761, and pK_{a3} = 6.396, and, thus H_2Cit^- is expected to be a predominant citrate anion at pH=4.5.

In the case of dried solutions of Mn nitrate and ammonium citrate with glycine or urea, much lower intensity of v(OH) stretching band at 3600 cm^{-1} is observed, which may be an indication that water ligands are substituted by glycine or urea in this case. The band of v_a(COO-) at 1580-1620 cm^{-1} is superposed with v(C-N) expected at 1590-1605 cm^{-1}, which makes the analysis of their expect positions complicated. However, FTIR spectra are in agreement with assumption of formation of strong Mn(II) complex with citrate ligands also in the presence of glycine or urea in the initial solution.

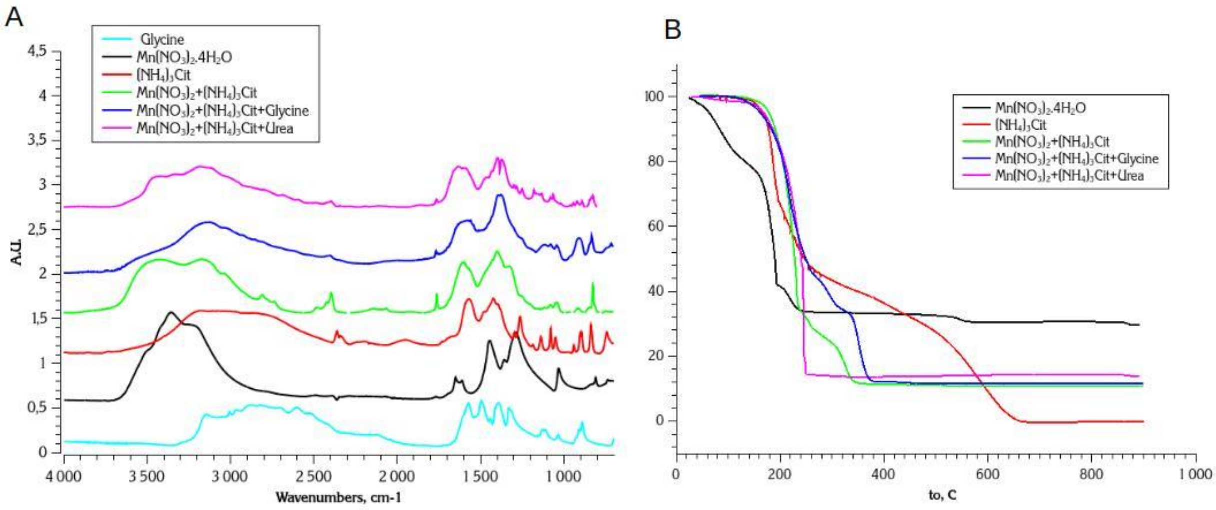

Figure 71: ATR-FTIR spectra of SCS solid mixtures with ammonium citrate (A) ; TGA curves of in-air decomposition of SCS solid mixtures (B).

TGA curves of the decomposition of the ammonium citrate and its mixture with Mn nitrate and with Mn nitrate and glycine are shown in Fig.71B. The thermal decomposition of ammonium citrate is not yet studied in details. The crystal structure of solid ammonium citrates is determined by hydrogen bonds, predominantly by N-H···O bonds [400], which are relatively weak and breaking with temperature. Thus, one may expect that thermal decomposition of ammonium citrate would have a similar mechanism to citric acid decomposition, which is a two-step process [401,402]. Namely, first step occurs simultaneously with melting of citric acid above 150 °C and results in formation of few stable intermediates, mostly *cis*- and *trans*-aconitic acid [402]. The intermediates are then slowly dehydrating forming corresponding anhydrides until total decomposition above 600 °C.

The dried mixture of Mn nitrate and ammonium citrate is stable up to the temperature of ≈150 ^oC before the decomposition of citrate starts. DRIFT spectra (Fig.72) shows only the loss of water, as indicated by a disappearance of ν(OH) band at 3600 cm^{-1} in this temperature range. At temperatures above 200 ^oC TGA curves shows rapid mass loss, in agreement with fast and simultaneous decrease of intensity of IR bands attributed to nitrate and citrate detected above 150^oC in DRIFT spectra. The decrease in the intensities of carbonyl-related bands (ν(OH) at 3200 cm^{-1} and ν(C-OH) at 1215 cm^{-1}) occurs at lower temperatures (150-200^oC) comparing to the carboxylate ($\nu_s(COO^-)$ at 1390 cm^{-1} and $\nu_a(COO^-)$ at 1610 cm^{-1}) groups, which starts above 200 ^oC. It confirms that the mechanism of decomposition of Mn-citrate complex is similar to the one of the decomposition of citric acid and proceeds first via elimination of carbonyl group of citrate and formation of aconate-type intermediates [402]. Contrary to slow second step of the decomposition of pure ammonium citrate, the decomposition of nitrate and citrate mixture is nearly finished above 340 ^oC, according to TGA. At the same temperature in DRIFT spectra one observes only remaining IR bands attributed to the rest of nitrate, as in the case of pure Mn nitrate decomposition, or Mn nitrate - glycine SCS synthesis, described in the previous section. One may suggest that Mn acts as a catalyst of the decomposition of citrate ligands, resulting in its faster decomposition comparing to pure ammonium citrate. A strong band centered at 602 cm^{-1} appears above 300 ^oC, and can be attributed to ν(Mn-O) stretching, reported for MnO_2 and Mn_2O_3 oxides [403].

The thermal decomposition of Mn nitrate - ammonium citrate - glycine mixture is similar to one of nitrate - citrate mixture, indicating that the presence of glycine does not influence the decomposition mechanism of manganese citrate complex. Contrary to nitrate-glycine mixture, there is no indication of autocatalytic decomposition of dried precursors neither in the case of nitrate-citrate nor in the case of nitrate-citrate-glycine mixtures. Moreover, one may argue from comparison of TGA curves for nitrate-citrate and nitrate-citrate-glycine mixtures that in the presence of glycine the decomposition of citrate is slower and is not finished yet below 380^oC (at least under the conditions of TGA measurements). It can be suggested that the intermediate products of the decomposition of citrate (aconate-type anions) are stabilized by the presence of the intermediates of glycine decomposition (amides). Nevertheless, in contrast to pure glycine, nearly no intermediates of glycine thermal decomposition remains above 380^oC in the case of Mn nitrate-citrate-glycine mixture.

A. $Mn(NO_3)_2+(NH_4)_3Cit$

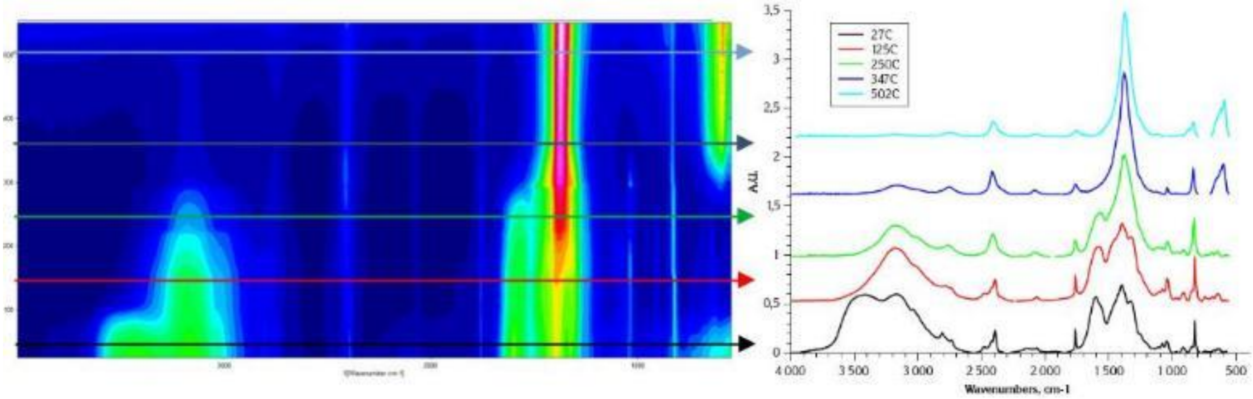

B. $Mn(NO_3)_2+(NH_4)_3Cit+Glycine$

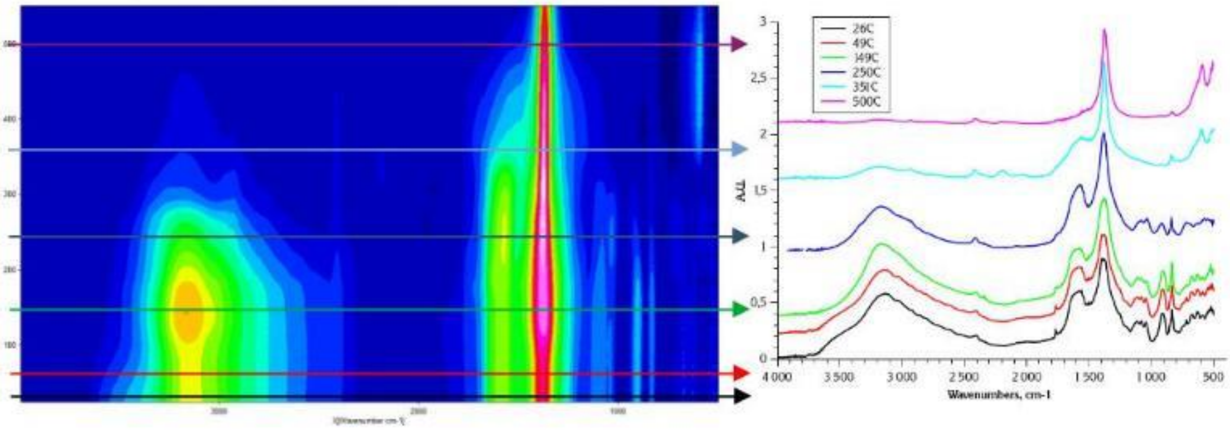

C. $Mn(NO_3)_2+(NH_4)_3Cit+Urea$

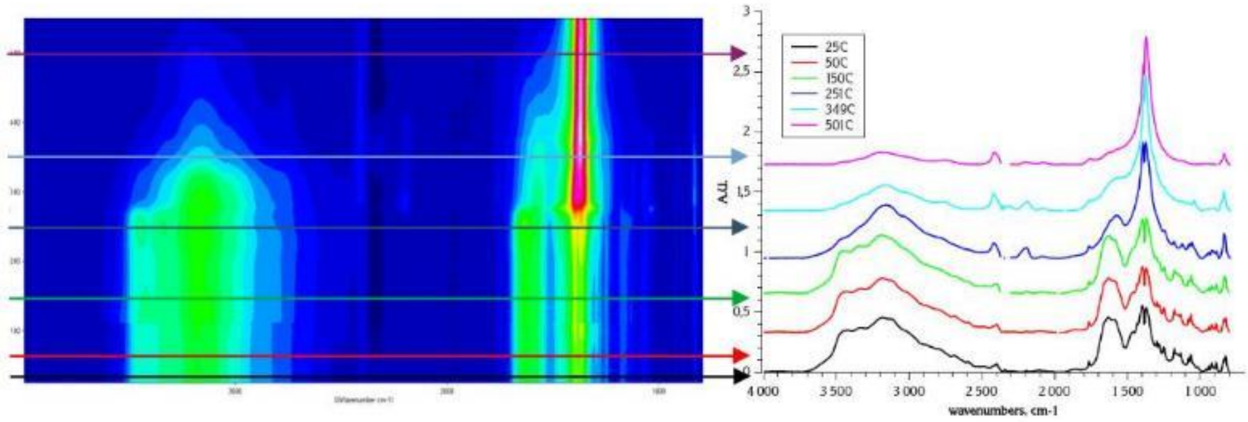

Figure 72: DRIFT spectra of decomposition of SCS mixtures with ammonium citrate. Arrows indicate the temperature of slice spectra presented at the right side.

Glycine may substitute water as a ligand in the initial mixture, as indicated by lower intensity of water-related ν(O-H) band. Also, the DRIFT spectra (Fig. 72) shows that the dehydration step occurs at somewhat lower temperature in the presence of glycine: the decrease in the intensity of ν(O-H) band is detected already below 100 °C, and it nearly disappears at 150 °C. However, after the dehydration step, the DRIFT observations and the TGA behavior are very similar in the case of presence and absence of glycine in nitrate-citrate mixture. The decomposition starts with elimination of carbonyl group at temperatures above 150 °C and then gradual decrease in the intensities of other bands related to citrate above 200 °C.

The mixture of Mn nitrate-citrate-urea also remains stable with no changes in chemical composition at least up to 150 °C (Fig. 72C). Above 200 °C one starts to observe a decrease in ν(OH) band related to carbonyl of citrate ligand, similarly to previous cases. Around 250 °C strong decrease in other citrate- and nitrate-related bands occurs with appearance of the band at 2200 cm^{-1}, which can be attributed to ν(-C=N) or ν(-C≡N). This band can indicate formation of intermediates of urea decomposition, such as cyanuric acid, cyanic acid, and cyanamide, as previous detailed studies of urea thermal decomposition suggested [404,405]. It is noteworthy that while the intermediates of the decomposition of citrate and urea are still detectable in DRIFT up to ca. 400 °C, the TGA measurements demonstrate that the decomposition is fast finished at ca. 250 °C, and no slow decomposition of intermediates occurs in this case. This discrepancy can be explained by the influence of KBr of DRIFT pellet, allowing more efficient dissipation of heat than in the case of TGA measurements, and hints to strong exothermic effect of the decomposition of nitrate-citrate-urea mixture.

- **SCS synthesis with ammonia citrate**

During SCS synthesis the dried mixtures of nitrate-citrate, nitrate-citrate-glycine, and nitrate-citrate-urea rapidly decomposes within first few (1-4) minutes after contacting the heating plate. Within this minutes one observes melting of the mixture and formation of water vapor. The decomposition reaction starts locally in one or few spots of the dried solid mixture and rapidly propagates within few or few tens of seconds until the whole solid mixture is converted and no further reaction is observed. However, it is important to emphasize that the propagation of reaction is not instantaneous as in the case of nitrate-glycine 1:1 mixture, indicating either lower heat effect end/or slower kinetics of the decomposition in the presence of citrate. It is noteworthy that the oxides MnOx-NCG and MnOx-NCU have smaller average size of crystallites as estimated by XRD in comparison with MnOx-NG oxide, while also smaller SSA (see Table 10). It may indicate that the particles of MnOx-NCG and MnOx-NCU samples are more agglomerated due to slower ignition conditions and, thus, less efficient heat evacuation.

As discussed above, presence of glycine and urea does not strongly influence the first step of decomposition of Mn citrate complex, which occurs in all cases at nearly the same temperature above 150°C. The self-propagating process is related to fast and exothermic decomposition of the intermediates of organic decomposition in the presence of Mn.

As SEM images in Fig. 73B-73D show, the oxides prepared by SCS using ammonium citrate have the morphology similar to one prepared by nitrate-glycine method, as described above : mesoporous structure consisted of partially agglomerated oxide nanoparticles. However, there are several important differences related to the utilization of ammonium citrate during the SCS synthesis.

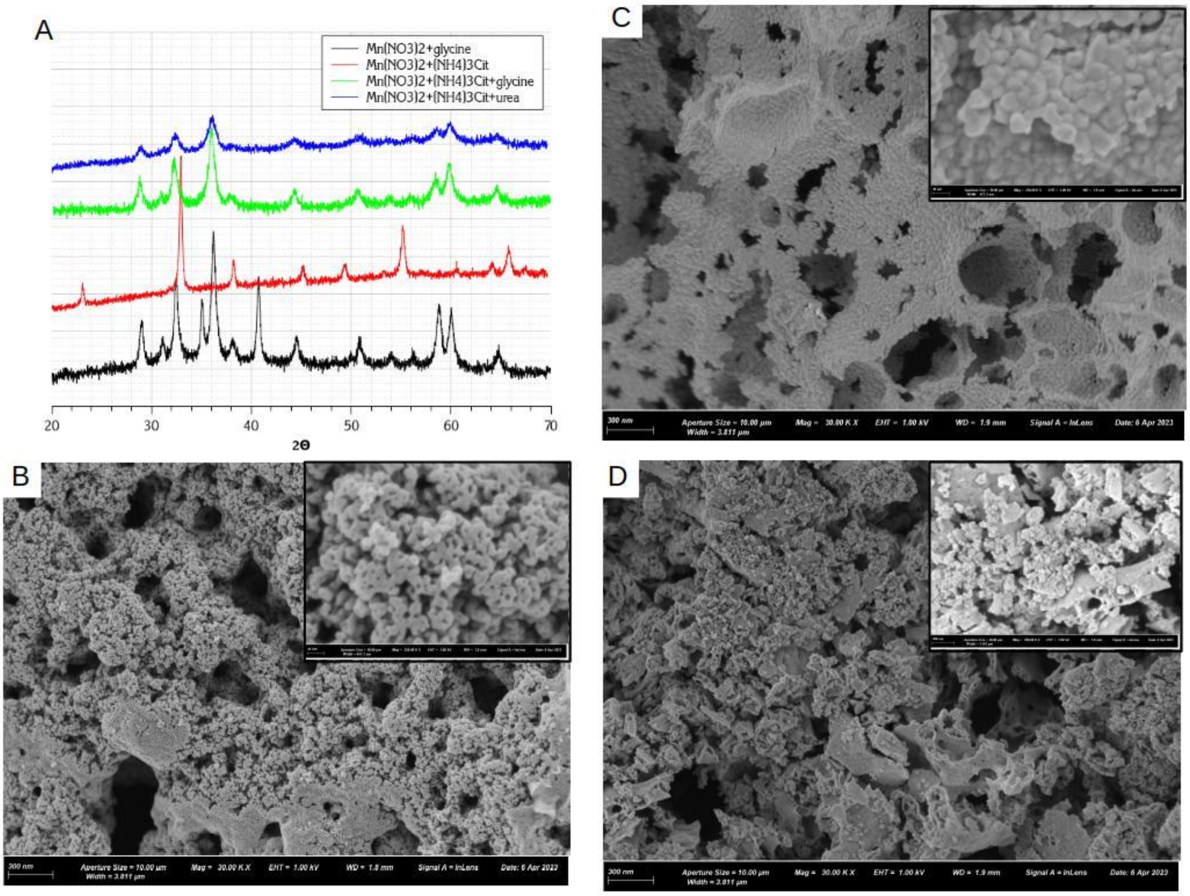

Figure 73: XRD diagrams of Mn oxides synthesized by SCS using 1-1 nitrate-glycine, nitrate-citrate, and 1-1-1 nitrate-citrate-glycine and nitrate-citrate-urea mixtures (A) Typical SEM images of oxide synthesized with 1-1 nitrate-citrate (B), 1-1-1 nitrate-citrate-glycine (C), and 1-1-1 nitrate-citrate-urea mixtures (D).

1. In all 3 cases (Mn nitrate-citrate, nitrate-citrate-glycine, and nitrate-citrate-urea) only one crystalline oxide phase was detected, despite slower kinetics of decomposition and less uniform conditions of reaction propagation, comparing to nitrate-glycine synthesis. This observation support the assumption that the main source of inhomogeneity in the final products of SCS is formation of various forms of Mn precursors, such as metal complexes, dried salt, and hydroxide, during slow step

of solvent evaporation. In the presence of citrate in the solution, Mn forms strong and stable complex with citrate ligands, which precipitates after solvent evaporation.

2. In the case of ammonium citrate being the only fuel of SCS process, the only product of the reaction is Mn_2O_3 (Fig. 73A), while in the presence of glycine and urea in the mixture, only Mn_3O_4 is formed. It can be argued that the presence of glycine or urea allows to reach higher temperature during the SCS reaction; alternatively, the decomposition of the intermediates of glycine or urea decomposition consumes oxygen resulting in lower local partial pressure $p(O_2)$. Both factors favorize formation of more reduced oxide, namely Mn_3O_4.

3. Both XRD estimation of crystallite size, measurements of specific surface area, and SEM images points to smaller particles size in the case of nitrate-citrate-urea comparing to nitrate-citrate-glycine mixture. We attribute this effect to faster kinetics of second step of decomposition of nitrate-citrate-urea mixture, in which case formation of larger amount of smaller particles is favored, while particles are less sintered due to shorter reaction time.

- **Electrochemical properties of Mn oxides prepared by SCS**

The CV curves of Mn oxide electrodes measured in 1M NaOH at 10 mV/s are shown in Fig. 74A. One detects a clear difference between the electrochemical properties of oxide samples MnOx-NG, MnOx-NCG, and MnOx-NCU, in comparison with oxide MnOx-NC. According to XRD data, the samples MnOx-NCG and MnOx-NCU contain only Mn_3O_4 oxide, which is also a predominant phase in MnOx-NG (with minor presence of MnO), while MnOx-NC consists of Mn_2O_3 oxide. Thus, observed difference can be attributed to the different electrochemical properties of two different Mn oxide phases.

Mn_3O_4 hausmannite has a spinel structure with Mn^{3+} cations occupying octahedral, and Mn^{2+} occupying tetrahedral sites. Despite mixed valency of Mn cations in spinel structure, it was demonstrated [356] that in aqueous solutions the average oxidation state of Mn at the surface is +3 or slightly above. The typical values of open circuit potential E_{OCP} of Mn oxide electrodes were typically measured as 0.00-0.10 V NHE, confirming that most of Mn at oxide surface are oxidized to Mn^{3+} state.

The CV curves in Fig. 74A are in agreement with previous studies [353,356] of Mn_3O_4, demonstrating clear pair of peaks around 0.15 V vs. NHE, attributed to the following reversible reaction.

$$Mn^{3+}O_x + \delta H_2O + \delta e^- \leftrightarrow Mn^{3+\delta}O_{x-\delta}(OH)_\delta + \delta OH^- \qquad \text{(R4)}.$$

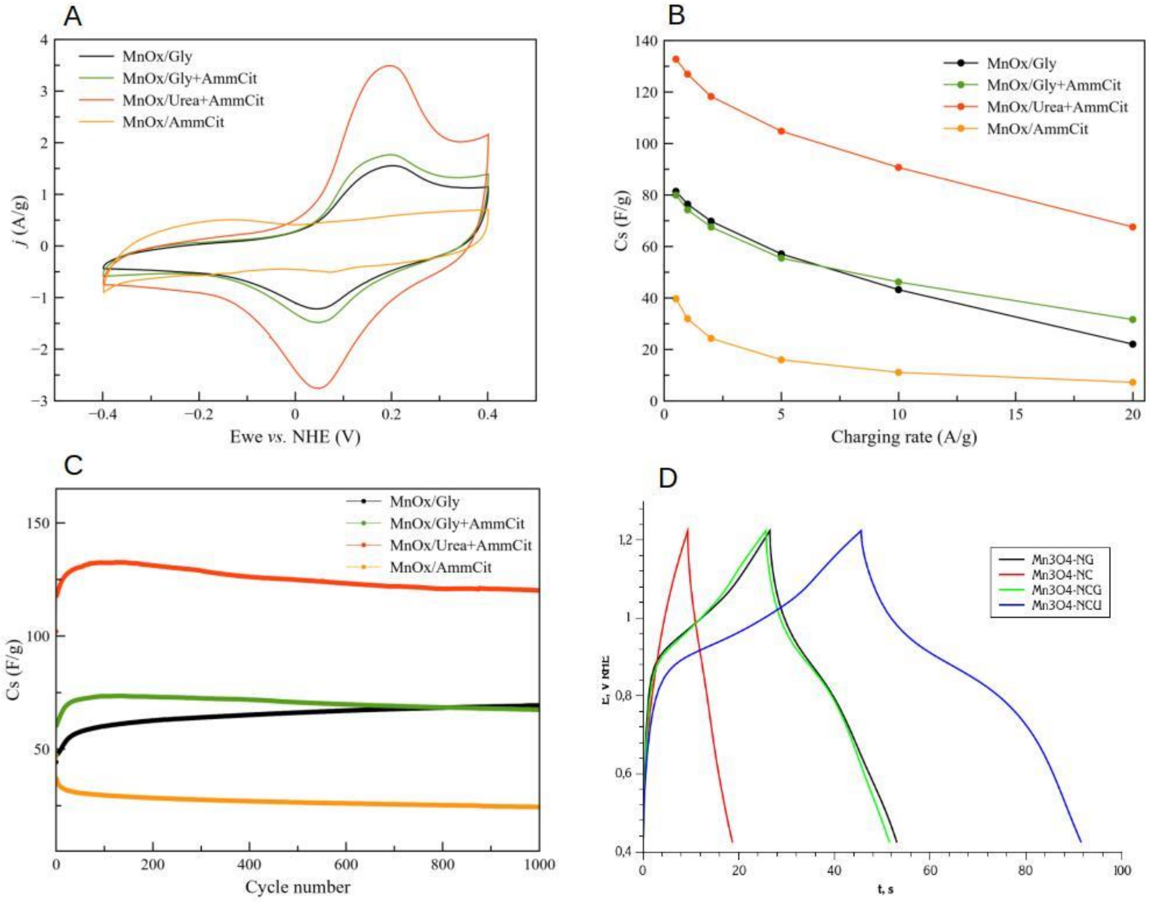

Figure 74: CV curves of MnOx electrode materials in 1M NaOH at 20 mV/s (A) ; dependence of specific capacitance of MnO_x on the charging rate (B) ; evolution of specific capacitance with galvanostatic charging cycling, measured at 2 A/g (C), chronopotentiogramms recorded during the galvanostatic cycling at 2 A/g.

Reaction (R4) can propagate further into the bulk of the oxide particles via solid state diffusion of a proton, thus giving the rise of pseudocapacitance phenomena via intercalation. The profile of CV curves and galvanostatic discharging curves (Fig. 74D) are in qualitative agreement with this mechanism [406]. The analysis of sweep rate dependence of the CV currents by Dunn method (Fig. 75) demonstrated that more than 90% of the CV current recorded at 10 mV/s is proportional to sweep rate and thus can be attributed to a process not limited by solid state diffusion. It confirms that the main charge storage mechanism in the case of Mn_3O_4 particles in 1M NaOH is a reversible pseudocapacitance via proton intercalation.

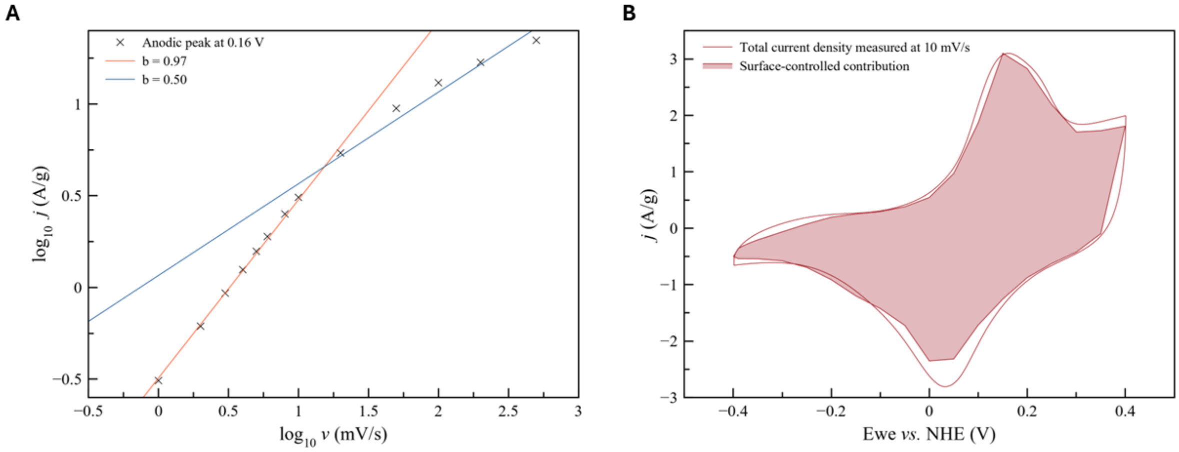

Figure 75: sweep rate dependence of the CV currents by Dunn method (A) with deconvolution of surface-controlled process for Mn_3O_4 synthetized with urea and ammonium citrate at a 10 mV/s scan rate in 1M NaOH (B).

In agreement with previous studies [407], the currents corresponding to reaction R4 in the case of Mn_2O_3 oxide are significantly weaker in comparison with Mn_3O_4 oxides. It has been also observed that the peaks related to reaction R4 of Mn_2O_3 are shifted ca. 40 mV to more positive potentials comparing to Mn_3O_4 oxide, indicating better stability of Mn^{III} sites of Mn_2O_3 towards oxidation. DFT modeling of water adsorption on Mn_3O_4 surface [408] demonstrated that the molecular water adsorption is facilitated on Mn^{II} tetrahedral sites due to their both electronic and geometric configuration. Stronger water adsorption on Mn_3O_4 surface and thermodynamically more facile oxidation of Mn^{III} sites are suggested as the factors explaining much higher currents of reaction R4 detected in the case of Mn_3O_4 oxides comparing to Mn_2O_3.

In contrast to Mn_2O_3, all Mn_3O_4 oxides demonstrate sufficient stability in 1000 galvanostatic cycles at 2 A/g (Fig. 74C). A rapid decrease in charge capacitance of Mn_3O_4 oxides with cycling is a general problem of this oxide electrodes, and is commonly associated to the dissolution of Mn [353,409]. Indeed, we did not detect and changes in crystallographic structure of Mn oxides after 1000 cycles by post-mortem XRD analysis, and, thus, attribute the degradation of capacitance observed for MnOx-NCG and MnOx-NCU samples to dissolution of Mn_3O_4 during galvanostatic cycles. According to Pourbaix diagram of Mn, at potentials below -0.2 V NHE in 1M NaOH one may expect reduction of Mn^{III} to Mn^{II} cations and formation of slightly soluble surface hydroxide $Mn(OH)_2$. This hydroxide is further dissolved in NaOH and can be partially re-deposited upon scan to higher potentials, and partially lost to the bulk of electrolyte. This mechanism may explain better stability of MnOx-NG sample, which contains minor amount of MnO : this oxide is dissolved as $Mn(OH)_2$ in 1M NaOH, thus creating higher local concentration of hydroxide and preventing the dissolution of Mn_3O_4 upon its reduction.

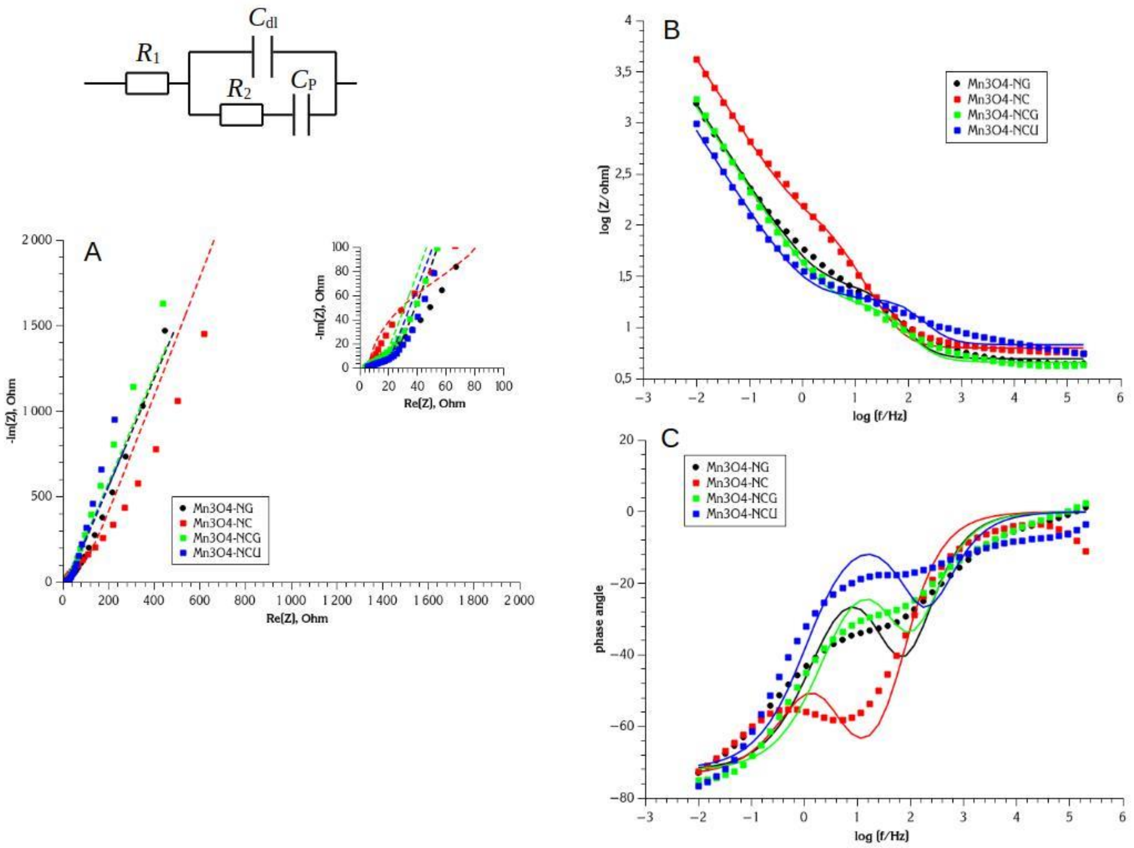

Figure 76: Nyquist plots (A) and Bode plots for total impedance (B) and phase angle (C) of Mn oxide electrodes, measured at 0.05 V RHE after 1000 of galvanostatic charging cycles. The points corresponds to the experimental data, and the lines are model fitting curves obtained with an equivalent circuit depicted above.

All oxide demonstrate a decrease in charge capacitance with an increase in charging rate (Fig. 74B). This decrease is strongest for Mn_2O_3 oxide (MnOx-NC), while it is approximately the same for all Mn_3O_4 oxides. This decrease can be attributed to limitations related to either slow kinetics of reaction R4 and/or diffusion-related limitations of the propagation of this reaction.

The charging rate-dependent electrochemical behavior of Mn oxide the electrochemical impedance spectroscopy has been studied by electrochemical impedance spectroscopy (Fig. 76). The impedance spectra have been analyzed by using an equivalent circuit depicted in Fig. 76, typically applied for pseudocapacitive materials [406]. This model includes the following elements : R_1 resistance, related to an electrolyte resistance between working electrode and point of the measurements of reference electrode potential (typically, the outlet of Luggin capillary); C_{dl}, attributed to the capacitance of electrical double layer at oxide / electrolyte interface; R_2, attributed to the resistance of interfacial charge transfer, reciprocal to the rate constant of interfacial electrochemical reaction related to pseudocapacitance reaction, and C_p, attributed the capacitance of charge storage by pseudocapacitance reaction. As one can see in Fig. 76, this simple model can explain the experimental data only qualitatively, while quantitative deviations can be detected, especially in the middle frequencies range. The deviation can be explained by different accessibility of the surface of electrodes depending on the position along the pore length : indeed, while at high frequencies predominantly pour openings are probed, and at low frequency the whole surface of pores are probed uniformly, frequency-dependent polarization of the signal is expected in the middle frequencies range. The inhomogeneities in surface properties can be partially taking into account by using CPE elements instead of perfect capacitors [339]. Indeed, for C_1, the CPE with constant α=0.95 and for C_2, the CPE with α=0.80 were used for the fitting : it is expected that the inhomogeneities have stronger effect on the processes related to interfacial charge transfer [410–412] , such as pseudocapacitance, than on pure double layer capacitance.

Despite these quantitative inconsistencies, the fitting parameters of the simple model can still be used for the analysis of the differences in properties of different samples. The fitting parameters are listed in the Table 12.

Table 12: *Parameters of fitting of the impedance data*

Sample		R_1, Ohm	C_{dl}, µF	R_2, Ohm	C_p, µF
MnOx-NG	initial	5.3	0.35	22.4	5.11
	after 1000 cycles	4.9	0.37	21.4	5.74
MnOx-NC	initial	5.1	0.33	22.9	2.20
	after 1000 cycles	6.3	0.51	143.5	1.83
MnOx-NCG	initial	4.9	0.45	21.9	6.31
	after 1000 cycles	4.6	0.33	12.9	6.09
MnOx-NCU	initial	9.3	0.45	6.4	12.9
	after 1000 cycles	6.7	0.15	12.5	10.8

The values of R_1 are mostly sensitive to the geometry of the electrochemical cell and contain little information about the properties of electrode level, and, thus, are not further analyzed. The values of C_{dl} and R_2 depend on the interfacial surface area (proportional and reciprocal respectively), while C_p is proporti*onal* to the amount of charge stored both at the interface and, at least partially, in the bulk of the oxide particles. Close initial values of C_{dl} of all oxides are in agreement with their similar values of SSA: noteworthy is that the C_{dl} of MnOx-NCG and MnOx-NCU is bigger than one for MnOx-NG, despite its large SSA. It may indicate that in the case of MnOx-NCG and MnOx-NCU oxides the surface is better accessible for an electrolyte, while the access to some surface of MnOx-NG may be blocked micropores formed by fast sintering of oxide particles.

MnOx-NC (Mn_2O_3 oxide) sample shows the smallest, and MnOx-NCU (Mn_3O_4) shows the biggest pseudocapacitance, in agreement with the data from CV and galvanostatic measurements. After 1000 galvanostatic cycles, the pseudocapacitance reaction on MnOx-NC become much slower, as reflected by strong increase in R_2, and the pseudocapacitance value C_p also decreases. This is in agreement with capacitance loss during the cycling, as shows Fig. 74C for this sample. This decrease cannot be explained by possible dissolution of Mn oxide : in fact, an increase in C_{dl} is detected, demonstrating no significant loss of material. One must assume the changes in the structure and/or composition of Mn_2O_3 surface upon cycling, which may result in a strong increase in interparticle contact resistance, thus further slowing down the kinetics of pseudocapacitance reaction. Similarly to MnOx-NC, a decrease in R_2 is observed also for MnOx-NCU sample, while in this case it can be explained by the loss of available surface area, as reflected by a decrease in C_{dl} value. MnOx-NG impedance data can be interpreted as a slight increase in active surface area (increase in C_{dl}, decrease in R_2) and resulting increase in pseudocapacitance, in agreement with the results of galvanostatic cycling. MnOx-NCG impedance data points to a moderate decrease in its surface area after galvanostatic cycling and in pseudocapacitance values. It is noteworthy that the pseudocapacitance reaction on MnOx-NCG samples seems to accelerate after galvanostatic cycling (decrease of R_2), despite decrease in interfacial surface area, hinting the change in surface morphology and composition. Unfortunately, post-mortem analysis of the samples by XRD and SEM methods did not provide any clear conclusions on the change in their structure of composition : these changes are either too subtle or too surface-confined to be detected by these methods. More detailed study of the processes occurring during the electrochemical performance of Mn oxide electrode materials by using *in situ* (for example, EQCM) and Near ambient pressure *operando* (NAP-XPS) methods are needed and planned for the future work.

The ensemble of electrochemical and physicochemical data allows to give the following tentative interpretation of the difference in structure, electrochemical properties, and cycling behavior of studied samples.

MnOx-NG sample consists of relatively large (ca. 20 nm) particles, which are not strongly sintered because of explosive character of SCS reaction. The explosive character of SCS process is related to the formation of a weak complex between Mn(II) nitrate and glycine, which is easily decomposed upon heating and provide significant exothermic effect for instantaneous self-propagation of the reaction. The final oxide product contains ca. 20%mol. of MnO and 80% of Mn_3O_4, and the presence of MnO is related to the hydrolysis of Mn nitrate during the slow evaporation of solvent before SCS reaction. The MnOx-NG electrode shows moderate charge capacitance (70 F/g at 2 A/g discharge) and very stable performance. MnO oxide is not stable in 1M NaOH and forms hydroxide, which does not contribute to the charge capacitance; however its presence allows to prevent dissolution of Mn_3O_4 oxide upon reduction in the form of Mn hydroxide, which is the main mechanism of this material degradation. The capacitance can be further significantly improved by forming a composite with carbon materials, as it is demonstrated in previous studies [353].

MnOx-NC sample consists of Mn_2O_3 oxide particles of ca. 20 nm, slightly sintered. Citrate forms stronger complex with Mn(II), and its decomposition is not sufficiently exothermic to generate temperature sufficient for Mn_3O_4 formation, which requires ca. 950 °C at $p(O_2)$=0.3 bar. MnOx-NC oxide demonstrate low charge capacitance in 1M NaOH (initially 22 F/g at 2 A/g), which is fast degrading upon galvanostatic cycling. The degradation cannot be explained only by possible dissolution of Mn oxide, but suggests changes in surface structure or composition, which my results in strong increase in contact interparticle resistance.

Addition of an equimolar amount of a fuel, either glycine (MnOx-NCG) or urea (MnOx-NCU), to Mn(II) nitrate - ammonium citrate mixture allows to increase an exothermic effect of the reaction and obtain Mn_3O_4 oxide nanoparticles. Formation of MnO is suppressed by the presence of citrate. The SCS reaction in these cases are slower than in the case of MnOx-NG, and take few seconds. The reaction is slower in the case of nitrate-citrate-glycine mixture in comparison with nitrate-citrate-urea mixture, which is explained by possible interactions between the intermediates of citrate and glycine decomposition. The slower rate of reaction results in more sintered particles in comparison to MnOx-NG synthesis. Nevertheless, MnOx-NCU oxide demonstrate highest charge capacitance due to strong and fast pseudocapacitance phenomena (130 F/g at 2 A/g). The high capacitance of this oxide can be explained by its relatively high SSA, providing fast charging rate, and moderate sintering of particles, decreasing the interparticle contact resistance. Upon cycling the capacitance of both MnOx-NCG and MnOx-NCU after initial increase within first 100 cycles, slowly decays, resulting from the dissolution of Mn_3O_4 upon reduction in the form of Mn(II) hydroxide. Further study of the mechanism of dissolution of Mn_3O_4 particles upon their electrochemical performance is needed to develop the strategy to avoid its degradation

- **Conclusion**

Solution combustion synthesis (SCS) was used and optimized in order to synthesize manganese oxide nanoparticles of various crystallite size and phases using different reactant mixtures. Temperature-dependent diffuse reflectance infrared with Fourier transform spectroscopy (TD-DRIFTS) allowed to study the evolution of IR bands of the reactants and mixtures upon heating as an analogue to the synthesis conditions. It was shown that the mixture of manganese nitrate and glycine resulted in the formation of a weak Mn(II)-glycine complex favorable to the self-propagating SCS process while providing mainly Mn_3O_4 nanoparticles. Nevertheless, some MnO formation is observed due to partial hydrolysis of manganese nitrate during the slow evaporation of the aqueous solvent. However, the addition of ammonium citrate in the mixture, either with glycine or urea, allowed to obtain pure hausmannite phase with crystallite size of ca. 11 and 9 nm respectively. The synthesis reaction appeared slower in these cases with relatively stronger sintering of nanoparticles. The best electrode material was obtained for the Mn(II)-Urea-Ammonium Citrate initial mixture with a specific capacitance up to 130 F/g at 2 A/g in 1M NaOH electrolyte with more than 90% of the total capacitance being under surface-controlled contribution.

- **Overview**

With this second part of research work, it has been shown that manganese oxide spinel Mn_3O_4 as a mesoporous nanostructure can be synthesized by solution combustion synthesis while detailing the formation process of the oxide. This work added knowledge in a possible synthesis route offered by SCS for the production of manganese oxide electrode materials directly applicable to supercapacitor applications. In complementarity with N-doped activated carbons, another type of materials – here a transition metal oxide coming from an abundant element – was presented as a performant supercapacitor electrode materials considering its high surface-specific capacitance (up to >370 $\mu F/cm^2$) due to surface-redox fast and reversible pseudocapacitive effect. Hence, both materials can be very performant depending on their specific application and still be in line with using electrode materials from abundant and low toxicity elements. This work not only showed how to obtain mesoporous Mn_3O_4 nanoparticles but also using an *in situ* TD-DRIFTS technique to assess the formation of this oxide. This characterization technique was here further developed for the specific use of EESD materials synthesis. This work allowed to enrich the global toolbox of available characterization method that could be used for other materials formation but why not directly study the electrode stability upon heating conditions to assess the evolution of the materials constituents by an *in situ* infrared method. Tested initially for supercapacitor applications, this manganese oxide spinel will also undergo test for applications as electrode for rechargeable Li-ion batteries. In link with this study, iron oxide spinel Fe_3O_4 is the other material electrode that will be presented for its EESD implementation.

Chapter 3: Engineering of Iron oxide nanoparticles for pseudocapacitors and lithium-ion batteries

• Abstract

Iron oxide spinels Fe_3O_4 are considered a promising material for electrochemical energy storage devices due its relatively high abundancy, low toxicity and high theoretical capacity of 924 mAh/g. Nanosizing and structural engineering are envisaged to enhance the performance of Fe_3O_4-based electrode by increasing the specific surface area of the material, its number of accessible electrochemical active sites and composites mixing to achieve interesting mechanical robustness. For these reasons, polyol method was employed to synthesize hollow iron oxide raspberry-shaped nanoparticles (RSN) and composites made out of few-layer graphene (FLG). For supercapacitor applications, the composite electrode of $RSN@TA@FLG_{100mg}$ tested in 1M NaOH allowed to obtain very high surface capacitance slightly above >350 µF/cm^2 at slow charge-discharge rate (0.5 A/g) assumed to be done the increased specific surface area and smaller nanograin size compared to the bare RSN sample and, the higher amount of active iron oxide RSN particles compared to the higher SSA $RSN@TA@FLG_{300mg}$ composite. Testing these electrodes as conversion-type negative electrode for rechargeable Li-ion batteries showed very interesting results as well. The addition of FLG, an electronically conductive carbon support, allowed to improve the cyclability of the electrode with better capacity retention, coulombic efficiency and thus reversibility of the conversion reaction. These benefits are translated by the hindered spatial and electronic isolation of the metallic phase iron nanoparticles deposited on the surface of FLG after subsequent cycling. Furthermore, the FLG could be responsible to "overcapacity" by participating as well to the charge storage. Therefore, maximum of 923 mAh/g of capacity could be obtained while retaining 27.0% of this performance after 50 cycles for the $RSN@TA@FLG_{300mg}$ sample.

• Introduction

To achieve the transition towards renewable energy sources and provide access to electricity for all, needs in highly efficient, reversible "green" energy storage devices, such as batteries and supercapacitors, are required[4,5]. Lithium-ion batteries represent a very mature energy storage technology but research is still needed to improve further their capacities and high-current rate applications. Supercapacitors tend to achieve very high power densities but at the expense of lower energy densities. Hence, non-toxic and abundant elements such as iron- electrode nanomaterials are studied to match such requirements in both systems. Nanostructured conversion-type anodes are very encouraged for development due to their higher theoretical capacities than conventional graphite anode (i.e. > 372 mAh/g) for high-rate applications and providing higher potential vs. Li^+/Li to avoid lithium plating[12]. For supercapacitors, the electrochemical properties of transition metal oxides are of particular interest due to their pseudocapacitive charge storage mechanism based on fast, reversible surface/sub-surface redox reactions[13]. Iron oxide spinel, Fe_3O_4, also known as magnetite, is considered a very promising material for both applications due to its abundancy, low toxicity and very theoretical capacitance of ca. 2300 F/g if involving an 8 electron redox process (two Fe^{2+} and one Fe^{3+}). To reach this theoretical value to the closest, nanostructuring of materials appears as one of the most promising way. This would allow to increase the surface-to-volume ratio and thus allowing the iron active surface sites to see its charge storage capacity being enhanced. In addition, engineering of nanoparticles with specific structural designs such as hollow structure could possibly improve the structural integrity of the electrode materials and hence its stability over cycling. This is particularly interesting considering that lithium insertion within the electrode implies volume expansion and hence mechanical stress on the materials implying a loss in stability. It is even more valid for conversion-type electrode materials where the material is going through severe structural changes. Another approach consists in making a composite material of oxide and another supporting materials that could prevent structural changes during cyclings. Different carbon supports can be used in that sense with graphene-type materials being favorized due to its remarkable properties such as high electronic conductivity brought by its *sp*^{2}-carbon core, strong mechanical stability, low molecular weight or even its cheapness and abundancy depending on its method of preparation.

On this work, Fe_3O_4 nanoparticles will be synthesized through a polyol solvothermal method to engineer its structure precisely[413,414]. This soft method particularly known for its low cost, high solubility of metal precursors in a variety of polyol solvents with different properties, high boiling points and coordinating functions for surface modification. Hence, hollow spherical raspberry-shaped iron nanoparticles (RSN) will be synthetized according to an already existing method with some modifications[415]. These particles in the shape of "raspberry" are hollow and composed of small nanograins of magnetite capable of accommodating lithium ions during cycling in sight of reducing the volume expansion and thus maintaining the structural integrity. Additionally, few-layer graphene obtained through a green method consisting of ultrasonication in an aqueous solvent with a green surfactant (i.e. tannic acid) will be used as a supporting conducting material to create iron oxide/carbon composite materials[16]. These compounds will be tested as electrode materials for supercapacitor applications as well as lithium-ion batteries.

- **Materials and methods**
  - Synthesis of iron raspberry-shaped nanoparticles (RSN) and composites with few-layer graphene (RSN@TA@FLG)

Few-layer graphene (FLG)

Few-layer graphene was obtained through an ultrasonication method in aqueous media assisted by tannic acid as a surfactant, giving a black colored 0.1wt.% dispersion. For that, 500 mg of expanded graphite and 250 mg of tannic acid (CAS: 1401-55-4, ACS reagent, Sigma-Aldrich) were added into a 1L graduated glass beaker with a magnetic stirrer. Then, 500 mL of ultrapure MilliQ water (resistivity of 18.2 MΩ·cm at 25 °C, Total of organic compound (TOC) ≤ 1 ppb) was poured in it. The beaker was after that placed in a thermostatic bath (room temperature) onto a stirring plate with a continuous agitation of ca. 1000 rpm creating a small vortex within the dispersion. The ultrasonotrode was immersed in it and ultrasonication was activated for 4 continuous hours at a 25% maximum frequency amplitude with a Branson 450 Digital Sonifier (400 W, 20 kHz). The surfactant assisted sonication allowed to exfoliate the graphene layers and prevent their further restacking in the dispersion thanks to the relatively big structure of tannic acid composed of multiple aromatic rings stacked onto the graphene layers surface with π- π interactions. The hydroxy groups of the tannic acid allow an optimal dispersion in aqueous solvent. Freeze-drying was used to remove water traces when FLG is needed for composite synthesis with the polyol method. For that, approximately 30 mL of FLG dispersion is poured into small glass vials with their lid covered with paper towel and a rubber. These vials are then frozen using liquid nitrogen prior to place them in the adequate freeze-drying machine compartment. The freeze-drying process is done over two nights to ensure complete removal of water solvent. The FLG is after used directly for synthesis or placed into a desiccator to avoid moist contamination.

Raspberry-shaped nanoparticles (RSN)

This method of synthesis has been developed previously to this project by the Dr. Sylvie Bégin-Colin's lab at the IPCMS institute, also part of this project. Helps on the synthesis' method assimilation and characterization were provided by two PhD students of this lab, Théo Lucante and Joana Vaz Ramos. The iron oxide raspberry-shaped nanoparticles (RSN) are synthetized by a polyol method using as an iron precursor 1.63g of iron(III) chloride hexahydrate $FeCl_3{\cdot}6H_2O$ (CAS: 10025-77-1, ≥99% purity, Sigma-Aldrich), 3.6g of urea (CAS: 57-13-6, 99.3+% purity, Alfa Aesar) and 0.24g of succinic acid (CAS: 110-15-6, ≥99.5% purity, ACS reagent, Sigma-Aldrich) in a 100 mL Erlenmeyer flask with a magnetic stirrer. Then, 60 mL of ethylene glycol (CAS: 107-21-1, 99% purity, Thermo Scientific Chemicals) is poured into the flask, covered with a cap and placed onto a magnetic plate with an agitation of 650 rpm for the dissolution of all the reactants for two hours. After that, the flask is sonicated three times 20 min in a sonication bath (changing the water bath each time to remain at a room temperature) to ensure complete dissolution of particles. The solution is then sealed in a Teflon chamber within a stainless steel autoclave. The latter is place in a programmed oven where the temperature is heated at a 1.5°C/min ramp until reaching the temperature of 200 °C and left at this isotherm for 10h30. The autoclave is then cool down to room temperature by removing in it from the oven. The precipitated blackish product is magnetically separated and decanted using a magnet. The dispersion is washed 9 times using a 75 mL mixture of ethanol:acetone in a 50:50 ratio. The obtained dispersion is placed in a small glass vial with ethanol for characterization. As for FLG, the RSN can also be freeze-dried (by changing first the ethanol to water solvent) for specific use such as making of electrode materials for electrochemical measurements.

Iron oxide raspberry-shaped nanoparticles with FLG composites (RSN@TA@FLG)

To make composites, the same protocol as for the synthesis of RSNs is used with some slight differences. First, freeze-dried FLG is weighted (either 100 mg or 300 mg) and put in a 100 mL Erlenmeyer flask with 60 mL of ethylene glycol and a magnetic stirrer. The flask is placed onto a magnetic plate and stirred for two hours at 650 rpm. Then, the same amount as listed above of iron(III) chloride hexahydrate, urea and succinic acid is poured in the same flask and let for stirring for two days. The dispersion is then sealed in a Teflon chamber within a stainless steel autoclave with the same program as before. The same washing step is also applied as well as the freeze-drying process.

- Physicochemical characterization

SEM measurements were done using a Zeiss 2600F microscope with a resolution of 5 nm. Transmission electronic microscopy (TEM) was also used with a Topcon 002B high-resolution transmission electron microscope operating at 200 kV where the samples were deposited on carbon-coated copper grids. XRD measurements were performed by Bruker D-8 Advance diffractometer with Cu Kα source (λ = 1.54184 Å). FTIR measurements were done with a Perkin Elmer Spectrum 100 spectrometer using KBr-based pellets. BET measurements were done using ASAP 2420 Micrometric analyzer measuring N_2 physisorption isotherm at 77 K after degassing the samples at 150 °C for 12 h. Raman spectra were recorded using LabRAM HORIBA ARAMIS spectrometer with CDD detector and laser line from 532 nm / 100 mW (YAG) Laser Quantum MPC600 PSU. XPS measurements were done using Multilab 2000 Thermoelectron spectrometer with Al Kα source (λ = 1486.6 eV). Thermogravimetric analysis (TGA) was performed with Q 5000 TA Instrument under air using platinum crucibles from room temperature to maximum 800-900°C with 5°C/min ramp.

- Electrochemical measurements

Ink preparation

First, a certain amount of oxide powder (active material), Vulcan XC-72 (conductive agent) and Nafion 0.5wt% (binder) is considered and all the products are weighted to obtain a 75:20:5 ratio respectively. The active material and conductive agent are mixed together in an agate mortar. Inks are prepared by adding a desired amount of the prepared mixture in a glass vial and the required volume of MilliQ water (resistivity of 18.2 MΩ·cm at 25 °C, Total of organic compound (TOC) ≤ 1 ppb) and Nafion 0.5wt% to obtain a 2 g/L concentrated ink. The ink is then shaken and sonicated in an ultrasonication bath for 20 minutes.

Ink deposition on glassy carbon rod

The active material was deposited by drop casting onto the surface of a glassy carbon rod electrode of 6 mm radius. The total deposited volume of ink is 75 µL divided by 5 deposition step of 15 µL in which the electrode is dried for 10 minutes in an oven programmed at 80 °C between each step. The loading of active material is approximated to 0.75 mg/cm^2. A final deposition of 15 µL Nafion 0.5 wt.% in mixture of lower aliphatic alcohols and water was added and dried to act as a binder.

Coin-cell assembly for lithium-ion battery test

The assembly and tests were realized by Dr. Régis Porhiel from the Institut de Chimie de Clermont-Ferrand, partner of this global research project, under the supervision of Dr. Katia Guérin Araujo da Silva (team leader) and Malika El Ghozzi (project responsible). The active material and the conductive agent (acetylene black) were first mixed together prior to the addition of 2.5% PVDF in NMP as binder to respect a 80:10:10 ratio. The mixture after mixing was deposited on a 0.5 mm thickness stainless steel disc. The latter was dried under at 60°C for two days in open air and then further dried at 110°C for 24 hours under vacuum before storage in an argon filled glovebox The coin cell was assembled in a glovebox under argon with the following layers: active material's electrode, polypropylene/glass fibers/polypropylene membranes, lithium foil with a 1M lithium hexafluorophosphate $LiPF_6$ salt in a ethylene carbonate/diethylene carbonate EC:DED 1:1 (v/v) solvent (commonly named LP40). The assembled coin was tested for electrochemistry using a Biologic battery cycler apparatus.

3-electrode cell set-up

A 3-electrode cell inside a Faraday cage is used for the electrochemical tests. A 100mL 1M NaOH electrolyte is poured in the cell followed by the addition of a platinum wire with a coil end counter electrode in the compartment separated by a fritted and a mercury/mercurous oxide electrode (Hg/HgO) in 1M NaOH internal solution in the compartment separated by Luggin capillary. The solution in the cell is then purged for at least 30 minutes under N_2 gas. The glassy carbon rod electrode with active material – the working electrode - is placed in a holder and then placed inside the electrochemical cell in order to only have a contact with the surface of the electrode. The N_2 gas is flushing above the electrolyte to keep a controlled atmosphere without O_2. The electrodes are connected to a SP-300 potentiostat from BioLogic.

- **Results and discussions**
    - Synthesis of materials

The details of the synthesis of the iron oxide raspberry-shaped nanoparticles was already presented by former members of the laboratory[415]. The reaction and formation of the RSNs starts with the creation of an amorphous gel after the four hours of reaction in the autoclave. This gel was attributed to an amorphous iron-organic complex structure. Starting from 5 hours of reaction, the gel-like structure is no longer present at the expense of plate-like lamellar structures with no particular shape and some already formed small (ca. 100 nm) of raspberry-shape particles. The plate-like structure disappears after 6 hours and give place to two populations of RSNs with size ca. 100 nm and 200 nm respectively. These RSNs are composed of very small nanograins of approximately 3-5 nm. After 7 hours of reaction, the RSNs size start to average around 250-300 nm and only the size of the nanograins increase further with the reaction time (ca. 5 nm at 9 hours and ca. 25 nm after 13 hours). This size increase is related to the creation of a cavity within the RSNs core making them structurally hollow. The plate-like structure is then referred as an intermediate compound with an intermediate spacing of ca. 1.1 nm without iron hydroxy species detected, comforting the hypothesis that it consists of an iron alkoxide complex with Fe^{3+} and Fe^{2+} bound to the oxygen atoms of a two carbon-chained alkoxide. Starting from 130°C, decomposition of urea into ammonium cations NH_4^+ and hydroxide anions HO^- occurs, basifying the mixture (i.e. pH increase) favorizing the co-precipitation of iron cations into iron oxides. The decomposition of urea is also responsible for the deprotonation of ethylene glycol serving as ligand for iron cations. The plate-like structure after 5 hours reaction is then acting as an iron reservoir inducing the nucleation of already formed RSNs. The final size of the nanostructures is dictated by the complete utilization of the plate-like intermediate after 7 hours of reaction. The further increase in size of the nanograins at prolonged reaction time is due to solubilization of nanoparticle-centered nanograins then recrystallizing on the outside of RSNs. The more accurate composition of the iron oxide spinel is actually $Fe_{3-x}O_{4-x}$ due to some surface oxidation under air (i.e. maghemite Fe_2O_3 presence). Obtention and confirmation of well-crystallized iron oxide spinel hollow raspberry nanoparticles can be seen by the X-ray diffraction characterization as seen in Fig. 77, with no other phase detected.

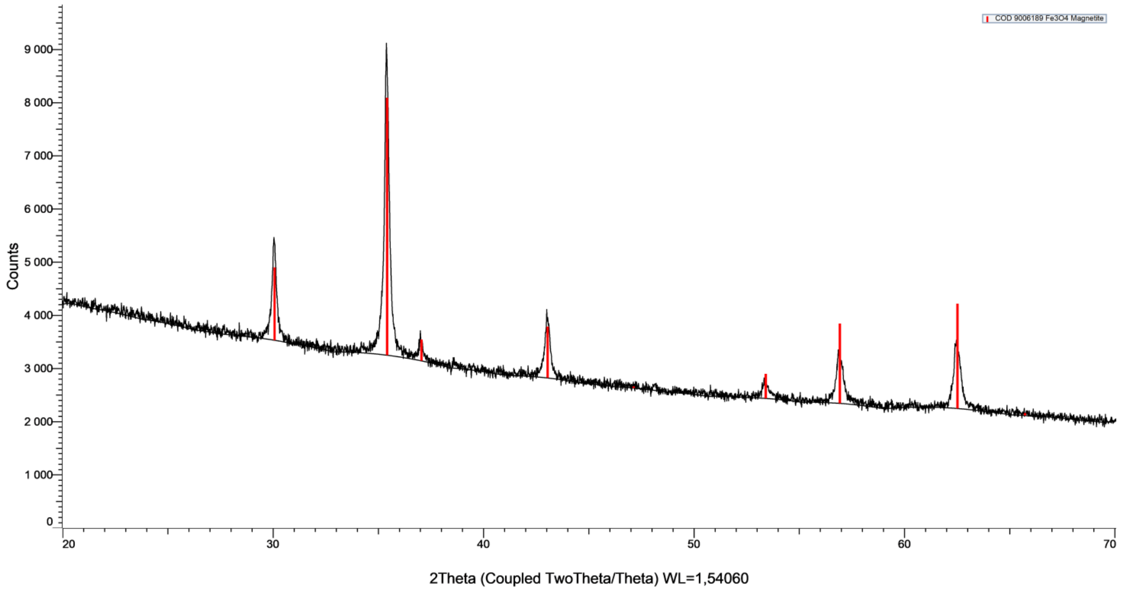

Figure 77: XRD diffractogram of synthetized RSN

In addition, the ability to perform magnetic decantation during the separation/washing steps confirm also the magnetic properties of the obtained particles, in other words, the magnetite Fe_3O_4 presence. The FTIR spectrum, realized with KBr, in the Fig. 78 shows the presence of IR vibrational peaks corresponding to Fe-O bonds but also to some water and ethylene glycol traces presence. Indeed, ν(Fe-O) stretching peak is located around 800-400 cm^{-1}, ν(O-H) broad stretching peak centered around 3500 cm^{-1} and δ(O-H) bending peak around 1650 cm^{-1} for water presence and, $\nu_{symmetrical}$(C-H)/$\nu_{asymmetrical}$(C-H) stretching modes around 3000 cm^{-1}, ν(C-C) stretching and ρ(CH_2) rocking modes from residual traces of ethylene glycol. Further washing steps cannot help getting rid of the latter traces.

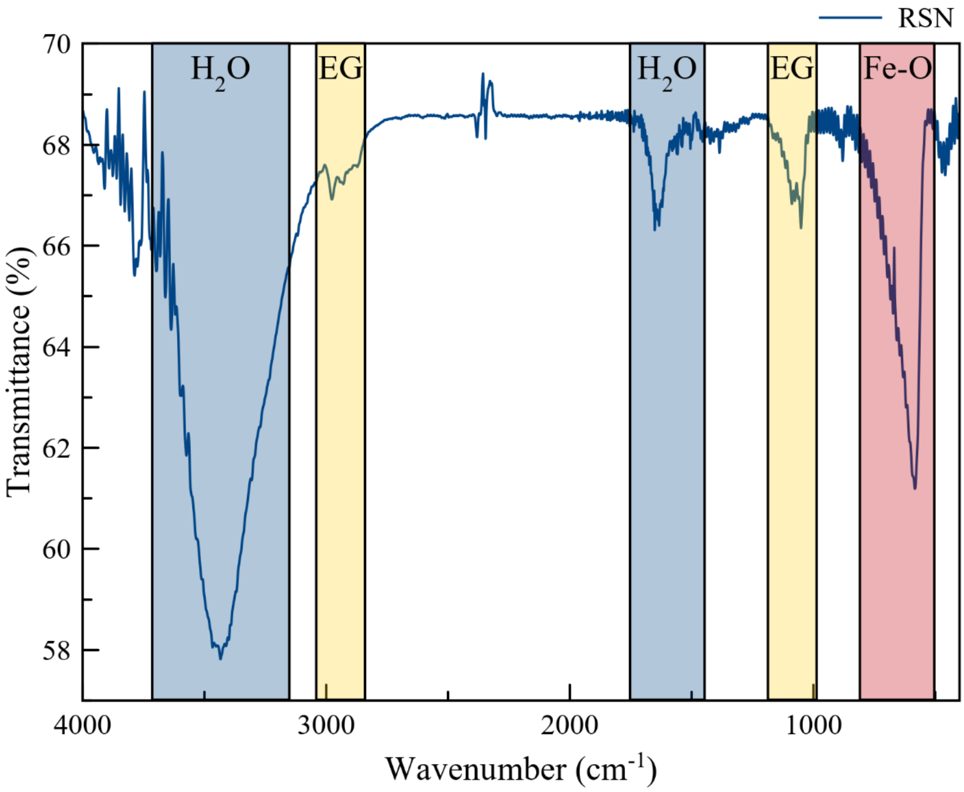

Figure 78: FTIR spectrum of RSN showing the presence of iron oxide but also water and ethylene glycol traces

N_2 adsorption-desorption characterization revealed a relatively small specific surface area of 13 m^2/g from a typical type IV isotherm (Fig. 79A) and showing a macroporous characteristic from the obtained pore size distribution. (Fig. 79B).

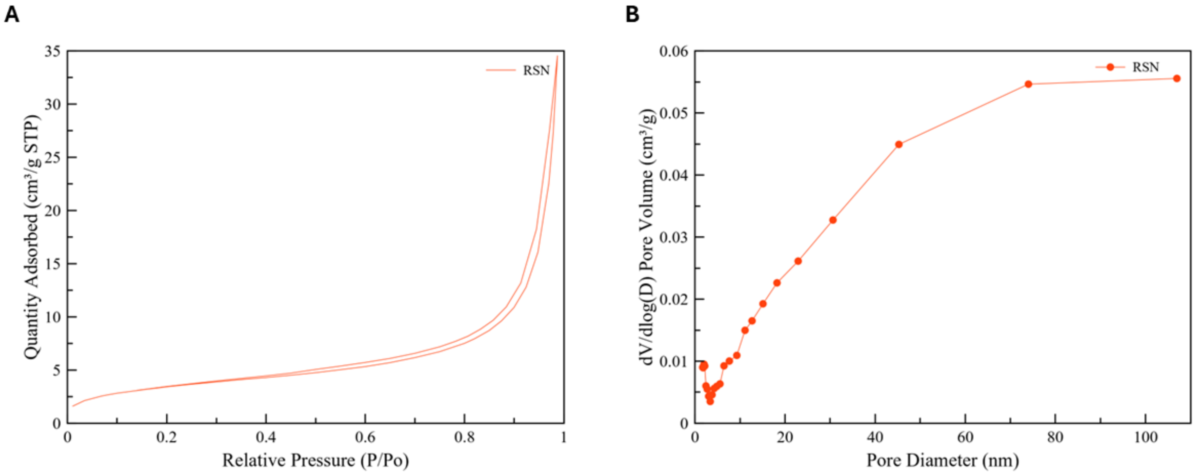

Figure 79: N_2 adsorption-desorption isotherm (A) and pore size distribution (B) of raspberry-shaped iron oxide nanostructures

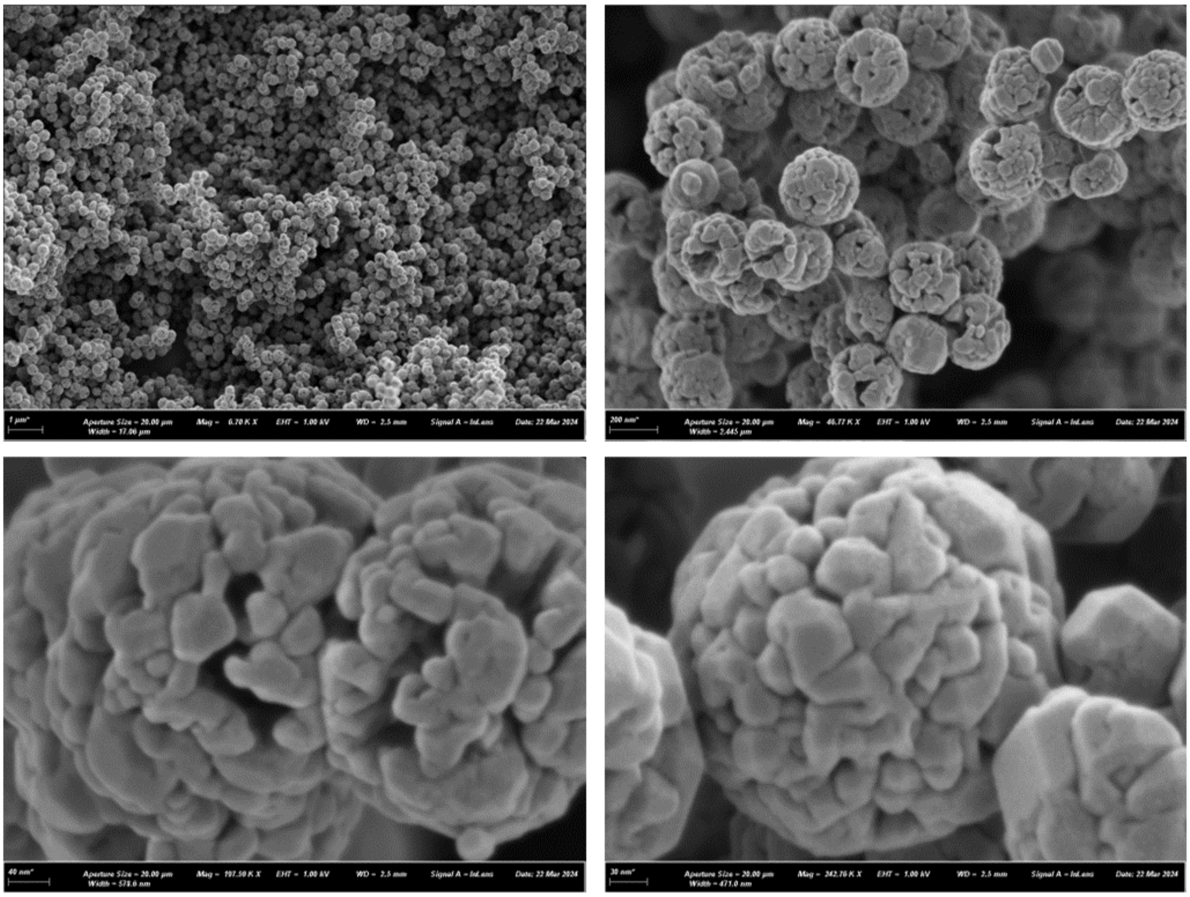

Figure 80: SEM images of bare raspberry-shaped nanoparticles at different magnifications

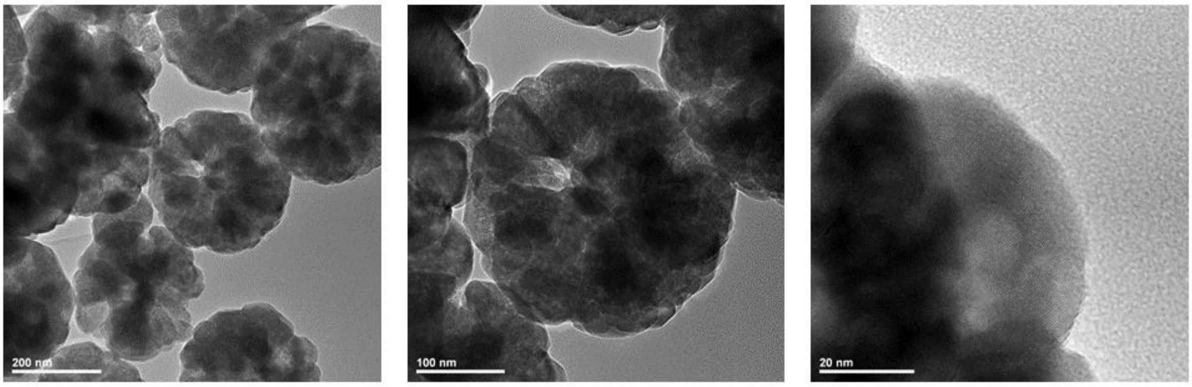

Figure 81: TEM images of bare raspberry-shaped nanoparticles at different magnifications

The images obtained from scanning and transmission electron microscopy (Fig. 80 and Fig. 81 respectively) confirmed the obtention of hollow raspberry-shaped nanoparticles of ca. 300 nm in size composed on nanograins of ca. 25-30 nm.

When synthetizing the composites using few-layer graphene containing tannic acid, RSNs grafted on FLG surfaces is obtained but with some differences in terms of RSN and nanograin size according to the amount of FLG added in the reaction mixture. It has been recently demonstrated from researchers of our lab[416] that the presence of tannic acid will impact the size of the structures for RSN alone and similar impact on the composites are observed in this work.

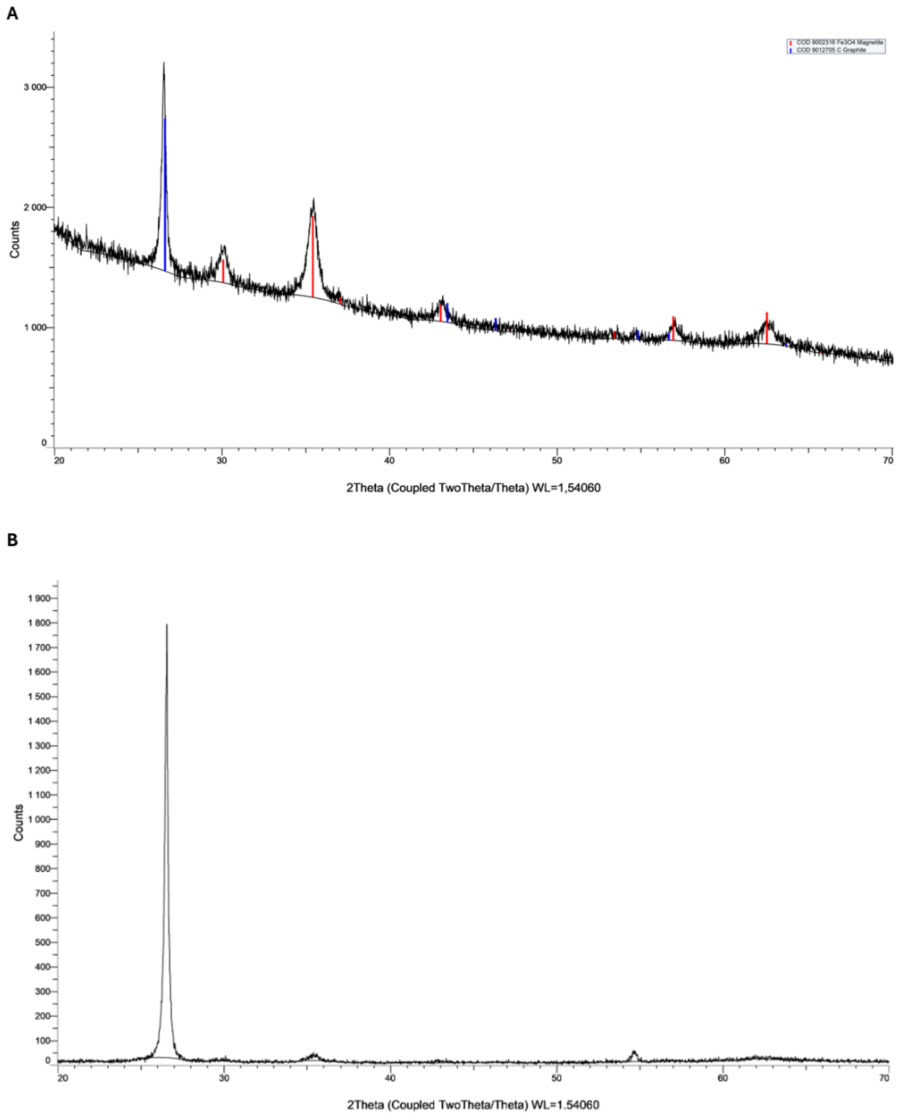

Figure 82: XRD diffractograms of RSN@TA@FLG$_{100mg}$ (A) and RSN@TA@FLG$_{300mg}$ (B)

Two different composites with FLG were made according to the amount of FLG added in the mixture. These samples are referred to as RSN@TA@FLG$_{100mg}$ and RSN@TA@FLG$_{300mg}$ for addition of 100mg or 300mg of freeze-dried FLG respectively. The obtained blackish dispersions were also magnetically decanted and washed multiples times as for the bare RSNs, indicating the highly probable obtention of magnetic magnetite particles. X-ray diffraction diffractograms of these samples are shown in the Figure 82 A and B, respectively. These data confirm the obtention of a composite with FLG with its characteristic graphite (002) peak around 26 2θ° with the most intense for the RSN@TA@FLG$_{300mg}$ sample (higher content in FLG). The presence of magnetite Fe_3O_4 is clearly visible with its diffraction peaks for the RSN@TA@FLG$_{100mg}$ sample compared to the RSN@TA@FLG$_{300mg}$ for which the graphite (002) diffraction peak is overtaking the magnetite diffraction peaks and "hiding" them. This is due to the possible higher content in FLG for this sample. To analyze the ratio between iron oxide raspberry-shaped nanoparticles and the FLG content, thermogravimetric analysis under air was done on both composite samples. The TGA curves of these two composites are presented in the Figure 83 A and B. From these data, the mass ratio of RSN:FLG@TA for RSN@TA@FLG$_{100mg}$ is 80:20 and for RSN@TA@FLG$_{300mg}$ is 48:52. These results are in adequation with the fact that the 300 mg FLG sample should have a higher content in graphitic carbons. Between 230°C and 400°C, the weight loss is associated with the decarboxylation of tannic acid followed by the oxidation of the latter into water, carbon monoxide and carbon dioxide at temperatures above 400°C [417].

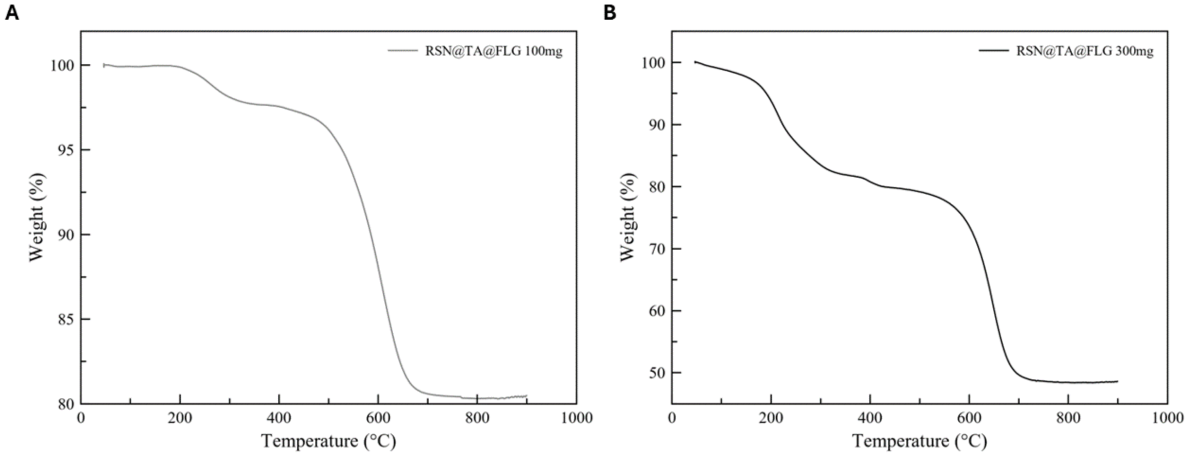

Figure 83: TGA curves of RSN@TA@FLG$_{100mg}$ (A) and RSN@TA@FLG$_{300mg}$ (B)

The well-synthesis of these composites were also confirmed using scanning and transmission electron microscopy techniques. SEM images (Fig. 84) demonstrate the synthesis of raspberry-shaped nanoparticles attached to few-layer graphene for the RSN@TA@FLG$_{100mg}$ sample. Using ImageJ, an image visualization software, a statistical evaluation of the size of the RSN particles onto the FLG surfaces showed the obtention of two populations centered around 325 and 450 nm (Supporting Information 3). These particles appeared well anchored to the FLG layers on both of their surfaces whether in-plane or on the edges.

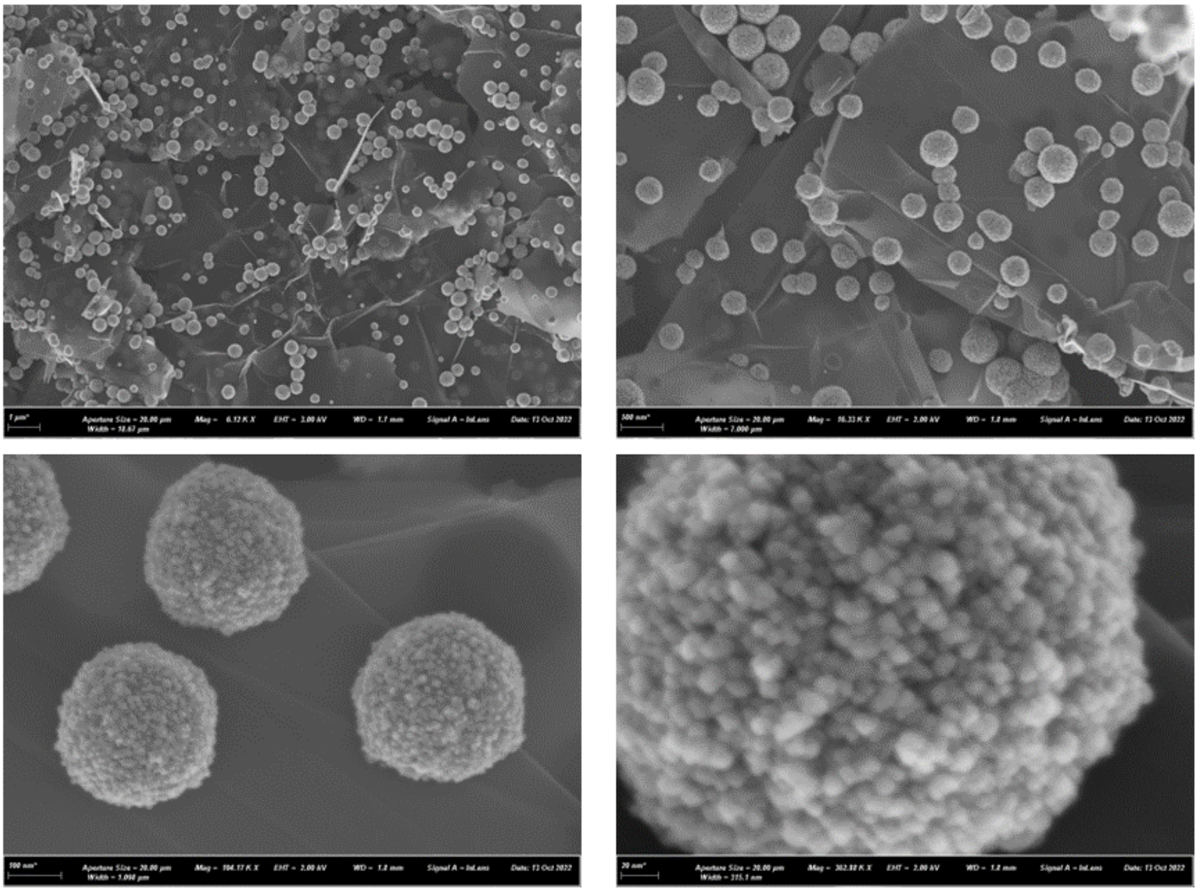

Figure 84: SEM images of RSN@TA@FLG$_{100mg}$ at different magnifications

The TEM images (Fig. 85) show that the nanograins' size is centered around 10 nm – also obtained thanks to statistical analysis using ImageJ (Supporting Information 3) - which is smaller than for the bare RSN nanoparticles' nanograins.

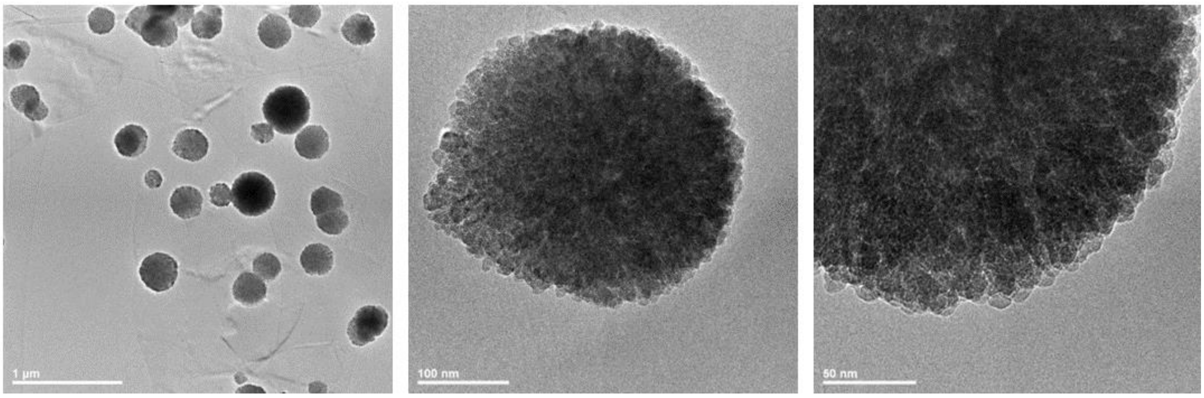

Figure 85: TEM images of RSN@TA@FLG$_{100mg}$ at different magnifications

Concerning the RSN@TA@FLG$_{300mg}$ sample, the SEM images are shown in Fig. 86 and demonstrate an average nanoparticle size centered around 275 nm (see statistical population in Supporting Information 3), so smaller than for the RSN@TA@FLG$_{100mg}$ sample. As for the latter, we can clearly see the presence of raspberry-shaped structures onto the surfaces of FLGs. From these pictures in higher magnification, it is already seen that the nanograins are already smaller than for the previous sample.

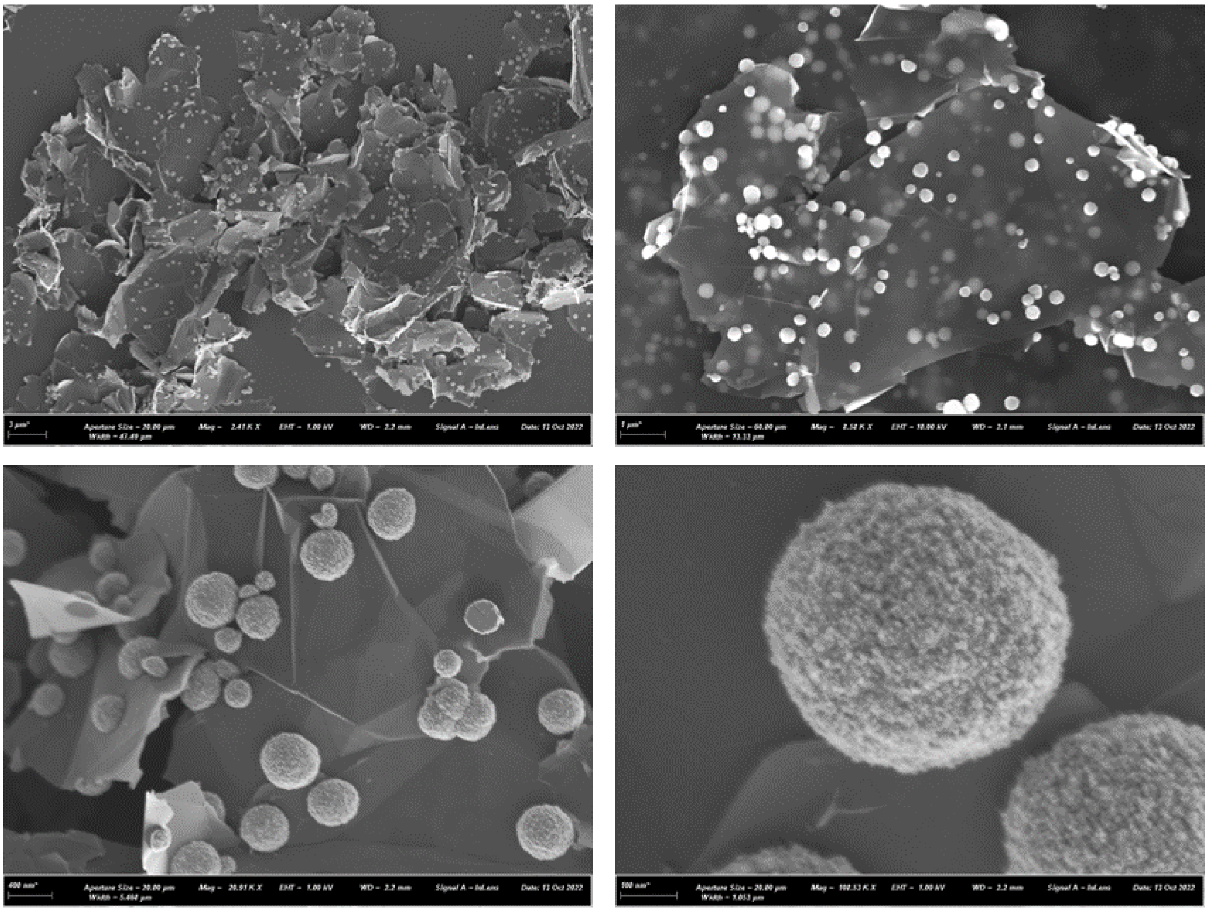

Figure 86: SEM images of RSN@TA@FLG$_{100mg}$ at different magnifications

The TEM images (Fig. 87) for this sample confirm the obtention of smaller nanograins for which its statistical counting resulted in an average population centered ca. 4.0-4.5 nm.

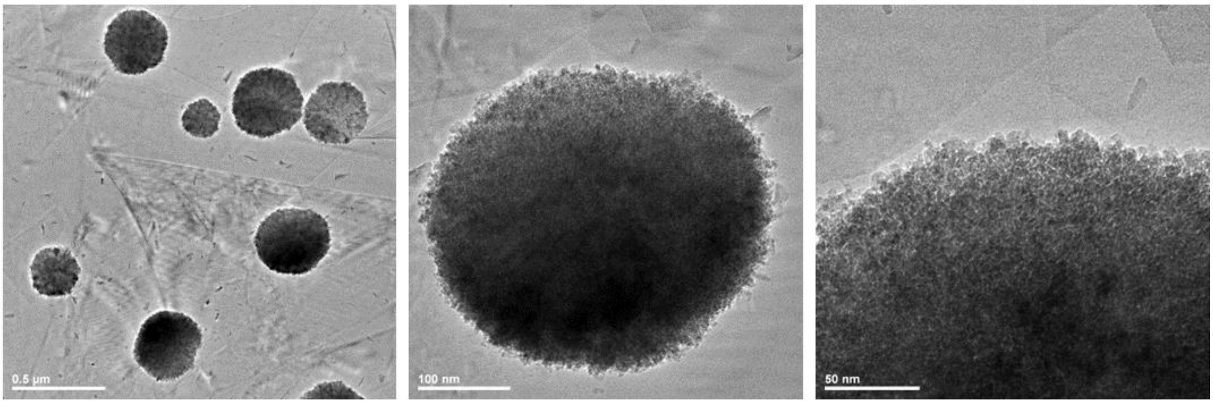

Figure 87: TEM images of RSN@TA@FLG$_{100mg}$ at different magnifications

The overall decrease in the nanograins size and the presence of FLG would imply a relatively higher specific surface area. Indeed, the obtained isotherms from nitrogen gas adsorption-desorption experiments (Fig. 88A and B) show that the RSN@TA@FLG$_{100mg}$ sample has a SSA of 29 m^2/g and the RSN@TA@FLG$_{300mg}$ sample a SSA of 61 m^2/g.

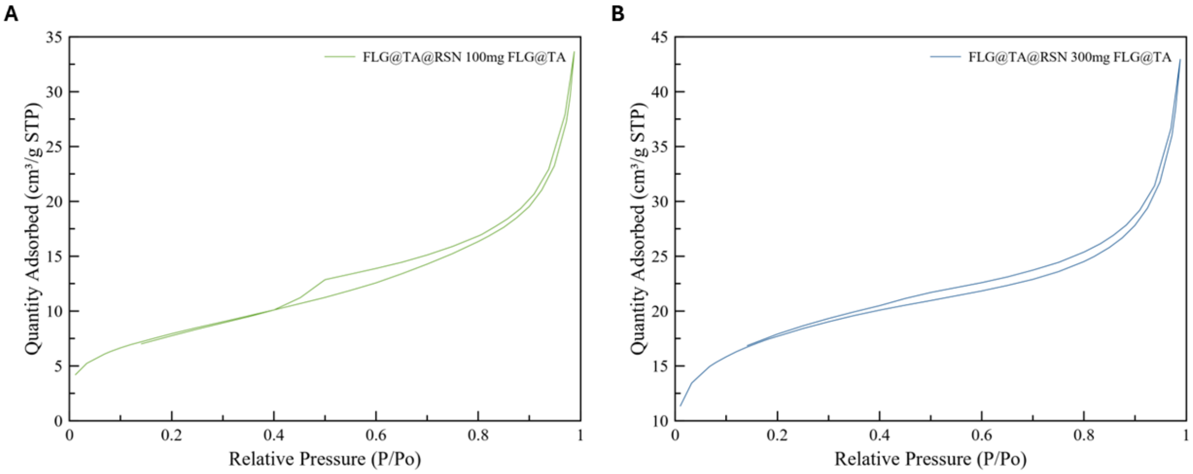

Figure 88: N_2 gas adsorption-desorption isotherms for RSN@TA@FLG$_{100mg}$ (A) and RSN@TA@FLG$_{300mg}$ (B)

Concerning the impact and the presence of tannic acid due to its attachment onto FLG layers since it was used as a surfactant during its exfoliation, it is clear that the more FLG@TA is added in the initial mixture with the reactants, hence more tannic acid, the smaller are the size of the nanograins. As a consequence, a higher specific surface area get be achieved for the composites. In addition, the SEM and TEM images tend to show that an increase in the amount of tannic acid result not only in smaller nanograins but also to a more dense and compact structure. It is noticeable from the SEM images that the for the RSN@TA@FLG$_{300mg}$ sample that the particles are more agglomerated, indicating the binder/”glue” role of tannic acid. The hypothesis on the role of tannic acid would be that the TA molecules would coat the RSN external surface with an accentuated agglomeration of the particles when a high amount of TA is present. Furthermore, the TA molecules would also coat the nanograins themselves to impede their complete overlap, hence creating small spaces between the nanograins resulting in a higher SSA as well. The denser structure of the composites would also suggest that there is no Oswald ripening occurring which was the for the bare RSNs where digestion of internal particles lead to the recrystallization of outer grains, increasing their size and forming a hollow structure. An already mentioned study report the absence of plate-like structure during the synthesis, which acted as an iron-reservoir for the bare RSNs without tannic acid, and hence would impede the growth of nanograins.

- Supercapacitor applications

The supercapacitor application tests were performed in a 3-electrode cell by using a mix of active material (RSN, RSN@TA@FLG$_{100mg}$ or RSN@TA@FLG$_{300mg}$) with Vulcan XC-72 (conductive agent) and Nafion 0.5 wt.% (binder) in a 75:20:5 weight ratio within a water:ethanol (50:50 volume ratio) mixture to obtain an 2 g/L ink. The drop-casted electrode material on a glassy carbon support (0.75 mg/cm^2 loading) is directly tested in a 1M sodium hydroxide NaOH electrolyte bubbled with nitrogen gas to remove traces of oxygen that could interfere with the electrochemical tests. The main electrochemical techniques used to assess the performance of RSN and its composites rely on cyclic voltammetry CV and galvanostatic charging with potential limitations GCPL (or also referred to as galvanostatic charge-discharge GCD). Cyclic voltammetries realized at 10 mV/s for the RSN sample are shown in Fig. 89 A and B, the first one being normalized to the theoretical mass calculated from the amount of ink drop-casted on top of the glassy carbon support (150 µg) and the second one normalized to the SSA of the RSN obtained from BET method thanks to the N_2 gas adsorption-desorption experiment.

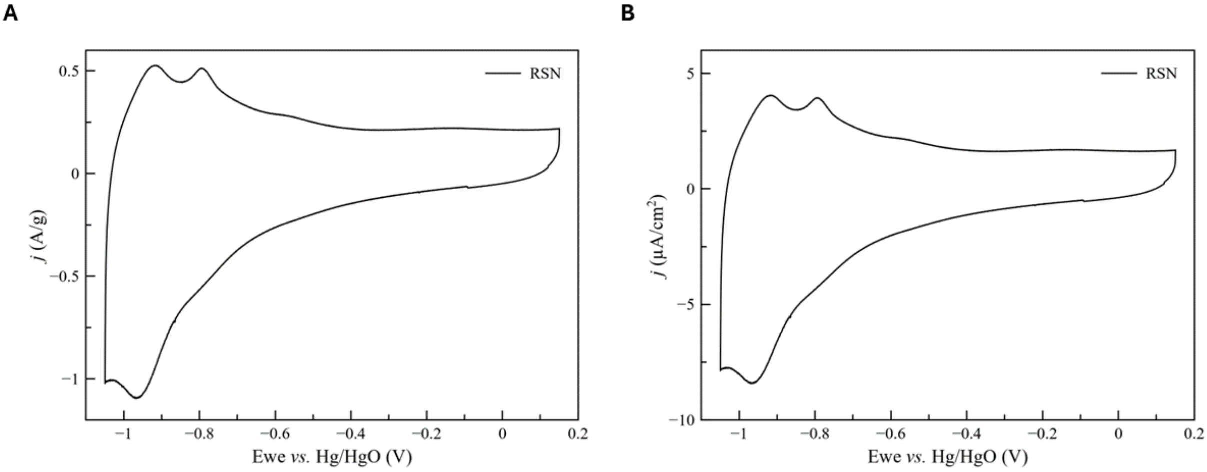

Figure 89: CVs of RSN electrode normalized to the mass of the electrode (A) or to the SSA of the RSN active material from BET analysis (B)

The CV shape indicates the presence of multiple redox transitions mainly located from -1.05 V to ca. -0.45 V vs. Hg/HgO, followed by a more rectangular shape at more positive potential above -0.4 V vs. Hg/HgO. Previous scientific articles reported the signification of such redox transition peaks, responsible for pseudocapacitive effect, in alkaline media for Fe_3O_4 particles[418,419]. The cathodic peak around -0.8 V vs. Hg/HgO would refer to redox transition from Fe^{3+} species to Fe^{2+}, with a more intense second cathodic peak at a more negative potential ca. -0.95 V vs. Hg/HgO representing a Fe^{2+} to Fe^0 transition. Going back to the anodic region starting from the negative potential limit, the first peak corresponds to an intermediate state formation of Fe(OH) around -0.925 V vs. Hg/HgO, followed by an oxidation to Fe^{2+} ca. -0.78 V vs. Hg/HgO and finally a transition to Fe^{3+} ca. -0.6 V vs. Hg/HgO. From the

GCPL curve realized at a charging rate of 2 A/g for 1000 cycles (Fig. 90 A and B). The A panel refers to specific capacitance normalized by the mass whereas the B panel is normalized by the specific surface area of the RSN particle. The dashed line represents the specific capacitance value by only considering the active mass of RSN in the electrode, hence 75wt.% of the total mass of the electrode. In terms of stability, we can see that the upon 1000 cycles, the capacitance is increased by 1.3x factor probably due to the electrochemical activation of the electrolyte. Nevertheless, even if the specific capacitance value of 36 F/g is not very high, the surface-normalized capacitance of 350 μF/cm^2 is quite high, especially compared to carbon materials, thanks to its pseudocapacitive charge storage mechanism and not only an electrical double-layer charge storage.

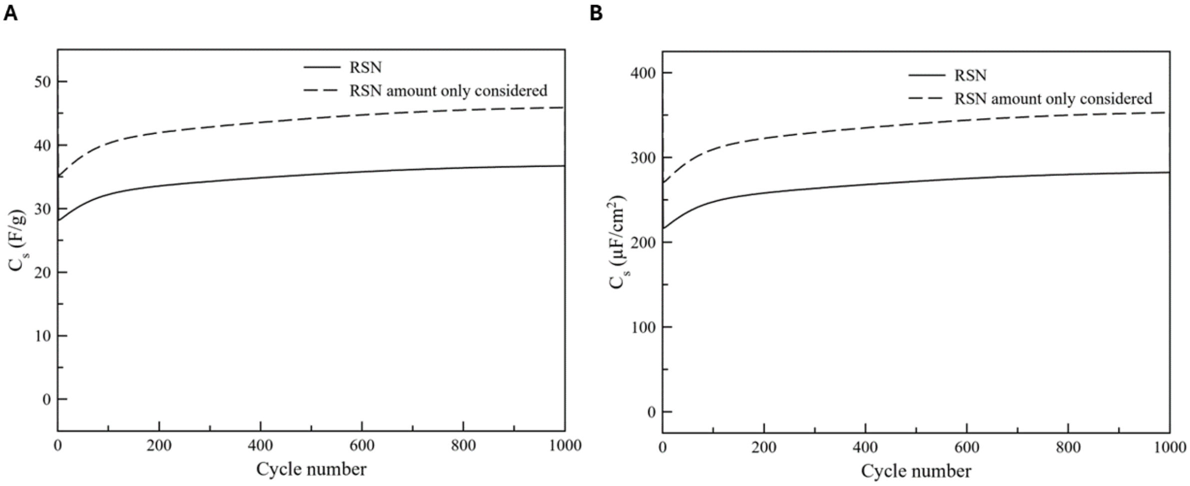

Figure 90: GCPL at 2 A/g of RSN electrode normalized to the mass of the electrode (A) or to the SSA of the RSN active material from BET analysis (B)

GCPL curves realized at various charging rates, ranging from 0.5 A/g to 20 A/g, are presented in Fig. 91 A and B, both being respectively normalized by the mass or the SSA. Values as high as 358 μF/cm^2 or 448 μF/cm^2 are obtained at 0.5 A/g by only considering the RSN amount whereas 192 μF/cm^2 and 240 μF/cm^2 at fast charging rate of 20 A/g. Considering that composites have higher surface area but also lower amount of iron oxide particles due to FLG presence, it will be interesting to compare the data obtained with bare RSN with the composites.

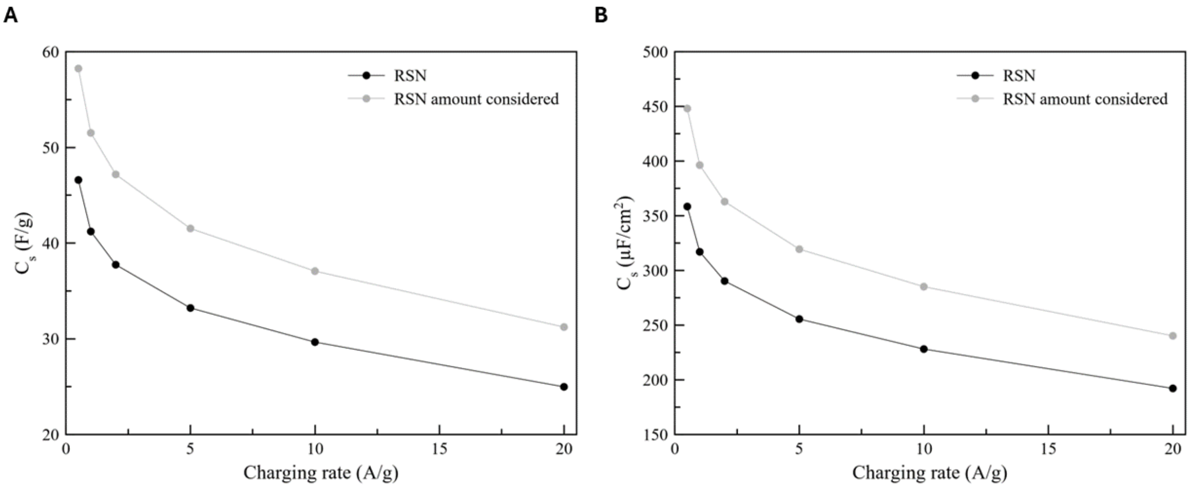

Figure 91: GCPL at various charging rates of RSN electrode normalized to the mass of the electrode (A) or to the SSA of the RSN active material from BET analysis (B)

The Figure 92 A and B represent, as it was the case for RSNs above, the cyclic voltammetry at 10 mV/s for the RSN@TA@FLG$_{100mg}$ either normalized by the electrode mass or the amount of RSN particles, which is in this case 60wt.% of the total mass of the electrode. This value is obtained by multiplying the amount of RSN@TA@FLG$_{100mg}$ within the electrode (75wt.% ratio) by the amount of RSN obtained from the TGA curve (80wt.% ratio). The CV curves present the same characteristic signal as for the Fe$_3$O$_4$ raspberry-shape nanoparticles. However, the current density values are already higher than for the RSN, especially when normalized to the mass of the electrode.

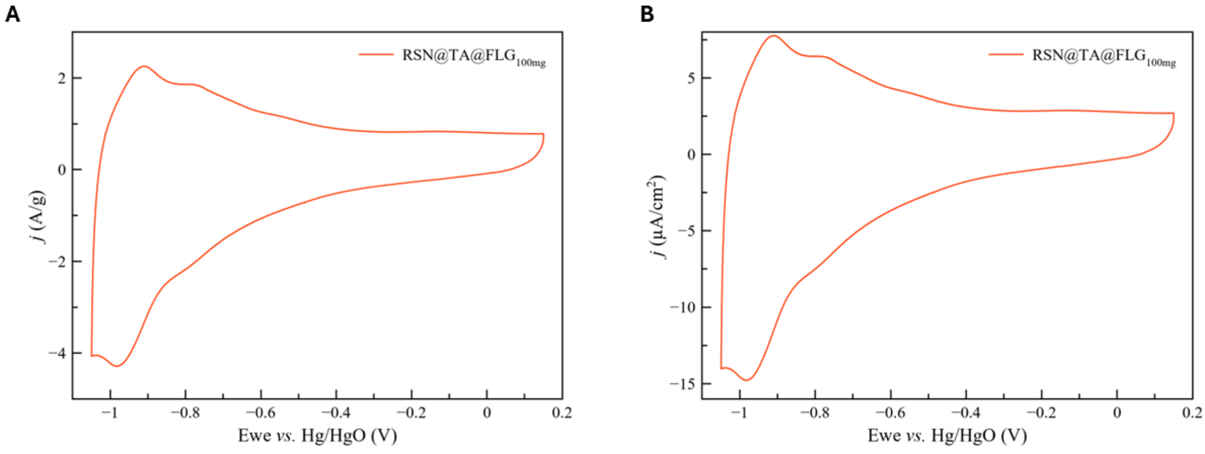

Figure 92: CVs of RSN@TA@FLG$_{100mg}$ electrode normalized to the mass of the electrode (A) or to the SSA of the active material from BET analysis (B)

The GCLP curves at constant charging rate of 2 A/g for the RSN@TA@FLG$_{100mg}$ sample are shown in the Figure 93 A and B. Compared to RSN, the mass-specific capacitance is almost four times higher with a value of 124 F/g (whole electrode mass considered) or 194 F/g (RSN amount considered). Interestingly as well, the surface-specific capacitance can reach up to 427 μF/cm^2 (whole electrode mass considered) or 668 µF/cm^2 (RSN amount considered) which are very high value but this time, two times higher than for the RSN sample.

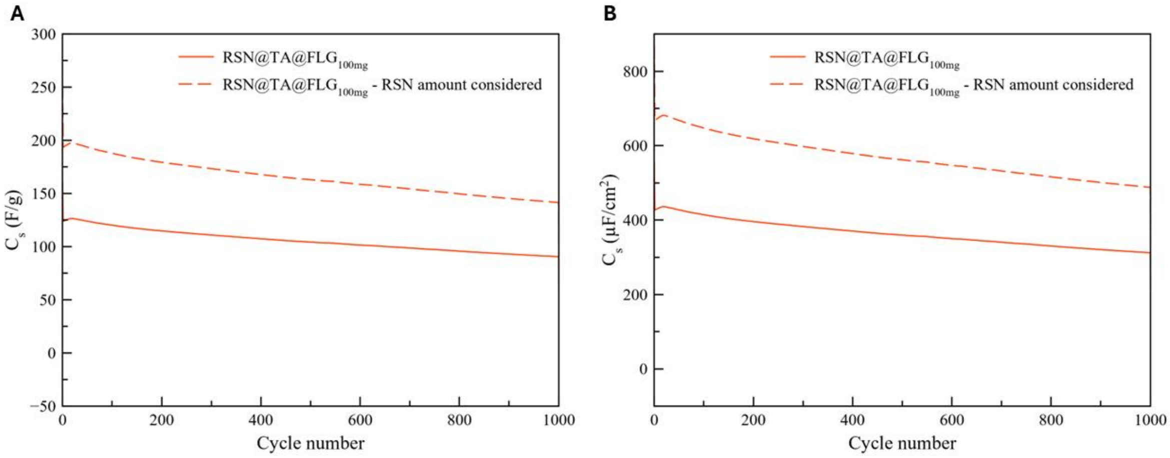

Figure 93: GCPL at 2 A/g of RSN@TA@FLG$_{100mg}$ electrode normalized to the mass of the electrode (A) or to the SSA of the active material from BET analysis (B)

The GPLC tests realized at various charging rates (Fig. 94 A and B) for the RSN@TA@FLG$_{100mg}$ sample show very high capacitance values going from 105 F/g – 361 µF/cm^2 at 0.5 A/g (163 F/g - 564 µF/cm^2 if only the amount of RSN is considered) and 64 F/g – 220 µF/cm^2 (100 F/g - 344 µF/cm^2 if only the amount of RSN is considered). For the mass-specific capacitance, these values are clearly higher than for the bare RSNs but not significantly different when a look is given to the surface-specific capacitance. However, a loss of 26.6% in stability is observed after 1000 cycles.

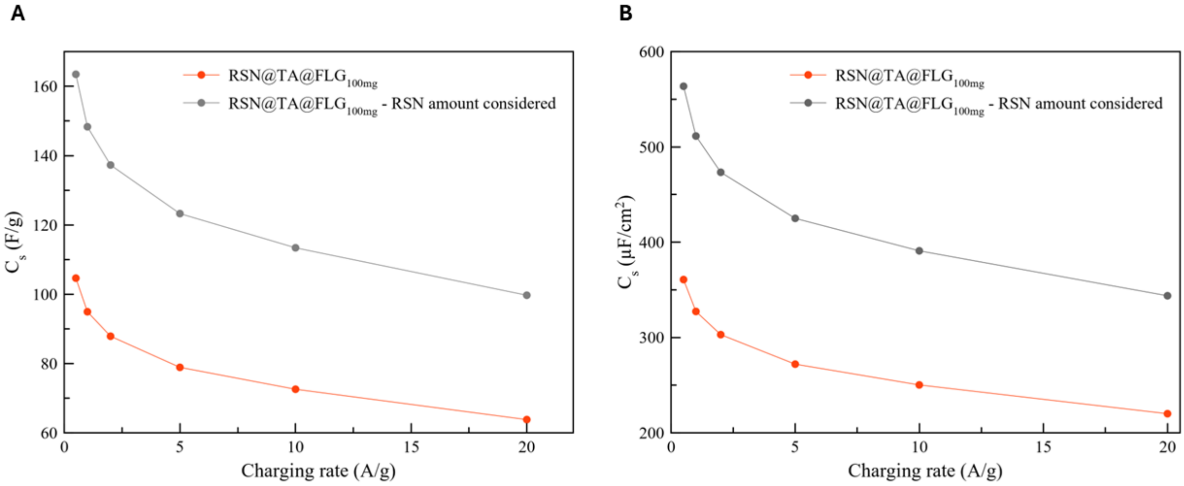

Figure 94: GCPL at various charging rates of RSN@TA@FLG$_{100mg}$ electrode normalized to the mass of the electrode (A) or to the SSA of the active material from BET analysis (B)

Before going into deep comparison between the tests made on RSN and RSN@TA@FLG$_{100mg}$, it will be interesting to also analyze the data obtained for the composite RSN@TA@FLG$_{300mg}$ presenting a higher amount of FLG at the expense of iron oxide nanoparticles but having a higher specific surface area and smaller nanograin size. The cyclic voltammetry measurements of this sample are shown in the following Figure 95 A and B.

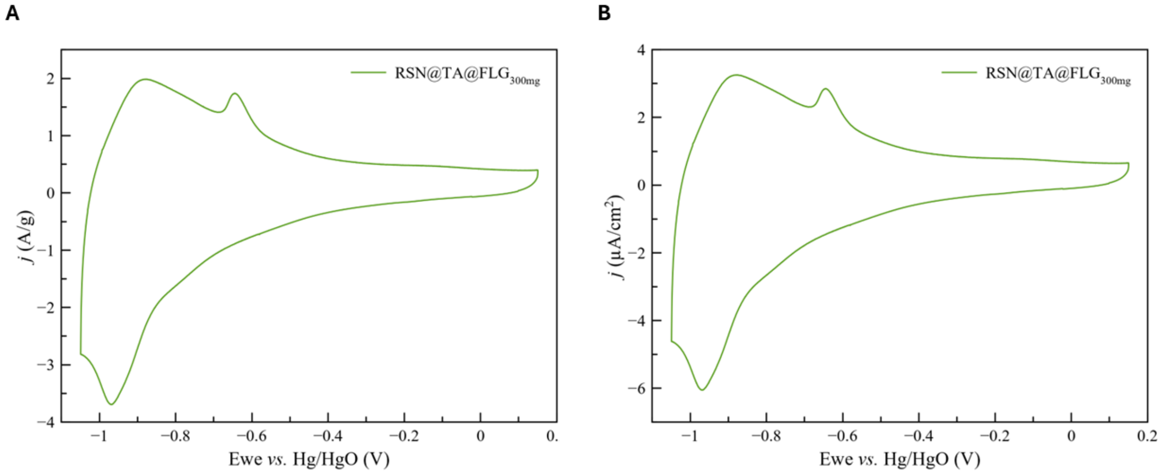

Figure 95: CVs of RSN@TA@FLG$_{300mg}$ electrode normalized to the mass of the electrode (A) or to the SSA of the active material from BET analysis (B)

The different transition peaks observed on the two other samples are still present here. However, the first two cathodic peaks corresponding to the Fe(OH) adsorption and the oxidation from Fe^0 to Fe^{2+} state are less perceptible and appear as a broaden peak. This broaden peak might be explained by the decrease in size of the nanograins from ca. 10 nm to ca. 4 nm that could affect directly the kinetics of these redox transitions. The peak transition to the Fe^{3+} state around -0.58 V vs. Hg/HgO appears more intense than for the other samples.

The GCPL curves at 2 A/g are presented in the Figure 96, showing a specific capacitance lower than for the RSN@TA@FLG$_{100mg}$ sample. Indeed, only up to 87 F/g (219 F/g with only the RSN amount considered) or 138 µF/cm^2 (364 µF/cm^2 with only the RSN amount considered). This difference with the RSN@TA@FLG$_{100mg}$ sample might be explained by the very low amount of RSN present in the composite material of RSN@TA@FLG$_{300mg}$. Indeed, according to the TGA curve, the weight percentage of RSN in the RSN@TA@FLG$_{300mg}$ is only of 48% and considering the 75wt.% ratio presence of the composite in the total mass of the electrode, the RSN amount would be about 36wt.%. Hence, a very low amount of active material is present, that would explain the lower performance in capacitance.

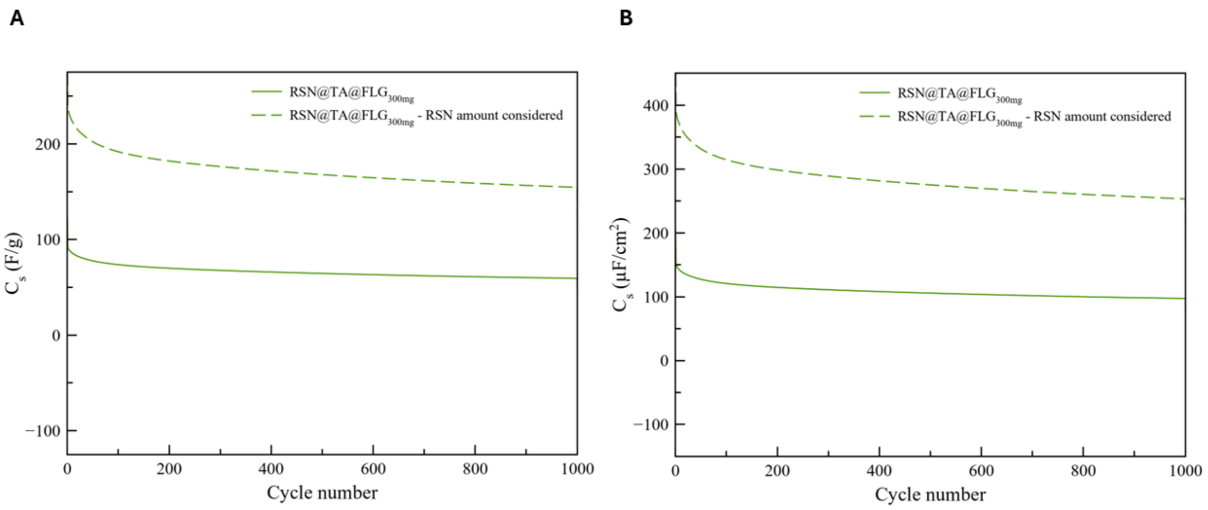

Figure 96: GCPL at 2 A/g of RSN@TA@FLG$_{300mg}$ electrode normalized to the mass of the electrode (A) or to the SSA of the active material from BET analysis (B)

The GCPL test realized at various charging rate comfort this observation as shown in Figure 97. The maximum specific capacitance achievable was only about 68 F/g or 112 µF/cm^2 at 0.5 A/g and 41 F/g or 67 µF/cm^2 at 20 A/g.

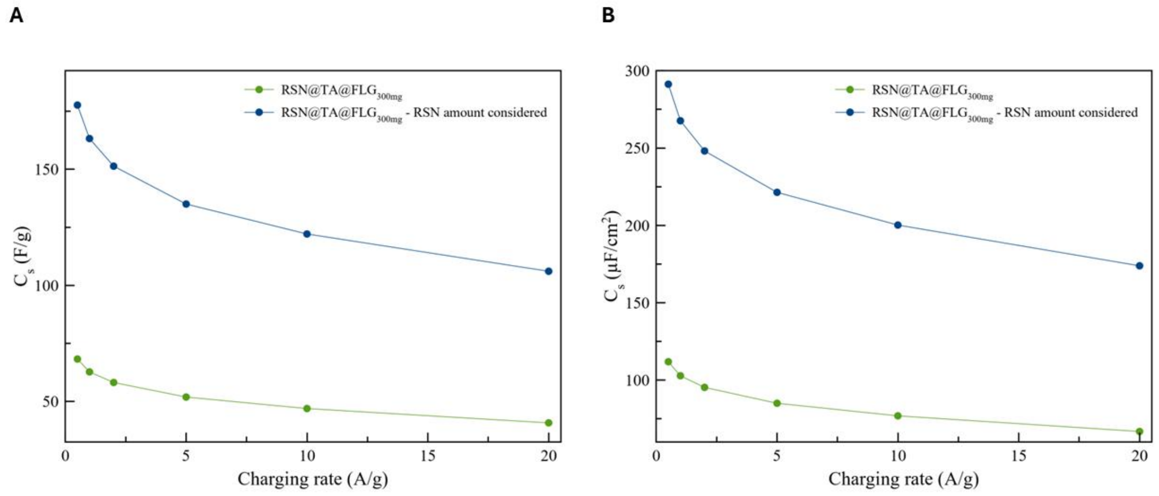

Figure 97: GCPL at various charging rates of RSN@TA@FLG$_{300mg}$ electrode normalized to the mass of the electrode (A) or to the SSA of the active material from BET analysis (B)

These higher performance values could be explained by the higher SSA of 29 m^2/g for the RSN@TA@FLG$_{100mg}$ sample compared to 13 m^2/g for the raspberry-shape nanoparticles alone. In addition, the smaller size of grains and thus a higher surface-to-volume ratio would allow a higher number of active sites for the surface-redox pseudocapacitive effect. This can already be seen from the current density intensities, and hence the aera under the curve synonym to the amount of charge stored/released, from the CVs of all three samples as shown in the Figure 98.

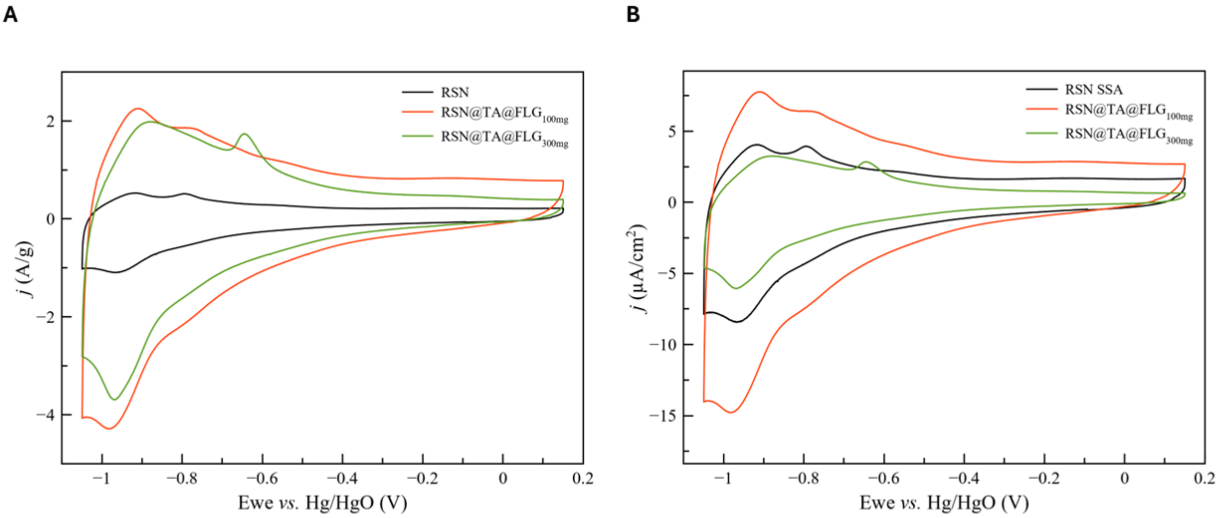

Figure 98: CVs of the different electrodes normalized to the mass of the electrode (A) or to the SSA of the active material from BET analysis (B)

It can be seen from the Fig. 98A that, when compared with the current density normalized to the mass of the electrode (i.e. in A/g), the RSN-based electrode has a very small area under the curve whereas both composites are similar. However, the RSN@TA@FLG$_{100mg}$ sample has clearly a higher charge storage capacity when we look at the Fig. 98B panel with the current normalized to the SSA of the active material. From this sample, it is interesting to note that the bare RSN electrode can store higher charge than RSN@TA@FLG$_{300mg}$. More information are given when a look is given to those electrode performances using the GCPL methods. At constant current cycling of 2 A/g for 1000 cycles (Fig. 99 A and B).

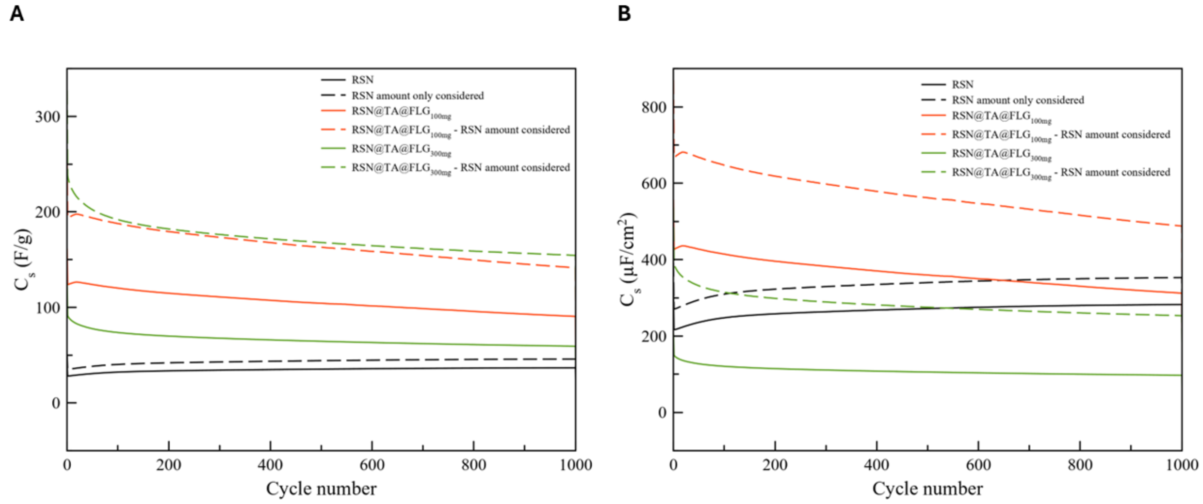

Figure 99: GCPL at 2 A/g during 1000 cycles of the electrodes normalized to the mass of the electrode (A) or to the SSA of the active material from BET analysis (B)

If we only give a look at the Fig. 99A panel, the mass-specific capacitance is the highest for the RSN@TA@FLG$_{100mg}$ sample, which was already expected from the comparison of the CVs at 10 mV/s.

However, if we only consider the amount of RSN in the electrode, both composites have relatively the same specific capacitance performance, indicating the improvement of performance by the formulation of FLG-based composites. When a look is given to test at surface-normalized performances (Fig. 99B), the RSN@TA@FLG$_{300mg}$ appear as the least performant whereas the RSN@TA@FLG$_{100mg}$ is still the superior one. Nevertheless, the decay in stability of RSN@TA@FLG$_{100mg}$ tend to join the performance of the bare RSN electrode. Considering now the tests at various charging rates (Fig. 100 A and B), the RSN@TA@FLG$_{100mg}$ is still the most performant electrode and the bare RSN the lowest if we only look at the mass of the electrode and in terms of mass-specific capacitance. With only taking into account the mass of RSN in the electrodes, the RSN@TA@FLG$_{300mg}$ sample is slightly superior to the RSN@TA@FLG$_{100mg}$ electrode, both outperforming the RSN electrode. The tendency is different when considering the surface-specific performance (Fig. 100B). With the totality of electrode, the same tendency as for GCPL test at 2 A/g for 1000 cycles appear with the RSN@TA@FLG$_{300mg}$ being the least performant and the RSN@TA@FLG$_{100mg}$ being only slightly better than the bare RSN electrode. With the RSN amount considered, the RSN@TA@FLG$_{100mg}$ would appear by far superior to the other materials, followed by the RSN and in the last the RSN@TA@FLG$_{300mg}$ sample.

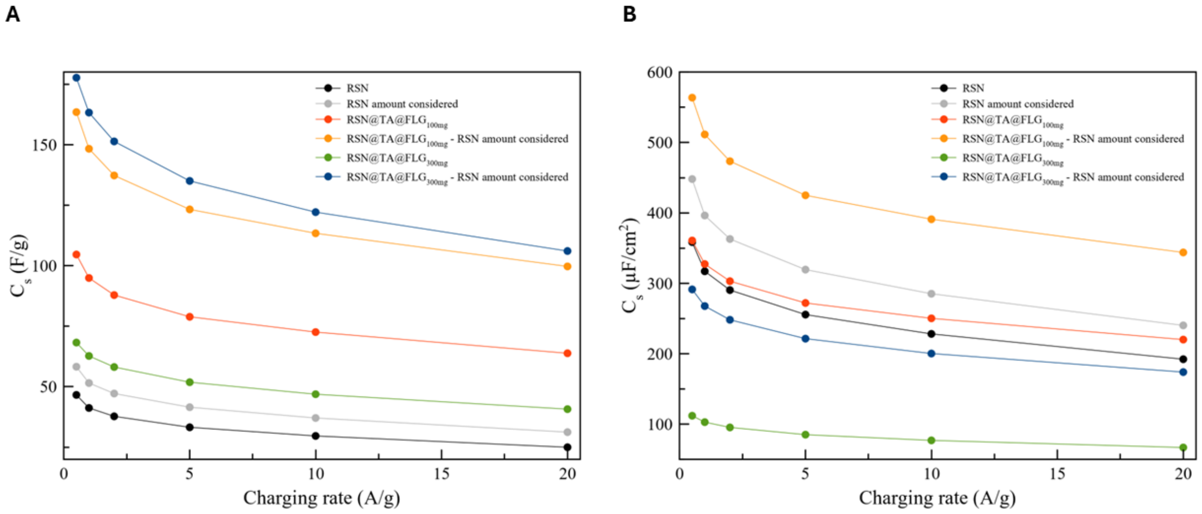

Figure 100: GCPL at various charging rate of the electrodes normalized to the mass of the electrode (A) or to the SSA of the active material from BET analysis (B)

Thus, increasing the SSA of the active material is not necessarily synonym of higher performance as we can that the RSN@TA@FLG$_{100mg}$ sample despite having a smaller SSA and slightly bigger nanograin size than RSN@TA@FLG$_{300mg}$, the former is more performant than the latter if the whole electrode mass and constituents (i.e. active material, conductive agent and binder) are considered, which is the most realistic case application of a supercapacitor electrode. However, at slow charging rate and by considering the surface of material instead of its mass, the RSN performance is close to the RSN@TA@FLG$_{100mg}$ composite, the latter being still more performant. The latter statement is true especially at higher charging rates (>10 A/g) with less loss in capacitance due to faster charge/discharge kinetics potentially due to smaller nanograins but also the support by the electronically conductive FLG.

- Conversion-type anode for Li-ion batteries

These materials are also very promising for usage in lithium-ion batteries by using them as conversion-type anode (or also called negative electrode). As stated in the introduction, the complete reduction of a Fe_3O_4 particle could result in very high theoretical capacity (ca. 926 mAh/g) considering that a complete electrochemical reduction of magnetite would involve an 8-electron exchange reaction:

$$Fe_3O_4 + 8Li^+ + 8e^- \rightleftarrows 4Li_2O + 3Fe$$

To test these materials, different electrochemical configurations are needed since it is involving the use of metallic lithium as a pseudo-reference electrode. The assembly of coin cells is done in an argon-purged glovebox. Prior to the assembly, the electrode were prepared by the protocol presented in the "Materials and methods" section. Formulated electrodes of RSN, RSN@TA@FLG$_{100mg}$ and RSN@TA@FLG$_{300mg}$ before assembly are presented in Fig. 101 A, B and C respectively.

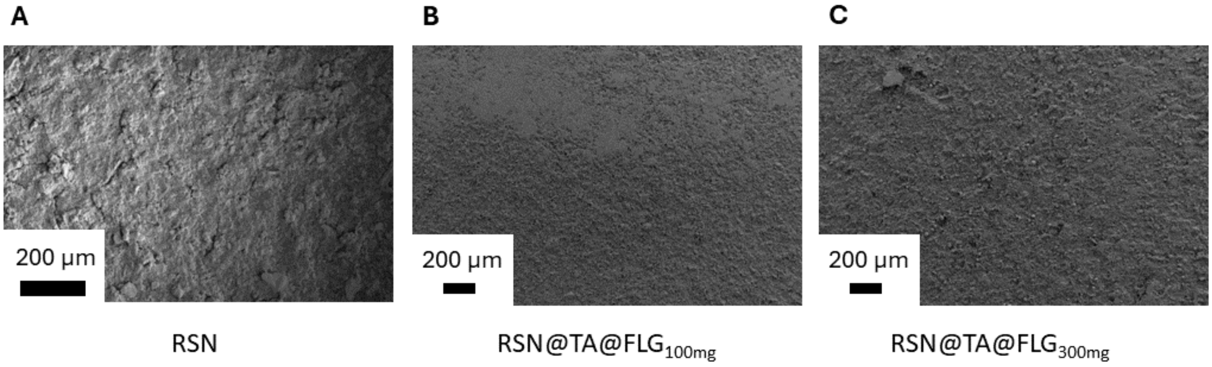

Figure 101: SEM images of freshly formulated electrode materials of RSN (A), RSN@TA@FLG$_{100mg}$ (B) and RSN@TA@FLG$_{300mg}$ (C)

First, a look is given to the test realized on the RSN electrode before checking the composites. A first galvanostatic charge/discharge (GCD) profile of the RSN electrode as well as its discharge capacity and coulombic efficiency at a C/20-rate and D/20-rate (i.e. a 20-hours discharge) are presented in the Fig. 102 A and B respectively. This experiment was done to analyze the electrode structure and morphology before and after few cycles only. For the first five cycles shown, the first discharge capacity can reach more than 740 mAh/g but rapidly decay to ca. 520 mAh/g after five cycles with approximately a 28.8% loss in capacity.

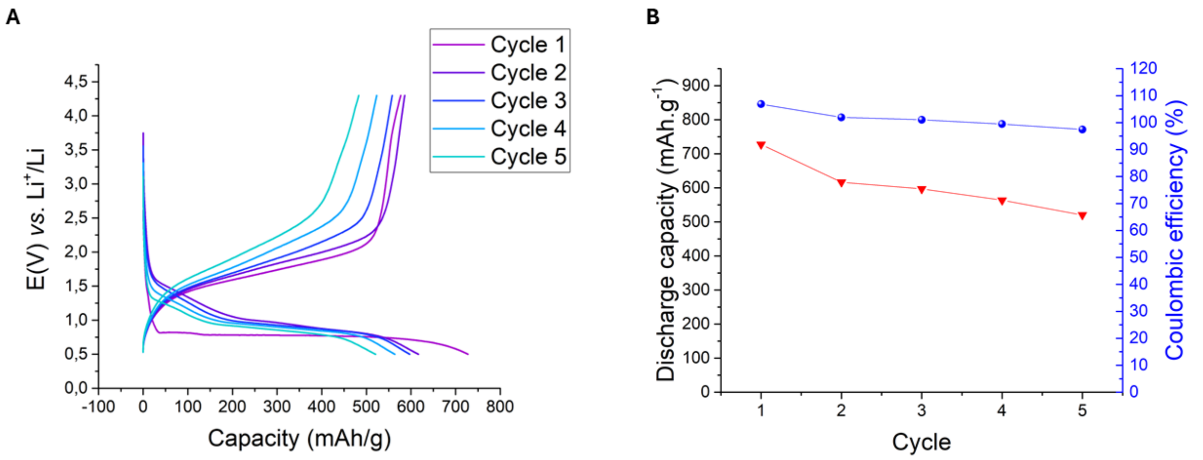

Figure 102: GCD profile realized at D/20 rate (A) and plot describing the evolution of the discharge capacity and coulombic efficiency for five cycles (B) of RSN electrode

Cyclic voltammetry at a scan rate of 0.05 mV/s was also realized for few cycles to assess the different transition occurring during charge and discharge. According to some in-depth studies made on Fe_3O_4 particles[119,420], iron oxide spinel can undergo an intercalation process for a lithium ion intercalation up to x=1, forming lithiated iron oxide of rock-salt structure:

$$Li^+ + e^- + Fe_3O_4 \rightleftarrows LiFe_3O_4$$

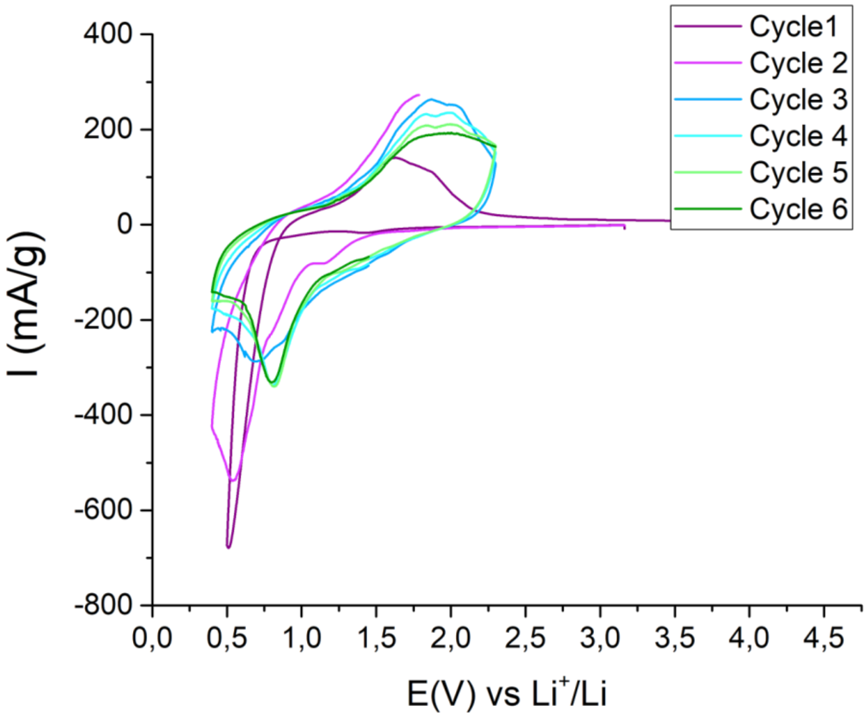

Figure 103: CVs at 0.05 mV/s of the RSN-based coin-cell

For subsequent lithium insertion, a competition occurs between the intercalation process with the formation of the $Li_xFe_3O_4$ rock-salt structure (with x<2) and the conversion reaction leading to Fe^0 and Li_2O formation. These two reactions overlapping for same single iron oxide spinel nanoparticle would lead to a difficult differentiation in the discharge curve. Nevertheless, the following conversion reaction is not totally reversed after the first lithiation cycle, with the main phase responsible for subsequent charge-discharge cycles being the rock-salt phase directly reacting with the metallic Fe^0. These observations, accompanied with the volume expansion of the electrode material upon the conversion reaction, explain the difference observed in the CV curves after the first few cycles and the rapid decay in capacity. In addition, the lithium oxide particles would kinetically hinder the reversible oxidation reaction of isolated Fe^0 nanoparticles. This decay and loss in performance is clearly observable not only after five cycles but tend to complete loss performance after tens of cycle as seen in the Figure 104.

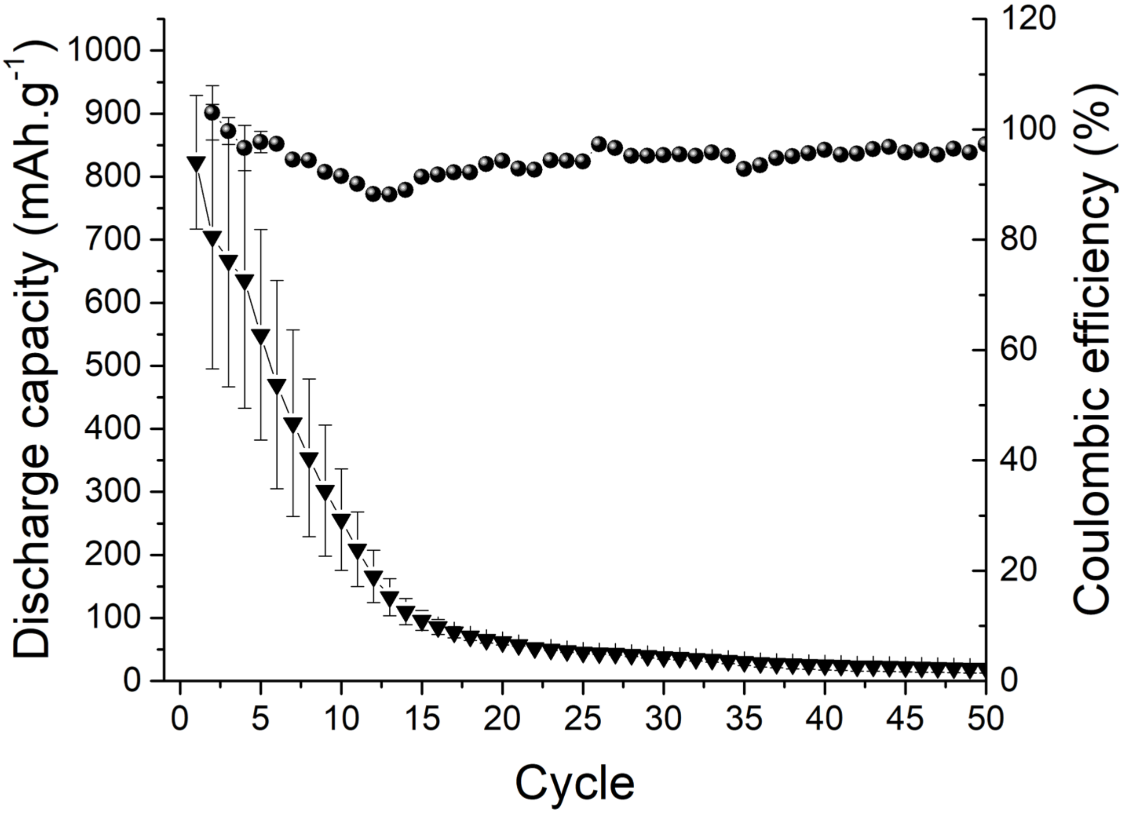

Figure 104: Plot describing the evolution of the discharge capacity and coulombic efficiency for 50 cycles (B) of RSN electrode

SEM images (Fig. 105) of the electrode before and after five cycles of cyclic voltammetry at 0.05 mV/s comforts the hypothesis stated above saying that the volume expansion of the electrode materials would end up as “destroying” the active material with mechanical fracture of the structure accompanied by the isolation of the metallic phase of iron during the completion of the conversion reaction. From these images it is evident that the raspberry-shaped nanoparticles, well-shaped in high magnification, did not retain their structure even after five cycles and electrode cracking is visible at low magnification.

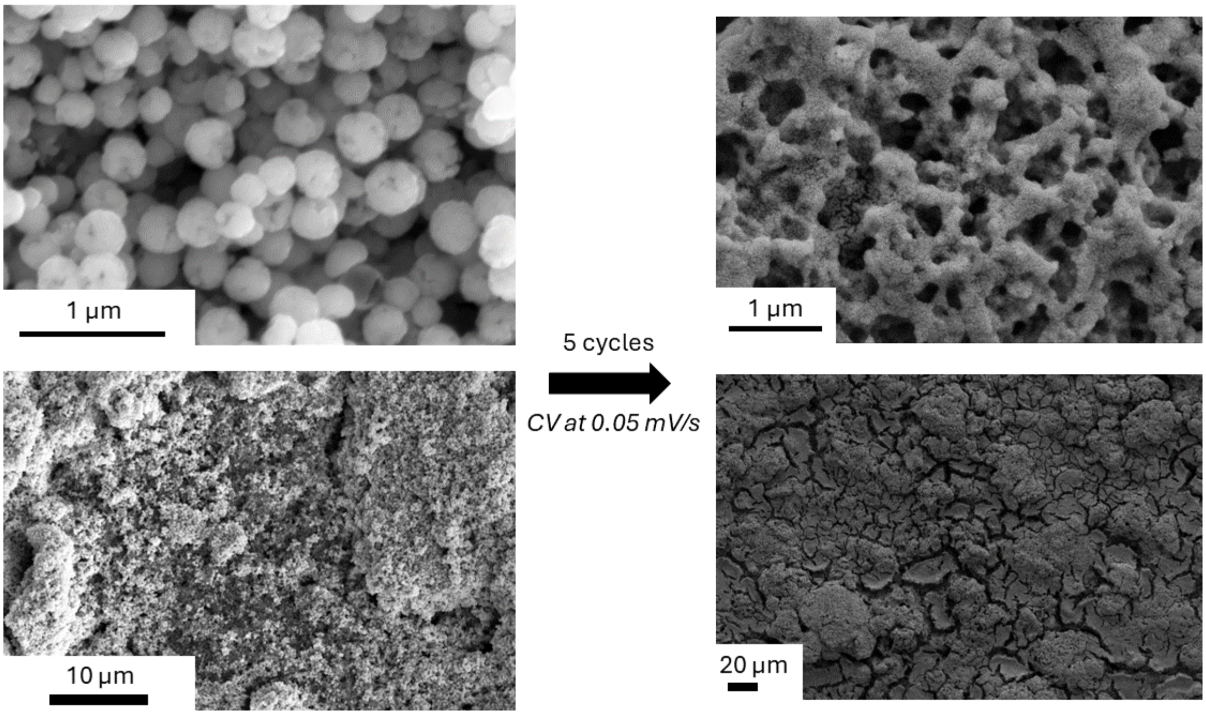

Figure 105: SEM images of RSN-based electrode before and after five cycles at 0.05 mV/s

The addition of FLG as an electronically conductive support could prevent the isolation of the metallic iron nanoparticles during the conversion reaction and hence, enhance the reversibility towards the oxidation reaction into iron oxides. The GCD curves of the RSN@TA@FLG$_{100mg}$ are presented in the Fig. 106.

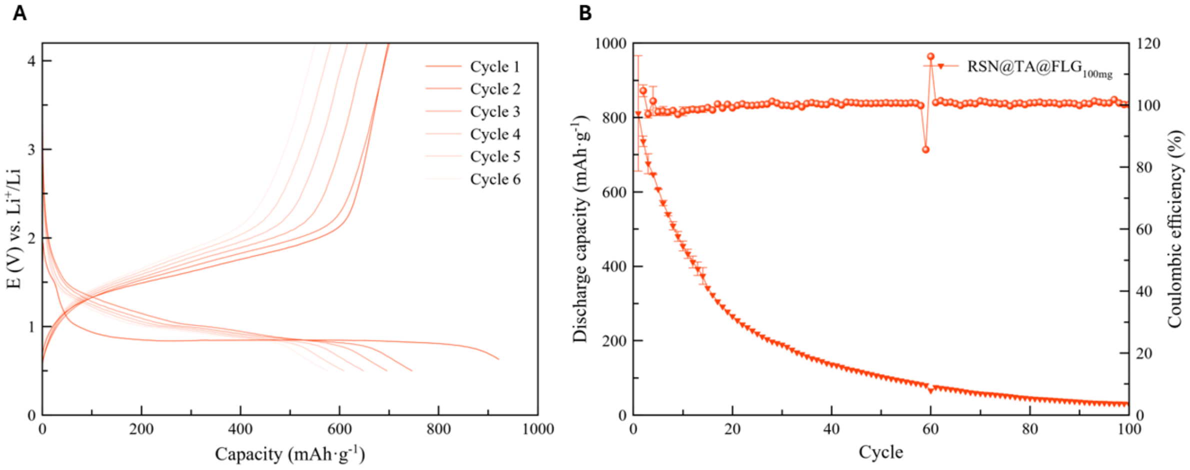

Figure 106: GCD curve at D/20 rate (A) and plot describing the evolution of the discharge capacity and coulombic efficiency for 100 cycles of RSN@TA@FLG$_{100mg}$ electrode (B)

Approximately 922 mAh/g of discharge capacity is achieved for the first cycle, followed by a drop to 746 mAh/g. Interestingly, the very high capacity is obtained for the consideration of the RSN amount as the electrochemically active compound. Hence, the high capacity of the first cycles can be due to two possible hypothesis with one being the electrolyte reduction to form a cathodic electrolyte interface (CEI). This might be explained as a second hypothesis to "overcapacity" provided by the FLG which also store lithium ions. In addition, despite a clearly visible decay in capacity loss over 100 cycling, the RSN@TA@FLG$_{100mg}$ electrode shows a less abrupt and more stable stability than for the RSN electrode with a discharge capacity of ca. 104 mAh/g at the 50th cycle versus 20 mAh/g for the RSN. Furthermore, it shows a better reversibility described by a better coulombic efficiency. Concerning the hypothesis of FLG overcapacity, this one rising from the cyclic voltammetry experiment (Fig. 107) with the presence of a peak visible in the cathodic region at ca. 0.58 V vs. Li$^+$/Li.

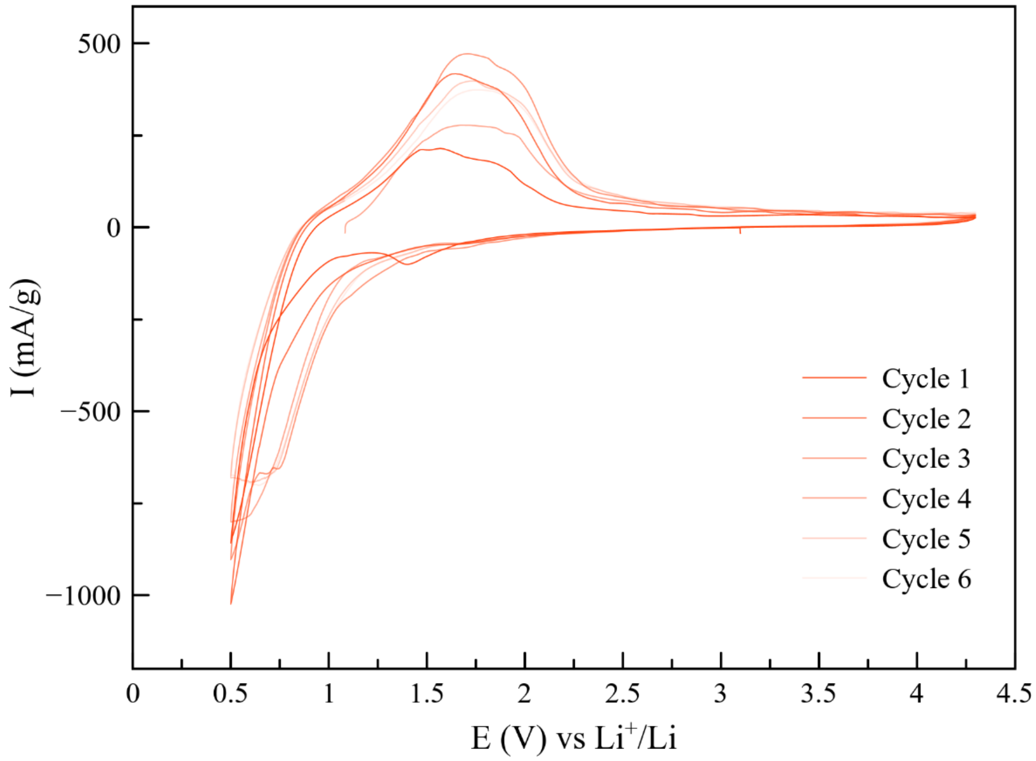

Figure 107: CVs for the RSN@TA@FLG$_{100mg}$ electrode at 0.2 mV/s of the RSN-based coin-cell

Underlying the positive effect of FLG support as conductive support for the RSN particles and preventing enlarged metallic iron nanoparticle isolation that would reduce the stability and reversibility of the conversion reaction, SEM images of the electrode before and after cycling is shown in Fig. 108.

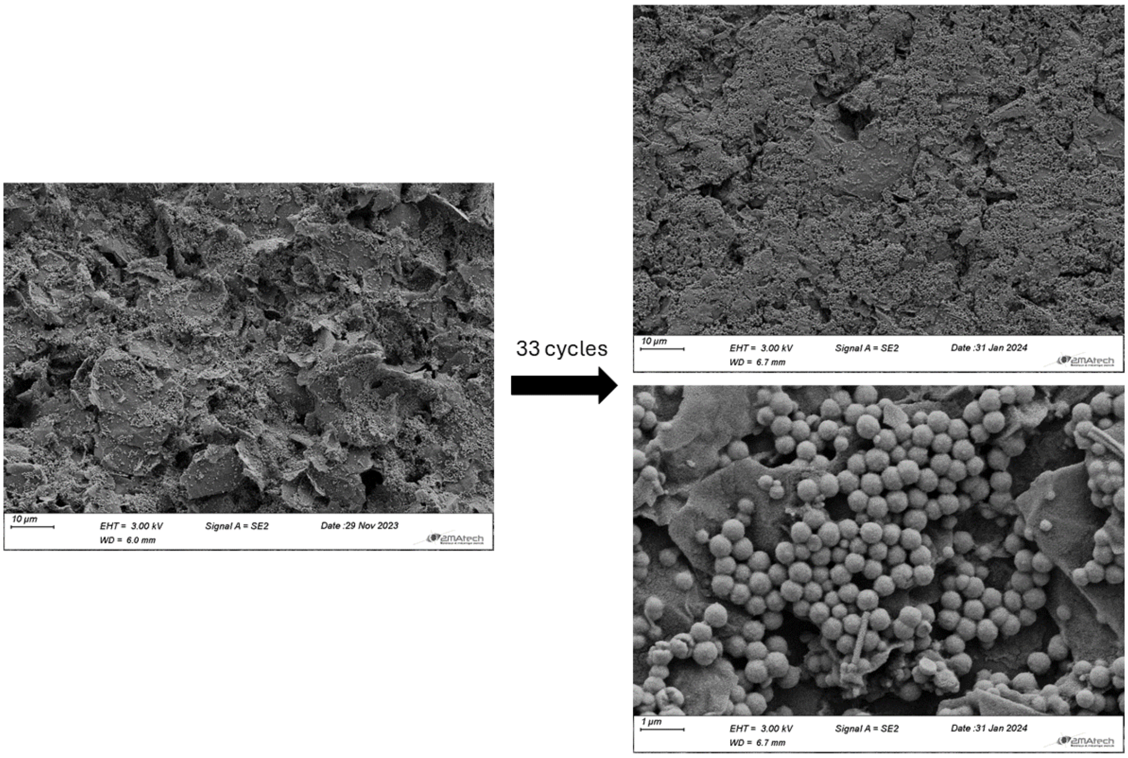

Figure 108: SEM images of the RSN@TA@FLG$_{100mg}$ electrode before and after 33 GCD cycles

We can see that the raspberry-shape structure is still present after 33 GCD cycles performed at a D/20 rate whereas it was already destroyed after 5 cycles in the case of bare RSN electrode (Fig. 105).

The GCD curves and performances over cycling of the RSN@TA@FLG$_{300mg}$ electrode are presented in the Fig. 109.

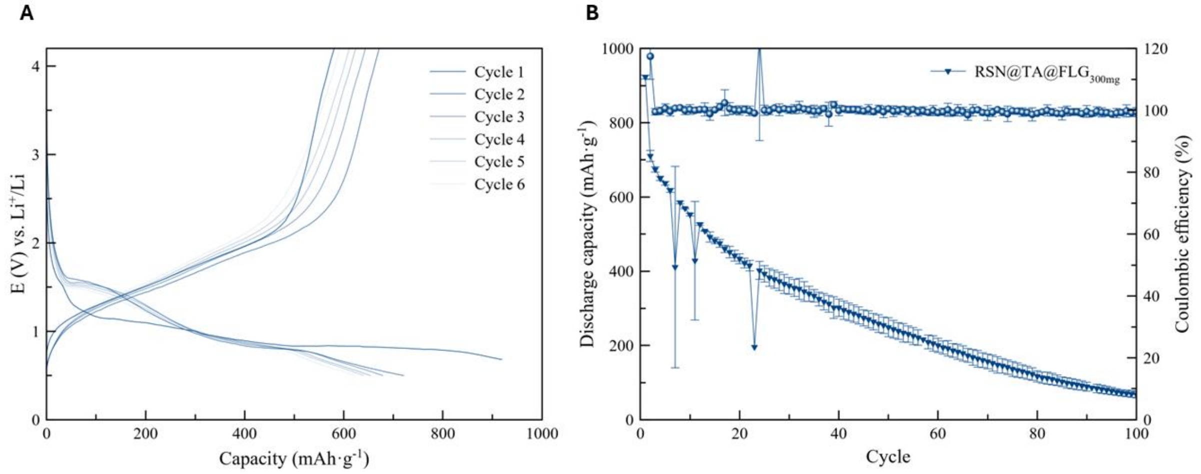

Figure 109: GCD curve at D/20 rate (A) and plot describing the evolution of the discharge capacity and coulombic efficiency for 100 cycles of RSN@TA@FLG$_{300mg}$ electrode (B)

The first discharge capacity reached the quasi-theoretical value of Fe_3O_4 with 923 mAh/g, with drop to 711 mAh/g at the second cycle but with less loss for the subsequent cycles compared to RSN@TA@FLG$_{100mg}$ (Fig. 109A). The same observations as for the RSN@TA@FLG$_{100mg}$ electrode can be underlined here at the slight difference that the electrode materials maintain a capacity retention of 27.0% after 50 cycles compared to 12.8% for the RSN@TA@FLG$_{100mg}$ electrode after the same number of cycle. The presence of the same peak that might be related to the FLG additional capacity is present and more visible for this sample, as seen in the Fig. 110.

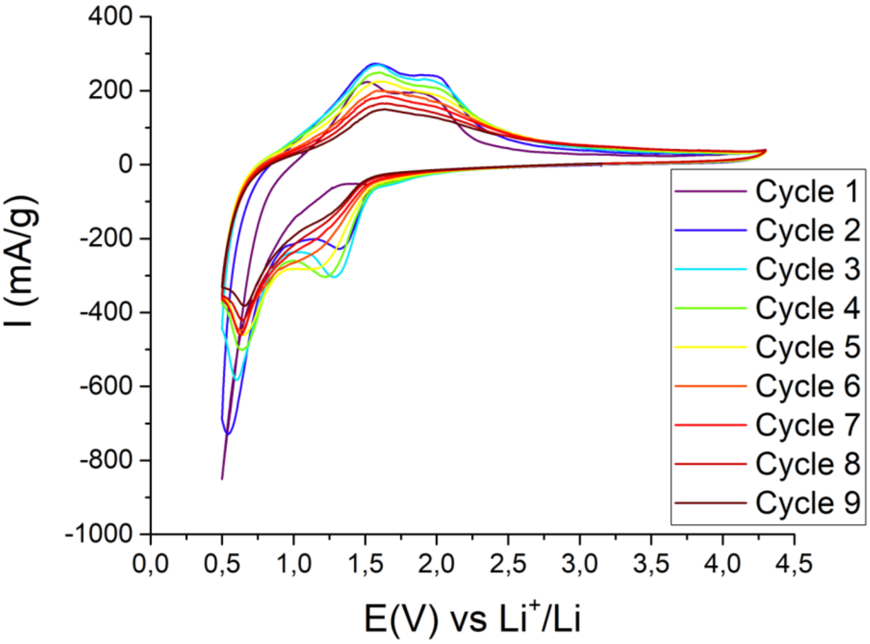

Figure 110: CVs for the RSN@TA@FLG$_{300mg}$ electrode at 0.2 mV/s of the RSN-based coin-cell

Furthermore, the SEM images of the electrode before and after GCD cycling (Fig. 111) show that the raspberry-shaped of the iron oxide nanoparticles grafted onto the FLG surfaces is also maintained. Hence, the positive effect brought by the addition of FLG as a support for the iron oxide RSNs allowed to once more enhance the discharge capacity of the electrode material and here, improve even more the capacity retention than for the composite sample with a lower amount of FLG. Important to note for both composites, small nanoparticles of probably iron oxide are present on the surfaces of few-layer graphene sheets. Thus, a complete integrity of raspberry-shaped particles seems difficult to achieve for a high number of cycling.

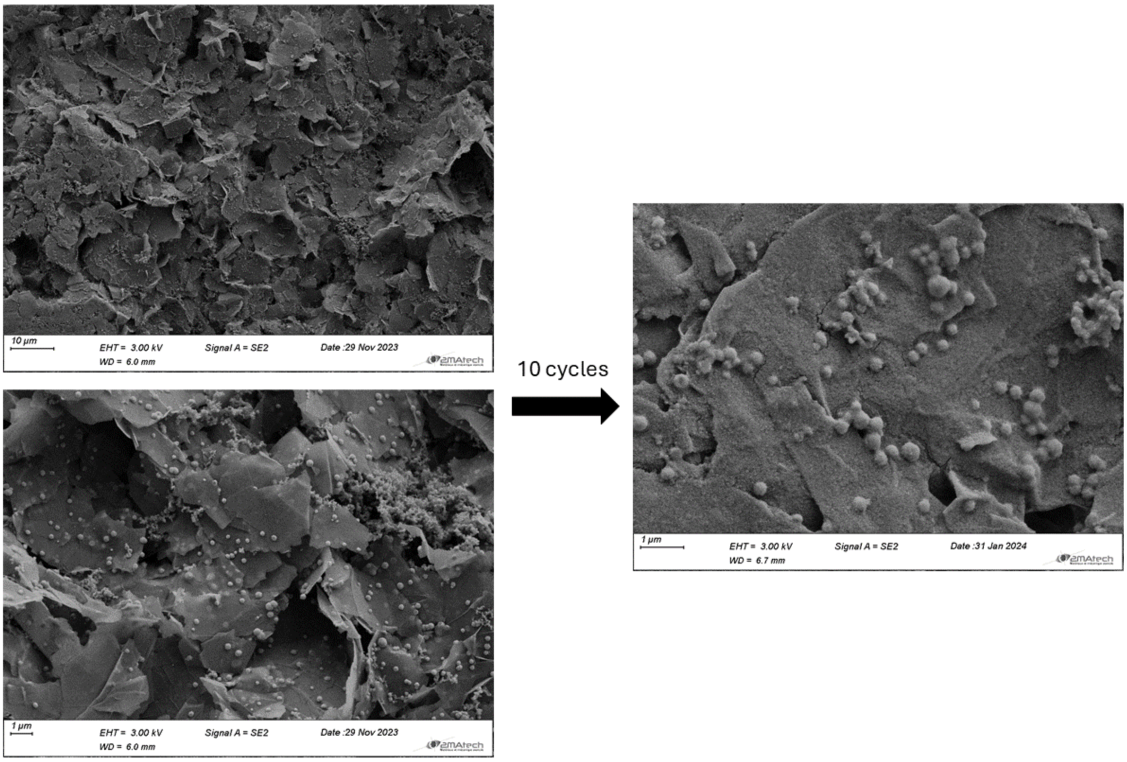

Figure 111: SEM images of the RSN@TA@FLG$_{300mg}$ electrode before and after 10 GCD cycles

By directly comparing all three electrodes' performance on a same plot (Fig. 112), it becomes evident that despite a very high first discharge capacity, the RSN electrode rapidly decay after the very first few cycles while showing a hindered coulombic efficiency. Both RSN@TA@FLG$_{100mg}$ and RSN@TA@FLG$_{300mg}$ composite electrodes showed improved performances compared to the RSN electrode with RSN@TA@FLG$_{300mg}$ showing the best stability over cycling. Scanning electronic microscopy from the electrodes before and after cycling revealed the improved maintenance in the structural integrity of the raspberry-shaped nanoparticles for the composite materials whereas it was completely destroyed after few cycles for the bare RSN electrode. Despite some visible and probable small iron oxide nanoparticles on the FLG surfaces after cycling, it seems that this electronically conductive support allow not only to enhance the capacity of electrode but also the coulombic efficiency (i.e. reversibility of the conversion reaction) and prevent some isolation of metallic iron nanoparticles after subsequent conversion reaction. From cyclic voltammetry of both composite electrodes, a peak at very low voltage appeared that might explain the high capacity obtained from these materials. This "overcapacity" due to the presence of FLG lies the hypothesis that the latter material participates also for the electrochemical energy storage of lithium ions.

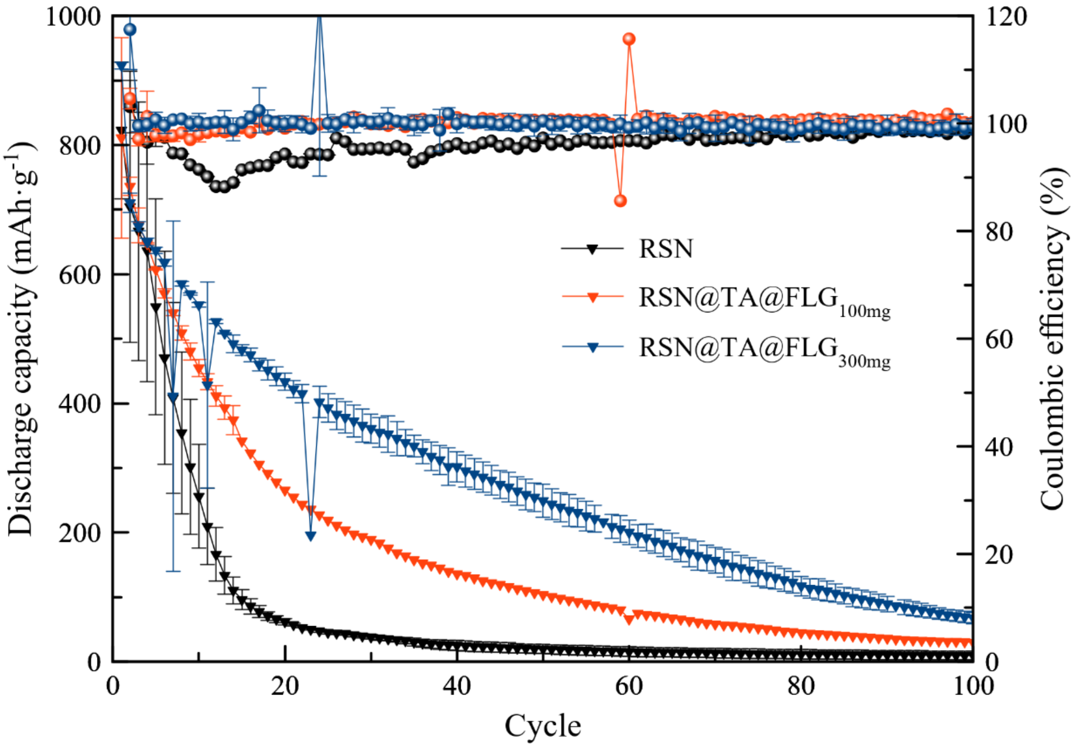

Figure 112: Plot describing the evolution of the discharge capacity and coulombic efficiency for 100 cycles of RSN, RSN@TA@FLG$_{100mg}$ and RSN@TA@FLG$_{300mg}$ electrodes

Operando Raman spectroscopy is nowadays conducted on these materials to assess the possible origin of this low voltage peak. For that, an EL-CELL Opto 10 cell with a sapphire window with the deposited electrode material on a copper disk within tetraethylene glycol dimethyl ether (or TEGDME) aprotic solvent is used to avoid the fluorescence phenomena that might hinder an optimal resolution of the results.

- **Conclusion**

Iron oxide spinel, Fe_3O_4, also known as magnetite is considered a very promising green material for applications as electrodes for either supercapacitors or Li-ion battery applications. Concerning its usage, nanostructuring and structural engineering of iron oxide in raspberry-shaped nanoparticles (RSN) would allow not only a higher number of electrochemical active sites – especially interesting for surface-redox pseudocapacitance driven energy storage for supercapacitors – but also maintaining the mechanical integrity during volume expansion during lithium ion insertion and conversion-type reactions. The addition of few-layer graphene (FLG), obtained from a green exfoliation method with tannic acid as a surfactant, is also a beneficial asset to improve the electrodes' overall performance.

Indeed, FLG is an electronically conductive support and would hindered the loss in conversion reaction due to its irreversibility with the metallic phase iron nanoparticles – obtained after reduction of iron oxide phases – being electronically and spatially isolated. During this work, it was shown that iron oxide spinel and its composites as supercapacitor electrodes were able to deliver very high surface capacitances (>350 µF/cm^2). Composite of RSN@TA@FLG$_{100mg}$ demonstrated highest performances even though it has an intermediate specific surface area and nanograin size in-between the bare RSN and RSN@TA@FLG$_{300mg}$ materials. It underlines the optimum mixture obtention to respect between the RSN active material and FLG support to enhance the electrochemical performance, reversibility of storage, mechanical stability of the materials but also the size of nanograins influenced by the presence of tannic acid surfactant onto the FLG surfaces. For usage as conversion-type negative electrode, the effect of FLG presence is even more noticeable. Whereas the raspberry-shaped nanostructures in the mere RSN electrode collapsed after only few cycles, the FLG conductive support comforted its benefits hypothesized earlier. Indeed, the composites electrodes saw their RSNs being structural maintained for higher cycling numbers with subsequent iron metallic phase nanoparticles lying onto the electronically conductive FLG layer surfaces enhancing the reversibility of the conversion reaction while preventing high dispersion and isolation of these particles. These beneficial effects are directly seen into the improved cyclability (i.e. capacity retention over cycling) of the composites materials with the RSN@TA@FLG$_{300mg}$ showing the best improvement in that sense. Furthermore, the composite electrodes show very high capacities at the first cycle (>920 mAh/g), surpassing the theoretical capacity of Fe_3O_4 alone if considering the amount of RSN within the electrode mixture. This effect is hypothesized to be due to the an "overcapacity" offered by the FLG which would participate to the charge storage. Nowadays, *operando* Raman spectroscopy is used to assess this possibility by tracking the evolution of Raman authorized vibrational peaks during cycling of the electrode.

- **Overview**

Iron oxide spinel Fe_3O_4 was considered to be a greener and efficient electrode for EESDs and this work emphasized this idea. Indeed, the polyol method was used to engineer nanoparticles in the shape of hollow raspberry shape. The synthesis of RSNs and its composite with FLG from a green exfoliation approach with tannic acid as surfactant and their applications as supercapacitor electrodes or as conversion-type anode was shown to be successful. Performance comparable with manganese oxide spinel proved that electrode materials coming from abundant and low toxic elements can still be very efficient as long as research is done to engineer and creates appropriate (nano)structures. The symbiosis between iron oxide RSNs and carbon-based FLG electronically conductive support allow to create not only performant materials for supercapacitors exceeding 350 µF/cm^2, but also improved cyclability for conversion-type anode which usually provide very high capacity but at the expense of drastic capacity retention loss due to particle collapse during volume expansion.

Therefore, all three elements – carbon, manganese and iron – which were initially thought to be used for greener EESDs were synthetized using different synthetic approaches, different strategies and various characterization tools. All these materials displayed very efficient performances and interests according to their use as supercapacitor electrode or for conversion-type anode in rechargeable Li-ion batteries. Humbly, the diversity and variety of methods and tools used from the synthesis of the active materials to their electrochemical studies in this PhD research work are thought to be in adequation with the initial scope of deepening the available knowledge in use of “greener” elements for performant electrochemical energy storage devices.

Conclusions

- **General point**

Energy storage is one of the most important objective of nowadays World with electrochemical energy storage devices being a promising technology for highly efficient charge storage and delivery with zero emissions of polluting gas. Hence, two main technologies – supercapacitors and rechargeable batteries – are studied either from an academic research point of view or by industrials. Supercapacitors which rely on fast charge storage mechanisms allow to store and deliver energy in a quick amount of time, i.e. high power density, at the expense of energy density making them complementary technology with classical rechargeable lithium-ion batteries. For both applications and by respecting green perspective and objectives, carbon and transition metal oxide based on abundant and low toxic element such as manganese and iron are judged as excellent candidates for electrode materials.

In this research work, a first look is given to carbon materials and how its doping with heteroatoms such as nitrogen and fluor would impact its performance as supercapacitor electrode. Its performance is not only looked at from cyclic voltammetry and galvanostatic charge-discharge tests but also from electrochemical impedance spectroscopy to relate the structural characteristics of this carbon – compared with other typical commercial carbons – with the capacitive performance at different frequencies of applied alternative current. In a second time, manganese oxide spinel Mn_3O_4, also known as hausmannite, is studied from its synthesis involving the solution combustion synthesis (SCS) – a self-propagating exothermic combustion reaction – to its application as a supercapacitor electrode with surface-redox driven pseudocapacitance charge storage phenomena. The formation of Mn_3O_4 nanoparticles obtained from using different mixture of fuels was studied by *in situ* temperature-dependent diffuse reflectance infrared Fourier transform spectroscopy (TD-DRIFTS) by analysing the evolution of vibration signals of various SCS mixtures upon heating, mimicking the combustion process. And last, engineering of iron oxide spinel magnetite Fe_3O_4 in hollow raspberry-shaped nanoparticles using a polyol method and also its composites with few-layer graphene (FLG), the latter obtained though a green surfactant-assisted aqueous exfoliation method using tannic acid. These materials were studied as supercapacitor electrode as for Mn_3O_4 but also as conversion-type negative electrode (or also referred as anode material in this context) for high capacity rechargeable lithium-ion batteries.

- **Activated carbons: doping by heteroatoms and impedance study**

Activated carbon is a very porous carbon material with high specific surface area (SSA), making it interesting for electrochemical double-layer-type of charge storage mechanisms in supercapacitor electrodes. However, the increase in SSA, even above 2000 m^2/g, is limited since the surface capacitance of carbon materials within their pores is only between 5-10 $\mu F/cm^2$. Thus, doping with heteroatoms is often seen as performance-enhancing thanks to redox-active functional groups that would additionally participate to the electrochemical charge storage with pseudocapacitance phenomena. For such purpose, nitrogen doping with various functional groups would bring better performances and this is what was studied here. Activated carbon was synthesized from a no-nitrogen containing carbon source, sucrose, and with ammonium citrate as a N-dopant during a KOH-assisted thermochemical activation process at three different pyrolysis temperatures (700°C, 800°C and 900°C) to see the impact on the structural properties of the carbons and their subsequent performance as electrode material. As already enlightened by older research, it was prospected that starting from 800°C of pyrolysis temperature, a structuration start to occur in the amorphous carbon with the creation of sp^2 electronically domain. Therefore, the higher the temperature of pyrolysis, the higher was the measured conductivity of the materials as obtained by conductivity measurements on powder. Following the same trend, less structural defects (e.g. dangling bonds) was observed through Raman spectroscopy but also with electron paramagnetic resonance (EPR) in a more advanced work that consisted on a study on fluor doping. The obtained N-doped activated carbons were highly microporous with SSA of 556 m^2/g (700°C), 1176 m^2/g (800°C) and 1534 m^2/g (900°C), measured by inert gas adsorption-desorption characterization. X-ray photoelectron spectroscopy (XPS) allowed to assess the different functional group percentage and it was seen that when the pyrolysis temperature increase the N content diminishes with more precisely increase in amino N, quaternary nitrogen (Q-N) and N-oxide/R-N groups, and decrease in pyridinic-N and pyrrolic/pyridinium-N groups. From electrochemical measurements in acidic media, the 800°C which has an intermediate content in N content compared to the two others showed very high specific capacitance more than 350 F/g (at 0.5 A/g of charge/discharge rate) and quasi-perfect capacitance retention over hundreds of cycles. This impressive performance was attributed to its sufficient electronically conductive carbon sp^2 matrix and redox-active N-pyrrolic nitrogen involving proton exchange. The high content in oxygen and nitrogen groups would also benefit the pore wettability and studies with organic electrolytes are thought to be done in further research works to see these N-doped activated carbons behavior in a non-aqueous media. Attempts on fluorinating these samples were done to see how fluor treatment could impact the carbonaceous structure and electrochemical properties. For the ACN-800°C sample which presented a certain amount of dangling bonds, a low amount of fluorination allowed to reduce them and high fluorination percentage (>8at.%) provoked high structural defects on both ACN-800°C and ACN-900°C. On the lower ordered ACN, fluorination probably caused damaged on the conductive carbon core and hence reducing the electronic conductivity of the material creating high resistance and decrease in performance. For the more ordered carbon, the fluorination on the other hand could improve the wettability of pores without damaging drastically the conductive carbonaceous core, which allow a very slight improvement at low fluorination level.

Furthermore, electrochemical impedance spectroscopy was used an electrochemical probe to assess the capacitance, and generally the performance and behavior of electrode materials, of three different carbons (Vulcan XC-72, AC Norit, ACN-800°C). All these three different samples having different structural porosity, their measured signal is also different, enlightening interesting observations and giving to EIS its honor as a complex but profound analysis tool. A model based on transition line model (TLM) was made by reducing the amount of adjustable parameters to a three-hierarchical pore levels with interfacial pore impedance evaluation and generational pore branching. Different loadings off active material was tested to allow an additional parameter adjustment of “macropores”. This simplified geometrical model could not take into account all structural considerations when compared to gas adsorption-desorption analysis but allowed interesting characterization of the pores accessibility of the electrolyte ions or even the polarizability of the pores interfaces. The carbon Vulcan XC-72 study shows that a more than 60% of the inner pores (7% in terms of total volume) contributes to the interfacial surface area with 45% of them being short micropores (tens of nanometers). Impedance modeling and its fitting with the geometric model allowed to add insight to SEM images that demonstrates the formation of a mesopore network, due to nanosized particles coalescing to form larger agglomerates, branching into meso- and micropores. For the AC Norit carbon, the inner pores have a significantly higher contribution to the total pore volume with 36%, with quasi 99% contributing to the total surface area with 94% presence of micropores. The latters are narrower and longer than what was characterized for the Vulcan XC-72 carbon, hindering the accessibility of the electrolyte ions, hence giving an electrochemical active specific surface area (460 m^2/g) lower than the measured 732 m^2/g surface area by nitrogen gas adsorption-desorption whereas for the XC-72 the values were closer (172 m^2/g for the ECSA vs. 236 m^2/g from BET analysis). The interface surface area being quasi involving micropores, their polarizability will directly determine the electrochemical performance of the AC Norit material. Despite a more complicated fitting for this carbon de to the interconnected network form quasi solely by the micropores, the modelling indicated a non-uniform polarization within the inner pores even at low frequencies. In the case of ACN-800°C, more than 98% of the interface is related to the narrow and long micropores with high accessibility for the electrolyte ions, explaining the closeness between the ECSA and experimentally obtained SSA. This carbon material would be formed of narrow and long mesopores creating a branching of interconnected long micropores. The polarization for these pores is clearly more uniform than the previous sample, indicating that a narrower dispersion of these micropores in comparison to AC Norit. Most of the pores are inner pores inside of the visible sheet structures in SEM images of several hundreds of nanometers to micrometers. The accessibility/wettability of these pores were expected due to the presence of polar functional groups with O and N heteroatoms.

- **Manganese oxide spinel, Mn_3O_4, formed by Solution Combustion Synthesis for applications in supercapacitors**

Manganese oxides are present in various polymorphs and the hausmannite spinel phase, Mn_3O_4, is studied as a potential promising candidate to be implemented in the supercapacitor as active electrode materials thanks to its high theoretical capacitance provided by surface-redox driven pseudocapacitive type of charge storage. The material is synthesized using the Solution Combustion Synthesis (SCS) process, which is a self-propagating exothermic reaction able to obtain small nanoparticles as a rapid method using commonly available metal nitrate precursors and fuels (e.g. glycine, urea, citric acid, etc…). Nevertheless, the SCS process is quite complex and result in different results according to the mixture of reactants. Indeed, mixed phases or various pure phases were obtained by changing the fuel (glycine or urea) but also by the addition of an additional ligand within the reacting mixture (ammonium citrate) which altered the resultant product as well. DRIFTS studies accompanied by thermogravimetric analysis (TGA) allowed to reach some interesting observations and conclusions. Glycine and manganese nitrate are actually forming a complex of either $[Mn(gly)(H_2O)_2](NO_3)_2$ or $[Mn(gly)(H_2O)_4](NO_3)_2$ ensuring a fine mixing of the reactants with uniformity. Furthermore, these Mn(II)-glycine complexes are less stable thermodynamically than many other transition metal complexes with their decomposition occurring at temperature lower than for pure glycine (160°C vs. 220°C). The faster decomposition for the glycine-Mn(II) nitrate mixture might indicate a lower activation energy for the decomposition reaction than for the pure separate reactants. Varying the metal precursor/fuel ratio was changed using glycine and manganese nitrate in order to be in oxygen lean, equilibrium or excess according to an ideal reaction equation to only obtain Mn_3O_4 phase with precise gas release. No practical pure phases were obtained with these mixtures, with the obtention of Mn_3O_4, Mn_2O_3 and MnO. These syntheses allowed to obtain mesoporous structures of partially agglomerated oxides nanoparticles of ca. 25-40 nm. For oxygen lean media, the main obtained phase was Mn_2O_3 whereas for oxygen equilibrium or excess, mixture of Mn_3O_4 (predominant) and MnO (minor) was present. The presence of different oxide phases in one mixture could be explained by the some partial reduction of a phase (i.e. Mn_3O_4 to MnO) due to high temperature combustion reaction but with only a minor presence thanks to effective heat release from produced gaseous species. But it can also be due to partial precipitation of manganese hydroxide $Mn(OH)_2$ during solvent evaporation in cause of its lower solubility comparing to nitrate. This hydroxide would then be decomposed into MnO which would not be further oxidized due to oxygen lean environment in the SCS reaction. The latter hypothesis tends to be more accurate since high excess in oxygen did not result in higher MnO amount.

Ammonium citrate was added to test its influence on the obtained products by doing mixtures of Mn nitrate/ammonium citrate (NC), Mn nitrate/glycine/ammonium citrate (NCG) and Mn nitrate/urea/ammonium citrate (NCU). Interestingly, the presence of ammonium citrate allowed to obtain pure phases in each case. Despite having slower kinetics of decomposition (in comparison to glycine mixtures), it is assumed that the main source of inhomogeneity of final products is due to less stable manganese (II) complexes in initial solution of reactants that would otherwise create other metal complexes, dried salts or even hydroxide. Indeed, the ammonium citrate ligand allow the creation strong and stable complex over the slow evaporation process of solvent. In the case of NC, only Mn_2O_3 was obtained whereas for NCG and NCU, the only detected phase was Mn_3O_4. The reasons for hausmannite obtention for the two latter cases can be due to higher temperatures reached with these two fuels and decomposition of glycine and urea intermediates consuming oxygen as well, thus diminishing the local partial pressure in oxygen. These two reasons would favorize the formation of a more reduce Mn_3O_4 oxide instead of Mn_2O_3. The Mn_3O_4 phase obtained with the NCU mixture provided higher SSA and smaller crystallite size compared to the NCG mixture, attributed to the faster decomposition kinetics resulting in the formation of smaller particles with less sintering.

Electrochemical tests on these materials were done for applications as supercapacitor electrode in aqueous basic media. Comparing the two different Mn_3O_4 obtained either by the NCG or NCU mixtures in basic aqueous media revealed higher performances for the one obtained for the NCU mixture. This is explained by the higher specific surface (35 m^2/g vs 24 m^2/g for NCG) due to smaller crystallite size (11.3 nm vs 9.3 nm for NCG), increasing as well the surface-to-volume ratio and therefore the interface between the electrolyte ions and the higher number of electrochemical active sites for surface-redox pseudocapacitance. Performance up to 130 F/g could be achieved for a cycling rate of 2 A/g, or the equivalent of 371 $\mu F/cm^2$. In addition, analysis conducted at different scan rate allowed to emphasizes the fast and reversible surface-redox process with 90% of the total capacitance provided by surface-controlled contribution. Interestingly, applications for lithium ion batteries are also envisaged and planned for these manganese oxide materials.

- **Iron oxide spinel, Fe_3O_4, structural engineering into raspberry-shaped nanoparticles and few-layer graphene-based composites as supercapacitor electrode and conversion-type negative electrode for Li-ion batteries**

Magnetite Fe_3O_4 is considered a promising green material candidate for applications as electrode in energy storage devices, for supercapacitors as well as for rechargeable lithium-ion batteries. This is due to iron element abundancy, low toxicity, environmentally low impacting and high theoretical capacity that would involve an 8 electron process for complete reduction of Fe^{2+} and Fe^{3+} states. Performance of electrode materials is strongly related to the materials' structure properties and morphology. Therefore, nanostructuring to increase the number of electrochemical active sites or structural engineering to alter the charge storage pathways/reactions for example. For such reasons, polyol method was used to synthetized hollow raspberry-shaped nanoparticles (RSN) composed of nanograins smaller than 30 nm and accommodation of lithium ions by lowering the mechanical stress induced by this volume expansion. Composites were also made with few-layer graphene (FLG), an electronically conductive carbon support obtained via a surfactant-assisted liquid exfoliation process in aqueous media. The FLG is interesting to prevent some loss in conversion reaction due to the conversion-type reaction irreversibility of the metallic phase iron nanoparticles that might be electronically and spatially isolated.

For supercapacitor applications, very high surface capacitances exceeding 350 µF/cm^2 in basic media were obtained thanks to partial reduction in size of the nanograins for the RSN@TA@FLG$_{100mg}$ composite due to presence of tannic acid. This charge storage mechanism is, as for manganese oxide, due to surface-redox driven pseudocapacitance phenomena with the iron valence state changes. The composite of RSN@TA@FLG$_{100mg}$ demonstrated the highest performances even though it has an intermediate specific surface area (29 m^2/g) and nanograin size (ca. 10 nm) in-between the bare RSN and RSN@TA@FLG$_{300mg}$ materials. It underlines the optimum mixture obtention to respect between the RSN active material and FLG support to enhance the electrochemical performance, reversibility of storage, mechanical stability of the materials but also the size of nanograins influenced by the presence of tannic acid surfactant onto the FLG surfaces. Since the RSN, and more precisely the Fe_3O_4, being the active material for electrochemical charge storage, a lower amount of the latter in the electrode composition would impede the obtention of high capacitance even though, the specific surface area is higher or nanograin size smaller. A complementary work for further investigation would be to synthesize more composites but with more variation of the tannic acid-assisted exfoliated FLG to analyze the trends both in terms of structural differences of the materials (e.g. size of particles, SSA, shape) and subsequent electrochemical performances.

Concerning the usage of Fe_3O_4 for rechargeable lithium ion batteries, it can be used as a conversion reaction-type negative electrode (also commonly referred to the anode electrode) providing very high capacity. Since the complete conversion reaction of Fe_3O_4 would involve its total reduction with the exchange of 8 electrons, a theoretical capacity of ca. 924 mAh/g is expected. However, the conversion reaction typically implies enormous structural modification of the electrode active materials due to very volume expansion that could reach more than 300% from the initial volume of the electrode, involving mechanical stress and cracks of the latter. Therefore, composites of iron oxide RSNs and FLG are very promising to enhance the stability of these electrodes. It was observed that the bare RSN-based electrode did not maintain its structure even after five cycles accompanied by a submit drop of capacity retention to almost 10 mAh/g after 50 cycles. However, the RSN structures of the composites did not collapse even after tens of cycles, enlightening the benefits of FLG support. Their cyclability and coulombic efficiency were enhanced thanks to the iron metallic phase nanoparticles laying onto the conductive FLG surfaces enhancing the reaction reversibility while preventing the electronic and spatial isolation of these particles. For such applications, the composite with the highest amount of FLG showed the best performances mostly underlined by its remarkable capacity retention of 27.0% after 50 cycles, way higher than for the other samples. Furthermore, the composites electrodes presented additional capacity brought by the FLG presence, hypothesizing that the FLG is also participating in the charge storage. This “overcapacity” is under investigation using *operando* Raman technique to assess the vibrational authorized Raman peaks changes during charge-discharge cycling.

Supplementary information

Supplementary information 1

N_2 isotherms and pore size distribution for:

- Vulcan XC-72

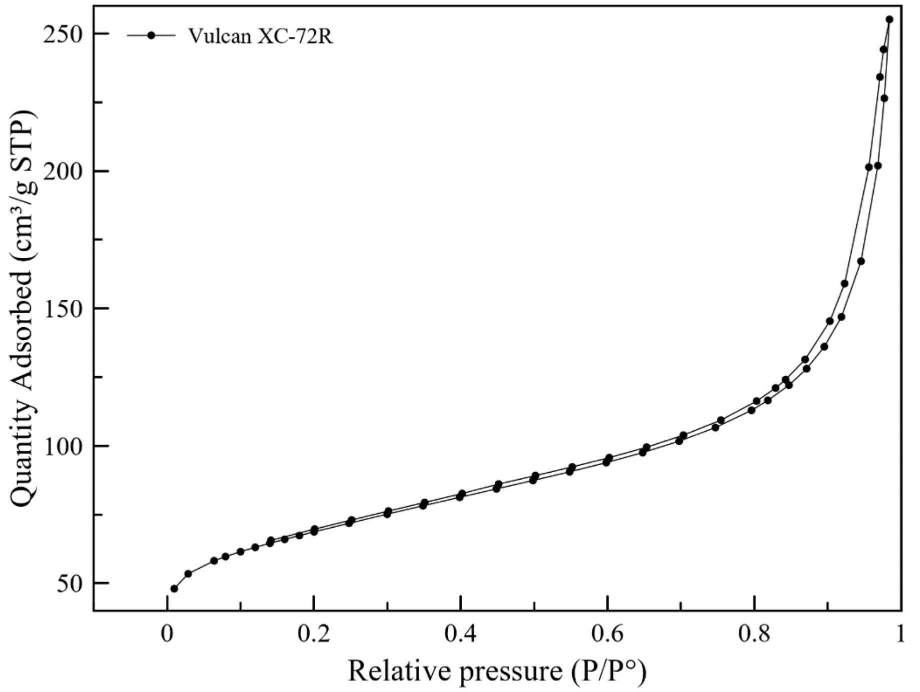

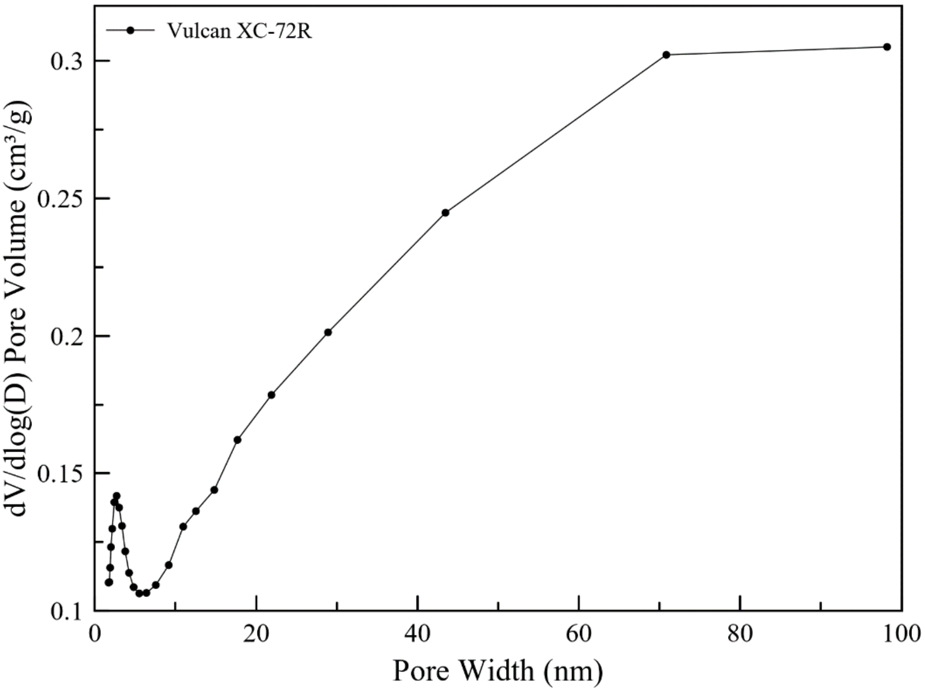

- AC Norit

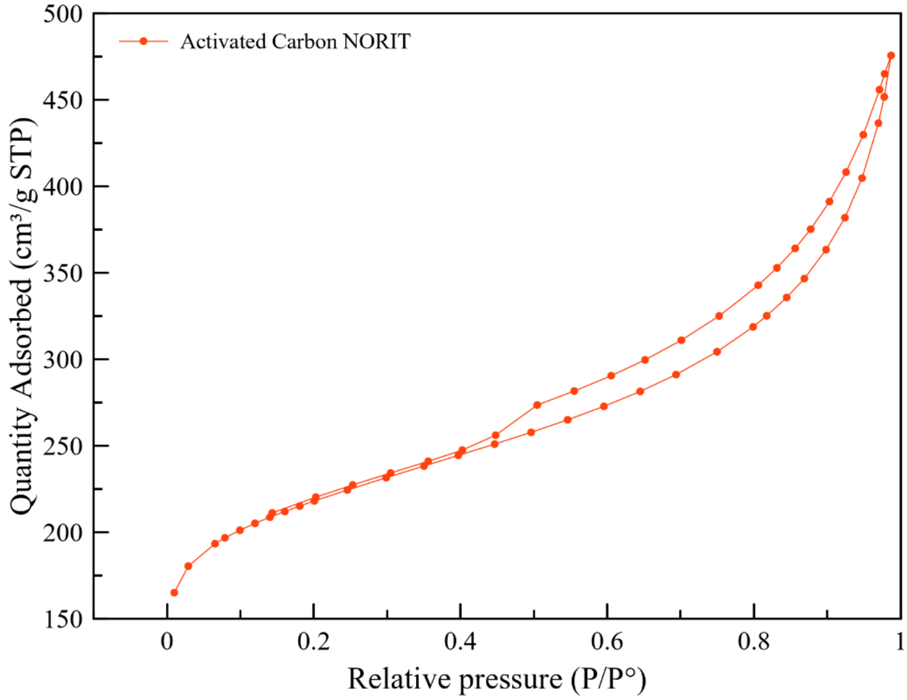
Activated Carbon NORIT
Quantity Adsorbed (cm³/g STP)
500
450
400
350
300
250
200
150
0
0.2
0.4
0.6
0.8
1
Relative pressure (P/P°)

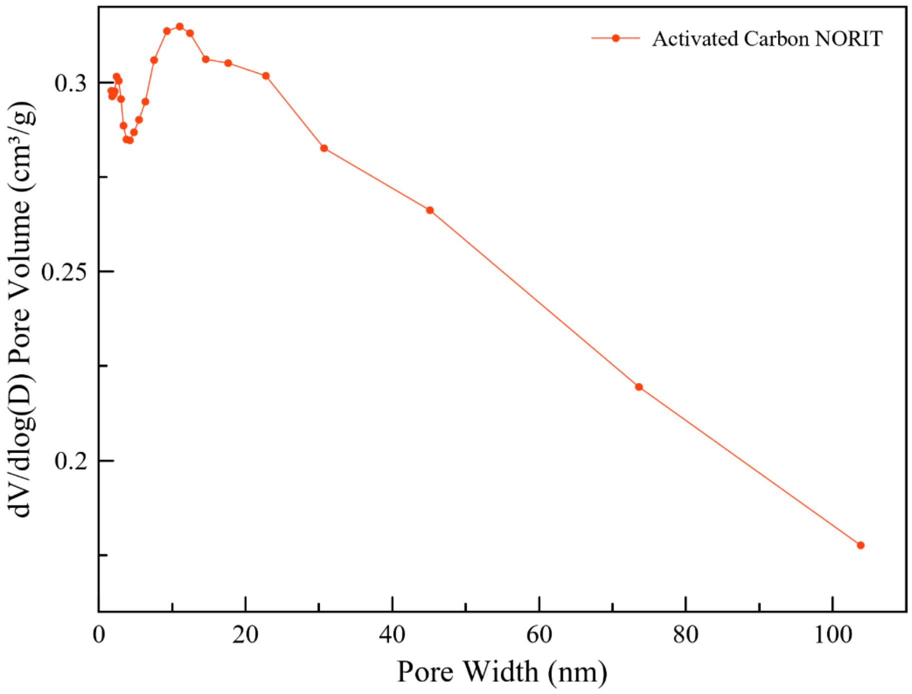
Activated Carbon NORIT
dV/dlog(D) Pore Volume (cm³/g)
0.3
0.25
0.2
0
20
40
60
80
100
Pore Width (nm)

- ACN-800°C

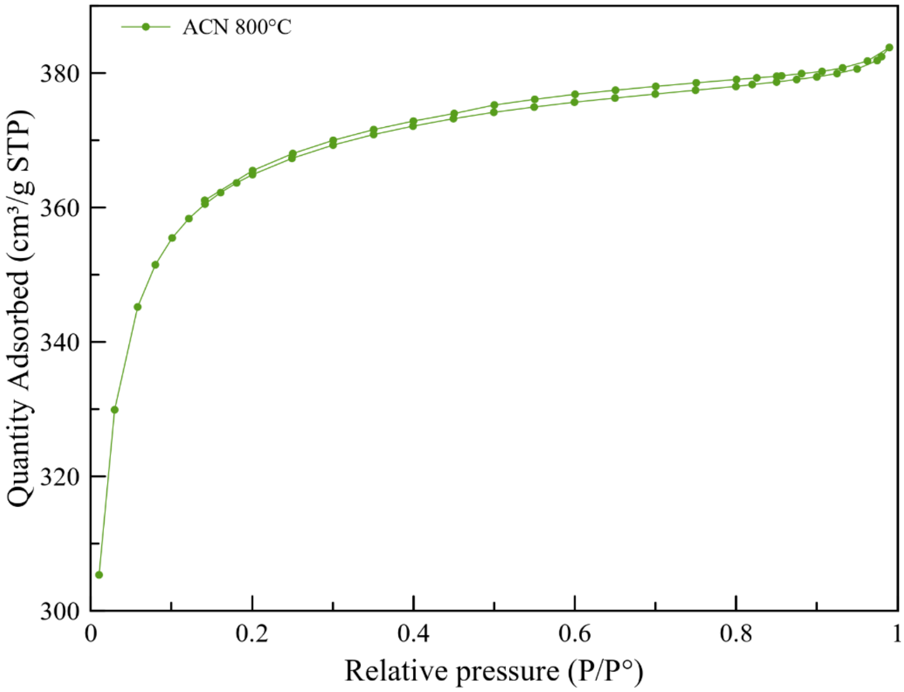
ACN 800°C
Quantity Adsorbed (cm³/g STP)
300
320
340
360
380
0
0.2
0.4
0.6
0.8
1
Relative pressure (P/P°)

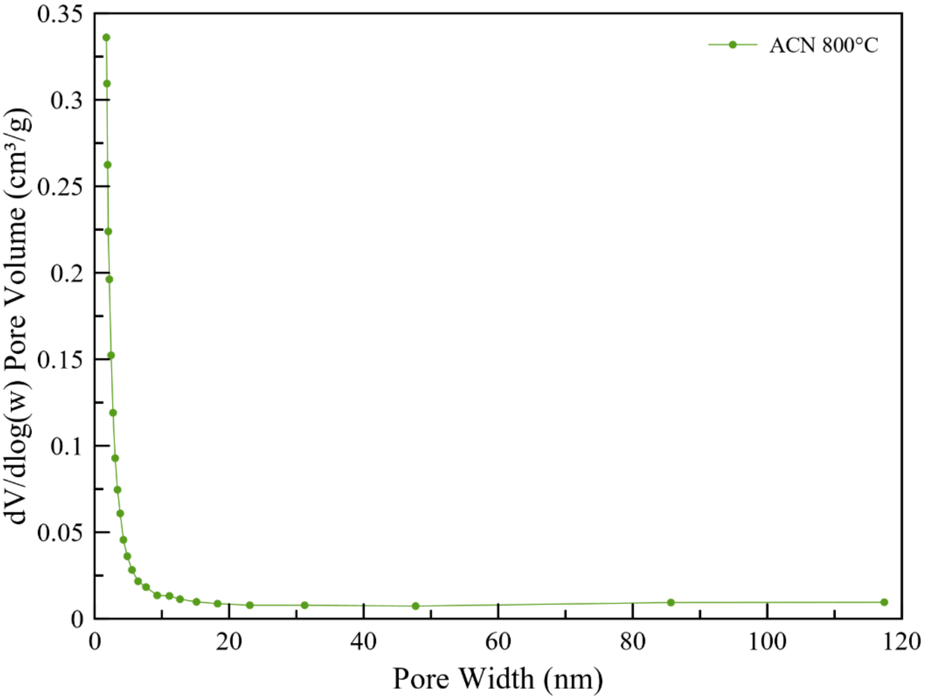
ACN 800°C
dV/dlog(w) Pore Volume (cm³/g)
0
0.05
0.1
0.15
0.2
0.25
0.3
0.35
0
20
40
60
80
100
120
Pore Width (nm)

Supplementary information 2

N_2 isotherms for:

- MnOx/Glycine

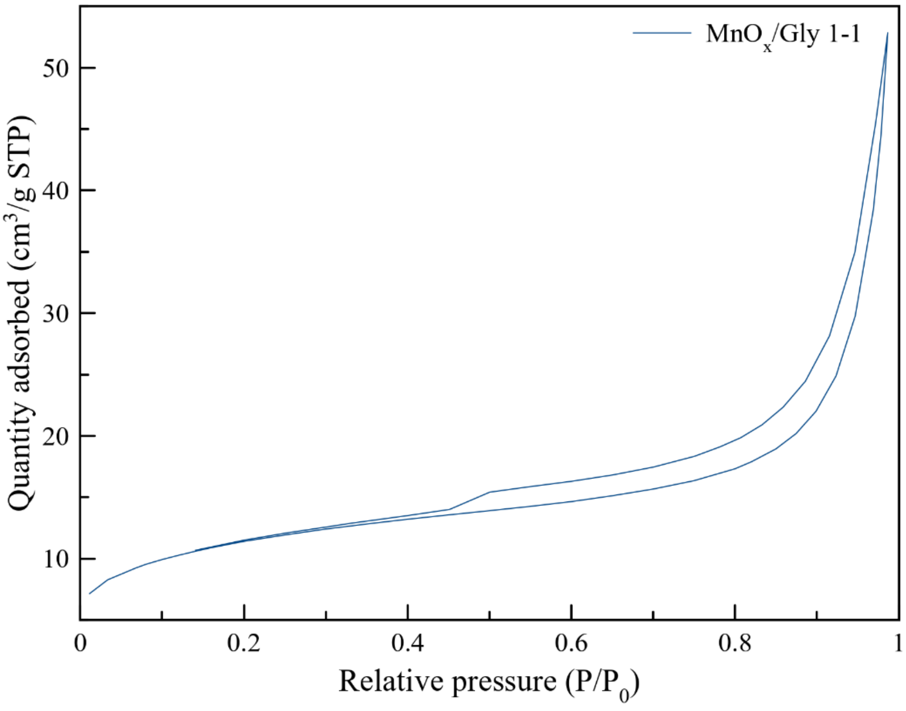

- MnOx/Gly at different ratio

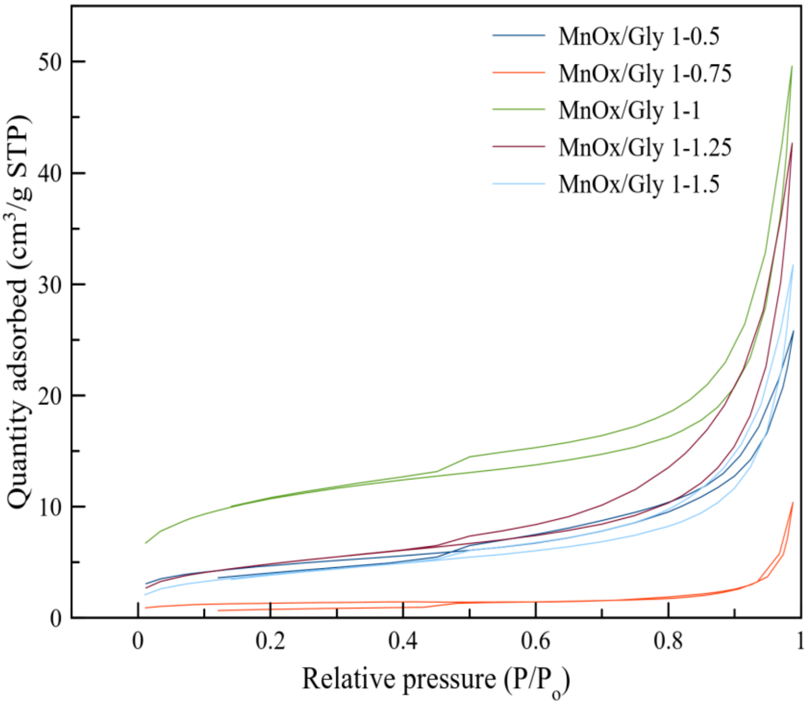

- MnOx/Urea

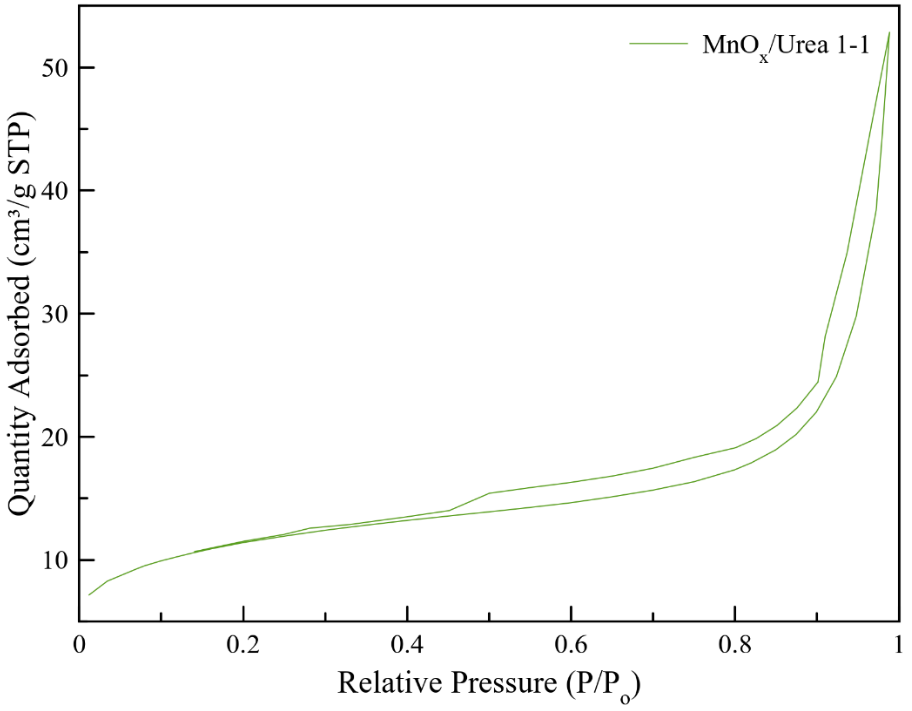

- MnOx/Glycine-Ammonium Citrate

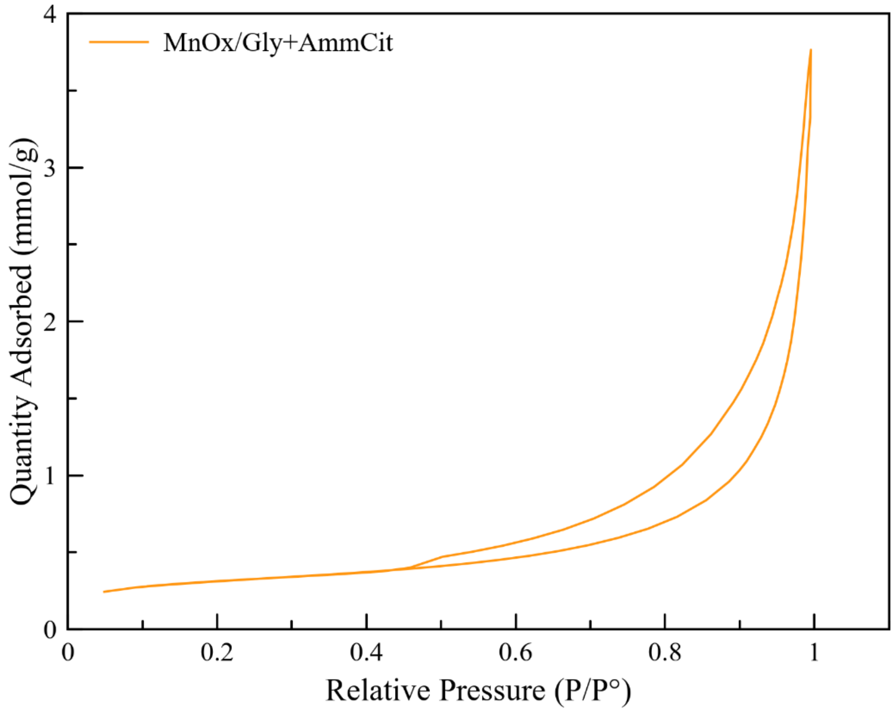

- MnOx/Urea-Ammonium Citrate

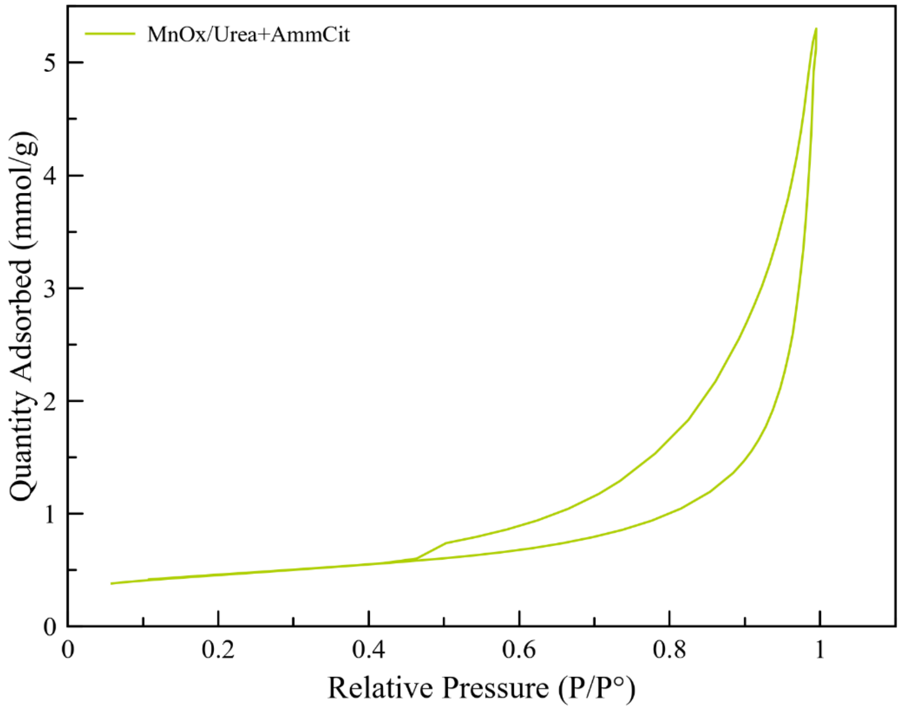

Supplementary information 3

- Statistical population of the RSN@TA@FLG$_{100mg}$ particles obtained from SEM images with ImageJ

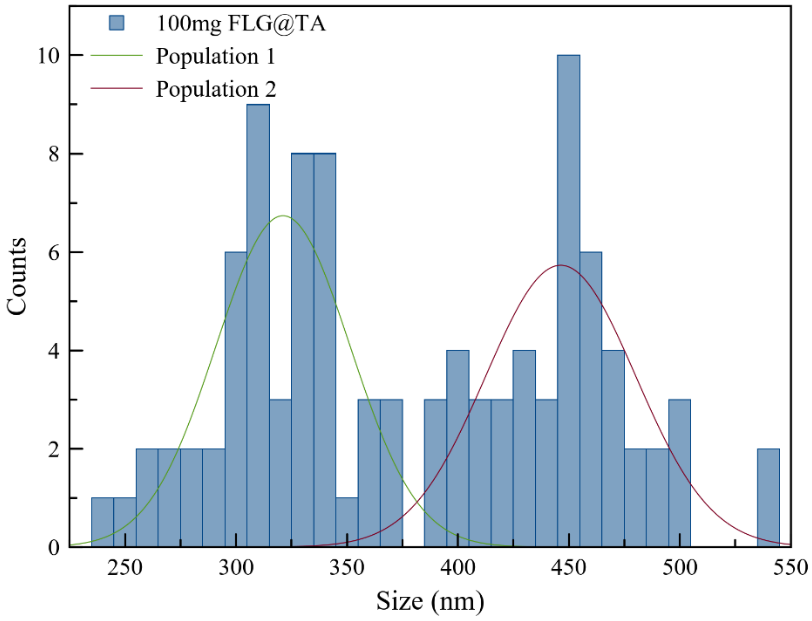

- Statistical population of the RSN@TA@FLG$_{100mg}$ nanograins obtained from TEM images with ImageJ

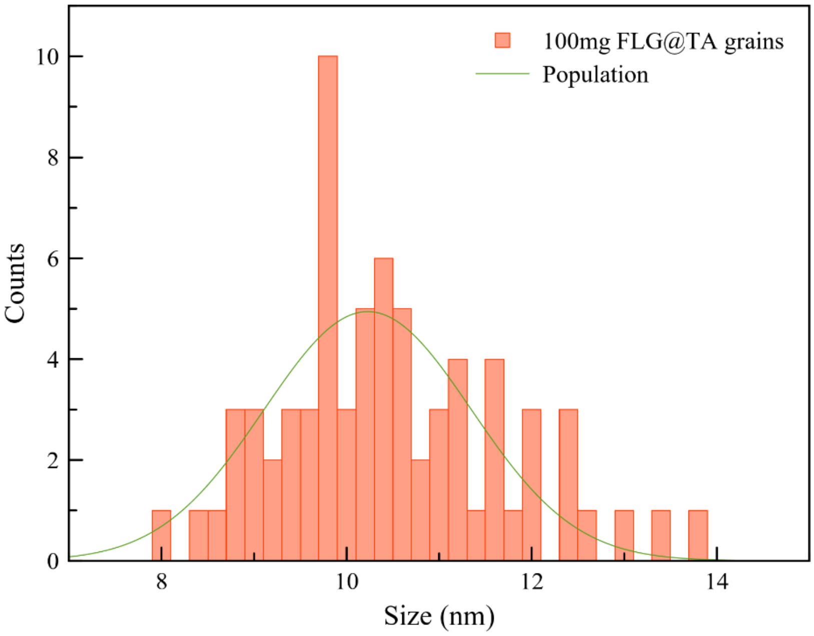

- Statistical population of the RSN@TA@FLG$_{300mg}$ particles obtained from SEM images with ImageJ

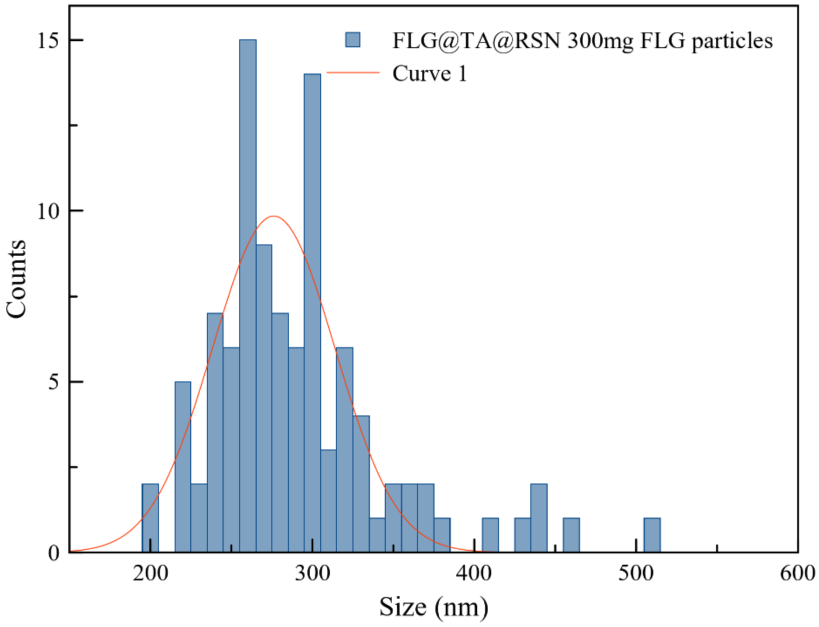

- Statistical population of the RSN@TA@FLG$_{300mg}$ nanograins obtained from TEM images with ImageJ

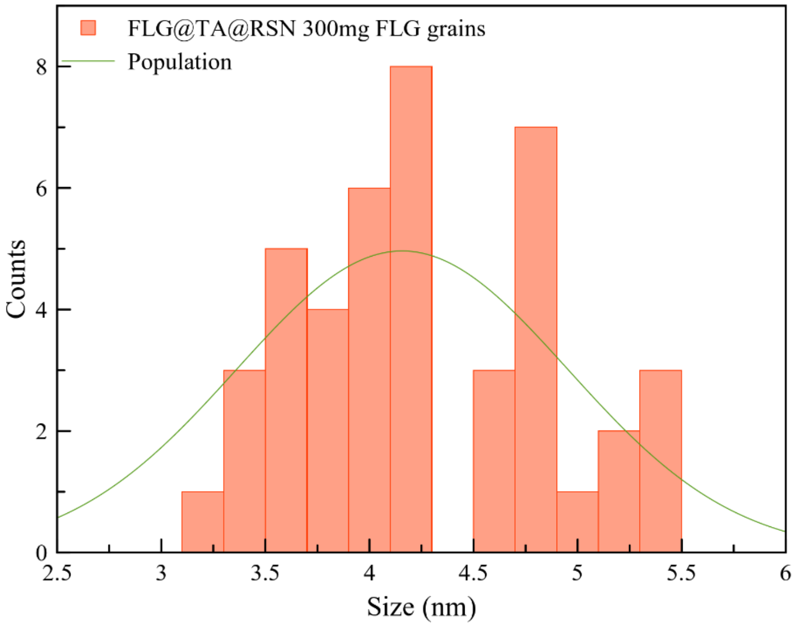

Publications and Communications

[1] Karakoç, T.; Ba, H.; Phuoc, L.T.; Bégin, D.; Pham-Huu, C.; Pronkin, S.N. Ultramicroporous N-Doped Activated Carbon Materials for High Performance Supercapacitors. *Batteries* **2023**, *9*, 436. https://doi.org/10.3390/batteries9090436

[2] Chniti, R.; Karakoç, T.; Kouass, S.; Ghodbane, O.; Pronkin, S.N. One-pot synthesis of low-cost CuS/Vulcan carbon composites applied as electrode materials for supercapacitors. *J Appl Electrochem* **2024**, https://doi.org/10.1007/s10800-024-02156-2

Poster presentation, « Ultramicroporous N-doped Activated Carbon Materials for High Performance Supercapacitors », 74th Annual Meeting of the International Society of Electrochemistry, September 2023, Lyon, France.

Bibliography

(1) *World Energy Outlook 2023 – Analysis*. IEA. https://www.iea.org/reports/world-energy-outlook-2023 (accessed 2024-01-08).

(2) *World Population Prospects 2022: Summary of Results - Population Division - United Nations*. https://www.un.org/development/desa/pd/content/World-Population-Prospects-2022 (accessed 2024-01-09).

(3) Dunn, B.; Kamath, H.; Tarascon, J.-M. Electrical Energy Storage for the Grid: A Battery of Choices. *Science* **2011**, *334* (6058), 928–935. https://doi.org/10.1126/science.1212741.

(4) Larcher, D.; Tarascon, J.-M. Towards Greener and More Sustainable Batteries for Electrical Energy Storage. *Nature Chem* **2015**, *7* (1), 19–29. https://doi.org/10.1038/nchem.2085.

(5) Shao, H.; Wu, Y.-C.; Lin, Z.; Taberna, P.-L.; Simon, P. Nanoporous Carbon for Electrochemical Capacitive Energy Storage. *Chem. Soc. Rev.* **2020**, *49* (10), 3005–3039. https://doi.org/10.1039/D0CS00059K.

(6) Karakoç, T.; Ba, H.; Phuoc, L. T.; Bégin, D.; Pham-Huu, C.; Pronkin, S. N. Ultramicroporous N-Doped Activated Carbon Materials for High Performance Supercapacitors. *Batteries* **2023**, *9* (9), 436. https://doi.org/10.3390/batteries9090436.

(7) de Levie, R. On Porous Electrodes in Electrolyte Solutions: I. Capacitance Effects. *Electrochimica Acta* **1963**, *8* (10), 751–780. https://doi.org/10.1016/0013-4686(63)80042-0.

(8) de Levie, R. On Porous Electrodes in Electrolyte Solutions—IV. *Electrochimica Acta* **1964**, *9* (9), 1231–1245. https://doi.org/10.1016/0013-4686(64)85015-5.

(9) Keiser, H.; Beccu, K. D.; Gutjahr, M. A. Abschätzung Der Porenstruktur Poröser Elektroden Aus Impedanzmessungen. *Electrochimica Acta* **1976**, *21* (8), 539–543. https://doi.org/10.1016/0013-4686(76)85147-X.

(10) Lasia, A. Impedance of Porous Electrodes. *Journal of Electroanalytical Chemistry* **1995**, *397* (1), 27–33. https://doi.org/10.1016/0022-0728(95)04177-5.

(11) Varma, A.; Mukasyan, A. S.; Rogachev, A. S.; Manukyan, K. V. Solution Combustion Synthesis of Nanoscale Materials. *Chem. Rev.* **2016**, *116* (23), 14493–14586. https://doi.org/10.1021/acs.chemrev.6b00279.

(12) Bresser, D.; Passerini, S.; Scrosati, B. Leveraging Valuable Synergies by Combining Alloying and Conversion for Lithium-Ion Anodes. *Energy Environ. Sci.* **2016**, *9* (11), 3348–3367. https://doi.org/10.1039/C6EE02346K.

(13) Fleischmann, S.; Mitchell, J. B.; Wang, R.; Zhan, C.; Jiang, D.; Presser, V.; Augustyn, V. Pseudocapacitance: From Fundamental Understanding to High Power Energy Storage Materials. *Chem. Rev.* **2020**, *120* (14), 6738–6782. https://doi.org/10.1021/acs.chemrev.0c00170.

(14) Gerber, O.; Pichon, B. P.; Ihiawakrim, D.; Florea, I.; Moldovan, S.; Ersen, O.; Begin, D.; Grenèche, J.-M.; Lemonnier, S.; Barraud, E.; Begin-Colin, S. Synthesis Engineering of Iron Oxide Raspberry-Shaped Nanostructures. *Nanoscale* **2016**, *9* (1), 305–313. https://doi.org/10.1039/C6NR07567C.

(15) Gerber, O.; Bégin-Colin, S.; Pichon, B. P.; Barraud, E.; Lemonnier, S.; Pham-Huu, C.; Daffos, B.; Simon, P.; Come, J.; Bégin, D. Design of Fe3–xO4 Raspberry Decorated Graphene Nanocomposites with High Performances in Lithium-Ion Battery. *Journal of Energy Chemistry* **2016**, *25* (2), 272–277. https://doi.org/10.1016/j.jechem.2016.01.021.

(16) Zhao, S.; Xie, S.; Zhao, Z.; Zhang, J.; Li, L.; Xin, Z. Green and High-Efficiency Production of Graphene by Tannic Acid-Assisted Exfoliation of Graphite in Water. *ACS Sustainable Chem. Eng.* **2018**, *6* (6), 7652–7661. https://doi.org/10.1021/acssuschemeng.8b00497.

(17) *Human Metabolism, Energy, Nutrients | Learn Science at Scitable*. https://www.nature.com/scitable/topicpage/nutrient-utilization-in-humans-metabolism-pathways-14234029/ (accessed 2024-01-08).

(18) *Energy | Definition, Types, Examples, & Facts | Britannica*. https://www.britannica.com/science/energy (accessed 2024-01-08).

(19) Murphy, D. J.; Hall, C. A. S. Year in Review—EROI or Energy Return on (Energy) Invested. *Annals of the New York Academy of Sciences* **2010**, *1185* (1), 102–118. https://doi.org/10.1111/j.1749-6632.2009.05282.x.

(20) Hall, C. A. S.; Lambert, J. G.; Balogh, S. B. EROI of Different Fuels and the Implications for Society. *Energy Policy* **2014**, *64*, 141–152. https://doi.org/10.1016/j.enpol.2013.05.049.

(21) Barnhart, C. J.; Dale, M.; Brandt, A. R.; Benson, S. M. The Energetic Implications of Curtailing versus Storing Solar- and Wind-Generated Electricity. *Energy Environ. Sci.* **2013**, *6* (10), 2804–2810. https://doi.org/10.1039/C3EE41973H.

(22) *World Population Prospects 2022 - Population Division - United Nations - Database*. https://population.un.org/wpp/Graphs/Probabilistic/POP/TOT/900 (accessed 2024-01-09).

(23) *Electrification - Energy System*. IEA. https://www.iea.org/energy-system/electricity/electrification (accessed 2024-01-10).

(24) *BATTERY 2030+ Roadmap*.

(25) Volta, A. XVII. On the Electricity Excited by the Mere Contact of Conducting Substances of Different Kinds. In a Letter from Mr. Alexander Volta, F. R. S. Professor of Natural Philosophy in the University of Pavia, to the Rt. Hon. Sir Joseph Banks, Bart. K.B. P. R. S. *Philosophical Transactions of the Royal Society of London* **1800**, *90*, 403–431. https://doi.org/10.1098/rstl.1800.0018.

(26) *CRC Handbook of Chemistry and Physics*, 95th ed.; Haynes, W. M., Ed.; CRC Press: Boca Raton, 2014. https://doi.org/10.1201/b17118.

(27) Bunsen, R. Darstellung Des Lithiums. *Justus Liebigs Annalen der Chemie* **1855**, *94* (1), 107–111. https://doi.org/10.1002/jlac.18550940112.

(28) Daniell, J. F. LXXIII. On the Constant Voltaic Battery. *The London, Edinburgh, and Dublin Philosophical Magazine and Journal of Science* **1842**, *21* (140), 421–422. https://doi.org/10.1080/14786444208621601.

(29) Daniell, M. J. F. Sur les piles à courant constant. *Annales de chimie et de physique* **1842**.

(30) Callaud, A. Essai Sur Les Piles. **1875**.

(31) Ayrton, W. E. *Practical Electricity*; London, Cassell, 1891.

(32) Silliman, B. *Principles of Physics, Or, Natural Philosophy: Designed for the Use of Colleges and Schools*; Theodore Bliss, 1861.

(33) *Linden's Handbook of Batteries*, 5th Edition.; Beard, K. W., Ed.; McGraw-Hill Education, 2019.

(34) Galvanic Battery. US373064A, November 15, 1887. https://patents.google.com/patent/US373064A/en (accessed 2024-02-12).

(35) De Wolff, P. M. Interpretation of Some γ-MnO2 Diffraction Patterns. *Acta Crystallographica* **1959**, *12* (4), 341–345. https://doi.org/10.1107/S0365110X59001001.

(36) Magnard, N. P. L.; Anker, A. S.; Aalling-Frederiksen, O.; Kirsch, A.; Jensen, K. M. Ø. Characterisation of Intergrowth in Metal Oxide Materials Using Structure-Mining: The Case of γ-MnO2. *Dalton Trans.* **2022**, *51* (45), 17150–17161. https://doi.org/10.1039/D2DT02153F.

(37) US EPA, O. *The Mercury-Containing and Rechargeable Battery Management Act - Public Law 104-142*; 1996. https://www.epa.gov/rcra/mercury-containing-and-rechargeable-battery-management-act-public-law-104-142 (accessed 2024-01-30).

(38) Lei, L.; Sun, Y.; Wang, X.; Jiang, Y.; Li, J. Strategies to Enhance Corrosion Resistance of Zn Electrodes for Next Generation Batteries. *Frontiers in Materials* **2020**, *7*.

(39) Durmus, Y. E.; Montiel Guerrero, S. S.; Tempel, H.; Hausen, F.; Kungl, H.; Eichel, R.-A. Influence of Al Alloying on the Electrochemical Behavior of Zn Electrodes for Zn–Air Batteries With Neutral Sodium Chloride Electrolyte. *Frontiers in Chemistry* **2019**, *7*.

(40) Energizer Brands, LLC. Energizer's Alkaline Manganese Dioxide Handbook and Application Manual, 2018. https://data.energizer.com/battery-handbook-crosssections/ (accessed 2024-02-12).

(41) Duracell. Duracell's Technical Bulletin for Alkaline-Manganese Dioxide Batteries. https://www.duracell.com/en-us/techlibrary/technical-bulletins/ (accessed 2024-02-12).

(42) *Galvani's voltaic pile | Science Museum Group Collection*. https://collection.sciencemuseumgroup.org.uk/objects/co143044/galvanis-voltaic-pile-voltaic-pile (accessed 2024-02-12).

(43) *Columbia Dry Cell Battery - Landmark*. American Chemical Society. https://www.acs.org/education/whatischemistry/landmarks/drycellbattery.html (accessed 2024-08-21).

(44) *Optimum - Duracell FR*. https://www.duracell.fr/optimum/?ref=duracell.com (accessed 2024-08-21).

(45) *Piles Energizer Alkaline Power - AA, AAA, C, D & 9V*. French. https://energizer.eu/fr/product/energizer-alkaline-power-aa/ (accessed 2024-08-21).

(46) Brande, W. T. *A Manual of Chemistry*, 2nd edition.; John Murray, 1821; Vol. 2.

(47) Lewis, G. N.; Keyes, F. G. THE POTENTIAL OF THE LITHIUM ELECTRODE. *J. Am. Chem. Soc.* **1913**, *35* (4), 340–344. https://doi.org/10.1021/ja02193a004.

(48) Hajek, J. Electrolyte Pour Électrodes de Poids Léger. https://data.inpi.fr/brevets/FR1000044?q=jan%20hajek#FR1000044 (accessed 2024-02-13).

(49) Harris, W. S. *Electrochemical Studies in Cyclic Esters*; UCRL-8381; Univ. of California, Berkeley, CA (United States), 1958. https://doi.org/10.2172/4305596.

(50) Meyers, W. F.; Simmons, J. W. Electric Current-Producing Cell with Anhydrous Organic Liquid Electrolyte. US3423242A, January 21, 1969. https://patents.google.com/patent/US3423242A/en (accessed 2024-03-01).

(51) Gabano, J.-P. Procédé de Préparation d'un Électrolyte Non Aqueux Pour Générateurs Électrochimiques Rechargeables, Électrolyte Ainsi Obtenu et Générateurs Utilisant Cet Électrolyte. 1.583.804, December 5, 1969.

(52) *SANYO Lithium Batteries | PDF | Battery (Electricity) | Rechargeable Battery*. Scribd. https://www.scribd.com/doc/316772569/SANYO-Lithium-batteries (accessed 2024-03-04).

(53) Watanabe, N.; Fukuda, M. Primary Cell for Electric Batteries. US3536532A, October 27, 1970. https://patents.google.com/patent/US3536532A/en?oq=US3536532 (accessed 2024-03-04).

(54) Watanabe, N.; Nakajima, T.; Hagiwara, R. Discharge Reaction and Overpotential of the Graphite Fluoride Cathode in a Nonaqueous Lithium Cell. *Journal of Power Sources* **1987**, *20* (1), 87–92. https://doi.org/10.1016/0378-7753(87)80095-2.

(55) Moser, J. R. Solid State Lithium-Iodine Primary Battery. US3660163A, May 2, 1972. https://patents.google.com/patent/US3660163A/en (accessed 2024-03-05).

(56) Carnot, S. *Réflexions sur la puissance motrice du feu et sur les machines propres à développer cette puissance*; Gauthier-Villars, 1824.

(57) Planté, G. A. du texte. *Recherches sur l'électricité / par Gaston Planté,...*; 1883.

(58) Faure, C. A. Perfectionnements Aux Batteries Galvaniques et Leur Application Aux Machines Locomotives Électriques. 139358, October 20, 1880.

(59) Faure, C. A. Perfectionnements Dans Les Dispositions et La Construction Des Couples-Batteries Galvaniques Secondaires. 141057, February 9, 1881.

(60) Gladstone, J. H.; Tribe, A. On the Chemistry of the Plants and Faure Accumulators. *Nature* **1882**, *25* (646), 461–463. https://doi.org/10.1038/025461c0.

(61) Harned, H. S.; Hamer, W. J. The Thermodynamics of Aqueous Sulfuric Acid Solutions from Electromotive Force Measurements1. *J. Am. Chem. Soc.* **1935**, *57* (1), 27–33. https://doi.org/10.1021/ja01304a009.

(62) *One of the first rechargeable batteries, about 1860 | Science Museum Group Collection*. https://collection.sciencemuseumgroup.org.uk/objects/co36401/one-of-the-first-rechargeable-batteries-about-1860-batteries (accessed 2024-03-08).

(63) Botte, G. G. Batteries: Basic Principles, Technologies, and Modeling. In *Encyclopedia of Electrochemistry*; John Wiley & Sons, Ltd, 2007. https://doi.org/10.1002/9783527610426.bard050007.

(64) Willems, J. J. G.; Buschow, K. H. J. From Permanent Magnets to Rechargeable Hydride Electrodes. *Journal of the Less Common Metals* **1987**, *129*, 13–30. https://doi.org/10.1016/0022-5088(87)90029-4.

(65) Lim, H. S.; Stadnick, S. J. Effect of Precharge on Nickel—Hydrogen Cell Storage Capacity. *Journal of Power Sources* **1989**, *27* (1), 69–79. https://doi.org/10.1016/0378-7753(89)80106-5.

(66) Whittingham, M. S. Electrical Energy Storage and Intercalation Chemistry. *Science* **1976**, *192* (4244), 1126–1127. https://doi.org/10.1126/science.192.4244.1126.

(67) Whittingham, M. S. Chemistry of Intercalation Compounds: Metal Guests in Chalcogenide Hosts. *Progress in Solid State Chemistry* **1978**, *12* (1), 41–99. https://doi.org/10.1016/0079-6786(78)90003-1.

(68) Lewis H. Gaines. Battery Having an Electrode Comprising Mixtures of Al and TiS2. 4091191, May 23, 1978.

(69) Fenton, D. E.; Parker, J. M.; Wright, P. V. Complexes of Alkali Metal Ions with Poly(Ethylene Oxide). *Polymer* **1973**, *14* (11), 589. https://doi.org/10.1016/0032-3861(73)90146-8.

(70) Wright, P. V. Electrical Conductivity in Ionic Complexes of Poly(Ethylene Oxide). *British Polymer Journal* **1975**, *7* (5), 319–327. https://doi.org/10.1002/pi.4980070505.

(71) Armand, M. B.; Chabagno, J. M.; Duclot, M. Second Intern. Meeting on Solid Electrolytes, 1978.

(72) Armand, M. The History of Polymer Electrolytes. *Solid State Ionics* **1994**, *69* (3), 309–319. https://doi.org/10.1016/0167-2738(94)90419-7.

(73) Jarratt, E. *The epic story of Moli Energy, pioneer of the rechargeable lithium battery*. Electric Autonomy Canada. https://electricautonomy.ca/2020/09/18/moli-energy-lithium-battery-technology/ (accessed 2024-04-05).

(74) Mizushima, K.; Jones, P. C.; Wiseman, P. J.; Goodenough, J. B. LixCoO2 (0<x<-1): A New Cathode Material for Batteries of High Energy Density. *Materials Research Bulletin* **1980**, *15* (6), 783–789. https://doi.org/10.1016/0025-5408(80)90012-4.

(75) Thackeray, M. M.; David, W. I. F.; Bruce, P. G.; Goodenough, J. B. Lithium Insertion into Manganese Spinels. *Materials Research Bulletin* **1983**, *18* (4), 461–472. https://doi.org/10.1016/0025-5408(83)90138-1.

(76) Thackeray, M. M.; Johnson, P. J.; de Picciotto, L. A.; Bruce, P. G.; Goodenough, J. B. Electrochemical Extraction of Lithium from LiMn2O4. *Materials Research Bulletin* **1984**, *19* (2), 179–187. https://doi.org/10.1016/0025-5408(84)90088-6.

(77) Li, M.; Lu, J.; Chen, Z.; Amine, K. 30 Years of Lithium-Ion Batteries. *Advanced Materials* **2018**, *30* (33), 1800561. https://doi.org/10.1002/adma.201800561.

(78) Reimers, J. N.; Dahn, J. R. Electrochemical and In Situ X-Ray Diffraction Studies of Lithium Intercalation in Li x CoO2. *J. Electrochem. Soc.* **1992**, *139* (8), 2091. https://doi.org/10.1149/1.2221184.

(79) Doh, C.-H.; Kim, D.-H.; Kim, H.-S.; Shin, H.-M.; Jeong, Y.-D.; Moon, S.-I.; Jin, B.-S.; Eom, S. W.; Kim, H.-S.; Kim, K.-W.; Oh, D.-H.; Veluchamy, A. Thermal and Electrochemical Behaviour of C/LixCoO2 Cell during Safety Test. *Journal of Power Sources* **2008**, *175* (2), 881–885. https://doi.org/10.1016/j.jpowsour.2007.09.102.

(80) Besenhard, J. O.; Fritz, H. P. Cathodic Reduction of Graphite in Organic Solutions of Alkali and NR4+ Salts. *Journal of Electroanalytical Chemistry and Interfacial Electrochemistry* **1974**, *53* (2), 329–333. https://doi.org/10.1016/S0022-0728(74)80146-4.

(81) Peled, E. The Electrochemical Behavior of Alkali and Alkaline Earth Metals in Nonaqueous Battery Systems—The Solid Electrolyte Interphase Model. *J. Electrochem. Soc.* **1979**, *126* (12), 2047. https://doi.org/10.1149/1.2128859.

(82) Goodenough, J. B.; Kim, Y. Challenges for Rechargeable Li Batteries. *Chem. Mater.* **2010**, *22* (3), 587–603. https://doi.org/10.1021/cm901452z.

(83) Gauthier, M.; Carney, T. J.; Grimaud, A.; Giordano, L.; Pour, N.; Chang, H.-H.; Fenning, D. P.; Lux, S. F.; Paschos, O.; Bauer, C.; Maglia, F.; Lupart, S.; Lamp, P.; Shao-Horn, Y. Electrode–Electrolyte Interface in Li-Ion Batteries: Current Understanding and New Insights. *J. Phys. Chem. Lett.* **2015**, *6* (22), 4653–4672. https://doi.org/10.1021/acs.jpclett.5b01727.

(84) Peljo, P.; Girault, H. H. Electrochemical Potential Window of Battery Electrolytes: The HOMO–LUMO Misconception. *Energy Environ. Sci.* **2018**, *11* (9), 2306–2309. https://doi.org/10.1039/C8EE01286E.

(85) Yoshino, A.; Sanechika, K.; Nakajima, T. Secondary Battery. US4668595A, May 26, 1987. https://patents.google.com/patent/US4668595A/en (accessed 2024-04-15).

(86) Xie, J.; Lu, Y.-C. A Retrospective on Lithium-Ion Batteries. *Nat Commun* **2020**, *11* (1), 2499. https://doi.org/10.1038/s41467-020-16259-9.

(87) Fong, R.; Sacken, U. von; Dahn, J. R. Studies of Lithium Intercalation into Carbons Using Nonaqueous Electrochemical Cells. *J. Electrochem. Soc.* **1990**, *137* (7), 2009. https://doi.org/10.1149/1.2086855.

(88) Nishi, Y. The Development of Lithium Ion Secondary Batteries. *The Chemical Record* **2001**, *1* (5), 406–413. https://doi.org/10.1002/tcr.1024.

(89) Guyomard, D.; Tarascon, J. M. Rechargeable Li1 + x Mn2 O 4 / Carbon Cells with a New Electrolyte Composition: Potentiostatic Studies and Application to Practical Cells. *J. Electrochem. Soc.* **1993**, *140* (11), 3071. https://doi.org/10.1149/1.2220987.

(90) Birkl, C. R.; Roberts, M. R.; McTurk, E.; Bruce, P. G.; Howey, D. A. Degradation Diagnostics for Lithium Ion Cells. *Journal of Power Sources* **2017**, *341*, 373–386. https://doi.org/10.1016/j.jpowsour.2016.12.011.

(91) Liu, Q.; Du, C.; Shen, B.; Zuo, P.; Cheng, X.; Ma, Y.; Yin, G.; Gao, Y. Understanding Undesirable Anode Lithium Plating Issues in Lithium-Ion Batteries. *RSC Adv.* **2016**, *6* (91), 88683–88700. https://doi.org/10.1039/C6RA19482F.

(92) Tallman, K. R.; Zhang, B.; Wang, L.; Yan, S.; Thompson, K.; Tong, X.; Thieme, J.; Kiss, A.; Marschilok, A. C.; Takeuchi, K. J.; Bock, D. C.; Takeuchi, E. S. Anode Overpotential Control via Interfacial Modification: Inhibition of Lithium Plating on Graphite Anodes. *ACS Appl. Mater. Interfaces* **2019**, *11* (50), 46864–46874. https://doi.org/10.1021/acsami.9b16794.

(93) Houreld, K.; Bashizi, A. *Despite reforms, mining for EV metals in Congo exacts steep cost on workers*. Washington Post. https://www.washingtonpost.com/world/interactive/2023/ev-cobalt-mines-congo/ (accessed 2024-04-15).

(94) Hou, X.; Liu, X.; Wang, H.; Zhang, X.; Zhou, J.; Wang, M. Specific Countermeasures to Intrinsic Capacity Decline Issues and Future Direction of LiMn2O4 Cathode. *Energy Storage Materials* **2023**, *57*, 577–606. https://doi.org/10.1016/j.ensm.2023.02.015.

(95) Yamada, A.; Miura, K.; Hinokuma, K.; Tanaka, M. Synthesis and Structural Aspects of LiMn2 O 4 ± δ as a Cathode for Rechargeable Lithium Batteries. *J. Electrochem. Soc.* **1995**, *142* (7), 2149. https://doi.org/10.1149/1.2044266.

(96) Tarascon, J. M.; McKinnon, W. R.; Coowar, F.; Bowmer, T. N.; Amatucci, G.; Guyomard, D. Synthesis Conditions and Oxygen Stoichiometry Effects on Li Insertion into the Spinel LiMn2 O 4. *J. Electrochem. Soc.* **1994**, *141* (6), 1421. https://doi.org/10.1149/1.2054941.

(97) Yang, X. Q.; Sun, X.; Balasubramanian, M.; McBreen, J.; Xia, Y.; Sakai, T.; Yoshio, M. The Population of Oxygen Vacancies in Li1 + y Mn2 − y O 4 − δ Type Cathode Materials: The Primary

Factor of Temperature Dependent Structural Changes. *Electrochem. Solid-State Lett.* **2001**, *4* (8), A117. https://doi.org/10.1149/1.1380549.

(98) Croguennec, L.; Palacin, M. R. Recent Achievements on Inorganic Electrode Materials for Lithium-Ion Batteries. *J. Am. Chem. Soc.* **2015**, *137* (9), 3140–3156. https://doi.org/10.1021/ja507828x.

(99) Yamada, S.; Fujiwara, M.; Kanda, M. Synthesis and Properties of LiNiO2 as Cathode Material for Secondary Batteries. *Journal of Power Sources* **1995**, *54* (2), 209–213. https://doi.org/10.1016/0378-7753(94)02068-E.

(100) Rougier, A.; Gravereau, P.; Delmas, C. Optimization of the Composition of the Li1 − z Ni1 + z O 2 Electrode Materials: Structural, Magnetic, and Electrochemical Studies. *J. Electrochem. Soc.* **1996**, *143* (4), 1168. https://doi.org/10.1149/1.1836614.

(101) Arai, H.; Okada, S.; Sakurai, Y.; Yamaki, J. Thermal Behavior of Li1−yNiO2 and the Decomposition Mechanism. *Solid State Ionics* **1998**, *109* (3), 295–302. https://doi.org/10.1016/S0167-2738(98)00075-7.

(102) Kang, K.; Meng, Y. S.; Bréger, J.; Grey, C. P.; Ceder, G. Electrodes with High Power and High Capacity for Rechargeable Lithium Batteries. *Science* **2006**, *311* (5763), 977–980. https://doi.org/10.1126/science.1122152.

(103) Ohzuku, T.; Ueda, A.; Kouguchi, M. Synthesis and Characterization of LiAl1 / 4Ni3 / 4 O 2 (R 3m) for Lithium-Ion (Shuttlecock) Batteries. *J. Electrochem. Soc.* **1995**, *142* (12), 4033. https://doi.org/10.1149/1.2048458.

(104) Guilmard, M.; Rougier, A.; Grüne, M.; Croguennec, L.; Delmas, C. Effects of Aluminum on the Structural and Electrochemical Properties of LiNiO2. *Journal of Power Sources* **2003**, *115* (2), 305–314. https://doi.org/10.1016/S0378-7753(03)00012-0.

(105) Xu, J.; Lin, F.; Doeff, M. M.; Tong, W. A Review of Ni-Based Layered Oxides for Rechargeable Li-Ion Batteries. *J. Mater. Chem. A* **2017**, *5* (3), 874–901. https://doi.org/10.1039/C6TA07991A.

(106) Jung, R.; Metzger, M.; Maglia, F.; Stinner, C.; Gasteiger, H. A. Oxygen Release and Its Effect on the Cycling Stability of LiNixMnyCozO2 (NMC) Cathode Materials for Li-Ion Batteries. *J. Electrochem. Soc.* **2017**, *164* (7), A1361. https://doi.org/10.1149/2.0021707jes.

(107) Noh, H.-J.; Youn, S.; Yoon, C. S.; Sun, Y.-K. Comparison of the Structural and Electrochemical Properties of Layered Li[NixCoyMnz]O2 (*x* = 1/3, 0.5, 0.6, 0.7, 0.8 and 0.85) Cathode Material for Lithium-Ion Batteries. *Journal of Power Sources* **2013**, *233*, 121–130. https://doi.org/10.1016/j.jpowsour.2013.01.063.

(108) Julien, C. M.; Mauger, A. NCA, NCM811, and the Route to Ni-Richer Lithium-Ion Batteries. *Energies* **2020**, *13* (23), 6363. https://doi.org/10.3390/en13236363.

(109) Padhi, A. K.; Nanjundaswamy, K. S.; Goodenough, J. B. Phospho-olivines as Positive-Electrode Materials for Rechargeable Lithium Batteries. *J. Electrochem. Soc.* **1997**, *144* (4), 1188. https://doi.org/10.1149/1.1837571.

(110) Julien, C. M.; Mauger, A.; Zaghib, K.; Groult, H. Comparative Issues of Cathode Materials for Li-Ion Batteries. *Inorganics* **2014**, *2* (1), 132–154. https://doi.org/10.3390/inorganics2010132.

(111) Colbow, K. M.; Dahn, J. R.; Haering, R. R. Structure and Electrochemistry of the Spinel Oxides LiTi2O4 and Li43<math><mtext>4</Mtext><mtext>3</Mtext></math>Ti53<math><mtext>5</Mtext><mtext>3</Mtext></math>O4. *Journal of Power Sources* **1989**, *26* (3), 397–402. https://doi.org/10.1016/0378-7753(89)80152-1.

(112) Ferg, E.; Gummow, R. J.; Kock, A. de; Thackeray, M. M. Spinel Anodes for Lithium-Ion Batteries. *J. Electrochem. Soc.* **1994**, *141* (11), L147. https://doi.org/10.1149/1.2059324.

(113) Julien, C. M.; Mauger, A. Fabrication of Li4Ti5O12 (LTO) as Anode Material for Li-Ion Batteries. *Micromachines* **2024**, *15* (3), 310. https://doi.org/10.3390/mi15030310.

(114) Poizot, P.; Laruelle, S.; Grugeon, S.; Dupont, L.; Tarascon, J.-M. Nano-Sized Transition-Metal Oxides as Negative-Electrode Materials for Lithium-Ion Batteries. *Nature* **2000**, *407* (6803), 496–499. https://doi.org/10.1038/35035045.

(115) Dedryvère, R.; Laruelle, S.; Grugeon, S.; Poizot, P.; Gonbeau, D.; Tarascon, J.-M. Contribution of X-Ray Photoelectron Spectroscopy to the Study of the Electrochemical Reactivity of CoO toward Lithium. *Chem. Mater.* **2004**, *16* (6), 1056–1061. https://doi.org/10.1021/cm0311269.

(116) Su, Q.; Zhang, J.; Wu, Y.; Du, G. Revealing the Electrochemical Conversion Mechanism of Porous Co3O4 Nanoplates in Lithium Ion Battery by *in Situ* Transmission Electron Microscopy. *Nano Energy* **2014**, *9*, 264–272. https://doi.org/10.1016/j.nanoen.2014.08.006.

(117) Wang, F.; Robert, R.; Chernova, N. A.; Pereira, N.; Omenya, F.; Badway, F.; Hua, X.; Ruotolo, M.; Zhang, R.; Wu, L.; Volkov, V.; Su, D.; Key, B.; Whittingham, M. S.; Grey, C. P.; Amatucci, G. G.; Zhu, Y.; Graetz, J. Conversion Reaction Mechanisms in Lithium Ion Batteries: Study of the Binary Metal Fluoride Electrodes. *J. Am. Chem. Soc.* **2011**, *133* (46), 18828–18836. https://doi.org/10.1021/ja206268a.

(118) Wang, F.; Yu, H.-C.; Chen, M.-H.; Wu, L.; Pereira, N.; Thornton, K.; Van der Ven, A.; Zhu, Y.; Amatucci, G. G.; Graetz, J. Tracking Lithium Transport and Electrochemical Reactions in Nanoparticles. *Nat Commun* **2012**, *3* (1), 1201. https://doi.org/10.1038/ncomms2185.

(119) Lin, F.; Nordlund, D.; Weng, T.-C.; Zhu, Y.; Ban, C.; Richards, R. M.; Xin, H. L. Phase Evolution for Conversion Reaction Electrodes in Lithium-Ion Batteries. *Nat Commun* **2014**, *5* (1), 3358. https://doi.org/10.1038/ncomms4358.

(120) Lu, Y.; Yu, L.; Lou, X. W. (David). Nanostructured Conversion-Type Anode Materials for Advanced Lithium-Ion Batteries. *Chem* **2018**, *4* (5), 972–996. https://doi.org/10.1016/j.chempr.2018.01.003.

(121) Ponrouch, A.; Taberna, P.-L.; Simon, P.; Palacín, M. R. On the Origin of the Extra Capacity at Low Potential in Materials for Li Batteries Reacting through Conversion Reaction. *Electrochimica Acta* **2012**, *61*, 13–18. https://doi.org/10.1016/j.electacta.2011.11.029.

(122) Martin, L.; Martinez, H.; Poinot, D.; Pecquenard, B.; Le Cras, F. Direct Observation of Important Morphology and Composition Changes at the Surface of the CuO Conversion Material in Lithium Batteries. *Journal of Power Sources* **2014**, *248*, 861–873. https://doi.org/10.1016/j.jpowsour.2013.10.015.

(123) Oumellal, Y.; Rougier, A.; Nazri, G. A.; Tarascon, J.-M.; Aymard, L. Metal Hydrides for Lithium-Ion Batteries. *Nature Mater* **2008**, *7* (11), 916–921. https://doi.org/10.1038/nmat2288.

(124) Cabana, J.; Monconduit, L.; Larcher, D.; Palacín, M. R. Beyond Intercalation-Based Li-Ion Batteries: The State of the Art and Challenges of Electrode Materials Reacting Through Conversion Reactions. *Advanced Materials* **2010**, *22* (35), E170–E192. https://doi.org/10.1002/adma.201000717.

(125) McDowell, M. T.; Lee, S. W.; Nix, W. D.; Cui, Y. 25th Anniversary Article: Understanding the Lithiation of Silicon and Other Alloying Anodes for Lithium-Ion Batteries. *Advanced Materials* **2013**, *25* (36), 4966–4985. https://doi.org/10.1002/adma.201301795.

(126) Idota, Y.; Kubota, T.; Matsufuji, A.; Maekawa, Y.; Miyasaka, T. Tin-Based Amorphous Oxide: A High-Capacity Lithium-Ion-Storage Material. *Science* **1997**, *276* (5317), 1395–1397. https://doi.org/10.1126/science.276.5317.1395.

(127) Sharma, R. A.; Seefurth, R. N. Thermodynamic Properties of the Lithium-Silicon System. *J. Electrochem. Soc.* **1976**, *123* (12), 1763. https://doi.org/10.1149/1.2132692.

(128) Beaulieu, L. Y.; Eberman, K. W.; Turner, R. L.; Krause, L. J.; Dahn, J. R. Colossal Reversible Volume Changes in Lithium Alloys. *Electrochem. Solid-State Lett.* **2001**, *4* (9), A137. https://doi.org/10.1149/1.1388178.

(129) Wu, H.; Cui, Y. Designing Nanostructured Si Anodes for High Energy Lithium Ion Batteries. *Nano Today* **2012**, *7* (5), 414–429. https://doi.org/10.1016/j.nantod.2012.08.004.

(130) Chan, C. K.; Peng, H.; Liu, G.; McIlwrath, K.; Zhang, X. F.; Huggins, R. A.; Cui, Y. High-Performance Lithium Battery Anodes Using Silicon Nanowires. *Nature Nanotech* **2008**, *3* (1), 31–35. https://doi.org/10.1038/nnano.2007.411.

(131) Cui, Y. Silicon Anodes. *Nat Energy* **2021**, *6* (10), 995–996. https://doi.org/10.1038/s41560-021-00918-2.

(132) *Electrochemical Supercapacitors*.

(133) Zhang, S.; Pan, N. Supercapacitors Performance Evaluation. *Advanced Energy Materials* **2015**, *5* (6), 1401401. https://doi.org/10.1002/aenm.201401401.

(134) Laheäär, A.; Przygocki, P.; Abbas, Q.; Béguin, F. Appropriate Methods for Evaluating the Efficiency and Capacitive Behavior of Different Types of Supercapacitors. *Electrochemistry Communications* **2015**, *60*, 21–25. https://doi.org/10.1016/j.elecom.2015.07.022.

(135) Gittins, J. W.; Chen, Y.; Arnold, S.; Augustyn, V.; Balducci, A.; Brousse, T.; Frackowiak, E.; Gómez-Romero, P.; Kanwade, A.; Köps, L.; Jha, P. K.; Lyu, D.; Meo, M.; Pandey, D.; Pang, L.; Presser, V.; Rapisarda, M.; Rueda-García, D.; Saeed, S.; Shirage, P. M.; Ślesiński, A.; Soavi, F.; Thomas, J.; Titirici, M.-M.; Wang, H.; Xu, Z.; Yu, A.; Zhang, M.; Forse, A. C. Interlaboratory Study Assessing the Analysis of Supercapacitor Electrochemistry Data. *Journal of Power Sources* **2023**, *585*, 233637. https://doi.org/10.1016/j.jpowsour.2023.233637.

(136) Conway, B. E.; Angerstein-Kozlowska, H. The Electrochemical Study of Multiple-State Adsorption in Monolayers. *Acc. Chem. Res.* **1981**, *14* (2), 49–56. https://doi.org/10.1021/ar00062a004.

(137) Angerstein-Kozlowska, H.; Conway, B. E.; Sharp, W. B. A. The Real Condition of Electrochemically Oxidized Platinum Surfaces: Part I. Resolution of Component Processes. *Journal of Electroanalytical Chemistry and Interfacial Electrochemistry* **1973**, *43* (1), 9–36. https://doi.org/10.1016/S0022-0728(73)80307-9.

(138) Costentin, C.; Porter, T. R.; Savéant, J.-M. How Do Pseudocapacitors Store Energy? Theoretical Analysis and Experimental Illustration. *ACS Appl. Mater. Interfaces* **2017**, *9* (10), 8649–8658. https://doi.org/10.1021/acsami.6b14100.

(139) Brousse, T.; Bélanger, D.; Long, J. W. To Be or Not To Be Pseudocapacitive? *J. Electrochem. Soc.* **2015**, *162* (5), A5185. https://doi.org/10.1149/2.0201505jes.

(140) Come, J.; Augustyn, V.; Kim, J. W.; Rozier, P.; Taberna, P.-L.; Gogotsi, P.; Long, J. W.; Dunn, B.; Simon, P. Electrochemical Kinetics of Nanostructured Nb2O5 Electrodes. *J. Electrochem. Soc.* **2014**, *161* (5), A718. https://doi.org/10.1149/2.040405jes.

(141) Deebansok, S.; Deng, J.; Le Calvez, E.; Zhu, Y.; Crosnier, O.; Brousse, T.; Fontaine, O. Capacitive Tendency Concept alongside Supervised Machine-Learning toward Classifying Electrochemical Behavior of Battery and Pseudocapacitor Materials. *Nat Commun* **2024**, *15* (1), 1133. https://doi.org/10.1038/s41467-024-45394-w.

(142) Shao, Y.; El-Kady, M. F.; Sun, J.; Li, Y.; Zhang, Q.; Zhu, M.; Wang, H.; Dunn, B.; Kaner, R. B. Design and Mechanisms of Asymmetric Supercapacitors. *Chem. Rev.* **2018**, *118* (18), 9233–9280. https://doi.org/10.1021/acs.chemrev.8b00252.

(143) Becker, H. I. Low Voltage Electrolytic Capacitor. US2800616A, July 23, 1957. https://patents.google.com/patent/US2800616A/en (accessed 2024-04-29).

(144) Rightmire, R. A. Electrical Energy Storage Apparatus. US3288641A, November 29, 1966. https://patents.google.com/patent/US3288641A/en (accessed 2024-04-29).

(145) Boos, D. L. Electrolytic Capacitor Having Carbon Paste Electrodes. US3536963A, October 27, 1970. https://patents.google.com/patent/US3536963A/en (accessed 2024-04-29).

(146) Jadhav, V. V.; Mane, R. S.; Shinde, P. V. Electrochemical Supercapacitors: History, Types, Designing Processes, Operation Mechanisms, and Advantages and Disadvantages. In *Bismuth-Ferrite-Based Electrochemical Supercapacitors*; Jadhav, V. V., Mane, R. S., Shinde, P. V., Eds.; Springer International Publishing: Cham, 2020; pp 11–36. https://doi.org/10.1007/978-3-030-16718-9_2.

(147) *Ultracapacitor Overview*. Maxwell Technologies. https://maxwell.com/products/ultracapacitors/ (accessed 2024-05-06).

(148) *PRISMATIC ULTRA THIN SUPERCAPS*. CAP-XX Designs & Manufactures the Thinnest, Highest Power Density Supercapacitors & Ultracapacitors. https://www.cap-xx.com/products/prismatic-overview/ (accessed 2024-05-06).

(149) Ugarte, D. Onion-like Graphitic Particles. *Carbon* **1995**, *33* (7), 989–993. https://doi.org/10.1016/0008-6223(95)00027-B.

(150) Bates, K. R.; Scuseria, G. E. Why Are Buckyonions Round? *Theor Chem Acc* **1998**, *99* (1), 29–33. https://doi.org/10.1007/s002140050299.

(151) Terrones, H.; Terrones, M. The Transformation of Polyhedral Particles into Graphitic Onions. *Journal of Physics and Chemistry of Solids* **1997**, *58* (11), 1789–1796. https://doi.org/10.1016/S0022-3697(97)00067-X.

(152) Kaur, S.; Krishnan, A.; Chakraborty, S. Recent Advances and Challenges of Carbon Nano Onions (CNOs) for Application in Supercapacitor Devices (SCDs). *Journal of Energy Storage* **2023**, *71*, 107928. https://doi.org/10.1016/j.est.2023.107928.

(153) Mykhailiv, O.; Zubyk, H.; Plonska-Brzezinska, M. E. Carbon Nano-Onions: Unique Carbon Nanostructures with Fascinating Properties and Their Potential Applications. *Inorganica Chimica Acta* **2017**, *468*, 49–66. https://doi.org/10.1016/j.ica.2017.07.021.

(154) Kuznetsov, V. L.; Chuvilin, A. L.; Moroz, E. M.; Kolomiichuk, V. N.; Shaikhutdinov, Sh. K.; Butenko, Yu. V.; Mal'kov, I. Yu. Effect of Explosion Conditions on the Structure of Detonation Soots: Ultradisperse Diamond and Onion Carbon. *Carbon* **1994**, *32* (5), 873–882. https://doi.org/10.1016/0008-6223(94)90044-2.

(155) Zeiger, M.; Jäckel, N.; Aslan, M.; Weingarth, D.; Presser, V. Understanding Structure and Porosity of Nanodiamond-Derived Carbon Onions. *Carbon* **2015**, *84*, 584–598. https://doi.org/10.1016/j.carbon.2014.12.050.

(156) Bartelmess, J.; Giordani, S. Carbon Nano-Onions (Multi-Layer Fullerenes): Chemistry and Applications. *Beilstein J. Nanotechnol.* **2014**, *5* (1), 1980–1998. https://doi.org/10.3762/bjnano.5.207.

(157) Permatasari, F. A.; Irham, M. A.; Bisri, S. Z.; Iskandar, F. Carbon-Based Quantum Dots for Supercapacitors: Recent Advances and Future Challenges. *Nanomaterials* **2021**, *11* (1), 91. https://doi.org/10.3390/nano11010091.

(158) Hu, C.; Li, M.; Qiu, J.; Sun, Y.-P. Design and Fabrication of Carbon Dots for Energy Conversion and Storage. *Chem. Soc. Rev.* **2019**, *48* (8), 2315–2337. https://doi.org/10.1039/C8CS00750K.

(159) Genc, R.; Alas, M. O.; Harputlu, E.; Repp, S.; Kremer, N.; Castellano, M.; Colak, S. G.; Ocakoglu, K.; Erdem, E. High-Capacitance Hybrid Supercapacitor Based on Multi-Colored Fluorescent Carbon-Dots. *Sci Rep* **2017**, *7* (1), 11222. https://doi.org/10.1038/s41598-017-11347-1.

(160) Cayuela, A.; Soriano, M. L.; Carrillo-Carrión, C.; Valcárcel, M. Semiconductor and Carbon-Based Fluorescent Nanodots: The Need for Consistency. *Chem. Commun.* **2016**, *52* (7), 1311–1326. https://doi.org/10.1039/C5CC07754K.

(161) Zhang, S.; Sui, L.; Dong, H.; He, W.; Dong, L.; Yu, L. High-Performance Supercapacitor of Graphene Quantum Dots with Uniform Sizes. *ACS Appl. Mater. Interfaces* **2018**, *10* (15), 12983–12991. https://doi.org/10.1021/acsami.8b00323.

(162) Tetsuka, H.; Nagoya, A.; Fukusumi, T.; Matsui, T. Molecularly Designed, Nitrogen-Functionalized Graphene Quantum Dots for Optoelectronic Devices. *Advanced Materials* **2016**, *28* (23), 4632–4638. https://doi.org/10.1002/adma.201600058.

(163) Wang, J.; Fang, Z.; Li, T.; ur Rehman, S.; Luo, Q.; Chen, P.; Hu, L.; Zhang, F.; Wang, Q.; Bi, H. Highly Hydrophilic Carbon Dots' Decoration on NiCo2O4 Nanowires for Greatly Increased Electric Conductivity, Supercapacitance, and Energy Density. *Advanced Materials Interfaces* **2019**, *6* (9), 1900049. https://doi.org/10.1002/admi.201900049.

(164) Wei, G.; Du, K.; Zhao, X.; Wang, Z.; Liu, M.; Li, C.; Wang, H.; An, C.; Xing, W. Carbon Quantum Dot-Induced Self-Assembly of Ultrathin Ni(OH)2 Nanosheets: A Facile Method for Fabricating Three-Dimensional Porous Hierarchical Composite Micro-Nanostructures with Excellent Supercapacitor Performance. *Nano Res.* **2017**, *10* (9), 3005–3017. https://doi.org/10.1007/s12274-017-1516-4.

(165) Iijima, S. Helical Microtubules of Graphitic Carbon. *Nature* **1991**, *354* (6348), 56–58. https://doi.org/10.1038/354056a0.

(166) Rathinavel, S.; Priyadharshini, K.; Panda, D. A Review on Carbon Nanotube: An Overview of Synthesis, Properties, Functionalization, Characterization, and the Application. *Materials Science and Engineering: B* **2021**, *268*, 115095. https://doi.org/10.1016/j.mseb.2021.115095.

(167) Thostenson, E. T.; Ren, Z.; Chou, T.-W. Advances in the Science and Technology of Carbon Nanotubes and Their Composites: A Review. *Composites Science and Technology* **2001**, *61* (13), 1899–1912. https://doi.org/10.1016/S0266-3538(01)00094-X.

(168) Belin, T.; Epron, F. Characterization Methods of Carbon Nanotubes: A Review. *Materials Science and Engineering: B* **2005**, *119* (2), 105–118. https://doi.org/10.1016/j.mseb.2005.02.046.

(169) Peigney, A.; Laurent, Ch.; Flahaut, E.; Bacsa, R. R.; Rousset, A. Specific Surface Area of Carbon Nanotubes and Bundles of Carbon Nanotubes. *Carbon* **2001**, *39* (4), 507–514. https://doi.org/10.1016/S0008-6223(00)00155-X.

(170) Kumar, N.; Ghosh, S.; Thakur, D.; Lee, C.-P.; Sahoo, P. K. Recent Advancements in Zero- to Three-Dimensional Carbon Networks with a Two-Dimensional Electrode Material for High-Performance Supercapacitors. *Nanoscale Adv.* **2023**, *5* (12), 3146–3176. https://doi.org/10.1039/D3NA00094J.

(171) Peng, C.; Zhang, S.; Jewell, D.; Chen, G. Z. Carbon Nanotube and Conducting Polymer Composites for Supercapacitors. *Progress in Natural Science* **2008**, *18* (7), 777–788. https://doi.org/10.1016/j.pnsc.2008.03.002.

(172) Augustyn, V.; Gogotsi, Y. 2D Materials with Nanoconfined Fluids for Electrochemical Energy Storage. *Joule* **2017**, *1* (3), 443–452. https://doi.org/10.1016/j.joule.2017.09.008.

(173) Novoselov, K. S.; Geim, A. K.; Morozov, S. V.; Jiang, D.; Zhang, Y.; Dubonos, S. V.; Grigorieva, I. V.; Firsov, A. A. Electric Field Effect in Atomically Thin Carbon Films. *Science* **2004**, *306* (5696), 666–669. https://doi.org/10.1126/science.1102896.

(174) Lee, C.; Wei, X.; Kysar, J. W.; Hone, J. Measurement of the Elastic Properties and Intrinsic Strength of Monolayer Graphene. *Science* **2008**, *321* (5887), 385–388. https://doi.org/10.1126/science.1157996.

(175) Lee, X. J.; Hiew, B. Y. Z.; Lai, K. C.; Lee, L. Y.; Gan, S.; Thangalazhy-Gopakumar, S.; Rigby, S. Review on Graphene and Its Derivatives: Synthesis Methods and Potential Industrial Implementation. *Journal of the Taiwan Institute of Chemical Engineers* **2019**, *98*, 163–180. https://doi.org/10.1016/j.jtice.2018.10.028.

(176) Jayasena, B.; Subbiah, S. A Novel Mechanical Cleavage Method for Synthesizing Few-Layer Graphenes. *Nanoscale Res Lett* **2011**, *6* (1), 95. https://doi.org/10.1186/1556-276X-6-95.

(177) Brodie, B. C. XIII. On the Atomic Weight of Graphite. *Philosophical Transactions of the Royal Society of London* **1859**, *149*, 249–259. https://doi.org/10.1098/rstl.1859.0013.

(178) Staudenmaier, L. Verfahren Zur Darstellung Der Graphitsäure. *Berichte der deutschen chemischen Gesellschaft* **1898**, *31* (2), 1481–1487. https://doi.org/10.1002/cber.18980310237.

(179) Hofmann, U.; König, E. Untersuchungen über Graphitoxyd. *Zeitschrift für anorganische und allgemeine Chemie* **1937**, *234* (4), 311–336. https://doi.org/10.1002/zaac.19372340405.

(180) Hummers, W. S. Jr.; Offeman, R. E. Preparation of Graphitic Oxide. *J. Am. Chem. Soc.* **1958**, *80* (6), 1339–1339. https://doi.org/10.1021/ja01539a017.

(181) Marcano, D. C.; Kosynkin, D. V.; Berlin, J. M.; Sinitskii, A.; Sun, Z.; Slesarev, A.; Alemany, L. B.; Lu, W.; Tour, J. M. Improved Synthesis of Graphene Oxide. *ACS Nano* **2010**, *4* (8), 4806–4814. https://doi.org/10.1021/nn1006368.

(182) Chua, C. K.; Pumera, M. Chemical Reduction of Graphene Oxide: A Synthetic Chemistry Viewpoint. *Chem. Soc. Rev.* **2013**, *43* (1), 291–312. https://doi.org/10.1039/C3CS60303B.

(183) Pei, S.; Cheng, H.-M. The Reduction of Graphene Oxide. *Carbon* **2012**, *50* (9), 3210–3228. https://doi.org/10.1016/j.carbon.2011.11.010.

(184) Ciesielski, A.; Samorì, P. Graphene via Sonication Assisted Liquid-Phase Exfoliation. *Chem. Soc. Rev.* **2013**, *43* (1), 381–398. https://doi.org/10.1039/C3CS60217F.

(185) Bhuyan, Md. S. A.; Uddin, Md. N.; Islam, Md. M.; Bipasha, F. A.; Hossain, S. S. Synthesis of Graphene. *Int Nano Lett* **2016**, *6* (2), 65–83. https://doi.org/10.1007/s40089-015-0176-1.

(186) Emtsev, K. V.; Bostwick, A.; Horn, K.; Jobst, J.; Kellogg, G. L.; Ley, L.; McChesney, J. L.; Ohta, T.; Reshanov, S. A.; Röhrl, J.; Rotenberg, E.; Schmid, A. K.; Waldmann, D.; Weber, H. B.; Seyller, T. Towards Wafer-Size Graphene Layers by Atmospheric Pressure Graphitization of Silicon Carbide. *Nature Mater* **2009**, *8* (3), 203–207. https://doi.org/10.1038/nmat2382.

(187) Mele, E. J. Interlayer Coupling in Rotationally Faulted Multilayer Graphenes. *J. Phys. D: Appl. Phys.* **2012**, *45* (15), 154004. https://doi.org/10.1088/0022-3727/45/15/154004.

(188) Riedl, C.; Coletti, C.; Starke, U. Structural and Electronic Properties of Epitaxial Graphene on SiC(0 0 0 1): A Review of Growth, Characterization, Transfer Doping and Hydrogen Intercalation. *J. Phys. D: Appl. Phys.* **2010**, *43* (37), 374009. https://doi.org/10.1088/0022-3727/43/37/374009.

(189) Li, X.; Cai, W.; An, J.; Kim, S.; Nah, J.; Yang, D.; Piner, R.; Velamakanni, A.; Jung, I.; Tutuc, E.; Banerjee, S. K.; Colombo, L.; Ruoff, R. S. Large-Area Synthesis of High-Quality and Uniform Graphene Films on Copper Foils. *Science* **2009**, *324* (5932), 1312–1314. https://doi.org/10.1126/science.1171245.

(190) Losurdo, M.; Giangregorio, M. M.; Capezzuto, P.; Bruno, G. Graphene CVD Growth on Copper and Nickel: Role of Hydrogen in Kinetics and Structure. *Phys. Chem. Chem. Phys.* **2011**, *13* (46), 20836–20843. https://doi.org/10.1039/C1CP22347J.

(191) Xia, J.; Chen, F.; Li, J.; Tao, N. Measurement of the Quantum Capacitance of Graphene. *Nature Nanotech* **2009**, *4* (8), 505–509. https://doi.org/10.1038/nnano.2009.177.

(192) Zhang, K.; Mao, L.; Zhang, L. L.; Chan, H. S. O.; Zhao, X. S.; Wu, J. Surfactant-Intercalated, Chemically Reduced Graphene Oxide for High Performance Supercapacitor Electrodes. *J. Mater. Chem.* **2011**, *21* (20), 7302–7307. https://doi.org/10.1039/C1JM00007A.

(193) Abraham, J.; Vasu, K. S.; Williams, C. D.; Gopinadhan, K.; Su, Y.; Cherian, C. T.; Dix, J.; Prestat, E.; Haigh, S. J.; Grigorieva, I. V.; Carbone, P.; Geim, A. K.; Nair, R. R. Tunable Sieving of Ions Using Graphene Oxide Membranes. *Nature Nanotech* **2017**, *12* (6), 546–550. https://doi.org/10.1038/nnano.2017.21.

(194) Banda, H.; Périé, S.; Daffos, B.; Taberna, P.-L.; Dubois, L.; Crosnier, O.; Simon, P.; Lee, D.; De Paëpe, G.; Duclairoir, F. Sparsely Pillared Graphene Materials for High-Performance Supercapacitors: Improving Ion Transport and Storage Capacity. *ACS Nano* **2019**, *13* (2), 1443–1453. https://doi.org/10.1021/acsnano.8b07102.

(195) Wang, G.; Sun, X.; Lu, F.; Sun, H.; Yu, M.; Jiang, W.; Liu, C.; Lian, J. Flexible Pillared Graphene-Paper Electrodes for High-Performance Electrochemical Supercapacitors. *Small* **2012**, *8* (3), 452–459. https://doi.org/10.1002/smll.201101719.

(196) Chen, L.; Shi, G.; Shen, J.; Peng, B.; Zhang, B.; Wang, Y.; Bian, F.; Wang, J.; Li, D.; Qian, Z.; Xu, G.; Liu, G.; Zeng, J.; Zhang, L.; Yang, Y.; Zhou, G.; Wu, M.; Jin, W.; Li, J.; Fang, H. Ion Sieving in Graphene Oxide Membranes via Cationic Control of Interlayer Spacing. *Nature* **2017**, *550* (7676), 380–383. https://doi.org/10.1038/nature24044.

(197) Banda, H.; Daffos, B.; Périé, S.; Chenavier, Y.; Dubois, L.; Aradilla, D.; Pouget, S.; Simon, P.; Crosnier, O.; Taberna, P.-L.; Duclairoir, F. Ion Sieving Effects in Chemically Tuned Pillared Graphene Materials for Electrochemical Capacitors. *Chem. Mater.* **2018**, *30* (9), 3040–3047. https://doi.org/10.1021/acs.chemmater.8b00759.

(198) Herrera-Alonso, M.; Abdala, A. A.; McAllister, M. J.; Aksay, I. A.; Prud'homme, R. K. Intercalation and Stitching of Graphite Oxide with Diaminoalkanes. *Langmuir* **2007**, *23* (21), 10644–10649. https://doi.org/10.1021/la0633839.

(199) Fleischmann, S.; Spencer, M. A.; Augustyn, V. Electrochemical Reactivity under Confinement Enabled by Molecularly Pillared 2D and Layered Materials. *Chem. Mater.* **2020**, *32* (8), 3325–3334. https://doi.org/10.1021/acs.chemmater.0c00648.

(200) Fleischmann, S.; Zhang, Y.; Wang, X.; Cummings, P. T.; Wu, J.; Simon, P.; Gogotsi, Y.; Presser, V.; Augustyn, V. Continuous Transition from Double-Layer to Faradaic Charge Storage in Confined Electrolytes. *Nat Energy* **2022**, *7* (3), 222–228. https://doi.org/10.1038/s41560-022-00993-z.

(201) Jeong, H. M.; Lee, J. W.; Shin, W. H.; Choi, Y. J.; Shin, H. J.; Kang, J. K.; Choi, J. W. Nitrogen-Doped Graphene for High-Performance Ultracapacitors and the Importance of Nitrogen-Doped Sites at Basal Planes. *Nano Lett.* **2011**, *11* (6), 2472–2477. https://doi.org/10.1021/nl2009058.

(202) Zhu, Y.; Murali, S.; Stoller, M. D.; Ganesh, K. J.; Cai, W.; Ferreira, P. J.; Pirkle, A.; Wallace, R. M.; Cychosz, K. A.; Thommes, M.; Su, D.; Stach, E. A.; Ruoff, R. S. Carbon-Based Supercapacitors Produced by Activation of Graphene. *Science* **2011**, *332* (6037), 1537–1541. https://doi.org/10.1126/science.1200770.

(203) Chen, S.; Zhu, J.; Wu, X.; Han, Q.; Wang, X. Graphene Oxide−MnO2 Nanocomposites for Supercapacitors. *ACS Nano* **2010**, *4* (5), 2822–2830. https://doi.org/10.1021/nn901311t.

(204) Qi, T.; Jiang, J.; Chen, H.; Wan, H.; Miao, L.; Zhang, L. Synergistic Effect of Fe3O4/Reduced Graphene Oxide Nanocomposites for Supercapacitors with Good Cycling Life. *Electrochimica Acta* **2013**, *114*, 674–680. https://doi.org/10.1016/j.electacta.2013.10.068.

(205) Zhang, K.; Zhang, L. L.; Zhao, X. S.; Wu, J. Graphene/Polyaniline Nanofiber Composites as Supercapacitor Electrodes. *Chem. Mater.* **2010**, *22* (4), 1392–1401. https://doi.org/10.1021/cm902876u.

(206) Hu, Z.; Srinivasan, M. P. Preparation of High-Surface-Area Activated Carbons from Coconut Shell. *Microporous and Mesoporous Materials* **1999**, *27* (1), 11–18. https://doi.org/10.1016/S1387-1811(98)00183-8.

(207) Hu, Z.; Srinivasan, M. P.; Ni, Y. Novel Activation Process for Preparing Highly Microporous and Mesoporous Activated Carbons. *Carbon* **2001**, *39* (6), 877–886. https://doi.org/10.1016/S0008-6223(00)00198-6.

(208) Sevilla, M.; Mokaya, R. Energy Storage Applications of Activated Carbons: Supercapacitors and Hydrogen Storage. *Energy Environ. Sci.* **2014**, *7* (4), 1250–1280. https://doi.org/10.1039/C3EE43525C.

(209) Zhang, L. L.; Zhao, X. S. Carbon-Based Materials as Supercapacitor Electrodes. *Chem. Soc. Rev.* **2009**, *38* (9), 2520–2531. https://doi.org/10.1039/B813846J.

(210) Fahimirad, S.; Hatami, M. Heavy Metal-Mediated Changes in Growth and Phytochemicals of Edible and Medicinal Plants. In *Medicinal Plants and Environmental Challenges*; Ghorbanpour, M., Varma, A., Eds.; Springer International Publishing: Cham, 2017; pp 189–214. https://doi.org/10.1007/978-3-319-68717-9_11.

(211) Chmiola, J.; Yushin, G.; Gogotsi, Y.; Portet, C.; Simon, P.; Taberna, P. L. Anomalous Increase in Carbon Capacitance at Pore Sizes Less Than 1 Nanometer. *Science* **2006**, *313* (5794), 1760–1763. https://doi.org/10.1126/science.1132195.

(212) Gogotsi, Y.; Nikitin, A.; Ye, H.; Zhou, W.; Fischer, J. E.; Yi, B.; Foley, H. C.; Barsoum, M. W. Nanoporous Carbide-Derived Carbon with Tunable Pore Size. *Nature Mater* **2003**, *2* (9), 591–594. https://doi.org/10.1038/nmat957.

(213) Tsai, W.-Y.; Taberna, P.-L.; Simon, P. Electrochemical Quartz Crystal Microbalance (EQCM) Study of Ion Dynamics in Nanoporous Carbons. *J. Am. Chem. Soc.* **2014**, *136* (24), 8722–8728. https://doi.org/10.1021/ja503449w.

(214) Presser, V.; Heon, M.; Gogotsi, Y. Carbide-Derived Carbons – From Porous Networks to Nanotubes and Graphene. *Advanced Functional Materials* **2011**, *21* (5), 810–833. https://doi.org/10.1002/adfm.201002094.

(215) Béguin, F.; Presser, V.; Balducci, A.; Frackowiak, E. Carbons and Electrolytes for Advanced Supercapacitors. *Advanced Materials* **2014**, *26* (14), 2219–2251. https://doi.org/10.1002/adma.201304137.

(216) MacFarlane, D. R.; Tachikawa, N.; Forsyth, M.; Pringle, J. M.; Howlett, P. C.; Elliott, G. D.; Davis, J. H.; Watanabe, M.; Simon, P.; Angell, C. A. Energy Applications of Ionic Liquids. *Energy Environ. Sci.* **2013**, *7* (1), 232–250. https://doi.org/10.1039/C3EE42099J.

(217) Forse, A. C.; Griffin, J. M.; Merlet, C.; Bayley, P. M.; Wang, H.; Simon, P.; Grey, C. P. NMR Study of Ion Dynamics and Charge Storage in Ionic Liquid Supercapacitors. *J. Am. Chem. Soc.* **2015**, *137* (22), 7231–7242. https://doi.org/10.1021/jacs.5b03958.

(218) Grahame, D. C. Properties of the Electrical Double Layer at a Mercury Surface. I. Methods of Measurement and Interpretation of Results. *J. Am. Chem. Soc.* **1941**, *63* (5), 1207–1215. https://doi.org/10.1021/ja01850a014.

(219) Conway, B. E.; Gileadi, E. Kinetic Theory of Pseudo-Capacitance and Electrode Reactions at Appreciable Surface Coverage. *Trans. Faraday Soc.* **1962**, *58* (0), 2493–2509. https://doi.org/10.1039/TF9625802493.

(220) Herrero, E.; Buller, L. J.; Abruña, H. D. Underpotential Deposition at Single Crystal Surfaces of Au, Pt, Ag and Other Materials. *Chem. Rev.* **2001**, *101* (7), 1897–1930. https://doi.org/10.1021/cr9600363.

(221) Trasatti, S.; Buzzanca, G. Ruthenium Dioxide: A New Interesting Electrode Material. Solid State Structure and Electrochemical Behaviour. *Journal of Electroanalytical Chemistry and Interfacial Electrochemistry* **1971**, *29* (2), A1–A5. https://doi.org/10.1016/S0022-0728(71)80111-0.

(222) Ardizzone, S.; Fregonara, G.; Trasatti, S. “Inner” and “Outer” Active Surface of RuO2 Electrodes. *Electrochimica Acta* **1990**, *35* (1), 263–267. https://doi.org/10.1016/0013-4686(90)85068-X.

(223) Zheng, J. P.; Cygan, P. J.; Jow, T. R. Hydrous Ruthenium Oxide as an Electrode Material for Electrochemical Capacitors. *J. Electrochem. Soc.* **1995**, *142* (8), 2699. https://doi.org/10.1149/1.2050077.

(224) Dmowski, W.; Egami, T.; Swider-Lyons, K. E.; Love, C. T.; Rolison, D. R. Local Atomic Structure and Conduction Mechanism of Nanocrystalline Hydrous RuO2 from X-Ray Scattering. *J. Phys. Chem. B* **2002**, *106* (49), 12677–12683. https://doi.org/10.1021/jp026228l.

(225) Yoshida, N.; Yamada, Y.; Nishimura, S.; Oba, Y.; Ohnuma, M.; Yamada, A. Unveiling the Origin of Unusual Pseudocapacitance of RuO2·nH2O from Its Hierarchical Nanostructure by Small-Angle X-Ray Scattering. *J. Phys. Chem. C* **2013**, *117* (23), 12003–12009. https://doi.org/10.1021/jp403402k.

(226) Majumdar, D.; Maiyalagan, T.; Jiang, Z. Recent Progress in Ruthenium Oxide-Based Composites for Supercapacitor Applications. *ChemElectroChem* **2019**, *6* (17), 4343–4372. https://doi.org/10.1002/celc.201900668.

(227) Lee, H. Y.; Goodenough, J. B. Supercapacitor Behavior with KCl Electrolyte. *Journal of Solid State Chemistry* **1999**, *144* (1), 220–223. https://doi.org/10.1006/jssc.1998.8128.

(228) Hong, M. S.; Lee, S. H.; Kim, S. W. Use of KCl Aqueous Electrolyte for 2 V Manganese Oxide/Activated Carbon Hybrid Capacitor. *Electrochem. Solid-State Lett.* **2002**, *5* (10), A227. https://doi.org/10.1149/1.1506463.

(229) Brousse, T.; Toupin, M.; Dugas, R.; Athouël, L.; Crosnier, O.; Bélanger, D. Crystalline MnO2 as Possible Alternatives to Amorphous Compounds in Electrochemical Supercapacitors. *J. Electrochem. Soc.* **2006**, *153* (12), A2171. https://doi.org/10.1149/1.2352197.

(230) Ghodbane, O.; Pascal, J.-L.; Favier, F. Microstructural Effects on Charge-Storage Properties in MnO2-Based Electrochemical Supercapacitors. *ACS Appl. Mater. Interfaces* **2009**, *1* (5), 1130–1139. https://doi.org/10.1021/am900094e.

(231) Toupin, M.; Brousse, T.; Bélanger, D. Charge Storage Mechanism of MnO2 Electrode Used in Aqueous Electrochemical Capacitor. *Chem. Mater.* **2004**, *16* (16), 3184–3190. https://doi.org/10.1021/cm049649j.

(232) Hsu, Y.-K.; Chen, Y.-C.; Lin, Y.-G.; Chen, L.-C.; Chen, K.-H. Reversible Phase Transformation of MnO2 Nanosheets in an Electrochemical Capacitor Investigated by in situRaman Spectroscopy. *Chem. Commun.* **2011**, *47* (4), 1252–1254. https://doi.org/10.1039/C0CC03902K.

(233) Chen, D.; Ding, D.; Li, X.; Waller, G. H.; Xiong, X.; El-Sayed, M. A.; Liu, M. Probing the Charge Storage Mechanism of a Pseudocapacitive MnO2 Electrode Using in Operando Raman Spectroscopy. *Chem. Mater.* **2015**, *27* (19), 6608–6619. https://doi.org/10.1021/acs.chemmater.5b03118.

(234) Boyd, S.; Ganeshan, K.; Tsai, W.-Y.; Wu, T.; Saeed, S.; Jiang, D.; Balke, N.; van Duin, A. C. T.; Augustyn, V. Effects of Interlayer Confinement and Hydration on Capacitive Charge Storage in Birnessite. *Nat. Mater.* **2021**, *20* (12), 1689–1694. https://doi.org/10.1038/s41563-021-01066-4.

(235) Yang, L.; Cheng, S.; Wang, J.; Ji, X.; Jiang, Y.; Yao, M.; Wu, P.; Wang, M.; Zhou, J.; Liu, M. Investigation into the Origin of High Stability of δ-MnO2 Pseudo-Capacitive Electrode Using Operando Raman Spectroscopy. *Nano Energy* **2016**, *30*, 293–302. https://doi.org/10.1016/j.nanoen.2016.10.018.

(236) Ghodbane, O.; Ataherian, F.; Wu, N.-L.; Favier, F. In Situ Crystallographic Investigations of Charge Storage Mechanisms in MnO2-Based Electrochemical Capacitors. *Journal of Power Sources* **2012**, *206*, 454–462. https://doi.org/10.1016/j.jpowsour.2012.01.103.

(237) Liu, J.; Bao, J.; Zhang, X.; Gao, Y.; Zhang, Y.; Liu, L.; Cao, Z. MnO2-Based Materials for Supercapacitor Electrodes: Challenges, Strategies and Prospects. *RSC Adv.* **2022**, *12* (55), 35556–35578. https://doi.org/10.1039/D2RA06664E.

(238) Conway, B. E. Two-Dimensional and Quasi-Two-Dimensional Isotherms for Li Intercalation and *Upd* Processes at Surfaces. *Electrochimica Acta* **1993**, *38* (9), 1249–1258. https://doi.org/10.1016/0013-4686(93)80055-5.

(239) Zukalová, M.; Kalbáč, M.; Kavan, L.; Exnar, I.; Graetzel, M. Pseudocapacitive Lithium Storage in TiO2(B). *Chem. Mater.* **2005**, *17* (5), 1248–1255. https://doi.org/10.1021/cm048249t.

(240) Wang, J.; Polleux, J.; Lim, J.; Dunn, B. Pseudocapacitive Contributions to Electrochemical Energy Storage in TiO2 (Anatase) Nanoparticles. *J. Phys. Chem. C* **2007**, *111* (40), 14925–14931. https://doi.org/10.1021/jp074464w.

(241) Dalton, A. S.; Belak, A. A.; Van der Ven, A. Thermodynamics of Lithium in TiO2(B) from First Principles. *Chem. Mater.* **2012**, *24* (9), 1568–1574. https://doi.org/10.1021/cm203283v.

(242) Hua, X.; Liu, Z.; Fischer, M. G.; Borkiewicz, O.; Chupas, P. J.; Chapman, K. W.; Steiner, U.; Bruce, P. G.; Grey, C. P. Lithiation Thermodynamics and Kinetics of the TiO2 (B) Nanoparticles. *J. Am. Chem. Soc.* **2017**, *139* (38), 13330–13341. https://doi.org/10.1021/jacs.7b05228.

(243) Brezesinski, K.; Wang, J.; Haetge, J.; Reitz, C.; Steinmueller, S. O.; Tolbert, S. H.; Smarsly, B. M.; Dunn, B.; Brezesinski, T. Pseudocapacitive Contributions to Charge Storage in Highly Ordered Mesoporous Group V Transition Metal Oxides with Iso-Oriented Layered Nanocrystalline Domains. *J. Am. Chem. Soc.* **2010**, *132* (20), 6982–6990. https://doi.org/10.1021/ja9106385.

(244) Kim, J. W.; Augustyn, V.; Dunn, B. The Effect of Crystallinity on the Rapid Pseudocapacitive Response of Nb2O5. *Advanced Energy Materials* **2012**, *2* (1), 141–148. https://doi.org/10.1002/aenm.201100494.

(245) Augustyn, V.; Come, J.; Lowe, M. A.; Kim, J. W.; Taberna, P.-L.; Tolbert, S. H.; Abruña, H. D.; Simon, P.; Dunn, B. High-Rate Electrochemical Energy Storage through Li+ Intercalation Pseudocapacitance. *Nature Mater* **2013**, *12* (6), 518–522. https://doi.org/10.1038/nmat3601.

(246) Griffith, K. J.; Forse, A. C.; Griffin, J. M.; Grey, C. P. High-Rate Intercalation without Nanostructuring in Metastable Nb2O5 Bronze Phases. *J. Am. Chem. Soc.* **2016**, *138* (28), 8888–8899. https://doi.org/10.1021/jacs.6b04345.

(247) Chen, D.; Wang, J.-H.; Chou, T.-F.; Zhao, B.; El-Sayed, M. A.; Liu, M. Unraveling the Nature of Anomalously Fast Energy Storage in T-Nb2O5. *J. Am. Chem. Soc.* **2017**, *139* (20), 7071–7081. https://doi.org/10.1021/jacs.7b03141.

(248) Maier, J. Thermodynamics of Electrochemical Lithium Storage. *Angewandte Chemie International Edition* **2013**, *52* (19), 4998–5026. https://doi.org/10.1002/anie.201205569.

(249) Fleischmann, S.; Kamboj, I.; Augustyn, V. Nanostructured Transition Metal Oxides for Electrochemical Energy Storage. In *Transition Metal Oxides for Electrochemical Energy Storage*; John Wiley & Sons, Ltd, 2022; pp 183–212. https://doi.org/10.1002/9783527817252.ch8.

(250) Gribb, A. A.; Banfield, J. F. Particle Size Effects on Transformation Kinetics and Phase Stability in Nanocrystalline TiO2. *American Mineralogist* **1997**, *82* (7–8), 717–728. https://doi.org/10.2138/am-1997-7-809.

(251) Kim, H.-S.; Cook, J. B.; Tolbert, S. H.; Dunn, B. The Development of Pseudocapacitive Properties in Nanosized-MoO2. *J. Electrochem. Soc.* **2015**, *162* (5), A5083. https://doi.org/10.1149/2.0141505jes.

(252) Maier, J. Size Effects on Mass Transport and Storage in Lithium Batteries. *Journal of Power Sources* **2007**, *174* (2), 569–574. https://doi.org/10.1016/j.jpowsour.2007.06.246.

(253) Naoi, K.; Kurita, T.; Abe, M.; Furuhashi, T.; Abe, Y.; Okazaki, K.; Miyamoto, J.; Iwama, E.; Aoyagi, S.; Naoi, W.; Simon, P. Ultrafast Nanocrystalline-TiO2(B)/Carbon Nanotube Hyperdispersion Prepared via Combined Ultracentrifugation and Hydrothermal Treatments for Hybrid Supercapacitors. *Advanced Materials* **2016**, *28* (31), 6751–6757. https://doi.org/10.1002/adma.201600798.

(254) Mathis, T. S.; Kurra, N.; Wang, X.; Pinto, D.; Simon, P.; Gogotsi, Y. Energy Storage Data Reporting in Perspective—Guidelines for Interpreting the Performance of Electrochemical Energy Storage Systems. *Advanced Energy Materials* **2019**, *9* (39), 1902007. https://doi.org/10.1002/aenm.201902007.

(255) Fan, Z.; Yan, J.; Wei, T.; Zhi, L.; Ning, G.; Li, T.; Wei, F. Asymmetric Supercapacitors Based on Graphene/MnO2 and Activated Carbon Nanofiber Electrodes with High Power and Energy Density. *Advanced Functional Materials* **2011**, *21* (12), 2366–2375. https://doi.org/10.1002/adfm.201100058.

(256) Shen, J.; Yang, C.; Li, X.; Wang, G. High-Performance Asymmetric Supercapacitor Based on Nanoarchitectured Polyaniline/Graphene/Carbon Nanotube and Activated Graphene Electrodes. *ACS Appl. Mater. Interfaces* **2013**, *5* (17), 8467–8476. https://doi.org/10.1021/am4028235.

(257) Anasori, B.; Lukatskaya, M. R.; Gogotsi, Y. 2D Metal Carbides and Nitrides (MXenes) for Energy Storage. *Nat Rev Mater* **2017**, *2* (2), 1–17. https://doi.org/10.1038/natrevmats.2016.98.

(258) Chaudhari, N. K.; Jin, H.; Kim, B.; Baek, D. S.; Joo, S. H.; Lee, K. MXene: An Emerging Two-Dimensional Material for Future Energy Conversion and Storage Applications. *J. Mater. Chem. A* **2017**, *5* (47), 24564–24579. https://doi.org/10.1039/C7TA09094C.

(259) Lukatskaya, M. R.; Kota, S.; Lin, Z.; Zhao, M.-Q.; Shpigel, N.; Levi, M. D.; Halim, J.; Taberna, P.-L.; Barsoum, M. W.; Simon, P.; Gogotsi, Y. Ultra-High-Rate Pseudocapacitive Energy Storage in Two-

Dimensional Transition Metal Carbides. *Nat Energy* **2017**, *2* (8), 1–6. https://doi.org/10.1038/nenergy.2017.105.

(260) Jiang, Q.; Kurra, N.; Alhabeb, M.; Gogotsi, Y.; Alshareef, H. N. All Pseudocapacitive MXene-RuO2 Asymmetric Supercapacitors. *Advanced Energy Materials* **2018**, *8* (13), 1703043. https://doi.org/10.1002/aenm.201703043.

(261) Yan, J.; Fan, Z.; Sun, W.; Ning, G.; Wei, T.; Zhang, Q.; Zhang, R.; Zhi, L.; Wei, F. Advanced Asymmetric Supercapacitors Based on Ni(OH)2/Graphene and Porous Graphene Electrodes with High Energy Density. *Advanced Functional Materials* **2012**, *22* (12), 2632–2641. https://doi.org/10.1002/adfm.201102839.

(262) Wang, X.; Liu, L.; Niu, Z. Carbon-Based Materials for Lithium-Ion Capacitors. *Mater. Chem. Front.* **2019**, *3* (7), 1265–1279. https://doi.org/10.1039/C9QM00062C.

(263) Khomenko, V.; Raymundo-Piñero, E.; Béguin, F. High-Energy Density Graphite/AC Capacitor in Organic Electrolyte. *Journal of Power Sources* **2008**, *177* (2), 643–651. https://doi.org/10.1016/j.jpowsour.2007.11.101.

(264) Wang, F.; Wang, C.; Zhao, Y.; Liu, Z.; Chang, Z.; Fu, L.; Zhu, Y.; Wu, Y.; Zhao, D. A Quasi-Solid-State Li-Ion Capacitor Based on Porous TiO2 Hollow Microspheres Wrapped with Graphene Nanosheets. *Small* **2016**, *12* (45), 6207–6213. https://doi.org/10.1002/smll.201602331.

(265) Deng, B.; Lei, T.; Zhu, W.; Xiao, L.; Liu, J. In-Plane Assembled Orthorhombic Nb2O5 Nanorod Films with High-Rate Li+ Intercalation for High-Performance Flexible Li-Ion Capacitors. *Advanced Functional Materials* **2018**, *28* (1), 1704330. https://doi.org/10.1002/adfm.201704330.

(266) Forse, A. C.; Merlet, C.; Griffin, J. M.; Grey, C. P. New Perspectives on the Charging Mechanisms of Supercapacitors. *J. Am. Chem. Soc.* **2016**, *138* (18), 5731–5744. https://doi.org/10.1021/jacs.6b02115.

(267) Bo, Z.; Yang, J.; Qi, H.; Yan, J.; Cen, K.; Han, Z. Revealing Ion Transport in Supercapacitors with Sub-2 Nm Two-Dimensional Graphene Channels. *Energy Storage Materials* **2020**, *31*, 64–71. https://doi.org/10.1016/j.ensm.2020.06.001.

(268) Zhang, E.; Wu, Y.-C.; Shao, H.; Klimavicius, V.; Zhang, H.; Taberna, P.-L.; Grothe, J.; Buntkowsky, G.; Xu, F.; Simon, P.; Kaskel, S. Unraveling the Capacitive Charge Storage Mechanism of Nitrogen-Doped Porous Carbons by EQCM and ssNMR. *J. Am. Chem. Soc.* **2022**, *144* (31), 14217–14225. https://doi.org/10.1021/jacs.2c04841.

(269) Liu, X.; Lyu, D.; Merlet, C.; Leesmith, M. J. A.; Hua, X.; Xu, Z.; Grey, C. P.; Forse, A. C. Structural Disorder Determines Capacitance in Nanoporous Carbons. *Science* **2024**, *384* (6693), 321–325. https://doi.org/10.1126/science.adn6242.

(270) Ghosh, S.; Barg, S.; Jeong, S. M.; Ostrikov, K. (Ken). Heteroatom-Doped and Oxygen-Functionalized Nanocarbons for High-Performance Supercapacitors. *Advanced Energy Materials* **2020**, *10* (32), 2001239. https://doi.org/10.1002/aenm.202001239.

(271) Hasegawa, G.; Deguchi, T.; Kanamori, K.; Kobayashi, Y.; Kageyama, H.; Abe, T.; Nakanishi, K. High-Level Doping of Nitrogen, Phosphorus, and Sulfur into Activated Carbon Monoliths and Their Electrochemical Capacitances. *Chem. Mater.* **2015**, *27* (13), 4703–4712. https://doi.org/10.1021/acs.chemmater.5b01349.

(272) Daems, N.; Sheng, X.; Vankelecom, I. F. J.; Pescarmona, P. P. Metal-Free Doped Carbon Materials as Electrocatalysts for the Oxygen Reduction Reaction. *J. Mater. Chem. A* **2014**, *2* (12), 4085–4110. https://doi.org/10.1039/C3TA14043A.

(273) Nguyen, T. H.; Yang, D.; Zhu, B.; Lin, H.; Ma, T.; Jia, B. Doping Mechanism Directed Graphene Applications for Energy Conversion and Storage. *J. Mater. Chem. A* **2021**, *9* (12), 7366–7395. https://doi.org/10.1039/D0TA11939C.

(274) Qiu, C.; Jiang, L.; Gao, Y.; Sheng, L. Effects of Oxygen-Containing Functional Groups on Carbon Materials in Supercapacitors: A Review. *Materials & Design* **2023**, *230*, 111952. https://doi.org/10.1016/j.matdes.2023.111952.

(275) Bleda-Martínez, M. J.; Maciá-Agulló, J. A.; Lozano-Castelló, D.; Morallón, E.; Cazorla-Amorós, D.; Linares-Solano, A. Role of Surface Chemistry on Electric Double Layer Capacitance of Carbon Materials. *Carbon* **2005**, *43* (13), 2677–2684. https://doi.org/10.1016/j.carbon.2005.05.027.

(276) Chen, C.-M.; Zhang, Q.; Yang, M.-G.; Huang, C.-H.; Yang, Y.-G.; Wang, M.-Z. Structural Evolution during Annealing of Thermally Reduced Graphene Nanosheets for Application in Supercapacitors. *Carbon* **2012**, *50* (10), 3572–3584. https://doi.org/10.1016/j.carbon.2012.03.029.

(277) Liu, F.; Xue, D. An Electrochemical Route to Quantitative Oxidation of Graphene Frameworks with Controllable C/O Ratios and Added Pseudocapacitances. *Chemistry – A European Journal* **2013**, *19* (32), 10716–10722. https://doi.org/10.1002/chem.201300679.

(278) Lee, J.; Abbas, M. A.; Bang, J. H. Exploring the Capacitive Behavior of Carbon Functionalized with Cyclic Ethers: A Rational Strategy To Exploit Oxygen Functional Groups for Enhanced Capacitive Performance. *ACS Appl. Mater. Interfaces* **2019**, *11* (21), 19056–19065. https://doi.org/10.1021/acsami.9b00929.

(279) Lee, Y.-H.; Chang, K.-H.; Hu, C.-C. Differentiate the Pseudocapacitance and Double-Layer Capacitance Contributions for Nitrogen-Doped Reduced Graphene Oxide in Acidic and Alkaline Electrolytes. *Journal of Power Sources* **2013**, *227*, 300–308. https://doi.org/10.1016/j.jpowsour.2012.11.026.

(280) Chen, C.-M.; Zhang, Q.; Zhao, X.-C.; Zhang, B.; Kong, Q.-Q.; Yang, M.-G.; Yang, Q.-H.; Wang, M.-Z.; Yang, Y.-G.; Schlögl, R.; Su, D. S. Hierarchically Aminated Graphene Honeycombs for Electrochemical Capacitive Energy Storage. *J. Mater. Chem.* **2012**, *22* (28), 14076–14084. https://doi.org/10.1039/C2JM31426F.

(281) Tian, K.; Wang, J.; Cao, L.; Yang, W.; Guo, W.; Liu, S.; Li, W.; Wang, F.; Li, X.; Xu, Z.; Wang, Z.; Wang, H.; Hou, Y. Single-Site Pyrrolic-Nitrogen-Doped Sp2-Hybridized Carbon Materials and Their Pseudocapacitance. *Nat Commun* **2020**, *11* (1), 3884. https://doi.org/10.1038/s41467-020-17727-y.

(282) Suktha, P.; Phattharasupakun, N.; Dittanet, P.; Sawangphruk, M. Charge Storage Mechanisms of Electrospun Mn3O4 Nanofibres for High-Performance Supercapacitors. *RSC Adv.* **2017**, *7* (16), 9958–9963. https://doi.org/10.1039/C6RA28499J.

(283) Lee, J. W.; Hall, A. S.; Kim, J.-D.; Mallouk, T. E. A Facile and Template-Free Hydrothermal Synthesis of Mn3O4 Nanorods on Graphene Sheets for Supercapacitor Electrodes with Long Cycle Stability. *Chem. Mater.* **2012**, *24* (6), 1158–1164. https://doi.org/10.1021/cm203697w.

(284) Wu, N.-L.; Wang, S.-Y.; Han, C.-Y.; Wu, D.-S.; Shiue, L.-R. Electrochemical Capacitor of Magnetite in Aqueous Electrolytes. *Journal of Power Sources* **2003**, *113* (1), 173–178. https://doi.org/10.1016/S0378-7753(02)00482-2.

(285) Wang, S.-Y.; Ho, K.-C.; Kuo, S.-L.; Wu, N.-L. Investigation on Capacitance Mechanisms of Fe3O4 Electrochemical Capacitors. *J. Electrochem. Soc.* **2005**, *153* (1), A75. https://doi.org/10.1149/1.2131820.

(286) Wang, L.; Ji, H.; Wang, S.; Kong, L.; Jiang, X.; Yang, G. Preparation of Fe3O4 with High Specific Surface Area and Improved Capacitance as a Supercapacitor. *Nanoscale* **2013**, *5* (9), 3793–3799. https://doi.org/10.1039/C3NR00256J.

(287) Taberna, P. L.; Mitra, S.; Poizot, P.; Simon, P.; Tarascon, J.-M. High Rate Capabilities Fe3O4-Based Cu Nano-Architectured Electrodes for Lithium-Ion Battery Applications. *Nature Mater* **2006**, *5* (7), 567–573. https://doi.org/10.1038/nmat1672.

(288) Lin, Z.; Goikolea, E.; Balducci, A.; Naoi, K.; Taberna, P. L.; Salanne, M.; Yushin, G.; Simon, P. Materials for Supercapacitors: When Li-Ion Battery Power Is Not Enough. *Materials Today* **2018**, *21* (4), 419–436. https://doi.org/10.1016/j.mattod.2018.01.035.

(289) Libich, J.; Máca, J.; Vondrák, J.; Čech, O.; Sedlaříková, M. Supercapacitors: Properties and Applications. *Journal of Energy Storage* **2018**, *17*, 224–227. https://doi.org/10.1016/j.est.2018.03.012.

(290) Borenstein, A.; Hanna, O.; Attias, R.; Luski, S.; Brousse, T.; Aurbach, D. Carbon-Based Composite Materials for Supercapacitor Electrodes: A Review. *Journal of Materials Chemistry A* **2017**, *5* (25), 12653–12672. https://doi.org/10.1039/c7ta00863e.

(291) Simon, P.; Gogotsi, Y. Capacitive Energy Storage in Nanostructured Carbon-Electrolyte Systems. *Acc. Chem. Res.* **2013**, *46* (Xx), 1094.

(292) Lv, S.; Ma, L.; Shen, X.; Tong, H. Recent Design and Control of Carbon Materials for Supercapacitors. *Journal of Materials Science* **2021**, *56* (3), 1919–1942. https://doi.org/10.1007/s10853-020-05351-6.

(293) Zahir, N.; Magri, P.; Luo, W.; Gaumet, J. J.; Pierrat, P. Recent Advances on Graphene Quantum Dots for Electrochemical Energy Storage Devices. *Energy and Environmental Materials* **2022**, *5* (1), 201–214. https://doi.org/10.1002/eem2.12167.

(294) Ke, Q.; Wang, J. Graphene-Based Materials for Supercapacitor Electrodes - A Review. *Journal of Materiomics* **2016**, *2* (1), 37–54. https://doi.org/10.1016/j.jmat.2016.01.001.

(295) Noked, M.; Soffer, A.; Arubach, D. The Electrochemistry of Activated Carbonaceous Materials: Past, Present, and Future. *Journal of Solid State Electrochemistry* **2011**, *15* (7–8), 1563–1578. https://doi.org/10.1007/s10008-011-1411-y.

(296) Ji, H.; Zhao, X.; Qiao, Z.; Jung, J.; Zhu, Y.; Lu, Y.; Zhang, L. L.; MacDonald, A. H.; Ruoff, R. S. Capacitance of Carbon-Based Electrical Double-Layer Capacitors. *Nature Communications* **2014**, *5* (3317), 1–7. https://doi.org/10.1038/ncomms4317.

(297) Ukanwa, K. S.; Patchigolla, K.; Sakrabani, R.; Anthony, E.; Mandavgane, S. A Review of Chemicals to Produce Activated Carbon from Agricultural Waste Biomass. *Sustainability (Switzerland)* **2019**, *11* (22), 1–35. https://doi.org/10.3390/su11226204.

(298) Köseoǀlu, E.; Akmil-Başar, C. Preparation, Structural Evaluation and Adsorptive Properties of Activated Carbon from Agricultural Waste Biomass. *Advanced Powder Technology* **2015**, *26* (3), 811–818. https://doi.org/10.1016/j.apt.2015.02.006.

(299) Abioye, A. M.; Ani, F. N. Recent Development in the Production of Activated Carbon Electrodes from Agricultural Waste Biomass for Supercapacitors: A Review. *Renewable and Sustainable Energy Reviews* **2015**, *52*, 1282–1293. https://doi.org/10.1016/j.rser.2015.07.129.

(300) Wei, L.; Yushin, G. Nanostructured Activated Carbons from Natural Precursors for Electrical Double Layer Capacitors. *Nano Energy* **2012**, *1* (4), 552–565. https://doi.org/10.1016/j.nanoen.2012.05.002.

(301) Jain, A.; Balasubramanian, R.; Srinivasan, M. P. Hydrothermal Conversion of Biomass Waste to Activated Carbon with High Porosity: A Review. *Chemical Engineering Journal* **2016**, *283*, 789–805. https://doi.org/10.1016/j.cej.2015.08.014.

(302) Lu, H.; Zhao, X. S. Biomass-Derived Carbon Electrode Materials for Supercapacitors. *Sustainable Energy and Fuels* **2017**, *1* (6), 1265–1281. https://doi.org/10.1039/C7SE00099E.

(303) Nunes, M.; Rocha, I. M.; Fernandes, D. M.; Mestre, A. S.; Moura, C. N.; Carvalho, A. P.; Pereira, M. F. R.; Freire, C. Sucrose-Derived Activated Carbons: Electron Transfer Properties and

Application as Oxygen Reduction Electrocatalysts. *RSC Adv.* **2015**, *5* (124), 102919–102931. https://doi.org/10.1039/C5RA20874B.

(304) Evans, M. J. B.; Halliop, E.; MacDonald, J. A. F. The Production of Chemically-Activated Carbon. *Carbon* **1999**, *37* (2), 269–274. https://doi.org/10.1016/S0008-6223(98)00174-2.

(305) Susanti, R. F.; Arie, A. A.; Kristianto, H.; Erico, M.; Kevin, G.; Devianto, H. Activated Carbon from Citric Acid Catalyzed Hydrothermal Carbonization and Chemical Activation of Salacca Peel as Potential Electrode for Lithium Ion Capacitor’s Cathode. *Ionics* **2019**, *25* (8), 3915–3925. https://doi.org/10.1007/s11581-019-02904-x.

(306) Lei, Q.; Kannan, S.; Raghavan, V. Uncatalyzed and Acid-Aided Microwave Hydrothermal Carbonization of Orange Peel Waste. *Waste Management* **2021**, *126*, 106–118. https://doi.org/10.1016/j.wasman.2021.02.058.

(307) Chen, F.; Zhang, Y.; Zheng, M.; Xiao, Y.; Hu, H.; Liang, Y.; Liu, Y.; Dong, H. Preparation of High-Performance Porous Carbon Materials by Citric Acid-Assisted Hydrothermal Carbonization of Bamboo and Their Application in Electrode Materials. *Energy & Fuels* **2022**. https://doi.org/10.1021/acs.energyfuels.2c01828.

(308) Del Menezzi, C.; Amirou, S.; Pizzi, A.; Xi, X.; Delmotte, L. Reactions with Wood Carbohydrates and Lignin of Citric Acid as a Bond Promoter of Wood Veneer Panels. *Polymers* **2018**, *10* (8), 833. https://doi.org/10.3390/polym10080833.

(309) Inagaki, M.; Toyoda, M.; Soneda, Y.; Morishita, T. Nitrogen-Doped Carbon Materials. *Carbon* **2018**, *132*, 104–140. https://doi.org/10.1016/j.carbon.2018.02.024.

(310) Frackowiak, E.; Lota, G.; Machnikowski, J.; Vix-Guterl, C.; Béguin, F. Optimisation of Supercapacitors Using Carbons with Controlled Nanotexture and Nitrogen Content. *Electrochimica Acta* **2006**, *51* (11), 2209–2214. https://doi.org/10.1016/j.electacta.2005.04.080.

(311) Béguin, F.; Presser, V.; Balducci, A.; Frackowiak, E. Carbons and Electrolytes for Advanced Supercapacitors. *Advanced Materials* **2014**, *26* (14). https://doi.org/10.1002/adma.201304137.

(312) Lin, T.; Chen, I.-W.; Liu, F.; Yang, C.; Bi, H.; Xu, F.; Huang, F. Nitrogen-Doped Mesoporous Carbon of Extraordinary Capacitance for Electrochemical Energy Storage. *Science* **2015**, *350* (6267), 1508–1513. https://doi.org/10.1126/science.aab3798.

(313) Richards, G.; Shafizadeh, F. Mechanism of Thermal Degradation of Sucrose. A Preliminary Study. *Aust. J. Chem.* **1978**, *31* (8), 1825. https://doi.org/10.1071/CH9781825.

(314) Lee, J. W.; Thomas, L. C.; Jerrell, J.; Feng, H.; Cadwallader, K. R.; Schmidt, S. J. Investigation of Thermal Decomposition as the Kinetic Process That Causes the Loss of Crystalline Structure in Sucrose Using a Chemical Analysis Approach (Part II). *J. Agric. Food Chem.* **2011**, *59* (2), 702–712. https://doi.org/10.1021/jf104235d.

(315) Sun, S.; Zhao, Z.; Umemura, K. Further Exploration of Sucrose-Citric Acid Adhesive: Synthesis and Application on Plywood. *Polymers* **2019**, *11* (11), 1875. https://doi.org/10.3390/polym11111875.

(316) Wibowo, E. S.; Kusumah, S. S.; Subyakto; Umemura, K. Modification of Novel Bio-Based Adhesive Made from Citric Acid and Sucrose by ZnCl2. *International Journal of Adhesion and Adhesives* **2021**, *108*, 102866. https://doi.org/10.1016/j.ijadhadh.2021.102866.

(317) Illingworth, J. M.; Rand, B.; Williams, P. T. Understanding the Mechanism of Two-Step, Pyrolysis-Alkali Chemical Activation of Fibrous Biomass for the Production of Activated Carbon Fibre Matting. *Fuel Processing Technology* **2022**, *235*, 107348. https://doi.org/10.1016/j.fuproc.2022.107348.

(318) Barroso Bogeat, A. Understanding and Tuning the Electrical Conductivity of Activated Carbon: A State-of-the-Art Review. *Critical Reviews in Solid State and Materials Sciences* **2021**, *46* (1), 1–37. https://doi.org/10.1080/10408436.2019.1671800.

(319) Biniak, S.; Szymański, G.; Siedlewski, J.; Świątkowski, A. The Characterization of Activated Carbons with Oxygen and Nitrogen Surface Groups. *Carbon* **1997**, *35* (12), 1799–1810. https://doi.org/10.1016/S0008-6223(97)00096-1.

(320) Shafeeyan, M. S.; Daud, W. M. A. W.; Houshmand, A.; Shamiri, A. A Review on Surface Modification of Activated Carbon for Carbon Dioxide Adsorption. *Journal of Analytical and Applied Pyrolysis* **2010**, *89* (2), 143–151. https://doi.org/10.1016/j.jaap.2010.07.006.

(321) Ferrari, A. C.; Meyer, J. C.; Scardaci, V.; Casiraghi, C.; Lazzeri, M.; Mauri, F.; Piscanec, S.; Jiang, D.; Novoselov, K. S.; Roth, S.; Geim, A. K. Raman Spectrum of Graphene and Graphene Layers. *Physical Review Letters* **2006**, *97* (18), 1–4. https://doi.org/10.1103/PhysRevLett.97.187401.

(322) Maslova, O. A.; Ammar, M. R.; Guimbretière, G.; Rouzaud, J.-N.; Simon, P. Determination of Crystallite Size in Polished Graphitized Carbon by Raman Spectroscopy. *Phys. Rev. B* **2012**, *86* (13), 134205. https://doi.org/10.1103/PhysRevB.86.134205.

(323) Weinberg, N. L.; Weinberg, H. R. Electrochemical Oxidation of Organic Compounds. *Chem. Rev.* **1968**, *68* (4), 449–523. https://doi.org/10.1021/cr60254a003.

(324) Roth, H. G.; Romero, N. A.; Nicewicz, D. A. Experimental and Calculated Electrochemical Potentials of Common Organic Molecules for Applications to Single-Electron Redox Chemistry. *Synlett* **2016**, *27* (5), 714–723. https://doi.org/10.1055/s-0035-1561297.

(325) Pronkin, S. N.; Shokina, N. Yu.; Pham-Huu, C. Redox Transitions in Pseudocapacitor Materials : Critera and Ruling Factors. In *Redox Chemistry - From Molecules to Energy Storage*; Intech Open, 2022; pp 1–22.

(326) Volfkovich, Y. M.; Bograchev, D. A.; Rychagov, A. Y.; Sosenkin, V. E.; Chaika, M. Y. Supercapacitors with Carbon Electrodes. Energy Efficiency: Modeling and Experimental Verification. *Journal of*

Solid State Electrochemistry **2015**, *19* (9), 2771–2779. https://doi.org/10.1007/s10008-015-2804-0.

(327) Volfkovich, Y. M.; Bograchev, D. A.; Mikhalin, A. A.; Bagotsky, V. S. Supercapacitor Carbon Electrodes with High Capacitance. *Journal of Solid State Electrochemistry* **2014**, *18* (5), 1351–1363. https://doi.org/10.1007/s10008-013-2271-4.

(328) Lobato, B.; Suárez, L.; Guardia, L.; Centeno, T. A. Capacitance and Surface of Carbons in Supercapacitors. *Carbon* **2017**, *122*, 434–445. https://doi.org/10.1016/j.carbon.2017.06.083.

(329) Vaik, K.; Schiffrin, D. J.; Tammeveski, K. Electrochemical Reduction of Oxygen on Anodically Pre-Treated and Chemically Grafted Glassy Carbon Electrodes in Alkaline Solutions. *Electrochemistry Communications* **2004**, *6* (1), 1–5. https://doi.org/10.1016/j.elecom.2003.10.003.

(330) Macdonald, J. R. Impedance Spectroscopy: Models, Data Fitting, and Analysis. *Solid State Ionics* **2005**, *176* (25), 1961–1969. https://doi.org/10.1016/j.ssi.2004.05.035.

(331) Pedersen, C.; Aslyamov, T.; Janssen, M. Equivalent Circuit and Continuum Modeling of the Impedance of Electrolyte-Filled Pores. *PRX Energy* **2023**, *2* (4), 043006. https://doi.org/10.1103/PRXEnergy.2.043006.

(332) Jang, J. H.; Oh, S. M. Complex Capacitance Analysis of Porous Carbon Electrodes for Electric Double-Layer Capacitors. *J. Electrochem. Soc.* **2004**, *151* (4), A571. https://doi.org/10.1149/1.1647572.

(333) Song, H.-K.; Sung, J.-H.; Jung, Y.-H.; Lee, K.-H.; Dao, L. H.; Kim, M.-H.; Kim, H.-N. Electrochemical Porosimetry. *J. Electrochem. Soc.* **2004**, *151* (3), E102. https://doi.org/10.1149/1.1641041.

(334) Eikerling, M.; Kornyshev, A. A.; Lust, E. Optimized Structure of Nanoporous Carbon-Based Double-Layer Capacitors. *J. Electrochem. Soc.* **2004**, *152* (1), E24. https://doi.org/10.1149/1.1825379.

(335) Itagaki, M.; Hatada, Y.; Shitanda, I.; Watanabe, K. Complex Impedance Spectra of Porous Electrode with Fractal Structure. *ELECTROCHIM ACTA* **2010**, *55* (21), 6255–6262. https://doi.org/10.1016/j.electacta.2009.10.016.

(336) Huang, Q.-A.; Li, Y.; Tsay, K.-C.; Sun, C.; ChangpingYang; Zhang, L.; Zhang, J. Multi-Scale Impedance Model for Supercapacitor Porous Electrodes: Theoretical Prediction and Experimental Validation. *Journal of Power Sources* **2018**, *400*, 69–86. https://doi.org/10.1016/j.jpowsour.2018.07.108.

(337) Pikma, P.; Ers, H.; Siinor, L.; Zhao, J.; Oll, O.; Romann, T.; Grozovski, V.; Siimenson, C.; Väärtnõu, M.; Paalo, M.; Härmas, R.; Lust, K.; Thomberg, T.; Jänes, A.; Nerut, J.; Jäger, R.; Valk, P.; Kivi, I.; Maide, M.; Möller, P.; Kanarbik, R.; Nurk, G.; Lust, E. The Review of Advances in Interfacial Electrochemistry in Estonia: Electrochemical Double Layer and Adsorption Studies for the

Development of Electrochemical Devices. *J Solid State Electrochem* **2023**, *27* (7), 1547–1591. https://doi.org/10.1007/s10008-022-05338-0.

(338) Brug, G. J.; van den Eeden, A. L. G.; Sluyters-Rehbach, M.; Sluyters, J. H. The Analysis of Electrode Impedances Complicated by the Presence of a Constant Phase Element. *Journal of Electroanalytical Chemistry and Interfacial Electrochemistry* **1984**, *176* (1), 275–295. https://doi.org/10.1016/S0022-0728(84)80324-1.

(339) Vivier, V.; Orazem, M. E. Impedance Analysis of Electrochemical Systems. *Chem. Rev.* **2022**, *122* (12), 11131–11168. https://doi.org/10.1021/acs.chemrev.1c00876.

(340) Kant, R.; Singh, M. B. Theory of the Electrochemical Impedance of Mesostructured Electrodes Embedded with Heterogeneous Micropores. *J. Phys. Chem. C* **2017**, *121* (13), 7164–7174. https://doi.org/10.1021/acs.jpcc.7b01287.

(341) Trasatti, S.; Petrii, O. A. Real Surface Area Measurements in Electrochemistry. *Journal of Electroanalytical Chemistry* **1992**, *327* (1), 353–376. https://doi.org/10.1016/0022-0728(92)80162-W.

(342) Ji, H.; Zhao, X.; Qiao, Z.; Jung, J.; Zhu, Y.; Lu, Y.; Zhang, L. L.; MacDonald, A. H.; Ruoff, R. S. Capacitance of Carbon-Based Electrical Double-Layer Capacitors. *Nat Commun* **2014**, *5* (1), 3317. https://doi.org/10.1038/ncomms4317.

(343) Jäckel, N.; Rodner, M.; Schreiber, A.; Jeongwook, J.; Zeiger, M.; Aslan, M.; Weingarth, D.; Presser, V. Anomalous or Regular Capacitance? The Influence of Pore Size Dispersity on Double-Layer Formation. *Journal of Power Sources* **2016**, *326*, 660–671. https://doi.org/10.1016/j.jpowsour.2016.03.015.

(344) Jäckel, N.; Simon, P.; Gogotsi, Y.; Presser, V. Increase in Capacitance by Subnanometer Pores in Carbon. *ACS Energy Lett.* **2016**, *1* (6), 1262–1265. https://doi.org/10.1021/acsenergylett.6b00516.

(345) Shiraishi, S.; Urita, K.; Nishihara, H.; Kondo, T. Extraordinary Capacitance and Stability of Carbon Electrode for Electrochemical Capacitors. *Electrochemistry* **2024**, *92* (7), 074001–074001. https://doi.org/10.5796/electrochemistry.24-70036.

(346) Tarascon, J. M.; Armand, M. Issues and Challenges Facing Rechargeable Lithium Batteries. *Nature* **2001**, *414* (6861), 359–367. https://doi.org/10.1038/35104644.

(347) Poizot, P.; Laruelle, S.; Grugeon, S.; Dupont, L.; Tarascon, J. M. Nano-Sized Transition-Metal Oxides as Negative-Electrode Materials for Lithium-Ion Batteries. *Nature* **2000**, *407* (6803), 496–499. https://doi.org/10.1038/35035045.

(348) Lin, Z.; Goikolea, E.; Balducci, A.; Naoi, K.; Taberna, P. L.; Salanne, M.; Yushin, G.; Simon, P. Materials for Supercapacitors: When Li-Ion Battery Power Is Not Enough. *Materials Today* **2018**, *21* (4), 419–436. https://doi.org/10.1016/j.mattod.2018.01.035.

(349) Thackeray, M. M. Manganese Oxides for Lithium Batteries. *Progress in Solid State Chemistry* **1997**, *25* (1–2), 1–71. https://doi.org/10.1016/S0079-6786(97)81003-5.

(350) Thackeray, M. M. Exploiting the Spinel Structure for Li-Ion Battery Applications: A Tribute to John B. Goodenough. *Advanced Energy Materials* **2021**, *11* (2), 1–8. https://doi.org/10.1002/aenm.202001117.

(351) Shah, H. U.; Wang, F.; Toufiq, A. M.; Khattak, A. M.; Iqbal, A.; Ghazi, Z. A.; Ali, S.; Li, X.; Wang, Z. Electrochemical Properties of Single-Crystalline Mn3O4 Nanostructures and Their Capacitive Performance in Basic Electrolyte. *International Journal of Electrochemical Science* **2016**, *11* (10), 8155–8162. https://doi.org/10.20964/2016.10.41.

(352) Shah, H. U.; Wang, F.; Toufiq, A. M.; Ali, S.; Khan, Z. U. H.; Li, Y.; Hu, J.; He, K. Electrochemical Properties of Controlled Size Mn3O4 Nanoparticles for Supercapacitor Applications. *Journal of Nanoscience and Nanotechnology* **2018**, *18* (1), 719–724. https://doi.org/10.1166/jnn.2018.14644.

(353) Kerangueven, G.; Faye, J.; Royer, S.; Pronkin, S. N. Electrochemical Properties and Capacitance of Hausmannite Mn3O4 - Carbon Composite Synthesized by in Situ Autocombustion Method. *Electrochimica Acta* **2016**, *222*, 755–764.

(354) Wang, J.-G.; Jin, D.; Zhou, R.; Li, X.; Liu, X.; Shen, C.; Xie, K.; Li, B.; Kang, F.; Wei, B. Highly Flexible Graphene/Mn3O4 Nanocomposite Membrane as Advanced Anodes for Li-Ion Batteries. *ACS Nano* **2016**, *10* (6), 6227–6234. https://doi.org/10.1021/acsnano.6b02319.

(355) Wang, H.; Cui, L.-F.; Yang, Y.; Sanchez Casalongue, H.; Robinson, J. T.; Liang, Y.; Cui, Y.; Dai, H. Mn3O4−Graphene Hybrid as a High-Capacity Anode Material for Lithium Ion Batteries. *J. Am. Chem. Soc.* **2010**, *132* (40), 13978–13980. https://doi.org/10.1021/ja105296a.

(356) Dosaev, K. A.; Istomin, S. Ya.; Strebkov, D. A.; Tsirlina, G. A.; Antipov, E. V.; Savinova, E. R. AMn2O4 Spinels (A - Li, Mg, Mn, Cd) as ORR Catalysts: The Role of Mn Coordination and Oxidation State in the Catalytic Activity and Their Propensity to Degradation. *Electrochimica Acta* **2022**, *428*, 140923. https://doi.org/10.1016/j.electacta.2022.140923.

(357) Patil, K. C.; Aruna, S. T.; Mimani, T. Combustion Synthesis: An Update. *Current Opinion in Solid State and Materials Science* **2002**, *6* (6), 507–512. https://doi.org/10.1016/S1359-0286(02)00123-7.

(358) Chick, L. A.; Pederson, L. R.; Maupin, G. D.; Bates, J. L.; Thomas, L. E.; Exarhos, G. J. Glycine-Nitrate Combustion Synthesis of Oxide Ceramic Powders. *Materials Letters* **1990**, *10* (1–2), 6–12. https://doi.org/10.1016/0167-577X(90)90003-5.

(359) Kingsley, J. J.; Suresh, K.; Patil, K. C. Combustion Synthesis of Fine-Particle Metal Aluminates. *J Mater Sci* **1990**, *25* (2), 1305–1312. https://doi.org/10.1007/BF00585441.

(360) Manoharan, S. S.; Patil, K. C. Combustion Synthesis of Metal Chromite Powders. *J American Ceramic Society* **1992**, *75* (4), 1012–1015. https://doi.org/10.1111/j.1151-2916.1992.tb04177.x.

(361) Arul Dhas, N.; Patil, K. C. Combustion Synthesis and Properties of Fine Particle Spinel Manganites. *Journal of Solid State Chemistry* **1993**, *102*, 440–445.

(362) Varma, A.; Mukasyan, A. S.; Rogachev, A. S.; Manukyan, K. V. Solution Combustion Synthesis of Nanoscale Materials. *Chemical Reviews* **2016**, *116* (23), 14493–14586. https://doi.org/10.1021/acs.chemrev.6b00279.

(363) De Bruijn, T. J. W.; De Ruiter, G. M. J.; De Jong, W. A.; Van Den Berg, P. J. Thermal Decomposition of Aqueous Manganese Nitrate Solutions and Anhydrous Manganese Nitrate. Part 2. Heats of Reaction. *Thermochimica Acta* **1981**, *45* (3), 279–292. https://doi.org/10.1016/0040-6031(81)85088-5.

(364) Nohman, A. K. H.; Ismail, H. M.; Hussein, G. A. M. Thermal and Chemical Events in the Decomposition Course of Manganese Compounds. *Journal of Analytical and Applied Pyrolysis* **1995**, *34* (2), 265–278. https://doi.org/10.1016/0165-2370(95)00896-M.

(365) Yablokov, V. Ya.; Smel'tsova, I. L.; Zelyaev, I. A.; Mitrofanova, S. V. Studies of the Rates of Thermal Decomposition of Glycine, Alanine, and Serine. *Russ J Gen Chem* **2009**, *79* (8), 1704–1706. https://doi.org/10.1134/S1070363209080209.

(366) Weiss, I. M.; Muth, C.; Drumm, R.; Kirchner, H. O. K. Thermal Decomposition of the Amino Acids Glycine, Cysteine, Aspartic Acid, Asparagine, Glutamic Acid, Glutamine, Arginine and Histidine. *BMC Biophys* **2018**, *11* (1), 2. https://doi.org/10.1186/s13628-018-0042-4.

(367) Mrozek, R.; Rz, Z. Thermal Analysis of Manganese(II) Complexes With Glycine. **2001**.

(368) Khaliullin, Sh. M.; Zhuravlev, V. D.; Bamburov, V. G. Solution-Combustion Synthesis of Oxide Nanoparticles from Nitrate Solutions Containing Glycine and Urea: Thermodynamic Aspects. *Int. J Self-Propag. High-Temp. Synth.* **2016**, *25* (3), 139–148. https://doi.org/10.3103/S1061386216030031.

(369) Yu, P.; Zhang, X.; Chen, Y.; Ma, Y. Solution-Combustion Synthesis of ε-MnO2 for Supercapacitors. *Materials Letters* **2010**, *64* (1), 61–64. https://doi.org/10.1016/j.matlet.2009.10.007.

(370) Puértolas, B.; Smith, A.; Vázquez, I.; Dejoz, A.; Moragues, A.; Garcia, T.; Solsona, B. The Different Catalytic Behaviour in the Propane Total Oxidation of Cobalt and Manganese Oxides Prepared by a Wet Combustion Procedure. *Chemical Engineering Journal* **2013**, *229*, 547–558. https://doi.org/10.1016/j.cej.2013.06.041.

(371) Piumetti, M.; Fino, D.; Russo, N. Mesoporous Manganese Oxides Prepared by Solution Combustion Synthesis as Catalysts for the Total Oxidation of VOCs. *Applied Catalysis B: Environmental* **2015**, *163*, 277–287. https://doi.org/10.1016/j.apcatb.2014.08.012.

(372) Kéranguéven, G.; Faye, J.; Royer, S.; Pronkin, S. N. Electrochemical Properties and Capacitance of Hausmannite Mn3O4 – Carbon Composite Synthesized by in Situ Autocombustion Method. *Electrochimica Acta* **2016**, *222*, 755–764. https://doi.org/10.1016/j.electacta.2016.11.032.

(373) Kéranguéven, G.; Bouillet, C.; Papaefthymiou, V.; Simonov, P. A.; Savinova, E. R. How Key Characteristics of Carbon Materials Influence the ORR Activity of LaMnO3- and Mn3O4-Carbon Composites Prepared by *in Situ* Autocombustion Method. *Electrochimica Acta* **2020**, *353*, 136557. https://doi.org/10.1016/j.electacta.2020.136557.

(374) Shi, J.; Sun, M.; Hu, H. One-Step Combustion Synthesis of C-Mn3O4/MnO Composites with High Electrochemical Performance for Supercapacitor. *Mater. Res. Express* **2018**, *6* (3), 035511. https://doi.org/10.1088/2053-1591/aaf58a.

(375) Guo, H.; Zhang, Z.; Jiang, Z.; Chen, M.; Einaga, H.; Shangguan, W. Catalytic Activity of Porous Manganese Oxides for Benzene Oxidation Improved via Citric Acid Solution Combustion Synthesis. *Journal of Environmental Sciences* **2020**, *98*, 196–204. https://doi.org/10.1016/j.jes.2020.06.008.

(376) Mollaei, Z.; Kermani, F.; Moosavi, F.; Kargozar, S.; Khakhi, J. V.; Mollazadeh, S. In Silico Study and Experimental Evaluation of the Solution Combustion Synthesized Manganese Oxide (MnO2) Nanoparticles. *Ceramics International* **2022**, *48* (2), 1659–1672. https://doi.org/10.1016/j.ceramint.2021.09.245.

(377) Vratny, F. Infrared Spectra of Metal Nitrates. *Appl Spectrosc* **1959**, *13* (3), 59–70. https://doi.org/10.1366/000370259774614960.

(378) Laulicht, I.; Pinchas, S.; Samuel, D.; Wasserman, I. The Infrared Absorption Spectrum of Oxygen-18-Labeled Glycine. *J. Phys. Chem.* **1966**, *70* (9), 2719–2725. https://doi.org/10.1021/j100881a003.

(379) Kumar, S.; Rai, A. K.; Singh, V. B.; Rai, S. B. Vibrational Spectrum of Glycine Molecule. *Spectrochimica Acta Part A: Molecular and Biomolecular Spectroscopy* **2005**, *61* (11–12), 2741–2746. https://doi.org/10.1016/j.saa.2004.09.029.

(380) Popov, D.; Herak, R.; Prelesnik, B.; Ribar, B. The Crystal Structure of Manganese Nitrate Tetrahydrate Mn(NO3)2 · 4H2O. *Zeitschrift für Kristallographie - Crystalline Materials* **1973**, *137* (4), 280–289. https://doi.org/10.1524/zkri.1973.137.4.280.

(381) Nakamoto, K. Applications in Coordination Chemistry. In *Infrared and Raman Spectra of Inorganic and Coordination Compounds*; John Wiley & Sons, Ltd, 2008; pp 1–273. https://doi.org/10.1002/9780470405888.ch1.

(382) Devereux, M.; Jackman, M.; McCann, M.; Casey, M. Preparation and Catalase-Type Activity of Manganese(II) Amino Acid Complexes. *Polyhedron* **1998**, *17* (1), 153–158. https://doi.org/10.1016/S0277-5387(97)00211-8.

(383) Komova, O. V.; Mukha, S. A.; Ozerova, A. M.; Odegova, G. V.; Simagina, V. I.; Bulavchenko, O. A.; Ishchenko, A. V.; Netskina, O. V. The Formation of Perovskite during the Combustion of an Energy-Rich Glycine–Nitrate Precursor. *Materials* **2020**, *13* (22), 5091. https://doi.org/10.3390/ma13225091.

(384) Hegedüs, A. J.; Horkay, K.; Székely, M.; Stefániay, W. Thermogravimetrische Untersuchung der Mangan(II)-oxid-Pyrolyse. *Mikrochim Acta* **1966**, *54* (4), 853–864. https://doi.org/10.1007/BF01223008.

(385) Greenberg, J.; Hallgren, L. J. Infrared Absorption Spectra of Alkali Metal Nitrates and Nitrites above and below the Melting Point. *The Journal of Chemical Physics* **1960**, *33* (3), 900–902. https://doi.org/10.1063/1.1731284.

(386) Gallagher, P. K.; Schrey, F.; Prescott, B. The Thermal Decomposition of Aqueous Manganese (II) Nitrate Solution. *Thermochimica Acta* **1971**, *2* (5), 405–412. https://doi.org/10.1016/0040-6031(71)85016-5.

(387) Huang, M.; Lv, S.; Zhou, C. Thermal Decomposition Kinetics of Glycine in Nitrogen Atmosphere. *Thermochimica Acta* **2013**, *552*, 60–64. https://doi.org/10.1016/j.tca.2012.11.006.

(388) Casale, A.; De Robertis, A.; De Stefano, C.; Gianguzza, A.; Patanè, G.; Rigano, C.; Sammartano, S. Thermodynamic Parameters for the Formation of Glycine Complexes with Magnesium(II), Calcium(II), Lead(II), Manganese(II), Cobalt(II), Nickel(II), Zinc(II) and Cadmium(II) at Different Temperatures and Ionic Strengths, with Particular Reference to Natural Fluid Conditions. *Thermochimica Acta* **1995**, *255*, 109–141. https://doi.org/10.1016/0040-6031(94)02181-M.

(389) Yamashita, H.; Nozaki, T.; Fukuda, Y.; Kabata, T. A Polarographic Study of the Glycine Complexes of Copper(II), Lead(II), Cadmium(II), and Manganese(II). *BCSJ* **1991**, *64* (2), 697–698. https://doi.org/10.1246/bcsj.64.697.

(390) Wen, W.; Wu, J.-M. Nanomaterials via Solution Combustion Synthesis: A Step Nearer to Controllability. *RSC Adv.* **2014**, *4* (101), 58090–58100. https://doi.org/10.1039/C4RA10145F.

(391) Fritsch, S.; Navrotsky, A. Thermodynamic Properties of Manganese Oxides. *Journal of the American Ceramic Society* **1996**, *79* (7), 1761–1768. https://doi.org/10.1111/j.1151-2916.1996.tb07993.x.

(392) Matzapetakis, M.; Karligiano, N.; Bino, A.; Dakanali, M.; Raptopoulou, C. P.; Tangoulis, V.; Terzis, A.; Giapintzakis, J.; Salifoglou, A. Manganese Citrate Chemistry: Syntheses, Spectroscopic Studies, and Structural Characterizations of Novel Mononuclear, Water-Soluble Manganese Citrate Complexes. *Inorganic Chemistry* **2000**, *39* (18), 4044–4051. https://doi.org/10.1021/ic9912631.

(393) Deng, Y. F.; Zhou, Z. H. Manganese Citrate Complexes: Syntheses, Crystal Structures and Thermal Properties. *Journal of Coordination Chemistry* **2009**, *62* (5), 778–788. https://doi.org/10.1080/00958970802376257.

(394) Strouse, J.; Layten, S. W.; Strouse, C. E. Structural Studies of Transition Metal Complexes of Triionized and Tetraionized Citrate. Models for the Coordination of the Citrate Ion to Transition Metal Ions in Solution and at the Active Site of Aconitase. *J. Am. Chem. Soc.* **1977**, *99* (2), 562–572. https://doi.org/10.1021/ja00444a041.

(395) Wang, W.; Zhang, X.; Chen, F.; Ma, C.; Chen, C.; Liu, Q.; Liao, D.; Li, L. Homo- and Hetero-Metallic Manganese Citrate Complexes: Syntheses, Crystal Structures and Magnetic Properties. *Polyhedron* **2005**, *24* (13), 1656–1668. https://doi.org/10.1016/j.poly.2005.04.031.

(396) Feick, G.; Hainer, R. M. On the Thermal Decomposition of Ammonium Nitrate . Temperatures and Reaction Rate. *Journal of the American Chemical Society* **1954**, *698* (5), 5860–5863.

(397) Chaturvedi, S.; Dave, P. N. Review on Thermal Decomposition of Ammonium Nitrate. *Journal of Energetic Materials* **2013**, *31* (1), 1–26. https://doi.org/10.1080/07370652.2011.573523.

(398) Babrauskas, V.; Leggett, D. Thermal Decomposition of Ammonium Nitrate. *Fire and Materials* **2019**, No. November, 1–19. https://doi.org/10.1002/fam.2797.

(399) Grzybowski, A. K.; Tate, S. S.; Datta, S. P. Magnesium and Manganese Complexes of Citric and Isocitric Acids. *J. Chem. Soc. A* **1970**, No. 0, 241–245. https://doi.org/10.1039/J19700000241.

(400) Wheatley, A. M.; Kaduk, J. A. Crystal Structures of Ammonium Citrates. *Powder Diffr.* **2019**, *34* (1), 35–43. https://doi.org/10.1017/S0885715618000829.

(401) Barbooti, M. M.; Dhoaib, A.-S. A. Thermal Decomposition of Citric Acid. *Thermochimica Acta* **1986**, *98*, 119–126.

(402) Wyrzykowski, D.; Hebanowska, E.; Nowak-Wiczk, G.; Makowski, M.; Chmurzyński, L. Thermal Behaviour of Citric Acid and Isomeric Aconitic Acids. *Journal of Thermal Analysis and Calorimetry* **2011**, *104* (2), 731–735. https://doi.org/10.1007/s10973-010-1015-2.

(403) Valletta, R. M.; Pliskin, W. A. Preparation and Characterization of Manganese Oxide Thin Films. *THIN FILMS* **1967**, *114* (9), 944–947.

(404) Paleckiene, R.; Sviklas, A.; Slinksiene, R. Reaction of Urea with Citric Acid. *Russ J Appl Chem* **2005**, *78* (10), 1651–1655. https://doi.org/10.1007/s11167-005-0579-2.

(405) Schaber, P. M.; Colson, J.; Higgins, S.; Thielen, D.; Anspach, B.; Brauer, J. Thermal Decomposition (Pyrolysis) of Urea in an Open Reaction Vessel. *Thermochimica Acta* **2004**, *424* (1–2), 131–142. https://doi.org/10.1016/j.tca.2004.05.018.

(406) Fleischmann, S.; Mitchell, J. B.; Wang, R.; Zhan, C.; Jiang, D.; Presser, V.; Augustyn, V. Pseudocapacitance: From Fundamental Understanding to High Power Energy Storage Materials. *Chem. Rev.* **2020**, *120* (14), 6738–6782. https://doi.org/10.1021/acs.chemrev.0c00170.

(407) Ryabova, A. S.; Napolskiy, F. S.; Poux, T.; Istomin, S. Ya.; Bonnefont, A.; Antipin, D. M.; Baranchikov, A. Ye.; Levin, E. E.; Abakumov, A. M.; Kéranguéven, G.; Antipov, E. V.; Tsirlina, G. A.; Savinova, E. R. Rationalizing the Influence of the Mn(IV)/Mn(III) Red-Ox Transition on the

Electrocatalytic Activity of Manganese Oxides in the Oxygen Reduction Reaction. *Electrochimica Acta* **2016**, *187*, 161–172. https://doi.org/10.1016/j.electacta.2015.11.012.

(408) Garcês Gonçalves, P. R.; De Abreu, H. A.; Duarte, H. A. Stability, Structural, and Electronic Properties of Hausmannite (Mn3O4) Surfaces and Their Interaction with Water. *Journal of Physical Chemistry C* **2018**, *122* (36), 20841–20849. https://doi.org/10.1021/acs.jpcc.8b06201.

(409) Zhu, J.; Wu, Q.; Li, J. Review And Prospect of Mn $_3$ O $_4$ -Based Composite Materials For Supercapacitor Electrodes. *ChemistrySelect* **2020**, *5* (33), 10407–10423. https://doi.org/10.1002/slct.202002544.

(410) Alexander, C. L.; Tribollet, B.; Vivier, V.; Orazem, M. E. Contribution of Surface Distributions to Constant-Phase-Element (CPE) Behavior: 3. Adsorbed Intermediates. *Electrochimica Acta* **2017**, *251*, 99–108. https://doi.org/10.1016/j.electacta.2017.08.081.

(411) Alexander, C. L.; Tribollet, B.; Vivier, V.; Orazem, M. E. Contribution of Surface Distributions to Constant-Phase-Element (CPE) Behavior: 1. Influence of Roughness. *Electrochimica Acta* **2017**, *251*, 416–424. https://doi.org/10.1016/j.electacta.2017.08.081.

(412) Alexander, C. L.; Tribollet, B.; Vivier, V.; Orazem, M. E. Contribution of Surface Distributions to Constant-Phase-Element (CPE) Behavior: 2. Capacitance. *Electrochimica Acta* **2017**, *251*, 566–573. https://doi.org/10.1016/j.electacta.2017.08.081.

(413) Feldmann, C. Polyol-Mediated Synthesis of Nanoscale Functional Materials. *Solid State Sciences* **2005**, *7* (7), 868–873. https://doi.org/10.1016/j.solidstatesciences.2005.01.018.

(414) Dong, H.; Chen, Y.-C.; Feldmann, C. Polyol Synthesis of Nanoparticles: Status and Options Regarding Metals, Oxides, Chalcogenides, and Non-Metal Elements. *Green Chem.* **2015**, *17* (8), 4107–4132. https://doi.org/10.1039/C5GC00943J.

(415) Gerber, O.; Pichon, B. P.; Ihiawakrim, D.; Florea, I.; Moldovan, S.; Ersen, O.; Begin, D.; Grenèche, J.-M.; Lemonnier, S.; Barraud, E.; Begin-Colin, S. Synthesis Engineering of Iron Oxide Raspberry-Shaped Nanostructures. *Nanoscale* **2016**, *9* (1), 305–313. https://doi.org/10.1039/C6NR07567C.

(416) Vaz-Ramos, J.; Lucante, T.; Greneche, J.-M.; Leuvrey, C.; Papaefthymiou, V.; Zafeiratos, S.; Carton, A.; Bégin, D.; Le Calvé, S.; Bégin-Colin, S. Impact of Tannic Acid on Iron Oxide Nanoclusters Synthesized by a Polyol Solvothermal Method. *Colloids and Surfaces A: Physicochemical and Engineering Aspects* **2024**, *689*, 133658. https://doi.org/10.1016/j.colsurfa.2024.133658.

(417) Xia, Z.; Singh, A.; Kiratitanavit, W.; Mosurkal, R.; Kumar, J.; Nagarajan, R. Unraveling the Mechanism of Thermal and Thermo-Oxidative Degradation of Tannic Acid. *Thermochimica Acta* **2015**, *605*, 77–85. https://doi.org/10.1016/j.tca.2015.02.016.

(418) Abdelrahim, A. M.; El-Moghny, M. G. A.; Abdelhady, H. H.; Wali, H. S.; Gamil, M. M.; Fahmy, S. R.; Abdel-Hamid, T. M.; Mohammed, G. K.; Ahmed, Y. A.; El-Deab, M. S. Tailoring a Facile Electronic and Ionic Pathway to Boost the Storage Performance of Fe3O4 Nanowires as Negative Electrode

for Supercapacitor Application. *Sci Rep* **2024**, *14* (1), 16807. https://doi.org/10.1038/s41598-024-66480-5.

(419) Li, R.; Wang, Y.; Zhou, C.; Wang, C.; Ba, X.; Li, Y.; Huang, X.; Liu, J. Carbon-Stabilized High-Capacity Ferroferric Oxide Nanorod Array for Flexible Solid-State Alkaline Battery–Supercapacitor Hybrid Device with High Environmental Suitability. *Advanced Functional Materials* **2015**, *25* (33), 5384–5394. https://doi.org/10.1002/adfm.201502265.

(420) He, K.; Zhang, S.; Li, J.; Yu, X.; Meng, Q.; Zhu, Y.; Hu, E.; Sun, K.; Yun, H.; Yang, X.-Q.; Zhu, Y.; Gan, H.; Mo, Y.; Stach, E. A.; Murray, C. B.; Su, D. Visualizing Non-Equilibrium Lithiation of Spinel Oxide via in Situ Transmission Electron Microscopy. *Nat Commun* **2016**, *7* (1), 11441. https://doi.org/10.1038/ncomms11441.

Université de Strasbourg

Taylan KARAKOÇ

EDSC
École Doctorale des Sciences Chimiques

Elaboration de matériaux composites oxyde inorganique / carbone pour optimiser leurs performances électrochimiques dans les dispositifs de stockage d'énergie

Résumé

Le dopage à l’azote de carbone activés microporeux montrèrent des performances électrochimiques en tant qu’électrodes pour supercondensateurs impressionnantes s’élevant à plus de 320 F/g en milieu acide. Cette étude mis en lumière l’atout que constitue le dopage par groupements fonctionnels azotés (ex : pyrrole) pouvant engendrer un stockage de charge additionnel par phénomène de pseudocapacitance. L’utilisation de modèle géométrique simplifié pour la modélisation des données d’impédance montra son utilité pour analyser en profondeur les propriétés d’électrodes carbonés poreux et leurs capacitances mesurées. Différentes observations obtenues par caractérisation *in situ* par spectroscopie infrarouge à transformée de Fourier par réflectance diffuse à température contrôlée (TD-DRIFTS) décrivent l’importance de la complexation de l’ion manganèse(II) dans la préparation de départ. L’ajout de citrate d’ammonium, un fort agent complexant, permet une meilleure uniformité et stabilité tout le long de l’évaporation de solvant, empêchant la formation d’hydroxyde et/ou d’autres sels/complexes métalliques. Des phases pures peuvent être produits, notamment la spinelle Mn_3O_4 mésoporeux qui montrèrent des capacitances à plus de 100 F/g et 370 µF/cm^2 dans un milieu basique aqueux. L’ingénierie de structure de spinelle de fer Fe_3O_4 fut permise par la méthode de synthèse polyol en nanostructure de type « framboise » creuse ainsi que de composites à base de graphène à quelques couches (FLG). Pour les supercondensateurs, un composite en teneur modérée en Fe_3O_4 mais non moins faible présenta des capacitances semblables à l’oxyde Mn_3O_4 avec plus de 350 µF/cm^2 atteignables. En tant que matériaux d’électrodes de type réaction de conversion, de très haute capacité à hauteur de 923 mAh/g furent atteintes avec une rétention de cycles améliorée par l’apport de FLG, servant de support électroniquement conducteur et empêchant l’isolation des particules métalliques de fer, améliorant la réversibilité de la réaction de conversion.

Supercondensateur – batteries Li-ion – carbone activé N-dopé – oxydes de manganèse et de fer

Résumé en anglais

Nitrogen doping of microporous activated carbon showed impressive electrochemical performances as electrodes for supercapacitors, reaching over 320 F/g in acidic media. This study highlighted the advantage of doping with nitrogen-containing functional groups (e.g. pyrrole), which can generate additional charge storage through pseudocapacitance. The use of a simplified geometric model to fit impedance data demonstrated its usefulness for in-depth analysis of the properties of porous carbon electrodes and their measured capacitances. Various observations obtained by *in situ* characterization using temperature-controlled diffuse reflectance Fourier transform infrared spectroscopy (TD-DRIFTS) describe the importance of manganese(II) ion complexation in the starting preparation. The addition of ammonium citrate, a strong complexing agent, provides greater uniformity and stability throughout solvent evaporation, preventing the formation of hydroxide and/or other metal salts/complexes. Pure phases can be produced, notably mesoporous Mn_3O_4 spinel, which showed capacitances in excess of 100 F/g and 370 µF/cm^2 in an aqueous basic medium. The engineering of Fe_3O_4 iron spinel structures was enabled by the polyol synthesis method in hollow "raspberry"-shaped nanostructures, as well as few-layer graphene composites (FLG). For supercapacitors, a composite with a moderate but low Fe_3O_4 content showed capacitances similar to Mn_3O_4 oxide, with over 350 µF/cm^2 achievable. As conversion reaction electrode materials, very high capacities of up to 923 mAh/g were achieved, with cycle retention enhanced by the addition of FLG, serving as an electronically conductive support and preventing the isolation of iron metal particles, improving the reversibility of the conversion reaction.

Supercapacitor - Li-ion batteries – N-doped activated carbon - manganese and iron oxides